



THE HONG KONG  
POLYTECHNIC UNIVERSITY

香港理工大學

Pao Yue-kong Library

包玉剛圖書館

---

## Copyright Undertaking

This thesis is protected by copyright, with all rights reserved.

**By reading and using the thesis, the reader understands and agrees to the following terms:**

1. The reader will abide by the rules and legal ordinances governing copyright regarding the use of the thesis.
2. The reader will use the thesis for the purpose of research or private study only and not for distribution or further reproduction or any other purpose.
3. The reader agrees to indemnify and hold the University harmless from and against any loss, damage, cost, liability or expenses arising from copyright infringement or unauthorized usage.

### IMPORTANT

If you have reasons to believe that any materials in this thesis are deemed not suitable to be distributed in this form, or a copyright owner having difficulty with the material being included in our database, please contact [lbsys@polyu.edu.hk](mailto:lbsys@polyu.edu.hk) providing details. The Library will look into your claim and consider taking remedial action upon receipt of the written requests.

**FIRE RESISTANCE OF FRP-STRENGTHENED RC  
BEAMS: NUMERICAL SIMULATION AND  
PERFORMANCE-BASED DESIGN**

**GAO WANYANG**

**Ph.D**

**The Hong Kong Polytechnic University**

**2013**



THE HONG KONG POLYTECHNIC UNIVERSITY  
DEPARTMENT OF CIVIL AND ENVIRONMENTAL ENGINEERING

**FIRE RESISTANCE OF FRP-STRENGTHENED RC  
BEAMS: NUMERICAL SIMULATION AND  
PERFORMANCE-BASED DESIGN**

**GAO Wanyang**

**A Thesis Submitted in Partial Fulfillment of the Requirements for  
the Degree of Doctor of Philosophy**

May 2013

# CERTIFICATE OF ORIGINALITY

I hereby declare that this dissertation entitled “*Fire Resistance of FRP-strengthened RC Beams: Numerical Simulation and Performance-based Design*” is my own work and that, to the best of my knowledge and belief, it reproduces no material previously published or written, nor material that has been accepted for the award of any other degree or diploma, except where due acknowledgement has been made in the text.

\_\_\_\_\_ (Signed)

Gao Wan-Yang (Name of student)

*To my family  
for their love and support*

## **ABSTRACT**

The wide use of externally bonded fiber reinforced polymer (FRP) laminates (including wet layup FRP sheets and pultruded FRP plates) in the strengthening of existing reinforced concrete (RC) structures has been a significant development in structural engineering over the past three decades. However, the technology also suffers from one serious limitation when employed for indoor applications in buildings: FRP composites have a poor resistance to fire as organic polymers (normally epoxies) used both as the matrix material and the bonding adhesive soften quickly around the glass transition temperature. Furthermore, when exposed to a high heat flux, the polymer matrix may ignite, resulting in flame spread and smoke generation. To facilitate a safe and economic use of the FRP strengthening technique in building applications, an in-depth understanding of the fire performance of FRP-strengthened RC members is deemed necessary. Against this background, this dissertation aims to develop a comprehensive approach to simulate the fire performance of un-protected and insulated FRP-strengthened RC beams.

The dissertation is composed of three main parts: (a) theoretical analyses on the bond-slip behavior of the FRP-to-concrete interface at elevated temperatures; (b) advanced finite element (FE) modeling of the structural behavior of un-protected and insulated FRP-strengthened RC beams exposed to fire; and (c) design-oriented solutions for predicting the fire resistance of un-protected and insulated FRP-strengthened RC beams.

In the first part of the dissertation, a set of closed-form theoretical solutions was developed for tracing the Mode II debonding process of FRP-to-concrete bonded joints subjected to combined thermal and mechanical loadings. In order to represent the behavior of a wide range of bonded joints, five different bond-slip models were considered in deriving the closed-form solutions, including the elastic-brittle, bi-linear, elastic-plastic-brittle, rigid-softening, and exponential models. For each

bond-slip model, explicit expressions for the debonding load, effective bond length, interfacial shear stress, interfacial slip as well as the load-displacement response were derived. It was found that the debonding of FRP-to-concrete interfaces may be delayed or accelerated by temperature variations (i.e., thermal loading) during service. The theoretical solutions indicate that, provided the bond length is sufficiently long, the debonding load of the FRP-to-concrete interface depends only on the interfacial fracture energy and the temperature variation. A temperature increase leads to an increase in both the debonding load and the effective bond length, and the rate of increase of the latter depends on the interfacial bond-slip model.

Based on the theoretical solutions, a nonlinear local bond-slip model was also developed for FRP externally bonded to concrete at elevated temperatures. Two key parameters of the proposed bond-slip model, the interfacial fracture energy  $G_f$  and the interfacial brittleness index  $B$ , were determined using existing shear test data of FRP-to-concrete bonded joints at elevated temperatures. The proposed bond-slip model provides the first-ever constitutive law for describing the local performance of the FRP-to-concrete interface at elevated temperatures.

In the second part of this dissertation, advanced FE models were developed to trace the thermal and structural responses of RC beams (i.e., equivalent to un-protected FRP-strengthened RC beams) and insulated FRP-strengthened RC beams exposed to fire. In the models, the temperature-dependent thermal and mechanical properties of concrete, steel, FRP and interfaces are all appropriately considered. The thermal and structural responses predicted by the FE models were compared with existing fire test data to examine their validity. For RC beams, the comparison showed that the inclusion of the steel-to-concrete interfacial behavior leads to more accurate predictions of the deflection. Besides, the proposed FE model allows the complex distribution and evolution of stresses in the reinforcing steel and concrete to be examined in detail, leading to a better understanding of the local responses of RC

beams exposed to fire. For insulated FRP-strengthened RC beams, FE predictions showed that the assumption of perfect bonding between FRP and concrete as adopted by previous numerical models leads to an underestimation of deflections and thus an unsafe prediction of fire resistance. Unless a very thick insulation layer is provided (usually an impractical solution), it was revealed that the main role of the insulation layer is to minimize the degradation of the original RC beam rather than to protect the FRP strengthening system. Therefore, the fire resistance evaluation of an insulated FRP-strengthened RC beam can be conservatively but closely approximated by that of an insulated un-strengthened RC beam.

In the third part of this dissertation, simple design-oriented solutions for predicting the fire resistance periods of un-protected and insulated FRP-strengthened RC beams are presented. For the un-protected FRP-strengthened RC beams (i.e., equivalent to bare RC beams), the validated FE model for RC beams was used for extensive parametric studies to investigate the effects of various influencing parameters on the fire resistance periods and to generate sufficient data for regressing explicit design formulae. For insulated FRP-strengthened RC beams under fire, a two-phase design-orientated approach was proposed to predict their fire resistance. The first phase is the development of explicit solutions for the temperature field analyses of insulated FRP-strengthened RC beams exposed to the standard fire. The second phase is the structural response analysis, for which the degradation of the load-carrying capacity of the beams are assessed using the “500 °C isotherm method” in combination with the temperature predictions of insulated beam sections. The fire resistance periods of insulated FRP-strengthened RC beams are defined to be reached when the fire load action exceeds the loading carrying-capacity of the beams during fire. In order to validate the simple design-oriented method, parametric studies using the advanced FE model were carried out to generate the fire-resistance data for comparisons. The comparisons showed that the simple design-oriented method provides a reliable prediction of the fire resistance periods for insulated FRP-strengthened RC beams.

# LIST OF PUBLICATIONS

## Refereed Journal Papers:

**Gao W.Y.**, Teng J.G., and Dai Jian-Guo, (2012), “Effect of temperature variation on the full-range behavior of FRP-to-concrete bonded joints”, *Journal of Composites for Construction, ASCE*, 16(6): 671-683.

Dai Jian-Guo, **Gao W.Y.**, and Teng J.G., (2013), “Bond-slip model for FRP laminates externally bonded to concrete at elevated temperature”, *Journal of Composites for Construction, ASCE*, 17(2): 217-228.

**Gao W.Y.**, Dai Jian-Guo and Teng J.G., (2013), “Finite element modeling of reinforced concrete beams exposed to fire”, *Engineering Structures*, 52: 488-501.

## Refereed Conference Papers:

Dai Jian-Guo, **Gao W.Y.**, and Teng, J.G., (2010), “Finite element modeling of insulated FRP-strengthened RC beams exposed to fire”, *Proceedings of the 5th International Conference on FRP Composites in Civil Engineering (CICE 2010)*, 27-29 September, Beijing, China, pp. 428-432. (**Best paper award**)

**Gao W.Y.**, Dai Jian-Guo, and Teng J.G., (2010), “Fire resistance of reinforced concrete beams: a three-dimensional finite element model”, *Proceedings of the 11th International Symposium on Structural Engineering (ISSE-11)*, 18-20 December, Guangzhou, China, pp. 2284-2289.

**Gao W.Y.**, Teng J.G., and Dai Jian-Guo, (2011), “Effect of temperature change on

the behavior of FRP-to-concrete bonded joints”, *Proceedings of the 4th International Conference on Durability & Sustainability of Fibre Reinforced Polymer (FRP) Composites for Construction & Rehabilitation (CDCC 2011)*, 20-22 July, Quebec, Canada, pp.37-46.

Dai Jian-Guo, **Gao W.Y.**, and Teng J.G., (2012), “Bond-slip model for interfaces between externally bonded FRP reinforcement and concrete at elevated temperatures”, *Proceedings of the 6th International Conference on FRP Composites in Civil Engineering (CICE 2012)*, 13-15 June, Roma, Italy, CD-ROM, Paper No. 03-783, 8 pages.

**Gao W. Y.**, Dai Jian-Guo, and Teng J.G., (2012), “A simplified approach for determining the temperature fields of concrete beams exposed to fire”, *Proceedings of the First International Conference on Performance-based and Life-cycle Structural Engineering (PLSE 2012)*, 5-7 December, Hong Kong, China, pp. 1457-1464.

## **ACKNOWLEDGEMENTS**

First and foremost, I would like to express my sincere gratitude to my chief supervisor, Dr. Jian-Guo Dai, for his enlightening guidance, valuable discussions, and continuous encouragements throughout the course of my research. During the past four years, I was very impressed by his deep insight into scientific problems, meticulous attitude to research, and responsibility to students and all of these qualities have greatly benefited me, not only in my PhD study but also in my future research work.

I would also like to express my profound appreciation to my co-supervisor, Prof. Jin-Guang Teng, for his enlightening guidance and enthusiastic supports throughout my PhD study. Prof Teng's rigorous attitude to academic research, broad depth and breadth of knowledge in structural engineering, creative and unique insight into many academic problems have demonstrated the essential merits that a good researcher should possess, and all of his merits not only bring me some new ideas for my research work, but also encourage me to pursue research innovation.

I am grateful to The Hong Kong Polytechnic University for providing me a PhD studentship as well as other necessary financial supports. I am also grateful to The Hong Kong Polytechnic University for providing me excellent research facilities.

I want to express my sincere thanks to my master supervisors Profs. Ke-Xu Hu and Zhou-Dao Lu at Tongji University. They both recommended and encouraged me to pursue my PhD degree and gave me many useful advises.

Special thanks are extended to my friends and colleagues at the Department of Civil and Environmental Engineering of the Hong Kong Polytechnic University, especially, Drs. Tao Yu, Guan-Ming Chen, Shi-Shun Zhang, Yue-Ming Hu, Fernando

Dilum, Hua-Nan He, Bing Wang, Xiao-Hui Wang, and Xiao-Yan Sun, Messrs. Qiong-Guan Xiao, Bing-Zhang, Jun-Liang Zhao, Guan-Lin, Yu-Lei Bai, Dian-Yu Sun, Jia-Zhan Su, Bao-Jian Zhang, Yi Yang, and Yang Chen, and Mss. Yue-Xin Zhang, Ming-Hui Shen, Shu-Qin Ye and Xiao-Hua Zhang, not only for their discussions and constructive comments, but also for their encouragement at the difficult times of my studies.

Last but, not the least, special thanks are given to my parents, my wife, my sister and my brother-in-law for their patience, love, support, and encouragement. They actually shared with me every moment of this work; to them all, this thesis shall be dedicated.

# CONTENTS

|  |       |
|--|-------|
| CERTIFICATE OF ORIGINALITY .....   | i     |
| ABSTRACT .....   | iii   |
| LIST OF PUBLICATIONS .....   | vi    |
| ACKNOWLEDGEMENTS .....   | viii  |
| LIST OF FIGURES.....   | xviii |
| LIST OF TABLES.....  | xxiv  |
| NOTATION.....  | xxv   |
| <br>   |       |
| CHAPTER 1 INTRODUCTION .....   | 1     |
| 1.1 GENERAL .....  | 1     |
| 1.2 FIRE SAFETY OF FRP-STRENGTHENED RC STRUCTURES .....                    | 1     |
| 1.3 STRENGTHENING OF RC BEAMS WITH FRP LAMINATES .....                     | 3     |
| 1.4 SCOPE, OBJECTIVES AND CONTENTS OF THIS DISSERTATION .....              | 4     |
| 1.5 REFERENCES.....  | 8     |
| <br>   |       |
| CHAPTER 2 LITERATURE REVIEW.....   | 13    |
| 2.1 GENERAL .....  | 13    |
| 2.2 PROPERTIES OF FRP COMPOSITES AT ELEVATED TEMPERATURES ...              | 13    |
| 2.2.1 Thermal Properties .....   | 14    |
| 2.2.2 Mechanical Properties.....   | 14    |
| 2.2.2.1 <i>Fibers</i> .....  | 15    |
| 2.2.2.2 <i>Matrix</i> .....  | 16    |
| 2.2.2.3 <i>FRPs</i> .....  | 16    |
| 2.3 BOND PROPERTIES AT ELEVATED TEMPERATURES.....                          | 17    |
| 2.4 PREVIOUS FIRE RESISTANCE TESTS OF FRP-STRENGTHENED RC<br>MEMBERS ..... | 19    |
| 2.4.1 FRP-Strengthened RC Slabs .....                                      | 20    |
| 2.4.2 FRP-Strengthened RC Beams .....                                      | 21    |

|  |    |
|--|----|
| 2.4.3 FRP-Strengthened RC Columns .....  | 24 |
| 2.5 EXISTING NUMERICAL MODELS FOR PREDICTING THE FIRE PERFORMANCE OF FRP-STRENGTHENED RC MEMBERS .....     | 25 |
| 2.6 EXISTING DESIGN PROVISIONS FOR THE FIRE SAFETY OF FRP-STRENGTHENED RC MEMBERS .....                    | 26 |
| 2.6.1 Fire Safety Design Provisions Recommended by ACI 440.2R-08 (2008)                                    | 26 |
| 2.6.2 Fire Safety Design Provisions Proposed by Kodur et al. (2007) .....                                  | 27 |
| 2.7 CONSLUSIONS AND RESEARCH NEEDS .....   | 28 |
| 2.8 REFERENCES .....   | 29 |
| <br>   |    |
| CHAPTER 3 EFFECT OF TEMPERATURE VARIATION ON THE FULL-RANGE BEHAVIOR OF FRP-TO-CONCRETE BONDED JOINTS..... | 37 |
| 3.1 INTRODUCTION .....   | 37 |
| 3.2 ANALYTICAL SOLUTION.....   | 38 |
| 3.2.1 Assumptions and Notation .....   | 39 |
| 3.2.2 Governing Equations.....   | 39 |
| 3.2.3 Bond-slip Model .....  | 41 |
| 3.2.4 Stages of the Debonding Process .....  | 41 |
| 3.2.5 Elastic Stage (Stage I) .....  | 42 |
| 3.2.6 Elastic-Softening Stage (Stage II).....  | 44 |
| 3.2.7 Elastic-Softening-Debonding Stage (Stage III) .....  | 46 |
| 3.2.8 Softening-Debonding Stage (Stage IV) .....   | 47 |
| 3.2.9 Load-Displacement Responses .....  | 50 |
| 3.3 VALIDATION OF THE ANALYTICAL SOLUTION .....  | 50 |
| 3.3.1 Klamer’s Tests.....  | 50 |
| 3.3.2 Comparisons with Test Results of Klamer (2006) .....   | 51 |
| 3.3.3 Comparisons with FE Predictions.....   | 52 |
| 3.4 RESPONSE OF THE FRP-TO-CONCRETE INTERFACE.....   | 54 |
| 3.4.1 Bonded Joint Exposed to a Temperature Increase .....   | 54 |
| 3.4.2 Bonded Joint Exposed to a Temperature Decrease .....   | 55 |

|  |    |
|--|----|
| 3.5 DETERMINATION OF INTERFACIAL FRACTURE ENERGY FROM SHEAR TESTS .....  | 56 |
| 3.6 CONCLUSIONS.....   | 57 |
| 3.7 REFERENCES.....  | 58 |
|  |    |
| CHAPTER 4 EFFECT OF BOND-SLIP MODEL ON THE MODE II DEBONDING BEHAVIOR OF BONDED JOINTS SUBJECTED TO COMBINED THERMAL AND MECHANICAL LOADINGS ..... | 72 |
| 4.1 INTRODUCTION .....   | 72 |
| 4.2 GOVERNING EQUATIONS .....  | 75 |
| 4.2.1 Assumptions and Notation .....   | 75 |
| 4.2.2 Governing Equations.....   | 75 |
| 4.3 BOND-SLIP MODEL.....   | 76 |
| 4.3.1 Mode I: Elastic-Brittle Model .....  | 77 |
| 4.3.2 Mode II: Bi-Linear Model.....  | 77 |
| 4.3.3 Mode III: Elastic-Plastic-Brittle Model .....  | 77 |
| 4.3.4 Mode IV: Rigid-Softening Model .....   | 78 |
| 4.3.5 Mode V: Exponential Model.....   | 78 |
| 4.4 PREDICTIONS OF THE FULL-RANGE DEBONDING BEHAVIOR.....  | 79 |
| 4.4.1 Elastic-Brittle Model.....   | 79 |
| 4.4.1.1 <i>Elastic stage</i> .....   | 79 |
| 4.4.1.2 <i>Elastic-debonding stage</i> .....   | 81 |
| 4.4.2 Bi-Linear Model.....   | 82 |
| 4.4.2.1 <i>Elastic stage</i> .....   | 82 |
| 4.4.2.2 <i>Elastic-softening stage</i> .....   | 82 |
| 4.4.2.3 <i>Elastic-softening-debonding stage</i> .....   | 83 |
| 4.4.3 Elastic-Plastic-Brittle Model.....   | 84 |
| 4.4.3.1 <i>Elastic stage</i> .....   | 85 |
| 4.4.3.2 <i>Elastic-plastic stage</i> .....   | 85 |
| 4.4.3.3 <i>Elastic-plastic-debonding stage</i> .....   | 87 |

|  |     |
|--|-----|
| 4.4.4 Rigid-Softening Model .....                                  | 88  |
| 4.4.4.1 Softening stage .....                                      | 88  |
| 4.4.4.2 Softening-debonding stage .....                            | 92  |
| 4.4.5 Exponential Model .....                                      | 92  |
| 4.5 NUMERICAL RESULTS AND DISCUSSIONS .....                        | 96  |
| 4.5.1 Interface Stress States and Load-Displacement Response ..... | 96  |
| 4.5.2 Effective Bond Length .....                                  | 98  |
| 4.5.3 Debonding Load .....   | 98  |
| 4.6 CONCLUSIONS .....  | 100 |
| 4.7 REFERENCES .....   | 101 |

CHAPTER 5 BOND-SLIP MODEL FOR FRP LAMINATES EXTERNALLY BONDED TO CONCRETE AT ELEVATED TEMPERATURES .....

|  |     |
|--|-----|
| 115  |     |
| 5.1 INTRODUCTION .....                                 | 115 |
| 5.2 FORMULATION OF THE BOND-SLIP MODEL .....           | 116 |
| 5.2.1 General .....                                    | 116 |
| 5.2.2 Theoretical Background .....                     | 117 |
| 5.2.2.1 Bond-slip model .....                          | 117 |
| 5.2.2.2 Interfacial slip distribution .....            | 119 |
| 5.2.2.3 Ultimate pull load .....                       | 120 |
| 5.2.2.4 Strain distributions in the FRP laminate ..... | 121 |
| 5.2.3 Determination of $G_f$ and $B$ .....             | 121 |
| 5.2.4 Expressions of $G_f$ and $B$ .....               | 125 |
| 5.3 VALIDATION OF THE BOND-SLIP MODEL .....            | 128 |
| 5.3.1 Ultimate Loads of Double-lap Shear Tests .....   | 128 |
| 5.3.2 Strain Distributions in the FRP Laminate .....   | 128 |
| 5.4 CONCLUSIONS .....                                  | 129 |
| 5.5 REFERENCES .....                                   | 130 |

CHAPTER 6 FE MODELING OF UN-PROTECTED FRP-STRENGTHENED RC

|   |     |
|---|-----|
| BEAMS EXPOSED TO FIRE .....   | 147 |
| 6.1 INTRODUCTION .....  | 147 |
| 6.2 MODELING OF CONCRETE .....  | 151 |
| 6.2.1 General .....   | 151 |
| 6.2.2. Thermal Properties of Concrete .....   | 151 |
| 6.2.3 Constitutive Model for Concrete.....  | 152 |
| 6.2.3.1 <i>Yield surface</i> .....  | 152 |
| 6.2.3.2 <i>Compressive behavior of concrete</i> .....                                 | 154 |
| 6.2.3.3 <i>Tensile behavior of concrete</i> .....                                     | 154 |
| 6.2.3.4 <i>Poisson's ratio</i> .....  | 156 |
| 6.2.3.5 <i>Decomposition of strain</i> .....  | 156 |
| 6.3 MODELING OF STEEL .....   | 157 |
| 6.3.1 Thermal Properties of Steel.....  | 157 |
| 6.3.2 Constitutive Model for Steel .....  | 157 |
| 6.4 MODELING OF STEEL-TO-CONCRETE INTERFACES .....                                    | 158 |
| 6.5 FINITE ELEMENT ANALYSIS .....   | 161 |
| 6.5.1 Fire Scenario Analysis.....   | 162 |
| 6.5.2 Heat Transfer Analysis .....  | 163 |
| 6.5.3 Mechanical Response Analysis.....   | 164 |
| 6.6 VALIDATION OF THE FE MODEL .....  | 165 |
| 6.6.1 Tests by Wu et al. (1993).....  | 165 |
| 6.6.2 Tests by Lin et al. (1981).....   | 167 |
| 6.6.3 Test by Detreppe and Franssen (1985).....                                       | 168 |
| 6.6.4 Local Behavior of RC beams Exposed to Fire.....                                 | 168 |
| 6.7 CONCLUSIONS.....  | 172 |
| 6.8 REFERENCES.....   | 173 |
| <br>  |     |
| CHAPTER 7 FE MODELING OF INSULATED FRP-STRENGTHENED RC<br>BEAMS EXPOSED TO FIRE ..... | 196 |
| 7.1 INTRODUCTION .....  | 196 |

|  |     |
|--|-----|
| 7.2 CONSTITUTIVE MODELS .....  | 197 |
| 7.2.1 General .....  | 197 |
| 7.2.2 Concrete and Reinforcing Steel at Elevated Temperatures .....  | 198 |
| 7.2.3 FRP Laminates at Elevated Temperatures .....   | 199 |
| 7.2.4 Interfaces at Elevated Temperatures .....  | 201 |
| 7.3 FINITE ELEMENT ANALYSIS .....  | 203 |
| 7.3.1 Procedure of Analysis .....  | 203 |
| 7.3.2 Heat Transfer Analysis .....   | 204 |
| 7.3.3 Mechanical Response Analysis .....   | 204 |
| 7.4 VALIDATION OF THE FE MODEL .....   | 205 |
| 7.4.1 Blontrock et al.'s Tests .....   | 205 |
| 7.4.2 Gao et al.'s Tests .....   | 208 |
| 7.4.3 William et al.'s Tests .....   | 210 |
| 7.5 FIRE RESISTANCE DESIGN OF INSULATED FRP-STRENGTHENED RC<br>BEAMS .....   | 211 |
| 7.6 CONCLUSIONS .....  | 213 |
| 7.7 REFERENCES .....   | 214 |
| <br>   |     |
| CHAPTER 8 SIMPLE METHOD FOR PREDICTING TEMPERATURES IN<br>BARE AND INSULATED RC BEAMS EXPOSED TO A STANDARD FIRE.... | 227 |
| 8.1 INTRODUCTION .....   | 227 |
| 8.2 EXISTING METHODS FOR TEMPERATURE PREDICTIONS .....   | 230 |
| 8.2.1 Wickstrom's Method .....   | 231 |
| 8.2.2 Desai's Method .....   | 232 |
| 8.2.3 Abbasi and Hogg's Method .....   | 233 |
| 8.3 PROPOSED METHOD FOR TEMPERATURES IN BARE RC BEAMS .....  | 234 |
| 8.3.1 General .....  | 234 |
| 8.3.2 FE Analyses .....  | 235 |
| 8.3.3 Factors Governing Temperature Fields .....   | 235 |
| 8.3.4 Mid-Width Temperatures in Wide Beams .....   | 236 |

|   |     |
|---|-----|
| 8.3.5 Effect of Beam Width.....   | 239 |
| 8.3.6 Temperatures of Corner Concrete .....   | 240 |
| 8.4 VERIFICATION OF THE PROPOSED METHOD FOR BARE RC BEAMS                             | 242 |
| 8.5 PROPOSED METHOD FOR TEMPERATURES IN INSULATED RC BEAMS                            |     |
| .....   | 244 |
| 8.5.1 General .....   | 244 |
| 8.5.2 Transformation of a Fire Insulation Layer to an Equivalent Concrete Layer       |     |
| .....   | 245 |
| 8.6 VERIFICATION OF THE PROPOSED METHOD FOR INSULATED RC                              |     |
| BEAMS.....  | 250 |
| 8.7 CONCLUSIONS.....  | 253 |
| 8.8 REFERENCES.....   | 253 |
| <br>  |     |
| CHAPTER 9 PERFORMANCE-BASED APPROACH FOR PREDICTING THE                               |     |
| FIRE RESISTANCE OF FRP-STRENGTHENED RC BEAMS .....                                    | 275 |
| 9.1 INTRODUCTION .....  | 275 |
| 9.2 AN EXPLICIT SOLUTION FOR PREDICTING THE FIRE RESISTANCE OF                        |     |
| UN-PROTECTED FRP-STRENGTHENED RC BEAMS .....  | 279 |
| 9.2.1 FE Parametric Study .....   | 279 |
| 9.2.1.1 Determination of the influencing parameters .....                             | 279 |
| 9.2.1.2 FE analytical results on the load-carrying capacity of RC beams at            |     |
| room temperature .....  | 282 |
| 9.2.1.3 Definition of the fire resistance period.....                                 | 282 |
| 9.2.2 FE Parametric Results vs. Predictions by Existing Design Methods.....           | 283 |
| 9.2.3 Simple Design Formulae.....   | 284 |
| 9.2.3.1 Configuration of the formulae.....  | 284 |
| 9.2.3.2 Function $\varphi(\gamma)$ for fire load ratio.....                           | 285 |
| 9.2.3.3 Function $\omega(c, \rho_s)$ for the combined effects of concrete cover depth |     |
| and tension steel reinforcement ratio .....   | 286 |

|            |  |     |
|------------|--|-----|
| 9.2.3.4    | Function $\psi\left(\frac{l}{d}, \rho_s\right)$ for beam span-to-depth ratio .....                             | 287 |
| 9.2.3.5    | Coefficient $\mu_{ag}$ for aggregate type of concrete .....  | 288 |
| 9.2.3.6    | Function $\xi\left(\frac{A_{sc}}{A_{st}}\right)$ for placement of tension steel rebars .....                   | 288 |
| 9.2.3.7    | Function $\phi(b)$ for beam width.....   | 289 |
| 9.2.4      | Validation of The Proposed Design Formulae .....   | 290 |
| 9.3        | SIMPLE METHOD FOR PREDICTING THE FIRE RESISTANCE OF INSULATED FRP-STRENGTHENED RC BEAMS.....                   | 292 |
| 9.3.1      | The 500 °C Isotherm Method.....  | 292 |
| 9.3.2      | Validation of The Proposed Simple Design-Oriented Method.....  | 294 |
| 9.4        | DESIGN APPLICABILITY FOR FRP-STRENGTHENED RC BEAMS.....  | 295 |
| 9.5        | CONCLUSIONS.....   | 297 |
| 9.6        | REFERENCES.....  | 297 |
|            | APPENDIX A .....   | 322 |
|            | <br>   |     |
| CHAPTER 10 | CONCLUSIONS AND RECOMMENDATIONS.....   | 324 |
| 10.1       | CONCLUSIONS.....   | 324 |
| 10.1.1     | Conclusions on Bond-Slip Behavior of FRP-to-Concrete Interfaces at Elevated Temperatures .....                 | 324 |
| 10.1.2     | Conclusions on Advanced FE Modeling of FRP-Strengthened RC Beams .....   | 326 |
| 10.1.3     | Conclusions on Performance-Based Approach for Predicting the Fire Resistance of FRP-Strengthened RC Beams..... | 327 |
| 10.2       | RECOMMENDATIONS FOR FUTURE RESEARCH .....  | 328 |
| 10.3       | REFERENCES.....  | 330 |

# LIST OF FIGURES

| Figure     | Caption   | Page |
|------------|---|------|
| Figure 1.1 | Typical flexural strengthening of an RC beam with an FRP laminate bonded to its soffit                          | 11   |
| Figure 1.2 | Failure modes of FRP strengthened RC beams (Teng et al. 2003)   | 11   |
| Figure 1.3 | Structure of the dissertation   | 12   |
| Figure 2.1 | Thermal properties of FRP composites (Griffis et al. 1981)  | 33   |
| Figure 2.2 | Property deteriorations of fibers and FRP composites at elevated temperatures                                   | 33   |
| Figure 2.3 | Temperature-dependent tensile strength degradations of fibers: test database vs. predictions (Bisby 2003)       | 34   |
| Figure 2.4 | Tensile strength degradations of CFRP composites at elevated temperatures (Bisby 2003)                          | 34   |
| Figure 2.5 | Elastic modulus degradations of CFRP composites at elevated temperatures (Bisby 2003)                           | 35   |
| Figure 2.6 | Cracking of calcium silicate cladding boards (Gao et al. 2010)  | 35   |
| Figure 2.7 | Appearance of CFRP sheets-strengthened RC beams after the removal of the insulation materials (Gao et al. 2010) | 36   |
| Figure 2.8 | Insulated FRP-strengthened concrete column before and after fire testing (Bisby et al. 2005b)                   | 36   |
| Figure 3.1 | Schematic diagram of a single-lap shear test  | 61   |
| Figure 3.2 | Bi-linear bond-slip model   | 61   |
| Figure 3.3 | Behavior of bonded joint at reference temperature   | 62   |
| Figure 3.4 | Test specimens of Klammer (2006)  | 64   |
| Figure 3.5 | Comparison with test results of Klammer (2006)  | 65   |
| Figure 3.6 | Finite element model  | 66   |
| Figure 3.7 | Bond-slip responses during slip reversals   | 66   |

|             |   |     |
|-------------|---|-----|
| Figure 3.8  | Effect of temperature variation on load-displacement response   | 67  |
| Figure 3.9  | Effect of temperature variation on ultimate load at different plate stiffness levels                            | 68  |
| Figure 3.10 | Bonded joint subjected to a temperature increase ( $\Delta T = 30^{\circ}\text{C}$ )                            | 68  |
| Figure 3.11 | Bonded joint subjected to a temperature decrease ( $\Delta T = -30^{\circ}\text{C}$ )                           | 70  |
| Figure 4.1  | Five local bond-slip models   | 105 |
| Figure 4.2  | Interfacial shear stress distributions for the elastic-brittle bond-slip model                                  | 107 |
| Figure 4.3  | Interfacial shear stress distributions for the bi-linear bond-slip model  | 108 |
| Figure 4.4  | Interfacial shear stress distributions for the elastic-plastic-brittle bond-slip model                          | 109 |
| Figure 4.5  | Interfacial shear stress distributions for the rigid-softening bond-slip model                                  | 110 |
| Figure 4.6  | Interfacial shear stress distributions for the exponential bond-slip model                                      | 111 |
| Figure 4.7  | Debonding loads and effective bond lengths predicted using the exponential bond-slip model                      | 112 |
| Figure 4.8  | Typical load-displacement curves for different bond-slip models   | 113 |
| Figure 4.9  | Effect of temperature variation on the effective bond length  | 113 |
| Figure 4.10 | Effect of bond length on the debonding load   | 114 |
| Figure 5.1  | Elastic modulus degradations of FRP sheets/bars at elevated temperatures  | 133 |
| Figure 5.2  | Effect of temperature on interfacial fracture energy  | 134 |
| Figure 5.3  | Effect of temperature on interfacial brittleness index  | 134 |
| Figure 5.4  | Predicted bond-slip curves at elevated temperatures   | 135 |
| Figure 5.5  | Comparisons between predicted and test ultimate loads of FRP-to-concrete bonded joints at elevated temperatures | 136 |
| Figure 5.6  | Comparisons between predicted and test strain distributions in FRP  | 137 |

|             |   |     |
|-------------|---|-----|
| Figure 6.1  | Thermal properties of concrete at elevated temperatures                                       | 181 |
| Figure 6.2  | Tensile behavior of concrete at elevated temperatures   | 182 |
| Figure 6.3  | Normalized bond strength and proposed upper and low bounds                                    | 183 |
| Figure 6.4  | Proposed local bond stress-slip curves at elevated temperatures                               | 184 |
| Figure 6.5  | Details of specimens (200 mm × 400 mm × 5400 mm)  | 185 |
| Figure 6.6  | Comparisons of the RC beams tested by Wu et al. (1993)  | 186 |
| Figure 6.7  | Comparisons of the RC beam tested by Lin et al. (1981)  | 188 |
| Figure 6.8  | Comparisons of the simply supported RC beam tested by Dotreppe and Franssen (1985)            | 189 |
| Figure 6.9  | Slip along the steel bar-to-concrete interface  | 190 |
| Figure 6.10 | Steel stress distributions in the longitudinal direction                                      | 192 |
| Figure 6.11 | Stress distributions over the mid-span cross-section  | 193 |
| Figure 6.12 | Evolutions of temperatures, strains and stresses over central layer at mid-span               | 194 |
| Figure 6.13 | Evolutions of temperatures, strains and stresses over exterior layer at mid-span              | 195 |
| Figure 7.1  | Variation of tensile strength of FRP sheets with temperature                                  | 217 |
| Figure 7.2  | Bond-slip curves of steel-to-concrete and FRP-to-concrete interfaces at elevated temperatures | 218 |
| Figure 7.3  | Load-deflection curves of Blontrock et al.'s (2000) reference beams                           | 219 |
| Figure 7.4  | Fire responses of plain RC beams tested by Blontrock et al. (2000)                            | 219 |
| Figure 7.5  | Fire responses of insulated CFRP-strengthened RC beams tested by Blontrock et al. (2000)      | 221 |
| Figure 7.6  | Fire responses of the insulated CFRP-strengthened RC beam tested by Gao et al. (2010)         | 222 |
| Figure 7.7  | Temperatures of CFRP-strengthened RC T-beams tested by Williams et al. (2008)                 | 223 |

|             |  |     |
|-------------|--|-----|
| Figure 7.8  | Effect of bond degradation on mid-span deflection  | 224 |
| Figure 7.9  | Effect of FRP strengthening system on temperatures in an insulated FRP-strengthened RC beam  | 225 |
| Figure 8.1  | Effects of beam dimensions on mid-width temperature rises  | 258 |
| Figure 8.2  | Mid-width temperature rises in a wide beam   | 259 |
| Figure 8.3  | $\theta_{d,120}$ defined as a function of distance from fire exposed surface   | 259 |
| Figure 8.4  | Temperature rises at different concrete depths with the fire exposure time   | 260 |
| Figure 8.5  | Comparisons of temperature rises at different concrete depths with the fire exposure time: predictions by proposed empirical equations vs. FE results. | 261 |
| Figure 8.6  | Effect of beam width on temperature rises at different concrete depths.  | 261 |
| Figure 8.7  | Mid-width temperature rises with exposure time: proposed explicit solution vs. FE prediction   | 262 |
| Figure 8.8  | Comparisons between predictions from simple methods and test data for Wu et al.'s (1993) beams   | 263 |
| Figure 8.9  | Comparisons between predictions from simple methods and test data for Lin et al.'s (1981) beam   | 264 |
| Figure 8.10 | Comparisons between predictions from simple methods and test data for Dotreppe and Franssen's (1985) beam  | 265 |
| Figure 8.11 | One-dimensional heat transfer problem  | 266 |
| Figure 8.12 | Comparisons of temperature profiles between bare and insulated concrete members  | 266 |
| Figure 8.13 | Optimization function vs. equivalent concrete thickness  | 267 |
| Figure 8.14 | Temperature profiles along the thickness direction in the insulated concrete member and the equivalent bare concrete member                            | 268 |
| Figure 8.15 | Determination of $d_a$ as a function of fire insulation thickness  | 268 |
| Figure 8.16 | Temperature history at the fire insulation layer-to-concrete interface as a function of fire exposure time   | 269 |
| Figure 8.17 | Effect of the thermal conductivity ( $\lambda_a$ ) on the equivalent concrete thickness  | 270 |

|             |   |     |
|-------------|---|-----|
| Figure 8.18 | Effect of the product of specific heat capacity and density ( $\rho_a c_a$ ) on the equivalent concrete thickness | 270 |
| Figure 8.19 | Predicted and measured temperature results for the insulated concrete beams tested by Blontrock et al. (2000)     | 271 |
| Figure 8.20 | Predicted and measured temperature results for the insulated concrete beams tested by William et al. (2008)       | 272 |
| Figure 8.21 | Comparisons of thermal resistance at the fire-to-insulation interface for beams tested by Williams et al. (2008)  | 273 |
| Figure 9.1  | Schematic of three-level performance-based fire resistance design   | 301 |
| Figure 9.2  | Effect of placement of tension steel rebars   | 301 |
| Figure 9.3  | Effects of loading scheme   | 302 |
| Figure 9.4  | Load-deflection responses of RC beams with different design parameters at ambient temperature                     | 303 |
| Figure 9.5  | Determination of fire-resistance periods of RC beams  | 303 |
| Figure 9.6  | Comparison between BS 8110 code predictions and FE results  | 304 |
| Figure 9.7  | Comparison between ACI code predictions and FE results  | 305 |
| Figure 9.8  | Comparison between FIP/CEB report predictions and FE results  | 305 |
| Figure 9.9  | Comparison between Eurocode predictions and FE results  | 306 |
| Figure 9.10 | Comparison between Kodur and Dwaikat's (2011) predictions and FE results  | 306 |
| Figure 9.11 | Effect of fire load ratio   | 307 |
| Figure 9.12 | Combined effects of concrete cover and ratio of tension steel reinforcement                                       | 307 |
| Figure 9.13 | Effect of span-to-depth ratio   | 308 |
| Figure 9.14 | Effect of aggregate type  | 308 |
| Figure 9.15 | Effect of rebar placement of tension steel reinforcement  | 309 |
| Figure 9.16 | Effect of beam width  | 309 |

|             |   |     |
|-------------|---|-----|
| Figure 9.17 | Comparisons between calculated fire resistance periods and data from FE parametric studies                        | 310 |
| Figure 9.18 | Comparison between the formulae predictions and the FE results (512 beams in total)                               | 312 |
| Figure 9.19 | Comparison between the formulae predictions with the data from further FE parametric analyses (60 beams in total) | 312 |
| Figure 9.20 | Comparison between formulae predictions and existing test data  | 313 |
| Figure 9.21 | Schematic of the 500 °C isotherm method   | 313 |
| Figure 9.22 | Effect of insulation thickness on the time-dependent moment capacity  | 314 |
| Figure 9.23 | Determination of fire resistance period of insulated CFRP-strengthened RC beams                                   | 315 |
| Figure 9.24 | Comparison between predicted fire resistance periods and FE results for insulated CFRP-strengthened RC beams      | 316 |

## LIST OF TABLES

| Table     | Caption   | Page |
|-----------|---|------|
| Table 5.1 | Double-lap shear test database: specimen details and results                        | 139  |
| Table 5.2 | Summary of predicted results for the test specimens                                 | 143  |
| Table 7.1 | Material and geometrical properties of insulated FRP-strengthened RC beams          | 226  |
| Table 8.1 | Cross-sections examined in the FE parametric study                                  | 274  |
| Table 8.2 | Coefficients $m_i$ determined through least-square regression analysis              | 274  |
| Table 9.1 | Design parameters of RC beams used in FE parametric analyses                        | 316  |
| Table 9.2 | Load-carrying capacity of beams at room temperature for parametric study            | 317  |
| Table 9.3 | Design parameters of RC beams used in further FE parametric analyses                | 317  |
| Table 9.4 | Comparisons between existing fire test data with formulae predictions               | 318  |
| Table 9.5 | Design parameters of insulated FRP-strengthened RC beams for FE parametric analyses | 319  |
| Table 9.6 | Load-carrying capacities of reference and FRP-strengthened RC beams                 | 319  |
| Table 9.7 | Fire resistance predictions of insulated CFRP-strengthened RC beams                 | 320  |

# NOTATION

*The main symbols used in this thesis are listed below:*

|                  |   |
|------------------|---|
| $\alpha_c$       | thermal expansion coefficient of the concrete                         |
| $\alpha_p$       | thermal expansion coefficient of the FRP laminate                     |
| $A$              | maximum strain reached in the FRP laminate                            |
| $A_{sc}$         | total area of corner tension rebars                                   |
| $A_{st}$         | total area of tension rebars  |
| $b$              | beam width  |
| $b_c$            | width of the concrete prism   |
| $b_p$            | width of the FRP laminate   |
| $B$              | interfacial brittleness index of the FRP-to-concrete bonded interface |
| $B_0$            | interfacial brittleness index at ambient temperature                  |
| $B(T)$           | interfacial brittleness index at an elevated temperature $T$          |
| $c$              | concrete cover depth  |
| $c_a$            | specific heat capacity of fire insulation                             |
| $c_c$            | specific heat capacity of concrete                                    |
| $c_{c,peak}$     | peak value of the specific heat capacity of concrete                  |
| $d$              | distance from the fire-exposed surface                                |
| $d_{equ}$        | thickness of the equivalent concrete layer                            |
| $d_i$            | thickness of the fire insulation layer                                |
| $d_c$            | damage variable used to define stiffness degradations in compression  |
| $d_t$            | damage variable used to define stiffness degradations in tension      |
| $\delta$         | interfacial slip of the FRP-to-concrete bonded interface              |
| $\delta_1$       | interfacial slip corresponding to the maximum shear stress            |
| $\delta_f$       | interfacial slip corresponding to the zero shear stress               |
| $\Delta$         | slip at the loaded end  |
| $\Delta T$       | service temperature variation (i.e., thermal loading)                 |
| $\varepsilon(x)$ | axial strain in the FRP laminate                                      |

|                           |   |
|---------------------------|---|
| $\varepsilon_m$           | heat emissivity of the exposed surfaces   |
| $\varepsilon_f$           | heat emissivity of the fire   |
| $\tilde{\varepsilon}_c^p$ | equivalent compressive plastic strain   |
| $\tilde{\varepsilon}_t^p$ | equivalent tensile plastic strain   |
| $\varepsilon_{tot}$       | total strain of concrete at elevated temperatures                                       |
| $\varepsilon_\sigma$      | stress-induced strain of concrete or steel at elevated temperatures                     |
| $\varepsilon_{th}$        | free thermal strain of concrete or steel at elevated temperatures                       |
| $\varepsilon_{cr}$        | classical creep strain of concrete  |
| $\varepsilon_{tr}$        | transient creep strain of concrete at elevated temperatures                             |
| $E_p$                     | elastic modulus of the FRP laminate   |
| $E_{p0}$                  | elastic modulus of FRP at ambient temperature   |
| $E_{pT}$                  | elastic modulus of FRP at an elevated temperature $T$                                   |
| $E_c$                     | elastic modulus of the concrete prism   |
| $E_{0,T}$                 | initial undamaged elastic modulus of concrete at an elevated temperature $T$            |
| $f_{b0,T}$                | initial equibiaxial compressive yield stress of concrete at an elevated temperature $T$ |
| $f_{c0,T}$                | initial uniaxial compressive yield stress of concrete at an elevated temperature $T$    |
| $f_{c,T}$                 | uniaxial compressive strength of concrete at an elevated temperature $T$                |
| $f_{pT}$                  | tensile strength of the FRP laminate at an elevated temperature $T$                     |
| $f_{p0}$                  | tensile strength of the FRP laminate at ambient temperature                             |
| $f_{t0,T}$                | initial uniaxial tensile yield stress of concrete at an elevated temperature $T$        |
| $f_{t,T}$                 | uniaxial tensile strength of concrete at an elevated temperature $T$                    |
| $G_f$                     | interfacial fracture energy of the FRP-to-concrete bonded interface                     |
| $G_{f0}$                  | interfacial fracture energy at ambient temperature                                      |
| $G_{f,T}$                 | interfacial fracture energy at an elevated temperature $T$                              |
| $G_F$                     | concrete fracture energy required to create a stress-free crack over a unit area        |
| $\gamma$                  | fire load ratio   |

|                      |  |
|----------------------|--|
| $h_c$                | convective heat transfer coefficient   |
| $\bar{I}_1$          | the first effective stress invariant   |
| $\bar{J}_2$          | the second effective deviatoric stress invariant   |
| $k$                  | thermal conductivity   |
| $k_b$                | coefficient accounting for the effect of beam width  |
| $k_\lambda$          | coefficient accounting for the effect of $\lambda_a$   |
| $k_t$                | coefficient accounting for the effect of fire exposure time                                    |
| $k_{\rho c}$         | coefficient accounting for the effect of $\rho_a c_a$  |
| $l$                  | RC beam span   |
| $L$                  | bond length of the FRP laminate  |
| $L_e$                | effective bond length of the FRP-to-concrete bonded interface                                  |
| $M_R$                | moment capacity of the insulated RC beam under fire  |
| $\sigma_c$           | axial stress in the concrete prism   |
| $\sigma_p$           | axial stress in the FRP laminate   |
| $\bar{\sigma}$       | effective stress tensor  |
| $\bar{\sigma}_{max}$ | algebraic maximum eigenvalue of the effective stress tensor                                    |
| $P$                  | applied load of the FRP-to-concrete bonded joint   |
| $P_u$                | debonding load of the FRP-to-concrete bonded joint   |
| $P_{u,T}$            | debonding load of the bonded joint at temperature $T$  |
| $\rho$               | density  |
| $\rho_a$             | density of fire insulation   |
| $\rho_s$             | reinforcement ratio of tension steel rebars  |
| $\lambda_a$          | thermal conductivity of fire insulation  |
| $s$                  | interfacial slip between the steel rebar and the concrete                                      |
| $\theta_{d,120}$     | reference temperature rise at $t = 120$ min for a certain depth $d$ and a beam width of 600 mm |
| $\tau$               | interfacial shear stress of the FRP-to-concrete bonded interface                               |
| $\tau_f$             | peak bond stress of the FRP-to-concrete bonded interface                                       |
| $\tau_{f,T}$         | residual bond strength of the FRP-to-concrete bonded interface at an elevated temperature $T$  |

|                |   |
|----------------|---|
| $\tau_{s,T}$   | local bond stress of the steel bar-to-concrete interface at an elevated temperature $T$ |
| $\tau_{max,T}$ | peak bond stress of the steel bar-to-concrete interface at an elevated temperature $T$  |
| $t$            | fire exposure time  |
| $t_c$          | thickness of the concrete prism   |
| $t_p$          | thickness of the FRP laminate   |
| $T_f$          | fire temperature measured in the furnace or determined from the standard fire curve     |
| $T_g$          | glass transition temperature  |
| $T_{g,a}$      | glass transition temperature of the bonding adhesive                                    |
| $T_{g,p}$      | glass transition temperature of the polymer matrix                                      |
| $T_z$          | absolute zero temperature   |
| $u_c$          | longitudinal displacement of the concrete substrate                                     |
| $u_p$          | longitudinal displacement of the FRP laminate   |

# CHAPTER 1

## INTRODUCTION

### 1.1 GENERAL

Maintaining and upgrading the safety of concrete structures is a massive long-term worldwide challenge, so better solutions have been constantly sought. A major breakthrough in the strengthening of concrete structures over the past three decades has been the development of bonded fibre-reinforced polymer (FRP) systems. The success of the FRP strengthening technology is attributed to its many advantages that arise from the high strength-to-weight ratio, excellent corrosion resistance and fast curing capability of FRP composites (Teng et al. 2002).

There are two categories of FRP strengthening applications for concrete structures: one is the bond-critical application, such as the flexural/shear strengthening of RC members using externally bonded FRP laminates; the other is the contact-critical application, such as the lateral confinement of RC columns using FRP wraps to increase their load-carrying capacity and ductility. Motivated by these two types of applications, extensive studies have been carried out in the past two decades, and all these research efforts have led to the development of various design codes and standards all over the world such as ACI 440.2R-08 (ACI 2008), *fib*-Bulletin 14 (fib 2001), Australian standard HB 305 (Oehlers et al. 2008), Japanese code (JSCE 2001), CNR-DT 200/2004 (CNR 2004) and Chinese code (GB 50608 2010).

### 1.2 FIRE SAFETY OF FRP-STRENGTHENED RC STRUCTURES

Despite its many advantages as mentioned above, the FRP strengthening technique suffers from one serious limitation, particularly for indoor applications: FRP laminates and the bonding adhesive soften quickly under fire exposure. This is because the polymer matrix of the composites and the bonding adhesive, both typically being epoxies, have a low glass transition temperature (e.g., generally in the

range of 45 °C~82 °C for FRP sheets formed through the wet lay-up process) (fib 2001; ACI 2008). When an epoxy is subjected to a temperature close to its glass transition temperature, it transforms into a soft and rubbery material with severe stiffness and strength degradations. In addition, the epoxy may burn unless a fire retardant is used, resulting in the generation of toxic smoke and the spread of flame. Therefore, the fire performance of FRP laminates and FRP-strengthened RC structures becomes a serious concern.

In RC buildings, structural members must be designed to satisfy appropriate fire resistance requirements specified in building codes. A direct approach for evaluating the fire resistance of RC members strengthened with FRP laminates is to conduct standard fire tests. Existing standard fire tests (Blontrock et al. 2000; Blontrock 2003; Bisby 2003; Williams 2004; Bisby et al. 2005a; Kodur et al. 2006; Chowdhury et al. 2007; Williams et al. 2008; Wu and Wan 2009; Gao et al. 2010; Ahmed 2010; Ahmed and Kodur 2011; Adelzadeh et al. 2012) have indicated qualitatively that FRP-strengthened RC members with appropriate design and insulation can achieve satisfactory fire performance. However, these tests have their own limitations, particularly in understanding the member degradation mechanisms at local levels. For example, it is difficult to investigate the behavior of the FRP-to-concrete interface in an insulated FRP-strengthened RC beam under fire exposure even though this interfacial behavior may have a significant effect on the global response of RC members strengthened in flexure or shear with FRP (Bisby et al. 2005b; Klamer 2006; Leone et al. 2009). Moreover, such standard fire tests are usually very expensive and time-consuming. It is therefore neither wise nor cost-effective to conduct systematic fire tests, which cover all the influencing parameters, to generate a comprehensive guideline for the fire safety design of FRP-strengthened RC members. Based on existing limited test results, the structural safety of FRP-strengthened RC members under fire events has not been fully addressed by researchers. The lack of sufficient fire research has imposed a significant limitation on the use of FRP laminates in the strengthening applications on RC structures, for which the fire safety is an important issue.

This dissertation aims at bridging the above knowledge gap and focusing on the fire safety evaluation of FRP-strengthened RC beams in flexure. In the following section,

a brief introduction of FRP-strengthened RC beams as well as the corresponding failure modes at room temperature is presented, while a detailed review of the fire performance (including high-temperature properties) of FRP laminates and FRP-strengthened RC members is given in the next chapter.

### **1.3 STRENGTHENING OF RC BEAMS WITH FRP LAMINATES**

Extensive experimental and analytical investigations have been carried out on RC beams strengthened by FRP laminates, leading to a good understanding of their behavior and failure modes (Ritchie et al. 1991; Triantafillou and Plevris 1992; Arduini and Nanni 1997; Teng et al. 2002; Smith and Teng 2002, 2003; Teng et al. 2003; Buyukozturk et al. 2004; Oehlers and Seracino 2004; Hollaway and Teng 2008; Teng and Chen 2009). Fig. 1.1 illustrates an FRP-strengthened RC beam in flexure by bonding an FRP laminate to its soffit. The FRP laminate may be a pultruded (i.e., prefabricated in factory) plate or an FRP sheet formed on-site using a wet lay-up process.

Several distinctive failure modes have been reported for FRP-strengthened RC beams (Triantafillou and Plevris 1992; Teng et al. 2003; Buyukozturk et al. 2004; Teng and Chen 2009), and can be broadly classified into the following three types: (a) tensile rupture of FRP (Fig. 1.2a) or compressive crushing of concrete (Fig. 1.2b); (b) brittle failure in shear (Fig. 1.2c) if the shear capacity is reached ahead of the flexural capacity of the strengthened beam; and (c) FRP debonding failures. In the former two types of conventional failure, the composite action between the FRP and the RC beam is maintained until the failure, while the last type of failure involves the loss of this composite action. According to the locations where the FRP debonding initiates, there are three different failure modes: (a) concrete cover separation (Fig. 1.2d); (b) plate end interfacial debonding (Fig. 1.2e); and (c) intermediate crack-induced debonding (i.e., IC debonding, Fig. 1.2f).

Based on the comprehensive understanding of the failure modes of FRP-strengthened RC beams, systematic theories have been available for the design of RC members strengthened in flexure with externally bonded FRP laminates in existing design guidelines (fib 2001; JSCE 2001; CNR 2004; Oehlers et al. 2008;

ACI 2008; GB 50608 2010). These design guidelines facilitate the structural safety of RC beams strengthened with FRP laminates at normal service conditions. However, these existing design guidelines do not provide systematic performance-based approaches for the fire safety design of FRP-strengthened RC beams although some of them have provided prescriptive design provisions (ACI 2008; fib 2001). For instance, it is conceptually specified that FRP-strengthened RC members should be designed in such a way that the nominal strength of the un-strengthened member under fire is greater than the service load acting on FRP-strengthened RC members for the required fire resistance rating.

#### **1.4 SCOPE, OBJECTIVES AND CONTENTS OF THIS DISSERTATION**

The primary aim of this dissertation is to develop a powerful computation tool to predict the fire performance of un-protected and insulated FRP-strengthened RC beams with the proposal and/or implementation of all necessary constitutive models for materials and interfaces, and to develop a performance-based design approach for predicting the fire resistance of FRP-strengthened RC beams. The specific objectives are as follows:

- ◆ to achieve an in-depth understanding of the bond-slip behavior of FRP-to-concrete interfaces under combined thermal and mechanical loadings;
- ◆ to develop advanced FE models for predicting the thermal and structural responses of FRP-strengthened RC beams with different fire insulation schemes (i.e., unprotected or fire insulated); and
- ◆ to conduct extensive parametric studies based on the validated FE models and then to develop a performance-based approach for the fire resistance design of FRP-strengthened RC beams.

A total of ten chapters are presented in this dissertation. Fig. 1.3 illustrates the structure of the whole dissertation.

As seen in the Fig. 1.3, seven main chapters are presented to address the above-mentioned three specific research objectives: three chapters (Chapters 3, 4, and 5) are presented on the debonding behavior and the corresponding bond-slip model of FRP-to-concrete interfaces under combined thermal and mechanical loadings; two

chapters (Chapter 6 and 7) are presented on the FE modeling of un-protected and insulated FRP-strengthened RC beams exposed to fire; two other chapters (Chapter 8 and 9) are presented on the development of a performance-based design approach for the fire resistance evaluation of FRP-strengthened RC beams.

Below are brief descriptions of all the chapters in this dissertation:

Chapter 1 presents a general introduction on the research background.

Chapter 2 presents a literature review on the thermal and mechanical properties of FRP composites as well as their constitutive materials (i.e., fibers and matrixes) at elevated temperatures. A detailed review is also conducted on the fire performance of FRP-strengthened RC members, including existing shear tests on FRP-to-concrete bonded joints at elevated temperatures, existing experimental tests and numerical modeling on the fire behavior of FRP-strengthened RC members, and existing prescriptive design provisions.

Chapter 3 presents an analytical solution for the full-range behavior of FRP-to-concrete bonded joints under combined thermal and mechanical loadings. The solution is based on a bilinear bond-slip model and leads to closed-form expressions. The validity of the solution is demonstrated through comparisons with both experimental results and finite element predictions. Numerical results from the solution are presented to illustrate the effects of thermal loading on the interfacial shear stress and slip distributions, as well as the global load-displacement response.

Chapter 4 discusses the influence of the shape of bond-slip models on the Mode-II debonding process of FRP-to-concrete bonded joints subjected to combined thermal and mechanical loadings, as the extension work of Chapter 3. Five different bond-slip models are considered in deriving the closed-form solutions, including the elastic-brittle, bi-linear, elastic-plastic-brittle, rigid-softening, and exponential models. For each type of bond-slip model, explicit expressions for the debonding load, effective bond length, interfacial shear stress, interfacial slip, as well as the load-displacement response are presented. A useful application of the closed-form solutions lies in the isolation of thermal effects from mechanical loading effects in

the interpretation of test data of bonded joints subjected to combined thermal and mechanical loadings. Such isolation is needed when such tests are used to determine the local bond-slip response of the interface.

Chapter 5 presents a nonlinear local bond-slip model for FRP laminates externally bonded to concrete at elevated temperature for future use in the numerical modeling of FRP-strengthened RC members exposed to fire. The model is an extension of an existing two-parameter bond-slip model for FRP-to-concrete interfaces at ambient temperature (Dai et al. 2005). The two key parameters employed in the proposed bond-slip model, the interfacial fracture energy  $G_f$  and the interfacial brittleness index  $B$ , are determined using existing shear test data of FRP-to-concrete bonded joints at elevated temperatures.

Chapter 6 presents a three-dimensional (3D) FE model for the accurate prediction of the thermal and mechanical behavior of un-protected FRP-strengthened RC beams. In the proposed FE model, both the thermal and mechanical properties of concrete and steel as well as the interfacial bond-slip behavior between the reinforcing steel and concrete are properly considered. Results obtained from the FE model are compared with the existing test data to examine the accuracy of the model. Predictions from this FE model also allow the complex distribution and evolution of stresses in the reinforcing steel and concrete to be examined in detail, leading to a better understanding of the local responses of RC beams exposed to fire. The developed FE model can be used for parametric analyses to propose a simple fire resistance design approach for un-protected FRP-strengthened RC beams, which are equivalent to bare RC beams prior to their strengthening in terms of the fire resistance.

Chapter 7 presents an advanced FE model for the fire performance evaluation of insulated FRP-strengthened RC beams. In this FE model, the temperature-dependent properties of concrete, steel, FRP and interfaces are all appropriately considered. Particular attention is paid to the modeling of interfacial bond-slip behavior between the externally bonded FRP laminates and the concrete, an aspect which has rarely been considered by previous numerical studies. Comparisons between FE

predictions and existing test data are presented to demonstrate the accuracy of the proposed FE model.

Chapter 8 presents a simple approach for predicting temperatures in RC beams under the standard fire exposure. Results from FE heat transfer analysis are first examined to identify the key parameters that influence the temperature fields of RC beams. On the basis of this knowledge, a simple method in the form of handy formulae and diagrams is derived from regression analysis of FE parametric studies, with due consideration of the effects of beam geometry and fire exposure duration. The accuracy of the proposed method is demonstrated by comparing its predictions with temperature data from both FE analyses and existing standard fire tests. For insulated FRP-strengthened RC beams, a set of formulae is also developed by which the fire insulation layer is equivalent to a concrete layer. The thickness of the equivalent concrete layer is expressed as a function of thickness and thermal properties of the fire insulation layer. As a consequence, the temperature field analysis of an insulated FRP-strengthened RC beam turns into that of an un-protected RC beam with enlarged sectional dimensions. The accuracy of the proposed equivalent method is demonstrated through comparing its predictions with the FE results and the existing standard fire tests on insulated FRP-strengthened RC beams.

Chapter 9 presents a performance-based approach for the fire resistance design of FRP-strengthened RC beams. A three-level design concept is proposed based on the tradeoff between the strength contribution of FRP strengthening system and the required fire resistance rating. For un-protected FRP-strengthened RC beams (i.e., the lowest level), extensive FE parametric studies are carried out to investigate the influences of various governing parameters. The fire resistance results generated from the FE parametric studies are then used to develop explicit design formulae with due consideration of the influences of various design parameters. The validity of the proposed formulae are demonstrated by comparing its predictions with fire-resistance data obtained from both FE parametric studies and existing standard fire tests. In addition, a design-oriented method is established based on the well-known “500°C isotherm method” to enable the moment capacity prediction of insulated FRP-strengthened RC beams (i.e., equivalent to insulated RC beams) under the

standard fire exposure. The fire resistance results obtained from the design-oriented method are in close agreement with the FE predictions.

Chapter 10 presents the conclusions derived from the research work in this dissertation, and recommends further research study on the fire safety evaluation of FRP-strengthened RC beams.

## 1.5 REFERENCES

- American Concrete Institute (ACI). (2008). "Guide for the design and construction of externally bonded FRP systems for strengthening concrete structures." *ACI 440.2R-08*, American Committee 440, Farmington Hills, Michigan, America.
- Adelzadeh, M., Benichou, N., and Green, M.F. (2012). "Behaviour of fibre reinforced polymer-strengthened T-beams and slabs in fire." *Proceedings of the ICE, Structures and Buildings*, Vol. 165, No. 7, pp. 361-371.
- Ahmed, A. (2010). "Behavior of FRP-strengthened reinforced concrete beams under fire conditions." Ph.D. thesis, Michigan State University, Michigan, America.
- Ahmed, A., and Kodur, V.K.R. (2011). "The experimental behavior of FRP-strengthened RC beams subjected to design fire exposure." *Engineering Structures*, Vol. 33, No. 7, pp. 2201-2211.
- Arduini, M., and Nanni, A. (1997). "Parametric study of beams with externally bonded FRP reinforcement." *ACI Structural Journal*, Vol. 94, No. 5, pp. 493-501.
- Bisby, L.A. (2003). "Fire behavior of fiber-reinforced polymer (FRP) reinforced or confined concrete." Ph.D. thesis, Queen's University, Kingston, Ontario, Canada.
- Bisby, L.A., Kodur, V.K.R., and Green, M.F. (2005a). "Fire endurance of Fiber-reinforced polymer-confined concrete columns." *ACI Structural Journal*, Vol. 102, No. 6, pp. 883-891.
- Bisby, L.A., Green, M.F., and Kodur, V.K.R. (2005b). "Response to fire of concrete structures that incorporate FRP." *Progress in Structural Engineering and Materials*, Vol. 7, No. 3, pp. 136-149.
- Blontrock, H., Taerwe, L., and Vandeveld, P. (2000). "Fire tests on concrete beams strengthened with fiber composite laminates." *Proceeding of the Third Ph.D. Symposium in Civil Engineering*, Vienna, Austria, pp. 151-161.
- Blontrock, H. (2003). "Analysis and modeling of the fire resistance of concrete elements with externally bonded FRP reinforcement." Ph.D. thesis, Ghent University, Ghent, Belgium.
- Buyukozturk, O., Gunes, O., and Karaca, E. (2004). "Progress on understanding debonding problems in reinforced concrete and steel members strengthened using FRP composites." *Construction and Building Materials*, Vol. 18, No. 11, pp. 9-19.

- Chowdhury, E.U., Bisby, L.A., Green, M.F., and Kodur, V.K.R. (2007). "Investigation of insulated FRP-wrapped reinforced concrete columns in fire." *Fire Safety Journal*, Vol. 42, No. 6-7, pp. 452-460.
- Consiglio Nazionale delle Ricerche (CNR). (2004). "Guide for the design and construction of externally bonded FRP systems for strengthening existing structures: Materials, RC and PC structures, masonry structures." *CNR-DT 200/2004*, Italian Research Council, Italian Advisory Committee on Technical Recommendations for Construction, CNR, Rome.
- Dai, J.G., Ueda, T., and Sato, Y. (2005). "Development of the nonlinear bond stress-slip model of fiber reinforced plastics sheet-concrete interfaces with a simple method." *Journal of Composites for Construction*, ASCE, Vol. 9, No. 1, pp. 52-62.
- Federation International du Beton (fib). (2001). "Externally bonded FRP reinforcement for RC structures." *fib Bulletin 14*, fib Task Group 9.3, fib, Lausanne, Switzerland.
- Hollaway, L.C. and Teng, J.G. (2008). *Strengthening and rehabilitation of civil infrastructures using fiber-reinforced polymer (FRP) composites*, Woodhead Publishing Ltd., UK.
- Gao, W.Y., Hu, K.X., and Lu, Z.D. (2010). "Fire resistance experiments of insulated CFRP strengthened reinforced concrete beams." *China Civil Engineering Journal*, Vol. 43, No. 3, pp. 15-23 (in Chinese).
- GB 50608. (2010). "Technical code for infrastructure application of FRP composites." *GB 50608-2010*, China Planning Press, Beijing, China.
- Klamer, E. (2006). "The influence of temperature on concrete structures strengthened with externally bonded CFRP." Research Report, Eindhoven University of Technology, Eindhoven, Netherlands.
- Kodur, V.K.R., Bisby, L.A., and Green, M.F. (2006). "Experimental evaluation of the fire behavior of insulated fibre-reinforced-polymer-strengthened reinforced concrete columns." *Fire Safety Journal*, Vol. 41, No. 7, pp. 547-557.
- Japan Society of Civil Engineers (JSCE). (2001). "Recommendation for upgrading of concrete structures with use of continuous fiber sheets." *Concrete Engineering Series 41*, Japan Society of Civil Engineers, Tokyo, Japan.
- Leone, M., Matthys, S., and Aiello, M.A. (2009). "Effect of elevated service temperature on bond between FRP EBR systems and concrete." *Composites Part B: Engineering*, Vol. 40, No. 1, pp. 85-93.
- Oehlers D.J., and Seracino, R. (2004). *Design of FRP and Steel Plated RC structures: Retrofitting Beams and Slabs for Strength, Stiffness and Ductility*. Elsevier, Oxford, UK.
- Oehlers D.J., Seracino R. and Smith S. (2008). "Design guideline for RC structures retrofitted with FRP and metal plates: beams and slabs." *HB 305-2008*, Standards Australia, Sydney, Australia.
- Ritchie, P.A., Thomas, D.A., Lu, L.W., and Connelly, G.M. (1991). "External reinforcement of concrete beams using fiber reinforced-plastics." *ACI Structural Journal*, Vol. 88, No. 4, pp. 490-500.

- Smith, S.T., and Teng, J.G. (2002). "FRP-strengthened RC beam-I: Review of debonding strength models." *Engineering Structures*, Vol. 24, No. 4, pp. 385-395.
- Smith, S.T., and Teng, J.G. (2003). "Shear-bending interaction in debonding failures of FRP-plated RC beams." *Advances in Structural Engineering*, Vol. 6, No. 3, pp. 183-199.
- Teng, J.G., Chen, J.F., Smith, S.T., and Lam, L. (2002). *FRP-strengthened RC structures*. John Wiley and Sons Ltd., Chichester, UK.
- Teng, J.G.; Chen, J.F.; Smith, S.T.; and Lam, L. (2003). "Behaviour and strength of FRP-strengthened RC structures: a state-of-the-art review." *Proceedings of the Institution of Civil Engineers, Structures & Buildings*, Vol. 156, No.1, pp. 51-62.
- Teng, J.G.; and Chen, J.F. (2009). "Mechanics of debonding in FRP-plated RC beams." *Proceedings of the Institution of Civil Engineers, Structures & Buildings*, Vol. 162, No.5, pp. 335-345.
- Triantafillou, T.C., and Plevris, N. (1992). "Strengthening of R/C beams with epoxy-bonded fiber composite materials." *Materials and Structures*, Vol. 25, No. 148, pp. 201-211.
- Williams, B. (2004). "Fire performance of FRP-strengthened reinforced concrete flexural members." Ph.D. thesis, Queen's University, Kingston, Ontario, Canada.
- Williams, B., Kodur, V.K.R., Green, M.F., and Bisby, L.A. (2008). "Fire endurance of fiber-reinforced polymer strengthened concrete T-beams." *ACI Structural Journal*, Vol. 105, No. 1, pp. 60-67.
- Wu, B., and Wan, Z.J. (2009). "Experimental investigation into fire resistance of reinforced concrete beams strengthened in flexure with Carbon Fiber Sheets." *Journal of South China University of Technology*, Vol.40, No.6, pp.26-41 (in Chinese).

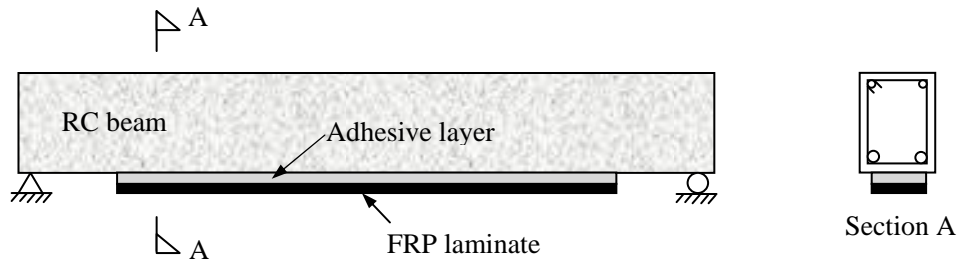


**Fig. 1.1** Typical flexural strengthening of an RC beam with an FRP laminate bonded to its soffit.

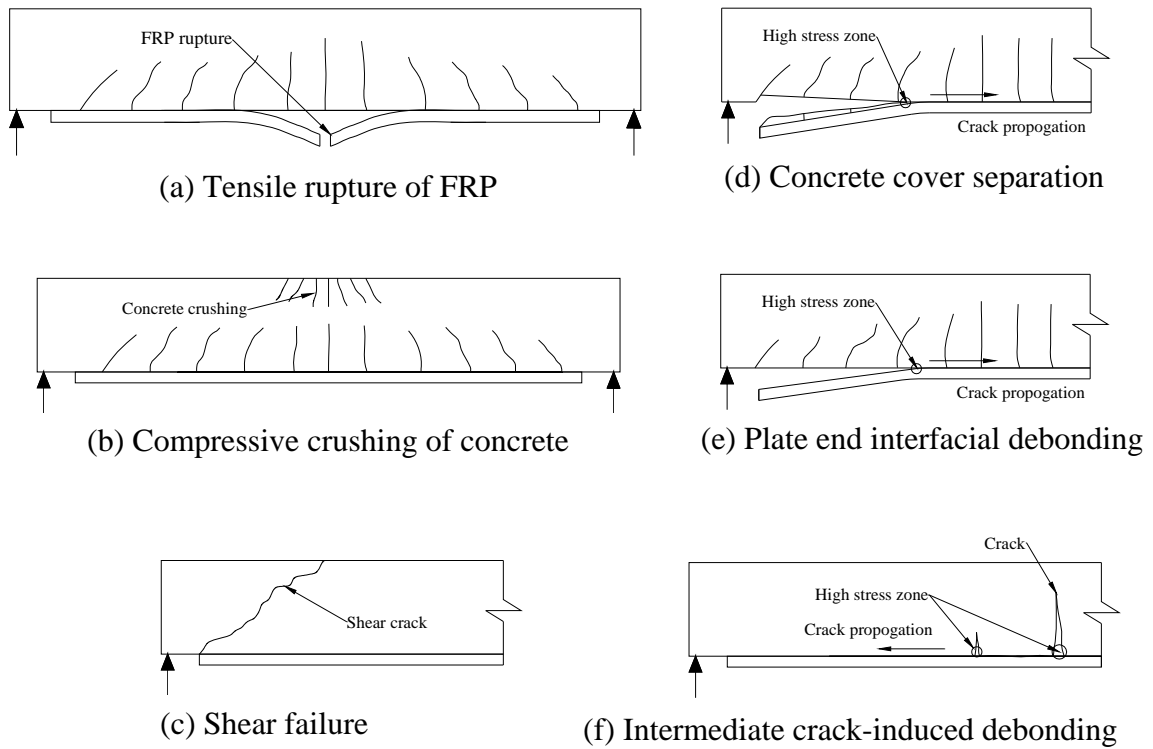


**Fig. 1.2** Failure modes of FRP strengthened RC beams (Teng et al. 2003).

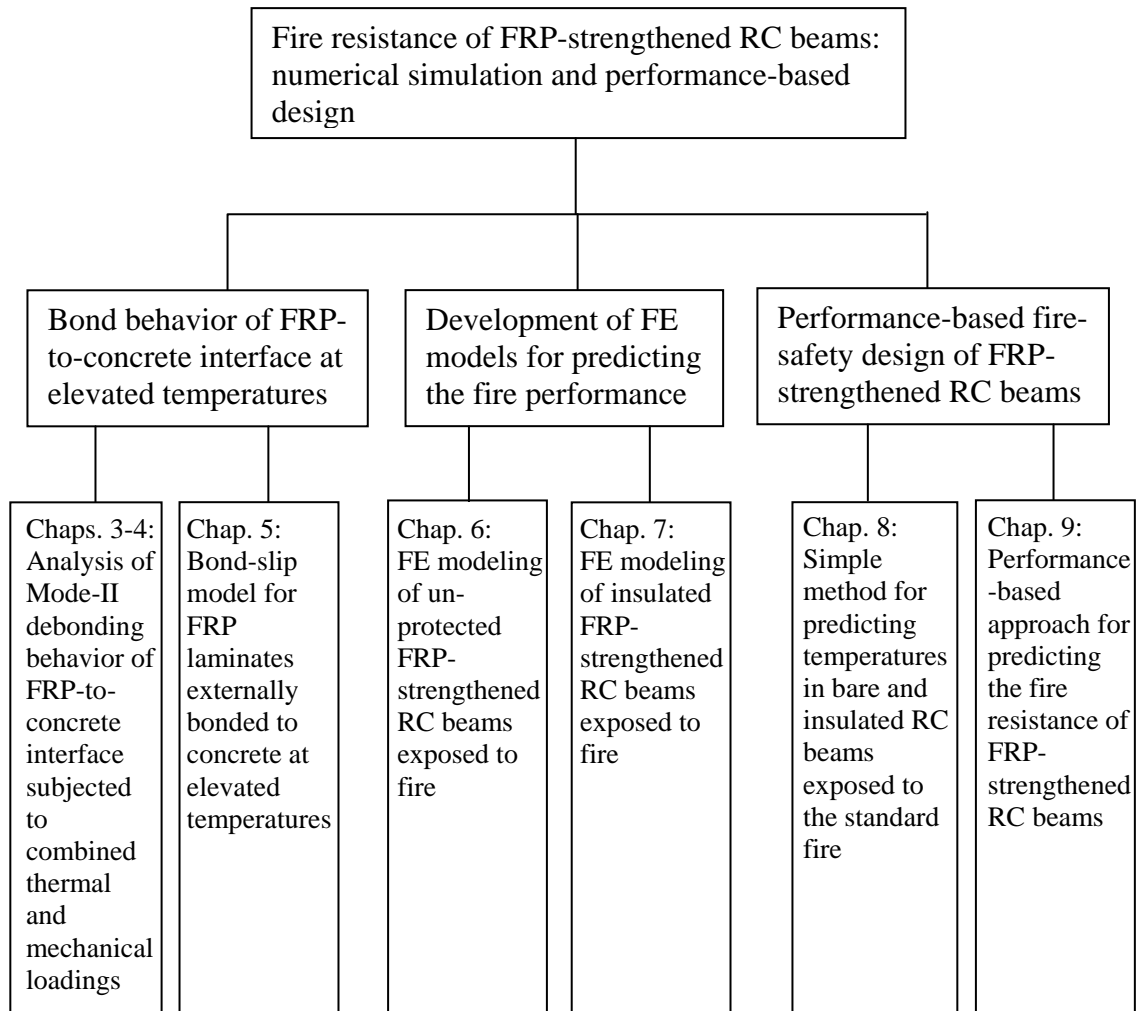


**Fig. 1.3** Structure of the dissertation.

## **CHAPTER 2**

### **LITERATURE REVIEW**

#### **2.1 GENERAL**

FRP composites were originally developed in marine, automotive and aerospace industries during the 1960s and 1970s as they were found to be useful in a wide variety of applications (Harries et al. 2003). In the last two decades, FRP composites have been extended to civil construction industry and are widely used for the strengthening and rehabilitation of RC structures due to their excellent mechanical properties, ease of installation and cost effectiveness. However, most of existing strengthening applications of FRP composites have been limited to outdoor structures such as bridges and naturally ventilated parking garages where the fire safety is not a major concern (Kodur et al. 2006). When FRP laminates are used in RC buildings, the fire safety of FRP-strengthened RC members becomes a serious concern as they have to satisfy the fire resistance requirements specified in building codes and standards. FRP composites have their own weaknesses, such as the poor performance of the organic polymer matrix under fire (flammability, smoke generation and rapid deterioration in its mechanical properties). This situation has motivated researchers to investigate the behavior of FRPs as well as FRP-strengthened RC members subjected to fire and elevated temperatures.

This chapter presents a review of existing knowledge on the fire performance of FRP composites and FRP-strengthened RC members, followed by a summary of the prescriptive provisions available in the current design codes and published documents, which are used conceptually for the fire safety design of FRP-strengthened RC members.

#### **2.2 PROPERTIES OF FRP COMPOSITES AT ELEVATED TEMPERATURES**

FRP composites are composed of reinforcing fibers, polymer matrix and some additives, such as coupling agents and fillers. The reinforcing fibers occupy the largest volume fraction and sustain the major portion of the loading acting on the composites. The polymer matrix acts as a binder for these fibers. The roles of the matrix in an FRP laminate are: (a) to transfer stresses between fibers, (b) to provide a barrier against an adverse environment, and (c) to protect the surface of the fibers from mechanical abrasion (Mallick 1993). However, when the polymer matrix suffers from an elevated temperature approaching its glass transition temperature ( $T_g$ ), it transforms from a rigid glass state to a soft rubbery state, resulting in a rapid reduction in both strength and stiffness (Bakis 1993; Blontrock et al. 1999). This property reduction limits the polymer's ability to transfer stresses between fibers and thus reduces the overall strength of the composites.

### ***2.2.1 Thermal Properties***

Thermal properties of FRP composites at elevated temperatures include the temperature-dependent variations of thermal conductivity, specific heat and density. Generally, polymers have relatively low thermal conductivities (Mallick 1993). This is a reason why polymers are commonly used as insulation materials for cables and wires. The fibers have much higher thermal conductivities than the polymers. As a composite material, the thermal conductivity of an FRP relies on the fiber type, the resin type of the polymer matrix, the orientation of fibers, and the fiber volume fraction (Bisby et al. 2005a). For unidirectional FRP laminates that are widely used in strengthening applications, the thermal conductivity relies heavily on the rate of heat transfer through the polymer matrix (Schwartz 1997). To date, raw experimental data on the thermal properties of FRP composites at elevated temperatures are extremely scarce in the literature. Griffis et al. (1981) conducted tests on a specific type of carbon FRP (CFRP) for aerospace applications by exposing the specimens to radiant heat, and reported changes in the thermal properties of the heated specimens for temperatures up to 1000 °C as shown in Fig. 2.1.

### ***2.2.2 Mechanical Properties***

### 2.2.2.1 Fibers

Fibers are more thermally stable than polymer matrix. The commonly used continuous fibers for the fabrication of FRP laminates are carbon, glass, aramid and basalt fibers (ACI 2008). The fire performance of these fibers varies with the types of fibers. Research has indicated that carbon fibers have high resistance to high temperatures and have the melting temperature as high as 4000 °C, aside from exhibiting a tendency to oxidize at temperatures above 400 °C (Bourbigot and Flambard 2002). Glass fibers exhibit different behavior as they do not oxidize at elevated temperatures, but they soften at temperatures approaching 800~1000 °C (Bakis 1993) and melt at temperatures approaching 1225~1370 °C (Bourbigot and Flambard 2002). Aramid fibers are flame-resistant because they form a burnt char when exposed to flame. However, aramid fibers oxidize at around 175 °C with an extreme strength degradation, thereby limiting their use at elevated temperatures (Bakis 1993). Bisby (2003) collected a test database on the tensile strengths and elastic moduli of carbon, glass and aramid fibers at elevated temperatures (e.g., see in Fig. 2.2 for tensile strengths), and suggested a semi-empirical analytical model [Eq. (2.1)] to describe the temperature-dependent variations of strength and stiffness of fibers at elevated temperatures:

$$\frac{f}{f_0} = \left(\frac{1-a}{2}\right) \cdot \tanh[-b(T - c)] + \left(\frac{1+a}{2}\right) \quad (2.1)$$

In Eq. (2.1),  $f_0$  and  $f$  are the strength or stiffness of fibers at ambient temperature and an elevated temperature  $T$ , respectively;  $a$ ,  $b$  and  $c$  are empirical constants. This sigmoid curve was employed to properly capture the property degradations of fibers as well as FRP composites at elevated temperatures (Bisby 2003). A schematic of this analytical model is shown in Fig. 2.2. For commonly used fibers, i.e., carbon, glass and aramid fibers, the constants in Eq. (2.1) were determined using least-squares regression analyses by Bisby (2003), and Fig. 2.3 shows the database collected by Bisby (2003) as well as the predictions by the proposed models.

#### 2.2.2.2 Matrix

As mentioned above, the glass transition temperature ( $T_{g,p}$ ) plays an important role in the behavior of polymer matrix at elevated temperatures. For wet layup FRP sheets, the matrix cannot be completely cured at ambient temperature (Silva and Biscaia 2008), and its  $T_{g,p}$  is normally low and within the range of 45 to 82 °C (fib 2001; ACI 2008). By contrast, the polymer matrix in a prefabricated FRP plate has a much higher  $T_{g,p}$  [around 130 °C (Clarke 1996)] as prefabrication allows curing at elevated temperature and pressure (Stratford et al. 2009). When exposed to a temperature close to  $T_{g,p}$ , the polymer transforms into a soften and viscous material, and significant portions of its strength and stiffness are lost. As a result, the mechanical properties of the FRP composite will degrade substantially due to the thermal softening and the property degradation of the polymer matrix (Mouritz 2002). With a further increase of elevated temperatures (beyond  $T_{g,p}$  and close to the decomposition temperature  $T_d$ ), the polymer matrix will be burnt and decomposed with a char layer. For commonly used epoxy matrixes, the decomposition temperature  $T_d$  is around 400 °C (Mouritz and Gibson 2006), depending on the cross-linking density, composition and curing temperature of the epoxy polymer (Mouritz 2002). The char layer formed during the decomposition process acts as a protective layer and protects the underlying composites, which slows the emission of toxic smokes and the spread of flames (Sorathia et al. 2001). However, such a protective char layer is not expected to form in thin composites typically used for the strengthening of concrete structures (Bisby et al. 2005a; Chowdhury et al. 2011).

#### 2.2.2.3 FRPs

As discussed in preceding sections, the fibers, especially the carbon fibers, perform well at elevated temperatures, whereas the polymer matrixes are extremely susceptible to elevated temperatures. As a whole, FRP composites experience significant degradations in mechanical properties at elevated temperatures (Blontrock et al. 1999). During the past several decades, numerous studies have been conducted to investigate the effect of elevated temperature on the mechanical properties of various FRP composites. Bisby (2003) collected all the data available at that time in the literature to describe the variations in strength and stiffness of

various FRP systems with temperature. Figs. 2.4 and 2.5 illustrate the test data and the proposed models for the tensile strength and the elastic modulus of CFRP composites at elevated temperatures (Bisby 2003). It should be noted that most of the collected data were from the tests on FRP bars or tendons, therefore may not accurately reflect the temperature-dependent properties of FRP sheets, which are commonly used to strengthen RC members and usually formed via a wet lay-up process. They possess a much lower  $T_{g,p}$  than prefabricated FRP products (as stated in Section 2.2.2.2).

### **2.3 BOND PROPERTIES AT ELEVATED TEMPERATURES**

The most common bonding adhesives (typically epoxies) used in FRP strengthening applications through the wet layup process have glass transition temperatures ( $T_{g,a}$ ) in the range of 45~82 °C (fib 2001; ACI 2008). Beyond the  $T_{g,a}$ , most of the bond action between FRP and concrete may be lost. Only a few experimental studies have been conducted to investigate how elevated temperatures influence the bond behavior between the bonded FRP laminate and the concrete substrate. Blontrock (2003) presented the first experimental study in which double-lap shear tests on CFRP-to-concrete bonded joints were conducted at four different temperatures (i.e., 20, 40, 55 and 70 °C). The ultimate load of the FRP-to-concrete bonded joint was found in this study to increase by 41% and 24% when the temperature was increased from 20 °C to 40 °C and 55 °C, respectively. However, when the temperature was further increased to 70 °C, the ultimate load was decreased by 19%.

Similar double-lap shear tests were carried out by Wu et al. (2005) on concrete specimens bonded with carbon fabric sheets. The wet lay-up FRP laminates were formed in two steps: a primer layer was first applied to the concrete surface, followed by the impregnation and placement of the fabric sheets with an epoxy resin. In one set of the specimens, an ordinary epoxy primer and an ordinary epoxy resin were used; in the other set, their thermo-resistant variants were used. The former specimens were tested at four different temperatures (i.e., 26, 30, 40 and 50 °C), while the latter were tested at 26, 40, 50 and 60 °C. For both types of primers and resins, the tests showed that the ultimate load decreased gradually as the temperature increased.

Klamer (2006, 2009) investigated the effect of temperature variation on the debonding behavior of CFRP-to-concrete interfaces using two different test set-ups: double-lap shear tests and small-scale three-point bending tests. Double-lap shear tests were conducted at eight different temperatures (-20, 20, 40, 50, 70, 80, 90 and 100 °C). The test results showed that the ultimate load increased initially as the temperature increased until it was around the glass transition temperature  $T_{g,a}$  of the bonding adhesive which was 62 °C (Klamer 2006). After that, a further temperature increase resulted in a decrease in the ultimate load due to the softening of the adhesive. The tests also indicated that debonding in the specimens was due to cohesion failure in the concrete adjacent to the adhesive layer at low to moderate temperatures (-20 °C to 50 °C), but at elevated temperatures (70 °C to 100 °C), debonding was due to adhesion failure at the adhesive-to-concrete interface. A similar trend for ultimate loads was also observed for the three-point bending tests: the ultimate load first increased with the temperature and then decreased with further temperature increases. Klamer et al. (2008) also tested four full-scale FRP-strengthened RC beams at each of three different temperatures (i.e., 20, 50 and 70 °C) to investigate the effect of temperature variation on the debonding mechanism. These tests showed that the average ultimate load and the failure mode at 50 °C were similar to those observed at ambient temperature (20 °C). However, at 70 °C, the specimens failed by adhesion failure at the adhesive-to-concrete interface, and the average ultimate load reduced considerably. Klamer et al. (2008) suggested that the strength contribution of the FRP strengthening system should be ignored once the temperature at the FRP-to-concrete interface reaches  $T_{g,a}$ .

Cai (2008) studied the bond behavior between CFRP sheets and concrete at temperatures ranging from 4 °C to 180 °C. An increase was seen in the average ultimate load by about 35% for specimens tested at 40 °C over specimens tested at ambient temperature (i.e., 4 °C). A further increase in temperature to 100 °C resulted in a 66% decrease in the average ultimate load. For temperatures exceeding 100 °C, the ultimate load showed no further decrease as the temperature increased; that is, the ultimate load remained almost unchanged.

Leone et al. (2009) investigated the effect of service temperature (i.e., 20, 50, 65 and 80 °C) on the bond behavior of FRP-to-concrete bonded joints. Three types of FRP reinforcement including wet lay-up CFRP and Glass FRP (GFRP) sheets as well as pultruded CFRP plates were used in the tests. In the case of CFRP sheets, a temperature increase in the range below  $T_{g,a}$  resulted in an increase in the ultimate load while at temperatures beyond  $T_{g,a}$ , the ultimate load decreased as the temperature increased. The GFRP sheet-to-concrete bonded joints were tested only at 20 °C and 80 °C, showing a significant loss of the ultimate load at 80 °C. However, a different trend was observed for the CFRP plate-to-concrete bonded joints as the ultimate load at 50 °C was found to be lower than those at 20 °C and 80 °C, probably due to the insufficient penetration of the bonding adhesive into the concrete in some areas as reported by Leone et al. (2009).

The existing laboratory tests as reviewed above have demonstrated clearly that elevated temperatures (or more generally temperature variations) have a significant effect on the bond behavior of FRP-to-concrete interfaces. In most of these existing studies, the ultimate load of the bonded joint was found to increase before the temperature reached the glass transition temperature. This was due to the effect of initial thermal stresses induced along the FRP-to-concrete interface (see more details in Chapters 3 and 4). The decrease of the ultimate load afterwards was due to degradations in the interfacial bond, which can be described using a degraded bond-slip model (see more details in Chapter 5). In the development of a bond-slip model for such degraded interfaces based on bonded joint tests at elevated temperature, the effect of thermal stresses needs to be isolated and excluded when interpreting the test results.

## **2.4 PREVIOUS FIRE RESISTANCE TESTS OF FRP-STRENGTHENED RC MEMBERS**

Over the past two decades, a number of experimental studies have been carried out on the behavior of FRP-strengthened RC members under fire conditions. Fire insulation was always used to prevent the fast temperature rise in the FRP

strengthening system. Results from these fire resistance tests on insulated and strengthened RC members are reviewed in detail in the following sections.

#### ***2.4.1 FRP-Strengthened RC Slabs***

The main research works on the performance of FRP externally bonded RC slabs subjected to fire are from Blontrock et al. (2001), Kodur et al. (2004) and Williams et al. (2006). The test program of Blontrock et al. (2001) included ten slabs, with a thickness of 150 mm, a width of 400 mm and a length of 3150 mm. Slab 1 (unstrengthened reference slab) and Slabs 2 and 3 (strengthened reference slabs) were statically loaded at room conditions to determine their load-carrying capacity. The other slabs, including Slabs 4 and 5 (un-protected RC slabs) and Slabs 6 to 10 (insulated and strengthened RC slabs), loaded to their service load level, were exposed to the ISO 834 standard fire to evaluate the fire resistance of these specimens. The temperature responses of fire tests showed that the slabs needed fire protection to maintain the integrity between the externally bonded FRP and the concrete substrate. Besides, the fire resistance of insulated and strengthened slabs is at least the same as that of un-protected RC slabs.

Research on the fire performance of FRP-strengthened RC members was also conducted by researchers at the Queen's University and the National Research Council (NRC) of Canada in collaboration with their industry partners. In total, four slabs, six T-beams, four circular columns and one square column were tested under the ASTM E119 standard fire exposure (Kodur et al. 2007; Green et al. 2007). Kodur et al. (2004) and Williams et al. (2006) reported the fire test results of the four CFRP plates strengthened RC slabs. The dimensions of these slabs were designed as an intermediate-scale of 954 mm × 1331 mm according to the slab furnace size, and a thickness of 150 mm was selected to represent typical RC building slabs. Two different insulation materials were used to protect the strengthened slabs, and some thermocouples were arranged along the slab thickness to measure the time-temperature responses during exposure to the ASTM E119 standard fire. Slabs 1 and 2 were protected with different thickness of a two-component fire protection system consisting of a layer of Tyfo<sup>®</sup> VG insulation (VG), applied to the exterior of the CFRP plates, followed by Tyfo<sup>®</sup> EI coating (EI), applied to the outside surface of the

VG. VG is a spray-applied fire-resistant plaster that was installed in thicknesses of 19 and 38 mm for Slabs 1 and 2, respectively. EI is an intumescent epoxy surface-hardening coating, which was used in a same thickness of 0.25 mm on the exterior of the VG insulation on both slabs. Slabs 3 and 4 were insulated with 38 mm thick MBrace<sup>®</sup> Insulation I and 38 mm thick MBrace<sup>®</sup> Insulation II, respectively, both of which were made with cementitious mortars incorporating lightweight fillers. Test results indicated that a four-hour fire resistance rating (based on thermal criteria only) can be achieved for the three slabs with a 38 mm fire protection and a two-hour for the slab with a 19 mm fire protection. However, the temperatures in the FRP-to-concrete interface exceeded the glass transition temperature of bonding adhesive (around 73 °C) at early fire stages although they were kept relatively low (i.e., below 350 °C) throughout the fire tests due to the successful fire protection.

#### ***2.4.2 FRP-Strengthened RC Beams***

The earliest fire tests on steel/FRP-strengthened RC beams were conducted at the Swiss Federal Laboratories for Materials Testing and Research (EMPA) in Switzerland by Deuring (1994). In this study, six beams with a span of 5 m and a cross-section of 400 mm × 300 mm were tested under the ISO 834 standard fire exposure. One un-strengthened RC beam served as the reference beam, another beam was strengthened with an adhesively bonded steel plate for comparison purposes, while the four remaining beams were strengthened with externally bonded CFRP plates. Among the four CFRP-strengthened RC beams, two were tested without insulation and two were protected with calcium silicate boards of different thicknesses. In the protected beams, the fire insulation helped to keep low temperatures at the CFRP-to-concrete interface. For the un-protected beams, the composite action between the CFRP and the concrete was lost within the first few minutes while maintained for about one hour in the protected beams.

The second test program, consisting of ten RC beams, was performed at Ghent University (Blontrock et al. 2000; Blontrock 2003): two RC beams (a reference RC beam and a reference strengthened RC beam) were statically loaded to failure; two plain RC beams were loaded to the service load level and then exposed to fire; the other six RC beams strengthened with CFRP plates were protected with different

insulation systems and tested under the ISO-834 standard fire exposure. All the beams had a section of 200 mm in width by 300 mm in depth and a span of 2.85 m. During fire exposure, the un-strengthened and strengthened beams were subjected to the service loads, which were approximately 45% and 38% of their ultimate loads, respectively. The test results indicated that the bond between CFRP and concrete significantly degraded when the temperature of the adhesive reached  $T_g$  (i.e., 62°C). The test results also demonstrated that, compared with a flat insulation system covering the bottom of the beam only, a U-shaped fire insulation system covering the two sides and the bottom of the beam was more effective in prolonging the fire exposure time before the loss of bond strength. In addition, a U-shaped insulation system had the additional advantage of postponing the temperature increase of the internal steel reinforcement, thereby maintaining the structural integrity with small deflections over a much longer fire exposure period.

Williams (2004) and Williams et al. (2008) reported the test results of two T-beams strengthened with CFRP plates and protected with a patented two-component insulation system. The insulation system, consisting of sprayed VG plaster, was applied to the exterior surface of the CFRP reinforcement, along with a topcoat of EI coating. The VG layers installed on the two T-beams had the thicknesses of 25 mm and 38 mm respectively. For both beams, the top layer coating had a nominal thickness of 0.1 mm and covered the entire length of the beam. The test results showed that the insulated beams achieved a fire resistance rating of more than four hours under the ASTM E119 standard fire condition although the temperature at the FRP-to-concrete interface exceeded the glass transition temperature within one hour fire exposure. The insulation system was effective in protecting the FRP-strengthened RC beams from heat penetration so that the strength and stiffness of the original RC beams were well protected. Adelzadeh et al. (2012) reported another two beam tests which were both protected by a 40 mm thick layer of cement-based fire protection mortar. Only the temperature responses of the insulation layer surface, the FRP-to-the insulation layer interface and the FRP-to-concrete interface at the mid-span section of the beams were presented. These test results showed that the temperature at the FRP-to-concrete interface reached  $T_g$  after approximate 30 minutes fire exposure.

Stratford et al. (2009) investigated the performance of bonded FRP laminates in a real compartment fire [i.e., the Dalmarnock fire tests (Rein et al. 2007)]. Both near-surface mounted and externally bonded FRP laminates were employed to strengthen the concrete structure, and they were protected using either an intumescent coating or gypsum boards. The test results showed that the FRP reinforcements were vulnerable during a real compartment fire as the temperatures of the bonded interfaces exceeded the glass transition temperature relatively early in all cases.

Another experimental study was conducted by Wu and Wan (2009) who tested one un-strengthened RC beam (i.e., a reference beam) and five RC beams strengthened with CFRP sheets under the ISO 834 standard fire exposure. All the five CFRP-strengthened RC beams were protected with a flat insulation system covering the bottom of the beam. The test parameters included the thickness of the fire protection mortar layer, the fire load ratio (defined as the ratio of the load sustained during fire exposure to the ultimate load) and the strengthening ratio. While all the CFRP-strengthened RC beams were designed to fail in flexure at ambient temperature, two of them failed in shear during fire exposure. Compared to the reference RC beam, the CFRP-strengthened RC beams, even under a higher level of load, achieved better fire performance.

Further experimental work was carried out by Gao et al. (2010), who tested three RC beams strengthened with CFRP sheets under the ISO 834 standard fire exposure. Two different fire insulation systems including cement-based fire protection mortar and calcium silicate cladding boards were used to protect the CFRP reinforcement. The effect of different anchorage configurations of the CFRP sheets was also investigated. Fig. 2.6 shows the cracking of calcium silicate cladding boards after fire exposure. The test results indicated that, when a 50 mm thick mortar layer or a 40 mm thick cladding board system was used, a fire resistance rating of more than two hours could be achieved for CFRP-strengthened RC beams. Besides, a 400 mm wide U-wrap of one-layer CFRP sheet, which was used for anchorage at each end of the CFRP reinforcement outside the fire exposure zone, effectively improved the fire resistance of the strengthened beam since the CFRP reinforcement survived as an unbonded tendon to contribute to the load-bearing capacity, as it has been pointed out by other researchers as well (Ahmed 2010; Ahmed and Kodur 2011a). Fig. 2.7

shows the post-fire failure mode of the strengthened beam insulated with the 40 mm thick cladding board. After the fire insulation materials were removed, it is clearly seen that the FRP sheets were detached from the RC beam (i.e., debonding) (Fig. 2.7).

Some small-scale tests were conducted by Barns and Fidell (2006) to study the behavior of CFRP-strengthened RC beams exposed to a standard cellulosic fire condition (BSI 1987). Twenty four RC beams with a cross-section of 100 mm × 150 mm were strengthened with 100 mm × 1 mm CFRP plates. Nine beams were tested at ambient temperature as control beams. The other fifteen beams for fire exposure tests were insulated by a 15 to 20 mm thick cement-based fire protection layer; they were first exposed to fire for one hour without any loading, and afterwards they were subjected to four-point bending till failure to determine their post-fire strength and stiffness. The test results showed that the bond between FRP and concrete was lost due to fire exposure, and the FRP strengthening system, even though protected with an insulation layer, was completely destroyed; the steel bolts provided to enhance the bond were not effective once the adhesive layer was destroyed. A similar study was conducted by Zhou (2010) and Tan and Zhou (2011) to investigate the flexural behavior of RC beams strengthened with glass FRP (GFRP) and basalt FRP (BFRP) sheets after subjecting them to elevated temperatures in an electrical furnace. It was also concluded that the strength and stiffness of the strengthened RC beams were generally decreased due to exposure to elevated temperatures regardless of the type of FRP.

All the above experimental studies clearly demonstrated that the tensile and bond properties of FRP laminates deteriorated severely under fire exposure, leading to significant strength and stiffness reductions of FRP-strengthened RC beams. In addition, these studies also showed that FRP-strengthened RC beams can achieve the required fire-resistance when a suitable fire insulation system is provided. However, the limited amount of fire testing available is far from being sufficient for the generation of generic and quantitative rules for the design of insulation systems for FRP-strengthened RC beams.

#### ***2.4.3 FRP-Strengthened RC Columns***

Canadian researchers (Bisby 2003; Bisby et al. 2005b; Kodur et al. 2005; Chowdhury et al. 2007; Chowdhury 2009) conducted a series of fire tests on FRP-confined RC columns. In total, four circular columns and one square column were prepared and tested under the ASTM E119 standard fire. The circular columns were strengthened by a single layer of unidirectional CFRP sheet with a 300 mm overlap length in the circumferential direction, while the square column was wrapped with three layers of GFRP sheets. All the specimens were insulated by a two-component fire protection system, which consisted of a cementitious VG plaster with a surface coating of intumescent EI paint.

All the insulated columns were found to be able to resist the full service load for more than four hours even though the glass transition temperature of the FRP was exceeded early in the test. Fig. 2.8 shows the photographs of a typical column before and after the fire test. To provide references, one strengthened column (#3) was tested in fire without any insulation (Chowdhury et al. 2007) and achieved a fire endurance of 210 minutes. The tests clearly demonstrated the effectiveness of the insulation systems in enhancing the strength of the original column in fire by maintaining the temperatures of the internal reinforcing steel and the core concrete at low levels.

## **2.5 EXISTING NUMERICAL MODELS FOR PREDICTING THE FIRE PERFORMANCE OF FRP-STRENGTHENED RC MEMBERS**

Numerical models are effective and attractive for use in evaluating the fire performance of FRP-strengthened RC members, since full-scale fire tests are very expensive and time-consuming. Limited attempts have so far been made to use numerical modeling, as an alternative to the standard fire test, for the fire resistance evaluation of FRP-strengthened RC members. Bisby et al. (2005c) and Chowdhury et al. (2012) developed computer programs based on the fiber-section analysis to evaluate the fire resistance of FRP-confined circular and rectangular columns, respectively. Similarly, Liu et al. (2009) and Kodur and Ahmed (2010) used the fiber-section analysis approach to predict the structural capacity of insulated FRP-strengthened RC beams subjected to fire exposure. Hawileh et al. (2009) employed a nonlinear finite element (FE) model to study the temperature field and structural

response of an insulated FRP-strengthened RC T-section beam tested by Williams et al. (2008). In most of these numerical studies, both the externally bonded FRP laminate and the internal steel reinforcement were assumed to be perfectly bonded with the concrete although debonding of FRP reinforcement from concrete is well-known as a common failure mode in FRP-strengthened RC beams at ambient temperature (Teng et al. 2002). At elevated temperatures, the bond between FRP and concrete may degrade more rapidly than the FRP laminate itself (Klamer 2006; Leone et al. 2009), but very little attention has been paid to the bond degradations at both the steel-to-concrete interface and the FRP-to-concrete interface in existing numerical studies. Only Ahmed and Kodur (2011b) proposed a modified fiber-section analysis with due consideration of shear slips between FRP and concrete, where the slips were attributed solely to the shear deformation of the adhesive layer. In their model, the degradation of the FRP-to-concrete bond strength at elevated temperatures was attributed to the shear modulus degradation of the bonding adhesive based on Leone et al.'s (2009) test results. Unfortunately, this simplification is not an accurate representation of the highly nonlinear bond-slip behavior of FRP-to-concrete interfaces at both ambient and elevated temperatures.

## **2.6 EXISTING DESIGN PROVISIONS FOR THE FIRE SAFETY OF FRP-STRENGTHENED RC MEMBERS**

### ***2.6.1 Fire Safety Design Provisions Recommended by ACI 440.2R-08 (2008)***

Information obtained from previous fire tests is not adequate for establishing performance-based approaches for the fire safety design of FRP-strengthened RC members. ACI 440.2R-08 (ACI 2008) recommends ignoring the contribution of FRP strengthening system due to the high temperatures associated with the fire as well as the low temperature resistance of the FRP system. Therefore, to achieve a satisfactory fire resistance rating, the member's structural resistance to fire should be larger than the service load action, with due considerations of reduced steel and concrete strengths as described by the following equation:

$$R_{n\theta} \geq S_{DL} + S_{LL} \quad (2.2)$$

The nominal resistance of a member at an elevated temperature  $R_{n\theta}$  can be determined using the guidelines outlined in ACI 216 (2007). The load effects,  $S_{DL}$  (dead load) and  $S_{LL}$  (live load), should be determined using the load requirements for the strengthened structure. Besides, the resistance should be computed for the time period required by the structure's fire-resistance rating and should ignore the contribution of the FRP strengthening system.

The fire resistance of FRP materials can be improved through the use of fire-resistant polymers or fire protection, as recommended by the design code (ACI 2008). If such methods are verified through testing to be able to increase the fire resistance of the FRP system and to meet the fire resistance rating of a structural component, the criteria put forth in Eq. (2.2) can be modified to reflect the level of protection provided. For insulated FRP-strengthened RC members, the fire resistance of the FRP strengthening system is usually defined in association with the glass transition temperature of the polymer. That is, the fire resistance of an FRP strengthening system is the time required for the polymer matrixes or adhesives used in the FRP system to reach their glass transition temperatures.

### ***2.6.2 Fire Safety Design Provisions Proposed by Kodur et al. (2007)***

Kodur et al. (2007) recommended that the increases in strength due to FRP strengthening should typically be limited to be between about 25% and 100% based on fire safety considerations. This recommendation was proposed based on the load resistance factors used in design and the live-to-dead load ratio for the strengthened member. The ratio of expected service load on the structures during fire to the one that may cause member collapse at room temperature is typically 0.5 or less. Other design considerations and good engineering judgment also suggest limiting the strength increase due to strengthening to be significantly less than 100%. When FRP-strengthened RC members are protected with supplemental fire insulation, the insulation allows the RC members to retain more of their pre-fire strength, even if the contribution of the FRP strengthening system is lost. Therefore, the fire load levels and the insulation schemes are considered to be critical factors influencing the fire safety of FRP-strengthened RC members. Further studies are deemed necessary

in order to accurately assess the fire performance FRP-strengthened RC members under different loading levels and fire insulation schemes.

## **2.7 CONCLUSIONS AND RESEARCH NEEDS**

In summary, existing fire tests on FRP-strengthened RC members were still limited and only very limited factors governing their fire resistance were covered in these tests. Based on these limited fire tests, some researchers concluded that a certain level of insulation is needed to satisfy fire resistance requirements for FRP-strengthened RC members. In addition, existing international design guidelines and published documents have provided some prescriptive provisions on the temperature or strength limit for the fire safety design of FRP-strengthened RC members. However, all these provisions are implicit and difficult to implement in practical design. To realize performance-based fire safety design of FRP-strengthened RC beams, the following issues need to be further addressed:

(1) Considering the high cost and the significant difficulty of fire tests, it is highly desirable to conduct advanced numerical simulations for the fire resistance evaluation of FRP-strengthened RC beams. Advanced FE models are needed for the numerical analyses of the thermal and the structural behavior of unprotected (i.e., RC beams) and insulated FRP-strengthened RC beams exposed to fire considering different loading and insulation schemes.

(2) The bond behavior between FRP laminate and concrete is well known as an important issue for FRP-strengthened RC members especially in bond-critical applications. To facilitate accurate FE modeling of the structural performance of FRP-strengthened RC beams exposed to fire, an in-depth understanding of the bond-slip behavior of FRP-to-concrete interfaces under combined thermal and mechanical loading at elevated temperatures is necessary.

(3) Based on the validated FE models, extensive parametric analyses on the fire behavior of unprotected and insulated FRP-strengthened RC members are needed with the aim to develop design-oriented approaches following the performance-based methodology.

## 2.8 REFERENCES

- American Concrete Institute (ACI). (2007). "Code Requirements for Determining Fire Resistance of Concrete and Masonry Construction Assemblies." *ACI 216.1*, American Concrete Institute, Farmington Hills, Michigan, America.
- American Concrete Institute (ACI). (2008). "Guide for the design and construction of externally bonded FRP systems for strengthening concrete structures." *ACI 440.2R-08*, American Concrete Institute, Farmington Hills, Michigan, America.
- Adelzadeh, M., Benichou, N., and Green, M.F. (2012). "Behaviour of fibre reinforced polymer -strengthened T-beams and slabs in fire." *Proceedings of the ICE, Structures and Buildings*, Vol. 165, No. 7, pp. 361-371.
- Ahmed, A. (2010). "Behavior of FRP-strengthened reinforced concrete beams under fire conditions." Ph.D. thesis, Michigan State University, Michigan, America.
- Ahmed, A., and Kodur, V.K.R. (2011a). "The experimental behavior of FRP-strengthened RC beams subjected to design fire exposure." *Engineering Structures*, Vol. 33, No. 7, pp. 2201-2211.
- Ahmed, A., and Kodur, V.K.R. (2011b). "Effect of bond degradation on fire resistance of FRP-strengthened reinforced concrete beams." *Composites Part B: Engineering*, Vol. 42, No. 2, pp. 226-237.
- Bakis, C.E. (1993). "FRP reinforcement: material and manufacturing." *Fiber-Reinforced-Plastic Reinforcement for Concrete Structures: Properties and Applications*, Elsevier Science, London, pp.13-58.
- Barnes, R., and Fidell, J. (2006). "Performance in fire of small-scale CFRP strengthened concrete beams." *Journal of Composites for Construction*, ASCE, Vol. 10, No. 6, pp. 503-508.
- Bisby, L.A. (2003). "Fire behavior of fiber-reinforced polymer (FRP) reinforced or confined concrete." Ph.D. thesis, Queen's University, Kingston, Ontario, Canada.
- Bisby, L.A., Williams, B.K., Kodur, V.K.R., Green, M.F., and Chowdhury, E. (2005a). "Fire performance of FRP systems for infrastructure: a state-of-the-art report." *Research report 179*, Queen's University, Kingston, Canada.
- Bisby, L.A., Kodur, V.K.R. & Green M.F. (2005b). "Fire endurance of Fiber-reinforced polymer-confined concrete columns", *ACI Structural Journal*, Vol.102, No.6, pp. 883-891.
- Bisby, L.A., Green, M.F., and Kodur, V.K.R. (2005c). "Modeling the behavior of fiber reinforced polymer-confined concrete columns exposed to fire." *Journal of Composites for Construction*, ASCE, Vol. 9, No. 1, pp. 15-24.
- Blontrock, H., Taerwe, L., and Matthys, S. (1999). "Properties of Fiber Reinforced Plastics at Elevated Temperatures with Regard to Fire Resistance of Reinforced Concrete Members." *Fibre Reinforced Polymer Reinforcement for Reinforced Concrete Structures*. A. Nanni, C.W. Dolan, and S.H. Rizkalla, eds., American Concrete Institute, Detroit, Michigan, pp. 43-54.

- Blontrock, H., Taerwe, L., and Vandeveld, P. (2000). "Fire tests on concrete beams strengthened with fiber composite laminates." *Proceeding of the Third Ph.D. Symposium in Civil Engineering*, Vienna, Austria, pp. 151-161.
- Blontrock, H., Taerwe, L. and Vandeveld, P. (2001). "Fire testing of concrete slabs strengthened with fibre composite laminates." *Fifth Annual Symposium on Fibre-Reinforced-Plastic reinforcement for Concrete Structures (FRPRCS-5)*. C. Burgoyne, ed., Thomas Telford, London, pp. 547-556.
- Blontrock, H. (2003). "Analysis and modeling of the fire resistance of concrete elements with externally bonded FRP reinforcement." Ph. D. thesis, Ghent University, Ghent, Belgium.
- Bourbigot, S., and Flambard, X. (2002). "Heat resistance and flammability of high performance fibres: A review." *Fire and Materials*, Vol.26, No.4-5, pp. 155-168.
- British Standards Institute (BSI). (1987). "Fire tests on building materials and structures. Part 20: Method for determination of the fire resistance of elements of construction (general principles)." *BS 476-20*, BSI, London.
- Cai, Z.H. (2008). "Research on bond property of FRP-to-concrete interface under elevated temperatures." Master's thesis, Tongji University, Shanghai, China.
- Chowdhury, E.U., Bisby, L.A., Green, M.F., Benichou, N. and Kodur, V.K.R. (2007). "Investigation of insulated FRP-wrapped reinforced concrete columns in fire." *Fire Safety Journal*, Vol.42, No.6-7, pp.452-460.
- Chowdhury, E.U. (2009). "Behavior of fiber reinforced polymer confined reinforced concrete columns under fire condition." Ph.D. thesis, Department of Civil Engineering, Queen's University, Kingston, Canada.
- Chowdhury, E.U., Eedson, R., Green, M.F., Bisby, L.A., and Benichou, N. (2011). "Mechanical characterization of fiber reinforced polymers materials at high temperature." *Fire Technology*, Vol. 47, No. 4, pp. 1063-1080.
- Chowdhury, E.U., Bisby, L.A., Green, M.F., Benichou, N., and Kodur, V.K.R. (2012). "Heat transfer and structural response modelling of FRP confined rectangular concrete columns in fire." *Construction and Building Materials*, Vol. 32, pp. 77-89.
- Clarke, J.L. (1996). *Structural design of polymer composites – Eurocomp design code and handbook*. E & FN Spon. Ltd., London, UK.
- Deuring, M. (1994). "Brandversuche an nachtraglich verstärkten tragern aus Beton." Research Report, No. 148'795, Swiss Federal Laboratories for Materials Testing and Research, Dubendorf, Switzerland.
- Fédération International du Béton (fib). (2001). "Externally bonded FRP reinforcement for RC structures." *fib Bulletin 14*, fib Task Group 9.3, fib, Lausanne, Switzerland.
- Gao, W.Y., Hu, K.X., and Lu, Z.D. (2010). "Fire resistance experiments of insulated CFRP strengthened reinforced concrete beams." *China Civil Engineering Journal*, Vol. 43, No. 3, pp. 15-23 (in Chinese).
- Green, M.F., Benichou N., Kodur, V.K.R., and Bisby, L.A. (2007). "Design guidelines for fire resistance of FRP-strengthened concrete structures." *The*

*Eighth International Conference on FRP in Reinforced Concrete Structures (FRPRCS-8)*, Paper No. 14-5, University of Patras, Patras, Greece.

- Griffis, C.A., Masmura, R.A. and Chang, C.I. (1981). "Thermal response of graphite epoxy composite subjected to rapid heating." *Journal of Composite Materials*, Vol.15, No.5, pp. 427-442.
- Harries, K.A., Porter, M.L., and Busel, J.P. (2003). "FRP materials and concrete - research needs." *Concrete International*, Vol. 25, No. 10, pp. 69-74.
- Hawileh, R.A., Naser, M., Zaidan, W., and Rasheed, H.A. (2009). "Modeling of insulated CFRP-strengthened reinforced concrete T-beam exposed to fire." *Engineering Structures*, Vol. 31, No. 12, pp. 3072-3079.
- Klamer, E. (2006). "The influence of temperature on concrete structures strengthened with externally bonded CFRP." Research Report, Eindhoven University of Technology, Eindhoven, Netherlands.
- Klamer, E.L., Hordijk, D.A., and Hermes, M.C.J. (2008). "The influence of temperature on RC beams strengthened with externally bonded CFRP reinforcement." *Heron*, Vol. 53, No. 3, pp. 157-185.
- Klamer, E. (2009). "Influence of temperature on concrete beams strengthened in flexure with CFRP." Ph.D. thesis, Eindhoven University of Technology, Eindhoven, Netherlands.
- Kodur, V.K.R., Green, M.F., Bisby, L.A., and Williams, B. (2004). "Evaluating the fire performance of FRP-strengthened structures." *Concrete Engineering International*, Vol. 8, No. 2, pp. 48-50.
- Kodur, V.K.R., Bisby, L.A., Green, M.F. and Chowdhury, E. (2005). "Fire endurance of insulated FRP-strengthened square concrete columns." *7th International Symposium on Fiber-Reinforced (FRP) Polymer Reinforcement for Concrete Structures*, ACI Special Publication 230-71, pp.1253-1267.
- Kodur, V.K.R., Bisby, L.A., and Green, M.F. (2006). "FRP retrofitted concrete under fire conditions." *Concrete International*, Vol. 28, No. 12, pp. 37-44.
- Kodur, V.K.R., Bisby, L.A., and Green, M.F. (2007). "Preliminary guidance for the design of FRP-strengthened concrete members exposed to fire", *Journal of Fire Protection Engineering*, Vol. 17, No. 5, pp. 5-26.
- Kodur, V.K.R., and Ahmed, A. (2010). "Numerical model for tracing the response of FRP-strengthened RC beams exposed to fire." *Journal of Composites for Construction*, ASCE, Vol. 14, No. 6, pp. 730-742.
- Leone, M., Matthys, S., and Aiello, M.A. (2009). "Effect of elevated service temperature on bond between FRP EBR systems and concrete." *Composites Part B: Engineering*, Vol. 40, No. 1, pp. 85-93.
- Liu, F.T., Wu, B., and Wei, D.M. (2009). "Failure modes of reinforced concrete beams strengthened with carbon fiber sheet in fire." *Fire Safety Journal*, Vol. 44, No. 7, pp. 941-950.
- Mallick, P.K. (1993). *Fiber-Reinforced Composites: Materials, Manufacturing and Design (Second Edition)*, Marcel-Dekker, New York, USA.

- Mouritz, A. P. (2002). "Post-fire flexural properties of fibre-reinforced polyester, epoxy and phenolic composites." *Journal of Materials Science*, Vol. 37, No.7, pp. 1377-1386.
- Mouritz, A. P., and Gibson, A. G. (2006). *Fire properties of polymer composite materials*, Springer, Dordrecht, Netherlands.
- Reni, G., Abecassis Empis, C., and Carvel, R. (2007). *The Dalmarnock Fire Tests: Experiments and Modelling*, School of Engineering and Electronics, The University of Edinburgh, Edinburgh, UK.
- Schwartz, M.M. (1997). *Composite Materials, Volume1: Properties, Non-Destructive Testing, and Repair*, Prentice Hall, Inc. NJ, USA.
- Silva, M.A.G., and Biscaia, H. (2008). "Degradation of bond between FRP and RC beams." *Composite Structures*, Vol. 85, No. 2, pp. 164-174.
- Stratford, T.J., Gillie, M., Chen, J.F., and Usmani, A.S. (2009). "Bonded fibre reinforced polymer strengthening in a real fire." *Advances in Structural Engineering*, Vol. 12, No. 6, pp. 867-878.
- Sorathia, U., Dapp, T., and Beck, C. (2001). "Fire performance of composites." *Material Engineering*, Vol. 109, No. 9, pp. 10-12.
- Tan, K.H., and Zhou, Y.Q. (2011). "Performance of FRP-strengthened beams subjected to elevated temperatures." *Journal of Composites for Construction*, ASCE, Vol. 15, No. 3, pp. 304-311.
- Teng, J.G., Chen, J.F., Smith, S.T., and Lam, L. (2002). *FRP-strengthened RC structures*. John Wiley and Sons Ltd., Chichester, UK.
- Williams, B. (2004). "Fire performance of FRP-strengthened reinforced concrete flexural members." Ph.D. thesis, Queen's University, Kingston, Ontario, Canada.
- Williams, B., Bisby, L., Kodur, V.K.R. and Green M.F. (2006). "Fire insulation schemes for FRP-strengthened concrete slabs." *Composites Part A: Applied Science and Manufacturing*, Vol. 37, No. 8, pp. 1151-1160.
- Williams, B., Kodur, V.K.R., Green, M.F., and Bisby, L.A. (2008). "Fire endurance of fiber-reinforced polymer strengthened concrete T-beams." *ACI Structural Journal*, Vol. 105, No. 1, pp. 60-67.
- Wu, Z.S., Iwashita, K., Yagashiro, S., Ishikawa, T., and Hamaguchi, Y. (2005). "Temperature effect on bonding and debonding behavior between FRP sheets and concrete." *Journal of the Society of Materials Science*, Vol. 54, No. 5, pp. 474-480.
- Wu, B., and Wan, Z.J. (2009). "Experimental investigation into fire resistance of reinforced concrete beams strengthened in flexure with Carbon Fiber Sheets." *Journal of South China University of Technology*, Vol.40, No.6, pp.26-41 (in Chinese).
- Zhou, Y.Q. (2010). "Performance of FRP-strengthened beams subjected to elevated temperatures." Ph.D. thesis, National University of Singapore, Singapore.

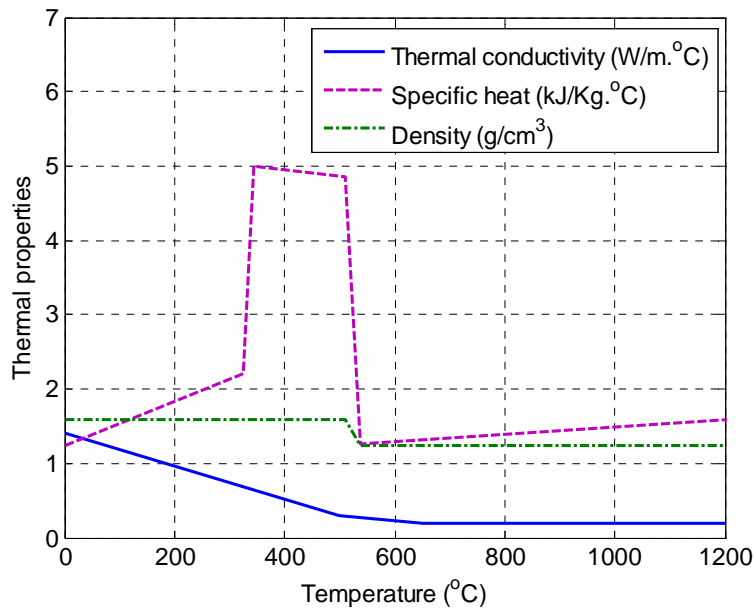


**Fig. 2.1** Thermal properties of FRP composites (Griffis et al. 1981).

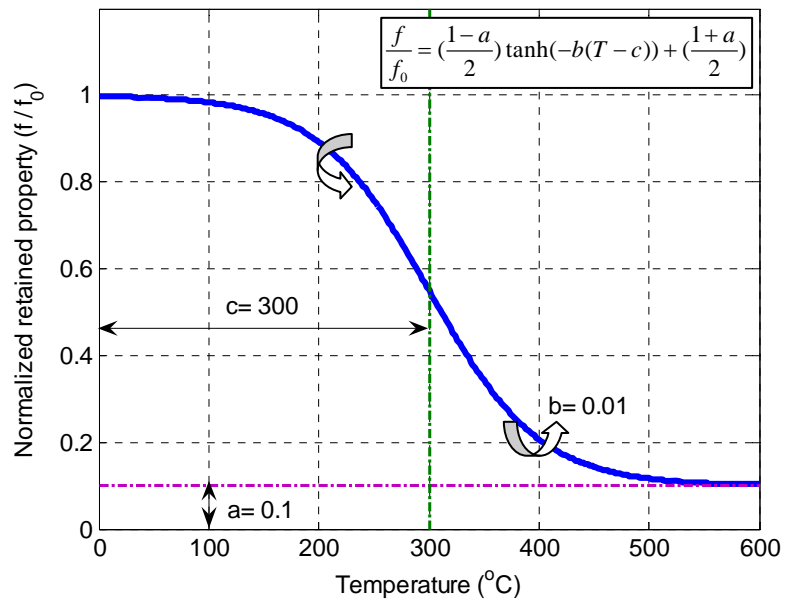


**Fig. 2.2** Property deteriorations of fibers and FRP composites at elevated temperatures.

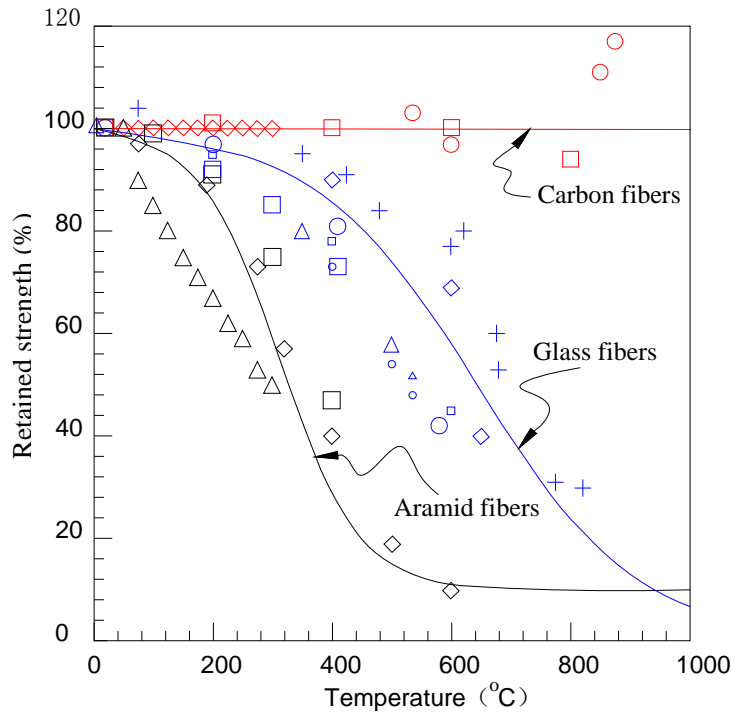


**Fig. 2.3** Temperature-dependent tensile strength degradations of fibers: test database vs. predictions (Bisby 2003).

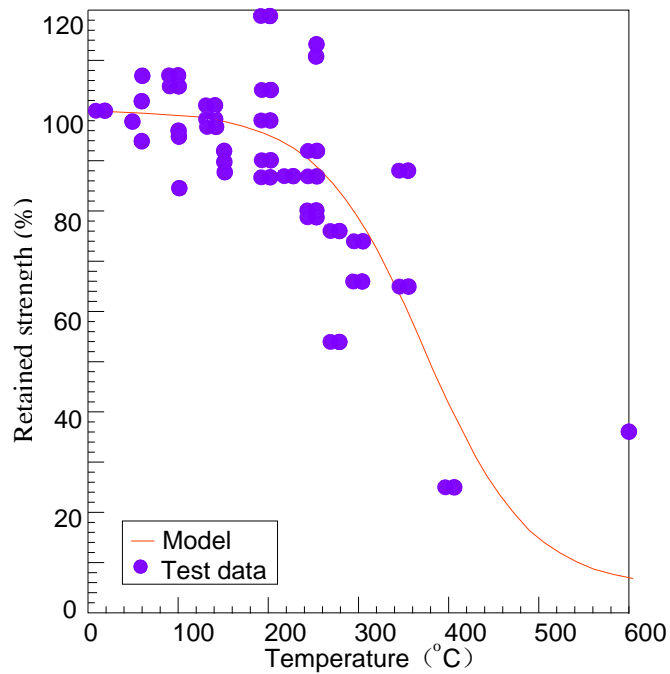


**Fig. 2.4** Tensile strength degradations of CFRP composites at elevated temperatures (Bisby 2003)

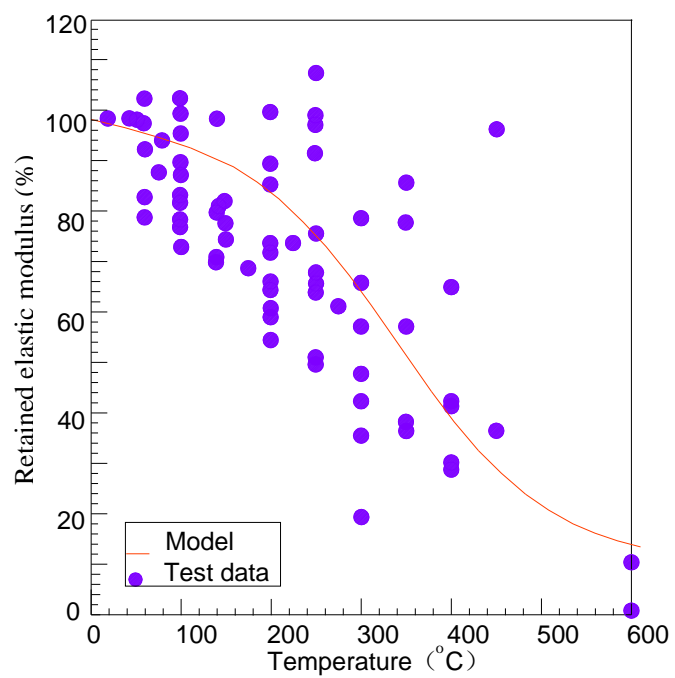


**Fig. 2.5** Elastic modulus degradations of CFRP composites at elevated temperatures (Bisby 2003)



**Fig. 2.6** Cracking of calcium silicate cladding boards (Gao et al. 2010)



**Fig. 2.7** Appearance of CFRP sheets-strengthened RC beams after the removal of the insulation materials (Gao et al. 2010)



**Fig. 2.8** Insulated FRP-strengthened concrete column before and after fire testing (Bisby et al. 2005b)

## CHAPTER 3

# EFFECT OF TEMPERATURE VARIATION ON THE FULL-RANGE BEHAVIOR OF FRP-TO-CONCRETE BONDED JOINTS

### 3.1 INTRODUCTION

In RC structures strengthened with externally bonded FRP reinforcement, the bond behavior between FRP and concrete often controls the load-carrying capacity of the strengthened structure (Teng et al. 2002; Hollaway and Teng 2008). As a result, many studies have been conducted on the bond behavior of FRP-to-concrete interfaces (e.g., Taljsten 1996; Chajes et al. 1996; Yuan et al. 2000; Brosens 2001; Chen and Teng 2001; De Lorenzis et al. 2001; Nakaba et al. 2001; Wu et al. 2002; Dai et al. 2005, 2006; Lu et al. 2005a, 2005b; Yao et al. 2005; Ferracuti et al. 2007; Wang 2007; Achintha 2009; Zhou et al. 2010; Cornetti and Carpinteri 2011). In particular, the single-lap shear test (Fig. 3.1) (or a double-lap shear test which can be seen as two single-lap shear tests being conducted simultaneously) has been widely used to study the ultimate load (i.e., the bond strength or the debonding load) of FRP-to-concrete bonded joints and the local bond-slip behavior of the FRP-to-concrete interface (e.g., Chajes et al. 1996; Brosens 2001; De Lorenzis et al. 2001; Nakaba et al. 2001; Dai et al. 2005; Yao et al. 2005).

FRP-strengthened RC structures in service are likely to experience significant temperature variations (e.g., seasonal ambient temperature changes and exposure to fire) and such variations can have a significant effect on the bond performance of FRP-to-concrete interfaces. To understand the bond behavior of FRP-to-concrete interfaces exposed to different temperature variations, the shear test has also been used (e.g., Blontrock 2003; Wu et al. 2005; Klammer 2006, 2009; Leone et al. 2009). Results from such tests reflect directly the combined effects of a number of factors including temperature-induced interfacial stresses and temperature-induced property changes in the bondline (the adhesive and the adjacent parts of the adherends) as

well as the adherends if the temperature becomes sufficiently high. A key purpose of such shear tests is to determine the bond-slip curve of the interface at a specific temperature variation, for which the effect of thermal interfacial stresses needs to be isolated from the effect of temperature-induced material property changes, as only the latter should be included in a bond-slip model for use in a theoretical model for FRP-strengthened RC structures subjected to temperature variations. This issue has received little attention and indeed in some existing studies, these thermal stresses were simply ignored in interpreting shear test results (e.g., Wu et al. 2005; Leone et al. 2009).

More recently, Rabinovitch (2010) employed linear elastic fracture mechanics (LEFM) and a high-order interfacial stress analysis to study the effect of temperature variation on debonding in FRP-strengthened concrete members. However, his analysis is incapable of predicting the full-range nonlinear behavior of the bonded interface between FRP and concrete. Indeed, given the importance of the softening behavior of the bonded interface after attaining the peak bond stress, an LEFM approach is in general inadequate. This chapter presents a theoretical study on the full-range behavior of FRP-to-concrete bonded joints at a specific temperature variation from the reference ambient temperature at installation (referred to as the reference temperature hereafter). An analytical solution, which is an extension of the existing analytical solution of Yuan et al. (2004) for mechanical loading only, is first presented, to predict the responses of FRP-to-concrete bonded joints under combined thermal and mechanical action. The validity of the analytical solution is demonstrated through comparisons with the limited available experimental results as well as results from a FE model. The effects of temperature variations on the load-displacement response, the ultimate load, the interfacial shear stress distribution and the interfacial slip distribution are all examined in this chapter. Finally, the relationship between the maximum pull load of FRP-to-concrete bonded joints and the interfacial fracture energy is proposed considering the temperature variation effects.

## **3.2 ANALYTICAL SOLUTION**

### 3.2.1 Assumptions and Notation

Fig. 3.1 shows the theoretical idealization of a single-lap bonded joint where both adherends are assumed to experience only membrane deformation. Moreover, it is assumed that the width and thickness of each of the three components (FRP laminate, adhesive layer and concrete prism) are constant in the longitudinal direction. In such a simplified theoretical model, the adhesive layer (representing the interface or the bondline whose deformation represents the deformation of the actual adhesive layer and that of the adjacent parts of the two adherends) is subjected to shear deformation, so that mode II interfacial fracture is the failure mode. This theoretical model is a close approximation of the behavior of a real bonded joint (Yuan et al. 2004; Teng et al. 2006; Chen et al. 2007). In addition, it is assumed that the interface is still within the linear elastic range of behavior and the properties of the adherends are not affected during the imposition of the thermal loading; these two assumptions means that the degree of temperature variation needs to be appropriately limited. The applicability of the solution to bonded joints whose adherends have experienced temperature-induced property degradations is discussed later in this chapter.

In Fig. 3.1,  $b_p$ ,  $t_p$  and  $L$  are the thickness, width and bond length of the FRP laminate, respectively, while  $b_c$  and  $t_c$  are the width and thickness of the concrete prism, respectively. The elastic moduli of the plate and the concrete are  $E_p$  and  $E_c$ , respectively. For convenience of presentation, the left end of the plate ( $x=0$ ) is referred to as the free end and the right end ( $x=L$ ) the loaded end hereafter.

### 3.2.2 Governing Equations

Based on the above assumptions, the horizontal equilibrium consideration of the FRP laminate and of the overall joint cross-section leads to the following equations:

$$\frac{d\sigma_p}{dx} - \frac{\tau}{t_p} = 0 \quad (3.1)$$

$$\sigma_p t_p b_p + \sigma_c t_c b_c = 0 \quad (3.2)$$

where  $\tau$  is the shear stress in the adhesive layer (the interfacial shear stress),  $\sigma_p$  is the axial stress in the FRP laminate and  $\sigma_c$  is the axial stress in the concrete prism. The constitutive equations for the adhesive layer and the two adherends are described by

$$\tau = f(\delta) \quad (3.3)$$

$$\sigma_p = E_p \left( \frac{du_p}{dx} - \alpha_p \Delta T \right) \quad (3.4)$$

$$\sigma_c = E_c \left( \frac{du_c}{dx} - \alpha_c \Delta T \right) \quad (3.5)$$

where  $u_p$  and  $u_c$  are the longitudinal displacements of the FRP laminate and the concrete, respectively;  $\alpha_p$  and  $\alpha_c$  are the coefficients of thermal expansion of the FRP laminate and the concrete, respectively; and  $\Delta T$  is the service temperature variation (thermal loading). The interfacial slip  $\delta$  is defined as the relative displacement between the two adherends; that is

$$\delta = u_p - u_c \quad (3.6)$$

From Eqs. (3.1)-(3.6), the following second-order differential equation can be derived:

$$\frac{d^2\delta}{dx^2} - \frac{2G_f}{\tau_f^2} \lambda^2 f(\delta) = 0 \quad (3.7)$$

where

$$\lambda^2 = \frac{\tau_f^2}{2G_f} \left( \frac{1}{E_p t_p} + \frac{b_p}{E_c t_c b_c} \right) \quad (3.8)$$

In Eqs. (3.7) and (3.8),  $\tau_f$  is the local bond strength (i.e., the maximum shear stress on the bond-slip curve) and  $G_f$  is the interfacial fracture energy (the area underneath the interfacial bond-slip curve). Substituting Eq. (3.6) into Eqs. (3.2), (3.4) and (3.5) yields

$$\sigma_p = \frac{\tau_f^2}{2G_f t_p \lambda^2} \left[ \frac{d\delta}{dx} - (\alpha_p - \alpha_c) \Delta T \right] \quad (3.9)$$

### 3.2.3 Bond-Slip Model

A bilinear bond-slip model has been widely used to study the bond behavior of FRP-to-concrete bonded joints (e.g., Yuan et al. 2004) as it closely reflects the actual bond-slip response (Lu et al. 2005a). Such a bilinear model is also adopted in the present study. As shown in Fig. 3.2, the bilinear bond-slip relationship consists of two segments: an initial linear elastic segment where the bond shear stress increases linearly with the interfacial slip until it reaches the peak stress  $\tau_f$  (the corresponding slip is denoted by  $\delta_1$ ) and a softening segment where the shear stress reduces with the interfacial slip until it becomes zero (the corresponding slip is denoted by  $\delta_f$ ). Note that the same shape is assumed for the bond-slip curve for shear stresses and slips in the opposite direction, but only the curve for positive values of  $\delta$  is shown in Fig. 3.2. This bond-slip model (Fig. 3.2) is described by the following equation:

$$f(\delta) = \begin{cases} \frac{\tau_f}{\delta_1} \delta & \text{when } 0 < \delta \leq \delta_1 \\ \frac{\tau_f}{\delta_f - \delta_1} (\delta_f - \delta) & \text{when } \delta_1 < \delta \leq \delta_f \\ 0 & \text{when } \delta > \delta_f \end{cases} \quad (3.10)$$

For the present analytical solution, it is assumed that the bond-slip law is fully reversible if slip reversals occur during the deformation process. The implications of this assumption are further discussed later in the chapter.

### 3.2.4 Stages of the Debonding Process

With the bond-slip model defined above and following the approach of Yuan et al. (2004), the governing equation [Eq. (3.7)] can be solved to find the interfacial shear stress distribution and interfacial slip distribution along the interface and the load-displacement response of the bonded joint under combined thermal and mechanical loadings.

For a bond-slip model as shown in Fig. 3.2, the entire deformation process can be divided into four stages (Yuan et al. 2004): (1) the elastic stage (Stage I), during which the load  $P$  is small and the interfacial shear stress stays below  $\tau_f$ ; (2) the elastic-softening stage (Stage II), during which the shear slip at the loaded end has exceeded  $\delta_1$  but is smaller than  $\delta_f$ ; (3) the elastic-softening-debonding stage (Stage III), during which the interfacial slip at the loaded end has exceeded the separation slip  $\delta_f$  and the shear stress there has reduced to zero; during this stage, interfacial debonding initiates at the loaded end and propagates along the interface; and (4) the softening-debonding stage (Stage IV), during which the elastic zone has disappeared as a result of propagation of debonding. For a bonded joint under mechanical load only, these stages are illustrated using the interfacial shear stress and slip distributions as well as the load-displacement response obtainable from Yuan et al.'s (2004) solution in Fig. 3.3; these results are for plate and concrete material properties from Klamer's (2006) tests and a bond-slip curve as described in Section 3.1. For a clearer presentation, the interfacial shear stresses and slips in Fig. 3.3 are normalized by  $\tau_f$  and  $\delta_f$ , respectively. The results shown in Fig. 3.3 also provide the reference point for the solution presented below.

### 3.2.5 Elastic Stage (Stage I)

During the elastic stage (Fig. 3.3a), the bond-slip curve is given by the first expression of Eq. (3.10). Substituting Eq. (3.10) into Eq. (3.7), the following differential equation is obtained:

$$\frac{d^2\delta}{dx^2} - \lambda_1^2 \delta = 0 \quad (3.11)$$

where

$$\lambda_1^2 = \frac{2G_f}{\delta_1 \tau_f} \lambda^2 = \frac{\tau_f}{\delta_1} \left( \frac{1}{E_p t_p} + \frac{b_p}{E_c t_c b_c} \right) \quad (3.12)$$

Substituting the boundary conditions ( $\sigma_p = 0$  at  $x = 0$ ;  $\sigma_p = \frac{P}{b_p t_p}$  at  $x = L$ ) into Eq. (3.11), the expressions for the interfacial slip, the interfacial shear stress and the axial stress in the plate are obtained:

$$\delta = \left\{ \frac{P \lambda_1 \delta_1}{b_p \tau_f} + \frac{(\alpha_p - \alpha_c) \Delta T [1 - \cosh(\lambda_1 L)]}{\lambda_1} \right\} \cdot \frac{\cosh(\lambda_1 x)}{\sinh(\lambda_1 L)} + \frac{(\alpha_p - \alpha_c) \Delta T}{\lambda_1} \cdot \sinh(\lambda_1 x) \quad (3.13)$$

$$\tau = \frac{\tau_f}{\delta_1} \left\{ \left[ \frac{P \lambda_1 \delta_1}{b_p \tau_f} + \frac{(\alpha_p - \alpha_c) \Delta T [1 - \cosh(\lambda_1 L)]}{\lambda_1} \right] \cdot \frac{\cosh(\lambda_1 x)}{\sinh(\lambda_1 L)} + \frac{(\alpha_p - \alpha_c) \Delta T}{\lambda_1} \cdot \sinh(\lambda_1 x) \right\} \quad (3.14)$$

$$\sigma_p = \frac{\tau_f}{\delta_1 t_p \lambda_1^2} \left\{ \left[ \frac{P \lambda_1^2 \delta_1}{b_p \tau_f} + (\alpha_p - \alpha_c) \Delta T [1 - \cosh(\lambda_1 L)] \right] \cdot \frac{\sinh(\lambda_1 x)}{\sinh(\lambda_1 L)} + (\alpha_p - \alpha_c) \Delta T \cdot \cosh(\lambda_1 x) - (\alpha_p - \alpha_c) \Delta T \right\} \quad (3.15)$$

The slip at the loaded end (i.e., the value of  $\delta$  at  $x=L$ ) is also referred to as the displacement of the bonded joint and is denoted by  $\Delta$ . Based on this definition, the load-displacement relationship is given by:

$$P = \Delta \times \left\{ \left[ 1 - \frac{(\alpha_p - \alpha_c) \Delta T}{\lambda_1 \Delta} \cdot \sinh(\lambda_1 L) \right] - \frac{(\alpha_p - \alpha_c) \Delta T [1 - \cosh(\lambda_1 L)]}{\lambda_1 \Delta \cdot \tanh(\lambda_1 L)} \right\} \cdot \frac{b_p \tau_f}{\lambda_1 \delta_1} \cdot \tanh(\lambda_1 L) \quad (3.16)$$

The initial displacement  $\Delta_0$  due to the temperature variation can be calculated as [i.e.  $P=0$  and  $x=L$  in Eq. (3.13)]:

$$\Delta_0 = \frac{(\alpha_p - \alpha_c) \Delta T [1 - \cosh(\lambda_1 L)]}{\lambda_1} \cdot \text{ctanh}(\lambda_1 L) + \frac{(\alpha_p - \alpha_c) \Delta T}{\lambda_1} \cdot \sinh(\lambda_1 L) \quad (3.17)$$

At the end of the elastic stage, the interfacial shear stress reaches  $\tau_f$  with a slip  $\delta_1$  at the loaded end. Substituting  $\Delta = \delta_1$  at  $x=L$  into Eq. (3.13) leads to the load at the initiation of interfacial softening (the beginning of the elastic-softening stage):

$$P_e = \left\{ \left[ 1 - \frac{(\alpha_p - \alpha_c) \Delta T}{\lambda_1 \delta_1} \cdot \sinh(\lambda_1 L) \right] - \frac{(\alpha_p - \alpha_c) \Delta T [1 - \cosh(\lambda_1 L)]}{\lambda_1 \delta_1 \cdot \tanh(\lambda_1 L)} \right\} \cdot \frac{b_p \tau_f}{\lambda_1} \cdot \tanh(\lambda_1 L) \quad (3.18)$$

For an infinite bond length, Eq. (3.18) reduces to

$$P_e = \left[ 1 - \frac{(\alpha_p - \alpha_c) \Delta T}{\lambda_1 \delta_1} \right] \cdot \frac{\tau_f b_p}{\lambda_1} \quad (3.19)$$

### 3.2.6 Elastic-Softening Stage (Stage II)

When the loaded end slip first exceeds  $\delta_1$ , the free end slip is still less than  $\delta_1$ , so the right part of the interface (i.e., the part near the loaded end) is now in a softening state while the left part of the interface (i.e., the part near the free end) is still in the linear elastic state (Fig. 3.3a). As the load  $P$  further increases, the length of the softening zone (denoted as  $a$ ) also increases. Substituting the relevant relationships given by Eq. (3.10) into Eq. (3.7), the following governing equations for the elastic-softening stage can be obtained:

$$\frac{d^2\delta}{dx^2} - \lambda_1^2 \delta = 0 \quad \text{for } 0 \leq \delta \leq \delta_1 \quad (3.20)$$

$$\frac{d^2\delta}{dx^2} + \lambda_2^2 \delta = \lambda_2^2 \delta_f \quad \text{for } \delta_1 < \delta \leq \delta_f \quad (3.21)$$

where

$$\lambda_2^2 = \frac{2G_f}{(\delta_f - \delta_1)\tau_f} \lambda^2 = \frac{\tau_f}{(\delta_f - \delta_1)} \left( \frac{1}{E_p t_p} + \frac{b_p}{E_c t_c b_c} \right) \quad (3.22)$$

The boundary conditions are defined as:

$$\sigma_p = 0 \quad \text{at } x = 0 \quad (3.23)$$

$$\sigma_p \text{ is continuous at } x = L - a \quad (3.24)$$

$$\tau = \tau_f \text{ at } x = L - a \quad (3.25)$$

$$\sigma_p = \frac{P}{b_p t_p} \text{ at } x = L \quad (3.26)$$

Making use of the boundary conditions, the solutions in the elastic zone ( $0 \leq x \leq L - a$ ,  $0 \leq \delta \leq \delta_1$ ) have the same form as Eqs. (3.13)-(3.15):

$$\delta = \frac{\lambda_1 \delta_1 - (\alpha_p - \alpha_c) \Delta T \sinh(\lambda_1(L-a))}{\lambda_1 \cosh(\lambda_1(L-a))} \cdot \cosh(\lambda_1 x) + \frac{(\alpha_p - \alpha_c) \Delta T}{\lambda_1} \cdot \sinh(\lambda_1 x) \quad (3.27)$$

$$\tau = \frac{\tau_f}{\delta_1} \left\{ \frac{\lambda_1 \delta_1 - (\alpha_p - \alpha_c) \Delta T \sinh(\lambda_1(L-a))}{\lambda_1 \cosh(\lambda_1(L-a))} \cdot \cosh(\lambda_1 x) + \frac{(\alpha_p - \alpha_c) \Delta T}{\lambda_1} \cdot \sinh(\lambda_1 x) \right\} \quad (3.28)$$

$$\sigma_p = \frac{\tau_f}{\lambda_1^2 t_p \delta_1} \left\{ \frac{\lambda_1 \delta_1 - (\alpha_p - \alpha_c) \Delta T \sinh(\lambda_1(L-a))}{\cosh(\lambda_1(L-a))} \cdot \sinh(\lambda_1 x) + [\cosh(\lambda_1 x) - 1](\alpha_p - \alpha_c) \Delta T \right\} \quad (3.29)$$

In the softening zone ( $L - a \leq x \leq L$ ,  $\delta_1 < \delta \leq \delta_f$ ), the interfacial slip, the interfacial shear stress and the axial stress in the FRP laminate are given by:

$$\delta = \delta_f + \frac{1}{\lambda_2} \left[ \lambda_1 \delta_1 \tanh(\lambda_1(L-a)) + \frac{(\alpha_p - \alpha_c) \Delta T}{\cosh(\lambda_1(L-a))} \right] \cdot \sin(\lambda_2(x-L+a)) + (\delta_1 - \delta_f) \cdot \cos(\lambda_2(x-L+a)) \quad (3.30)$$

$$\tau = -\tau_f \left\{ \frac{1}{\lambda_2(\delta_f - \delta_1)} \left[ \lambda_1 \delta_1 \cdot \tanh(\lambda_1(L-a)) + \frac{(\alpha_p - \alpha_c) \Delta T}{\cosh(\lambda_1(L-a))} \right] \cdot \sin(\lambda_2(x-L+a)) - \cos(\lambda_2(x-L+a)) \right\} \quad (3.31)$$

$$\sigma_p = -\frac{\tau_f}{\lambda_1^2 t_p \delta_1} (\alpha_p - \alpha_c) \Delta T + \frac{\tau_f}{t_p \lambda_1^2 \delta_1} \left[ \lambda_1 \delta_1 \tanh(\lambda_1(L-a)) + \frac{(\alpha_p - \alpha_c) \Delta T}{\cosh(\lambda_1(L-a))} \right] \cdot \cos(\lambda_2(x-L+a)) + \frac{\tau_f}{t_p \lambda_2} \cdot \sin(\lambda_2(x-L+a)) \quad (3.32)$$

Substituting the boundary condition  $\sigma_p = \frac{P}{b_p t_p}$  at the loaded end ( $x=L$ ) into Eq. (3.32) yields

$$P = -\frac{b_p \tau_f}{\lambda_1^2 \delta_1} (\alpha_p - \alpha_c) \Delta T + \frac{b_p \tau_f}{\lambda_1^2 \delta_1} \left[ \lambda_1 \delta_1 \tanh(\lambda_1(L-a)) + \frac{(\alpha_p - \alpha_c) \Delta T}{\cosh(\lambda_1(L-a))} \right] \cdot \cos(\lambda_2 a) + \frac{b_p \tau_f}{\lambda_2} \cdot \sin(\lambda_2 a) \quad (3.33)$$

and the displacement  $\Delta$  at the loaded end can be found from Eq. (3.30) (i.e.,  $x=L$ ) to be

$$\Delta = \delta_f + \frac{1}{\lambda_2} \left[ \lambda_1 \delta_1 \tanh(\lambda_1(L-a)) + \frac{(\alpha_p - \alpha_c) \Delta T}{\cosh(\lambda_1(L-a))} \right] \cdot \sin(\lambda_2 a) + (\delta_1 - \delta_f) \cdot \cos(\lambda_2 a)$$

(3.34)

Eqs. (3.33) and (3.34) can be used to predict the load-displacement relationship for the elastic-softening stage by varying the value of  $a$ .

### 3.2.7 Elastic-Softening-Debonding Stage (Stage III)

At the end of Stage II (Fig. 3.3a), the slip at the loaded end  $\Delta$  reaches  $\delta_f$ , indicating the initiation of debonding at the loaded end. The corresponding value of  $a$  is its maximum possible value (denoted by  $a_d$ ) and is determined using the following equation which is obtained from Eq. (3.34):

$$\frac{1}{\lambda_2} \left[ \lambda_1 \delta_1 \tanh(\lambda_1(L - a_d)) + \frac{(\alpha_p - \alpha_c)\Delta T}{\cosh(\lambda_1(L - a_d))} \right] \cdot \sin(\lambda_2 a_d) + (\delta_1 - \delta_f) \cdot \cos(\lambda_2 a_d) = 0 \quad (3.35)$$

Substituting Eq. (3.35) into Eq. (3.33) yields

$$P_u = \frac{b_p \tau_f}{\lambda_2} \cdot \frac{\delta_f}{\delta_f - \delta_1} \cdot \sin(\lambda_2 a_d) - \frac{b_p \tau_f}{\lambda_1^2 \delta_1} (\alpha_p - \alpha_c) \Delta T \quad (3.36)$$

For an infinite bond length, Eq. (3.35) reduces to

$$a_d = \frac{1}{\lambda_2} \arctan \left\{ \frac{\lambda_1}{\lambda_2} \right\} \quad (3.37)$$

and Eq. (3.36) reduces to

$$P_u = \frac{b_p \tau_f}{\lambda} - \frac{b_p \tau_f}{\lambda_1^2 \delta_1} (\alpha_p - \alpha_c) \Delta T \quad (3.38)$$

As the debonding crack propagates, the location of the peak shear stress  $\tau_f$  moves away from the loaded end towards the free end, and as a result, the total length of the intact interface reduces and the pull load starts to decrease (unless the bond length is infinitely long for which the pull load remains constant during crack propagation).

Assuming that the length of the debonded interface is  $d$  (see Fig. 3.3a), the equations derived for Stage II for the interfacial slip, the interfacial shear stress, the FRP laminate axial stress [Eqs. (3.27)-(3.32)] and the pull load [Eq. (3.33)] are still valid for Stage III if  $L$  is replaced by  $(L-d)$ . The displacement can be evaluated with the consideration of thermal deformation in the debonded zone and is given by the following equation:

$$\Delta = \delta_f + \frac{P}{b_p} \left( \frac{1}{E_p t_p} + \frac{b_p}{E_c t_c b_c} \right) d + (\alpha_p - \alpha_c) \Delta T d \quad (3.39)$$

### 3.2.8 Softening-Debonding Stage (Stage IV)

The softening-debonding stage initiates when  $L - d = a_u$  (Fig. 3.3a), and it is governed by Eq. (3.21) with the following boundary conditions:

$$\sigma_p = 0 \text{ at } x = 0 \quad (3.40)$$

$$\delta = \delta_f \text{ and } \sigma_p = \frac{P}{b_p t_p} \text{ at } x = a_u \quad (3.41)$$

The following solution can thus be found for  $0 \leq x \leq a_u$

$$\delta = \delta_f + A \sin(\lambda_2 x) + B \cos(\lambda_2 x) \quad (3.42)$$

$$\tau = \frac{\tau_f}{\delta_f - \delta_1} \cdot (\delta_f - \delta) \quad (3.43)$$

$$\sigma_p = \frac{\tau_f}{\lambda_2^2 t_p (\delta_f - \delta_1)} [A \lambda_2 \cos(\lambda_2 x) - B \lambda_2 \sin(\lambda_2 x) - (\alpha_p - \alpha_c) \Delta T] \quad (3.44)$$

where

$$A = \frac{1}{\lambda_2} (\alpha_p - \alpha_c) \Delta T \quad (3.45)$$

$$B = - \left[ \frac{(\alpha_p - \alpha_c) \Delta T}{\lambda_2} + \frac{P \lambda_2 (\delta_f - \delta_1)}{b_p \tau_f} \right] \sin(\lambda_2 a_u) \quad (3.46)$$

$$a_u = \frac{1}{\lambda_2} \cdot \arccos \left[ \frac{\frac{1}{\lambda_2}(\alpha_p - \alpha_c)\Delta T}{\frac{1}{\lambda_2}(\alpha_p - \alpha_c)\Delta T + \frac{P\lambda_2(\delta_f - \delta_1)}{b_p\tau_f}} \right] \quad (3.47)$$

Eq. (3.47) indicates that as the pull load increases, the softening zone length  $a_u$  (over which interfacial shear stresses exist) increases if  $\Delta T > 0$  but decreases if  $\Delta T < 0$ . The load-displacement relationship can be obtained by replacing  $d$  with  $(L - a_u)$  in Eq. (3.39):

$$\Delta = \delta_f + \frac{P}{b_p} \left( \frac{1}{E_p t_p} + \frac{b_p}{E_c t_c b_c} \right) (L - a_u) + (\alpha_p - \alpha_c)\Delta T(L - a_u) \quad (3.48)$$

During this softening-debonding stage, if there is no thermal loading, Eq. (3.47) indicates that  $a_u$  is a constant (Yuan et al. 2004; Fig. 3.3b) and the slip at the loaded end reduces linearly with the load as indicated by Eq. (3.48). At the same time, the slip at the free-end increases as the load reduces and when this slip reaches  $\delta_f$ , the slip values everywhere along the interface are equal to  $\delta_f$  (Fig. 3.3b), which means that the entire interface has debonded and the pull load is now zero. Note that during the entire deformation process, although slip reversals occur near the loaded end, these reversals are never large enough to reduce a slip value larger than  $\delta_f$  to below  $\delta_f$ ; that is, slip reversals do not have any implication for the assumed bond-slip model. However, when thermal loading exists, the response of the bonded joint becomes more complicated during this stage and depends on whether  $\Delta T > 0$  or  $\Delta T < 0$ .

When  $\Delta T < 0$ , the softening zone length  $a_u$  with active shear stresses becomes shorter than that of the reference temperature case (Fig. 3.11d). Similar to the reference temperature case, when the slip at the free end reaches  $\delta_f$ , the slip values everywhere along the entire interface are larger than  $\delta_f$  (Fig. 3.11d) (hence the softening zone length  $a_u$  reduces to zero) and the pull load becomes zero.

When  $\Delta T > 0$ , the softening zone length  $a_u$  becomes greater than that of the reference temperature case (Fig. 3.10d) and before the entire interface reaches

debonding, parts of the interface have experienced slip reversals to values below  $\delta_f$  (Figs. 3.10d and 3.10e). Due to these slip reversals, the analytical solution depends on the assumed behavior of the bond-slip model during such slip reversals. For simplicity of solution, it is assumed for the present solution that the bond-slip relationship is fully reversible when local slip reversals occur. The effect of assuming a different unloading path for slip reversals is examined later using an FE model (Figs. 3.10d and 3.10e). Under the assumption of a fully reversible bond-slip law, the softening zone expands towards the loaded end during this stage, due to the assumed ability of the debonded interface to regain resistance. This expansion ends when the slip at the free end reaches  $\delta_f$  and the softening zone length  $a_u$  reaches its maximum possible value  $a_{umax}$  (Fig. 3.10d). Afterwards, the boundary condition described by Eq. (3.41) is no longer valid. Different from the case of  $\Delta T < 0$ , the fact that the free-end slip reaches  $\delta_f$  does not mean that interfacial slip values at other locations of the interface are larger than  $\delta_f$ . After the free-end slip reaches  $\delta_f$  (referred to as Stage IV'), the boundary condition at the free end becomes:

$$\tau = 0 \text{ and } \sigma_p = 0 \text{ at } x = 0 \quad (3.49)$$

Substituting Eq. (3.49) into the governing equation [i.e., Eq. (3.21)] leads to a solution that has the same form as Eqs. (3.42)-(3.44) with the parameters  $A$  and  $B$  being given by

$$A = \frac{1}{\lambda_2} (\alpha_p - \alpha_c) \Delta T \quad (3.50)$$

$$B = 0 \quad (3.51)$$

During Stage IV', the bond length with active bond stresses (i.e., defined as  $a'_u$ ) decreases from  $a_{umax}$  and the load-displacement response can be obtained from the following equations:

$$P = \frac{\tau_f b_p}{\lambda_2^2 (\delta_f - \delta_1)} [(\alpha_p - \alpha_c) \Delta T \cos(\lambda_2 a'_u) - (\alpha_p - \alpha_c) \Delta T] \quad (3.52)$$

$$\Delta = \delta_f + \frac{1}{\lambda_2} (\alpha_p - \alpha_c) \Delta T \sin(\lambda_2 a'_u) \quad (3.53)$$

Eq. (3.52) clearly indicates that  $P$  is always zero if there is no thermal loading (i.e.,  $\Delta T = 0$ ), which means that Stage IV' does not exist when  $\Delta T = 0$ .

### 3.2.9 Load-Displacement Responses

According to the closed-form solution presented above, the entire load-displacement curve of an FRP-to-concrete bonded joint subjected to combined thermal and mechanical loadings can be obtained. Fig. 3.3c shows the load-displacement response of a typical bonded joint at reference temperature, in which the segments from OA, AB, BC and CD correspond to the elastic stage (Stage I), elastic-softening stage (Stage II), elastic-softening-debonding stage (Stage III) and softening-debonding stage (Stage IV), respectively. During the elastic stage, the pull load increases linearly with the displacement, followed by a nonlinear increase up to a peak value, which is reached at the slip value of  $\delta_f$ . The ultimate load remains basically unchanged (i.e., reduces very slowly) during the elastic-softening-debonding stage for a range of displacement values if the bond length is sufficiently long. Afterwards, the load-displacement curve exhibits a descending part first and then a snapback part, which ends at a displacement value of  $\delta_f$ .

## 3.3 VALIDATION OF THE ANALYTICAL SOLUTION

To verify the analytical solution, analytical predictions are compared in this section with the limited experimental results available in the literature (Klamer 2006, 2009). In addition, a simple FE model was developed to provide FE predictions to further demonstrate the validity of the analytical solution.

### 3.3.1 Klamer's Tests

Klamer (2006, 2009) conducted a series of shear tests on double-lap FRP-to-concrete bonded joints (Fig. 3.4a) at temperatures ranging from  $-20$  °C to  $100$  °C. The test specimens (including the installation of strain gauges on the FRP plate) were

prepared at 20 °C (the reference temperature) but the tests were conducted at a different temperature (-20 °C, 20 °C, 40 °C, 50 °C, 70 °C, 80 °C or 100 °C). The thicknesses of the FRP pultruded plate and the adhesive layer were 1.2 mm and 1.5 mm, respectively, while the bond length was 300 mm. In making the predictions, the following geometric and material properties were used as provided by Klamer (2006):  $b_p = 100$  mm,  $t_c = 75$  mm,  $b_c = 150$  mm,  $E_p = 165$  GPa,  $E_c = 26.8$  GPa,  $\alpha_c = 10.2 \times 10^{-6}/^\circ\text{C}$  and  $\alpha_p = 0.3 \times 10^{-6}/^\circ\text{C}$ . From the experimental load-displacement curves of the two specimens tested at reference temperature (20 °C), the load and slip values corresponding to the initiation of softening were identified (i.e., defined based on inspection) to be 20 kN and 0.09 mm, respectively. The ultimate load was averaged from the two test values to be 45.92 kN and hence the interfacial fracture energy was found to be 0.57 N/mm (Yuan et al. 2004). The other two parameters of the bond-slip curve, namely  $\delta_f$  and  $\tau_f$ , were identified by least square analysis to obtain a best-fit curve for the combined data of the two test load-displacement curves. The results turned out to be:  $\delta_f = 0.41$  mm and  $\tau_f = 2.77$  MPa. Fig. 3.4b shows a comparison between the two test load-displacement curves and the corresponding curve predicted using the analytical solution of Yuan et al. (2004) (which is a special case of the present solution) and based on the identified bond-slip curve, indicating that the identified bond-slip curve leads to close predictions of the test results.

### ***3.3.2 Comparisons with Test Results of Klamer (2006)***

Fig. 3.5a presents a comparison between the predicted thermal strains in the CFRP plate and the experimental values for one of the specimens which was subjected to a temperature increase of 30 °C (i.e.,  $\Delta T = 30$  °C) before the mechanical load was applied [Klamer (2006) reported the thermal strains of the FRP plate only for this specimen]. The close agreement between the test results and the analytical predictions demonstrates the validity of the present closed-form solution when only the thermal loading is considered.

Fig. 3.5b shows a comparison between the ultimate loads of FRP-to-concrete bonded joints obtained from Klamer's (2006) tests and the analytical solution. In this figure, the ultimate loads are normalized by the corresponding (experimental or predicted)

value for the reference temperature of 20 °C for a clearer comparison. It is seen that the experimental ultimate load initially increases as the temperature increases (or decreases as the temperature reduces) but the trend reverses when the temperature is around the glass transition temperature  $T_{g,a}$  of the bonding adhesive which was 62 °C [as provided by the manufacturer and reported by Klamer (2006)]. As shown in Fig. 3.5b, the analytical ultimate load increases monotonically with the temperature. The difference between the experimental ultimate load and the analytical prediction for temperatures above the glass transition temperature is due to the omission of the effect of softening of the bonding adhesive: in the present predictions, the bilinear bond-slip law was identified from the test results for the reference temperature of 20 °C. In addition, any softening of the adherends was also ignored. The reasonably close agreement between the experimental results and the analytical predictions for temperatures below  $T_{g,a}$  further verify the reliability of the closed-form solution.

### ***3.3.3 Comparisons with FE Predictions***

In the FE model (Fig. 3.6), two-node truss elements are used to represent the FRP plate and the concrete prism in accordance with the assumption adopted for the analytical solution that both adherends experience only membrane deformation. The bond-slip behavior between the two adherends is modeled using zero-thickness cohesive elements. All nodes of the bottom surface of the concrete prism are restrained against vertical movement and the node at the bottom right corner is additionally restrained against horizontal displacement. The FE model was implemented with ABAQUS (2008) and the well-known arc-length method was employed to trace the full-range load-displacement response that involves the snapback phenomenon.

In the analytical solution, it is assumed that the bond-slip response is fully reversible when slip reversals occur (Fig. 3.7a). In the FE model, a more realistic assumption for the effect of slip reversal can also be used: the bond resistance is no longer recoverable once the interfacial slip has exceeded  $\delta_f$  (Fig. 3.7b); the softening part of the bond-slip curve is still assumed to be fully recoverable. The use of the bond-slip

model of Fig. 3.7b in the analytical solution would create difficulty for the derivation of a closed-form solution.

Fig. 3.8a presents load-displacement curves of bonded joints for different temperature variations predicted by both the analytical solution and the FE model using geometric and material properties (including the identified bond-slip curve) of Klamer's (2006) two reference test specimens. The bond-slip response of Fig. 3.7a was used in both approaches for obtaining the results shown in Fig. 3.8a. Obviously, the two approaches lead to identical results, confirming the validity and accuracy of both approaches.

In Fig. 3.8b, FE predictions based on the two different bond-slip laws of Fig. 3.7a and Fig. 3.7b are compared. Only a small difference between the two bond-slip laws is seen during the softening-debonding stage for  $\Delta T > 0$  while no difference is seen for  $\Delta T < 0$ . Results obtained based on the linear damage model of Fig. 3.7c, if shown in Fig. 3.8b, are indistinguishable from those based on Fig. 3.7b and are thus not included in Fig. 3.8b. Similar to Fig. 3c, the segments of OA, AB, BC and CD in Fig. 3.8b correspond to the elastic, elastic-softening, elastic-softening-debonding and softening-debonding stages, respectively. If  $\Delta T > 0$ , the softening-debonding stage CD can be further divided into two sub-stages, CC' and C'D (Stage VI'), as explained earlier. At point O, an initial displacement exists due to the thermal action. This displacement has usually been ignored in previous studies when interpreting the test results of FRP-to-concrete bonded joints subjected to a positive or negative temperature change (Klamer 2006; Leone et al. 2009), which is inappropriate. The snapback portion ends at a displacement value of  $\delta_f$  when  $\Delta T \geq 0$  but at a larger value when  $\Delta T < 0$ ; this is because the debonded part of the interface cannot be reloaded in the case of  $\Delta T < 0$  as discussed previously.

Fig. 3.9 presents numerical results from the analytical solution to examine the effect of temperature variation on the normalized ultimate load for FRP plates of different thicknesses (i.e., different tensile stiffnesses), with  $\Delta T = 0$  °C being for the reference case. It is clearly seen that for the same temperature rise, the increase in the ultimate load is larger when a thicker FRP plate is used. If a 2.4 mm thick FRP plate is used,

a temperature decrease of 50 °C (e.g., from an installation temperature of 25 °C to a winter temperature of -25 °C) leads to approximately a 26% decrease in the ultimate load. This detrimental effect of temperature decrease on bond resistance needs to be properly considered in further research when an FRP-strengthened structure is subjected to significant service temperature variations.

### **3.4 RESPONSE OF THE FRP-TO-CONCRETE INTERFACE**

Interfacial shear stress and slip distributions at various deformation states of bonded joints exposed to a positive and a negative temperature variation are illustrated in Figs. 3.10 and 3.11 respectively. In these figures, analytical predictions for characteristic deformation states are represented using continuous or dashed lines while a dotted line is used to represent an intermediate deformation state to illustrate the evolution of stresses and slips. Note that these results were obtained for plate and concrete material properties from Klamer's tests (2006) and the same bond-slip parameters as described in Section 3.1. In addition, FE predictions are shown as hollow circles only for the intermediate deformation state to confirm the agreement between analytical and FE predictions. The focus of the discussions in the remainder of this section is on the effect of temperature variation on interfacial behaviour.

#### ***3.4.1 Bonded Joint Exposed to a Temperature Increase***

Fig. 3.10 shows how the interfacial shear stress distribution and the interfacial slip distribution vary as deformation progresses for a temperature increase of 30°C (i.e.,  $\Delta T = 30^\circ\text{C}$  and  $T = 50^\circ\text{C}$ ) in comparison with corresponding results for the reference temperature of 20°C. When only the thermal loading is applied (point O in Fig. 3.8b), both the interfacial shear stress and the slip due to a temperature increase are anti-symmetrically distributed, with the slip at the load end being negative. The interfacial shear stresses and slips from the pull load are opposite in direction to those from the thermal loading, so the two types of load lead to interfacial shear stresses and slips that counteract each other. That is, part of the pull load in a bonded joint exposed to a temperature increase is resisted by the thermal stresses and as a result, a temperature increase leads to an increase in the load levels of all characteristic deformation states except the completely unloaded state when the pull

load is reduced back to zero (Fig. 3.8b). The phenomenon of an increase in the ultimate load due to a temperature increase has previously been discussed by Rabinovitch (2010) who correctly attributed the phenomenon to counteracting interfacial stresses.

Once the interfacial shear stress at the loaded end reaches its maximum value  $\tau_f$  (with a corresponding slip of  $\delta_1$ ) (point A in Fig. 3.8b), the FRP-to-concrete interface enters the elastic-softening stage (segment AB in Fig. 3.8b), as described in Fig. 3.10b. Afterwards, debonding initiates first at the loaded end (point B in Fig. 3.8b) and then propagates along the bond length until the slip at the free end reaches  $\delta_1$  (point C in Fig. 3.8c), as illustrated in Fig. 3.10c. Figs. 3.10b and 3.10c show that a positive temperature variation leads to a slightly longer length for the softening zone and a slightly shorter length for the debonded zone than those for the reference temperature. Furthermore, Fig. 3.10d shows that the softening zone expands towards the loaded end in the unloading stage (segment CD in Fig. 3.8b); this expansion is due to reductions of slip values to below  $\delta_f$  coupled with the assumption of a fully reversible bond-slip law (Fig. 3.7a) which allows the debonded part of the bond length to regain bond resistance.

When the interfacial shear stress at the free end reduces to zero, the slip values of the entire interface are equal to  $\delta_f$  for a bonded joint not exposed to a temperature variation (Fig. 3.10d), which signifies complete debonding of the entire interface. However, the situation is different for a bonded joint exposed to a temperature increase: when the interfacial shear stress at the free end reduces to zero, the interface enters the second sub-stage (Stage VI') of the soft-debonding stage as represented by segment C'D in Fig. 3.8b; debonding starts at the free end and propagates towards the loaded end until the whole interface is fully separated (Fig. 3.10e). At the end of debonding, the slip at the loaded end equals to  $\delta_f$  while the slip values at other locations are greater than  $\delta_f$  by an amount due to thermal expansion (Fig. 3.10e).

#### ***3.4.2 Bonded Joint Exposed to a Temperature Decrease***

Similar to Fig. 3.10, the response of a bonded joint exposed to a temperature decrease of 30°C (i.e.,  $\Delta T = -30^\circ\text{C}$  and  $T = -10^\circ\text{C}$ ) is examined in Fig. 3.11; the results for the reference temperature case are again shown for comparison. Naturally, a temperature decrease alone leads to interfacial shear stresses and slips that are opposite in direction to those due to a temperature increase of the same magnitude (Fig. 3.11a), and this means that the pull load leads to interfacial shear stresses and slips in the same direction as the thermal loading in the zone near the loaded end. These thermal stresses are detrimental to the ultimate load and reduce the load values of the characteristic deformation states (Fig. 3.8b). A temperature decrease is seen to lead to a slightly shorter softening zone and a slightly longer debonding zone (Figs 3.11b and 3.11c). Unlike a bonded joint exposed to a temperature increase (Figs. 3.10d-3.10e), the slip values along the entire interface of a bonded joint exposed to a temperature reduction increase monotonically during the first three deformation stages (Figs. 3.11a-3.11c). During the softening-debonding stage (Fig. 3.11d), slip reversals occur but these reversals are never large enough to reduce a slip value larger than  $\delta_f$  to below  $\delta_f$ ; that is, the assumption of a fully reversible bond-slip law has no consequence. At the end of debonding, the slip value at the free end reaches  $\delta_f$  while the slip values elsewhere are all greater than  $\delta_f$ , indicating the end of debonding.

### **3.5 DETERMINATION OF INTERFACIAL FRACTURE ENERGY FROM SHEAR TESTS**

It is now clear that the ultimate load of an FRP-to-concrete bonded joint can be significantly affected by a temperature variation from the reference temperature (i.e., the installation temperature). This has a significant implication when shear test results are used to derive bond-slip curves. In such a derivation, the interfacial fracture energy  $G_f$  is directly related to the ultimate load of the bonded joint when temperature variations are not involved (e.g., Wu et al. 2002; Dai and Ueda. 2003; Lu et al. 2005a). When shear tests are used to derive bond-slip laws at a temperature variation, previous authors have followed the same approach (Wu et al. 2005). In the correct approach, the effect of thermal stresses on the ultimate load needs to be eliminated and the revised ultimate load can then be used to determine the interfacial

fracture energy for the establishment of the bond-slip curve which may include the effect of softening of the bonding adhesive. That is, the interfacial fracture energy at temperature  $T$  is related to the experimental ultimate load  $P_{u,T}$  by the following equation:

$$G_{f,T} = \frac{\left\{ P_{u,T} + \frac{\tau_f b_p}{\lambda_1^2 \delta_1} (\alpha_p - \alpha_c) \Delta T \cdot \left[ 1 - \frac{\cos(\lambda_2 a_d)}{\cosh(\lambda_1 (L - a_d))} \right] \right\}^2}{2b_p^2 E_p t_p} \quad (3.54)$$

The problem with the above equation is that  $a_d$  is implicitly defined by Eq. (3.35) and can only be found by iterations. However it can be shown that for a sufficiently long bond length  $L$  and with the simplification that  $\cosh(\lambda_1 (L - a_d))$  is infinite, Eq. (3.54) reduces to

$$G_{f,T} = \frac{\left[ P_{u,T} + \frac{\tau_f b_p}{\lambda_1^2 \delta_1} (\alpha_p - \alpha_c) \Delta T \right]^2}{2b_p^2 E_p t_p} \quad (3.55)$$

If the test involves softening of the adherends as well, the above equations can still be used provided that the thermally induced deteriorations of material properties of the adherends are properly considered, such as using the model proposed in Chapter 5 for FRP laminates at elevated temperatures.

### 3.6 CONCLUSIONS

This chapter has presented a closed-form analytical solution for the full-range behavior of FRP-to-concrete bonded joints under combined thermal and mechanical loadings. A bilinear local bond-slip relationship is employed in the solution, but the general characteristics observed from the solution are applicable to interfaces with a similar bond-slip model. The solution provides closed-form expressions for the interfacial slip, the interfacial shear stress, the axial stress in the FRP laminate as well as the load-displacement response for the entire deformation process. The predictions of the closed-form solution have been compared with the existing test data available and FE results, demonstrating close agreement between results from the three different approaches if the exposed temperature is less than the glass

transition temperature  $T_{g,a}$  of the bonding adhesive. It has been shown that, provided the material properties are not affected by temperature variations, a temperature rise increases the ultimate load while a temperature reduction decreases the ultimate load; the latter can have serious implications for the safety of the strengthened structure. A useful function of the closed-form solution lies in the interpretation of shear test results: the solution allows the effect of thermal stresses to be isolated from the effect of property changes of the bondline in obtaining bond-slip responses from shear tests.

It is worth noting that while the solution is developed with particular reference to FRP-to-concrete bonded joints, it is also applicable to similar bonded joints made of other materials (e.g., FRP-to-steel bonded joints) where the interfacial bond-slip law can be approximated as bi-linear. Furthermore, the solution can also be applied to situations where differential expansions between the two adherends are induced by factors other than thermal loading (e.g., moisture-induced differential expansions).

### 3.7 REFERENCES

- ABAQUS. (2008). *ABAQUS standard user's manual*, Volumes I-III, Version 6.8. Hibbitt, Karlsson & Sorensen, Inc., Pawtucket, America.
- Achintha, P.M.M. (2009). "Fracture analysis of debonding mechanism for FRP plates." Ph.D. thesis, University of Cambridge, UK.
- Blontrock, H. (2003). "Analysis and modeling of the fire resistance of concrete elements with externally bonded FRP reinforcement." Ph.D. thesis, Ghent University, Belgium.
- Brosens, K. (2001). "Anchoring of externally bonded steel plates and CFRP laminates for the strengthening of concrete elements." Ph.D. thesis, Katholieke University Leuven, Belgium.
- Chajes, M.J., Finch, W.W., Januszka, T.F., and Thomson, T.A. (1996). "Bond and force transfer of composite material plates bonded to concrete." *ACI Structural Journal*, Vol. 93, No. 2, pp. 208-217.
- Chen, J.F., and Teng, J.G. (2001). "Anchorage strength models for FRP and steel plates bonded to concrete." *Journal of Structural Engineering*, ASCE, Vol. 127, No. 7, pp. 784-791.
- Chen, J.F., Yuan, H., and Teng, J.G. (2007). "Debonding failure along a softening FRP-to-concrete interface between two adjacent cracks in concrete members." *Engineering Structures*, Vol. 29, No. 2, pp. 259-270.

- Cornetti, P., and Carpinteri, A. (2011). "Modeling the FRP-concrete delamination by means of an exponential softening law." *Engineering Structures*, Vol. 33, No. 6, pp. 1998-2001.
- Dai, J.G., and Ueda, T. (2003). "Local bond stress slip relationship for FRP composites-concrete interfaces." *Proceedings of the Sixth International Symposium on FRP Reinforcement for Concrete Structures (FRPRCS-6)*, Singapore, pp. 143-152.
- Dai, J.G., Ueda, T., and Sato, Y. (2005). "Development of the nonlinear bond stress-slip model of fiber reinforced plastics sheet-concrete interfaces with a simple method." *Journal of Composites for Construction*, ASCE, Vol. 9, No. 1, pp. 52-62.
- Dai, J.G., Ueda, T., and Sato, Y. (2006). "Unified analytical approaches for determining shear bond characteristics of FRP-concrete interfaces through pullout tests." *Journal of Advanced Concrete Technology*, JSCE, Vol. 4, No. 1, pp. 133-145.
- De Lorenzis, L., Miller, B., and Nanni, A. (2001). "Bond of fiber-reinforced polymer laminates to concrete." *ACI Material Journal*, Vol. 98, No. 1, pp. 256-264.
- Ferracuti, B., Savoia, M., and Mazzotti, C. (2007). "Interface law for FRP-concrete delamination." *Composite Structures*, Vol. 80, No. 4, pp. 523-531.
- Hollaway, L.C., and Teng, J.G. (2008). *Strengthening and Rehabilitation of Civil Infrastructures Using FRP Composites*. Woodhead Publishing Limited, Cambridge, UK.
- Klamer, E. (2006). "The influence of temperature on concrete structures strengthened with externally bonded CFRP." Research Report, Eindhoven University of Technology, Netherlands.
- Klamer, E. (2009). "Influence of temperature on concrete beams strengthened in flexure with CFRP." Ph.D. Thesis, Eindhoven University of Technology, Netherlands.
- Leone, M., Matthys, S., and Aiello, M.A. (2009). "Effect of elevated service temperature on bond between FRP EBR systems and concrete." *Composites Part B: Engineering*, Vol. 40, No. 1, pp.85-93.
- Lu, X.Z., Teng, J.G., Ye, L.P., and Jiang, J.J. (2005a). "Bond-slip models for FRP sheets/plates bonded to concrete." *Engineering Structures*, Vol. 27, No. 6, pp. 920-937.
- Lu, X.Z., Ye, L.P., Teng, J.G. and Jiang, J.J. (2005b). "Meso-scale finite element model for FRP sheets/plates bonded to concrete." *Engineering Structures*, Vol. 27, No. 4, pp. 564-575.
- Nakaba, K., Kanakubo, T., Furuta, T., and Yoshizawa, H. (2001). "Bond behavior between fiber-reinforced polymer laminate and concrete." *ACI Structural Journal*, Vol. 98, No. 3, pp. 359-367.
- Rabinovitch, O. (2010). "Impact of thermal loads on interfacial debonding in FRP strengthened beams." *International Journal of Solids and Structures*, Vol. 47, No. 24, pp. 3234-3244.

- Taljsten, B. (1996). "Strengthening of concrete prisms using the plate-bonding technique." *International Journal of Fracture*, Vol. 82, No. 3, pp. 253-266.
- Teng, J.G., Chen, J.F., Smith, S.T. and Lam, L. (2002). *FRP-Strengthened RC Structures*. John Wiley and Sons Ltd., Chichester, UK.
- Teng, J.G., Yuan, H., and Chen, J.F., (2006). "FRP-to-concrete interface between two adjacent cracks: Theoretical model for debonding failure." *International Journal of Solid and Structures*, Vol. 43, Nos 18-19, pp. 5750-5778.
- Wang, J. (2007). "Cohesive-bridging zone model for FRP-concrete interface debonding." *Engineering Fracture Mechanics*, Vol. 74, No. 17, pp. 2643-2658.
- Wu, Z.S., Yuan, H. and Niu, H. (2002). "Stress transfer and fracture propagation in different kinds of adhesive joints." *Journal of Engineering Mechanics*, ASCE, Vol. 128, No. 5, pp. 562-573.
- Wu, Z.S., Iwashita, K., Yagashiro, S., Ishikawa, T., and Hamaguchi, Y. (2005). "Temperature effect on bonding and debonding behavior between FRP sheets and concrete." *Journal of the Society of Materials Science*, Vol. 54, No. 5, pp. 474-480.
- Yao, J., Teng, J.G., and Chen, J.F. (2005). "Experimental study on FRP-to-concrete bonded joints." *Composites Part B: Engineering*, Vol. 36, No. 2, pp. 99-113.
- Yuan, H., Wu, Z.S. and Yoshizawa, H. (2000). "Theoretical solutions on interfacial stress transfer of externally bonded steel/composite laminates." *Journal of Structural Mechanics and Earthquake Engineering*, JSCE, Vol. 18, No. 1, pp. 27-39.
- Yuan, H., Teng, J.G., Seracino, R., Wu, Z.S. and Yao, J. (2004). "Full-range behavior of FRP-to-concrete bonded joints." *Engineering Structures*, Vol. 26, No. 5, pp. 553-565.
- Zhou, Y.W., Wu, Y.F. and Yun, Y. (2010). "Analytical modeling of the bond-slip relationship at FRP-concrete interfaces for adhesively-bonded joints." *Composites Part B: Engineering*, Vol. 41, No. 6, pp. 423-433.

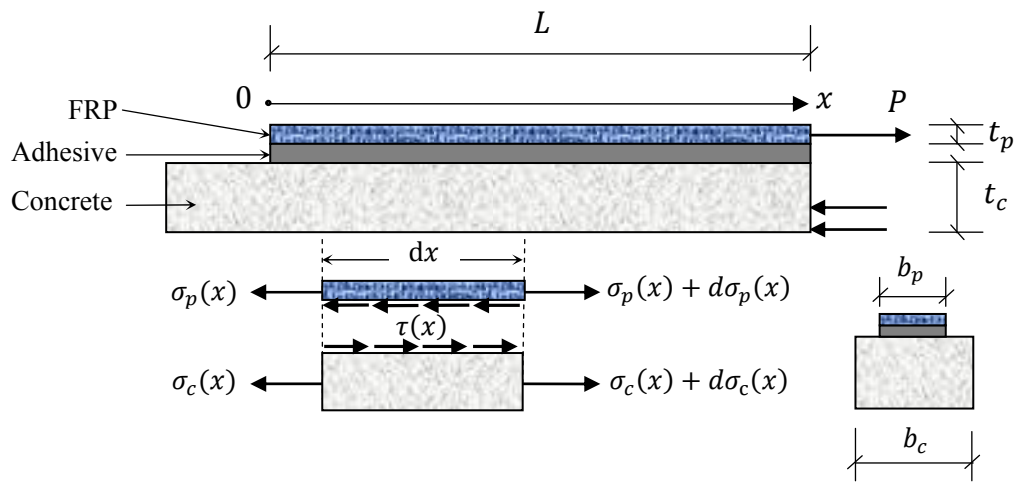


**Fig. 3.1** Schematic diagram of a single-lap shear test.

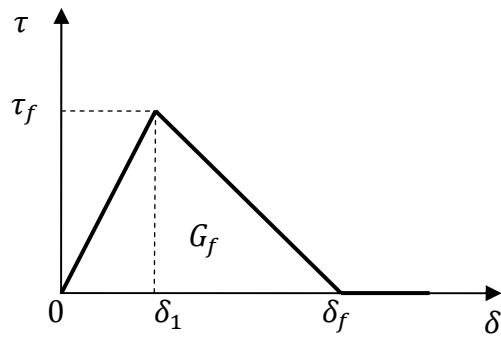
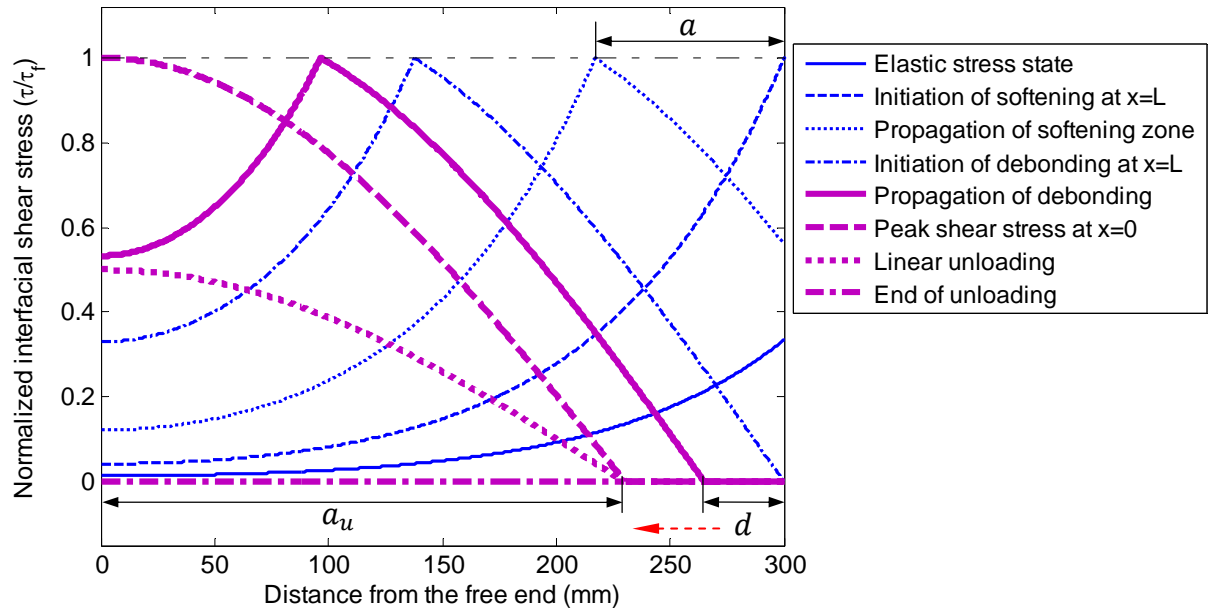
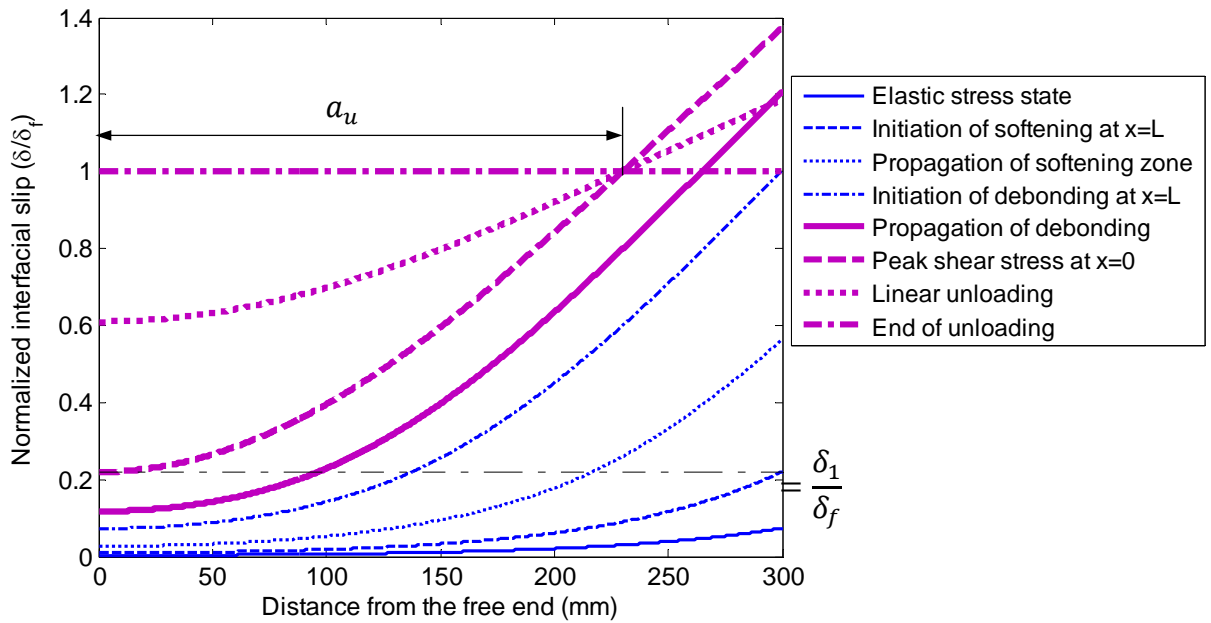


**Fig. 3.2** Bi-linear bond-slip model.

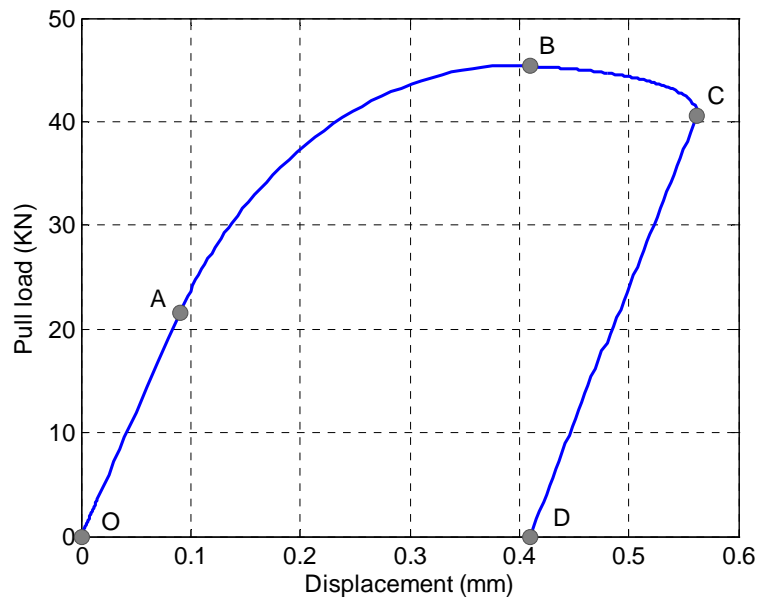


(a) Interfacial shear stress distribution



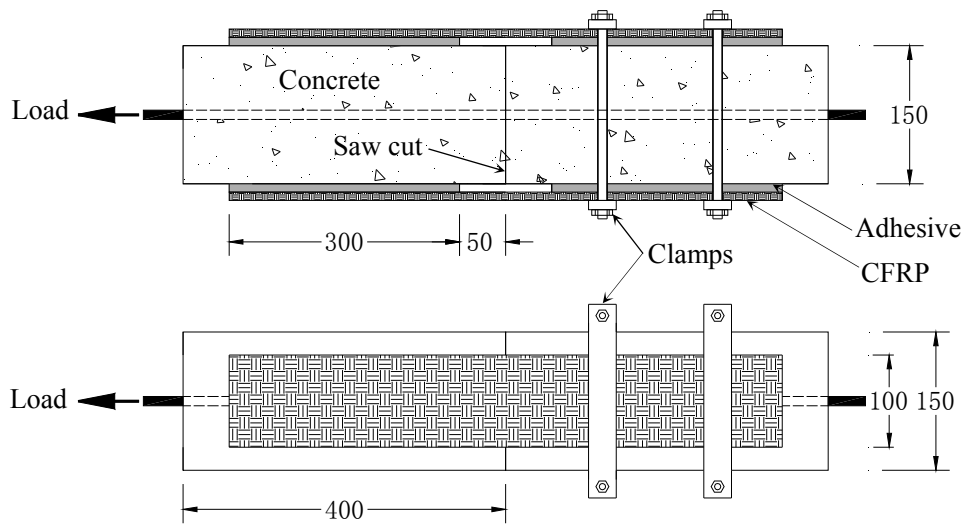
(b) Interfacial slip distribution

**Fig. 3.3** Behavior of bonded joint at reference temperature.

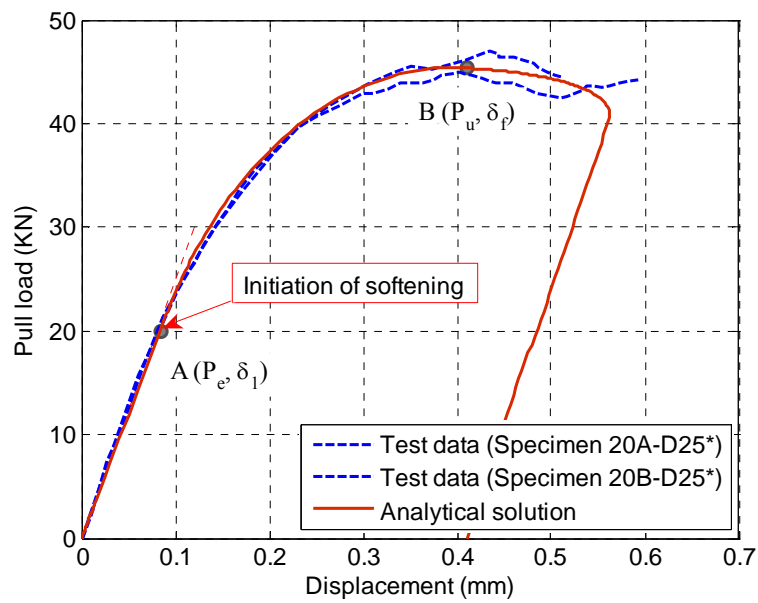


(c) Load-displacement response

**Fig. 3.3** Behavior of bonded joint at reference temperature (cont'd).

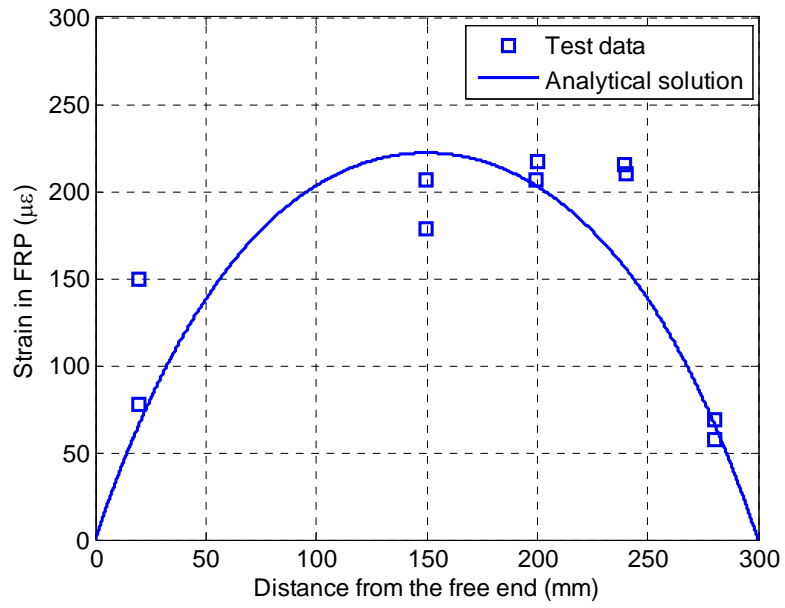


(a) Specimen details

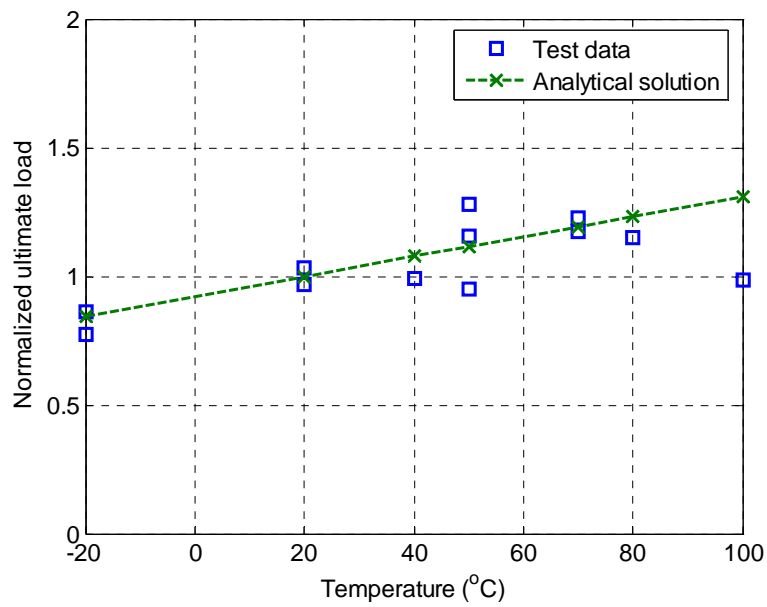


(b) Load-displacement curves

**Fig. 3.4** Test specimens of Klammer (2006).



(a) Thermal strain distribution in the FRP.



(b) Normalized ultimate load vs. temperature.

**Fig. 3.5** Comparison with test results of Klamer (2006).

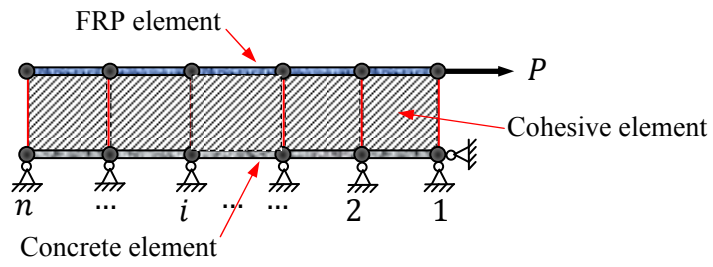
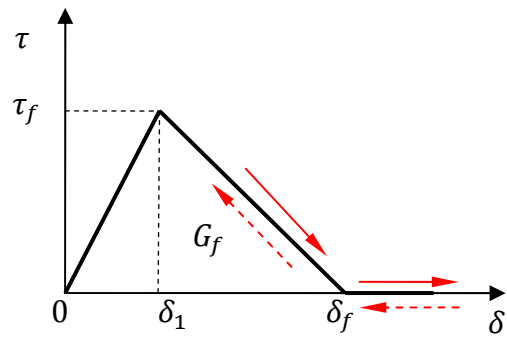
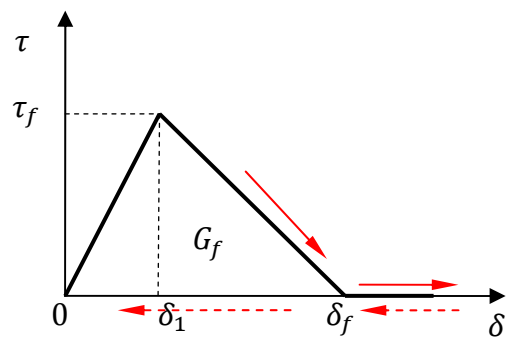


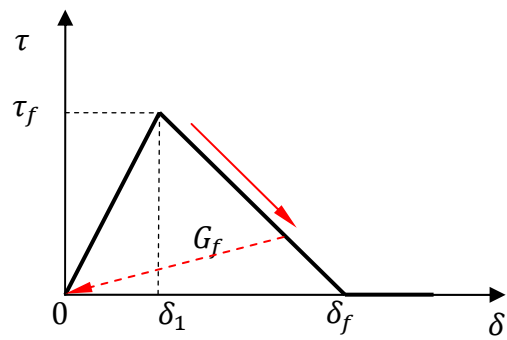
**Fig. 3.6** Finite element model



(a) Fully reversible

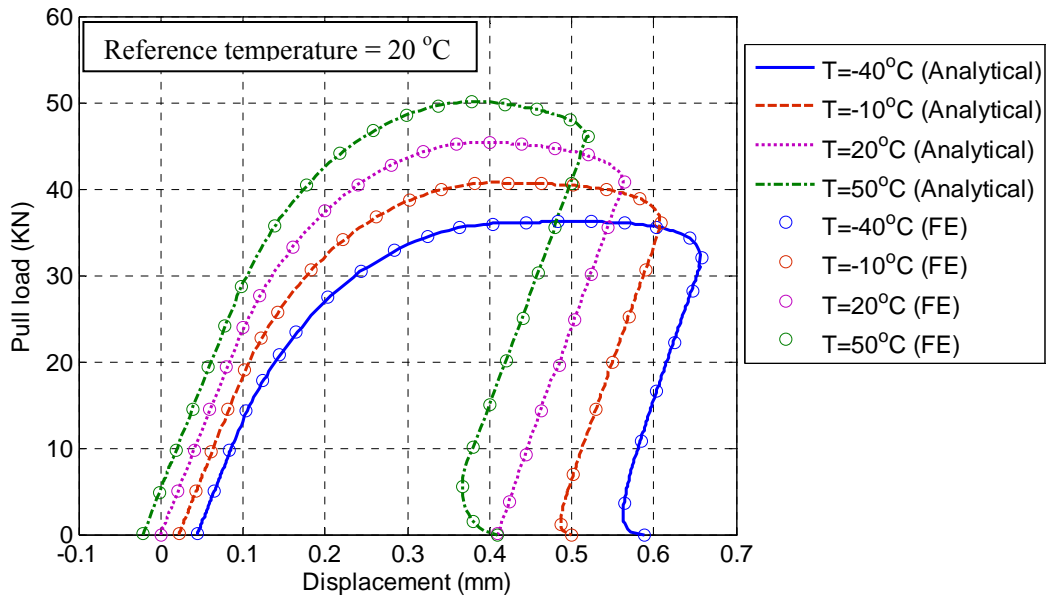


(b) Non-reversible after complete separation

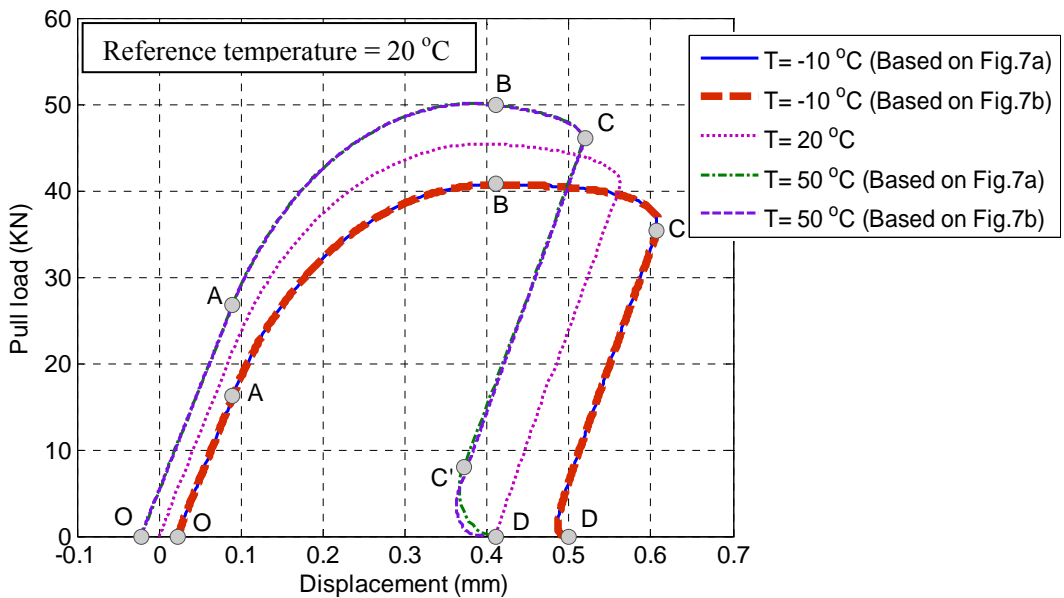


(c) Linear damage model

**Fig. 3.7** Bond-slip responses during slip reversals.



(a) Comparison between analytical and FE predictions.



(b) Comparison between predictions based on different slip reversal responses.

**Fig. 3.8** Effect of temperature variation on load-displacement response.

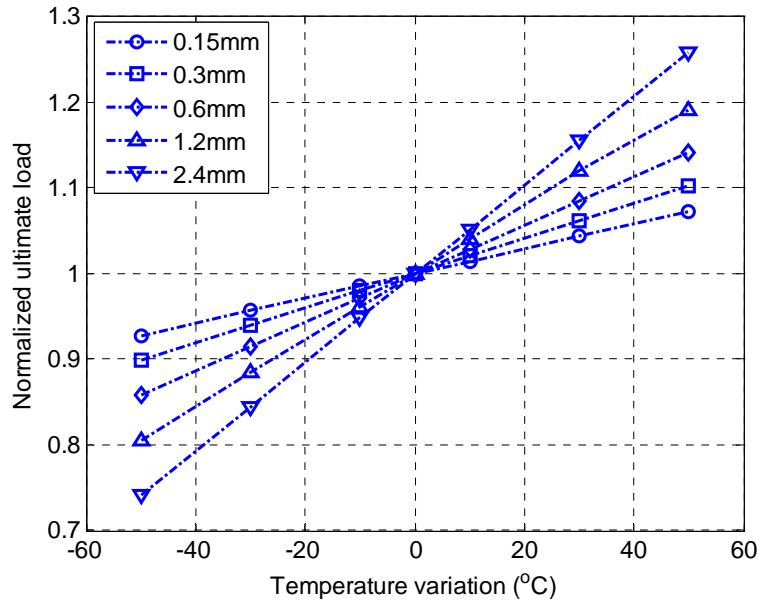


**Fig. 3.9** Effect of temperature variation on ultimate load at different plate stiffness levels.

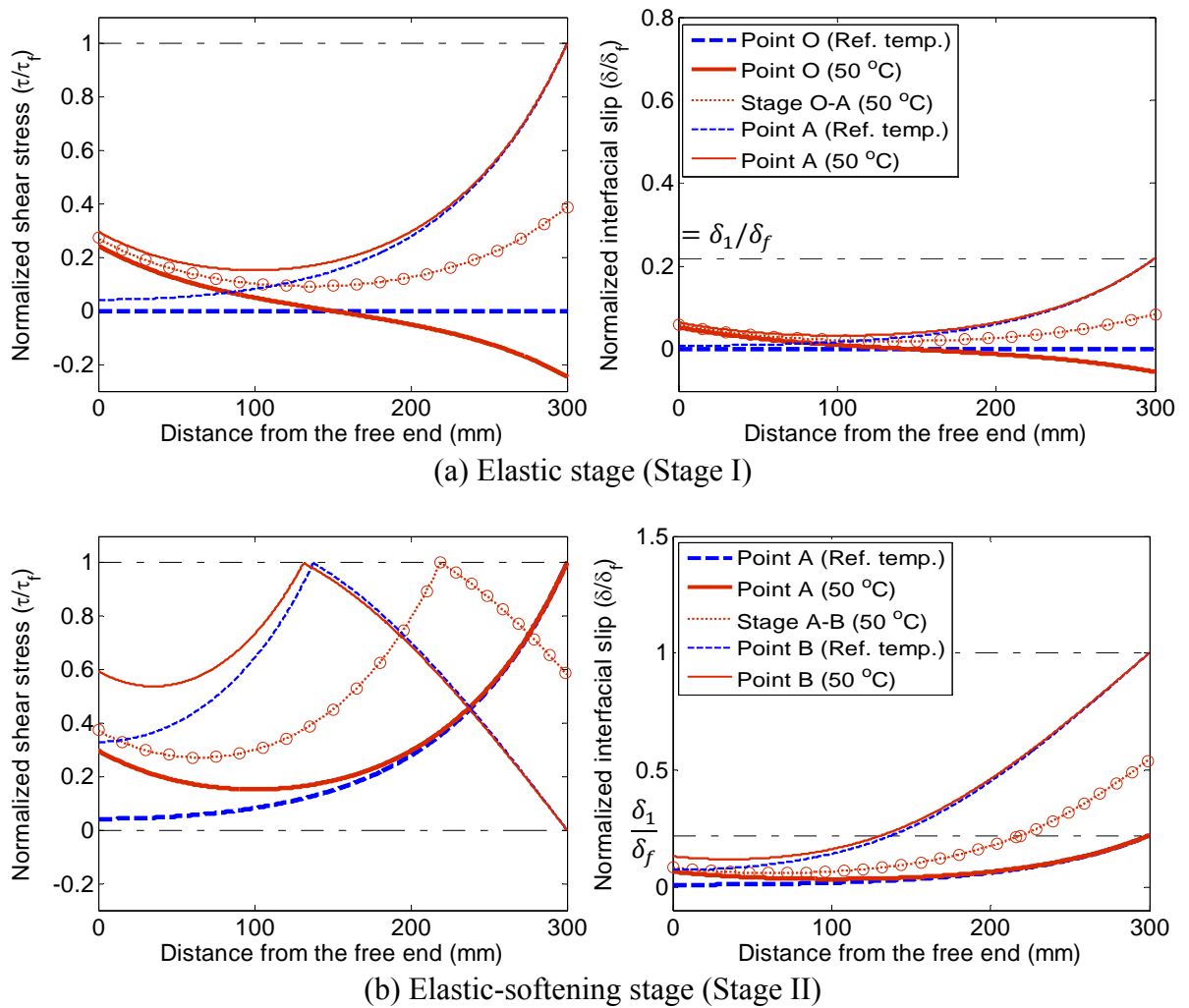
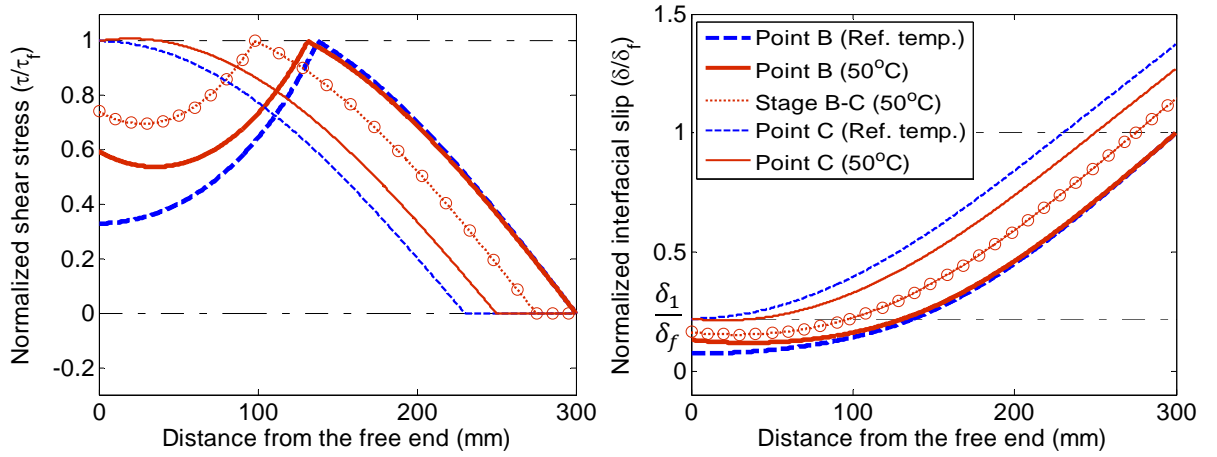
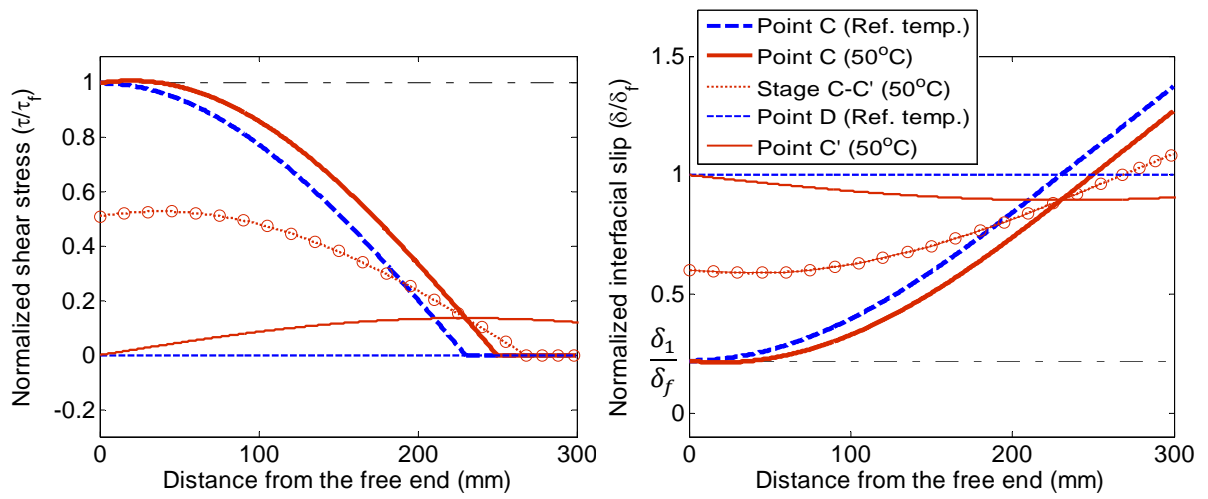


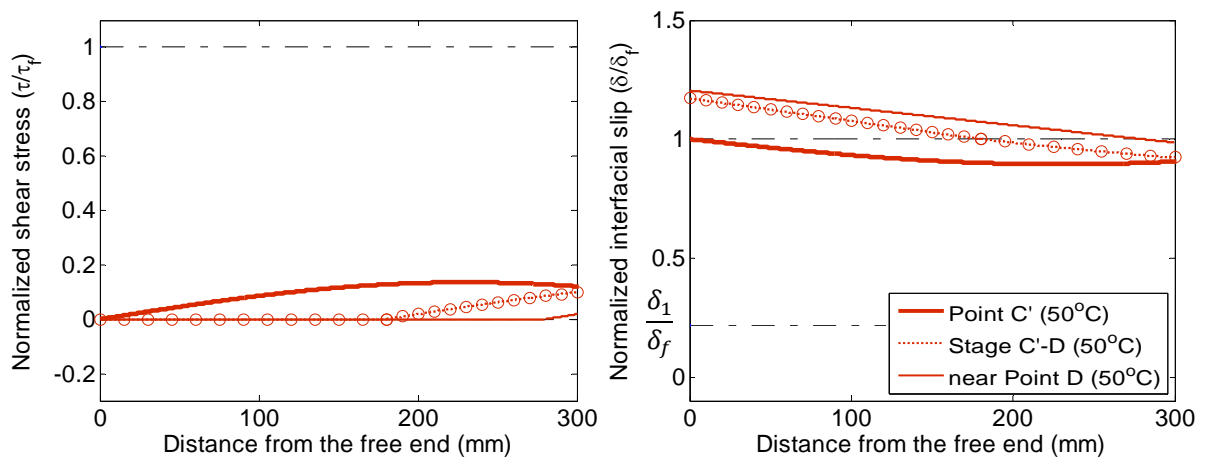
**Fig. 3.10** Bonded joint subjected to a temperature increase ( $\Delta T = 30^\circ\text{C}$ ).



(c) Elastic-softening-debonding stage (Stage III)

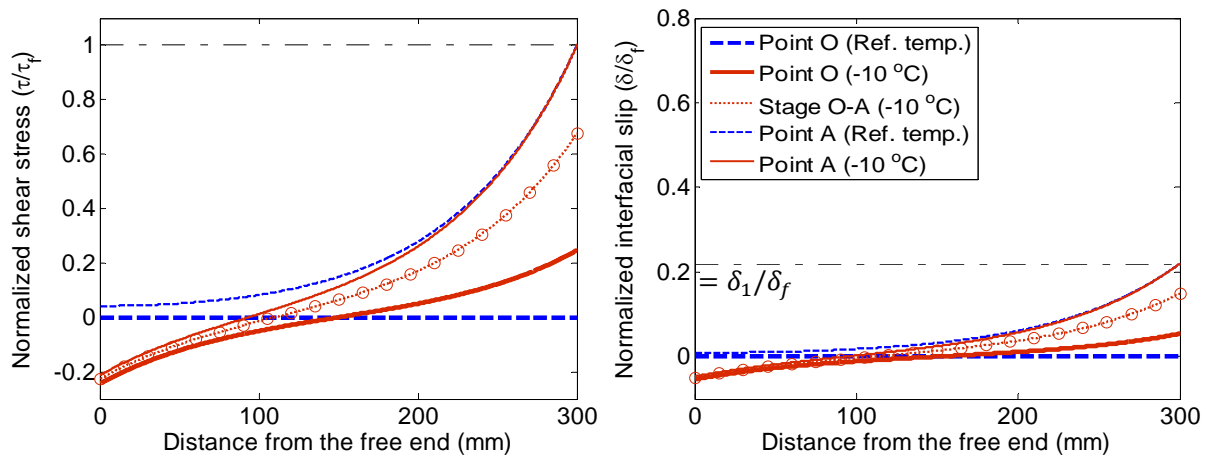


(d) Softening-debonding stage (Stage IV)

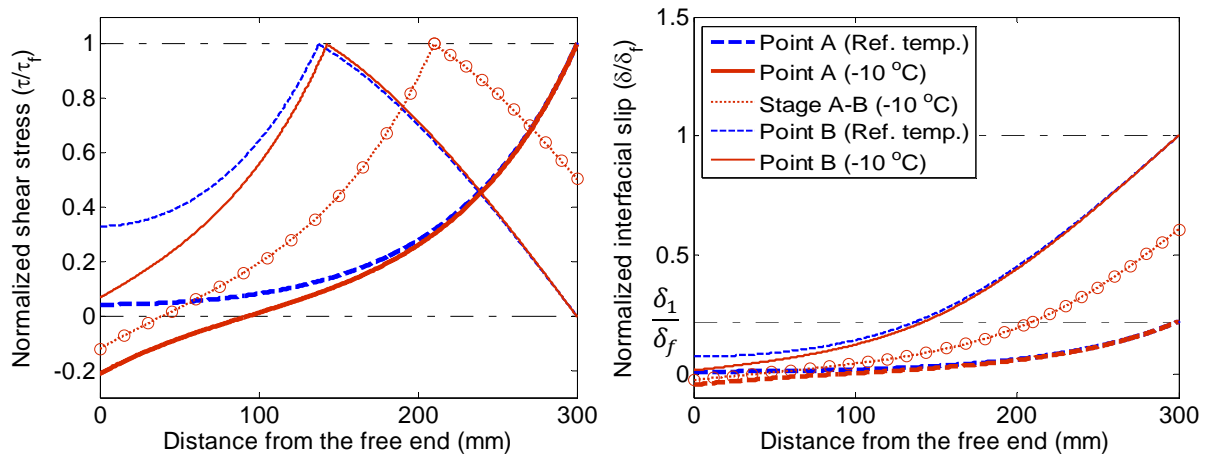


(e) Softening-debonding stage (Stage IV')

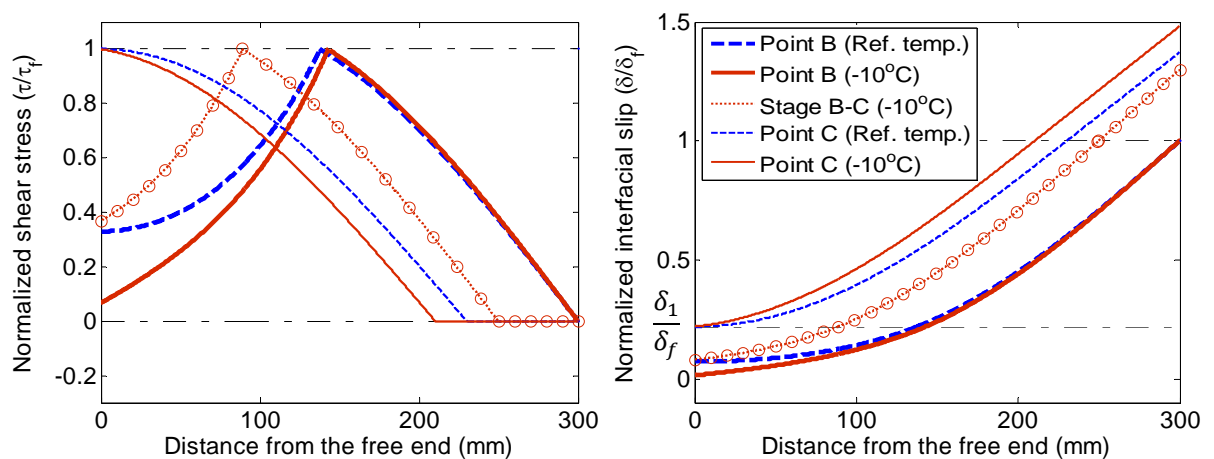
**Fig. 3.10** Bonded joint subjected to a temperature increase ( $\Delta T = 30^\circ\text{C}$ ) (cont'd).



(a) Elastic stage (Stage I)



(b) Elastic-softening stage (Stage II)



(c) Elastic-softening-debonding stage (Stage III)

**Fig. 3.11** Bonded joint subjected to a temperature decrease ( $\Delta T = -30^\circ\text{C}$ ).

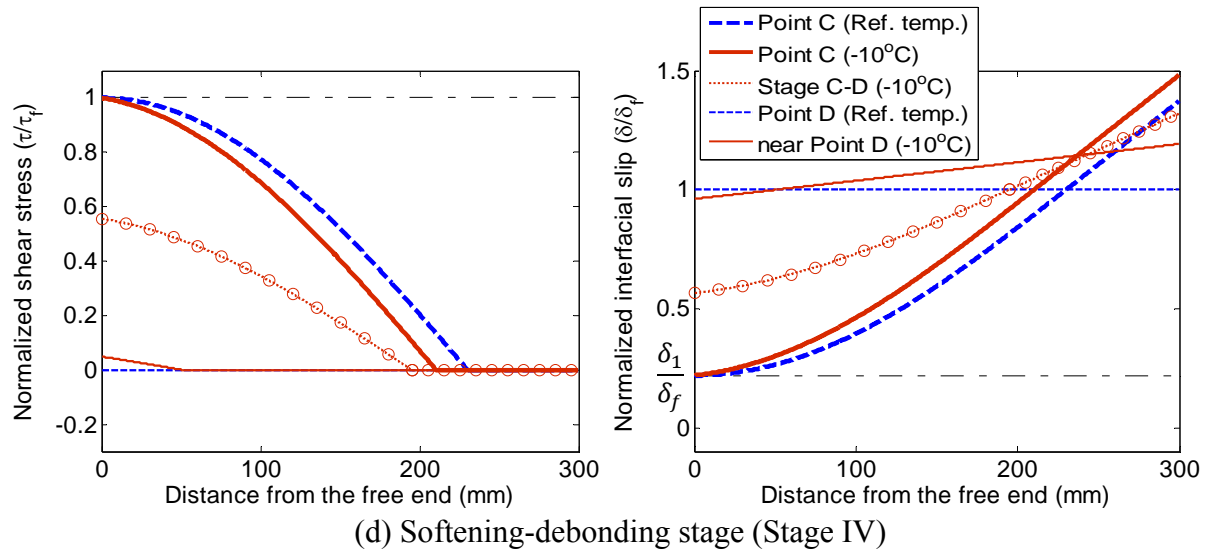


**Fig. 3.11** Bonded joint subjected to a temperature decrease ( $\Delta T = -30^{\circ}\text{C}$ ) (cont'd).

## CHAPTER 4

# EFFECTS OF BOND-SLIP MODELS ON THE MODE II DEBONDING BEHAVIOR OF BONDED JOINTS SUBJECTED TO COMBINED THERMAL AND MECHANICAL LOADINGS

### 4.1 INTRODUCTION

Mode II (i.e., pure shear) debonding of the FRP-to-concrete interface is often a dominant failure mode in concrete structures strengthened with externally bonded FRP reinforcement (e.g., Teng et al. 2002; Teng et al. 2003; Teng and Chen 2009), particularly in bond critical applications (e.g., flexural and shear strengthening of flexural members). Many experimental and theoretical studies have been carried out to investigate the behavior of FRP-to-concrete bonded joints subjected to Mode II loading (e.g., Taljsten 1996; Chen and Teng 2001; Dai et al. 2003, 2005; Lu et al. 2005a, 2005b; Leung and Yang 2006; Seracino et al. 2007; Wang 2007). In particular, the single-lap shear test (Fig. 3.1) or double-lap shear test has been widely used to study the bond characteristics of FRP-to-concrete interfaces subjected to Mode II loading, including the debonding load (i.e., the ultimate load of the bonded joint due to debonding failure which is also referred to as the bond strength of the joint), the effective bond length, the bond-slip model, and the full-range deformation behavior (e.g., Chajes et al. 1996; Maeda et al. 1997; Brosens and van Gemert 1999; Bizindavyi and Neale 1999; Focacci et al. 2000; Brosens 2001; Nakaba et al. 2001; Yao et al. 2005; Dai et al. 2005, 2006; Ferracuti et al. 2007; Ferrier et al. 2010). It is worth noting that the bond-slip model is the most fundamental law describing the bond characteristics of FRP-to-concrete interfaces subjected to Mode II loading. Once the bond-slip law is known, the full-range deformation behavior of an FRP-to-concrete interface subjected to Mode II loading can be determined (e.g., Yuan et al. 2001; Yuan et al. 2004; Dai et al. 2006).

The shape of the bond-slip model of FRP-to-concrete interfaces depends on the properties of the bonding adhesive and/or the properties and conditions of the

substrate. Existing bond-slip models proposed for FRP-to-concrete interfaces can be classified into five typical categories as follows: (a) the elastic-brittle model (Taljsten 1996; Maeda et al. 1997; Yuan et al. 2001; Wu et al. 2002); (b) the bi-linear model (Holzenkampfer 1994; Taljsten 1996; Brosens and van Gemert 1998; Yuan et al. 2001 ; Wu et al. 2002; Yuan et al. 2004; Lu et al. 2005a; Teng et al. 2006; Mohamed Ali et al. 2006, 2008); (c) the elastic-plastic-brittle model (Sato et al. 1997; Gao et al. 2001; Maeda et al. 2001; De Lorenzis et al. 2001), which includes as a special case the rigid-plastic-brittle model (Taljsten 1996); (d) the rigid-softening model (Taljsten 1996; Yuan et al. 2001; Mohamed Ali et al. 2006, 2008; Chen et al. 2007); and (e) the nonlinear model (Focacci et al. 2000; Nakaba et al. 2001; Dai and Ueda 2003; Dai et al. 2005; Lu et al. 2005a; Ferracuti et al. 2007). These five types of bond-slip models are likely to cover most of the cases of bond-slip behavior for various substrate materials such as concrete, steel, masonry and timber. Fig. 4.1 illustrates these five types of bond-slip models (i.e.,  $\tau$ - $\delta$  relationships). The nonlinear model is represented by an exponential shape proposed by Dai et al. (2005). Similar shapes have often been used to describe the nonlinear bond-slip behavior of FRP-to-concrete interfaces by various researchers (Focacci et al. 2000; Nakaba et al. 2001; Dai and Ueda 2003; Dai et al. 2005; Lu et al. 2005a; Ferracuti et al. 2007).

Among these five types of bond-slip models, the bi-linear model has been the most popular and has also been adopted in several design guidelines (e.g., fib 2001; CNR 2004) due to its simplicity as well as reasonable accuracy in representing interfacial softening behavior. While some issues regarding the calibration of its parameters (i.e., the interfacial fracture energy and the local-slip parameters) need further examination (Bilotta et al. 2012), the bi-linear bond-slip model is still an attractive option as it offers convenience for the development of closed-form solutions for the full-range behavior of FRP-to-concrete interfaces. For the elastic-brittle, bi-linear and rigid-softening types of bond-slip models, Yuan et al. (2001) presented rigorous closed-form analytical solutions for predicting the full-range debonding behavior of FRP-to-concrete bonded joints subjected to Mode II loading. Similarly, Dai et al. (2006) developed a closed-form solution for predicting the full-range debonding behavior of FRP-to-concrete bonded joints subjected to Mode II loading for an exponential bond-slip model based on the assumption that there is a sufficiently long bond length available between the FRP plate and the concrete substrate.

Despite the existing work as discussed above, very limited analytical work has been conducted to date to investigate the influence of service temperature variations (i.e., thermal loading) on the debonding behavior of FRP-to-concrete interfaces subjected to Mode II loading. It is obvious that FRP-strengthened RC structures may be subjected to significant temperature variations (e.g., due to ambient temperature changes or fire exposure). Such variations may have two different effects on the bond behavior of FRP-to-concrete interfaces. The first effect is related to the thermal stresses induced at the interface due to the thermal incompatibility between the FRP and the concrete substrate (e.g., Rabinovitch 2010). The thermal expansion of FRP in the longitudinal direction is dominated by the thermal expansion of the reinforcing fibers and can differ considerably from that of concrete. For instance, the thermal expansion coefficient of CFRP is generally close to zero (ACI 2008) and can be either negative or positive depending on the fiber used, the fiber array and the fiber volumetric fraction (Sen et al. 1999; Masmoudi et al. 2005). As a consequence, the interfacial thermal stresses may have a significant influence on the bond strength of FRP-to-concrete interfaces when they are subjected to combined thermal and mechanical loadings. The second effect is related to the changes in material properties. Temperature variations may influence the material properties (i.e., stiffness and strength) of the bonding adhesive between the FRP and the concrete substrate as well as the properties of the FRP (and even those of the substrate in extreme cases); hence the debonding behavior of FRP-to-concrete interfaces is affected. This chapter considers directly only the first effect based on the assumption that the properties of the bonding adhesive and the adherends are not affected by the imposition of thermal loading. The analytical solutions derived on the basis of this assumption can, however, be easily adapted for application to cases where material properties may change by replacing the original material properties with the modified material properties in the analytical solutions.

As mentioned in Chapter 3, some researchers have conducted single-lap or double-lap shear tests on FRP-to-concrete interfaces to understand their bond behavior at different temperatures (e.g., Blontrock 2003; Wu et al. 2005; Klamer 2006, 2009; Leone et al. 2009). A key purpose of such shear tests is to determine the bond-slip model of the interface at a specific temperature variation, for which the effect of

thermal interfacial stresses needs to be isolated from the effect of temperature-induced material property changes, as only the latter should be included in a bond-slip model for use in the theoretical performance modeling of FRP-strengthened structures subjected to temperature variations. This issue has been little explored, and indeed in some existing studies, these thermal stresses were simply ignored in interpreting the shear test results (e.g., Wu et al. 2005; Leone et al. 2009). Chapter 3 has presented an analytical solution for the full-range behavior of FRP-to-concrete bonded joints subjected to combined thermal loading and Mode II mechanical loading based on a bi-linear interfacial bond-slip model. This closed-form solution provides a rigorous explanation of the effect of thermal stresses on the debonding load and can be used to isolate the former from the latter. The analytical results showed clearly that an increase/decrease of the service temperature leads to a corresponding increase/decrease of the Mode II debonding load.

This chapter complements the study of Chapter 3 by presenting corresponding closed-form analytical solutions for other bond-slip models. The present study has the following purposes: (1) to investigate the effect of a different bond-slip model on the shear stress transfer mechanism and the associated debonding propagation of FRP-to-substrate bonded joints subjected to combined thermal and mechanical loadings; and (2) to develop theoretical models for the debonding load and the effective bond length accounting for the effect of temperature variations.

## **4.2 GOVERNING EQUATIONS**

### ***4.2.1 Assumptions and Notation***

Fig. 3.1 shows a theoretical idealization of a single-lap bonded joint, in which both adherends are assumed to experience only membrane (i.e., in-plane) deformation. This theoretical model is a close approximation of the behavior of a real bonded joint (Yuan et al. 2004; Teng et al. 2006; Chen et al. 2007). The detailed assumptions and notation can be found in Section 3.2.1.

### ***4.2.2 Governing Equations***

The governing equations for the FRP-to-concrete bonded joints subjected to combined thermal and mechanical loadings can be described as follows:

$$\frac{d\sigma_p}{dx} - \frac{\tau}{t_p} = 0 \quad (4.1)$$

$$\sigma_p t_p b_p + \sigma_c t_c b_c = 0 \quad (4.2)$$

$$\tau = f(\delta) \quad (4.3)$$

$$\sigma_p = E_p \left( \frac{du_p}{dx} - \alpha_p \Delta T \right) \quad (4.4)$$

$$\sigma_c = E_c \left( \frac{du_c}{dx} - \alpha_c \Delta T \right) \quad (4.5)$$

$$\delta = u_p - u_c \quad (4.6)$$

$$\frac{d^2\delta}{dx^2} - \frac{2G_f}{\tau_f^2} \lambda^2 f(\delta) = 0 \quad (4.7)$$

$$\text{where } \lambda^2 = \frac{\tau_f^2}{2G_f} \left( \frac{1}{E_p t_p} + \frac{b_p}{E_c t_c b_c} \right) \quad (4.8)$$

$$\sigma_p = \frac{\tau_f^2}{2G_f t_p \lambda^2} \left[ \frac{d\delta}{dx} - (\alpha_p - \alpha_c) \Delta T \right] \quad (4.9)$$

The detailed descriptions and notation of the above equations can be found in Section 3.2.2; here these equations are listed for a clear presentation for the following analytical solution sections.

### 4.3 BOND-SLIP MODEL

The governing equation [i.e., Eq. (4.7)] can be solved if an appropriate bond-slip relationship [i.e., Eq. (4.3)] is provided. Five bond-slip models as reviewed in Section 4.1 and illustrated in Fig. 4.1 are considered in the following analysis. For

comparison purposes, the areas underneath the five  $\tau$ - $\delta$  models are assumed to be the same. For FRP-to-concrete interfaces subjected to Mode II loading only, previous studies have demonstrated that its Mode II debonding load is proportional to the square root of  $G_f$  regardless of the shape of bond-slip model (Taljsten 1996; Yuan et al. 2001; Wu et al. 2002; Dai et al. 2003). Details of the five bond-slip models are given below.

#### **4.3.1 Model I: Elastic-Brittle Model**

In the elastic-brittle model (Fig. 4.1a), the bond stress-slip relationship follows a linear ascending branch before the occurrence of interface fracture where the peak stress is reached with an interfacial slip  $\delta_f$ ; afterwards, the interfacial shear stress drops abruptly to zero without any interfacial softening behavior. This bond-slip model is described by the following equation:

$$f(\delta) = \begin{cases} \frac{\tau_f}{\delta_f} \delta & \text{when } 0 < \delta \leq \delta_f \\ 0 & \text{when } \delta > \delta_f \end{cases} \quad (4.10)$$

#### **4.3.2 Model II: Bi-Linear Model**

The bilinear bond-slip model (Fig. 4.1b) consists of two segments: a linear ascending segment where the shear bond stress increases linearly with the interfacial slip until it reaches the peak shear stress  $\tau_f$  (the corresponding slip is denoted by  $\delta_1$ ) and a linear softening segment where the shear bond stress decreases linearly with the interfacial slip to zero (the corresponding slip is denoted by  $\delta_f$ ). This bond-slip model (Fig. 4.1b) is described by the following equation:

$$f(\delta) = \begin{cases} \frac{\tau_f}{\delta_1} \delta & \text{when } 0 < \delta \leq \delta_1 \\ \frac{\tau_f}{\delta_f - \delta_1} (\delta_f - \delta) & \text{when } \delta_1 < \delta \leq \delta_f \\ 0 & \text{when } \delta > \delta_f \end{cases} \quad (4.11)$$

#### **4.3.3 Model III: Elastic-Plastic-Brittle Model**

For the elastic-plastic-brittle model (Fig. 4.1c), the shear stress increases linearly to reach its peak  $\tau_f$  at an interfacial slip of  $\delta_1$ . Afterwards, the shear stress is kept constant before it drops abruptly to zero. The elastic-plastic-brittle model is described by the following equation:

$$f(\delta) = \begin{cases} \frac{\tau_f}{\delta_1} \delta & \text{when } 0 < \delta \leq \delta_1 \\ \tau_f & \text{when } \delta_1 < \delta \leq \frac{\delta_1 + \delta_f}{2} \\ 0 & \text{when } \delta > \frac{\delta_1 + \delta_f}{2} \end{cases} \quad (4.12)$$

#### 4.3.4 Model IV: Rigid-Softening Model

The rigid-softening model (Fig. 4.1d) has only a softening branch and can be obtained from the bi-linear model by omitting the linear ascending branch (i.e.,  $\delta_1 = 0$ ). This rigid-softening model is described by the following equation:

$$f(\delta) = \begin{cases} \tau_f - \frac{\tau_f}{\delta_f} \delta & \text{when } 0 < \delta \leq \delta_f \\ 0 & \text{when } \delta > \delta_f \end{cases} \quad (4.13)$$

#### 4.3.5 Model V: Exponential Model

The exponential model (Fig. 4.1e) was proposed by Dai et al. (2005) and is controlled by two parameters: the interfacial fracture energy  $G_f$  and the interfacial brittleness index  $B$ . The model is described by the following equation:

$$f(\delta) = 2 \cdot B \cdot G_f (e^{-B\delta} - e^{-2B\delta}) \quad (4.14)$$

It should be noted that in Figs. 4.1a to 4.1e the bond-slip relationships are illustrated for positive slip values. When the slip is negative, its absolute value needs to be used in Eqs. (4.10) to (4.14) to calculate the bond stress, which should then be given a negative sign. Once the bond-slip relationship is defined, the governing equation [i.e., Eq. (4.7)] can be solved to predict the interfacial shear stress/slip distributions along

the bonded length and the load-displacement response of the bonded joint subjected to combined thermal and mechanical loadings as shown in the following sections.

Figs. 4.2 to 4.6 illustrate the evolution of interfacial shear stress distributions for bonded joints subjected to a positive temperature variation ( $\Delta T = 30^\circ\text{C}$ , left column) and a negative temperature variation ( $\Delta T = -30^\circ\text{C}$ , right column) respectively for different stages of the deformation process. These figures are based on results from the analytical solutions to be presented later, but they are shown in advance for convenience of presentation and discussion. The slip state of the loaded end, as depicted in Fig. 4.1, is used to indicate the state of the interface. For example, “Point O” means that the bond state of the loaded end is that of the beginning point of the bond-slip model and “Point A” means that the bond state of the loaded end is that of the point when the maximum shear bond stress is first reached. Such states are referred to as the characteristic states while states of the interface between these characteristic states are referred to as the transition states.

## 4.4 PREDICTIONS OF THE FULL-RANGE DEBONDING BEHAVIOR

### 4.4.1 Elastic-Brittle Model

For an elastic-brittle bond-slip model as shown in Fig. 4.1a, the debonding process can be divided into two stages: the elastic stage (Fig. 4.2a) and the elastic-debonding stage (Fig. 4.2b). As the bond stress descends abruptly to zero (Fig. 4.1a), the softening process does not exist.

#### 4.4.1.1 Elastic stage

When the slip at the loaded end is less than  $\delta_f$ , the entire interface is elastic (Fig. 4.2a). Substituting Eq. (4.10) for the case of  $0 < \delta \leq \delta_f$  into Eq. (4.7) gives the following differential equation:

$$\frac{d^2\delta}{dx^2} - \lambda^2\delta = 0 \quad \text{for } 0 \leq \delta \leq \delta_f \quad (4.15)$$

Using the boundary conditions at the two ends of the FRP plate [ $\sigma_p = 0$  at  $x = 0$  and  $\sigma_p = P/(b_p t_p)$  at  $x = L$ ], the interfacial slip, the interfacial shear stress and the axial stress in the FRP plate can be found by solving Eq. (4.15):

$$\delta = \left[ \frac{P \cdot 2G_f \lambda^2}{b_p \tau_f^2} + (\alpha_p - \alpha_c) \Delta T (1 - \cosh(\lambda L)) \right] \frac{\cosh(\lambda x)}{\lambda \sinh(\lambda L)} + \frac{(\alpha_p - \alpha_c) \Delta T}{\lambda} \sinh(\lambda x) \quad (4.16)$$

$$\tau = \frac{\tau_f}{\delta_f} \left\{ \left[ \frac{P \cdot 2G_f \lambda^2}{b_p \tau_f^2} + (\alpha_p - \alpha_c) \Delta T (1 - \cosh(\lambda L)) \right] \frac{\cosh(\lambda x)}{\lambda \sinh(\lambda L)} + \frac{(\alpha_p - \alpha_c) \Delta T}{\lambda} \sinh(\lambda x) \right\} \quad (4.17)$$

$$\sigma_p = \frac{\tau_f^2}{2G_f t_p \lambda^2} \left\{ \left[ \frac{P \cdot 2G_f \lambda^2}{b_p \tau_f^2} + (\alpha_p - \alpha_c) \Delta T (1 - \cosh(\lambda L)) \right] \frac{\sinh(\lambda x)}{\sinh(\lambda L)} + (\alpha_p - \alpha_c) \Delta T \cdot \cosh(\lambda x) - (\alpha_p - \alpha_c) \Delta T \right\} \quad (4.18)$$

During this stage, the slip at the loaded end (i.e., the value of  $\delta$  at  $x=L$ ) is the same as the displacement of the loaded end of the FRP plate (also referred to as the displacement of the bonded joint),  $\Delta$ . Therefore, the load-displacement relationship can be deduced from Eq. (4.16) to be:

$$P = \Delta \times \left\{ 1 - \frac{(\alpha_p - \alpha_c) \Delta T}{\lambda \Delta} \cdot \sinh(\lambda L) - \frac{(\alpha_p - \alpha_c) \Delta T [1 - \cosh(\lambda L)]}{\lambda \Delta \cdot \tanh(\lambda L)} \right\} \cdot \frac{b_p \tau_f}{\lambda \delta_f} \cdot \tanh(\lambda L) \quad (4.19)$$

At the end of the elastic stage, the interfacial shear stress reaches  $\tau_f$  with a slip  $\delta_f$  at the loaded end (point A in Fig. 4.1a). Substituting  $\Delta = \delta_f$  into Eq. (4.19) leads to the load at the initiation of interfacial debonding (the beginning of the elastic-debonding stage):

$$P_u = \left[ 1 + \frac{(\alpha_p - \alpha_c) \Delta T}{\lambda \delta_f \sinh(\lambda L)} - \frac{(\alpha_p - \alpha_c) \Delta T \operatorname{ctanh}(\lambda L)}{\lambda \delta_f} \right] \cdot \frac{b_p \tau_f}{\lambda} \cdot \tanh(\lambda L) \quad (4.20)$$

For an infinite bond length, Eq. (4.20) converges to

$$P_u = \frac{b_p \tau_f}{\lambda} - \frac{b_p \tau_f}{\lambda^2 \delta_f} (\alpha_p - \alpha_c) \Delta T \quad (4.21)$$

Theoretically, the load that can be resisted by the interface keeps increasing as the length of the interface increases, and the maximum possible load that can be resisted by the bonded joint corresponds to an infinitely long bond length. For any practical applications, when the bond length is sufficiently long, the debonding load of the bonded joint is so close to that given by Eq. (4.21) that any further increase due a longer bond length is negligible. Based on this consideration, the concept of an effective bond length has been well-established in the existing literature (e.g., Chen and Teng 2001). In the present study, following Yuan et al. (2004), the effective bond length ( $L_e$ ) is defined as the bond length over which the interfacial shear stresses resist 97% of the debonding load for a joint with an infinite bond length. Based on this definition and Eqs. (4.20)-(4.21), the effective bond length can be determined from the following equation:

$$\tanh(\lambda L_e) = 0.97 - 0.97 \frac{(\alpha_p - \alpha_c)\Delta T}{\lambda \delta_f} - \frac{(\alpha_p - \alpha_c)\Delta T}{\lambda \delta_f} \frac{1 - \cosh(\lambda L_e)}{\sinh(\lambda L_e)} \quad (4.22)$$

The solution to the above equation leads to:

$$L_e = \frac{1}{\lambda} \operatorname{acosh} \left[ \frac{1}{2} \cdot \frac{m - \sqrt{m^2 - (m+n-1)(4-2n)}}{m+n-1} \right] \quad (4.23)$$

$$\text{where } m = \frac{(\alpha_p - \alpha_c)\Delta T}{\lambda \delta_f}, \quad n = 0.97 - 0.97 \frac{(\alpha_p - \alpha_c)\Delta T}{\lambda \delta_f}.$$

#### 4.4.1.2 Elastic-debonding stage

When the slip at the loaded end exceeds  $\delta_f$ , debonding initiates at the loaded end and then propagates towards the free end with an almost constant (exactly constant if the bond length is infinitely long) debonding load (Fig. 4.2b). By denoting the debonded length of the interface by  $d$ , the solutions for the elastic stage [Eqs. (4.16)-(4.18)] can be simply modified by replacing  $L$  with  $(L-d)$  for the elastic-debonding stage. However, the displacement of the bonded joint, now differing from the slip of the FRP plate at the loaded end due to the presence of thermal expansion of the substrate, can be evaluated with due consideration of thermally induced slip in the debonded zone and is given by the following equation:

$$\Delta = \delta_f + \frac{P}{b_p} \left( \frac{1}{E_p t_p} + \frac{b_p}{b_c E_c t_c} \right) d + (\alpha_p - \alpha_c) \Delta T d \quad (4.24)$$

#### 4.4.2 Bi-Linear Model

The debonding process of a bonded joint with a bi-linear bond-slip relationship (Fig. 4.1b) can be divided into three stages (Yuan et al. 2004): (a) the elastic stage (Fig. 4.3a), during which the slip at the loaded end is below  $\delta_1$  and the interfacial shear stress stays below  $\tau_f$ ; (b) the elastic-softening stage (Fig. 4.3b), during which the slip at the loaded end is greater than  $\delta_1$  but smaller than  $\delta_f$ ; (c) the elastic-softening-debonding stage (Fig. 4.3c), during which the interfacial slip at the loaded end is greater than the separation slip  $\delta_f$  and the corresponding shear stress is zero; during this stage, interfacial debonding initiates at the loaded end and propagates along the interface. Since the detailed solutions for the interfacial shear stress/slip distributions during these three stages have already been given in Chapter 3, here only the expressions for the load-displacement relationship are provided to facilitate the determination of the debonding load and the effective bond length.

##### 4.4.2.1 Elastic stage

During the elastic stage (Fig. 4.3a), the linear load-displacement relationship corresponding to the linearly ascending segment in Fig. 4.1b is described by:

$$P = \Delta \times \left\{ \left[ 1 - \frac{(\alpha_p - \alpha_c) \Delta T}{\lambda_1 \Delta} \cdot \sinh(\lambda_1 L) \right] - \frac{(\alpha_p - \alpha_c) \Delta T [1 - \cosh(\lambda_1 L)]}{\lambda_1 \Delta \cdot \tanh(\lambda_1 L)} \right\} \cdot \frac{b_p \tau_f}{\lambda_1 \delta_1} \cdot \tanh(\lambda_1 L) \quad (4.25)$$

$$\text{where } \lambda_1^2 = \frac{2G_f}{\delta_1 \tau_f} \quad \lambda^2 = \frac{\tau_f}{\delta_1} \left( \frac{1}{E_p t_p} + \frac{b_p}{b_c E_c t_c} \right).$$

##### 4.4.2.2 Elastic-softening stage

When the loaded end slip first exceeds  $\delta_1$  (beyond point A in Fig. 4.1b), the free end slip is still less than  $\delta_1$ , so the right part of the interface (i.e., the part near the loaded end) is now in the softening state while the left part of the interface (i.e., the part near the free end) is still in the linear elastic state (Fig. 4.3b). Denoting the length of the

softening zone by  $a$ , the load-displacement response can be expressed as a function of the softening zone length  $a$ :

$$P = -\frac{b_p \tau_f}{\lambda_1^2 \delta_1} (\alpha_p - \alpha_c) \Delta T + \frac{b_p \tau_f}{\lambda_1^2 \delta_1} \left\{ \lambda_1 \delta_1 \tanh[\lambda_1 (L - a)] + \frac{(\alpha_p - \alpha_c) \Delta T}{\cosh[\lambda_1 (L - a)]} \right\} \cdot \cos(\lambda_2 a) + \frac{b_p \tau_f}{\lambda_2} \cdot \sin(\lambda_2 a) \quad (4.26)$$

$$\text{where } \lambda_2^2 = \frac{2G_f}{(\delta_f - \delta_1) \tau_f} \lambda^2 = \frac{\tau_f}{(\delta_f - \delta_1)} \left( \frac{1}{E_p t_p} + \frac{b_p}{E_c t_c b_c} \right).$$

$$\Delta = \delta_f + \frac{1}{\lambda_2} \left\{ \lambda_1 \delta_1 \tanh[\lambda_1 (L - a)] + \frac{(\alpha_p - \alpha_c) \Delta T}{\cosh[\lambda_1 (L - a)]} \right\} \cdot \sin(\lambda_2 a) + (\delta_1 - \delta_f) \cdot \cos(\lambda_2 a) \quad (4.27)$$

#### 4.4.2.3 Elastic-softening-debonding stage

At the end of the elastic-softening stage, the slip at the loaded end  $\Delta$  reaches  $\delta_f$  (point C in Fig. 4.1b), indicating the initiation of debonding at the loaded end (Fig. 4.3c). The corresponding value of  $a$  reaches its maximum possible value (denoted by  $a_d$ ) and is determined using the following equation which is obtained from Eq. (4.27):

$$\frac{1}{\lambda_2} \left\{ \lambda_1 \delta_1 \tanh[\lambda_1 (L - a_d)] + \frac{(\alpha_p - \alpha_c) \Delta T}{\cosh[\lambda_1 (L - a_d)]} \right\} \cdot \sin(\lambda_2 a_d) + (\delta_1 - \delta_f) \cdot \cos(\lambda_2 a_d) = 0 \quad (4.28)$$

Substituting Eq. (4.28) into Eq. (4.26), the debonding load is obtained:

$$P_u = \frac{b_p \tau_f}{\lambda_2} \cdot \frac{\delta_f}{\delta_f - \delta_1} \cdot \sin(\lambda_2 a_d) - \frac{b_p \tau_f}{\lambda_1^2 \delta_1} (\alpha_p - \alpha_c) \Delta T \quad (4.29)$$

For an infinite bond length, Eq. (4.28) becomes

$$a_d = \frac{1}{\lambda_2} \arctan \left( \frac{\lambda_1}{\lambda_2} \right) \quad (4.30)$$

Substituting Eq. (4.30) into Eq. (4.29) yields

$$P_u = \frac{b_p \tau_f}{\lambda} - \frac{b_p \tau_f}{\lambda_1^2 \delta_1} (\alpha_p - \alpha_c) \Delta T \quad (4.31)$$

By defining the effective bond length as a bond length that allows 97% of  $P_u$ , to be resisted by the bonded joint, Eq. (4.28) can be solved to yield the following equation:

$$L_e = a + \frac{\ln \left\{ \frac{-(\alpha_p - \alpha_c) \Delta T + \sqrt{[(\alpha_p - \alpha_c) \Delta T]^2 + [\lambda_2 (\delta_f - \delta_1) \text{ctg}(\lambda_2 a) - \lambda_1 \delta_1] [\lambda_2 (\delta_f - \delta_1) \text{ctg}(\lambda_2 a) + \lambda_1 \delta_1]}}{\lambda_2 (\delta_f - \delta_1) \text{ctg}(\lambda_2 a) - \lambda_1 \delta_1} \right\}}{\lambda_1} \quad (4.32)$$

where the corresponding softening length can be obtained from Eqs. (4.29) and (4.31):

$$a = \frac{1}{\lambda_2} \arcsin \left[ 0.97 \sqrt{\frac{\delta_f - \delta_1}{\delta_f}} + 0.03 \frac{1}{\lambda_2 \delta_f} (\alpha_p - \alpha_c) \Delta T \right] \quad (4.33)$$

As debonding propagates, the location of the peak shear stress  $\tau_f$  moves towards the free end (Fig. 4.3c), and as a result, the total length of the intact interface reduces. Assuming that the length of the debonded portion of the interface is  $d$ , the load-displacement response [Eq. (4.26)] is still valid if  $L$  is replaced by  $(L-d)$ . The displacement can still be evaluated using Eq. (4.24) with due consideration of thermally induced slips in the debonded zone.

#### 4.4.3 Elastic-Plastic-Brittle Model

For a bonded joint with an elastic-plastic-brittle bond-slip characteristic as shown in Fig. 4.1c, the entire debonding process can be divided into three stages: (a) the entire interface is in the elastic stage (i.e., the slip at the loaded end is below  $\delta_1$  and the interfacial shear stress stays below  $\tau_f$ ) (Fig. 4.4a); (b) when the slip at the loaded end exceeds  $\delta_1$ , the right part of the interface enters into the plastic state whereas the remaining part is still in the elastic state (referred to as the elastic-plastic stage) (Fig. 4.4b); (c) when the slip at the loaded end exceeds  $\frac{\delta_f + \delta_1}{2}$  (note that this debonding slip is different from the value defined in other bond-slip models due to the same fracture energy assumed underneath the bond-slip curves), interfacial debonding initiates at

the loaded end, and then the plastic zone moves towards the free end; the interface is now in the elastic-plastic-debonding stage (Fig. 4.4c). Detailed solutions for these three stages are presented below.

#### 4.4.3.1 Elastic stage

During the elastic stage (Fig. 4.4a), the bond-slip behavior is described by the first part of Eq. (4.12). Similar to the elastic stage for the elastic-brittle model, the expressions for the interfacial slip, the interfacial shear stress and the axial stress in the FRP plate can be obtained from Eqs. (4.16)-(4.18) by replacing  $\lambda$  with  $\lambda_1$ . The load-displacement relationship can be deduced from Eq. (4.19) by substituting  $\lambda_1$  and the corresponding slip  $\delta_1$  at the loaded end into this equation.

#### 4.4.3.2 Elastic-plastic stage

When the pull load on the FRP plate is further increased so that the loaded end slip first exceeds  $\delta_1$  (point A in Fig. 4.1c), the interface enters into the elastic-plastic stage (Fig. 4.4b). Substituting Eq. (4.12) into Eq. (4.7), the following differential equations for the elastic-plastic stage can be obtained:

$$\frac{d^2\delta}{dx^2} - \lambda_1^2 \delta = 0 \quad \text{for } 0 \leq \delta \leq \delta_1 \quad (4.34)$$

$$\frac{d^2\delta}{dx^2} - \frac{2G_f}{\tau_f} \lambda^2 = 0 \quad \text{for } \delta_1 \leq \delta \leq \frac{\delta_1 + \delta_f}{2} \quad (4.35)$$

If the length of plastic zone is denoted by  $l_p$ , the boundary conditions for the interface during the elastic-plastic stage can be defined as follows:

$$\sigma_p = 0 \quad \text{at } x = 0 \quad (4.36)$$

$$\sigma_p \text{ is continuous at } x = L - l_p \quad (4.37)$$

$$\delta = \delta_1 \quad \text{at } x = L - l_p \quad (4.38)$$

$$\sigma_p = \frac{P}{b_p t_p} \text{ at } x = L \quad (4.39)$$

With the above boundary conditions, the solutions for the elastic zone ( $0 \leq x \leq L - l_p$ ,  $0 \leq \delta \leq \delta_1$ ) can be obtained as follows:

$$\delta = \frac{\lambda_1 \delta_1 - (\alpha_p - \alpha_c) \Delta T \sinh[\lambda_1(L - l_p)]}{\lambda_1 \cosh[\lambda_1(L - l_p)]} \cdot \cosh(\lambda_1 x) + \frac{(\alpha_p - \alpha_c) \Delta T}{\lambda_1} \cdot \sinh(\lambda_1 x) \quad (4.40)$$

$$\tau = \frac{\tau_f}{\delta_1} \left\{ \frac{\lambda_1 \delta_1 - (\alpha_p - \alpha_c) \Delta T \sinh[\lambda_1(L - l_p)]}{\lambda_1 \cosh[\lambda_1(L - l_p)]} \cdot \cosh(\lambda_1 x) + \frac{(\alpha_p - \alpha_c) \Delta T}{\lambda_1} \cdot \sinh(\lambda_1 x) \right\} \quad (4.41)$$

$$\sigma_p = \frac{\tau_f}{\lambda_1^2 t_p \delta_1} \left\{ \frac{\lambda_1 \delta_1 - (\alpha_p - \alpha_c) \Delta T \sinh[\lambda_1(L - l_p)]}{\cosh[\lambda_1(L - l_p)]} \cdot \sinh(\lambda_1 x) + [\cosh(\lambda_1 x) - 1](\alpha_p - \alpha_c) \Delta T \right\} \quad (4.42)$$

For the plastic zone ( $L - l_p \leq x \leq L$ ,  $\delta_1 < \delta \leq \frac{\delta_1 + \delta_f}{2}$ ), the interfacial slip, the interfacial shear stress and the axial stress in the FRP plate are given by:

$$\delta = \frac{G_f}{\tau_f} \lambda^2 [x - (L - l_p)]^2 + \left\{ \lambda_1 \delta_1 \tanh[\lambda_1(L - l_p)] + \frac{(\alpha_p - \alpha_c) \Delta T}{\cosh[\lambda_1(L - l_p)]} \right\} [x - (L - l_p)] + \delta_1 \quad (4.43)$$

$$\tau = \tau_f \quad (4.44)$$

$$\sigma_p = \frac{\tau_f^2}{2G_f t_p \lambda^2} \left\{ \frac{2G_f}{\tau_f} \lambda^2 [x - (L - l_p)] + \lambda_1 \delta_1 \tanh[\lambda_1(L - l_p)] + \frac{1 - \cosh[\lambda_1(L - l_p)]}{\cosh[\lambda_1(L - l_p)]} (\alpha_p - \alpha_c) \Delta T \right\} \quad (4.45)$$

The load-displacement relationship can be obtained from Eqs. (4.43) and (4.45) as

$$\Delta = \frac{G_f}{\tau_f} \lambda^2 \cdot l_p^2 + \left\{ \lambda_1 \delta_1 \cdot \tanh[\lambda_1(L - l_p)] + \frac{(\alpha_p - \alpha_c) \Delta T}{\cosh[\lambda_1(L - l_p)]} \right\} l_p + \delta_1 \quad (4.46)$$

$$P = b_p \tau_f l_p + \frac{b_p \tau_f^2}{2G_f \lambda^2} \left\{ \lambda_1 \delta_1 \cdot \tanh[\lambda_1(L - l_p)] + \frac{1 - \cosh[\lambda_1(L - l_p)]}{\cosh[\lambda_1(L - l_p)]} (\alpha_p - \alpha_c) \Delta T \right\} \quad (4.47)$$

The plastic stage ends when the slip at the loaded end reaches  $\frac{\delta_1 + \delta_f}{2}$  (point B in Fig. 4.1c). That is, when

$$\frac{G_f}{\tau_f} \lambda^2 \cdot l_p^2 + \left\{ \lambda_1 \delta_1 \cdot \tanh[\lambda_1(L - l_p)] + \frac{(\alpha_p - \alpha_c)\Delta T}{\cosh[\lambda_1(L - l_p)]} \right\} l_p + \delta_1 = \frac{\delta_1 + \delta_f}{2} \quad (4.48)$$

Combining Eq. (4.48) and Eq. (4.47) yields

$$P_u = b_p \tau_f l_p + \frac{b_p \tau_f^2}{2G_f \lambda^2} \left\{ \frac{\delta_f - \delta_1}{2l_p} - \frac{G_f}{\tau_f} \lambda^2 l_p - (\alpha_p - \alpha_c)\Delta T \right\} \quad (4.49)$$

For an infinite bond length, Eq. (4.48) becomes

$$l_{p,max} = \frac{-\lambda_1 \delta_1 + \sqrt{(\lambda_1 \delta_1)^2 + (\delta_f - \delta_1)\delta_f \lambda^2}}{\delta_f \lambda^2} \quad (4.50)$$

With the replacement of  $l_p$  with  $l_{p,max}$ , Eq. (4.49) becomes

$$P_u = \frac{b_p \tau_f}{\lambda} - \frac{b_p \tau_f}{\lambda^2 \delta_f} (\alpha_p - \alpha_c)\Delta T \quad (4.51)$$

If the effective bond length  $L_e$  is still defined as a bonded length needed to resist 97% of  $P_u$ , replacing  $P$  with  $0.97P_u$  in Eq. (4.47) yields:

$$L_e = l_p + \frac{1}{\lambda_1} \ln \left[ \frac{-(\alpha_p - \alpha_c)\Delta T + \sqrt{[(\alpha_p - \alpha_c)\Delta T]^2 + 4(\lambda_1 \delta_1 + p)^2}}{2(\lambda_1 \delta_1 + p)} \right] \quad (4.52)$$

where  $p = \frac{0.5(\delta_f - \delta_1) - 0.5\delta_f \lambda^2 l_p^2}{l_p}$  and the length of the plastic zone,  $l_p$ , can be obtained from Eqs. (4.49) and (4.51) as follows:

$$l_p = \frac{0.97\lambda\delta_f + 0.03(\alpha_p - \alpha_c)\Delta T + \sqrt{[0.97\lambda\delta_f + 0.03(\alpha_p - \alpha_c)\Delta T]^2 - \delta_f(\delta_f - \delta_1)\lambda^2}}{\delta_f \lambda^2} \quad (4.53)$$

#### 4.4.3.3 Elastic-plastic-debonding stage

Assuming that the length of the debonded part of the interface is  $d$ , the solutions for

the elastic-plastic-debonding are given by Eqs. (4.40)-(4.45) with  $L$  replaced by  $(L-d)$ . During this stage, the plastic zone (i.e.,  $L - l_{p,max} - d \leq x \leq L - d$ ) has a constant shear stress  $\tau_f$  (the plastic plateau) and this plateau moves towards the free end as debonding progresses (i.e., as  $d$  increases) (Fig. 4.4c). Therefore, the displacement at the loaded end can be obtained with due consideration of thermally induced slip at the debonded length:

$$\Delta = \frac{\delta_1 + \delta_f}{2} + \frac{P}{b_p} \left( \frac{1}{E_p t_p} + \frac{b_p}{b_c E_c t_c} \right) d + (\alpha_p - \alpha_c) \Delta T d \quad (4.54)$$

It is worth noting that if a rigid-plastic-brittle bond-slip model (e.g., Taljsten 1996) is incorporated into the above analyses, the elastic stage does not exist and the detailed solutions for the other stages are still valid by setting  $\delta_1 = 0$ .

#### **4.4.4 Rigid-Softening Model**

For a rigid-softening bond-slip model as shown in Fig. 4.1d, the debonding process can be divided into two stages: (1) the softening stage (Fig. 4.5a), during which the slip at the loaded end is less than  $\delta_f$ ; (2) the softening-debonding stage (Fig. 4.5b), during which the slip at the loaded end exceeds  $\delta_f$  and the interfacial debonding propagates from the loaded end towards the free end. The analytical solutions for these two stages are discussed below.

##### **4.4.4.1 Softening stage**

If the bonded joint is subjected to thermal loading only (i.e., temperature change denoted by  $\Delta T$ ), softening initiates at the two ends (point O) in an anti-symmetrical manner and propagates inwards (Fig. 4.5a). Substituting Eq. (4.13) for the case of  $0 < |\delta| \leq \delta_f$  into Eq. (4.7) gives the following differential equations:

$$\frac{d^2 \delta}{dx^2} + \lambda^2 \delta = -\lambda^2 \delta_f \quad \text{for } -\delta_f \leq \delta \leq 0 \quad (4.55a)$$

$$\frac{d^2 \delta}{dx^2} + \lambda^2 \delta = \lambda^2 \delta_f \quad \text{for } 0 \leq \delta \leq \delta_f \quad (4.55b)$$

If the length of the two softening regions is denoted by  $a_1$ , the boundary conditions at the free and the loaded ends ( $x = 0, L$ ) and at the softening fronts ( $x = a_1, L - a_1$ ) can be obtained for the condition of thermal loading only:

$$\sigma_p = 0 \text{ at } x = 0 \text{ and } x = L \quad (4.56)$$

$$\delta = 0 \text{ at } x = a_1 \text{ and } x = L - a_1 \quad (4.57)$$

$$\sigma_p \text{ is continuous at } x = a_1 \text{ and } x = L - a_1 \quad (4.58)$$

The interfacial slip, the interfacial shear stress and the axial stress in the FRP plate can be found by solving Eqs. (4.55a) and (4.55b). If  $(\alpha_p - \alpha_c)\Delta T > 0$ , the thermal expansion of the FRP plate is constrained by the substrate and negative (i.e., compressive) axial stresses are induced in the FRP plate. Under this condition, the solutions for the left softening region (Fig. 4.5a) of the interface ( $-\delta_f \leq \delta \leq 0$  within  $0 \leq x \leq a_1$ ) are given by

$$\delta + \delta_f = A \sin[\lambda(x - a_1)] + B \cos[\lambda(x - a_1)] \quad (4.59)$$

$$\tau = -\frac{\tau_f}{\delta_f} \{A \sin[\lambda(x - a_1)] + B \cos[\lambda(x - a_1)]\} \quad (4.60)$$

$$\sigma_p = \frac{\tau_f}{\lambda^2 t_p \delta_f} \{A\lambda \cos[\lambda(x - a_1)] - B\lambda \sin[\lambda(x - a_1)] - (\alpha_p - \alpha_c)\Delta T\} \quad (4.61)$$

and those for the right softening region ( $0 \leq \delta \leq \delta_f$  within  $L - a_1 \leq x \leq L$ ) are given by

$$\delta - \delta_f = C \sin[\lambda(x - L + a_1)] + D \cos[\lambda(x - L + a_1)] \quad (4.62)$$

$$\tau = -\frac{\tau_f}{\delta_f} \{C \sin[\lambda(x - L + a_1)] + D \cos[\lambda(x - L + a_1)]\} \quad (4.63)$$

$$\sigma_p = \frac{\tau_f}{\lambda^2 t_p \delta_f} \{ C\lambda \cos[\lambda(x - L + a_1)] - D\lambda \sin[\lambda(x - L + a_1)] - (\alpha_p - \alpha_c)\Delta T \} \quad (4.64)$$

Within the rigid region of the interface ( $a_1 \leq x \leq L - a_1$ ), there is no interfacial slip or interfacial shear stress, so the axial stress in the FRP can be found from Eq. (4.61) as

$$\sigma_p = \frac{\tau_f}{\lambda^2 t_p \delta_f} [A\lambda - (\alpha_p - \alpha_c)\Delta T] \quad (4.65)$$

The constants  $A$ ,  $B$ ,  $C$  and  $D$  in Eqs. (4.59)-(4.64) can be obtained as follows by substituting Eqs. (4.56)-(4.58) into Eqs. (4.59), (4.61), (4.62) and (4.64):

$$A = 0, B = \delta_f, C = 0, D = -\delta_f \quad (4.66)$$

Therefore, by substituting Eq. (4.66) into Eqs. (4.59)-(4.61), the solutions for the left softening region ( $0 \leq x \leq a_1$ ) become:

$$\delta = \delta_f \cos[\lambda(x - a_1)] - \delta_f \quad (4.67)$$

$$\tau = -\tau_f \cos[\lambda(x - a_1)] \quad (4.68)$$

$$\sigma_p = \frac{\tau_f}{\lambda^2 t_p \delta_f} \{ -\lambda\delta_f \sin[\lambda(x - a_1)] - (\alpha_p - \alpha_c)\Delta T \} \quad (4.69)$$

and those for the right softening region of the interface ( $L - a_1 \leq x \leq L$ ) [i.e., Eqs. (4.62)-(4.64)] become:

$$\delta = \delta_f - \delta_f \cos[\lambda(x - L + a_1)] \quad (4.70)$$

$$\tau = \tau_f \cos[\lambda(x - L + a_1)] \quad (4.71)$$

$$\sigma_p = \frac{\tau_f}{\lambda^2 t_p \delta_f} \{ \lambda\delta_f \sin[\lambda(x - L + a_1)] - (\alpha_p - \alpha_c)\Delta T \} \quad (4.72)$$

If there is no mechanical loading (i.e.,  $P = 0$ ), the softening zones are anti-symmetrically located on the interface and the value of  $a_1$  can be obtained from the following equation:

$$\frac{\tau_f}{\lambda^2 t_p \delta_f} [\lambda \delta_f \sin(\lambda a_1) - (\alpha_p - \alpha_c) \Delta T] = 0 \quad (4.73)$$

If  $(\alpha_p - \alpha_c) \Delta T < 0$ , the thermal contraction of the FRP plate is constrained by the substrate, and tensile (positive) axial stresses are induced in the FRP plate. The solutions presented above are also valid with the boundary conditions redefined as  $0 \leq \delta \leq \delta_f$  within  $0 \leq x \leq a_1$  and  $-\delta_f \leq \delta \leq 0$  within  $L - a_1 \leq x \leq L$ .

After a pull load is now applied on the FRP plate, the softening region near the loaded end is extended and the corresponding length is denoted by  $a_2$  (Fig. 4.5a). The governing equation [i.e. Eq. (4.55)] is always suitable for the interface whereas the boundary condition at the loaded end is changed to

$$\sigma_p = \frac{P}{b_p t_p} \text{ at } x = L \quad (4.74)$$

Therefore, the solutions in Eqs. (4.72)-(4.74) are still valid if the softening length  $a_1$  is replaced by  $a_2$  and the value of  $a_2$  can be obtained from the following equation:

$$\frac{\tau_f}{\lambda^2 t_p \delta_f} [\lambda \delta_f \sin(\lambda a_2) - (\alpha_p - \alpha_c) \Delta T] = \frac{P}{b_p t_p} \quad (4.75)$$

Clearly, two softening regions appear at the free and the loaded end respectively, and the length of the softening region  $a_2$  increases with the pull load. The displacement at the loaded end can be expressed as a function of the length  $a_2$  (i.e.,  $x = L$  in Eq. 70) as follows:

$$\Delta = \delta_f - \delta_f \cos(\lambda a_2) \quad (4.76)$$

In Eq. (4.75), the pull load  $P$  reaches its maximum value when the derivative of Eq. (4.75) with respect to  $a_2$  is equal to zero. Therefore, the softening length  $(a_2)_{max}$  at the debonding load (point C in Fig. 4.1d) can be obtained as

$$(a_2)_{max} = \frac{\pi}{2\lambda} \quad (4.77)$$

By substituting Eq (4.77) into Eq. (4.75), the debonding load can be found as

$$P_u = \frac{b_p \tau_f}{\lambda^2 \delta_f} [\lambda \delta_f - (\alpha_p - \alpha_c) \Delta T] \quad (4.78)$$

If the effective bond length  $L_e$  is still defined as one that can resist 97% of the debonding load of an infinitely bonded joint subjected to combined thermal and mechanical loadings, it can be obtained from Fig. 4.5a as

$$L_e = a_2 + |a_1| = \frac{1}{\lambda} \arcsin(0.97) + \frac{1}{\lambda} \arcsin \left| \frac{(\alpha_p - \alpha_c) \Delta T}{\lambda \delta_f} \right| \quad \text{for } \Delta T \geq 0 \quad (4.79a)$$

$$L_e = a_2 - |a_1| = \frac{1}{\lambda} \arcsin(0.97) - \frac{1}{\lambda} \arcsin \left| \frac{(\alpha_p - \alpha_c) \Delta T}{\lambda \delta_f} \right| \quad \text{for } \Delta T < 0 \quad (4.79b)$$

#### 4.4.4.2. Softening-debonding stage

When the slip at the loaded end is larger than  $\delta_f$ , interfacial debonding propagates from the loaded end towards the free end without any change in the pull load (Fig. 4.5b). If the length of the debonded portion of the interface is denoted by  $d$ , the solutions for softening-debonding stage are the same as those for the softening stage [Eqs. (4.70)-(4.76)] except for the replacement of  $L$  by  $(L-d)$ . The displacement at the loaded end has the same expression as Eq. (4.24).

#### 4.4.5 Exponential model

For the exponential bond-slip model as shown in Fig. 4.1e, the axial stress in the FRP plate can be obtained by substituting Eqs. (4.2), (4.6) and (4.14) into Eqs. (4.4)-(4.5) as follows:

$$\sigma_p = \frac{E_p}{\left(1 + \frac{b_p E_p t_p}{b_c E_c t_c}\right)} \left[ \frac{d\delta}{dx} - (\alpha_p - \alpha_c) \Delta T \right] \quad (4.80)$$

With the use of Eq. (4.1) and Eq. (4.14), the item  $\sigma_p$  can be eliminated from Eq. (4.80), which then becomes:

$$\frac{d^2\delta}{dx^2} = \frac{2BG_f}{t_p} \left( \frac{1}{E_p} + \frac{b_p t_p}{b_c E_c t_c} \right) (e^{-B\delta} - e^{-2B\delta}) \quad (4.81)$$

Recognizing that  $\frac{d^2\delta}{dx^2} = \frac{d}{dx} \left( \frac{d\delta}{dx} \right) = \frac{d}{d\delta} \left( \frac{d\delta}{dx} \right) \frac{d\delta}{dx} = \frac{1}{2} \frac{d}{d\delta} \left( \left( \frac{d\delta}{dx} \right)^2 \right)$  and substituting it into Eq. (4.81) leads to:

$$\frac{d}{d\delta} \left( \left( \frac{d\delta}{dx} \right)^2 \right) = \frac{4BG_f}{t_p} \left( \frac{1}{E_p} + \frac{b_p t_p}{b_c E_c t_c} \right) (e^{-B\delta} - e^{-2B\delta}) \quad (4.82)$$

Integrating Eq. (4.82) gives (Dai et al. 2006)

$$\frac{d\delta}{dx} = \sqrt{\frac{2G_f}{t_p} \left( \frac{1}{E_p} + \frac{b_p t_p}{b_c E_c t_c} \right) (1 - e^{-B\delta})^2 + c_1} \quad (4.83)$$

where  $c_1$  is a constant.

When a sufficiently long bond length  $L$  is provided (i.e., a bond length larger than the effective bond length defined later in this chapter), the following boundary conditions exist for the bonded joint subjected to combined thermal and mechanical loadings:

$$\left. \frac{d\delta}{dx} \right|_{x=0} = 0 \text{ and } \left. \delta \right|_{x=\frac{L}{2}} = 0 \quad (4.84)$$

Substituting Eq. (4.84) into Eq. (4.83),  $c_1 = 0$  can be obtained. Eq. (4.83) can then be solved and the slip distribution along the interface can be obtained as:

$$\delta(x) = \frac{1}{B} \ln[e^{B(Ax+c_2)} + 1] \quad (4.85)$$

where  $A = \sqrt{\frac{2G_f}{t_p} \left( \frac{1}{E_p} + \frac{b_p t_p}{b_c E_c t_c} \right)}$ .  $c_2$  is a constant and can be solved by substituting Eq. (4.85) into Eq. (4.80) using the boundary condition at the loaded end (i.e.,  $\sigma_p = \frac{P}{t_p b_p}$ ):

$$c_2 = \frac{1}{B} \ln \left\{ \frac{\frac{1}{A} \left[ P \frac{\left(1 + \frac{b_p E_p t_p}{b_c E_c t_c}\right)}{b_p E_p t_p} + (\alpha_p - \alpha_c) \Delta T \right]}{1 - \frac{1}{A} \left[ P \frac{\left(1 + \frac{b_p E_p t_p}{b_c E_c t_c}\right)}{b_p E_p t_p} + (\alpha_p - \alpha_c) \Delta T \right]} \right\} - AL \quad (4.86)$$

Substituting Eq. (4.86) into Eq. (4.80), the axial stress in the FRP plate can be expressed as

$$\sigma_p = \frac{E_p}{\left(1 + \frac{b_p E_p t_p}{b_c E_c t_c}\right)} \{A(1 - e^{-B\delta}) - (\alpha_p - \alpha_c) \Delta T\} \quad (4.87)$$

Eqs. (4.14), (4.85) and (4.87) define the distributions of interfacial shear stress, interfacial shear stress slip and axial stress in the FRP. When only thermal loading is applied, the temperature-induced interfacial shear stress distribution near the free end is anti-symmetrical to that near the loaded end. It can be assumed that these initial temperature-induced interfacial shear stresses near the free end are not affected by the applied pull load on the FRP plate if bonded length is sufficiently long.

The load-displacement relationship at the loaded end (i.e.,  $\delta = \Delta$ ) of the bonded joint subjected to combined thermal and mechanical loadings can be obtained from Eq. (4.87) as:

$$P = \frac{b_p E_p t_p}{\left(1 + \frac{b_p E_p t_p}{b_c E_c t_c}\right)} [A(1 - e^{-B\Delta}) - (\alpha_p - \alpha_c) \Delta T] \quad (4.88)$$

For an infinite bond length (i.e.,  $\delta \rightarrow \infty$ ), Eq. (4.88) converges to

$$P_u = \frac{b_p E_p t_p}{\left(1 + \frac{b_p E_p t_p}{b_c E_c t_c}\right)} [A - (\alpha_p - \alpha_c) \Delta T] \quad (4.89)$$

$P_u$  given by Eq. (4.89) can never be achieved in reality since it corresponds to an infinite bonded length. Similarly to the case of a bi-linear model, the effective bond length can be defined as the bonded length required to resist  $0.97P_u$ . However, no explicit relationship can be found between the debonding load and the bond length for a bonded joint with an exponential bond-slip model. As an approximation, Dai et al. (2006) defined the effective bond length  $L_e$  as the length of the most active bond zone of an infinitely long interface at  $P_u$ . Within such a zone the FRP strain increases from  $(1 - \alpha)\varepsilon_{max}/2$  to  $(1 + \alpha)\varepsilon_{max}/2$ , where  $\varepsilon_{max}$  is the maximum strain in the FRP plate at  $P_u$  and  $\alpha = P/P_u$ , in which  $P$  is the pull load transferred by interfacial shear stresses within the most active bond zone. As a result, the effective bond length can be obtained as:

$$L_e = \frac{\sqrt{2E_p t_p}}{B\sqrt{G_f}} \ln\left(\frac{1+\alpha}{1-\alpha}\right) \quad (4.90)$$

However, this approximation is not suitable for a bonded joint subjected to combined thermal and mechanical loadings because at  $P_u$  the strain distribution in the FRP plate no longer has a monotonically decreasing trend (see Fig. 4.6). To examine the relationship between the debonding load and the bond length for a bonded joint subjected to combined mechanical and thermal loadings, FE analyses were conducted. In the FE model, truss elements are used to represent the FRP plate and the substrate, whereas cohesive elements with a zero thickness are used to depict the bond behavior between them following the same assumptions as adopted in deriving the closed-form solutions. The properties of the FRP plate and the concrete substrate are assumed as follows:  $E_p = 165$  GPa,  $b_p = 100$  mm,  $t_p = 1.2$  mm,  $E_c = 26.8$  GPa,  $b_c = 150$  mm,  $t_c = 75$  mm,  $\alpha_p = 0.3 \times 10^{-6}/^\circ\text{C}$ ,  $\alpha_c = 10.2 \times 10^{-6}/^\circ\text{C}$  according to Klamer's (2006) tests. The parameters to define the bond-slip curve are determined according to Section 3.3.1 as:  $\delta_1 = 0.09$  mm,  $\delta_f = 0.41$  mm,  $\tau_f = 2.77$  Mpa,  $G_f = 0.57$  N/mm,  $B = 9.72$  mm<sup>-1</sup>.

Fig. 4.7a shows the relationships between the debonding load and the bond length of a bonded joint exposed to different temperature variations. The effective bond length  $L_e$ , as defined earlier in the paper, can be easily deduced from such a relationship. Fig. 4.7b illustrates how the temperature variation affects the effective bond length for a bonded joint with an exponential bond-slip model. In the figure, the values of  $L_e$  of a bonded joint with a bilinear bond-slip model are also shown for comparison. It is clearly seen that both the bi-linear and the exponential models lead to the same linearly increasing trend, but the latter leads to a slightly larger  $L_e$  at all temperature variations. Eq. (4.32) multiplied by a factor of 1.05 can be used to predict closely the  $L_e$  value of a bonded joint with an exponential bond-slip model (Fig. 4.7b).

## 4.5 NUMERICAL RESULTS AND DISCUSSIONS

### 4.5.1 Interfacial Stress States and Load-Displacement Response

Interfacial shear stress distributions at different loading states for both a temperature rise of 30 °C and a temperature reduction of 30 °C are shown in parallel for the five different bond-slip models examined above in Figs. 4.2-4.6 respectively. In all the analyses, the properties of the FRP plate and the substrate were taken from Klamer's (2006) tests. A bond length of 450 mm was used for the bonded joints to represent a length longer than the effective bond length. For easy comparisons, the interfacial shear stresses in Figs. 4.2-4.6 are all normalized by the value of  $\tau_f$  of the relevant bond-slip model.

In Figs. 4.2-4.5, the continuous and dashed lines represent the predicted shear stress distributions for the characteristic states (corresponding to the characteristic points on the bond-slip curves in Fig. 4.1), while the dotted lines with hollow circles represent transition states between these characteristic states to indicate the evolution of interfacial shear stresses. In Fig. 4.6 which is for the exponential model case, the FE predictions are also shown for comparison with results from the closed-form solution since the latter is for an infinite bond length instead of a finite bond length of 450 mm. This comparison shows that the results from the closed-form solution agree closely with the FE predictions for all the loading stages (Figs. 4.6a, 4.6b and

4.6c), indicating that the closed-form solution has good accuracy for FRP-to-substrate bonded joints with a finite bond length that is longer than the effective bond length.

In each of Figs. 4.2-4.6, the left column shows how the interfacial shear stress distribution develops as loading progresses for a temperature increase of 30 °C (i.e.,  $\Delta T = 30^{\circ}\text{C}$ ) in comparison with the reference case of no temperature change (i.e., mechanical loading only) for each of the five different bond-slip models. Before applying the mechanical loading (i.e., Point O in Fig. 4.1), the interfacial shear stresses due to a temperature increase are anti-symmetrically distributed. At the initial stage of mechanical loading, the interfacial shear stresses near the loaded end due to Mode-II loading (i.e., the horizontal pull load on the FRP plate) are opposite in direction to those due to the temperature increase (i.e., thermal loading). Therefore, the two types of loadings lead to interfacial shear stresses that counteract each other. That is, part of the pull load in a bonded joint exposed to a temperature increase is resisted by the thermal interfacial stresses, and as a result, a positive temperature variation leads to an increase of the load resisted by the joint during all stages.

The right column of each of Figs. 4.2-4.6 shows how the interfacial shear stress distribution develops as loading progresses for a temperature decrease of 30 °C (i.e.  $\Delta T = -30^{\circ}\text{C}$ ) in comparison with the reference temperature case of no temperature change for each of the five different bond-slip models. It is no surprise that a temperature decrease alone leads to interfacial shear stresses which are opposite in direction to those due to a temperature increase. As a result, the interfacial shear stresses in the zone near the loaded end induced by the pull load have the same direction as those induced by the thermal loading. Therefore, these thermally-induced shear stresses reduce the debonding load of the bonded joint.

Figs. 4.2-4.6 also show clearly that the interfacial shear stress distribution and the propagation of debonding are both influenced by the bond-slip characteristics of the interface. To further clarify this issue, Fig. 4.8 shows the typical load-displacement curves of a bonded joint subjected to a temperature increase of 30 °C obtained from the close-form solutions presented in this paper for the five bond-slip models. These curves are all for the ideal case of an infinitely long bond length. In the figure, both

the pull load and the corresponding displacement are normalized by the corresponding values of  $P_u$  and  $\delta_f$ , respectively. The rigid-plastic-brittle model and the rigid-softening model are seen to lead to a higher initial stiffness for the load-displacement curve. The largest difference among these load-displacement curves is found between the rigid-plastic-brittle model and the elastic-brittle model as the differences between these two bond-slip models are also the greatest. The other two models, which are the bi-linear and the exponential models, yield very similar load-displacement responses.

#### ***4.5.2. Effective bond length***

The effective bond length,  $L_e$ , is an important design parameter of FRP-to-concrete bond interfaces since the debonding load no longer increases beyond that length (Chen and Teng 2001). From Eqs. (4.23), (4.32), (4.52) and (4.79), it is clear that the effective bond length for a bonded joint under combined thermal and mechanical loadings depends on the shape of the bond-slip model as well as the properties of the substrate and the FRP plate. As an example, Fig. 4.9 shows how the effective bond length changes with the temperature variation for an FRP-to-concrete interface characterized by each of the five of bond-slip models discussed above. Obviously, with a positive temperature variation, the effective bond length always increases regardless of the shape of the bond-slip model. For a given temperature variation, a bonded joint with an elastic-brittle bond-slip model has the largest effective bond length whereas a rigid-plastic-brittle bond-slip model almost leads to the smallest value. In terms the rate of increase in the effective bond length as the temperature increases, the elastic-plastic-brittle and the elastic-brittle bond-slip models belong to one group while the other three bond-slip models (i.e., rigid-softening, bi-linear and exponential models) belong to the other group. For each group, the rates of increase are similar, and between the two groups, the rates of increase are significantly different. These results indicate that the influence of the temperature variation on the effective bond length should be paid more attention in practical strengthening projects where significant temperature variations are expected during service.

#### ***4.5.3. Debonding load***

The debonding loads of FRP-to-concrete bonded joints subjected to combined thermal and mechanical loadings can be calculated using Eqs. (4.21), (4.31), (4.51), (4.78) and (4.89), respectively for the five different bond-slip models. Provided that the bonded length  $L$  is sufficiently long, all these five equations reduce to the following unified form:

$$P_u = b_p \sqrt{2G_f \frac{E_p t_p}{\left(1 + \frac{b_p E_p t_p}{b_c E_c t_c}\right)} - \frac{b_p E_p t_p}{\left(1 + \frac{b_p E_p t_p}{b_c E_c t_c}\right)} (\alpha_p - \alpha_c) \Delta T} \quad (4.91)$$

Eq. (4.91) demonstrates clearly that the debonding load of the bonded joints is independent of the shape of the bond-slip model once the bond length is long enough. It is only dependent on the interfacial fracture energy  $G_f$  and the temperature variation  $\Delta T$  as well as the material and geometrical properties of the FRP and the substrate.

Figs. 4.10a and 4.10b show the relationships between the debonding load and the bond length for two different thermal loading cases (i.e.,  $\Delta T = -30$  °C and  $30$  °C). Note that the debonding loads in these figures were obtained from the FE model when the bond lengths are less than the effective bond length. These figures show that while these relationships depend on the bond-slip model, they all eventually converge to a single unique value as predicted by Eq. (4.91). The largest differences are observed between the rigid-plastic-brittle bond-slip model and the elastic-brittle bond-slip model as can be expected because the two bond-slip models differ most significantly from each other in shape.

Besides, as long as the interfacial fracture energy and the peak bond stress are kept the same (the same values were chosen for obtaining the curves in Fig. 4.10), the bi-linear and exponential bond-slip models lead to very similar debonding load predictions. The very similar predictions of these two bond-slip models for both the effective bond lengths (Fig. 4.9) and the debonding loads (Fig. 4.10) at different temperature variations further indicate that an exponential bond-slip model can be closely represented by the much simpler bi-linear model.

## 4.6 CONCLUSIONS

This chapter has presented a set of closed-form analytical solutions for the Mode II debonding behavior of FRP-to-substrate bonded joints subjected to combined thermal and mechanical loadings. In order to reveal the stress transfer mechanism and the debonding propagation process in such bonded joints with different bond-slip characteristics, five different bond-slip models have been considered in the study. Explicit closed-form expressions for the interfacial shear stress, the interfacial slip, the axial stress in the FRP plate as well as the load-displacement relationship of such bonded joints have been presented for each of the five bond-slip models. These analytical solutions are applicable to bonded joints between a thin plate and a substrate of many materials (e.g., FRP and concrete, FRP and steel, steel and concrete, aluminum and concrete, and FRP and aluminum) subjected to combined thermal and mechanical loadings. Based on the results and discussions presented in this chapter, the following conclusions can be drawn.

- (a) The bond-slip characteristics of the FRP-to-concrete interface have been found to influence the bond stress transfer mechanism and the propagation of debonding when the interface is subjected to combined thermal and mechanical loadings.
- (b) Provided that the exposed temperature is less than the glass transition temperature, a temperature increase leads to an increase in the debonding load of the bonded joint, regardless of the shape of the bond-slip models.
- (c) If a sufficiently long bond length exists, the debonding load of an FRP-to-concrete bonded joint depends only on the interfacial fracture energy and the temperature variation but is independent of the bond-slip characteristics.
- (d) The effective bond length increases with a positive temperature variation and the increase rate depends on the bond-slip characteristics. The increase rates of elastic-brittle and elastic-plastic-brittle bond-slip models are much higher than those of the other three bond-slip models (i.e., rigid-softening, bi-linear and exponential models).

- (e) The analytical solutions provide a theoretical basis for the interpretation of test results of bonded joints subjected to combined mechanical and thermal loadings; in particular, these solutions can be used to isolate the thermal stress effect due to thermal incompatibility between the two adherends from the effect of mechanical loading.

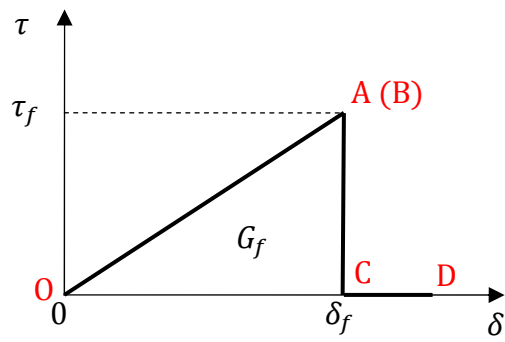
#### 4.7 REFERENCES

- American Concrete Institute (ACI). (2008). "Guide for the design and construction of externally bonded FRP systems for strengthening concrete structures." *ACI 440.2R-08*, American Committee 440, Farmington Hills, Michigan, America.
- Bilotta, A., Faella, C., Martinelli, E., and Nigro, E. (2012). "Indirect identification method of bilinear interface laws for FRP bonded on a concrete substrate." *Journal of Composites for Construction*, ASCE, Vol. 16, No. 2, pp. 171-184.
- Bizindavyi, B.L. and Neale, K.W. (1999). "Transfer lengths and bond strengths for composites bonded to concrete." *Journal of Composites for Construction*, ASCE, Vol. 3, No. 4, pp. 153-160.
- Blontrock, H., "Analysis and Modeling of the Fire Resistance of Concrete Elements with Externally Bonded FRP Reinforcement." Ph.D. thesis, Ghent University, Ghent, Belgium, 2003.
- Brosens, K. and van Gemert, D. (1998). "Plate end shear design for external CFRP laminate." *Proceeding of the Third International Conference on Fracture Mechanics of Concrete and Concrete Structures*, Freiburg, Germany, pp. 1793-1804.
- Brosens, K. and van Gemert, D. (1999). "Anchorage design for externally bonded carbon fiber polymer laminates." *Proceeding of the Fourth International Symposium on Fiber Reinforced Polymer Reinforcement for Concrete Structures*, Baltimore, USA, pp. 635-645.
- Brosens, K. (2001). "Anchoring of externally bonded steel plates and CFRP laminates for the strengthening of concrete elements." Ph.D. thesis, Department of Civil Engineering, Katholieke University Leuven, Belgium.
- Chajes, M.J., Finch, W.W., Januszka, T.F. and Thomson, T.A. (1996). "Bond and force transfer of composite material plates bonded to concrete." *ACI Structural Journal*, Vol. 93, No. 2, pp. 208-217.
- Chen, J.F. and Teng, J.G. (2001). "Anchorage strength models for FRP and steel plates bonded to concrete." *Journal of Structural Engineering*, ASCE, Vol. 127, No. 7, pp. 784-791.
- Chen, J.F., Yuan, H. and Teng, J.G. (2007). "Debonding failure along a softening FRP-to-concrete interface between two adjacent cracks in concrete members." *Engineering Structures*, Vol. 29, No. 2, pp. 259-270.

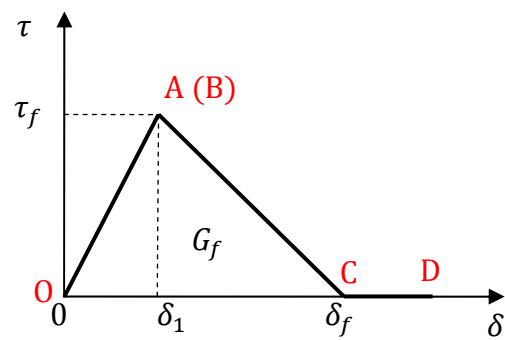
- Consiglio Nazionale delle Ricerche (CNR). (2004). "Guide for the design and construction of externally bonded FRP systems for strengthening existing structures: Materials, RC and PC structures, masonry structures." *CNR-DT 200/2004*, Italian Research Council, Italian Advisory Committee on Technical Recommendations for Construction, CNR, Rome.
- Dai, J.G. and Ueda, T. (2003). "Local bond stress slip relationship for FRP composites-concrete interfaces." *Proceedings of the Sixth International Symposium on FRP Reinforcement for Concrete Structures (FRPRCS-6)*, Singapore, pp. 143-152.
- Dai, J.G., Ueda, T. and Sato, Y. (2005). "Development of the nonlinear bond stress-slip model of fiber reinforced plastics sheet-concrete interfaces with a simple method." *Journal of Composites for Construction*, ASCE, Vol. 9, No. 1, pp. 52-62.
- Dai, J.G., Ueda, T. and Sato, Y. (2006). "Unified analytical approaches for determining shear bond characteristics of FRP-concrete interfaces through pullout tests." *Journal of Advanced Concrete Technology*, JSCE, Vol. 4, No. 1, pp. 133-145.
- De Lorenzis, L., Miller, B. and Nanni, A. (2001). "Bond of fiber-reinforced polymer laminates to concrete." *ACI Material Journal*, Vol. 98, No. 1, pp. 256-264.
- Ferracuti, B., Savoia, M. and Mazzotti, C. (2007). "Interface law for FRP-concrete delamination." *Composite Structures*, Vol. 80, No. 4, pp. 523-531.
- Ferrier, E., Quiertant, M., Benzarti, K. and Hamelin, P. (2010). "Influence of the properties of externally bonded CFRP on the shear behavior of concrete/composite adhesive joints." *Composites Part B: Engineering*, Vol. 41, No. 5, pp. 354-362.
- Federation International du Beton (fib). (2001). "Externally bonded FRP reinforcement for RC structures." *fib Bulletin 14*, fib Task Group 9.3, fib, Lausanne, Switzerland.
- Focacci, F., Nanni, A. and Bakis, C.E. (2000). "Local bond-slip relationship for FRP reinforcement in concrete." *Journal of Composites for Construction*, ASCE, Vol. 4, No. 1, pp. 24-31.
- Gao, B., Leung, W. H., Cheung, C. M., Kim, J.-K. and Leung, C. K. Y. (2001). "Effects of adhesive properties on strengthening of concrete beams with composite strips." *Proceedings of the International Conference on FRP Composites in Civil Engineering*, Hong Kong, pp. 423-432.
- Holzenkämpfer, O. (1994). "Ingenieurmodelle des Verbunds geklebter Bewehrung für Betonbauteile." Ph.D. thesis, TU Braunschweig, Germany.
- Klamer, E. (2006). "The influence of temperature on concrete structures strengthened with externally bonded CFRP." Research Report, Eindhoven University of Technology, Eindhoven, Netherlands.
- Klamer, E. (2009). "Influence of temperature on concrete beams strengthened in flexure with CFRP." Ph.D. thesis, Eindhoven University of Technology, Eindhoven, Netherlands.

- Leone, M., Matthys, S. and Aiello, M.A. (2009). "Effect of elevated service temperature on bond between FRP EBR systems and concrete." *Composites Part B: Engineering*, Vol. 40, No. 1, pp. 85-93.
- Leung, C.K.Y. and Yang, Y. (2006). "Energy-based modeling approach for debonding of FRP plate from concrete substrate." *Journal of Engineering Mechanics*, ASCE, Vol. 132, No. 6, pp. 583-593.
- Lu, X.Z., Teng, J.G., Ye, L.P. and Jiang, J.J. (2005a). "Bond-slip models for FRP sheets/plates bonded to concrete." *Engineering Structures*, Vol. 27, No. 6, pp. 920-937.
- Lu, X.Z., Ye, L.P., Teng, J.G. and Jiang, J.J. (2005b). "Meso-scale finite element model for FRP sheets/plates bonded to concrete." *Engineering Structures*, Vol. 27, No. 4, pp. 564-575.
- Maeda, T., Asano, Y., Sato, Y., Ueda, T. and Kakuta, Y. (1997). "A study on bond mechanism of carbon fiber sheet." *Proceeding of the Third International Symposium of Non-Metallic (FRP) Reinforced for Concrete Structures*, Sapporo, Japan, pp. 279-286.
- Maeda, T., Komaki, H., Tsubouchi, K. and Murakami, K. (2001). "Strengthening behavior of carbon fiber sheet using flexible layer." *Transactions of the Japan Concrete Institute*, Vol. 23, No. 1, pp. 817-822.
- Masmoudi, R., Zaidi, A. and Gerada, P. (2005). "Transverse thermal expansion of FRP bars embedded in concrete." *Journal of Composites for Construction*, ASCE, Vol. 9, No. 5, pp. 377-387.
- Mohamed Ali, M.S., Oehlers, D.J. and Seracino, R. (2006). "Vertical shear interaction model between external FRP transverse plates and internal steel stirrups." *Engineering Structures*, Vol. 28, No. 3, pp. 381-389.
- Mohamed Ali, M.S., Oehlers, D.J., Griffith, M.C. and Seracino, R., (2008). "Interfacial stress transfer of near-surface-mounted FRP-to-concrete joints." *Engineering Structures*, Vol. 30, No. 7, pp. 1861-1868.
- Nakaba, K., Kanakubo, T., Furuta, T. and Yoshizawa, H. (2001). "Bond behavior between fiber-reinforced polymer laminate and concrete." *ACI Structural Journal*, Vol. 98, No. 3, pp. 359-367.
- Rabinovitch, O. (2010). "Impact of thermal loads on interfacial debonding in FRP strengthened beams." *International Journal of Solids and Structures*, Vol. 47, No. 24, pp. 3234-3244.
- Sato, Y., Kimura, K. and Kobatake, Y. (1997). "Bond Behavior between CFRP Sheet and Concrete (Part 1)." *Journal of Structural and Construction Engineering*, Architectural Institute of Japan, Vol. 62, No. 500, pp. 75-82.
- Sen, R., Shahawy, M., Rosas, J. and Sukumar., S. (1999). "Durability of aramid fiber reinforced plastic pretensioned elements under tidal/thermal cycles." *ACI Structural Journal*, Vol. 96, No. 1, pp. 95-104.
- Seracino, R., Saifulnaz, M.R.R. and Oehlers, D.J. (2007). "Generic debonding resistance of EB and NSM plate-to-concrete joints." *Journal of Composites for Construction*, ASCE, Vol. 11, No. 1, pp. 62-70.

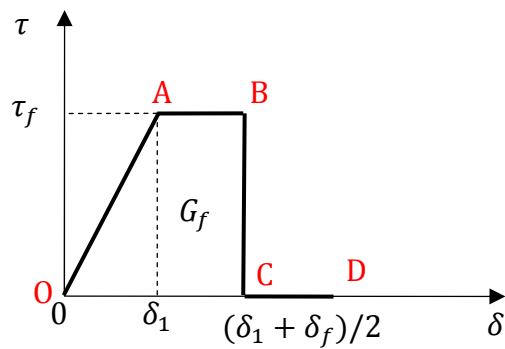
- Taljsten, B. (1996). "Strengthening of concrete prisms using the plate-bonding technique." *International Journal of Fracture*, Vol. 82, No. 3, pp. 253-266.
- Teng, J.G., Chen, J.F., Smith, S.T. and Lam, L. (2002). *FRP-Strengthened RC Structures*, John Wiley and Sons Ltd., Chichester, UK.
- Teng, J.G., Smith, S.T., Yao, J. and Chen, J.F. (2003). "Intermediate crack-induced debonding in RC beams and slabs", *Construction and Building Materials*, Vol. 17, No. 6-7, pp. 447-462.
- Teng, J.G., Yuan, H. and Chen, J.F., (2006). "FRP-to-concrete interface between two adjacent cracks: Theoretical model for debonding failure", *International Journal of Solids and Structures*, Vol. 43, No. 18-19, pp. 5750-5778.
- Teng, J.G. and Chen, J.F. (2009). "Mechanics of debonding in FRP-plated RC beams", *Proceedings of the ICE, Structures and Buildings*, Vol. 162, No. 5, pp. 335-345.
- Wang, J. (2007). "Cohesive-bridging zone model for FRP-concrete interface debonding." *Engineering Fracture Mechanics*, Vol. 74, No. 17, pp. 2643-2658.
- Wu, Z.S., Yuan, H. and Niu, H. (2002). "Stress transfer and fracture propagation in different kinds of adhesive joints." *Journal of Engineering Mechanics*, ASCE, Vol. 128, No. 5, pp. 562-573.
- Wu, Z.S., Iwashita, K., Yagashiro, S., Ishikawa, T. and Hamaguchi, Y. (2005). "Temperature effect on bonding and debonding behavior between FRP sheets and concrete." *Journal of the Society of Materials Science*, Vol. 54, No. 5, pp. 474-480.
- Yao, J., Teng, J.G. and Chen, J.F. (2005). "Experimental study on FRP-to-concrete bonded joints." *Composites Part B: Engineering*, Vol. 36, No. 2, pp. 99-113.
- Yuan, H., Wu, Z.S. and Yoshizawa, H. (2001). "Theoretical solutions on interfacial stress transfer of externally bonded steel/composite laminates." *Journal of Structural Mechanics and Earthquake Engineering*, JSCE, Vol. 18, No. 1, pp. 27-39.
- Yuan, H., Teng, J.G., Seracino, R., Wu, Z.S. and Yao, J. (2004). "Full-range behavior of FRP-to-concrete bonded joints." *Engineering Structures*, Vol. 26, No. 5, pp. 553-565.



(a) Elastic-brittle model

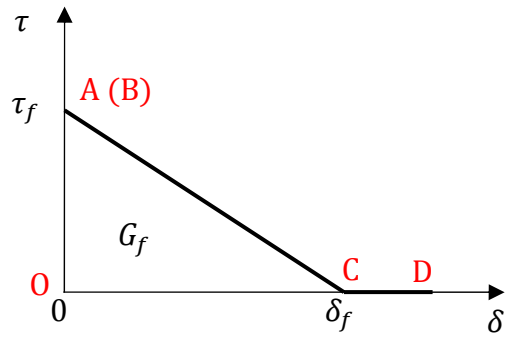


(b) Bi-linear model

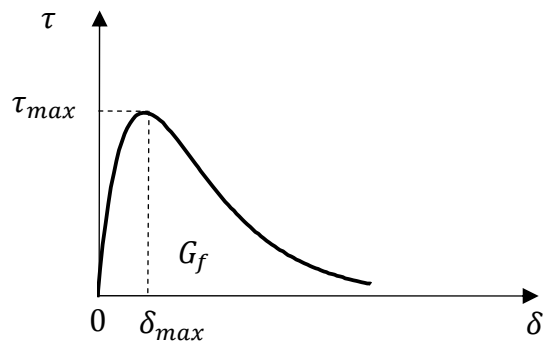


(c) Elastic-plastic-brittle model

**Fig. 4.1** Five local bond-slip models.

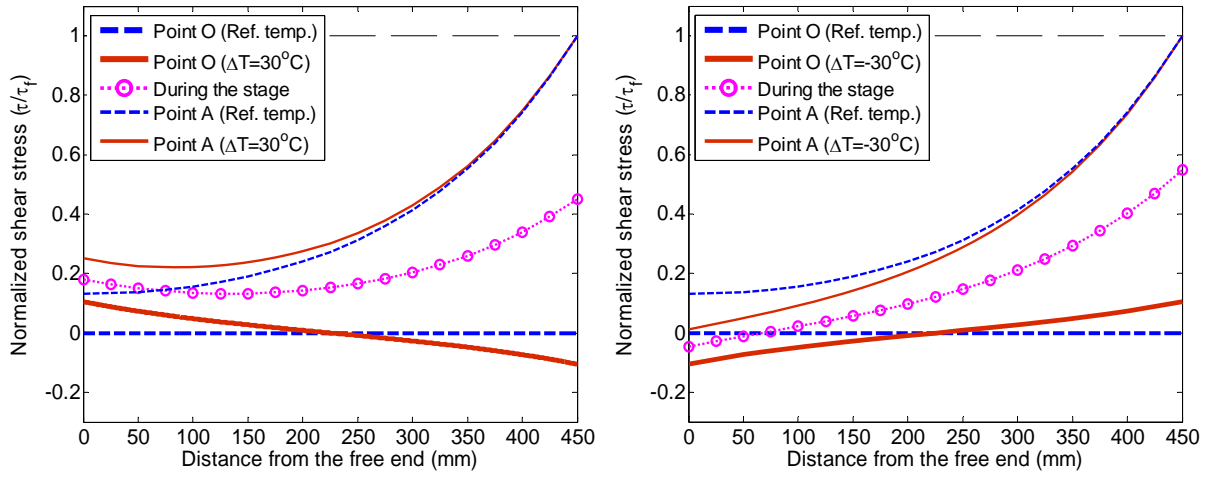


(d) Rigid-softening model

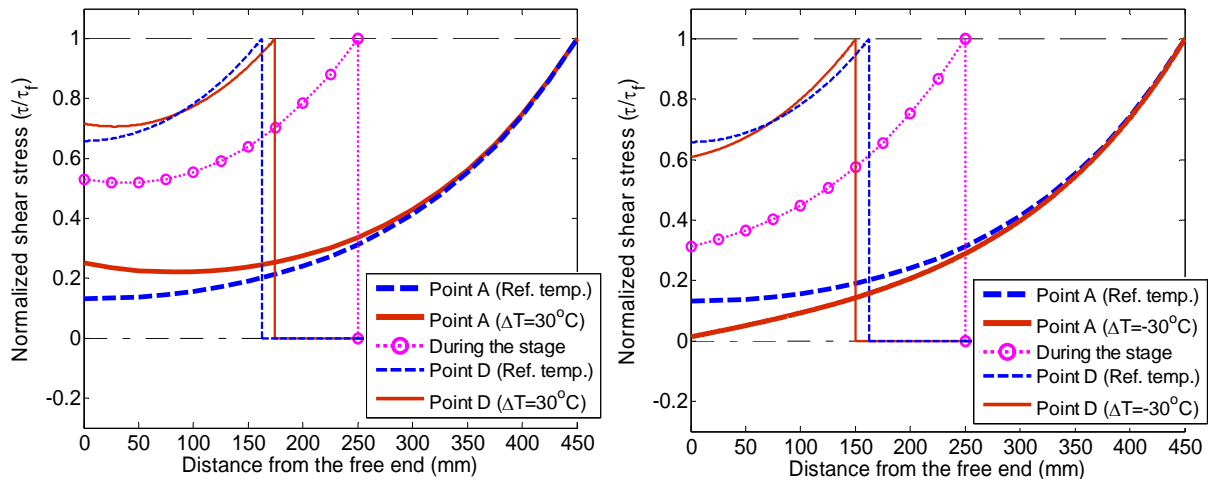


(e) Exponential model

**Fig. 4.1** Five local bond-slip models (Cont'd).



(a) Elastic stage



(b) Elastic-debonding stage

**Fig. 4.2** Interfacial shear stress distributions for the elastic-brittle bond-slip model.

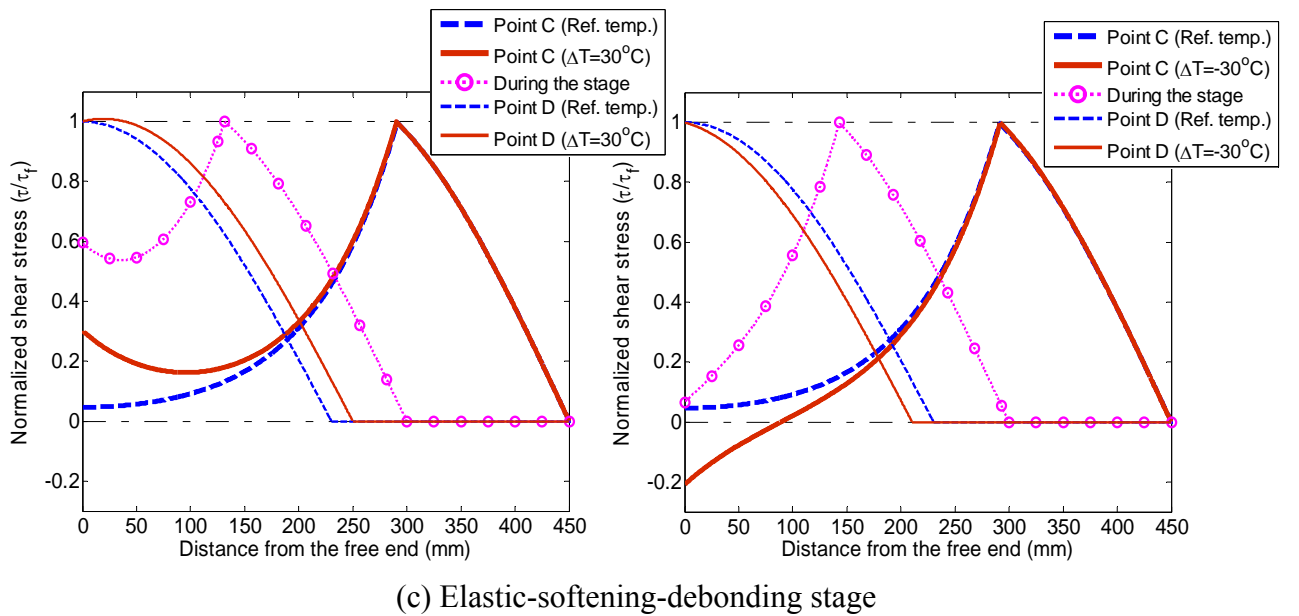
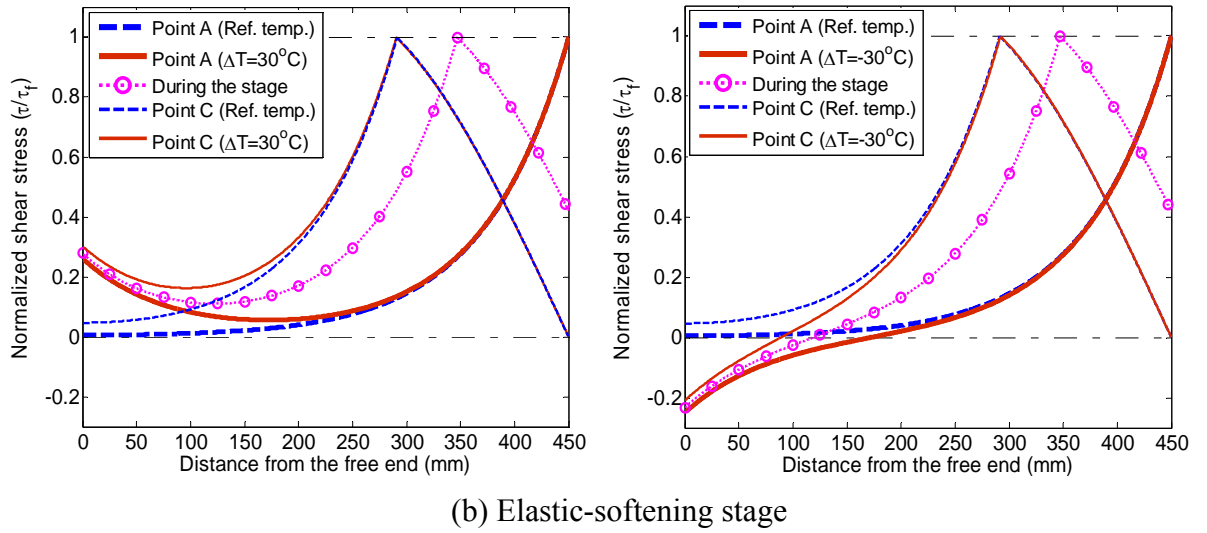
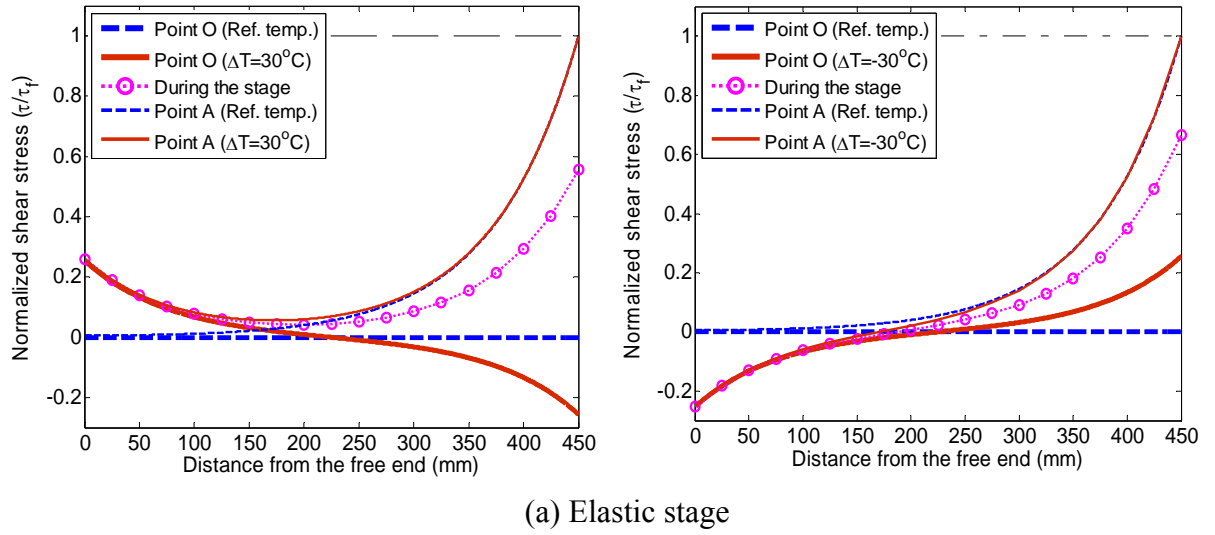
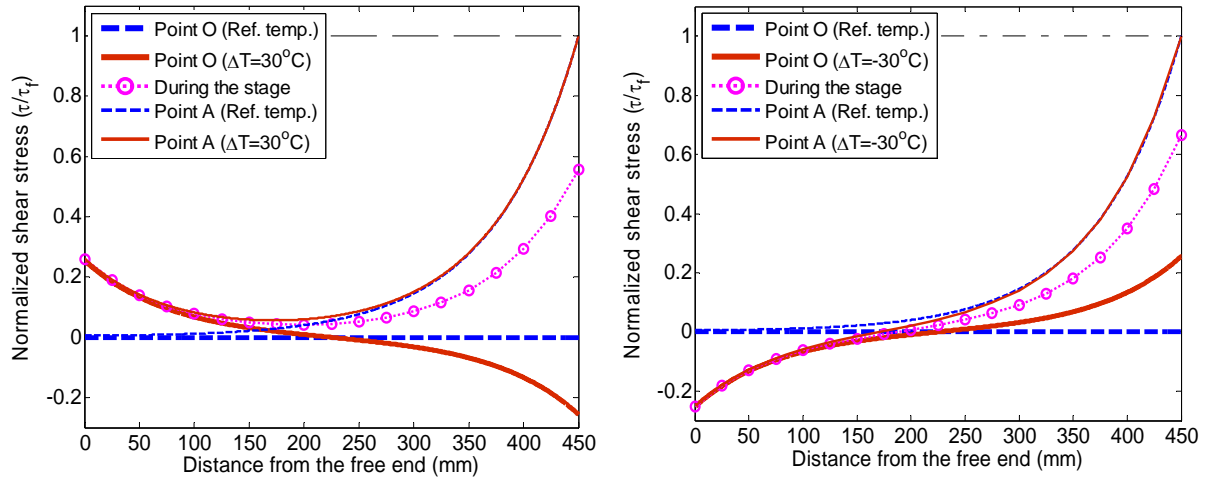
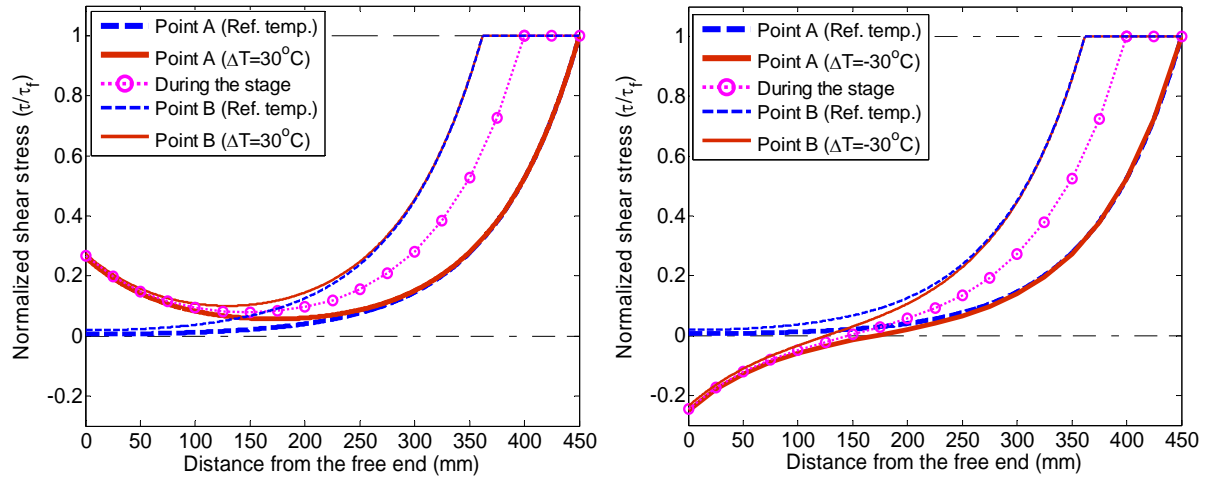


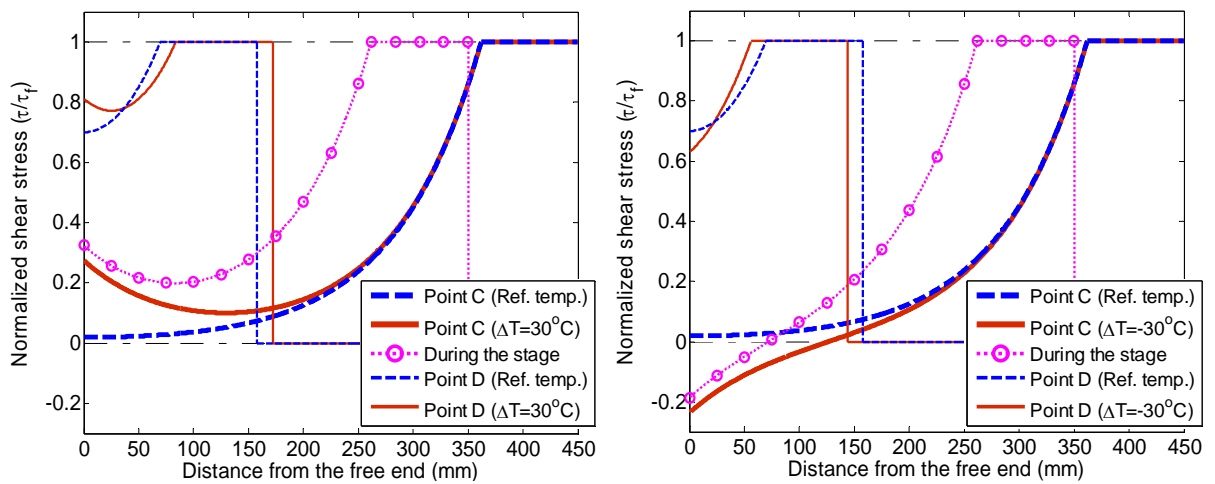
**Fig. 4.3** Interfacial shear stress distributions for the bi-linear bond-slip model.



(a) Elastic stage

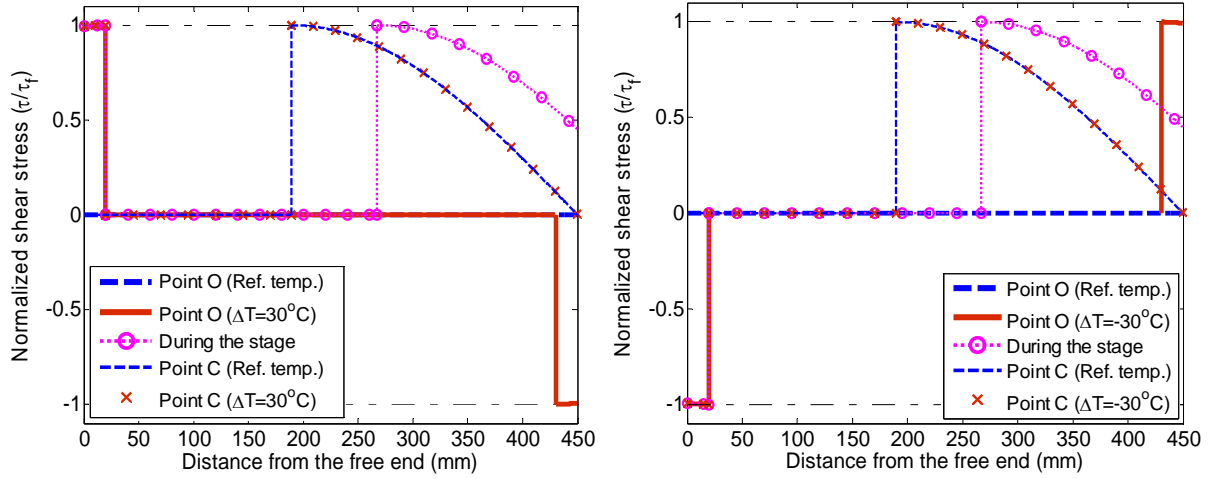


(b) Elastic-plastic stage

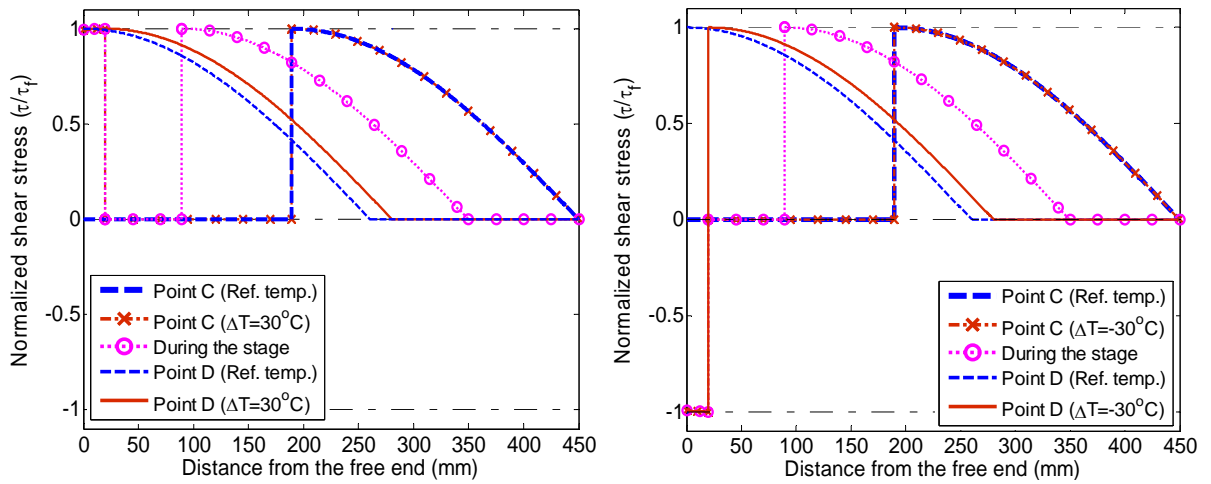


(c) Elastic-plastic-debonding stage

**Fig. 4.4** Interfacial shear stress distributions for the elastic-plastic-brittle bond-slip model



(a) Softening stage



(b) Softening-debonding stage

**Fig. 4.5** Interfacial shear stress distributions for the rigid-softening bond-slip model.

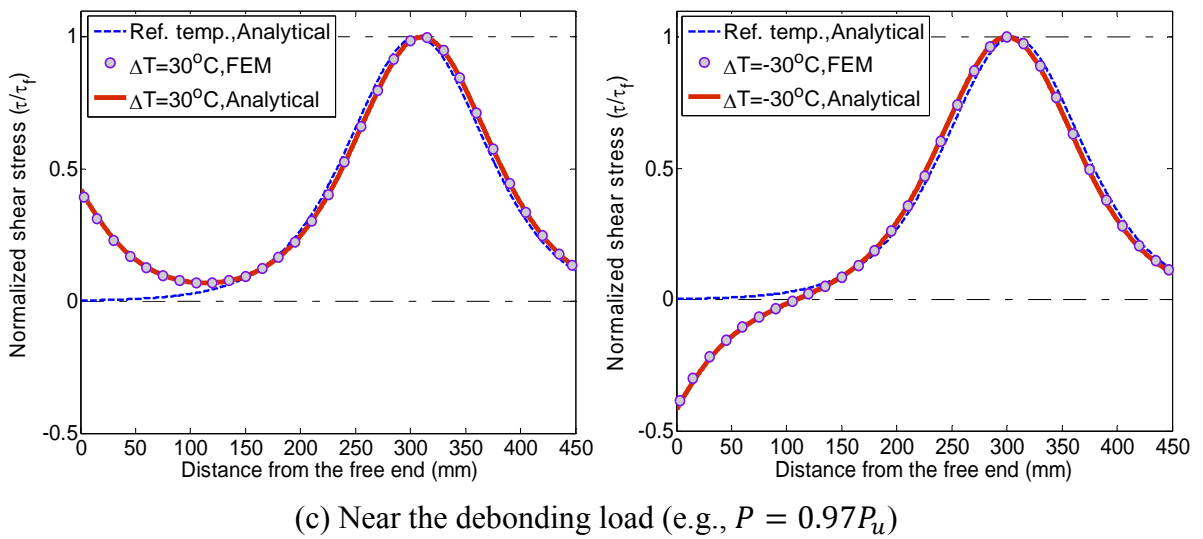
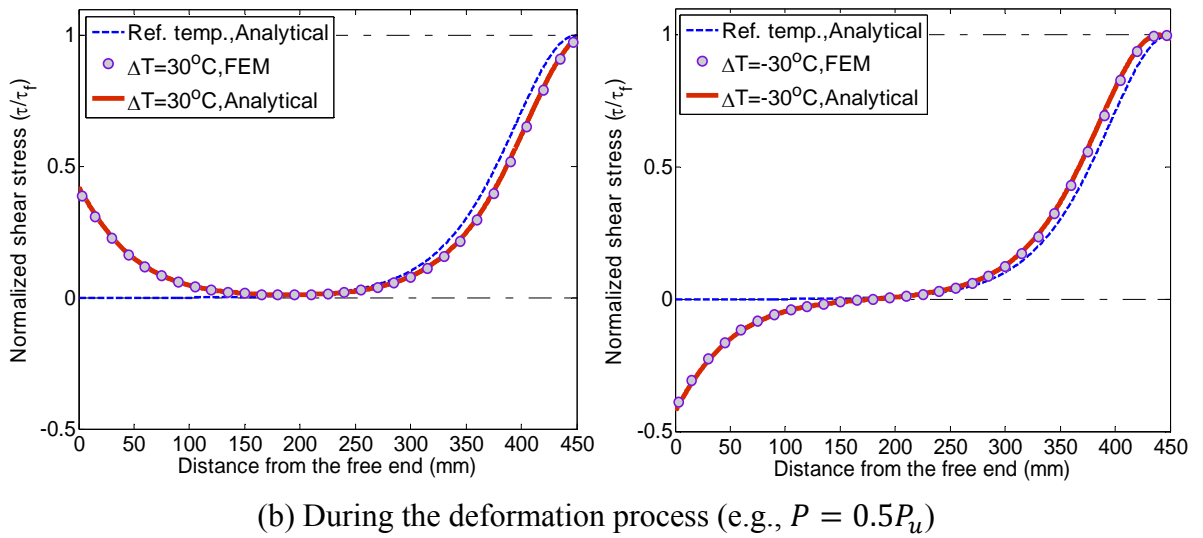
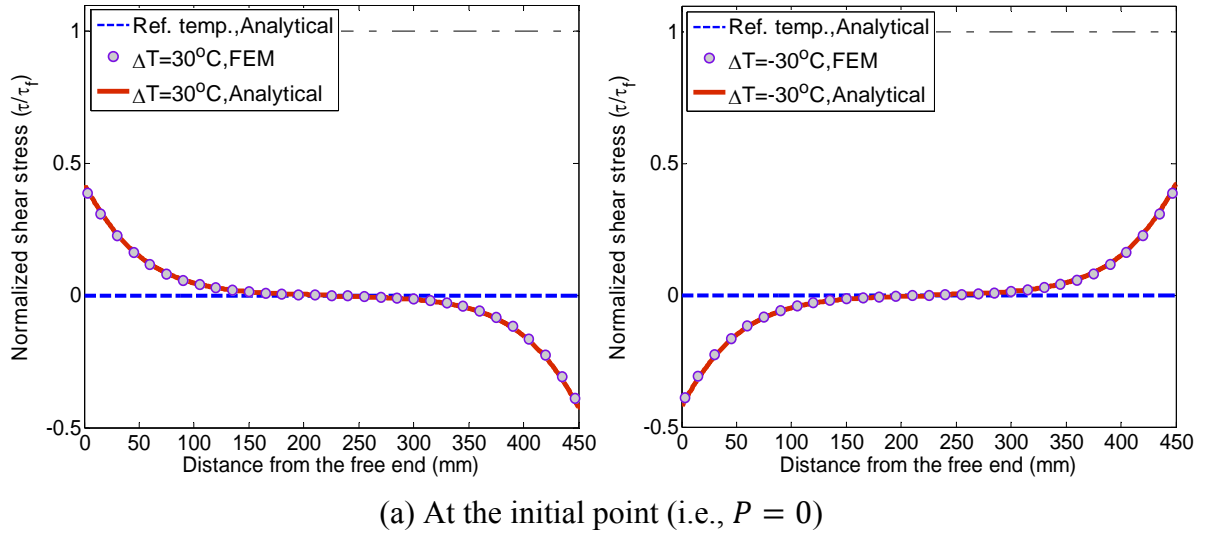
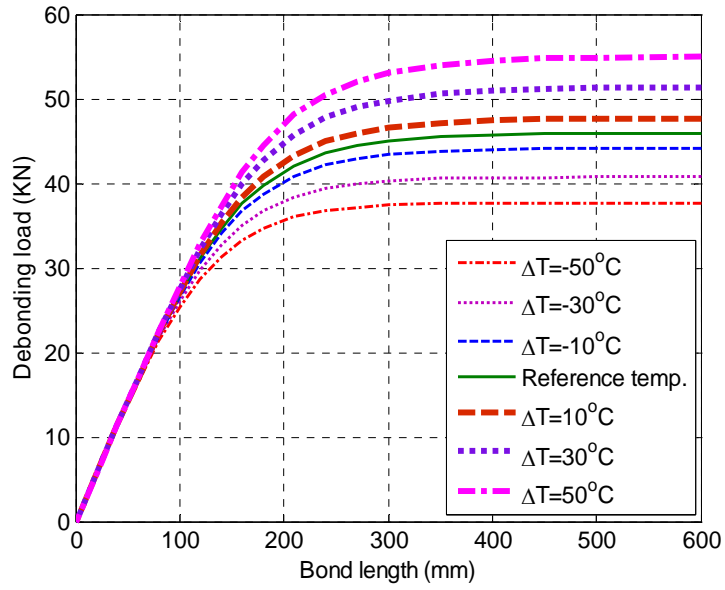
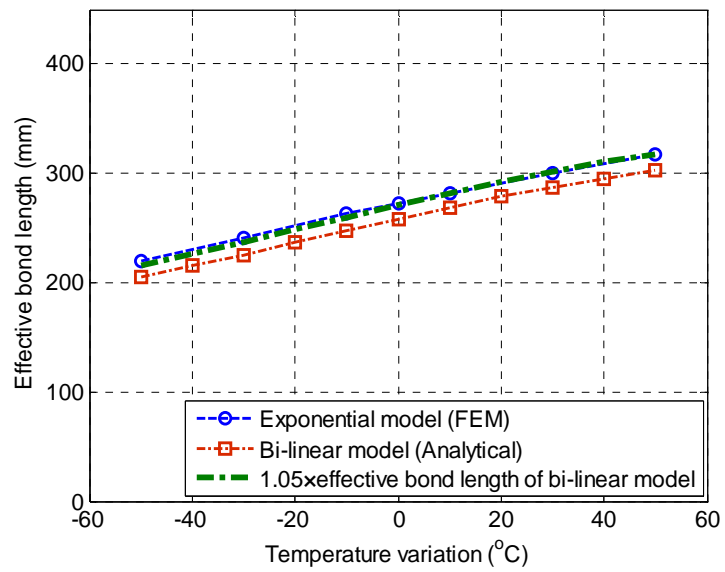


**Fig. 4.6** Interfacial shear stress distributions for the exponential bond-slip model.



(a) Debonding load versus bond length



(b) Effective bond length

**Fig. 4.7** Debonding loads and effective bond lengths predicted using the exponential bond-slip model.

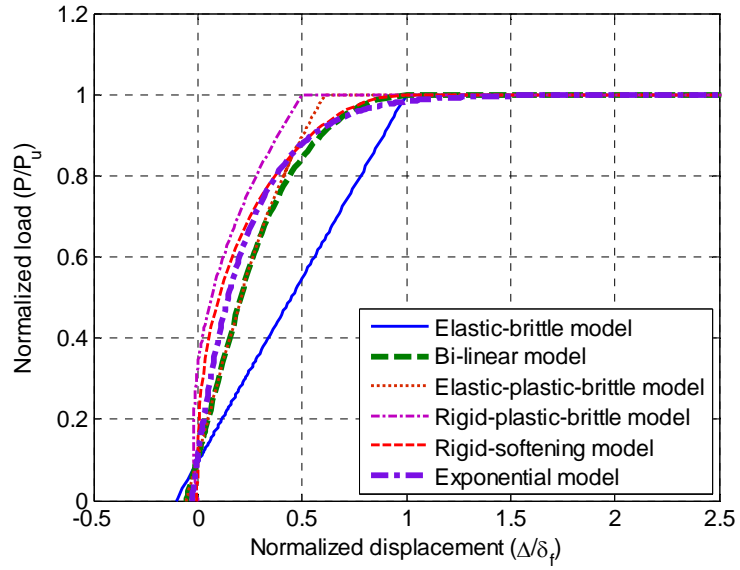


**Fig. 4.8** Typical load-displacement curves for different bond-slip models.

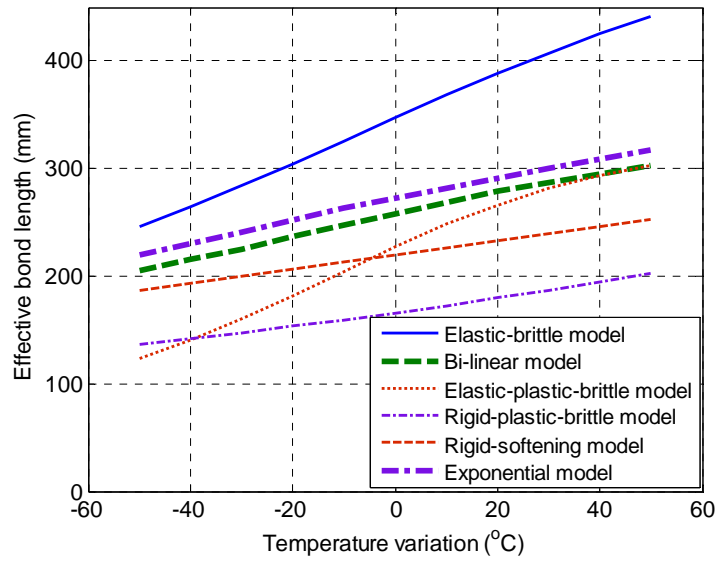
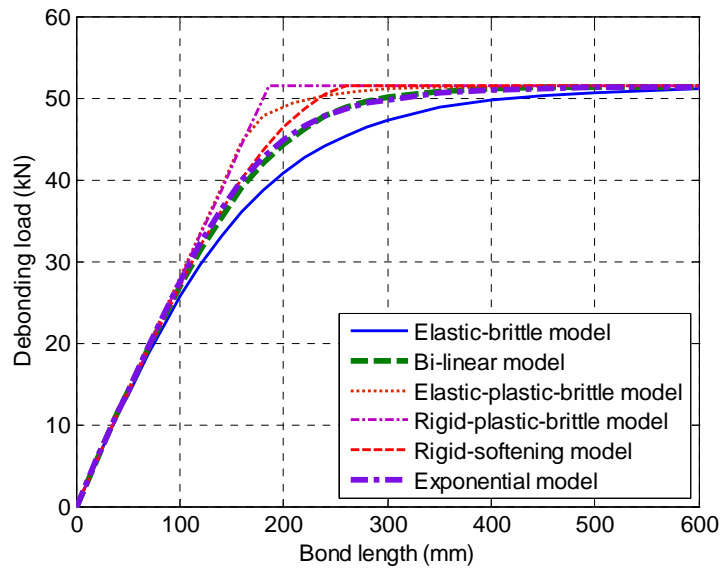
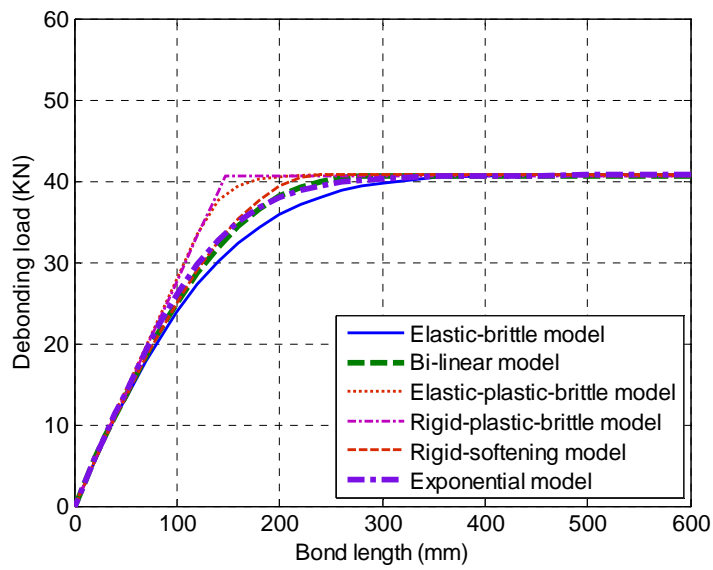


**Fig. 4.9** Effect of temperature variation on the effective bond length.



(a)  $\Delta T = 30^{\circ}\text{C}$



(b)  $\Delta T = -30^{\circ}\text{C}$

**Fig. 4.10** Effect of bond length on the debonding load.

## CHAPTER 5

# BOND-SLIP MODEL FOR FRP LAMINATES EXTERNALLY BONDED TO CONCRETE AT ELEVATED TEMPERATURES

### 5.1 INTRODUCTION

The fire-resistance problem of FRP-strengthened RC structures may be solved by covering the bonded FRP system with a fire protection layer so that the temperature in the FRP stays below its glass transition temperature for a sufficiently long period during a fire (Bisby et al. 2005; Williams et al. 2008); the structural resistance of such a sufficiently protected FRP-strengthened RC structure will remain basically unaffected during this time period. However, existing studies (e.g., Gamage et al. 2006; Gao et al. 2010) have shown that this approach is usually impractical because the fire protection layer needed can be excessively thick (e.g., 70mm for achieving a two-hour fire resistance rating for the epoxy). As a result, the attractiveness of the FRP strengthening technology in terms of its minimal alterations to the dimensions and appearance of the structure is greatly compromised. In addition, this solution may not be cost-effective.

A more practical solution is to adopt a relatively thin fire protection layer to achieve only partial insulation for the bonded FRP system; such an insulation layer is aimed at preventing flame spread and smoke generation, and in the meantime, ensuring that an adequate structural resistance is retained during a fire. Depending on the situation, the latter requirement may mean that the contribution of the bonded FRP system is allowed to totally disappear, but the structural resistance of the original RC structure is completely or largely preserved after exposure to a fire; it may also mean that the resistance offered by the bonded FRP system is only partially lost during a fire (e.g., due to the deterioration of the bondline).

To be able to explore the benefits of different fire protection strategies and to develop corresponding design procedures, an analysis capability for predicting the behavior of FRP-strengthened RC structures with fire protection of various levels needs to be established. For the development of such an analysis capability, a key component is a bond-slip model for FRP-to-concrete interfaces at elevated temperatures. Indeed, as the bond capacity between FRP and concrete may degrade faster than the FRP system itself during a fire (Ahmed and Kodur 2011), the partial loss of the structural resistance offered by the bonded FRP system may be due directly to degradation in bond performance. In addition to fire exposure, FRP-strengthened RC structures are also found in harsh service environments, where temperatures up to 50 °C or more may occur (e.g., hot climates and industrial conditions). For such service conditions, it is also essential for designers to understand how FRP-to-concrete interfaces behave at elevated temperatures and consequently how their degradation influences the safety of FRP-strengthened RC structures. This chapter therefore presents a study aimed at the development of the first ever bond-slip model for FRP-to-concrete interfaces at elevated temperatures.

## **5.2 FORMULATION OF THE BOND-SLIP MODEL**

### ***5.2.1 General***

There are basically three different ways of developing a bond-slip model for FRP-to-concrete interfaces: (a) based directly on readings from closely-spaced strain gauges installed on the surface of the FRP laminate (e.g., Chajes et al. 1996; Nakaba et al. 2001; Bilotta et al. 2012); (b) based on detailed meso-scale finite element modeling of debonding failures in conjunction with test data (e.g., distributions of strains in the FRP laminate along the bond length) (Lu et al. 2005a); (c) based on the global load-displacement responses of FRP-to-concrete bonded joints (Dai et al. 2005). Method (a) suffers from a number of problems and has not been used successfully for this purpose; in particular, the test data shows considerable scatter due to factors such as the local bending of the FRP laminate and heterogeneity of the concrete substrate due to non-uniform aggregate and crack distributions. Method (b) is based on rigorous numerical modeling and has led to the well-known bond-slip model of Lu et al. (2005b). Method (a) was not employed in the present study due to not only the

scatter problem but also the lack of sufficient strain measurement data. Method (b) was also not attempted in the present study due to a lack of understanding of detailed local material degradations of FRP-to-concrete interfaces at elevated temperatures; the modeling of adhesion failure at the adhesive-concrete interface for the bonded joint subjected to an elevated temperature close to or higher than  $T_{ga}$  poses a particular challenge to this approach. Therefore, Method (c) was adopted, and indeed the proposed model represents an extension of the two-parameter bond-slip model developed by Dai et al. (2005) for FRP-to-concrete interfaces at ambient temperature.

The advantage of Dai et al.'s approach lies in its simplicity as only two parameters need to be determined from test data without the need for sophisticated finite element modeling. Another justification for using Dai et al.'s approach in the present study is that the softening of adhesives at elevated temperatures can be implicitly reflected in these two parameters. Although the use of two parameters only to define the bond-slip law may impose some unnecessary constraint in achieving an accurate description of the shape of highly non-linear bond-slip curves, the extension of Dai et al. (2005) model for the present purpose represents a good first attempt within the context of available information for FRP-to-concrete interfaces exposed to elevated temperatures.

### ***5.2.2 Theoretical Background***

The single-lap or double-lap shear test is a popular method for studying the bond characteristics of FRP-to-concrete interfaces (Fig. 3.1). In deriving local bond-slip curves using Dai et al.'s (2005) approach, load-displacement responses from such tests are interpreted in accordance with the theoretical framework presented below.

#### ***5.2.2.1 Bond-slip model***

At any location of the FRP-to-concrete interface of an FRP-to-concrete bonded joint with the free end of the FRP laminate subjected to a pull load, the relationship between the axial strain in the FRP and the interfacial slip between the FRP and the concrete can be expressed as follows:

$$\varepsilon(x) = f(\delta(x)) \quad (5.1)$$

By assuming that the  $\tau\sim\delta$  relationship is unique along the FRP-to-concrete interface, Eq. (5.1) is valid for all locations of a sufficiently long bond length (Dai et al. 2005, 2006). Here, the sufficiently long bond length is defined as a bond length larger than the effective bond length of the bonded joints (see Chapter 4.4.5 for more details). Therefore, Eq. (5.1) can be simply obtained from the pull load (from which the strain in the FRP at the loaded end can be found) and the relative interfacial slip between the FRP and the concrete at the loaded end. It should be noted that, when the FRP-to-concrete interface is subjected to combined mechanical and thermal loadings, the strain in the FRP at the loaded end consists of both the load-induced and the thermally induced components as shown later.

From an interpretation of extensive experimental results of bonded joints tested at ambient temperature, the following exponential expression was found to represent  $f(\delta(x))$  with sufficient accuracy (Dai et al. 2005):

$$\varepsilon(x) = f(\delta(x)) = A(1 - e^{-B\cdot\delta(x)}) \quad (5.2)$$

where  $A$  and  $B$  are parameters to be determined from regression analysis of bonded joint test results. The physical meaning of  $A$  is the maximum strain reached in the FRP laminate if its bond length is longer than the effective bond length.  $B$  can be regarded as the brittleness index that controls the shape of the bond-slip curve: a larger  $B$  value corresponds to a steeper ascending branch (i.e., a larger initial interfacial stiffness) and a steeper descending branch.

Note that

$$\tau(x) = \frac{E_p t_p}{(1+\alpha)} \frac{d\varepsilon(x)}{dx} \quad (5.3)$$

and

$$\varepsilon(x) = \frac{d\delta(x)}{dx} \quad (5.4)$$

where  $\frac{E_p t_p}{(1+\alpha)}$  is a stiffness ratio of the bonded joint with  $\alpha = \frac{E_p t_p b_p}{E_c t_c b_c}$ ;  $b_p$  and  $t_p$  are the width and thickness of the FRP laminate;  $b_c$  and  $t_c$  are the width and thickness of the concrete prism;  $E_p$  and  $E_c$  are the elastic moduli of the FRP laminate and the concrete, respectively.

Combining Eqs. (5.2)-(5.4) yields the following equation for the bond-slip model of FRP-to- concrete interfaces:

$$\tau(x) = A^2 B \frac{E_p t_p}{(1+\alpha)} (e^{-B\delta(x)} - e^{-2B\delta(x)}) \quad (5.5)$$

If  $G_f$  is used to denote the interfacial fracture energy, which is the area underneath the  $\tau \sim \delta$  curve (i.e.,  $\int_0^\infty \tau(x) d\delta(x) = G_f$ ), the following expression can be obtained from Eq. (5.5):

$$A = \sqrt{\frac{2G_f}{E_p t_p} (1 + \alpha)} \quad (5.6)$$

By substitution of Eq. (5.6) into Eq. (5.5), the bond-slip model can be rewritten as

$$\tau(x) = 2G_f B (e^{-B\delta(x)} - e^{-2B\delta(x)}) \quad (5.7)$$

### 5.2.2.2 Interfacial slip distribution

Using Eqs. (5.3)-(5.5), the governing differential equation for the FRP-to-concrete interface subjected to shear stresses can also be expressed in terms of the local interfacial slip  $\delta(x)$  as follows:

$$\frac{d^2\delta(x)}{dx^2} = A^2 B (e^{-B\delta(x)} - e^{-2B\delta(x)}) \quad (5.8)$$

For an FRP-to-concrete interface with a sufficiently long bond length and subjected to combined thermal and mechanical loadings, the solution to Eq. (5.8) can be found in Section 4.4.5 as follows:

$$\delta(x) = \frac{1}{B} \ln[e^{B(Ax+c_2)} + 1] \quad (5.9)$$

where  $c_2$  is a constant given by the following equation:

$$c_2 = \frac{1}{B} \ln \left\{ \frac{\frac{1}{A} \left[ \frac{P(1+\alpha)}{E_p t_p b_p} + (\alpha_p - \alpha_c) \Delta T \right]}{1 - \frac{1}{A} \left[ \frac{P(1+\alpha)}{E_p t_p b_p} + (\alpha_p - \alpha_c) \Delta T \right]} \right\} - AL \quad (5.10)$$

where  $P$  is the pull load acting on the FRP laminate at the loaded end;  $L$  is the bond length; and  $\Delta T$  is the temperature variation (a positive value means a temperature increase).

It should be mentioned that viscoelastic deformation of FRP-to-concrete interfaces is not considered in the proposed model, while such deformation may become significant at elevated temperatures when the interface is subjected to sustained loading. In all existing shear tests on FRP-to-concrete joints at elevated temperatures, the specimen was usually first heated up to the desired temperature and was then subjected to instantaneous loading to failure. The interfacial stresses induced by the thermal mismatch between FRP and concrete are generally low, so they are also not expected to induce significant viscoelastic deformation.

### 5.2.2.3 Ultimate pull load

Considering the differential thermal expansion between FRP and concrete, at any location of the interface, the pull load  $P(x)$  acting on the FRP laminate can be calculated as

$$P(x) = \frac{E_p t_p b_p}{(1+\alpha)} [\varepsilon(x) - (\alpha_p - \alpha_c) \Delta T] \quad (5.11)$$

Substituting Eq. (5.2) into Eq. (5.11), the pull load-displacement relationship (i.e.,  $P$ - $\Delta$  relationship) at the loaded end can be obtained as

$$P = \frac{E_p t_p b_p}{(1+\alpha)} [A(1 - e^{-B\Delta}) - (\alpha_p - \alpha_c)\Delta T] \quad (5.12)$$

If the second term on the right hand side is removed, Eq. (5.12) is identical to the pull load-slip relationship derived by Dai et al. (2005) for FRP-to-concrete interfaces at ambient temperature.

If there is an infinite bond length (e.g., at least a bond length longer than the effective bond length) to provide a large enough slip  $\Delta$  at the loaded end, Eq. (5.12) converges to the following form:

$$P_{uT} = b_p \sqrt{2G_f \frac{E_p t_p}{(1+\alpha)} - \frac{E_p t_p b_p}{(1+\alpha)} (\alpha_p - \alpha_c)\Delta T} \quad (5.13)$$

where  $P_{uT}$  is the ultimate pull load of the FRP-to-concrete interface subject to combined mechanical and thermal loadings. When  $\Delta T = 0$ , Eq. (5.13) reduces to the familiar relationship between the ultimate pull load and the interfacial fracture energy of an FRP-to-concrete interface at ambient temperature (e.g., Taljsten 1996; Brosens 2001; Wu et al. 2002; Yuan et al. 2004).

#### 5.2.2.4 Strain distributions in the FRP laminate

Since  $\delta(x)$  is known, with the use of Eqs. (5.6), (5.9), (5.10) and (5.13), the strain distribution,  $\varepsilon(x)$ , in the FRP laminate along the FRP-to-concrete interface at different pull load levels can also be obtained as

$$\varepsilon(x) = \frac{A}{1 + e^{BA(L-x)} \cdot \frac{P_{uT} - P}{P + \frac{E_p t_p b_p}{(1+\alpha)} (\alpha_p - \alpha_c)\Delta T}} \quad (5.14)$$

#### 5.2.3 Determination of $G_f$ and $B$

With the above theoretical framework, the values of the two key parameters,  $G_f$  and  $B$ , for the bond-slip model, can be determined from the pull test result without difficulty for a given FRP-to-concrete interface subjected to combined mechanical and thermal loadings. For a single-lap shear test or one of the four interfaces in a double-lap shear test (the latter has been widely used to evaluate the bond behavior of FRP-to-concrete interfaces at elevated temperatures as reviewed earlier), the interfacial fracture energy  $G_f$  can be calculated from the ultimate pull load and Eq. (5.13) as follows provided that the bond length is longer than the effective bond length:

$$G_f(T) = (1 + \alpha) \frac{(P_{uT} - \Delta P)^2}{2E_p t_p b_p^2} \quad (5.15)$$

where  $\Delta P = -\frac{E_p t_p b_p}{(1+\alpha)} (\alpha_p - \alpha_c) \Delta T$ , which is induced by the thermal incompatibility between FRP and concrete. It is seen that the difference in thermal expansion between FRP and concrete has a positive influence on the ultimate load when the bonded joint is exposed to a moderate temperature increase and vice versa provided no material degradation of the bondline has occurred. Therefore, when deducing the temperature-dependent fracture energy from the pull load, the thermal stress-induced component  $\Delta P$  needs to be eliminated first.

It should also be noted that the elastic modulus  $E_p$  of the FRP laminate in Eq. (5.15) may change with the temperature increase. Bisby (2003) collected existing test data and proposed a sigmoid function model for the strength and elastic modulus degradation of pre-fabricated FRP products at elevated temperatures. However, Bisby's model may not be suitable for wet layup FRP sheets as they possess a much lower  $T_{g,p}$  than prefabricated FRP products. For wet layup FRP sheets, the matrix and the bonding materials are generally the same epoxy material which cannot be completely cured at ambient temperature (Silva and Biscaia 2008), and its  $T_{g,p}$  is normally within the range of 45 °C to 82 °C (fib 2001; ACI 2008). By contrast, the polymer matrix in a prefabricated FRP composite has a much higher  $T_{g,p}$  [around 130 °C (Clarke 1996)] as prefabrication allows curing at elevated temperatures and pressure (Stratford et al. 2009).

Unfortunately, previous researchers did not provide details of the temperature-dependent properties (e.g., elastic modulus) of FRP laminates when reporting their test results of FRP-to-concrete bonded joints at elevated temperatures, which made it difficult to interpret the joint test results. To tackle this problem, the authors collected the available test data of the elastic modulus of FRP sheets at elevated temperatures from other published studies (Chowdhury et al. 2008; Chowdhury et al. 2011). It was assumed that all FRP sheets have a similar degradation trend at elevated temperatures and the actual degradation process depends on the glass transition temperature  $T_{g,p}$ . Fig. 5.1a shows the available test data for the elastic modulus of FRP sheets at elevated temperatures. The test data from Zhou (2005) and Wang et al. (2007) for FRP bars and the two models proposed by Bisby (2003) for CFRP and GFRP respectively are also shown there for comparison. In the figure, the elastic modulus at elevated temperatures is normalized by the corresponding value obtained at ambient temperature. It is clearly seen that the elastic modulus degradation of FRP sheets is more severe than that of FRP bars. As the performance of FRP sheets/bars at elevated temperatures depends predominately on the glass transition temperature  $T_{g,p}$  of the polymer matrix,  $T_{g,p}$  needs to be taken as a key parameter in any elastic modulus degradation model. Therefore, Bisby's (2003) model was modified, by taking account of the  $T_{g,p}$  value ( $^{\circ}\text{C}$ ), into the following equation to describe the elastic modulus degradation of FRP sheets:

$$\frac{E_{pT}}{E_{p0}} = \left(\frac{1-a_1}{2}\right) \times \tanh\left(-a_2 \times \left(\frac{T}{T_{g,p}} - a_3\right)\right) + \left(\frac{1+a_1}{2}\right) \quad (5.16)$$

where  $E_{p0}$  and  $E_{pT}$  are the elastic modulus of FRP at ambient temperature and that at an elevated temperature  $T$  ( $^{\circ}\text{C}$ ), respectively; and  $a_1 = 0.729$ ,  $a_2 = 9.86$  and  $a_3 = 0.607$  are empirical factors derived based on multivariable least-squares regression analysis of existing test data. Fig. 5.2b shows this proposed relationship where the elastic modulus is normalized by its corresponding ambient value and the temperature is normalized by the  $T_{g,p}$  value ( $^{\circ}\text{C}$ ) of the polymer matrix. The highest test temperature covered by Fig. 5.1b is  $200^{\circ}\text{C}$ . While this temperature is still much lower than the decomposition temperature of polymer matrix [denoted by  $T_d$ , around

400 °C (Mouritz and Gibson 2006)], the proposed model is adequate for bond critical applications as the FRP-to-concrete interface has lost most of its bond capacity around this temperature. For contact critical applications (e.g., FRP-confined columns), further work is needed to define the stiffness degradation of FRP sheets beyond 200 °C for accurate predictions of member residual strengths at higher temperatures. Due to the lack of test data for  $T_{g,p}$  as well as the elastic modulus of FRP plates at elevated temperatures (Wang et al. 2011), the original Bisby's (2003) model developed for FRP bars is directly used in the present study to predict the elastic modulus of FRP plates at elevated temperatures.

Once the value of  $G_f$  (i.e.,  $A$ ) is known [Eq. (5.15)], the value of  $B$  can be obtained from least-squares regression analysis of the experimental relationship between the pull load and the local slip at the loaded end. Unfortunately, of the existing experimental studies, only Klamer (2006, 2009) reported the global pull load-displacement curves of FRP-to-concrete bonded joints at elevated temperatures. Such relationships were not reported for the tests conducted by other researchers. Instead, the strain distributions over the FRP laminate at different pull load levels were often reported. As the measured strains in the FRP include various local effects (e.g., local bending of the FRP laminate and non-uniform distributions of coarse aggregate and cracks in the substrate concrete), the global load-displacement curve, if available, was used in determining the value of  $B$  from each joint test. If this was not available, Eq. (5.14), which represents the theoretical strain distribution in the FRP, was compared with the test strain distribution to determine the value of  $B$ .

If the measured strains at different pull load levels ( $P_i, i = 1, \dots, m$ ) and at different locations ( $j = 1, \dots, n$ , where  $n$  is the total number of strain gages on the FRP laminate) are denoted by  $(\varepsilon_{i,j})^{\text{test}}$  and the corresponding strains predicted by Eq. (5.14) are denoted by  $(\varepsilon_{i,j})^{\text{pred}}$ , the value of  $B$  can be determined through least square minimization of the difference between  $(\varepsilon_{i,j})^{\text{test}}$  and  $(\varepsilon_{i,j})^{\text{pred}}$ . That is, for each bonded joint test, a value for  $B$  can be found to minimize (Dai and Ueda 2003):

$$e = \sum_{i=1}^m \sum_{j=1}^n [(\varepsilon_{i,j})^{\text{pred}} - (\varepsilon_{i,j})^{\text{test}}]^2 \quad (5.17)$$

When the global pull load-displacement curve was used to obtain the value of  $B$  for test joint, a similar procedure was followed.

It should be noted that in most existing tests of FRP-to-concrete bonded joints at elevated temperatures, strain readings were not taken during the heating process; that is, the reported strain readings did not include the initial strains in the FRP laminate induced by thermal incompatibility between FRP and concrete (Blontrock 2003; Wu et al. 2005; Leone et al. 2009). Therefore, when such data are used in regression analysis, the initial thermal strains need also be eliminated from the predicted strains.

#### **5.2.4 Expressions for $G_f$ and $B$**

The test data of 79 bonded joint shear tests conducted at ambient and elevated temperatures were assembled from the existing experimental studies reviewed earlier (Blontrock 2003; Klamer 2006; Wu et al. 2005; Cai 2008; Leone et al. 2009) to examine the dependence of  $G_f$  and  $B$  on temperature following the approach explained above. All these test results were from double-lap shear tests with a sufficient FRP bond length. Details of all the specimens and their test results are shown in Table 5.1. In the tests of Cai (2008) and Lenoe et al. (2009), the  $T_g$  values (including both  $T_{g,a}$  and  $T_{g,p}$ ) were determined by the researchers using the differential scanning calorimetry (DSC) method, while in the tests of Blontrock (2003), Wu et al. (2005) and Klamer (2006), the  $T_g$  values were provided by the material suppliers. In the case of FRP sheets, as the bonding adhesive is also used as the polymer matrix, the values of  $T_{g,a}$  and  $T_{g,p}$  are usually identical. Only Wu et al. (2008) used two different thermo-resistant resins as the bonding adhesive and the polymer matrix of the FRP sheets respectively, and hence the values of  $T_{g,a}$  and  $T_{g,p}$  for their tests are different.

A summary of the predicted values for  $\Delta P$ ,  $G_f$ ,  $A$  and  $B$  are given in Table 5.2. Specimens C-L-20 to C-L-80 in Leone et al.'s (2009) tests were not included in the analysis since they suffered from insufficient penetration of the bonding adhesive into the concrete substrate as reported by the authors. Specimens B1-100 and B2-70 from Klamer (2006) were excluded in the determination of  $B$  because of suspected

measurement errors: the global pull force was recorded to increase abruptly with almost zero slip at the loaded end in the initial loading stage. Through a careful analysis of the test data, the following observations can be made:

- (1) When the temperature increases from ambient temperature but remains below the glass transition temperature of the bonding adhesive ( $T_{g,a}$ ), the interfacial fracture energy  $G_f$  of the FRP-to-concrete interface remains almost constant (Fig. 5.2). For the few specimens tested by Blontrock (2003), Leone et al. (2009) and Cai (2008), an initial increase in the interfacial fracture energy is also observed. Post-curing at elevated temperatures (Klamer 2006) is believed to be the main reason for this phenomenon. During this stage, no degradation of the interface occurred.
- (2) As the temperature increases further, the interfacial fracture energy  $G_f$  is initially almost constant but starts to decrease when the glass transition temperature is being approached; a rapid decrease is seen to occur when the temperature exceeds the glass transition temperature of the bonding adhesive (Fig. 5.2). This decrease is mainly attributed to the mechanical degradation of the bonding adhesive.
- (3) The value of  $B$  also shows a decreasing trend as the temperature increases (Fig. 5.3), but this decrease is almost completed when the glass transition temperature is reached, which is different from that observed for the interfacial fracture energy. A decrease in the  $B$  value means a decrease in the interfacial stiffness due to the softening of the bonding adhesive (Dai et al. 2005).

As the properties of a bonding adhesive at elevated temperatures relies highly on its glass transition temperature, the value of  $T_{g,a}$  ( $^{\circ}\text{C}$ ) needs to be properly accounted for in establishing mathematical expressions for  $G_f$  and  $B$ . Figs. 5.3 and 5.4 show how the values of  $G_f$  and  $B$  normalized by their ambient values vary with the value of temperature normalized by  $T_{g,a}$  ( $^{\circ}\text{C}$ ). Through multivariable least-squares regression analysis, the following two expressions for Eq. (5.7) can be derived to completely define a temperature-dependent bond-slip model:

$$\frac{G_f(T)}{G_{f0}} = \frac{1}{2} \times \tanh\left(-b_2 \times \left(\frac{T}{T_{g,a}} - b_3\right)\right) + \frac{1}{2} \quad (5.18)$$

$$\frac{B(T)}{B_0} = \frac{(1-c_1)}{2} \times \tanh\left(-c_2 \times \left(\frac{T}{T_{g,a}} - c_3\right)\right) + \frac{(1+c_1)}{2} \quad (5.19)$$

where  $B_0$  ( $\text{mm}^{-1}$ ) and  $G_{f0}$  (N/mm) are respectively the interfacial brittleness index and the interfacial fracture energy at ambient temperature; and  $b_2= 3.21$ ,  $b_3= 1.31$ ,  $c_1= 0.485$ ,  $c_2= 14.05$  and  $c_3= 0.877$ . Eqs. (5.18) and (5.19) approximate the test results reasonably well given the larger scatter of the test data (Figs. 5.2 and 5.3). The average of the predicted-to-test fracture energy ratios and its coefficient of variation are 1.025 and 32.857%, while the average of the predicted-to-test brittleness index ratios and its coefficient of variation are 1.084 and 20.163%. The values of  $B_0$  and  $G_{f0}$  may vary over a wide range and depend mainly on the strength of concrete and the properties of adhesive (Dai et al. 2005; Lu et al. 2005b; Bilotta et al. 2011; Toutanji et al. 2011). A joint shear test should be conducted to determine the values of these two parameters for a specific type of FRP laminate (and adhesive). If such a test cannot be conducted for whatever reason, the interfacial fracture energy  $G_{f0}$  can be estimated from Lu et al.'s (2005b) model; for example, Lu et al.'s (2005b) model predicts a value of 0.545 N/mm for  $G_{f0}$  for a concrete cylinder compressive strength of 35 MPa and a commonly available bonding adhesive.  $B_0$  may also be determined from Lu et al.'s (2005b) model; the values of  $B_0$  predicted by Lu et al.'s (2005b) model range from around 8 to around 14.1 for normal strength concrete with a cylinder strength varying from around 15MPa to around 50MPa. Therefore, for simplicity, a simple reference value of 10.4 may be used for  $B_0$  according to Dai et al. (2006) if a conventional bonding adhesive is used.

Predictions from the proposed bond-slip model [Eqs (5.7), (5.18) and (5.19)] at various temperatures are presented in Figs. 5.4a and 5.4b for Blontrock's (2003) specimens (specimens Zijde-20 to Zijde-70) and some of Klammer's (2006) specimens (specimens B1-20 to B1-100), respectively. The values of  $G_{f0}$  and  $B_0$  for Klammer's (2006) specimens were averaged from the two identical specimens tested at ambient

temperature. It is clearly seen that as the temperature increases, the initial stiffness of the bond-slip curve decreases while the descending branch becomes more gentle. The area enclosed by the bond-slip curve shrinks as the temperature increases, indicating degradations in the interfacial fracture energy.

### 5.3 VALIDATION OF THE BOND-SLIP MODEL

#### 5.3.1 Ultimate Loads of Double-lap Shear Tests

Fig. 5.5a presents a comparison between the ultimate load  $P_{uT, \text{pred}}$  predicted using the proposed bond-slip model and the test ultimate load  $P_{uT, \text{test}}$ . The average of the predicted-to-test load ratios and its coefficient of variation are 1.01 and 20.23%, respectively. This comparison indicates that the proposed bond-slip model can be used to predict the ultimate load of a bonded joint at elevated temperatures with good accuracy. While this close agreement can be expected because the interfacial fracture energy  $G_f$ , upon which the ultimate load depends directly, was regressed from the test ultimate loads, it at least demonstrates that the complex relationships among  $G_f$ , the temperature of the FRP-to-concrete interface and the glass transition temperature of the bonding adhesive have all been well captured by Eq. (5.18). Fig. 5.5b shows the dependence of the predicted-to-test load ratio on the temperature of the interface. It is seen that the debonding load is reasonably well predicted at temperatures over a wide range (up to 180 °C).

#### 5.3.2 Strain Distributions in the FRP Laminate

With the proposed bond-slip model, Eq. (5.14) can be used to predict strain distributions along the FRP laminate at various load levels. In Figs. 5.6a-5.6d, predicted strain distributions are compared with experimental strain distributions for four bonded joints at different load levels and different temperatures. The first specimen (Zijde-20) was tested by Blontrock (2003) at ambient temperature (Fig. 5.6a) while the second specimen (Zijde-55) was tested by Blontrock (2003) at the elevated temperature of 55 °C (Fig. 5.6b). The bond lengths of both specimens are 300 mm, which is longer than the effective bond length. The predicted strain

distributions shown in Figure 5.7a were obtained from Eq. (5.14) with  $B_0 = 10.29 \text{ mm}^{-1}$ , which was regressed from the corresponding experimental FRP strain distributions. In Fig. 5.6b, two sets of predicted FRP strain distributions are provided. One was predicted using Eq. (5.14) and  $B = 5.97 \text{ mm}^{-1}$ , which was regressed from the experimental strain distributions; another was predicted using Eq. 14 and  $B = 7.25 \text{ mm}^{-1}$ , which was calculated from the proposed equation for  $B$  [Eq. (5.19)]. It is seen that both sets of predictions are in close agreement with the test results. By comparing the strain distributions between specimen Zijde-20 and specimen Zijde-55, it can be seen that due to the temperature increase, the strain distributions become more gentle due to the softening of the bonding adhesive. Similar comparisons of strain distributions are shown in Figs. 5.6c and 5.6d for the specimens tested by Leone et al. (2009) at ambient temperature (G-S-20, 20 °C) and at an elevated temperature (G-S-80, 80 °C) respectively. Once again, the predicted strain distributions are in close agreement with the measured distributions throughout the loading process. The above comparisons clearly demonstrate the validity of the proposed bond-slip model at least within the parameter ranges of the assembled test database.

## 5.4 CONCLUSIONS

A general approach has been presented to interpret and model the bond-slip behavior of FRP-to-concrete interfaces at elevated temperatures. Based on a careful analysis of the existing test data which includes 79 tests of FRP-to-concrete bonded joints at temperatures ranging from 4 °C to 180 °C, a nonlinear temperature-dependent local bond-slip model for FRP-to-concrete interfaces has been formulated. This model is an extension of the two-parameter bond-slip model previously proposed by Dai et al. (2005) for FRP-to-concrete interfaces at ambient temperature. The two key parameters employed in the bond-slip model, the interfacial fracture energy  $G_f$  (i.e., the area beneath the bond-slip curve) and the interfacial brittleness index  $B$  (a shape parameter for the bond-slip curve), were determined from regression analysis of existing test data at elevated temperatures. During the interpretation of the test data and the derivation of  $G_f$  and  $B$ , the influences of both temperature-induced thermal stress and temperature-induced bond degradation were carefully considered. It has

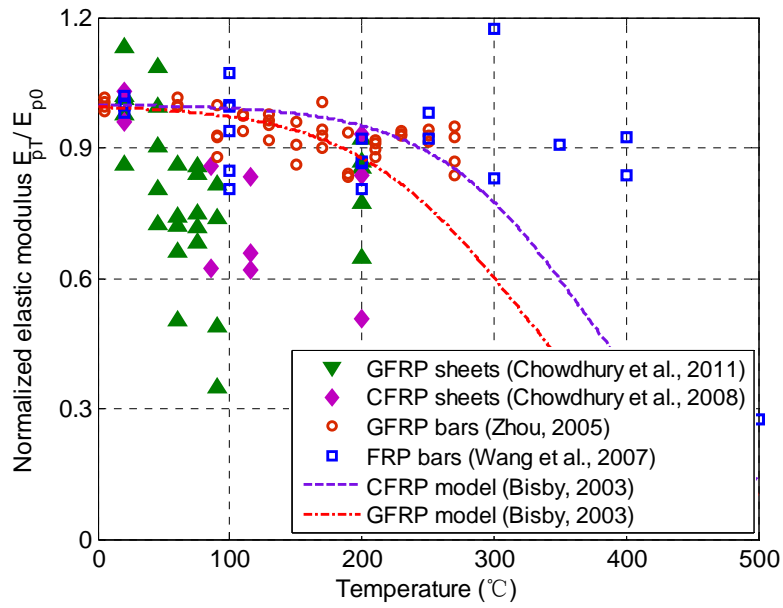
been shown that the interfacial fracture energy  $G_f$  is initially almost constant but starts to decrease as the temperature approaches the glass transition temperature; the interfacial brittleness index  $B$  also exhibits a decreasing trend, but the decrease is almost completed before reaching the glass transition temperature. The proposed temperature-dependent bond-slip model has been shown to provide a reasonably close representation of the test data upon which it is based, despite the large scatter of the test data. The proposed bond-slip model is expected to be useful in the numerical modeling of FRP-strengthened RC members exposed to fire or extremely hot climates.

## 5.5 REFERENCES

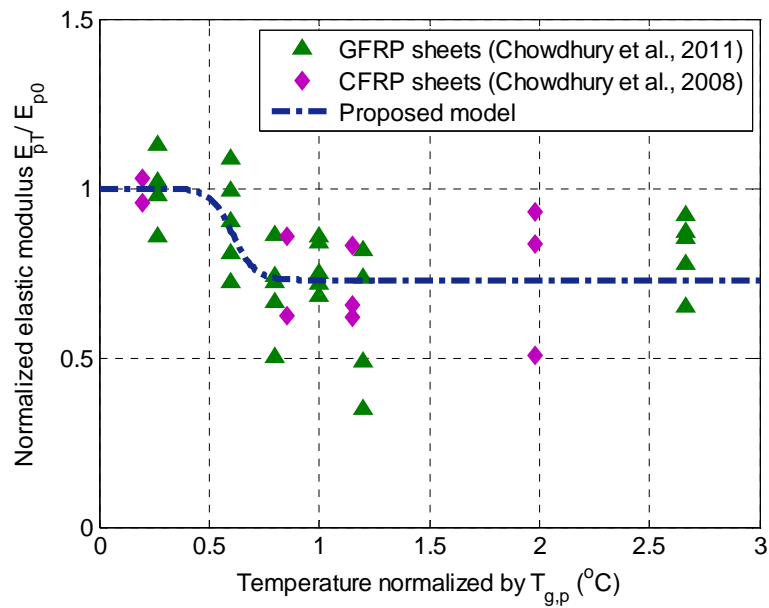
- American Concrete Institute (ACI). (2008). "Guide for the design and construction of externally bonded FRP systems for strengthening concrete structures." *ACI 440.2R-08*, Farmington Hills, Michigan, America.
- Ahmed, A., and Kodur, V.K.R. (2011). "Effect of bond degradation on fire resistance of FRP-strengthened reinforced concrete beams." *Composites Part B: Engineering*, Vol. 42, No. 2, pp. 226-237.
- Bilotta, A., Faella, C., Martinelli, E., and Nigro, E. (2012). "Indirect identification method of bilinear interface laws for FRP bonded on a concrete substrate." *Journal of Composites for Construction*, ASCE, Vol. 16, No. 2, pp. 171-184.
- Bisby, L. (2003). "Fire behavior of fiber-reinforced polymer (FRP) reinforced or confined concrete." Ph. D. thesis, Queen's University, Kingston, Ontario, Canada.
- Bisby, L.A., Kodur, V.K.R., and Green, M.F. (2005). "Fire endurance of fiber-reinforced polymer-confined concrete columns." *ACI Structural Journal*, Vol. 102, No. 6, pp. 883-891.
- Blontrock, H. (2003). "Analysis and modeling of the fire resistance of concrete elements with externally bonded FRP reinforcement." Ph. D. thesis, Ghent University, Ghent, Belgium.
- Brosens, K. (2001). "Anchoring of externally bonded steel plates and CFRP laminates for the strengthening of concrete elements." Ph.D. thesis, Department of Civil Engineering, Katholieke University Leuven, Belgium.
- Cai, Z.H. (2008). "Research on bond property of FRP-to-concrete interface under elevated temperatures." Master's thesis, Tongji University, Shanghai, China.
- Chajes, M.J., Finch, W.W., Januszka, T.F., and Thomson, T.A. (1996). "Bond and force transfer of composite material plates bonded to concrete." *ACI Structural Journal*, Vol. 93, No. 2, pp. 208-217.
- Chowdhury, E.U., Eedson, R., Bisby, L.A., Green, M.F., Benichou, N., and Kodur, V.K.R. (2008). "Mechanical characterization of fibre reinforced polymers for

- numerical fire endurance modelling.” *Proceeding of the Fifth International Conference on Structures in Fire*, Singapore, pp. 499-507.
- Chowdhury, E.U., Eedson, R., Green, M.F., Bisby, L.A., and Benichou, N. (2011). “Mechanical characterization of fiber reinforced polymers materials at high temperature.” *Fire Technology*, Vol. 47, No. 4, pp. 1063-1080.
- Clarke, J.L. (1996). *Structural design of polymer composites – Eurocomp design code and handbook*. E & FN Spon. Ltd., London, UK.
- Dai, J.G., and Ueda, T. (2003). “Local bond stress slip relationship for FRP composites-concrete interfaces.” *Proceedings of the Sixth International Symposium on FRP Reinforcement for Concrete Structures (FRPRCS-6)*, Singapore, pp. 143-152.
- Dai, J.G., Ueda, T., and Sato, Y. (2005). “Development of the nonlinear bond stress-slip model of fiber reinforced plastics sheet-concrete interfaces with a simple method.” *Journal of Composites for Construction*, ASCE, Vol. 9, No. 1, pp. 52-62.
- Dai, J.G., Ueda, T., and Sato, Y. (2006). “Unified analytical approaches for determining shear bond characteristics of FRP-concrete interfaces through pullout tests.” *Journal of Advanced Concrete Technology*, JSCE, Vol. 4, No. 1, pp. 133-145.
- Fédération International du Béton (fib). (2001). “Externally bonded FRP reinforcement for RC structures.” *fib Bulletin 14*, fib Task Group 9.3, fib, Lausanne, Switzerland.
- Gamage, J.C.P.H., Al-Mahaidi, R., and Wong, M.B. (2006). “Bond characteristics of CFRP plated concrete members under elevated temperatures.” *Composite Structures*, Vol. 75, No. 1-4, pp. 199-205.
- Gao, W.Y., Hu, K.X., and Lu, Z.D. (2010). “Fire resistance experiments of insulated CFRP strengthened reinforced concrete beams.” *China Civil Engineering Journal*, Vol. 43, No. 3, pp. 15-23 (in Chinese).
- Klamer, E. (2006). “The influence of temperature on concrete structures strengthened with externally bonded CFRP.” *Research Report*, Eindhoven University of Technology, Eindhoven, Netherlands.
- Klamer, E. (2009). “Influence of temperature on concrete beams strengthened in flexure with CFRP.” Ph.D. thesis, Eindhoven University of Technology, Eindhoven, Netherlands.
- Leone, M., Matthys, S., and Aiello, M.A. (2009). “Effect of elevated service temperature on bond between FRP EBR systems and concrete.” *Composites Part B: Engineering*, Vol. 40, No. 1, pp. 85-93.
- Lu, X.Z., Ye, L.P., Teng, J.G., and Jiang, J.J. (2005a). “Meso-scale finite element model for FRP sheets/plates bonded to concrete.” *Engineering Structures*, Vol. 27, No. 4, pp. 564-575.
- Lu, X.Z., Teng, J.G., Ye, L.P., and Jiang, J.J. (2005b). “Bond-slip models for FRP sheets/plates bonded to concrete.” *Engineering Structures*, Vol. 27, No. 6, pp. 920-937.

- Mouritz, A. P., and Gibson, A. G. (2006). *Fire properties of polymer composite materials*, Springer, Dordrecht, Netherlands.
- Nakaba, K., Kanakubo, T., Furuta, T., and Yoshizawa, H. (2001). "Bond behavior between fiber-reinforced polymer laminate and concrete." *ACI Structural Journal*, Vol. 98, No. 3, pp. 359-367.
- Silva, M.A.G., and Biscaia, H. (2008). "Degradation of bond between FRP and RC beams." *Composite Structures*, Vol. 85, No. 2, pp. 164-174.
- Stratford, T.J., Gillie, M., Chen, J.F., and Usmani, A.S. (2009). "Bonded fibre reinforced polymer strengthening in a real fire." *Advances in Structural Engineering*, Vol. 12, No. 6, pp. 867-878.
- Taljsten, B. (1996). "Strengthening of concrete prisms using the plate-bonding technique." *International Journal of Fracture*, Vol. 82, No. 3, pp. 253-266.
- Toutanji, H., Han, M., and Ghorbel, E. (2011). "Interfacial bond strength characteristics of FRP and RC substrates." *Journal of Composites for Construction*, ASCE, Vol. 16, No. 1, pp. 35-46.
- Wang, K., Young, B., and Smith, S.T. (2011). "Mechanical properties of pultruded carbon fibre-reinforced polymer (CFRP) plates at elevated temperatures." *Engineering Structures*, Vol. 33, No. 7, pp. 2154-2161.
- Wang, Y.C., Wong, P.M.H., and Kodur, V. (2007). "An experimental study of the mechanical properties of fibre reinforced polymer (FRP) and steel reinforcing bars at elevated temperatures." *Composite Structures*, Vol. 80, No. 1, pp. 131-140.
- Williams, B., Kodur, V.K.R., Green, M.F., and Bisby, L. (2008). "Fire endurance of fiber-reinforced polymer strengthened concrete T-beams." *ACI Structural Journal*, Vol. 105, No. 1, pp. 60-67.
- Wu, Z.S., Iwashita, K., Yagashiro, S., Ishikawa, T., and Hamaguchi, Y. (2005). "Temperature effect on bonding and debonding behavior between FRP sheets and concrete." *Journal of the Society of Materials Science*, Vol. 54, No. 5, pp. 474-480.
- Wu, Z.S., Yuan, H., and Niu, H. (2002). "Stress transfer and fracture propagation in different kinds of adhesive joints." *Journal of Engineering Mechanics*, ASCE, Vol. 128, No. 5, pp. 562-573.
- Yuan, H., Teng, J.G., Seracino, R., Wu, Z.S., and Yao, J. (2004). "Full-range behavior of FRP-to-concrete bonded joints", *Engineering Structures*, Vol. 26, No. 5, pp. 553-565.
- Zhou, C.D. (2005). "Fire performance of GFRP reinforced concrete." Research Report, Department of Civil Engineering, Tongji University, Shanghai, China (in Chinese).



(a) Effect of temperature on normalized elastic modulus



(b) Effect of normalized temperature ( $T/T_{g,p}$ ) on normalized elastic modulus

**Fig. 5.1** Elastic modulus degradations of FRP sheets/bars at elevated temperatures.

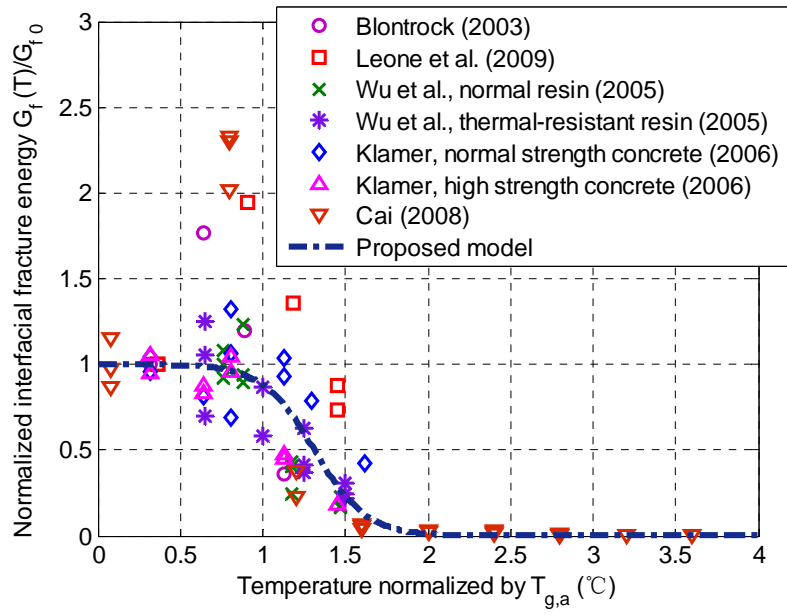


**Fig. 5.2** Effect of temperature on interfacial fracture energy

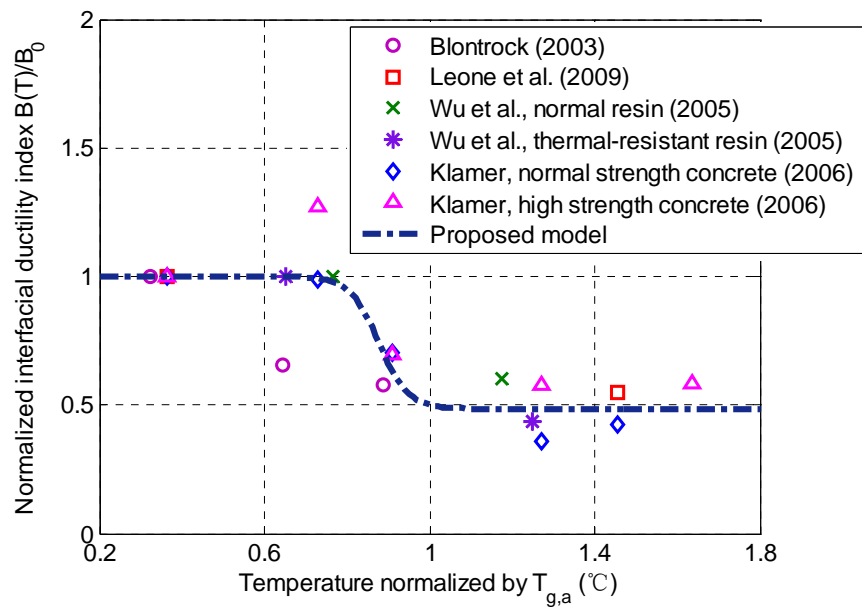
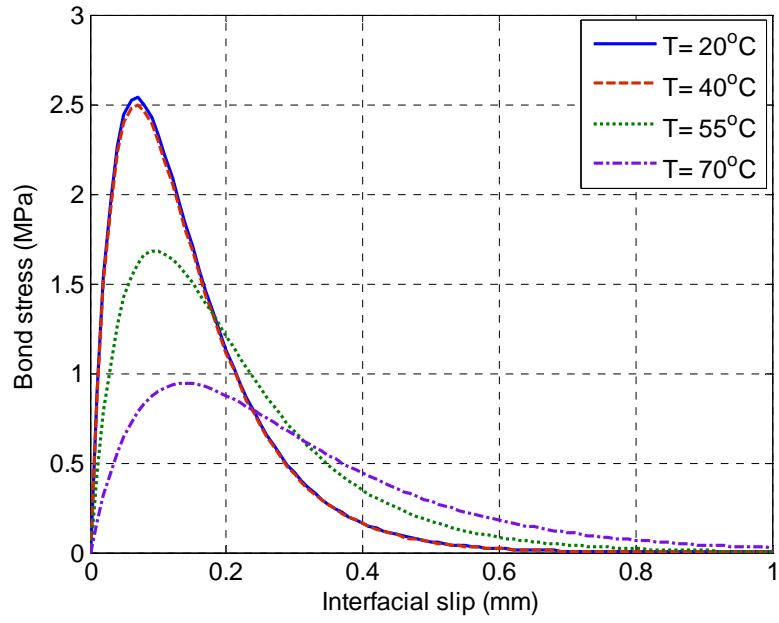
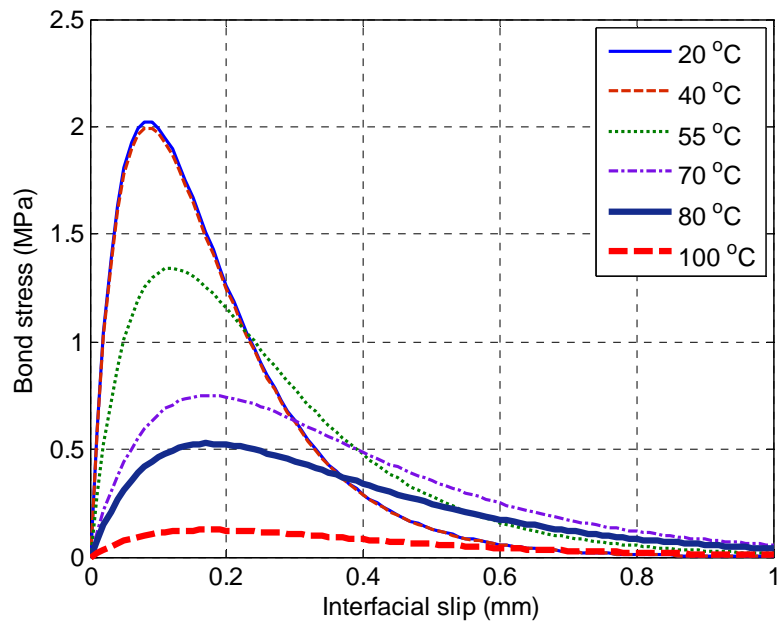


**Fig. 5.3** Effect of temperature on interfacial brittleness index

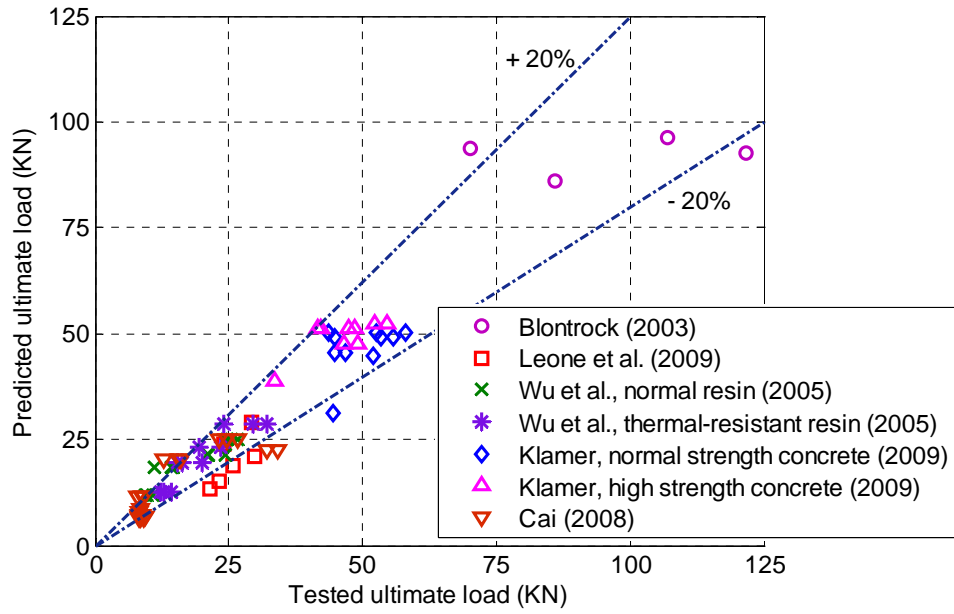


(a) Blontrock's (2003) specimens

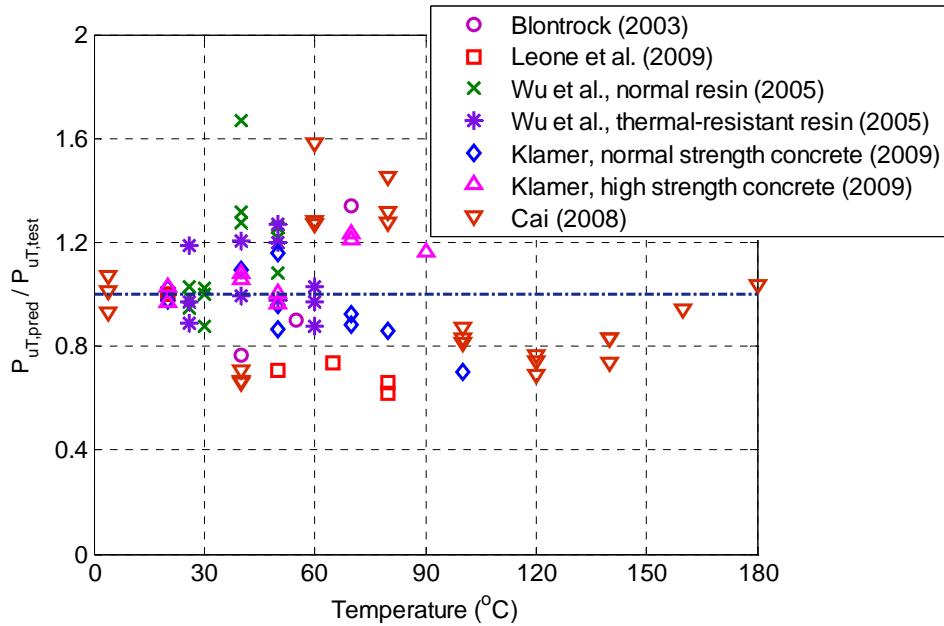


(b) Klamer's (2006) specimens

**Fig. 5.4** Predicted bond-slip curves at elevated temperatures.



(a) Comparisons between predicted and test ultimate loads



(b) Effect of temperature on the predicted-to-test ultimate load ratio

**Fig. 5.5** Comparisons between predicted and test ultimate loads of FRP-to-concrete bonded joints at elevated temperatures.

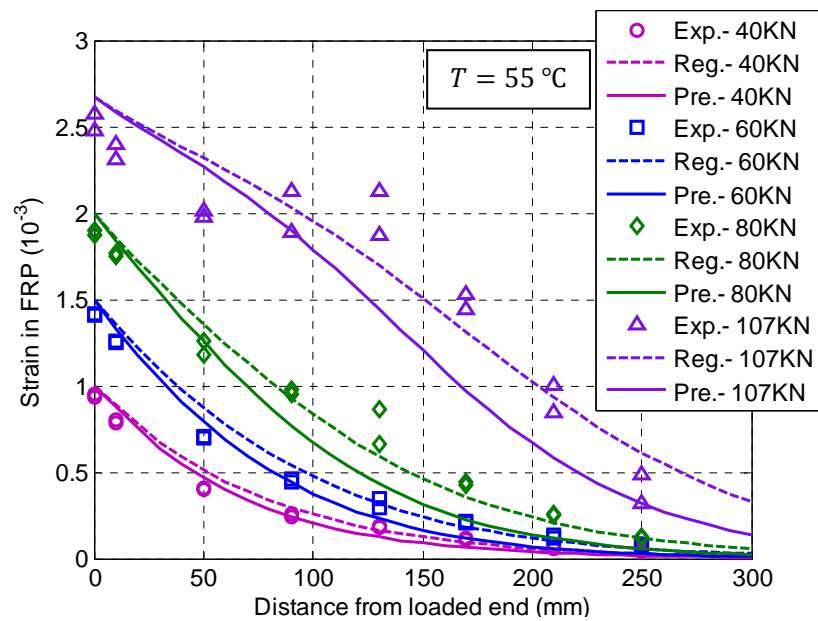
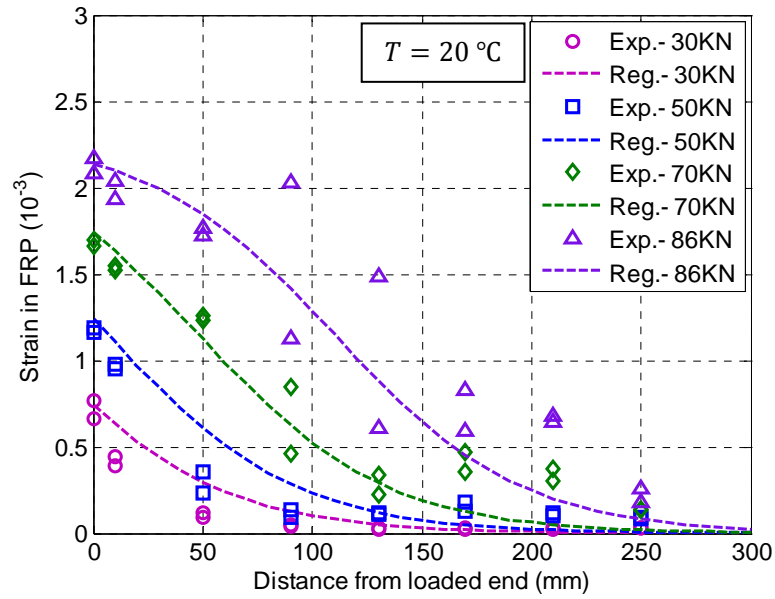
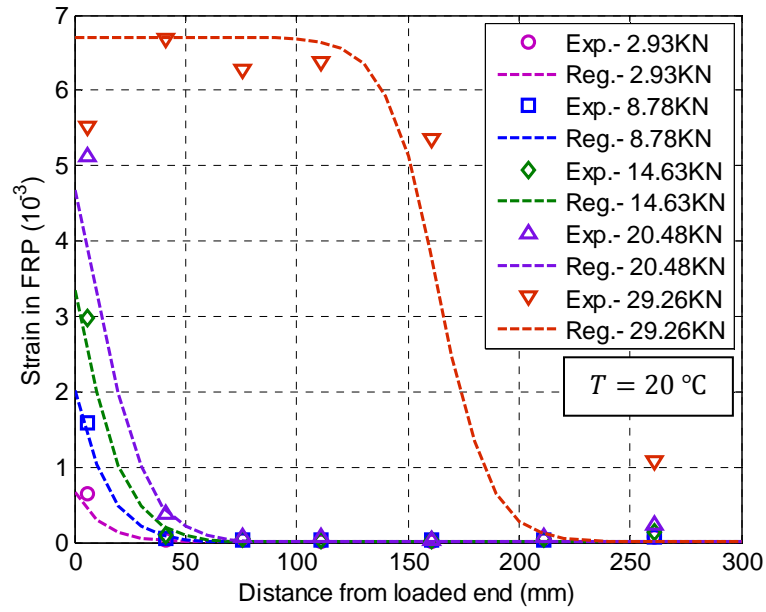
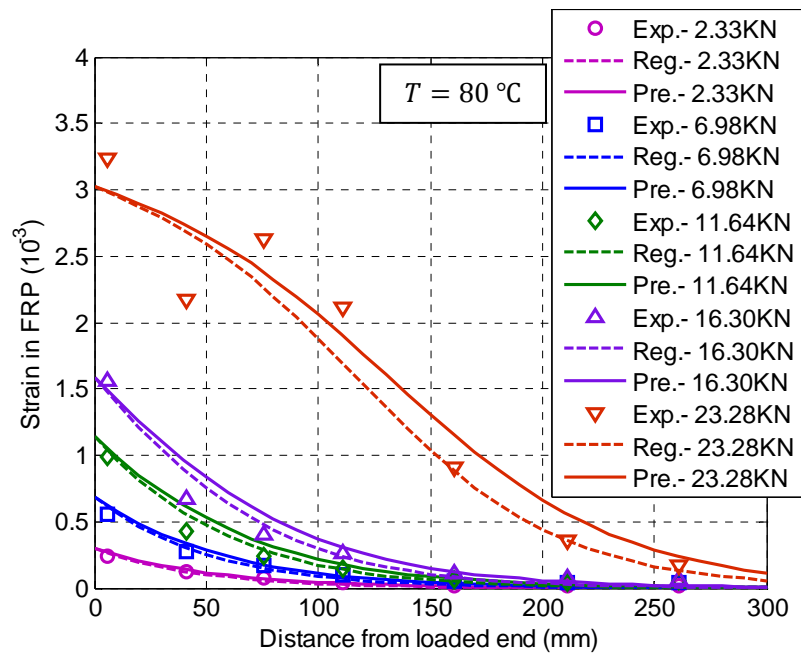


**Fig. 5.6** Comparisons between predicted and test strain distributions in FRP.



(c) Specimen G-S-20 (Leone et al. 2009)



(d) Specimen G-S-80 (Leone et al. 2009)

**Fig. 5.6** Comparisons between predicted and test strain distributions in FRP (Cont'd).

**Table 5.1** Double-lap shear test database: specimen details and results.

| Specimen name <sup>a,b</sup> | Temp (°C) | FRP laminates |            |             |             |           | Adhesive              |           | Bond zone |            | Ultimate load $P_{uT,test}$ (kN) | Failure mode <sup>c</sup> |
|------------------------------|-----------|---------------|------------|-------------|-------------|-----------|-----------------------|-----------|-----------|------------|----------------------------------|---------------------------|
|                              |           | type          | $t_p$ (mm) | $E_p$ (GPa) | $f_p$ (MPa) | $T_{g,p}$ | type                  | $T_{g,a}$ | $L$ (mm)  | $b_p$ (mm) |                                  |                           |
| Zijde-20                     | 20        | CFRP          | 1.2        | 165         | 2800        | --        |                       | 62        | 300       | 100        | 86                               | DB-C                      |
| Zijde-40                     | 40        | CFRP          | 1.2        | --          | --          | --        | Sikadur-30            | 62        | 300       | 100        | 121.6                            | DB-C                      |
| Zijde-55                     | 55        | CFRP          | 1.2        | --          | --          | --        |                       | 62        | 300       | 100        | 107                              | DB-C                      |
| Zijde-70                     | 70        | CFRP          | 1.2        | --          | --          | --        |                       | 62        | 300       | 100        | 70                               | DB-A                      |
| C-S-20                       | 20        | CFRP          | 0.117      | 225.6       | 2600        | 55        |                       | 55        | 300       | 100        | 23.98                            | DB-C                      |
| C-S-50                       | 50        | CFRP          | 0.117      | --          | --          | 55        | PC5800                | 55        | 300       | 100        | 29.7                             | DB-C                      |
| C-S-65                       | 65        | CFRP          | 0.117      | --          | --          | 55        | CARBO                 | 55        | 300       | 100        | 25.64                            | DB-C/A                    |
| C-S-80                       | 80        | CFRP          | 0.117      | --          | --          | 55        |                       | 55        | 300       | 100        | 21.48                            | DB-A                      |
| C-L-20                       | 20        | CFRP          | 1          | 176         | 2450        | --        | PC5800<br>/BL         | 81        | 300       | 100        | 80.94                            | DB-C/A                    |
| C-L-50                       | 50        | CFRP          | 1          | --          | --          | --        |                       | 81        | 300       | 100        | 68.66                            | DB-C/A                    |
| C-L-80                       | 80        | CFRP          | 1          | --          | --          | --        |                       | 81        | 300       | 100        | 88.04                            | DB-C/A                    |
| G-S-20                       | 20        | GFRP          | 0.3        | 73          | 780         | 55        | PC5800                | 55        | 300       | 100        | 29.26                            | DB-C                      |
| G-S-80                       | 80        | GFRP          | 0.3        | --          | --          | 55        | CARBO                 | 55        | 300       | 100        | 23.28                            | DB-A                      |
| O-26                         | 26        | CFRP          | 0.111      | 235         | 3400        | 34        |                       | 34        | 200       | 50         | 26.6                             | DB-C                      |
| O-26                         | 26        | CFRP          | 0.111      | 235         | 3400        | 34        |                       | 34        | 200       | 50         | 25.55                            | DB-C                      |
| O-26                         | 26        | CFRP          | 0.111      | 235         | 3400        | 34        |                       | 34        | 200       | 50         | 24.5                             | DB-C                      |
| O-30                         | 30        | CFRP          | 0.111      | --          | --          | 34        |                       | 34        | 200       | 50         | 24.3                             | DB-C                      |
| O-30                         | 30        | CFRP          | 0.111      | --          | --          | 34        |                       | 34        | 200       | 50         | 21.25                            | DB-C                      |
| O-30                         | 30        | CFRP          | 0.111      | --          | --          | 34        | Normal<br>epoxy resin | 34        | 200       | 50         | 20.75                            | DB-A                      |
| O-40                         | 40        | CFRP          | 0.111      | --          | --          | 34        |                       | 34        | 200       | 50         | 14.6                             | DB-A                      |
| O-40                         | 40        | CFRP          | 0.111      | --          | --          | 34        |                       | 34        | 200       | 50         | 14.15                            | DB-A                      |
| O-40                         | 40        | CFRP          | 0.111      | --          | --          | 34        |                       | 34        | 200       | 50         | 11.15                            | DB-A                      |
| O-50                         | 50        | CFRP          | 0.111      | --          | --          | 34        |                       | 34        | 200       | 50         | 10.85                            | DB-A                      |
| O-50                         | 50        | CFRP          | 0.111      | --          | --          | 34        |                       | 34        | 200       | 50         | 9.65                             | DB-A                      |
| O-50                         | 50        | CFRP          | 0.111      | --          | --          | 34        |                       | 34        | 200       | 50         | 9.35                             | DB-A                      |

**Table 5.1** Double-lap shear test database: specimen details and results (Cont'd).

| Specimen name <sup>a,b</sup> | Temp (°C) | FRP laminates |            |             |             |           | Adhesive                     |           | Bond zone |            | Ultimate load $P_{uT,test}$ (kN) | Failure mode <sup>c</sup> |
|------------------------------|-----------|---------------|------------|-------------|-------------|-----------|------------------------------|-----------|-----------|------------|----------------------------------|---------------------------|
|                              |           | type          | $t_p$ (mm) | $E_p$ (GPa) | $f_p$ (MPa) | $T_{g,p}$ | type                         | $T_{g,a}$ | $L$ (mm)  | $b_p$ (mm) |                                  |                           |
| T-26                         | 26        | CFRP          | 0.111      | 235         | 3400        | 55        |                              | 40        | 200       | 50         | 32.2                             | DB-C                      |
| T-26                         | 26        | CFRP          | 0.111      | 235         | 3400        | 55        |                              | 40        | 200       | 50         | 29.55                            | DB-C                      |
| T-26                         | 26        | CFRP          | 0.111      | 235         | 3400        | 55        |                              | 40        | 200       | 50         | 24.05                            | DB-C                      |
| T-40                         | 40        | CFRP          | 0.111      | --          | --          | 55        |                              | 40        | 200       | 50         | 23.55                            | DB-C                      |
| T-40                         | 40        | CFRP          | 0.111      | --          | --          | 55        | Thermo-resistant epoxy resin | 40        | 200       | 50         | 23.54                            | DB-A                      |
| T-40                         | 40        | CFRP          | 0.111      | --          | --          | 55        |                              | 40        | 200       | 50         | 19.35                            | DB-A                      |
| T-50                         | 50        | CFRP          | 0.111      | --          | --          | 55        |                              | 40        | 200       | 50         | 19.95                            | DB-A                      |
| T-50                         | 50        | CFRP          | 0.111      | --          | --          | 55        |                              | 40        | 200       | 50         | 16.25                            | DB-A                      |
| T-50                         | 50        | CFRP          | 0.111      | --          | --          | 55        |                              | 40        | 200       | 50         | 15.35                            | DB-A                      |
| T-60                         | 60        | CFRP          | 0.111      | --          | --          | 55        |                              | 40        | 200       | 50         | 14.25                            | DB-A                      |
| T-60                         | 60        | CFRP          | 0.111      | --          | --          | 55        |                              | 40        | 200       | 50         | 12.85                            | DB-A                      |
| T-60                         | 60        | CFRP          | 0.111      | --          | --          | 55        |                              | 40        | 200       | 50         | 12.1                             | DB-A                      |
| B1-20                        | 20        | CFRP          | 1.2        | 165         | 2800        | 62        |                              | 62        | 300       | 50         | 44.71                            | DB-C                      |
| B1-20                        | 20        | CFRP          | 1.2        | 165         | 2800        | 62        |                              | 62        | 300       | 50         | 46.69                            | DB-C                      |
| B1-40                        | 40        | CFRP          | 1.2        | --          | --          | 62        |                              | 62        | 300       | 50         | 44.89                            | DB-C                      |
| B1-50                        | 50        | CFRP          | 1.2        | --          | --          | 62        |                              | 62        | 300       | 50         | 43.51                            | DB-C                      |
| B1-50                        | 50        | CFRP          | 1.2        | --          | --          | 62        | Sikadur-30                   | 62        | 300       | 50         | 52.69                            | DB-C                      |
| B1-50                        | 50        | CFRP          | 1.2        | --          | --          | 62        |                              | 62        | 300       | 50         | 58.11                            | DB-C                      |
| B1-70                        | 70        | CFRP          | 1.2        | --          | --          | 62        |                              | 62        | 300       | 50         | 55.82                            | DB-A                      |
| B1-70                        | 70        | CFRP          | 1.2        | --          | --          | 62        |                              | 62        | 300       | 50         | 53.36                            | DB-A                      |
| B1-80                        | 80        | CFRP          | 1.2        | --          | --          | 62        |                              | 62        | 300       | 50         | 51.86                            | DB-A                      |
| B1-100                       | 100       | CFRP          | 1.2        | --          | --          | 62        |                              | 62        | 300       | 50         | 44.54                            | DB-A                      |
| B2-20                        | 20        | CFRP          | 1.2        | 165         | 2800        | 62        |                              | 62        | 300       | 50         | 49.16                            | DB-C                      |
| B2-20                        | 20        | CFRP          | 1.2        | 165         | 2800        | 62        |                              | 62        | 300       | 50         | 46.59                            | DB-C                      |

**Table 5.1** Double-lap shear test database: specimen details and results (Cont'd).

| Specimen name <sup>a,b</sup> | Temp (°C) | FRP laminates |            |             |             | Adhesive  |            | Bond zone |          | Ultimate load $P_{uT,test}$ (kN) | Failure mode <sup>c</sup> |            |
|------------------------------|-----------|---------------|------------|-------------|-------------|-----------|------------|-----------|----------|----------------------------------|---------------------------|------------|
|                              |           | type          | $t_p$ (mm) | $E_p$ (GPa) | $f_p$ (MPa) | $T_{g,p}$ | type       | $T_{g,a}$ | $L$ (mm) |                                  |                           | $b_p$ (mm) |
| B2-40                        | 40        | CFRP          | 1.2        | --          | --          | 62        |            | 62        | 300      | 50                               | 48.52                     | DB-C       |
| B2-40                        | 40        | CFRP          | 1.2        | --          | --          | 62        |            | 62        | 300      | 50                               | 47.33                     | DB-C       |
| B2-50                        | 50        | CFRP          | 1.2        | --          | --          | 62        |            | 62        | 300      | 50                               | 54.62                     | DB-C       |
| B2-50                        | 50        | CFRP          | 1.2        | --          | --          | 62        | Sikadur-30 | 62        | 300      | 50                               | 52.38                     | DB-C       |
| B2-70                        | 70        | CFRP          | 1.2        | --          | --          | 62        |            | 62        | 300      | 50                               | 41.56                     | DB-A       |
| B2-70                        | 70        | CFRP          | 1.2        | --          | --          | 62        |            | 62        | 300      | 50                               | 42.31                     | DB-A       |
| B2-90                        | 90        | CFRP          | 1.2        | --          | --          | 62        |            | 62        | 300      | 50                               | 33.46                     | DB-A       |
| CS-4                         | 4         | CFRP          | 0.165      | 260         | 2900        | 50        |            | 50        | 120      | 80                               | 26.7                      | DB-C       |
| CS-4                         | 4         | CFRP          | 0.165      | 260         | 2900        | 50        |            | 50        | 120      | 80                               | 23.2                      | DB-C/A     |
| CS-4                         | 4         | CFRP          | 0.165      | 260         | 2900        | 50        |            | 50        | 120      | 80                               | 24.6                      | DB-C       |
| CS-40                        | 40        | CFRP          | 0.165      | --          | --          | 50        |            | 50        | 120      | 80                               | 34.2                      | DB-C       |
| CS-40                        | 40        | CFRP          | 0.165      | --          | --          | 50        |            | 50        | 120      | 80                               | 34.0                      | DB-C       |
| CS-40                        | 40        | CFRP          | 0.165      | --          | --          | 50        |            | 50        | 120      | 80                               | 32.0                      | DB-C       |
| CS-60                        | 60        | CFRP          | 0.165      | --          | --          | 50        |            | 50        | 120      | 80                               | 15.9                      | DB-A       |
| CS-60                        | 60        | CFRP          | 0.165      | --          | --          | 50        |            | 50        | 120      | 80                               | 15.8                      | DB-A       |
| CS-60                        | 60        | CFRP          | 0.165      | --          | --          | 50        | HM 300     | 50        | 120      | 80                               | 12.8                      | DB-A       |
| CS-80                        | 80        | CFRP          | 0.165      | --          | --          | 50        |            | 50        | 120      | 80                               | 8.0                       | DB-A       |
| CS-80                        | 80        | CFRP          | 0.165      | --          | --          | 50        |            | 50        | 120      | 80                               | 9.1                       | DB-A       |
| CS-80                        | 80        | CFRP          | 0.165      | --          | --          | 50        |            | 50        | 120      | 80                               | 8.8                       | DB-A       |
| CS-100                       | 100       | CFRP          | 0.165      | --          | --          | 50        |            | 50        | 120      | 80                               | 8.7                       | DB-A       |
| CS-100                       | 100       | CFRP          | 0.165      | --          | --          | 50        |            | 50        | 120      | 80                               | 8.1                       | DB-A       |
| CS-100                       | 100       | CFRP          | 0.165      | --          | --          | 50        |            | 50        | 120      | 80                               | 8.5                       | DB-A       |
| CS-120                       | 120       | CFRP          | 0.165      | --          | --          | 50        |            | 50        | 120      | 80                               | 8.3                       | DB-A       |
| CS-120                       | 120       | CFRP          | 0.165      | --          | --          | 50        |            | 50        | 120      | 80                               | 8.6                       | DB-A       |

**Table 5.1** Double-lap shear test database: specimen details and results (Cont'd).

| Specimen name <sup>a,b</sup> | Temp (°C) | FRP laminates |            |             |             |           | Adhesive |           | Bond zone |            | Ultimate load $P_{uT,test}$ (kN) | Failure mode <sup>c</sup> |
|------------------------------|-----------|---------------|------------|-------------|-------------|-----------|----------|-----------|-----------|------------|----------------------------------|---------------------------|
|                              |           | type          | $t_p$ (mm) | $E_p$ (GPa) | $f_p$ (MPa) | $T_{g,p}$ | type     | $T_{g,a}$ | $L$ (mm)  | $b_p$ (mm) |                                  |                           |
| CS-120                       | 120       | CFRP          | 0.165      | --          | --          | 50        |          | 50        | 120       | 80         | 9.2                              | DB-A                      |
| CS-140                       | 140       | CFRP          | 0.165      | --          | --          | 50        |          | 50        | 120       | 80         | 8.3                              | DB-A                      |
| CS-140                       | 140       | CFRP          | 0.165      | --          | --          | 50        | HM 300   | 50        | 120       | 80         | 9.3                              | DB-A                      |
| CS-140                       | 140       | CFRP          | 0.165      | --          | --          | 50        |          | 50        | 120       | 80         | 8.3                              | DB-A                      |
| CS-160                       | 160       | CFRP          | 0.165      | --          | --          | 50        |          | 50        | 120       | 80         | 8.2                              | DB-A                      |
| CS-180                       | 180       | CFRP          | 0.165      | --          | --          | 50        |          | 50        | 120       | 80         | 8.4                              | DB-A                      |

<sup>a</sup> Some of the specimen names are assigned by the present authors as they are not available in the original papers.

<sup>b</sup> Specimens Zijde-20 to Zijde-70 are from Blontrock (2003); Specimens C-S-20 to G-S-80 are from Leone et al. (2009); Specimens O-26 to T-60 are from Wu et al. (2005); Specimens B1-20 to B2-90 are from Klamer (2006); Specimens CS-4 to CS-180 are from Cai (2008). Note that specimens B1-20 to B1-100 were prepared with normal strength concrete whereas specimens B2-20 to B2-90 were prepared with high strength concrete.

<sup>c</sup> Failure mode: DB-C = Debonding failure in the concrete substrate; DB-A = Debonding failure within the adhesive layer or at the adhesive/concrete interface; DB-C/A = DB-C and DB-A were both observed.

**Table 5.2** Summary of predicted results for the test specimens.

| Specimen name | FRP laminates $E_p^d$ (GPa) | $\Delta P$ (kN) | $P_{uT,test} - \Delta P$ | $G_f$ (N/mm) | $A$ ( $10^{-2}$ ) | $B$ ( $\text{mm}^{-1}$ ) | Ultimate load |                           |
|---------------|-----------------------------|-----------------|--------------------------|--------------|-------------------|--------------------------|---------------|---------------------------|
|               |                             |                 |                          |              |                   |                          | $P_{uT,pred}$ | $P_{uT,pred}/P_{uT,test}$ |
| Zijde-20      | 165                         | 0               | 86.00                    | 0.493        | 0.229             | 10.29                    | 85.93         | 1.00                      |
| Zijde-40      | 164.47                      | 7.474           | 114.13                   | 0.871        | 0.305             | 6.75                     | 92.76         | 0.76                      |
| Zijde-55      | 164.31                      | 13.068          | 93.93                    | 0.591        | 0.252             | 5.96                     | 96.23         | 0.90                      |
| Zijde-70      | 164.11                      | 18.646          | 51.35                    | 0.177        | 0.138             | --                       | 93.67         | 1.34                      |
| C-S-20        | 225.6                       | 0               | 23.98                    | 0.274        | 0.454             | --                       | 23.95         | 1.00                      |
| C-S-50        | 164.62                      | 1.149           | 28.55                    | 0.532        | 0.742             | --                       | 20.91         | 0.70                      |
| C-S-65        | 164.46                      | 1.723           | 23.92                    | 0.374        | 0.621             | --                       | 18.85         | 0.74                      |
| C-S-80        | 164.46                      | 2.297           | 19.18                    | 0.240        | 0.498             | --                       | 13.28         | 0.62                      |
| G-S-20        | 73                          | 0               | 29.26                    | 0.492        | 0.671             | 12.78                    | 29.23         | 1.00                      |
| G-S-80        | 52.22                       | 0.381           | 22.90                    | 0.359        | 0.672             | 6.98                     | 15.31         | 0.66                      |
| O-26          | 235                         | 0               | 26.60                    | 1.364        | 1.026             | --                       | 25.19         | 0.95                      |
| O-26          | 235                         | 0               | 25.55                    | 1.259        | 0.985             | --                       | 25.19         | 0.99                      |
| O-26          | 235                         | 0               | 24.50                    | 1.157        | 0.945             | 3.67                     | 25.19         | 1.03                      |
| O-30          | 171.59                      | 0.076           | 24.22                    | 1.549        | 1.279             | --                       | 21.26         | 0.86                      |
| O-30          | 171.59                      | 0.076           | 21.17                    | 1.184        | 1.118             | --                       | 21.26         | 1.00                      |
| O-30          | 171.59                      | 0.076           | 20.67                    | 1.129        | 1.092             | --                       | 21.26         | 1.03                      |
| O-40          | 171.32                      | 0.265           | 14.34                    | 0.543        | 0.757             | 2.21                     | 18.62         | 1.28                      |
| O-40          | 171.32                      | 0.265           | 13.89                    | 0.509        | 0.733             | --                       | 18.62         | 1.32                      |
| O-40          | 171.32                      | 0.265           | 10.89                    | 0.313        | 0.575             | --                       | 18.62         | 1.67                      |
| O-50          | 171.32                      | 0.454           | 10.40                    | 0.286        | 0.549             | --                       | 11.74         | 1.08                      |
| O-50          | 171.32                      | 0.454           | 9.20                     | 0.223        | 0.486             | --                       | 11.74         | 1.22                      |
| O-50          | 171.32                      | 0.454           | 8.90                     | 0.209        | 0.470             | --                       | 11.74         | 1.26                      |

**Table 5.2** Summary of predicted results for the test specimens (Cont'd).

| Specimen name | FRP laminates $E_p^d$ (GPa) | $\Delta P$ (kN) | $P_{uT, test} - \Delta P$ | $G_f$ (N/mm) | $A$ ( $10^{-2}$ ) | $B$ ( $\text{mm}^{-1}$ ) | Ultimate load  |                             |
|---------------|-----------------------------|-----------------|---------------------------|--------------|-------------------|--------------------------|----------------|-----------------------------|
|               |                             |                 |                           |              |                   |                          | $P_{uT, pred}$ | $P_{uT, pred}/P_{uT, test}$ |
| T-26          | 235                         | 0               | 32.20                     | 1.999        | 1.242             | 3.81                     | 28.60          | 0.89                        |
| T-26          | 235                         | 0               | 29.55                     | 1.683        | 1.139             | --                       | 28.60          | 0.97                        |
| T-26          | 235                         | 0               | 24.05                     | 1.115        | 0.927             | --                       | 28.60          | 1.19                        |
| T-40          | 176.76                      | 0.273           | 23.28                     | 1.387        | 1.192             | --                       | 23.74          | 1.00                        |
| T-40          | 176.76                      | 0.273           | 23.27                     | 1.386        | 1.191             | --                       | 23.74          | 1.00                        |
| T-40          | 176.76                      | 0.273           | 19.08                     | 0.931        | 0.977             | --                       | 23.74          | 1.23                        |
| T-50          | 171.48                      | 0.455           | 19.50                     | 1.003        | 1.029             | --                       | 19.52          | 0.98                        |
| T-50          | 171.48                      | 0.455           | 15.80                     | 0.658        | 0.833             | --                       | 19.52          | 1.20                        |
| T-50          | 171.48                      | 0.455           | 14.90                     | 0.585        | 0.786             | 1.67                     | 19.52          | 1.27                        |
| T-60          | 171.32                      | 0.644           | 13.61                     | 0.489        | 0.719             | --                       | 12.49          | 0.88                        |
| T-60          | 171.32                      | 0.644           | 12.21                     | 0.393        | 0.645             | --                       | 12.49          | 0.97                        |
| T-60          | 171.32                      | 0.644           | 11.46                     | 0.347        | 0.605             | --                       | 12.49          | 1.03                        |
| B1-20         | 165                         | 0               | 44.71                     | 0.521        | 0.233             | 8.28                     | 45.67          | 1.02                        |
| B1-20         | 165                         | 0               | 46.69                     | 0.569        | 0.244             | 8.15                     | 45.67          | 0.98                        |
| B1-40         | 164.47                      | 3.78            | 41.11                     | 0.442        | 0.215             | 8.10                     | 49.11          | 1.09                        |
| B1-50         | 164.37                      | 5.67            | 37.84                     | 0.375        | 0.198             | 8.29                     | 50.44          | 1.16                        |
| B1-50         | 164.37                      | 5.67            | 47.02                     | 0.579        | 0.246             | 6.07                     | 50.44          | 0.96                        |
| B1-50         | 164.37                      | 5.67            | 52.44                     | 0.720        | 0.275             | 3.00                     | 50.44          | 0.87                        |
| B1-70         | 164.18                      | 9.44            | 46.38                     | 0.564        | 0.243             | 4.11                     | 49.31          | 0.88                        |
| B1-70         | 164.18                      | 9.44            | 43.92                     | 0.506        | 0.230             | 1.75                     | 49.31          | 0.92                        |
| B1-80         | 163.94                      | 11.32           | 40.54                     | 0.431        | 0.213             | 3.49                     | 44.69          | 0.86                        |
| B1-100        | 163.50                      | 15.05           | 29.49                     | 0.229        | 0.155             | --                       | 31.30          | 0.70                        |
| B2-20         | 165                         | 0               | 49.16                     | 0.628        | 0.255             | 7.39                     | 47.85          | 0.97                        |
| B2-20         | 165                         | 0               | 46.59                     | 0.564        | 0.242             | 7.68                     | 47.85          | 1.03                        |

**Table 5.2** Summary of predicted results for the test specimens (Cont'd).

| Specimen name | FRP laminates $E_p^d$ (GPa) | $\Delta P$ (kN) | $P_{uT,test} - \Delta P$ | $G_f$ (N/mm) | $A$ ( $10^{-2}$ ) | $B$ ( $\text{mm}^{-1}$ ) | Ultimate load |                           |
|---------------|-----------------------------|-----------------|--------------------------|--------------|-------------------|--------------------------|---------------|---------------------------|
|               |                             |                 |                          |              |                   |                          | $P_{uT,pred}$ | $P_{uT,pred}/P_{uT,test}$ |
| B2-40         | 164.47                      | 3.80            | 44.72                    | 0.521        | 0.233             | 10.67                    | 51.29         | 1.06                      |
| B2-40         | 164.47                      | 3.80            | 43.53                    | 0.494        | 0.227             | 8.49                     | 51.29         | 1.08                      |
| B2-50         | 164.37                      | 5.70            | 48.92                    | 0.624        | 0.255             | 3.37                     | 52.60         | 0.96                      |
| B2-50         | 164.37                      | 5.70            | 46.68                    | 0.568        | 0.243             | 7.12                     | 52.60         | 1.00                      |
| B2-70         | 164.11                      | 9.48            | 32.08                    | 0.269        | 0.167             | --                       | 51.26         | 1.23                      |
| B2-70         | 164.11                      | 9.48            | 32.83                    | 0.281        | 0.171             | 4.35                     | 51.26         | 1.21                      |
| B2-90         | 163.74                      | 13.24           | 20.22                    | 0.107        | 0.106             | 4.42                     | 39.00         | 1.17                      |
| CS-4          | 260                         | 0               | 26.70                    | 0.328        | 0.393             | --                       | 24.87         | 0.93                      |
| CS-4          | 260                         | 0               | 23.20                    | 0.247        | 0.341             | --                       | 24.87         | 1.07                      |
| CS-4          | 260                         | 0               | 24.60                    | 0.278        | 0.362             | --                       | 24.87         | 1.01                      |
| CS-40         | 191.08                      | 1.77            | 32.43                    | 0.661        | 0.653             | --                       | 22.65         | 0.66                      |
| CS-40         | 191.08                      | 1.77            | 32.23                    | 0.653        | 0.649             | --                       | 22.65         | 0.67                      |
| CS-40         | 191.08                      | 1.77            | 30.23                    | 0.575        | 0.608             | --                       | 22.65         | 0.71                      |
| CS-60         | 189.54                      | 2.75            | 13.15                    | 0.109        | 0.265             | --                       | 20.21         | 1.27                      |
| CS-60         | 189.54                      | 2.75            | 13.05                    | 0.107        | 0.263             | --                       | 20.21         | 1.28                      |
| CS-60         | 189.54                      | 2.75            | 10.05                    | 0.063        | 0.202             | --                       | 20.21         | 1.58                      |
| CS-80         | 189.54                      | 3.74            | 4.26                     | 0.011        | 0.086             | --                       | 11.61         | 1.45                      |
| CS-80         | 189.54                      | 3.74            | 5.36                     | 0.018        | 0.108             | --                       | 11.61         | 1.28                      |
| CS-80         | 189.54                      | 3.74            | 5.06                     | 0.016        | 0.102             | --                       | 11.61         | 1.32                      |
| CS-100        | 189.54                      | 4.72            | 3.38                     | 0.007        | 0.068             | --                       | 7.06          | 0.87                      |
| CS-100        | 189.54                      | 4.72            | 3.98                     | 0.010        | 0.080             | --                       | 7.06          | 0.81                      |
| CS-100        | 189.54                      | 4.72            | 3.78                     | 0.009        | 0.076             | --                       | 7.06          | 0.83                      |
| CS-120        | 189.54                      | 5.71            | 2.59                     | 0.004        | 0.052             | --                       | 6.36          | 0.77                      |
| CS-120        | 189.54                      | 5.71            | 2.89                     | 0.005        | 0.058             | --                       | 6.36          | 0.74                      |

**Table 5.2** Summary of predicted results for the test specimens (Cont'd).

| Specimen name | FRP laminates $E_p^d$ (GPa) | $\Delta P$ (kN) | $P_{uT,test} - \Delta P$ | $G_f$ (N/mm) | $A$ ( $10^{-2}$ ) | $B$ ( $\text{mm}^{-1}$ ) | Ultimate load |                           |
|---------------|-----------------------------|-----------------|--------------------------|--------------|-------------------|--------------------------|---------------|---------------------------|
|               |                             |                 |                          |              |                   |                          | $P_{uT,pred}$ | $P_{uT,pred}/P_{uT,test}$ |
| CS-120        | 189.54                      | 5.71            | 3.49                     | 0.008        | 0.070             | --                       | 6.36          | 0.69                      |
| CS-140        | 189.54                      | 6.69            | 1.61                     | 0.002        | 0.032             | --                       | 6.87          | 0.83                      |
| CS-140        | 189.54                      | 6.69            | 2.61                     | 0.004        | 0.053             | --                       | 6.87          | 0.74                      |
| CS-140        | 189.54                      | 6.69            | 1.61                     | 0.002        | 0.032             | --                       | 6.87          | 0.83                      |
| CS-160        | 189.54                      | 7.67            | 0.53                     | 0.0002       | 0.011             | --                       | 7.72          | 0.94                      |
| CS-180        | 189.54                      | 8.66            | -0.26                    | -0.00004     | -0.005            | --                       | 8.67          | 1.03                      |
|               |                             |                 |                          |              |                   |                          | Mean          | 1.01                      |

<sup>d</sup>The elastic modulus degradation of prefabricated FRP plates was evaluated using Bisby's (2003) model:  $E_{pT}/E_{p0} = (1 - a_1)/2 \times \tanh(-a_2 \times (T - a_3)) + (1 + a_1)/2$ ; for CFRP plates:  $a_1=0.05$ ,  $a_2=8.68 \times 10^{-3}$ ,  $a_3=367.41$ ; for GFRP plates:  $a_1=0.05$ ,  $a_2=7.91 \times 10^{-3}$ ,  $a_3=320.35$ . The elastic modulus degradation of FRP sheets was evaluated using the present proposed model:  $E_{pT}/E_{p0} = (1 - a_1)/2 \times \tanh(-a_2 \times (T/T_g - a_3)) + (1 + a_1)/2$ , where  $a_1=0.729$ ,  $a_2=9.856$ ,  $a_3=0.607$ .

# FE MODELING OF UN-PROTECTED FRP-STRENGTHENED RC BEAMS EXPOSED TO FIRE

## 6.1 INTRODUCTION

When there is no additional fire insulation provided for FRP-strengthened RC beams, FRP composites will be burnt up in several minutes under a fire exposure (Li et al. 2008). That means the contribution of FRP strengthening can be simply ignored for the fire safety design of un-protected FRP-strengthened RC beams (Han et al. 2006), which analysis converts to that of an RC beam exposed to fire.

In current design codes, such as BS 8110-2 (1985), FIP/CEB (2004), ACI 216.1 (2007) and AS 3600 (2009), the fire resistance period of an RC member is usually determined using a prescriptive approach, such as the tabulated method which specifies some deemed-to-satisfy requirements of the minimum member dimensions and the minimum concrete cover for the reinforcing steel. These requirements are usually derived from empirical approaches and rely heavily on the limited results from fire resistance tests of RC members in which an RC member is commonly pre-loaded and exposed to a prescribed temperature-time curve as defined by BS 476-20 (1987), ISO 834-1 (1999) or ASTM E119 (2008).

The prescriptive approach as mentioned above generally results in a conservative design, but it is not based on an accurate understanding of the thermal and mechanical behavior of RC members exposed to fire. As a result, the prescriptive approach provides little insight into the effects of many important factors, including

the geometrical configuration, load level, restraint condition, temperature-dependent material properties, cracking and tension stiffening behavior of concrete, and acceptable failure criterion of RC members exposed to fire (Kodur and Dwaikat 2007; Kodur et al. 2008).

Recent years have seen a gradual transition from the prescriptive approach to the performance-based approach in the fire safety design of RC members since the latter provides a more cost-effective, flexible and rational tool and allows designers to use multiple routes to achieve the required fire safety (Grosshandler 2002; The Institution of Structural Engineers 2003, 2007; Beyler et al. 2007). The performance-based fire safety design approach requires tools for the accurate fire resistance analysis of RC members (or systems), which has motivated the development of numerical simulation tools with the desired capability. Such a numerical simulation tool is generally capable of a three-step analysis: (a) fire scenario analysis, (b) heat transfer analysis, and (c) mechanical response analysis (EN 1992-1-2 2004; Bailey 2004, 2009).

Many numerical models have been presented to simulate the thermal and mechanical behavior of RC beams exposed to fire. In these numerical models, the heat transfer analysis is conducted mostly using the finite difference method or the FE method (Dotrepe and Franssen 1985; Ellingwood and Lin 1991; Bratina et al. 2003, 2007; Capua and Mari 2007; Kodur and Dwaikat 2007, 2008; El-Fitiany and Youssef 2009; Kodur et al. 2009; Wu and Lu 2009) although empirical formulas have occasionally been used (Purkiss et al. 1989; Desai 1998). The mechanical response of RC beams is evaluated using either the traditional sectional analysis (Purkiss et al. 1989; Desai 1998; Capua and Mari 2007; Kodur and Dwaikat 2007, 2008; El-Fitiany and Youssef 2009; Kodur et al. 2009) or the FE method; in the latter case, beam elements (Dotrepe and Franssen 1985; Pulmano and Shin 1987; Ellingwood and Lin 1991; Bratina et al. 2003, 2007; Riva and Franssen 2008; Wu and Lu 2009; Huang et al.

2009) or isoparametric four-node quadrilateral elements (Huang and Platten 1997) have both been employed. The focus of the existing studies has been on the reliable prediction of strength degradation, deflection or rate of deflection, which can be used as a performance index to define the fire limit state.

Exposure of an RC beam to elevated temperatures during a fire leads to significant losses in the strength and stiffness of the concrete and the reinforcing steel as well as the bond between them. However, in all existing numerical models, except the model presented in a recent publication by Huang (2010), the reinforcing steel is usually assumed to be fully or perfectly bonded to the concrete at elevated temperatures. This assumption may be appropriate for predicting deteriorations in the load-carrying capacity of an RC beam exposed to fire since the critical factors are the temperature history and the deterioration in material strength. However, in performance-based fire safety design, the deflection or the rate of deflection may become a significant performance index for defining the failure limit of an RC member (Kodur and Dwaikat 2008). It is obvious that the bond-slip response of the reinforcing steel may significantly influence the deflection or the rate of deflection of an RC beam at elevated temperatures. Indeed, early pull-out tests found that the bond between steel and concrete degrades faster than the reinforcing steel itself at elevated temperatures (Diederichs and Schneider 1981; Morley and Royles 1983). It is worth mentioning that, for an un-bonded post-tensioned RC beam exposed to fire, the bond between steel and concrete in the anchorage zones is a critical issue since sudden structural failure may occur due to the loss of anchorage bond (Purkiss 2007).

It should also be mentioned that the tension-stiffening effect of concrete derived from the bond between reinforcing steel and concrete has been widely recognized as a fundamental mechanism that governs the deflection response of an RC member at room temperature; it has thus attracted extensive research attention. However,

research on RC members subjected to elevated temperatures is still very limited. Recently, Pothisiri and Panedpojaman (2012) analyzed the bond degradation and pull-out behavior of reinforcing steel in concrete subject to elevated temperatures by considering the effect of elevated temperature on the tension softening behavior of concrete. Huang (2010) modeled both the steel-to-concrete interface and RC beams subjected to elevated temperatures and concluded that the perfect bond assumption in the analysis of RC structures exposed to fire is un-conservative, but he did not propose a bond-stress slip model for the steel-to-concrete interface at elevated temperatures.

Apart from the deflection, another important issue in the performance-based fire safety design of RC members is the localized cracking behavior of reinforced concrete and its effect on structural integrity, which is usually ignored in the existing numerical models. Concrete cracking in RC beams exposed to fire has a number of important consequences. First, the bond behavior between steel and concrete is associated with the extent of localized damage (crack propagation) in the concrete surrounding the reinforcing steel (Rots 1985; fib 2000; Cervenka et al. 2003). Second, concrete cracking (and its effect on the bond) affects the local exposure condition of the reinforcing steel. Third, concrete cracking has a significant bearing on structural integrity and post-fire serviceability or reparability; in particular, when the beam is insulated or externally strengthened with a dissimilar layer of material on the beam surface, cracking of concrete may have a serious consequence. Indeed, it has been clearly established that debonding failure of the externally bonded strengthening layer depends strongly on the pattern and widths of cracks in the RC beam (Chen et al. 2011).

Against the above background, this chapter presents a more accurate three-dimensional (3D) FE model for the thermal and mechanical analysis of RC beams

exposed to fire. This 3D FE model inherits the important features of existing numerical models with respect to fire scenario analysis, heat transfer analysis and mechanical response analysis. In addition, the model includes a rigorous procedure to account for the tension-stiffening effect of concrete for accurate predictions of cracks and deflections; the latter is achieved through the accurate modeling of the bond behavior between reinforcing steel and interface. The accuracy of the FE model is demonstrated through comparisons with existing test results while its capability is illustrated through an examination of local responses predicted by the model.

## **6.2 MODELLING OF CONCRETE**

### ***6.2.1. General***

The thermal and mechanical responses of RC beams exposed to fire depend strongly on the material properties of both concrete and reinforcing steel. Extensive studies conducted over the past few decades have led to a comprehensive understanding of the thermal and mechanical properties of concrete and steel at elevated temperatures, and this information is now widely available (ASCE 1992; EN 1992-1-2 2004; Kodur et al. 2008). The modeling of the behavior of concrete in the present FE model is discussed in this section based on this information while that of reinforcing steel is dealt with in the next section.

### ***6.2.2. Thermal Properties of Concrete***

The thermal conductivity and specific heat capacity of concrete are defined according to EN 1992-1-2 (2004) (Figs. 6.1a and 6.1b); the density of concrete is taken to have a constant value of  $2300 \text{ kg/m}^3$ . The effect of moisture in concrete is implicitly considered by introducing a latent heat of evaporation component to the

specific heat capacity of concrete; the value of this latent heat is denoted by  $c_{c,peak}$ , when the temperature is between 100 °C and 115 °C, and decreases linearly when the temperature is between 115 °C and 200 °C. As shown in Fig. 6.1b,  $c_{c,peak}$  is equal to 1470 J/(kg. °C) and 2020 J/(kg. °C) respectively, for the moisture contents of 1.5% or 3.0% by weight. For other moisture contents, a linear interpolation is adopted.

### 6.2.3. Constitutive Model for Concrete

At elevated temperatures, the mechanical behavior of concrete is complex, involving strong nonlinearity, different failure mechanisms under compression and tension (crushing or cracking), and other temperature-dependent effects such as thermal expansion and creep. In the present FE model, the mechanical behavior of concrete is modeled using a damaged plasticity constitutive model (ABAQUS 2008). The key aspects of this model are summarized below.

#### 6.2.3.1 Yield surface

The yield surface used in the constitutive model for concrete was initially proposed by Lubliner et al. (1989) and later modified by Lee and Fenves (1998) to reflect the different responses of concrete in tension and compression. The yield surface is described by:

$$F(\bar{\sigma}, \tilde{\varepsilon}_t^p, \tilde{\varepsilon}_c^p) = \frac{1}{1-A} \left( A\bar{I}_1 + \sqrt{3}\bar{J}_2 + B\langle \bar{\sigma}_{max} \rangle - C\langle -\bar{\sigma}_{max} \rangle \right) - \bar{\sigma}_c(\tilde{\varepsilon}_c^p) \quad (6.1)$$

where  $\tilde{\varepsilon}_t^p$  and  $\tilde{\varepsilon}_c^p$  are the equivalent tensile and compressive plastic strains, which are determined from uniaxial tension and compression tests, respectively;  $\bar{I}_1$  and  $\bar{J}_2$  are the first effective stress invariant and the second effective deviatoric stress invariant, respectively;  $\bar{\sigma}_{max}$  denotes the algebraic maximum eigenvalue of the effective stress tensor  $\bar{\sigma}$  (Compressive stresses are defined as negative while tensile

stresses are defined to be positive);  $\langle \rangle$  is the McAuley bracket (i.e.,  $\langle x \rangle = x$  for  $x \geq 0$  and  $\langle x \rangle = 0$  for  $x < 0$ ); and  $A, B$  are dimensionless material constants and can be calculated using the following equations:

$$A = \frac{f_{b0,T} - f_{c0,T}}{2f_{b0,T} - f_{c0,T}} \quad 0 \leq A \leq 0.5 \quad (6.2)$$

$$B(\tilde{\varepsilon}_t^p, \tilde{\varepsilon}_c^p) = \frac{\bar{\sigma}_{c,T}(\tilde{\varepsilon}_c^p)}{\bar{\sigma}_{t,T}(\tilde{\varepsilon}_t^p)}(1 - A) - (1 + A) \quad (6.3)$$

where  $f_{b0,T}$  is the initial equibiaxial compressive yield stress at temperature  $T$ ; and  $f_{c0,T}$  and  $f_{t0,T}$  are the initial uniaxial compressive and tensile yield stress at temperature  $T$ , respectively. The value of  $f_{b0,T}/f_{c0,T}$  increases with the temperature because the uniaxial compressive strength degrades faster than the biaxial compressive strength, causing the yield surface to exhibit a nearly elliptical shape at low temperatures but to become egg-shaped at elevated temperatures (Khennane and Baker 1992). Based on experimental data, it has been proposed that the ratio  $f_{b0,T}/f_{c0,T}$  starts with a value of 1.16 at 20 °C and increases linearly to 1.30 at 300 °C and up to 1.70 at 750 °C (Kordina et al. 1985).  $\bar{\sigma}_{c,T}(\tilde{\varepsilon}_c^p)$  and  $\bar{\sigma}_{t,T}(\tilde{\varepsilon}_t^p)$  are the effective uniaxial compressive stress and effective uniaxial tensile stress respectively which can be determined from the corresponding uniaxial stress-strain relationships under compression ( $\sigma_{c,T}, \varepsilon_c$ ) and tension ( $\sigma_{t,T}, \varepsilon_t$ ) at temperature  $T$ :

$$\bar{\sigma}_{c,T}(\tilde{\varepsilon}_c^p) = \frac{\sigma_{c,T}}{(1-d_c)} = E_{0,T}(\varepsilon_c - \tilde{\varepsilon}_c^p) \quad (6.4)$$

$$\bar{\sigma}_{t,T}(\tilde{\varepsilon}_t^p) = \frac{\sigma_{t,T}}{(1-d_t)} = E_{0,T}(\varepsilon_t - \tilde{\varepsilon}_t^p) \quad (6.5)$$

where  $E_{0,T}$  is the initial undamaged elastic modulus at temperature  $T$ ;  $d_c$  and  $d_t$  are the damage variables used to define stiffness degradations in compression and

tension, respectively. The definition of damage variables is important in modeling shear failures in RC beams as the shear retention factor is dependent upon the damage variables (Chen et al. 2011). In the present study, no damage was defined as shear failure is not a critical failure mode under consideration. In biaxial compression where  $\bar{\sigma}_{max} = 0$ , the surface defined above becomes the Drucker-Prager yield function. The coefficient  $C$  is only required for triaxial compressive stress states, when  $\bar{\sigma}_{max} < 0$  and a typical value of  $C = 3$  is recommended for normal concrete by Lubliner et al. (1989).

#### *6.2.3.2 Compressive behavior of concrete*

The response of concrete under compression is assumed to be linear elastic until the initial yield surface is reached. The subsequent yield surfaces (i.e. loading surfaces) are controlled by a hardening variable, which is a function of the equivalent plastic strain. Therefore, based on the concept of effective stress and equivalent plastic strain, it is possible to find loading surfaces under multiaxial compression from the uniaxial compressive stress-strain relationship. In the present study, the Eurocode model (EN 1992-1-2 2004) is adopted to define the uniaxial compressive stress-strain relationship of concrete at elevated temperatures. The compressive response of concrete is assumed to be linear elastic until the axial stress reaches the initial uniaxial yield stress which is taken to be  $0.33 f_{c,T}$  ( $f_{c,T}$  denotes the uniaxial compressive strength of concrete at temperature  $T$ ). This is followed by a strain-hardening curve up to the peak compressive stress and then a descending branch representing the post-peak softening behavior of concrete.

#### *6.2.3.3 Tensile behavior of concrete*

Before cracking, the tensile behavior of concrete is assumed to be linear elastic. The behavior of cracked concrete is simulated using an elastic-plastic constitutive model (which is a smeared crack approach) in combination with the crack band model

(Bazant and Oh 1983). In this smeared crack model, crack initiates when the specified yield surface (i.e. which is the same as the failure surface for tension-dominated behavior) is reached. Consequently, the tensile stress within the crack band gradually decreases while the strain increases (referred to as tension softening). In a smeared crack model, the predicted strain of cracked concrete depends on the element size (Bazant and Planas 1998). In order to obtain objective (i.e., mesh-insensitive) results, a tensile stress-crack opening displacement curve rather than a tensile stress-strain curve is needed to define the softening behavior of cracked concrete. Such a tensile stress-crack opening displacement curve is defined in terms of material parameters such as the tensile strength and the fracture energy of the concrete (Hillerborg et al. 1976). The tensile strength  $f_{t,T}$  at temperature  $T$  is taken as  $0.1 f_{c,T}$  (Ellobody and Bailey 2009). The fracture energy  $G_f$  of concrete at ambient temperature is determined using the following equation (CEB-FIP 1993):

$$G_f = (0.0469 d_a^2 - 0.5 d_a + 26) \left( \frac{f_{c0}}{10} \right)^{0.7} \quad (6.6)$$

where  $f_{c0}$  is the compressive strength of concrete at ambient temperature;  $d_a$  is the maximum coarse aggregate size. For concrete beams analyzed in this study,  $d_a = 20$  mm is assumed if this information is not reported. Very limited test results are available on the effect of elevated temperature on the fracture energy of concrete probably because the determination of fracture energy of concrete at elevated temperatures requires sophisticated measurements. Existing tests on the fracture energy of concrete at elevated temperatures were conducted using different test methods and different types of test specimens (Bazant and Part 1985; Baker 1996; Zhang and Bicanic 2000, 2006; Nielsen and Bicanic 2003; Tang and Lo 2009). In addition, the loading tests in these studies were not always conducted at elevated temperatures (Bazant and Part 1985; Zhang and Bicanic 2006); that is, loading tests in some of these studies were conducted at an ambient temperature after the

specimen had cooled down (Baker 1996; Zhang and Bicanic 2000, 2006; Nielsen and Bicanic 2003; Tang and Lo 2009). The existing test data suggest that the fracture energy of concrete does not show clear dependence on temperature (as shown in Fig. 6.2a). In Fig. 6.2a, results from loading tests conducted at both elevated and ambient temperatures are included, and the fracture energy of concrete at elevated temperatures is normalized by the value obtained at ambient temperature. Therefore, the fracture energy of concrete is assumed to be independent of temperature in the present FE model. Based on Ellobody and Bailey (2009), a linearly descending branch is used in the present FE model to describe the relationship between the tensile stress and the crack opening displacement of concrete (Fig. 6.2b); a small residual tensile stress ( $0.05f_{t,T}$ ) is assumed when  $w > 0.95 w_u$ , where  $w$  is the crack opening displacement of concrete and  $w_u$  is the calculated stress-free crack opening displacement, to avoid possible difficulty in achieving numerical stability.

#### 6.2.3.4 Poisson's ratio

Based on the test data of Marechal (1972) and a model proposed by Elghazouli and Izzuddin (2001), the Poisson's ratio of concrete is taken as 0.20 at 20 °C and to remain constant until 150 °C. Beyond the latter temperature, the Poisson's ratio is assumed to decrease linearly to 0.1 at 400 °C and to further decrease linearly down to zero at 1200 °C.

#### 6.2.3.5 Decomposition of strain

The total strain of concrete at elevated temperatures includes four parts: the free thermal strain, the instantaneous stress-induced strain, the classical creep strain, and the transient creep strain (Khoury et al. 1985; Schneider 1986; Buchanan 2001), as shown in the following expression:

$$\varepsilon_{tot} = \varepsilon_{th}(T) + \varepsilon_{\sigma}(\bar{\sigma}, T) + \varepsilon_{cr}(\bar{\sigma}, T, t) + \varepsilon_{tr}(\bar{\sigma}, T) \quad (6.7)$$

where  $\varepsilon_{tot}$  is the total strain;  $t$  is the fire-exposure time;  $\varepsilon_{\sigma}$  is the stress-induced strain obtained from the above-mentioned constitutive law;  $\varepsilon_{th}$  is the free thermal strain and is determined according to EN 1992-1-2 (2004);  $\varepsilon_{cr}$  is the classical creep strain and can be ignored due to its small value compared to the other three components; and  $\varepsilon_{tr}$  is the transient creep strain which is defined as a function of stress and temperature. Transient creep appears only during the first heating cycle but not during the subsequent cooling and heating cycles (Khoury et al. 1985). It is noted that the uniaxial compressive stress-strain relationship provided by the EN 1992-1-2 (2004) has implicitly incorporated the effect of transient creep as pointed out in previous studies (fib 2007; Biondini and Nero 2011); furthermore, transient creep exists for concrete in compression rather than in tension. Therefore, the transient creep strain is not considered as a separate strain component in the present FE model. The phenomenon of concrete spalling is not considered in the present model since how it should be modeled is still controversial (Pearce et al. 2006; Huang et al. 2008). Besides, the concrete spalling has a minor effect on the fire performance of the RC beams analyzed in this study as they were made of normal strength concrete.

## **6.3 MODELLING OF STEEL**

### ***6.3.1 Thermal properties of steel***

The temperature-dependent variations of thermal conductivity and specific heat capacity of steel as specified in EN 1993-1-2 (2005) are adopted in the present FE model. The density of steel is taken to be 7800 kg/m<sup>3</sup>.

### ***6.3.2 Constitutive model for steel***

The total strain of steel at elevated temperatures includes two parts: the free thermal strain  $\varepsilon_{th}$  and the stress-induced strain  $\varepsilon_{\sigma}$  (i.e., tensile stress-strain curve). Both are defined in the present FE model according to EN 1992-1-2 (2004).

## **6.4 MODELLING OF STEEL-TO-CONCRETE INTERFACES**

Plain concrete under tension exhibits a softening post-peak response. In RC members, the tensile behavior of cracked concrete is more complicated due to bond interaction with the reinforcing steel. Although the tensile concrete located between flexural cracks does not significantly affect the load-bearing capacity of an RC beam, its ability to carry some tensile stresses after cracking does offer a stiffening effect to the steel bars. This stiffening effect is realized through the bond between the steel tension bars and the surrounding concrete and is referred to as the tension-stiffening phenomenon. Accurate modeling of this tension-stiffening effect, by accounting for slips between the steel bars and the concrete, is important in predicting the deflection of RC beams in the post-cracking range of concrete.

To model the tension-stiffening effect, various approaches have been explored. Scanlon and Murray (1974) proposed the use of an average stress-strain relationship for the tensile concrete in the descending branch. Gilbert and Warner (1978) proposed to modify the stress-strain relationship of the tension steel to indirectly consider the contribution of concrete on the basis of the assumption that the concrete has zero tensile resistance after cracking. These empirical approaches are able to account for the tension stiffening effect at the member level but not at the local level. A more generic approach is based on the modeling of local bond stress-slip responses of the steel-to-concrete interface using fictitious spring elements (Ngo and Scordelis 1967; Schafer 1975; de Groot et al. 1981; Ogura et al. 2008; Li et al. 2009).

In a typical FE implementation of this approach, the concrete and the reinforcing steel are represented by two different sets of elements, and node pairs at the interface (i.e., at the same location) are connected using interfacial spring elements. In the present 3D FE model, three spring elements are used at each node pair: one to represent the shear bond behavior according to a bond-slip relationship and the other two to represent the normal bond behavior in the vertical directions; the latter are assumed to be rigid (Rots 2002) for simplicity by assigning a large spring stiffness to the normal springs.

Limited experimental work exists on the bond behavior between reinforcing steel and concrete at elevated temperatures. The earliest pull-out test at elevated temperatures found in the published literature was conducted by Milovanov and Salmanov (1954). Their specimens were heated to several elevated temperatures and then allowed to cool down to ambient temperature before testing. In later studies, pull-out tests were conducted either at elevated temperatures (Diederichs and Schneider 1981; Morley and Rolys 1983; Hu 1989) or at ambient temperature after cooling (Reichel 1978; Hu 1989; Haddad et al. 2008). These test results suggest that the degradation of bond strength due to a temperature increase is slightly greater than that of the tensile strength of steel (Reichel 1978; Diederichs and Schneider 1981; Morley and Rolys 1983; Haddad et al. 2008). Moreover, the test results show that the degree of bond strength loss is influenced by the steel bar type (deformed or smooth), rib area and surface roughness of deformed bar, and type of aggregate. In addition, the details of the test method adopted, including the heating rate, size and shape of specimen, loading rate, and location of the reinforcing bar were also found to affect the test results. Fig. 6.3 provides a summary of the existing pull-out test results for deformed steel bars, indicating a wide scatter; the bond strength at elevated temperature is normalized by its value at ambient temperature for clearer comparison. The diameters of the steel bars covered by Fig. 6.3 range from 12 mm to 20 mm

while their embedded lengths range from 40 mm to 300 mm. While the bond strength generally decrease as the temperature increases, some of the test results show an opposite trend in the initial range of elevated temperatures up to around 300 °C. This unexpected increase is attributed to slightly different thermal expansion coefficients (e.g., increased confinement from the concrete to the steel) as the mechanical properties of both concrete and steel are unlikely to have changed within this temperature range. The complex scatter of the test data means difficulty in formulating an explicit equation to represent them. For the purpose of the present study, an “upper-bound” and a “lower-bound” trend line for the normalized bond strength variation are proposed for incorporation into the FE model to reflect the effect of temperature-induced bond strength loss on the deflection of RC beams. The upper-bound line is taken to have a value of 1.25 at 300 °C and to decrease to 0.63 at 800 °C; the “lower-bound” line is taken to have a value of 0.75 at 400 °C and to decrease to 0.15 at 700 °C (Fig. 6.3).

No information has been found in the published literature on the local bond-slip relationship of reinforcing steel at elevated temperatures. In the present FE model, the CEB-FIP bond-slip model for reinforcing steel is adopted to depict ambient temperature behavior; it is also modified for the prediction of bond-slip behavior at elevated temperatures by incorporating bond strength deteriorations as discussed above. That is, the bond-slip curve for a given elevated temperature is assumed to differ from a corresponding ambient temperature curve only in the value of the peak bond shear stress. Given the limited test data available, this assumption represents a realistic approach, and any future refinement of the bond-slip model for elevated temperatures can be easily incorporated into the FE model presented here. Based on the above considerations, the bond-slip model of reinforcing steel is given as follows:

$$\tau_{s,T} = \tau_{max,T} \left( \frac{s}{s_1} \right)^{0.4}, \quad s \leq s_1 \quad (6.8a)$$

$$\tau_{s,T} = \tau_{max,T}, \quad s_1 < s \leq s_2 \quad (6.8b)$$

$$\tau_{s,T} = \tau_{max,T} - \frac{\tau_{max,T} - \tau_{f,T}}{s_3 - s_2} (s - s_2), \quad s_2 < s \leq s_3 \quad (6.8c)$$

$$\tau_{s,T} = \tau_{f,T}, \quad s > s_3 \quad (6.8d)$$

where  $\tau_{s,T}$  is the local bond stress at temperature  $T$ ;  $s$  is the interfacial slip between reinforcing steel and concrete;  $s_1$ ,  $s_2$  and  $s_3$  are assumed to be independent of temperature and are equal to 0.6 mm, 0.6 mm, and 1.0 mm respectively;  $\tau_{max,T}$  is the peak bond stress at temperature  $T$ , which is proportional to the normalized bond strength as shown in Fig. 6.3; and  $\tau_{f,T}$  ( $= 0.15\tau_{max,T}$ ) is the residual bond strength at large slips ( $>1.0$  mm). As a result, a set of temperature-dependent bond-slip curves can be derived (Figs. 6.4a and 6.4b) for both the upper-bound and the lower-bound conditions. Following the existing studies (Ngo and Scordelis 1967; Schafer 1975; de Groot et al. 1981; Ogura et al. 2008; Li et al. 2009), fictitious spring elements were used to represent the bond-slip response of the steel-to-concrete interface at elevated temperatures in the present FE model. Therefore, the tangential force transmitted via a spring element parallel to a single reinforcing steel bar is found from the following equation:

$$F_{b,T} = \pi \times D \times l_s \times \tau_{s,T} \quad (6.9)$$

where  $D$  is the diameter of the reinforcing bar;  $l_s$  is the average length of the two adjacent elements and  $\tau_{s,T}$  is the bond stress calculated from Eqs. (6.8a)-(6.8d).

## 6.5 FINITE ELEMENT ANALYSIS

The FE software package ABAQUS (2008) was used to realize the proposed FE model. The temperature-dependent bond-slip model described above was implemented into ABAQUS as a user-defined spring element. The constitutive models for concrete and steel were defined within the framework of the software package; the modeling of RC beams exposed to fire was undertaken using the sequentially coupled thermo-mechanical procedure. In this procedure, the mechanical analysis depends on the heat transfer analysis, but no reverse dependency exists. Therefore, the FE analysis included three steps: (a) a fire scenario analysis to determine the temperature evolution of a compartment fire; (b) a heat transfer analysis of the RC beam exposed to this fire; and (c) a mechanical analysis based on the heat transfer analysis.

#### ***6.5.1 Fire Scenario Analysis***

The temperature evolution inside a compartment fire can be evaluated by means of the two-zone fire model or computational fluid dynamics (CFD). The two-zone fire model (based on the division of a given compartment into a top hot-layer and a bottom cold-layer) has been implemented into several free programs, such as Ozone [developed at the University of Liege, Belgium (Cadorin and Franssen 2003)] and CFAST [developed at the National Institute of Standard and Technology (NIST), United States (Peacock et al. 2008)]. The rapid growth of computational power as well as CFD has also led to the development of CFD-based field models such as the computer program FDS [developed at NIST, United States (McGrattan et al. 2010)]. In principle, the present FE model is capable of fire resistance analysis of RC beams exposed to any given temperature-time curve of a real compartment fire. However, since the available fire resistance tests of RC beams were conducted under the standard fire following ASTM E119 (2008) or ISO 834-1 (1999), the standard

temperature-time relationship was employed in all the fire resistance numerical simulations presented in this paper.

### 6.5.2 Heat Transfer Analysis

To obtain the transient temperature field of an RC beam in a fire, three modes of heat transfer, namely convection, radiation and conduction should be appropriately considered. In a fire test furnace, heat fluxes flow to the outermost surfaces of the RC beam and exchange heat with them by convection and radiation, whereas heat transfer occurs within the concrete body through conduction. The time-dependent distribution of the temperature gradient in an RC beam is described by Fourier's differential equation for heat conduction (Purkiss 2007):

$$\frac{\partial}{\partial x} \left( k \frac{\partial T}{\partial x} \right) + \frac{\partial}{\partial y} \left( k \frac{\partial T}{\partial y} \right) + \frac{\partial}{\partial z} \left( k \frac{\partial T}{\partial z} \right) + Q = \rho C_c \frac{\partial T}{\partial t} \quad (6.10)$$

where  $k$ ,  $\rho$  and  $C_c$  denote the temperature-dependent thermal conductivity, density and specific heat capacity, respectively;  $Q$  is the inherently generated heat; and  $t$  is the time variable. For the purpose of heat transfer analysis of an RC beam, the inherently generated heat  $Q$  is not active (i.e.,  $Q = 0$ ). The solution of the above differential equation requires the initial temperature distribution and proper boundary conditions. The initial temperature distribution in an RC beam at  $t = 0$  is described by:

$$T(x, y, z, t)|_{t=0} = T_0(x, y, z) \quad (6.11)$$

where  $T_0(x, y, z)$  is the ambient temperature of the test specimen; in an actual fire test, its value is usually measured using thermocouples and the measured value varies from one test to another.

The heat fluxes exchange heat with the outermost surfaces of the RC beam via convection and radiation, which can be depicted by means of the Robin boundary conditions (Purkiss 2007):

$$-k \frac{\partial T}{\partial n} = h_c (T - T_f) + \sigma \varepsilon_m \varepsilon_f \left[ (T - T_z)^4 - (T_f - T_z)^4 \right] \quad (6.12)$$

where  $n$  represents the outward normal direction of the beam surface;  $h_c$  is the convective heat transfer coefficient and the value is taken as 25 W/(m<sup>2</sup>.K) (EN 1992-1-2 2002);  $T_f$  denotes the fire temperature measured in the furnace or determined from the standard fire curve;  $T_z$  is the absolute zero temperature;  $\sigma$  is the Stefan-Boltzmann constant and is equal to  $5.67 \times 10^{-8}$  W/(m<sup>2</sup>.K<sup>4</sup>);  $\varepsilon_m$  and  $\varepsilon_f$  are the heat emissivities of the exposed surfaces and the fire, respectively. According to EN 1991-1-2 (2002),  $\varepsilon_f = 1.0$  for the standard fire condition, and  $\varepsilon_m = 0.8$  for concrete. For the un-exposed surfaces, a constant value of 9 W/(m<sup>2</sup>.K) is assumed for the convective heat transfer coefficient  $h_c$ . In the FE heat transfer analysis of the present study, the concrete and the reinforcing steel were modeled using eight-node continuum (DC3D8) and two-node link (DC1D2) thermal elements, respectively.

### ***6.5.3 Mechanical Response Analysis***

During the mechanical response analysis, the FE mesh remained the same as that used in the preceding heat transfer analysis, but the thermal elements were replaced with stress elements, which were the eight-node continuum element with reduced integration (C3D8R) for concrete and the two-node link element (T3D2) for the reinforcing steel. The total fire exposure period was divided into small time steps. The magnitude of each time step was automatically chosen by the computer program, and the minimum time step adopted was very small (i.e.,  $t_i = 0.2$  min) to ensure

numerical convergence even for a highly nonlinear problem. To investigate the convergence of the FE mesh, the beam tested by Wu et al. (1993), with a section of 200 mm × 400 mm, was modeled using different meshes. Converged results for the displacement response of the beam (i.e. with a displacement tolerance of 1%) were achieved when an element size of 25 mm × 25 mm × 25 mm was used. Therefore, this element size was adopted in all the subsequent numerical simulations to strike a good balance between accuracy and efficiency.

As RC beams in fire generally experience large deflections, the effect of geometric nonlinearity was included in FE analysis using the updated Lagrangian method (ABAQUS 2008). Similar to other studies (Rafi et al. 2008; Wu and Lu 2009), the Newton-Raphson method was employed as the solution method with a tolerance of 0.05 for the displacement norm as the convergence criterion. In addition, the line search function (Crisfield 1982; Schweizerhof 1993) was activated to achieve more rapid convergence.

## **6.6 VALIDATION OF THE FE MODEL**

RC beams tested under fire by Wu et al. (1993), Lin et al. (1981) and Dotreppe and Franssen (1985) respectively were selected and analyzed to illustrate the capability and accuracy of the present FE model. These tests were selected because their results have been reported in detail to facilitate FE simulations and detailed comparisons.

### ***6.6.1 Tests by Wu et al. (1993)***

As part of a joint research project on the fire resistance of housing in China between the Fire Bureau of China and the Institute for Research in Construction of Canada, three RC beams were tested at Tianjin Fire Research Institute, China (Wu et al.

1993). These beam specimens (Beam I, Beam II and Beam III) were designed to be identical. The dimensions and reinforcement details of these beams are shown in Fig. 5. The reinforcing steel had a yield stress and a tensile strength of 240 MPa and 380 MPa, respectively. The measured cube compressive strength of the concrete at 28 days was 24.2 MPa. The beams were 5.1 m in span with 4.0 m of the span exposed to fire (Fig. 6.5). During the fire test, an overlaying slab was placed on the beam; this slab was 80 mm thick for Beams I and II but 120 mm thick for Beam III. A distributed load (i.e.,  $300 \text{ kg/m}^2$ ) was applied on the top of the overlaying slab, so the total load acting on the beam during the fire consisted of two parts: the applied distributed load and the self-weight of the overlaying slab.

During the heat transfer analysis, the beam was subjected to the ISO 834 standard fire from its bottom and two sides. Fig. 6.6a compares the predicted temperature increases at various locations in the beam with the experimental results, showing very close agreement in general. The temperature at 100 mm from the bottom face is somewhat underestimated within the first 40 minutes of fire exposure, which may be attributed to the migration of moisture toward the inner part of the beam. However, the mechanical properties of concrete and steel remain almost unchanged during this stage as the temperature is still relatively low (around  $100 \text{ }^\circ\text{C}$ ), this underestimation of temperature has little effect on the predicted fire performance of the RC beam. Figs. 6.6b and 6.6c present comparisons between the measured mid-span deflections and the FE predictions for the three beams. The three predicted curves in each figure correspond to three different assumptions for the bond behavior between steel and concrete: (a) perfect bond; (b) the upper-bound bond-slip model (Fig. 6.4a); and (c) the lower-bound bond-slip model (Fig. 6.4b). Clearly, the FE model provides closer predictions of deflections when the temperature-dependent local bond-slip behavior is included. The close agreement between the predictions and the test results demonstrates the validity and accuracy of the proposed FE model.

### **6.6.2. Tests by Lin et al. (1981)**

Another series of fire tests on RC beams were conducted at the Fire Research Laboratory of the Portland Cement Association and reported by Lin et al. (1981). A total of eleven full-scale rectangular beams were tested under the ASTM E119 standard fire. The effects of several parameters such as the aggregate type, moment redistribution and beam continuity on the fire resistance of RC beams were examined. Each beam had a total length of 9,760 mm and was installed in the fire furnace with a 6,100 mm distance between the two supports and with an 1,830 mm cantilever span beyond each support. Only one beam, named beam B-124, was simply supported during the test while all other beams were continuous at their supports, with either one or both cantilevered spans subjected to a concentrated load. As the effect of beam continuity over supports is beyond the scope of this study, only beam B-124 was modeled. Beam B -124 had a section of 305 mm × 355 mm reinforced with four 19 mm steel tension bars and two 19 mm steel compression bars. The bottom and side concrete cover were 25 mm and 38 mm, respectively. The yield stress of reinforcing steel was 435.8 MPa while the cylinder compressive strength of the concrete was 29.46 MPa. The RC beam was symmetrically loaded with four concentrated loads at 1500 mm apart, and each load had a constant value of 20 kN during the test. The corner rebar temperature and mid-span deflection predicted by the proposed FE model are compared with the test data in Figs. 7, showing close agreement between the two sets of results throughout the fire exposure period. The lower-bound bond-slip model leads to more accurate predictions of the mid-span deflection whereas the perfect bond assumption leads to underestimation of the deflection, indicating that the inclusion of bond degradation at elevated temperatures leads to more accurate predictions.

### ***6.6.3. Test by Dotreppe and Franssen (1993)***

The last test simulated was conducted by Dotreppe and Franssen (1993) who reported only the fire test of one simply supported beam. The beam had a span of 6,500 mm, a width of 200 mm and a depth of 600 mm. This beam was symmetrically loaded in four-point bending with a constant moment zone of 3,150 mm. The two concentrated loads were 32.5 kN each. The bottom concrete cover was 40 mm. Comparisons between test and FE results for the temperature increase of the central tension rebar and the mid-span deflection of the beam respectively are compared in Figs. 8a and 8b. These comparisons indicate that the FE model provides consistent and satisfactory predictions of the test results throughout the entire duration of fire exposure.

### ***6.6.4. Local Behavior of RC Beams Exposed to Fire***

The validated FE model can be deployed to understand aspects of structural performance which cannot be easily clarified through fire tests. The local behavior of Wu et al. (1993)'s test beam, (i.e., Beams I and II) is examined herein as an example. Figs. 6.9a-6.9c present the steel-concrete interfacial slip distributions for the middle tension bar along the beam span. As expected, the distribution of interfacial slips is nearly anti-symmetric with regard to the mid-span of the beam, due to the symmetry of loading and geometry of the RC beam except for the slightly different support conditions at the two ends (i.e., one end was restrained against longitudinal displacements but the other end was not), which are not expected to affect the slip distribution (Fig. 6.5a). The maximum slip obtained with the lower-bound bond model is around twice of that obtained with the upper-bound bond model. At ambient temperature, the maximum slip always occurs near the mid-span of the beam (Fig. 6.9a) due to the mid-span crack which is the widest among all cracks in

the beam. At elevated temperatures, the maximum slip at the steel-to-concrete interface occurs unexpectedly in the transition zone between the heated and the unheated areas within the anchorage zone (Figs. 6.9b-6.9c). These results indicate that slips at elevated temperatures are mainly caused by the different thermal deformations between concrete and reinforcing steel, and these thermally-induced slips are much larger than load-induced slips at ambient temperature. In a real compartment fire, the fire exposure condition is similar to the test condition of this beam: the central part of the RC beam is exposed to fire while the parts adjacent to the beam ends are much cooler. After such fire exposure, the steel-to-concrete interface may have experienced unrecoverable slips, which may influence the residual strength and serviceability of the fire-damaged RC beam.

The variations of longitudinal distributions of stresses in the middle and the corner steel tension bars with the fire exposure time are shown in Figs. 10a and 10b. These distributions clearly indicate that all steel bars had a similar maximum tensile stress of around 50 MPa at mid-span before the fire exposure. During the fire exposure, the stresses in the tension bars increased significantly with time, and the corner bars behaved very differently from the middle bar. In the transition zone, the corner bars even developed compressive stresses, indicating that their thermal expansion was restrained by the adjacent regions (Fig. 6.5). When the fire exposure time exceeded about 60 minutes, the maximum stress in the middle bar experienced little further changes, whereas the maximum stress in the corner bars first increased and then decreased because of their faster deterioration due to the larger temperature increase at the corners.

Figs. 6.11a-6.11f present the predicted distributions of axial stresses in concrete over the beam cross-section at the mid-span as a function of fire exposure time obtained with the lower-bound bond model. At the beginning of fire tests ( $t = 0$  min), the top

concrete fibers are subject to compression and the bottom concrete fibers are subject to tension (Fig. 6.11a) as is expected. However, as the temperature increases, compressive stresses appear in the four corner zones of the section (Fig. 6.11b) due to the temperature gradient (i.e. U-shaped distribution) in the section. This unique stress distribution over the section causes the neutral axis to shift downward and also results in the yielding of the middle steel bar (Fig. 6.10a). These complex stress variations are due to a combined effect of thermal stresses and interaction between reinforcing steel and concrete through interfacial bond.

Even though the spalling of concrete has not been considered in the present FE model, the predicted stress distributions shown in Fig. 6.11 provide a good qualitative explanation for the spalling phenomenon observed in fire tests of high strength concrete (HSC) beams. Existing explanations of concrete spalling can be classified into two categories: (a) thermal stress-induced spalling (compressive stress); and (b) spalling due to the build-up of pore pressure within concrete (Ko et al. 2011). Moreover, previous tests showed that concrete spalling occurs during the first 20-60 minutes in a fire (Khoury 2000). As shown in Fig. 6.11f, the spalling zones observed in the fire tests of HSC beams (Choi and Shin 2011; Dwaikat and Kodur 2009) are almost identical to the compressive stress zones predicted by the FE model (Figs. 6.11b and 6.11c). This consistency demonstrates that the predicted stresses can be used for predicting concrete spalling. Therefore, the present FE analysis, due to its three-dimensional nature, has good potential for extension into a realistic predictive model for concrete spalling and for achieving improved fire-resistance analysis of HSC beams exposed to fire.

To further understand the thermal and mechanical responses of the RC beam, Figs. 6.12-6.13 show the predicted evolutions with time of temperatures, axial strains and axial stresses of concrete over two vertical paths of the mid-span beam section: one

is along the integration points of the central layer of elements (Fig. 6.12) (i.e., near the mid-width of the beam section) and the other is along the integration points of the exterior layer of elements (Fig. 6.13) (i.e., near the beam side). In the FE model, the element size was 25 mm, leading to 8 elements across the beam width. As the integration point is at the centre of the element, the temperature of the integration point is taken as the average temperature of the eight nodes of the element.

As expected, before fire exposure, the axial stresses of concrete at mid-span vary linearly in the compressive zone. This is consistent with the plane section assumption. Nonlinear tension-softening is observed for the cracked concrete below the neutral axis of the mid-span section (Figs. 6.12d and 6.13d). After the commencement of fire exposure, the temperature- induced thermal strain and thus the total strain varies in a nonlinear manner down the beam height (Figs. 6.12b-6.12c and 6.13b-6.13c). As a result, the stress distribution over the beam depth also becomes nonlinear. The axial stresses of the central layer elements generally decrease with the fire exposure time in both the tensile and compressive zones (Fig. 6.12d) although at 106 minutes, a small zone of large compressive stresses exists near the top edge of the beam; for the exterior layer elements, the compressive zone of concrete expands with the fire exposure time while the bottom concrete changes from a tensile state into a compressive state (Fig. 6.13d). These stress distributions indicate that it is difficult to define a neutral axis for such a beam section exposed to fire, which also illustrates the importance of three-dimensional analysis of RC members exposed to fire. These complex stress distributions are also difficult to incorporate in a relatively simple fire resistance design approach such as the widely used sectional analysis approach.

Some abrupt fluctuations at small stresses around the zero stress line are observed down both vertical paths at different times of fire exposure (Figs. 6.12d and 6.13d). These fluctuations are difficult to explain, but may be attributed to the high

nonlinearity of the problem and the numerical procedure adopted by ABAQUS. Similar stress fluctuations have also been reported by Nechnech et al. (2002) for an RC slab exposed to fire.

## **6.7 CONCLUSIONS**

This chapter has presented a 3D FE model for predicting the behavior of RC beams exposed to fire. In the proposed FE model, the bond-slip response of the interface between reinforcing steel and concrete at elevated temperatures is explicitly considered to enable more accurate predictions of deflections. The FE predictions of both the thermal and mechanical responses of RC beams have been found to be in close agreement with existing test results. These comparisons have also clarified for the first time that while the inclusion of this interfacial behavior in the FE model leads to more accurate predictions, the effect is often rather limited and may be ignored when the objective of the analysis is to obtain the global response of an RC beam. However, the 3D FE model allows an in-depth examination of the local behavior of RC beams exposed to fire in terms of stress and deformation states in both the concrete and the steel as well as their complex interaction. The proposed 3D FE model may be used directly in performance-based fire safety design of RC beams as a cost-effective numerical tool; it may also be employed in parametric studies to develop simple design rules.

A key element of the proposed FE model is the temperature-dependent bond-slip model for the reinforcing steel. In the present FE model, a lower-bound and an upper-bound bond model was proposed for use in the FE model based on the limited test results available. More work is needed to define the bond-slip relationship more accurately so that the local behavior of an RC beam exposed to fire can be more

accurately predicted; the predicted global response of the beam benefits little from a more accurate bond-slip model for the steel-to-concrete interface.

## 6.8 REFERENCES

- ABAQUS. (2008). *ABAQUS Standard User's Manual*, Volumes I-III, Version 6.8. Hibbitt, Karlsson & Sorensen, Inc., Pawtucket, America.
- ACI 216.1. (2007). *Code Requirements for Determining Fire Resistance of Concrete and Masonry Construction Assemblies*. American Concrete Institute, Michigan, America.
- AS 3600. (2009). *Concrete Structures*. Standards Association of Australia, Sydney, Australia.
- ASCE. (1992). *Structural Fire Protection*. Manuals and Reports on Engineering Practice No. 78, ASCE Committee on Fire Protection, Structural Division, American Society of Civil Engineers, New York, America.
- ASTM E119. (2008). *Standard Test Methods for Fire Test of Building Construction and Materials*. American Society for Testing and Materials, Pennsylvania, America.
- Bazant, P. Z. and Oh, B. H. (1983). "Crack band theory for fracture of concrete." *Materials and Structures*, Vol. 16, No. 3, pp. 155-177.
- Bazant, P. Z. and Prat, C. P. (1985). "Effect of temperature and humidity on fracture energy of concrete." *ACI Material Journal*, Vol. 85, No. 4, pp. 262-271.
- Bazant, P. Z. and Planas, J. (1998). *Fracture and size effect in concrete and other quasibrittle materials*, CRC press, Boca Raton, America.
- Bailey, C. (2004). "Structural fire design: core or specialist subject?" *The Structural Engineer*, Vol. 82, No. 9, pp. 32-38.
- Bailey, C. (2009). "Science and technology developments in structural fire engineering." *Structural Engineering International*, Vol. 19, No. 2, pp. 155-164.
- Baker, G. (1996). "The effect of exposure to elevated temperatures on the fracture energy of plain concrete." *Materials and Structures*, Vol. 29, No. 19, pp. 383-388.
- Beyler, C., Beitel, J., Iwankiw, N. and Lattimer, B. (2007). "Fire resistance testing for performance-based fire design of buildings." Research Report, Fire Protection Research Foundation of the NFPA, Quincy, MA, America.

- Biondini, F.M. and Nero, A. (2011). "Cellular finite beam element for nonlinear analysis of concrete structures under fire." *Journal of Structural Engineering*, ASCE, Vol. 137, No. 5, pp. 543-558.
- Bratina, S., Planinc, I., Saje, M., and Goran, T. (2003). "Non-linear fire-resistance analysis of reinforced concrete beams." *Structural Engineering and Mechanics*, Vol. 16, No. 6, pp. 695-712.
- Bratina, S., Saje, M., and Planinc, I., Saje, M. (2007). "The effects of different strain contributions on the response of RC beams in fire." *Engineering Structures*, Vol. 29, No. 3, pp. 418-430.
- BS 476-20. (1987). *Fire Tests on Building Materials and Structures --- Part 20: Methods for Determination of the Fire Resistance of Elements of Construction (General Principles)*. British Standards Institute, Milton Keynes, UK.
- BS 8110-2. (1985). *Structural Use of Concrete--- Part 2: Code of Practice for Special Circumstance*. British Standards Institute, Milton Keynes, UK.
- Buchanan, A.H. (2001). *Structural Design for Fire Safety*. Wiley, Chichester, UK.
- Cadorin, J.F. and Franssen, J.M. (2003). "A tool to design steel elements submitted to compartment fires---OZone V2. Part 1: pre- and post-flashover compartment fire model." *Fire Safety Journal*, Vol. 38, No. 5, pp. 395-427.
- Capua, D.D. and Mari, A.R. (2007). "Nonlinear analysis of reinforced concrete cross-sections exposed to fire." *Fire Safety Journal*, Vol. 42, No. 2, pp. 139-149.
- CEB-FIP. (1993). *CEB-FIP Model Code 90*, Thomas Telford Ltd., London.
- Cervenka, V., Cervenka, J. and Jendele, L. (2003). "Bond in finite element modelling of reinforced concrete", *Proceeding of the Euro-C Conference 2003: Computational Modeling of Concrete Structures*, N. Bicanic, R. de Borst, H. Mang and G. Meschke, eds., St Johann im Pongau, Austria, pp. 189-194.
- Chen, G.M.; Teng, J.G. and Chen, J.F. (2011). "Finite-element modeling of intermediate crack debonding in FRP-plated RC beams", *Journal of Composites for Construction*, ASCE, Vol. 15, No. 3, pp. 339-353.
- Choi, E.G. and Shin, Y.S. (2011). "The structural behavior and simplified thermal analysis of normal-strength and high-strength concrete beams under fire." *Engineering Structures*, Vol. 33, No. 4, pp. 1123-1132.
- Crisfield, M.A. (1982). "Accelerated solution techniques and concrete cracking." *Computer Methods in Applied Mechanics and Engineering*, Vol. 33, No. 1-3, pp. 585-607.
- de Groot, A.K., Kusters, G.M.A. and Monnier, T. (1981). "Numerical modelling of bond-slip behavior." *Heron*, Vol. 26, No. 1B, pp.6-38.

- Desai, S.B. (1998). "Design of reinforced concrete beams under fire exposure conditions." *Magazine of Concrete Research*, Vol. 50, No. 1, pp. 75-83.
- Dwaikat, M.B. and Kodur, V.K.R. (2009). "Response of restrained concrete beams under design fire exposure." *Journal of Structural Engineering*, ASCE, Vol. 135, No. 11, pp. 1408-1417.
- Diederichs, U. and Schneider, U. (1981). "Bond strength at high temperature." *Magazine of Concrete Research*, Vol. 33, No. 115, pp. 75-84.
- Dotreppe, J.C. and Franssen, J.M. (1985). "The use of numerical models for the fire analysis of reinforced concrete and composite structures." *Engineering Analysis*, Vol. 2, No. 2, pp. 67-74.
- EI-Fitiany, S.F. and Youssef, M.A. (2009). "Assessing the flexural and axial behaviour of reinforced concrete members at elevated temperatures using sectional analysis." *Fire safety Journal*, Vol. 44, No.5, pp. 691-703.
- Elghazouli, A.Y. and Izzuddin, B.A. (2001). "Analytical assessment of the structural performance of composite floors subject to compartment fires." *Fire Safety Journal*, Vol. 36, No. 8, pp. 769-793.
- Ellingwood, B. and Lin, T.D. (1991). "Flexural and shear behaviour of concrete beams during fires." *Journal of Structural Engineering*, ASCE, Vol. 117, No. 2, pp. 440-458.
- Ellobody, E.A.M. and Bailey, C.G. (2009). "Modelling of unbonded post-tensioned concrete slabs under fire conditions." *Fire Safety Journal*, Vol. 44, No.2, pp. 159-167.
- EN 1991-1-2 (2002). *Eurocode 1: Actions on Structures --- Part 1-2: General Actions --- Actions on Structures Exposed to Fire*, British Standards Institution, London, UK.
- EN 1992-1-2 (2004). *Eurocode 2: Design of Concrete Structures --- Part 1-2: General Rules --- Structural Fire Design*, British Standards Institution, London, UK.
- EN 1993-1-2 (2005). *Eurocode 3: Design of Steel Structures --- Part 1-2: General Rules --- Structural Fire Design*, British Standards Institution, London, UK.
- fib. (2000). *Bond of Reinforcement in Concrete: State-of-the Art Report*, fib Bulletin 10, Lausanne, Switzerland.
- fib. (2007). *Fire Design of Concrete Structures --- Materials, Structures and Modelling*, fib Bulletin 38, Lausanne, Switzerland.
- FIP/CEB (2004). *FIP/CEB Report on Methods of Assessment of the Fire Resistance of Concrete Structural Members*, Cement and Concrete Association, Slough. UK.

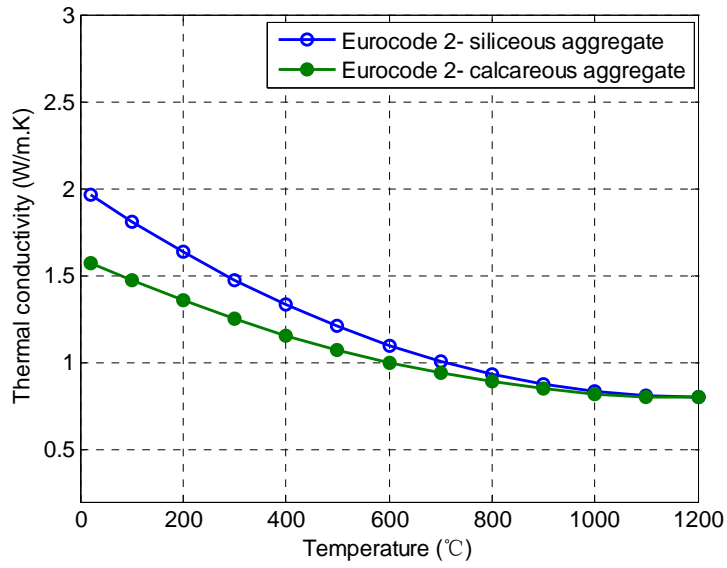
- Gilbert, R.I. and Warner, R.F. (1978). "Tension stiffening in reinforced concrete slabs." *Journal of the Structural Division*, ASCE, Vol. 104, No. 12, pp. 1885-1900.
- Grosshandler, W. (2002). *Proceedings of Fire Resistance Determination and Performance Prediction Research Needs Workshop*, NISTIR 6890, National Institute of Standards and Technology, Gaithersburg, MD, America.
- Haddad, R.H., Al-Saleh, R.J. and Al-Akhras, N.M. (2008). "Effect of elevated temperature on bond between reinforcing steel and fiber reinforced concrete." *Fire Safety Journal*, Vol. 43, No. 6, pp. 334-343.
- Han, L.H., Zheng, Y.Q., and Teng, J.G. (2006). "Fire resistance of RC and FRP-confined RC columns." *Magazine of Concrete Research*, Vol. 58, No. 8, pp. 533-546.
- Hillerborg, A., Modeer, M. and Petersson, P.E. (1976). "Analysis of crack formation and crack growth in concrete by means of fracture mechanics and finite elements." *Cement and Concrete Research*, Vol. 6, No. 6, pp. 773-782.
- Huang, Z.F., Tan, K.H., Toh, W.S. and Phng, G.H. (2008). "Fire resistance of composite columns with embedded I-section steel --- effects of section size and load level." *Journal of Constructional Steel Research*, Vol. 64, No. 3, pp. 312-325.
- Huang, Z.H. (2010). "Modelling the bond between concrete and reinforcing steel in a fire." *Engineering Structures*, Vol. 32, No. 11, pp. 3660-3669.
- Huang, Z.H. and Platten, A. (1997). "Nonlinear finite element analysis of planar reinforced concrete members subjected to fires." *ACI Structural Journal*, Vol. 94, No. 3, pp. 272-282.
- Huang, Z.H., Burgess, I.W. and Plank, R.J. (2009). "Three-dimensional analysis of reinforced concrete beam-column structures in fire." *Journal of Structural Engineering*, ASCE, Vol. 135, No. 10, pp. 1201-1212.
- Hu, K.X. (1989). "Researches on the bond-slip behaviour between concrete and steel bar at elevated temperatures and the fire resistance of reinforced concrete portal frames." MSc thesis, Tongji University, China.
- ISO 834-1 (1999). *Fire Resistance Tests --- Elements of Building Construction --- Part 1: General Requirement*. International Organization for Standardization, Geneva, Switzerland.
- Khennane, A. and Baker, G. (1992). "Plasticity models for the biaxial behaviour of concrete at elevated temperatures, Part I: Failure criterion." *Computer Methods in Applied Mechanics and Engineering*, Vol. 100, No. 2, pp. 207-223.

- Khoury, G.A. (2000). "Effect of fire on concrete and concrete structures." *Progress in Structural Engineering and Materials*, Vol. 2, No. 4, pp. 429-447.
- Khoury, G.A., Grainger, B.N. and Sullivan, P.J.E. (1985). "Transient thermal strain of concrete: literature review, conditions within specimens and behaviour of individual constituents." *Magazine of Concrete Research*, Vol. 37, No. 132, pp. 131-144.
- Ko, J., Noguchi, T. and Ryu, D. (2011). "The spalling mechanism of high-strength concrete under fire." *Magazine of Concrete Research*, Vol. 63, No. 5, pp. 357-370.
- Kodur, V.K.R. and Dwaikat, M.B. (2007). "Performance-based fire safety design of reinforced concrete beams." *Journal of Fire Protection Engineering*, Vol. 17, No. 4, pp. 293-320.
- Kodur, V.K.R. and Dwaikat, M.B. (2008). "A numerical model for predicting the fire resistance of reinforced concrete beams." *Cement and Concrete Composites*, Vol. 30, No. 5, pp. 431-443.
- Kodur, V.K.R., Dwaikat, M.M.S. and Dwaikat, M.B. (2008). "High-temperature properties of concrete for fire resistance modelling of structures." *ACI Material Journal*, Vol. 105, No. 5, pp. 517-527.
- Kodur, V.K.R., Dwaikat, M.M.S. and Raut, N. (2009). "Macroscopic FE model for tracing the fire response of reinforced concrete structures." *Engineering Structures*, Vol. 31, No. 10, pp. 2368-2379.
- Kordina, K., Ehm, C. and Schneider, U. (1985). "Effect of biaxial loading on the high temperature behaviour of concrete." *Proceeding of the First International Symposium on Fire Safety Science*, Gaithersburg, MD, pp. 281-290.
- Lee, J. and Fenves, G. (1998). "Plastic damage model for cyclic loading of concrete structures." *Journal of Engineering Mechanics*, ASCE, Vol. 124, No. 8, pp. 892-900.
- Li, B., Tran, C.T.N. and Pan, T-C. (2009). "Experimental and numerical investigation on the seismic behaviour of lightly reinforced concrete beam-column joints." *Journal of Structural Engineering*, ASCE, Vol. 135, No. 9, pp. 1007-1018.
- Li, G.F., Li, G.Q., Li, X.G., Pang, S.S., and Jones, R. (2008). "Experimental study of FRP tube encased concrete cylinders exposed to fire." *Composite Structures*, Vol. 85, No. 2, pp. 149-154.
- Lin, T.D., Gustaferro, A.H. and Abrams, M.S. (1981). *Fire Endurance of Continuous Reinforced Concrete Beams.* RD 072.01B, Research and Development Bulletin, Portland Cement Association, America.

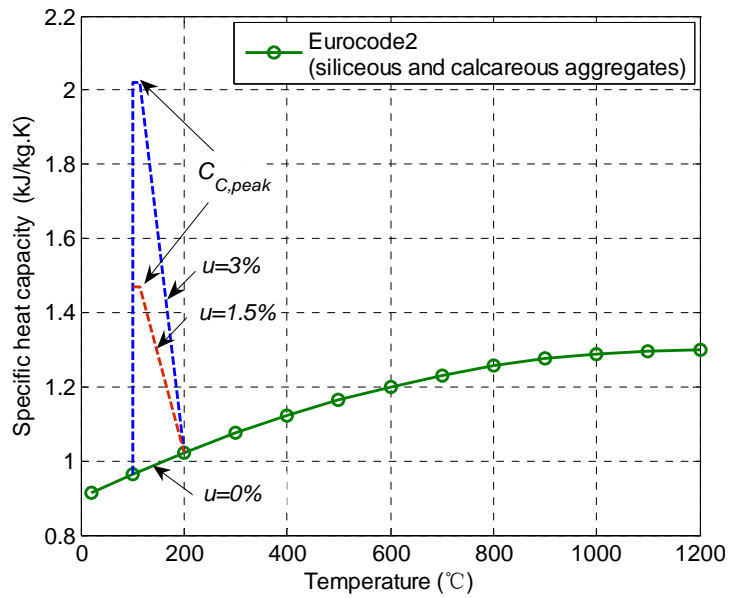
- Lublinter, J., Oliver, J., Oller, S. and Onate, E. (1989). "A plastic-damage model for concrete." *International Journal of Solids and Structures*, Vol. 25, No. 3, pp. 299-326.
- Marechal, J.C. (1972). "Variations of the modulus of elasticity and Poisson's ratio with temperature." *Concrete for Nuclear Reactors*, ACI SP-34, Vol.1, pp.495-503.
- McGrattan, K., McDermott, R., Hostikka, S. and Floyd, J. (2010). *Fire Dynamics Simulator (Version 5)*. NIST Special Publication 1019-5, National Institute of Standards and Technology, Gaithersburg, MD, America.
- Milovanov, A.F. and Salmanov, G.D. (1954). "The influence of high temperature upon the properties of reinforcing steels and bond strength between reinforcement and concrete." *Issledovanija Po Zharoupornym Betonu I Zhelezobetonu*, pp. 203-223.
- Morley, P.D. and Royles, R. (1983). "Response of the bond in reinforced concrete to high temperature." *Magazine of Concrete Research*, Vol. 35, No. 123, pp. 67-74.
- Nechnech, W., Meftah, F., and Reynouard, J.M. (2002). "An elasto-plastic damage model for plain concrete subjected to high temperatures." *Engineering Structures*, Vol. 24, No. 5, pp. 597-611.
- Ngo, D. and Scordelis, A.C. (1967). "Finite element analysis of reinforced concrete beams." *ACI Journal*, Vol. 67, No. 3, pp.152-163.
- Nielsen, C.V. and Bicanic, N. (2003). "Residual fracture energy of high-performance and normal concrete subjected to high temperatures." *Materials and Structures*, Vol. 36, No. 262, pp. 515-521.
- Ogura, N., Bolander, J.E. and Ichinose, T. (2008). "Analysis of bond splitting failure of deformed bars within structural concrete." *Engineering Structures*, Vol. 30, No. 2, pp. 428-435.
- Peacock, R., Jones, W.W., Reneke, P.A. and Forney, G.P. (2008). *CFAST --- Consolidated Model of Fire Frowth and Smoke Transport (Version 6)*. NIST Special Publication 1041, National Institute of Standards and Technology, Gaithersburg, MD, America.
- Pearce, C. J., Kukla, K. and Bicanic, N. (2006). "Modelling of transport processes in concrete at elevated temperatures --- an alternative formulation for sorption isotherms." *EURO-C 2006 --- Computational Modelling of Concrete Structures*, Mayrhofen, Tirol, Austria, pp. 623-632.
- Pothisiri, T. and Panedpojaman, P. (2012). "Modeling of bonding between steel rebar and concrete at elevated temperatures." *Construction and Building Materials*, Vol. 27, No. 1, pp. 130-140.

- Pulmano, A.V. and Shin, S.Y. (1987). "Simplified finite-element analysis of deflections of reinforced concrete beams." *ACI Structural Journal*, Vol. 84, No. 4, pp. 342-348.
- Purkiss, J.A. (2007). *Fire Safety Engineering Design of Structures*, 2nd Edition, Oxford, Butterworth-Heinemann, England.
- Purkiss, J.A., Claridge, S.L. and Durkin, P.S. (1989). "Calibration of simple methods of calculating the fire safety of flexural reinforced concrete members." *Fire Safety Journal*, Vol. 15, No. 3, pp. 245-263.
- Rafi, M.M., Nadjai, A. and Ali, F. (2008). "Finite element modelling of carbon fiber-reinforced polymer reinforced concrete beams under elevated temperatures." *ACI Structural Journal*, Vol. 105, No. 6, pp. 701-710.
- Reichel, V. (1978). "How fire affects steel-to-concrete bond." *Building Research and Practice*, Vol. 6, No. 3, pp. 176-186.
- Riva, P. and Franssen, J.M. (2008). "Non-linear and plastic analysis of RC beams subjected to fire." *Structural Concrete*, Vol. 9, No. 1, pp. 30-43.
- Rots, J.G. (1985). "Bond-slip simulation using smeared cracks and/or interface element." Research Report 85.01, Structural Mechanics Group, Department of Civil Engineering, Delft University of Technology, The Netherlands.
- Rots, J.G. (2002). "Comparative study of crack models." *Proceedings of the Third DIANA World Conference*, M.A.N. Hendriks and J.G. Rots, eds., Tokyo, Japan, pp. 17-28.
- Scanlon, A. and Murray, D. (1974). "Time-dependent reinforced concrete slab deflections." *Journal of the Structural Division*, ASCE, Vol. 100, No. 9, pp. 1911-1924.
- Schafer, H. (1975). "A contribution to the solution of contact problems with the aid of bond elements." *Computer Methods in Applied Mechanics and Engineering*, Vol. 6, No. 3, pp.335-353.
- Schneider, U. (1986). *Properties of Materials at High Temperatures --- Concrete*, 2nd Edition, RILEM --- Technical Committee 44-PHT, Technical University of Kassel, Kassel.
- Schweizerhof, K. (1993). "Consistent concept for line search algorithms in combination with arc-length constraints." *Communications Numerical Methods in Engineering*, Vol. 9, No. 9, pp. 773-784.
- Tang, W.C. and Lo, T.Y. (2009). "Mechanical and fracture properties of normal and high strength concretes with fly ash after exposure to high temperatures." *Magazine of Concrete Research*, Vol. 61, No. 5, pp. 323-330.

- The Institution of Structural Engineers. (2003). *Introduction to the Fire Safety Engineering of Structures*, Institution of Structural Engineers, London.
- The Institution of Structural Engineers. (2007). *Guide to the Advanced Fire Safety Engineering of Structures*, Institution Of Structural Engineers, London.
- Wu, B. and Lu, J.Z. (2009). "A numerical study of the behaviour of restrained RC beams at elevated temperatures." *Fire Safety Journal*, Vol. 44, No. 4, pp. 522-531.
- Wu, H.J., Lie, T.T. and Hu, J.Y. (1993). "Fire resistance of beam-slab specimens --- experimental studies." Internal Report No. 641, Institute for Research in Construction, National Research Council Canada, Canada.
- Zhang, B. and Bicanic, N. (2000). "Residual fracture properties of normal- and high-strength concrete subject to elevated temperatures." *Magazine of Concrete Research*, Vol. 52, No. 2, pp. 123-136.
- Zhang, B. and Bicanic, N. (2006). "Fracture energy of high-performance concrete at high temperature up to 450 °C: the effects of heating temperatures and testing conditions (hot and cold)." *Magazine of Concrete Research*, Vol. 58, No. 5, pp. 277-288.

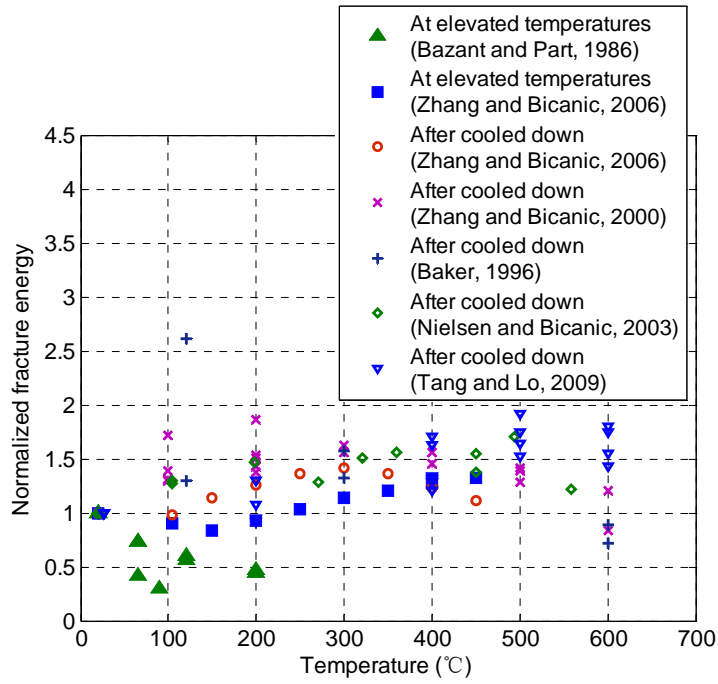


(a) Thermal conductivity

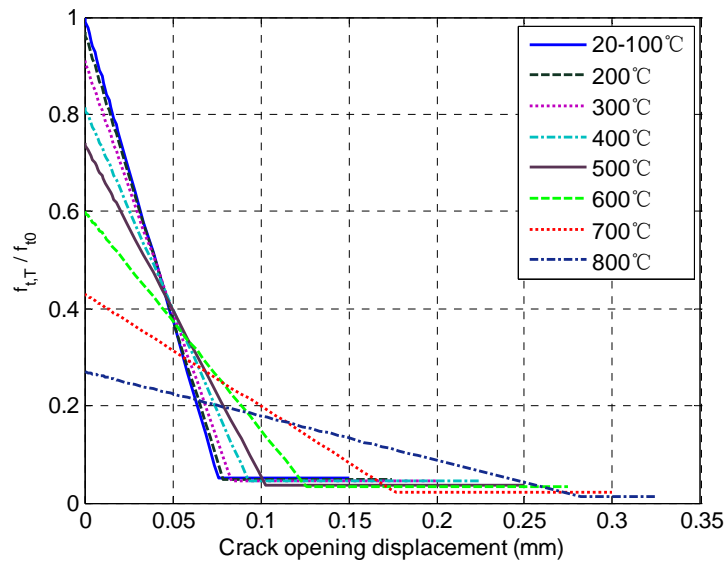


(b) Specific heat capacity

**Fig. 6.1** Thermal properties of concrete at elevated temperatures.



(a) Normalized fracture energy



(b) Tensile stress-crack opening displacement curves

**Fig. 6.2** Tensile behavior of concrete at elevated temperatures.

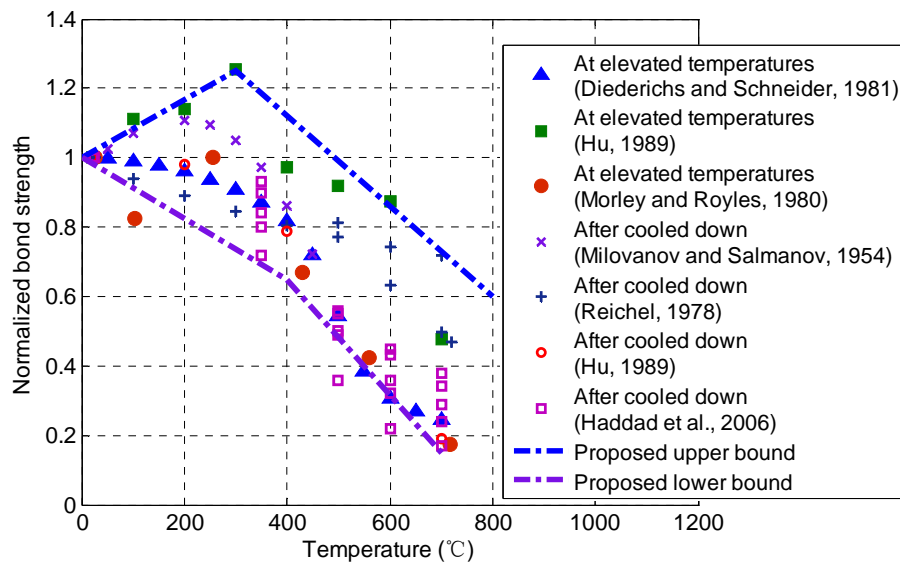
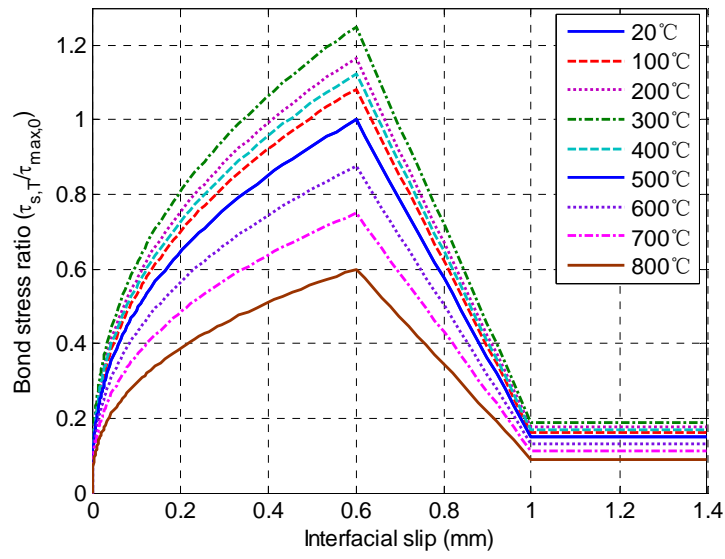
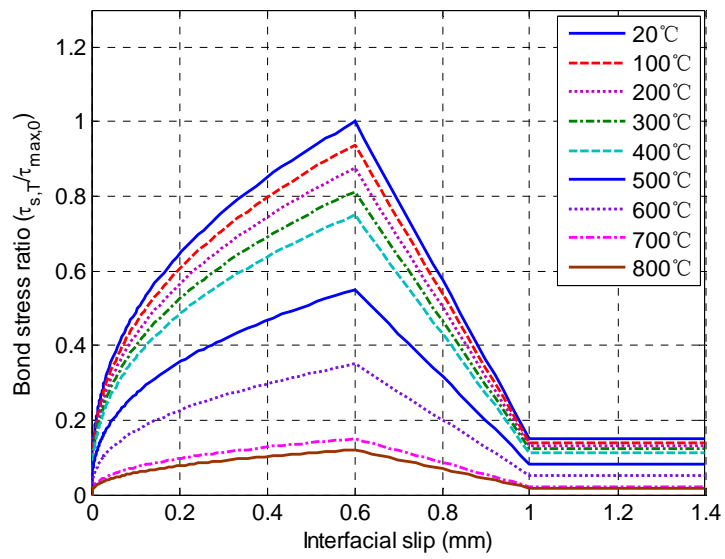


**Fig. 6.3** Normalized bond strength and proposed upper and low bounds.

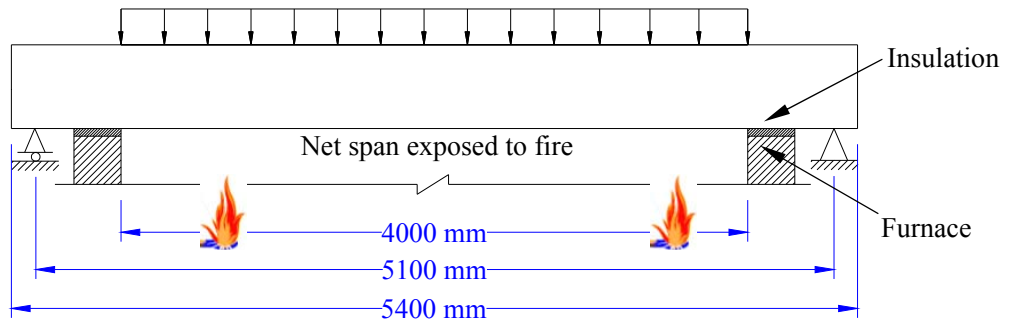


(a) Upper-bound model

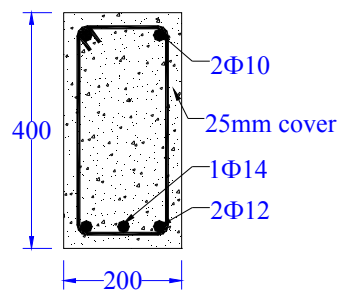


(b) Lower-bound model

**Fig. 6.4** Proposed local bond stress-slip curves at elevated temperatures.

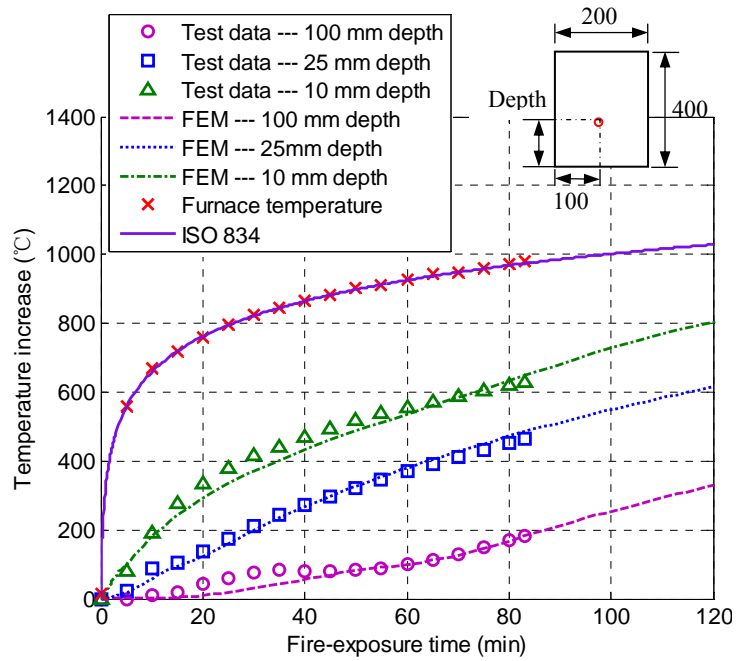


(a) Elevation

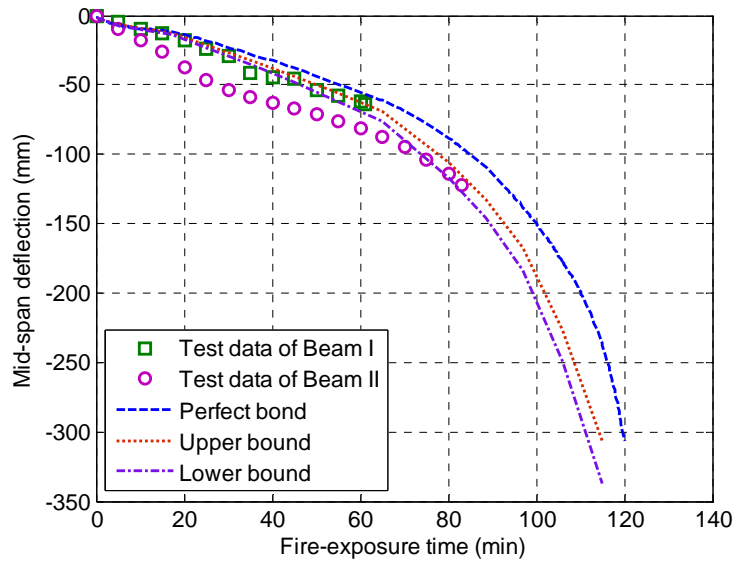


(b) Cross-section

**Fig. 6.5** Details of specimens (200 mm × 400 mm × 5400 mm).

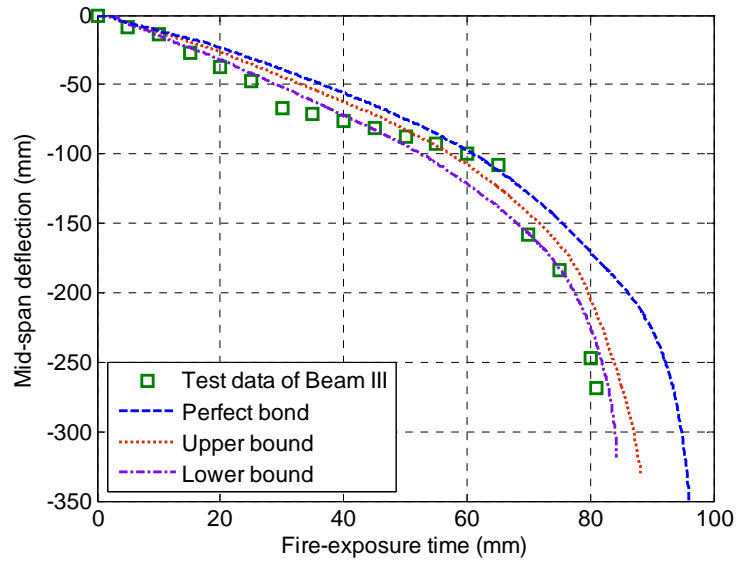


(a) Predicted and measured temperatures at various locations



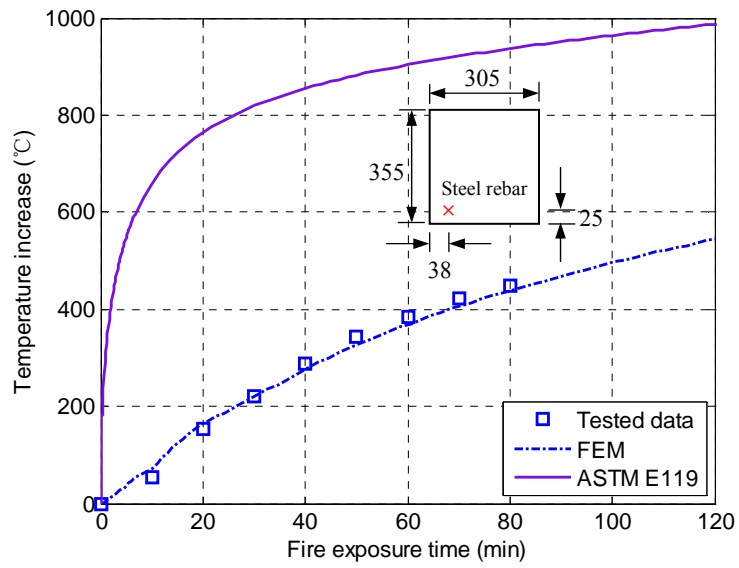
(b) Predicted and measured mid-span deflections of Beams I and II

**Fig. 6.6** Comparisons of the RC beams tested by Wu et al. (1993).

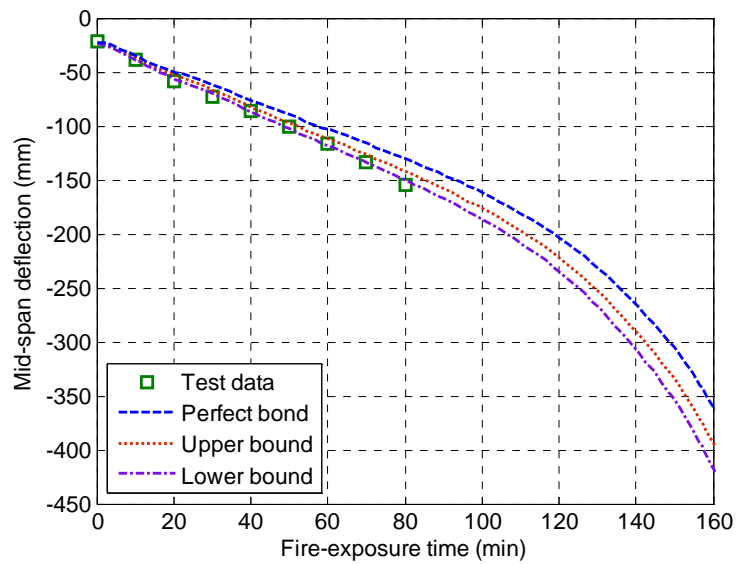


(c) Predicted and measured mid-span deflections of Beams III

**Fig. 6.6** Comparisons of the RC beams tested by Wu et al. (1993) (Cont'd).

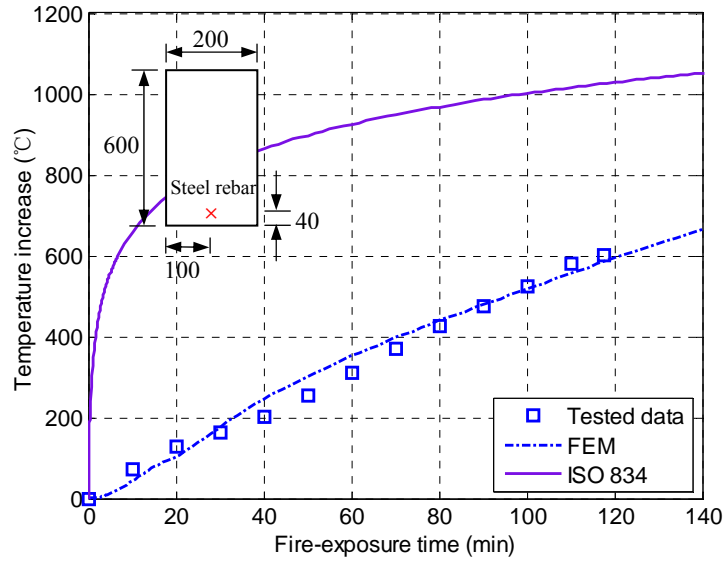


(a) Predicted and measured rebar temperatures

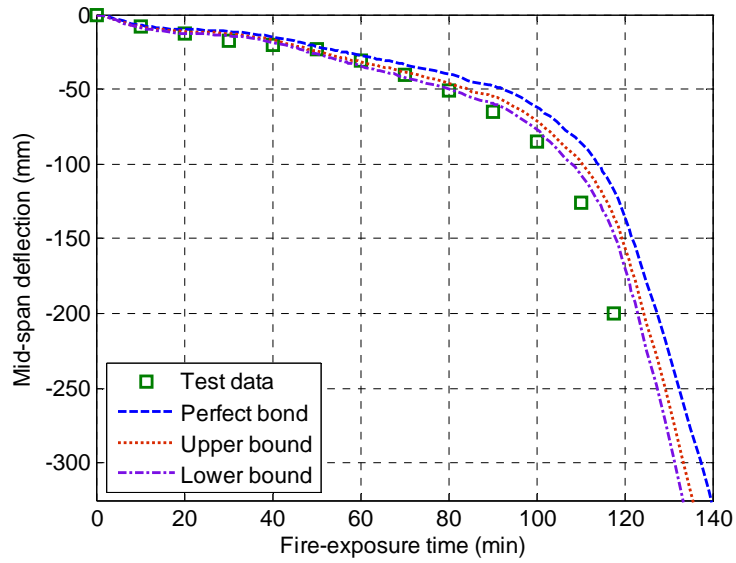


(b) Predicted and measured mid-span deflections

**Fig. 6.7** Comparisons of the RC beam tested by Lin et al. (1981).

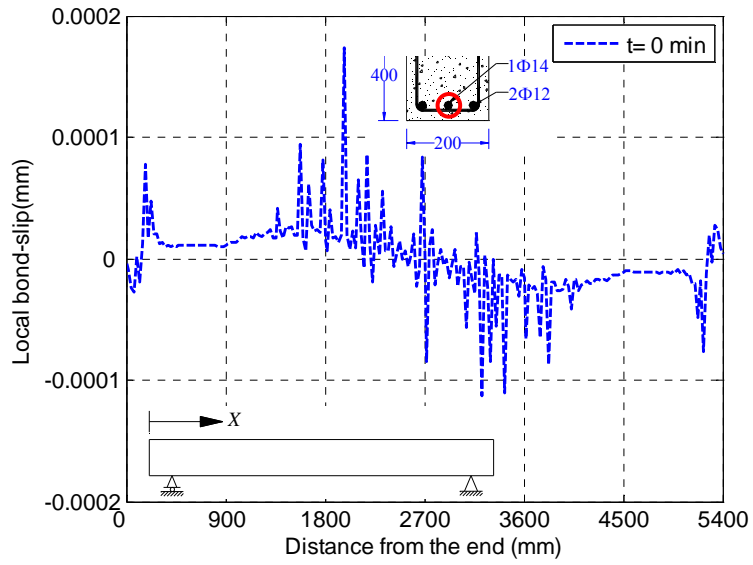


(a) Predicted and measured rebar temperatures

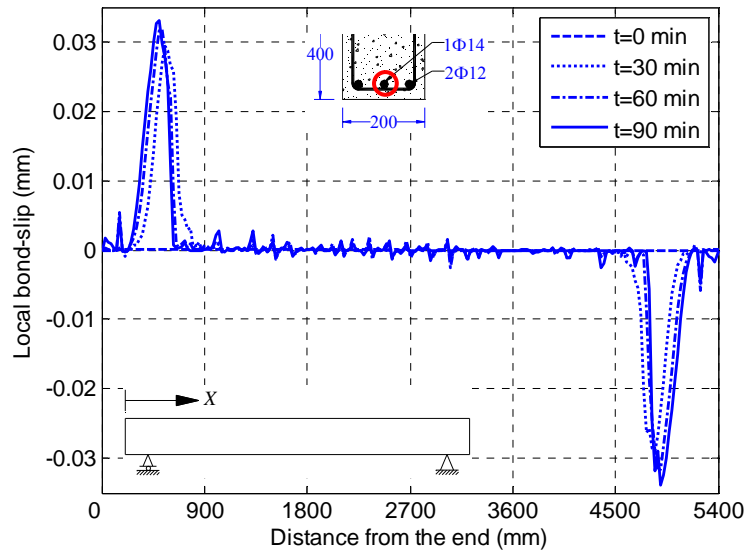


(b) Predicted and measured mid-span deflections

**Fig. 6.8** Comparisons of the simply supported RC beam tested by Dotreppe and Franssen (1985).

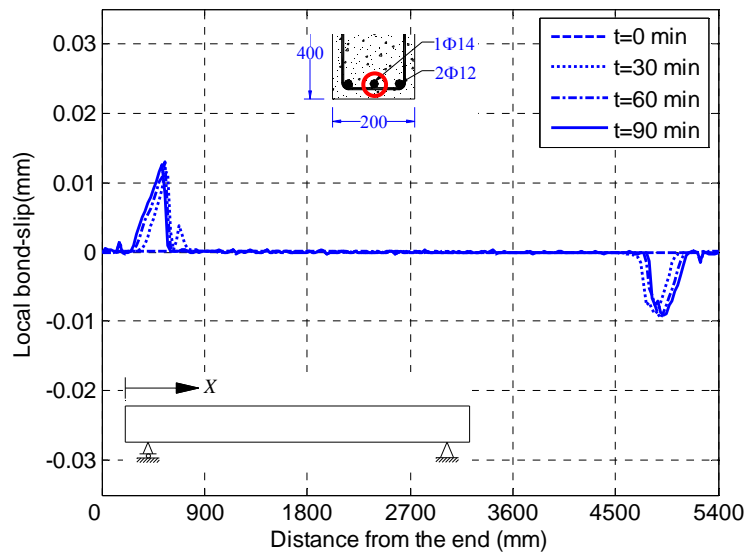


(a)  $t = 0$  min.



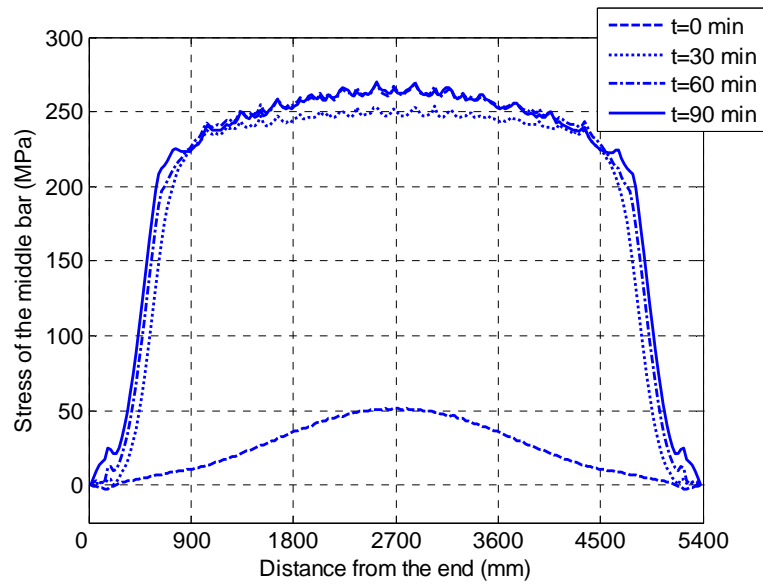
(b)  $t = 0, 30, 60$  and  $90$  min with the lower-bound bond condition.

**Fig. 6.9** Slip along the steel bar-to-concrete interface.

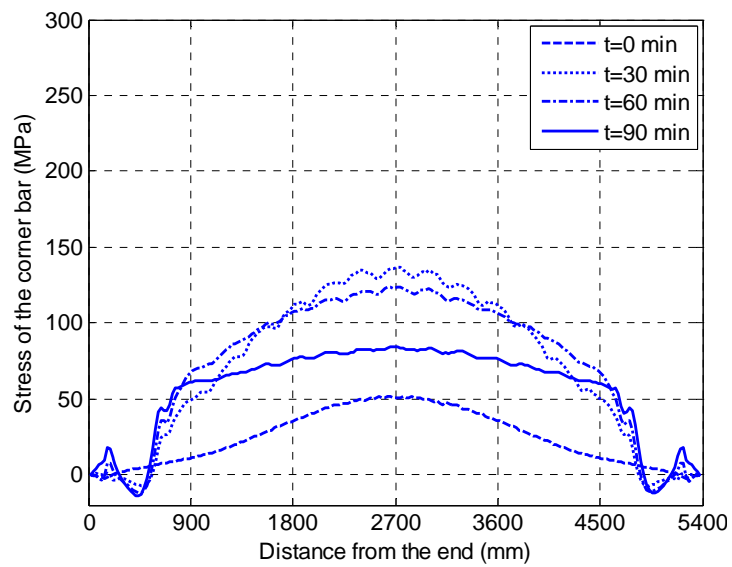


(c)  $t = 0, 30, 60$  and  $90$  min with the upper-bound bond condition.

**Fig. 6.9** Slip along the steel bar-to-concrete interface (Cont'd).

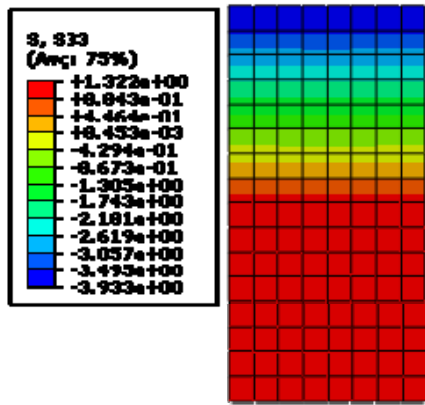


(a) Middle bar

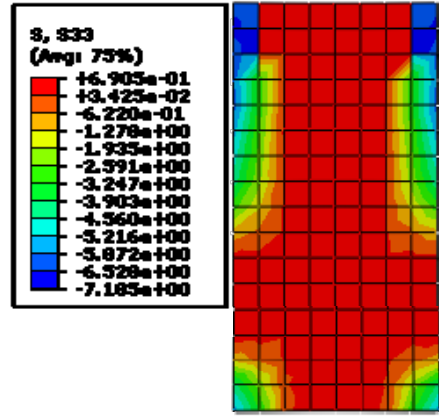


(b) Corner bar

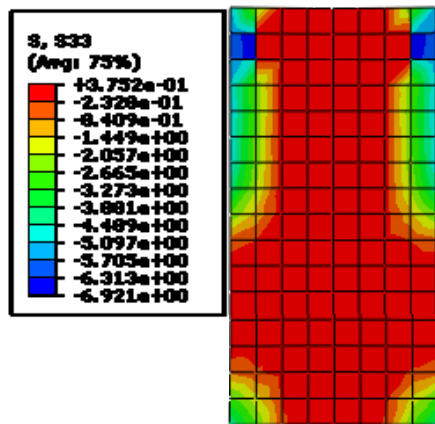
**Fig. 6.10** Steel stress distributions in the longitudinal direction.



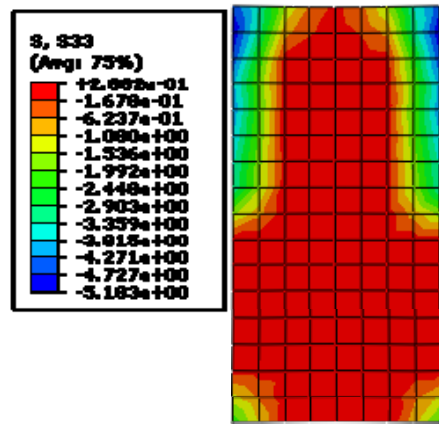
(a)  $t = 0$  min



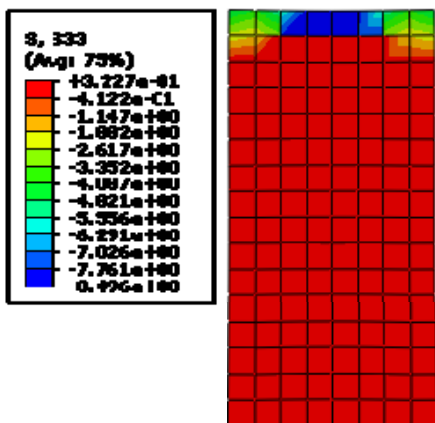
(b)  $t = 30$  min



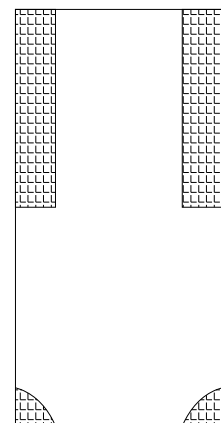
(c)  $t = 60$  min



(d)  $t = 90$  min

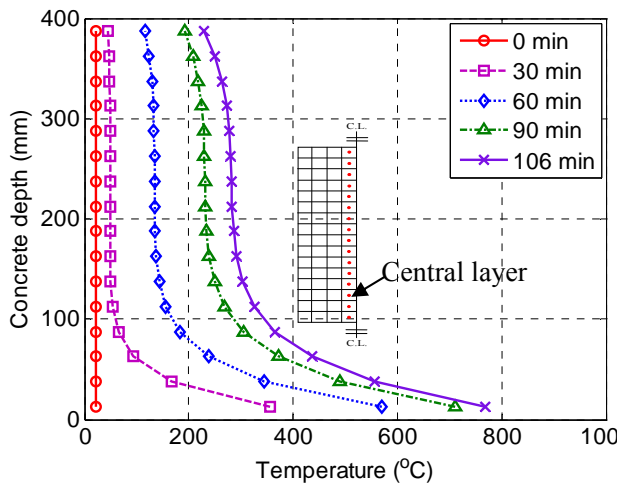


(e)  $t = 106$  min

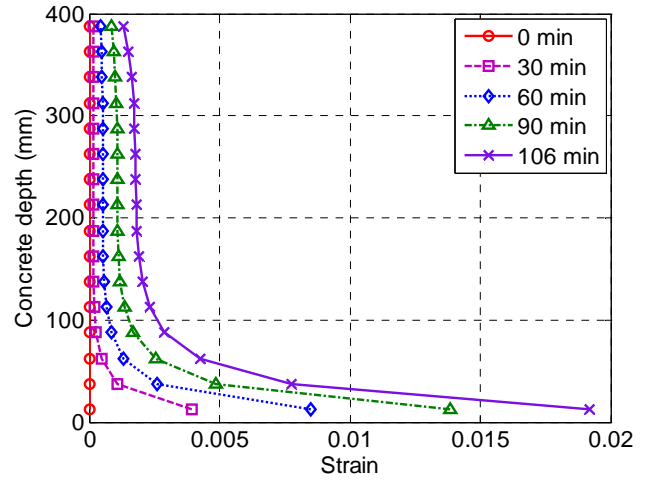


(f) Concrete spalling zones

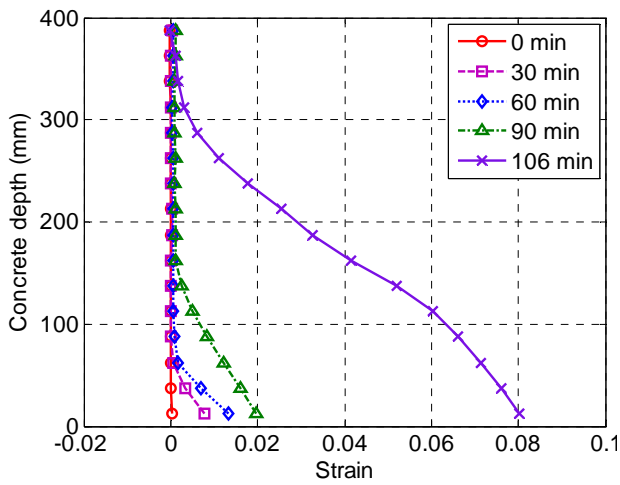
Fig. 6.11 Stress distributions over the mid-span cross-section.



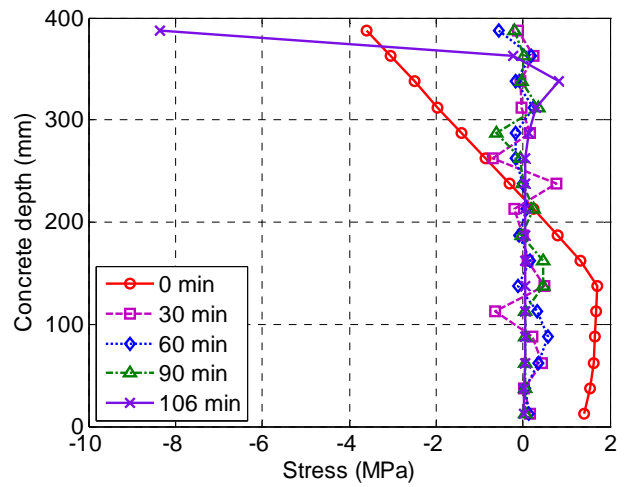
(a) Temperature distributions



(b) Thermal strain distributions

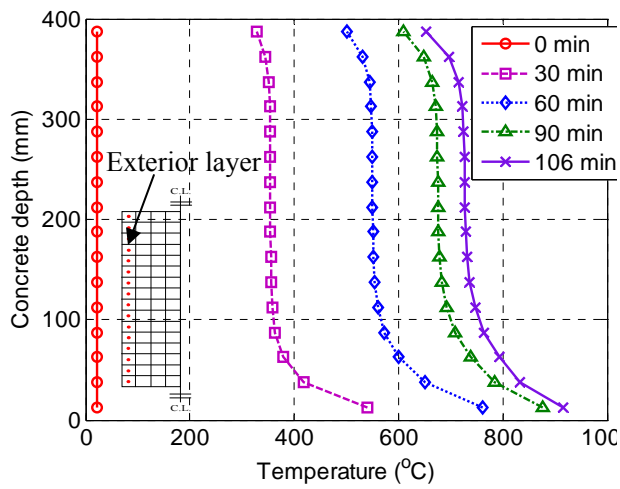


(c) Total strain distributions

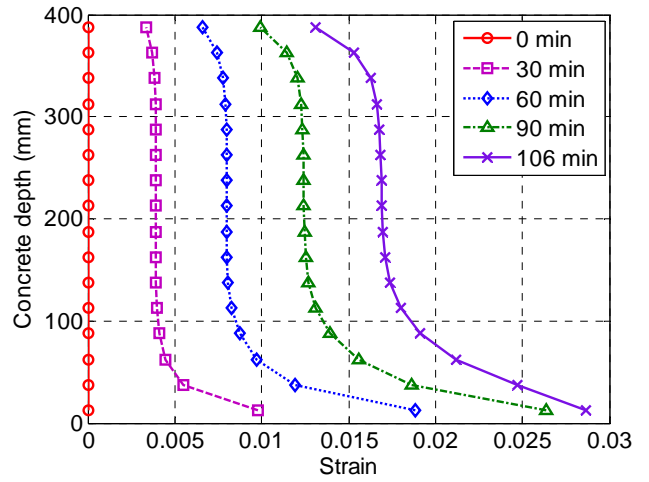


(d) Stress distributions

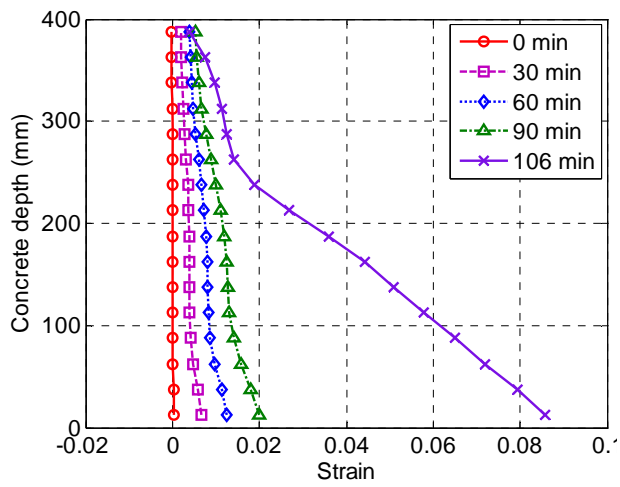
**Fig. 6.12** Evolutions of temperatures, strains and stresses over central layer at mid-span.



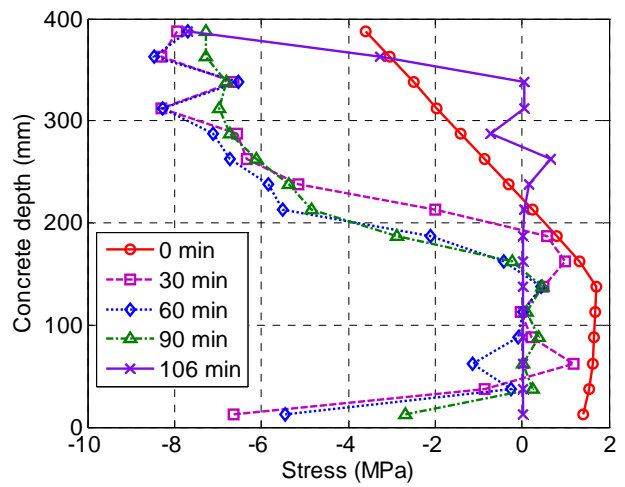
(a) Temperature distributions



(b) Thermal strain distributions



(c) Total strain distributions



(d) Stress distributions

**Fig. 6.13** Evolutions of temperatures, strains and stresses over exterior layer at mid-span.

## CHAPTER 7

# FE MODELING OF INSULATED FRP-STRENGTHENED RC BEAMS EXPOSED TO FIRE

### 7.1 INTRODUCTION

FRP laminates exhibit a poor performance at elevated temperatures, and therefore, a layer of insulation material is often adopted to protect the bonded FRP reinforcement as well as the original RC member for obtaining the required fire resistance. A direct approach for accessing the fire performance of insulated FRP-strengthened RC members is to conduct standard fire tests (e.g., Blontrock et al. 2000; Blontrock 2003; Bisby 2003; Williams 2004; Bisby et al. 2005; Kodur et al. 2006; Chowdhury et al. 2007; Williams et al. 2008; Wu and Wan 2009; Gao et al. 2010; Ahmed 2010; Ahmed and Kodur 2011a; Adelzadeh et al. 2012). However, the available fire test data are limited and far from being sufficient to generate a generic and quantitative guideline for the insulation scheme design of FRP-strengthened RC beams. Considering the high cost and the significant difficulty of fire tests, it is pursued to conduct advanced numerical simulations to supplement fire test results for the development of design guidelines.

In most of existing numerical simulations, both the externally bonded FRP laminate and the internal steel reinforcement were assumed to be perfectly bonded with the concrete (e.g., Liu et al. 2009; Hawileh et al. 2009; Kodur and Ahmed 2010). The bond degradation of FRP-to-concrete interfaces due to elevated temperatures is no longer a concern if the bonded FRP laminate is so well protected during a fire that the temperature at the FRP-to-concrete interface is kept below the critical temperature (s) of the polymer(s) forming the FRP strengthening system. However, to realize such a “full” protection of FRP laminates, a thick insulation layer is usually needed, which greatly compromises the advantages of the FRP strengthening technique in terms of ease of installation and minimal alterations of structural dimensions. Therefore, a more practical solution is to employ a relatively thin fire

protection layer which is aimed at preventing flame spread and smoke generation of the FRP laminate as well as ensuring the retention of adequate structural resistance during a fire. The latter requirement generally means that the structural resistance offered by the original RC member is retained but the structural resistance offered by the bonded FRP system can be completely or partially lost during a fire (e.g., due to the deterioration of the bonded interface between FRP and concrete).

To explore the benefits of different fire protection strategies and to develop corresponding design procedures, a reliable numerical tool for the fire performance evaluation of FRP-strengthened RC members with fire protection of various levels needs to be established. Indeed, the fire resistance analysis of insulated FRP-strengthened RC members is more challenging than that of un-protected FRP-strengthened RC members as the contribution of FRP in the latter case can simply be ignored [e.g., Han et al. (2006)]. This chapter presents a generic and advanced FE model to accurately simulate the thermal and structural behaviour of insulated FRP-strengthened RC beams exposed to fire. The FE model takes into account the bond behaviour between the concrete and both the internal steel and the external FRP reinforcements using interfacial elements with appropriate temperature-dependent bond-slip properties. Furthermore, the mechanical properties of FRP sheets at elevated temperatures are also properly considered. Predictions from the FE model of a number of FRP-strengthened RC test beams with different fire insulation configurations are then compared with test results to demonstrate the reliability of the FE model. Finally, a parametric study conducted using the verified FE model is presented to identify issues important for the future development of fire resistance design approaches for insulated FRP-strengthened RC beams.

## **7.2 CONSTITUTIVE MODELS**

### ***7.2.1 General***

The thermal and mechanical responses of FRP-strengthened RC beams exposed to fire depend strongly on the material properties of concrete, steel and FRP as well as their interfaces. Extensive studies conducted over the past few decades have led to a good understanding of the thermal and mechanical properties of concrete and steel at

elevated temperatures, and this information is now widely available (ASCE 1992; EN 1992-1-2 2004; Kodur et al. 2008). By contrast, there exists limited information on the thermal and mechanical properties of FRP laminates at elevated temperatures. Furthermore, there is little information on the degradations of interfaces between the concrete and both the internal steel reinforcement and the external FRP laminate at elevated temperatures, but this information is essential for accurate numerical simulation of FRP-strengthened RC members exposed to fire. In the present study, tensile test data of FRP coupons were collected from the published literature to develop temperature-dependent material models for FRP laminates. Appropriate bond-slip models for both the steel-to-concrete interface and the FRP-to-concrete interface at elevated temperatures were incorporated into the FE model based upon the work in previous chapters (i.e., Chapters 5 and 6). Detailed descriptions of all relevant constitutive models used in the present FE model are presented in the following sections.

### ***7.2.2 Concrete and reinforcing steel at elevated temperatures***

A damaged plasticity model for concrete available in ABAQUS (2008) served as the basis for the constitutive model of concrete at elevated temperatures. This model uses concepts of isotropic compressive and tensile plasticity in combination with scalar damage to describe the irreversible reduction in stiffness during the fracturing process. To define this constitutive model, the temperature-dependent elastic and inelastic parameters as well as the coefficient of thermal expansion (CTE) of concrete are needed.

The elastic modulus and Poisson's ratio are the two basic parameters to define the elastic mechanical behaviour of concrete. The inelastic response of concrete at elevated temperatures is defined by a yield surface, a plastic flow rule in combination with equivalent uniaxial stress-strain relationships of concrete under tension and compression. Concrete damage due to cracking is described by a scalar damage variable, which is defined to correspond to the softening curve using the linear damage model as explained in Chen et al. (2011). For reinforcing steel, the tensile stress-strain relationship and the CTE at elevated temperatures are determined based on EN 1992-1-2 (2004). Further details of the constitutive models for concrete

and steel at elevated temperatures can be found in Chapter 6, which presents accurate finite element simulations of conventional RC beams exposed to fire.

### ***7.2.3 FRP laminates at elevated temperatures***

Little information is available on the tensile behaviour of FRP laminates for structural strengthening applications at elevated temperatures in the published literature. Bisby (2003) collected the available test data and proposed a sigmoid function model for the strength and stiffness of FRP laminates at elevated temperatures. It should be noted that most of the test data collected by Bisby (2003) were from the tensile tests of FRP bars or tendons. Therefore, Bisby's (2003) model may not be suitable for wet lay-up FRP sheets commonly used to strengthen RC beams as such FRP sheets possess a much lower glass transition temperature than pre-fabricated FRP products. Based on the existing coupon test data (Chowdhury et al. 2008; Chowdhury et al. 2011), a sigmoid function has been proposed in Section 5.5.3 to describe the elastic modulus degradation of FRP sheets at elevated temperatures (see Fig. 5.1 for more details). This model is incorporated into the present FE model to predict the temperature-dependent elastic modulus of FRP sheets at elevated temperatures.

Fig. 7.1a shows the available coupon test data for the tensile strength of FRP sheets at elevated temperatures (Chowdhury et al. 2008; Cao et al. 2009; Cao et al. 2011; Chowdhury et al. 2011). The test data from Wang et al. (2011) for CFRP plates, and Wang et al. (2007) and Zhou (2005) for FRP bars as well as the models proposed by Bisby (2003) are also shown in the figure for comparison. In the figure, the tensile strength values of FRP composites at different temperatures are normalized by that obtained at ambient temperature. It is clearly seen that the strength of FRP sheets degrades more significantly than that of FRP bars/plates. The residual tensile strengths of FRP sheets at elevated temperatures are attributed to the strength contribution of the corresponding fibers, since at these temperatures (around 200 °C) the most strengths of fibers are reserved even though the strength of the epoxy polymers has been significantly diminished (Cao et al. 2009, 2011). Similarly, the

temperature can be normalized by the  $T_{g,p}$  value ( $^{\circ}\text{C}$ ), and a sigmoid function can be used to describe the strength degradation of FRP sheets as follows:

$$\frac{f_{pT}}{f_{p0}} = \left(\frac{1-b_1}{2}\right) \times \tanh\left(-b_2 \times \left(\frac{T}{T_{g,p}} - b_3\right)\right) + \left(\frac{1+b_1}{2}\right) \quad (7.1)$$

where  $f_{p0}$  and  $f_{pT}$  are the tensile strengths at ambient temperature and at an elevated temperature  $T$ , respectively; and  $b_1 = 0.593$ ,  $b_2 = 4.50$  and  $b_3 = 0.967$ . Fig. 7.1b shows a comparison between the predictions of Eq. (7.1) and the test results. It is seen that good agreement is achieved over the whole range of considered temperatures. For pre-fabricated FRP plates at elevated temperatures, Bisby's (2003) models are directly used in this study to describe the tensile strength and elastic modulus degradations due to the lack of test data for the value of  $T_{g,p}$  as well as the material properties of FRP plates at elevated temperatures (Wang et al. 2011).

It should be noted that the highest test temperature for the existing test data is about  $200^{\circ}\text{C}$  (Figs. 5.1b and 7.1b). While this temperature is still much lower than the decomposition temperature of the polymer matrix [denoted by  $T_d$ , which has been reported to be around  $400^{\circ}\text{C}$  (Mouritz and Gibson 2006)], the proposed models shown in Figs. 5.1b and 7.1b are believed to be sufficiently reliable for use in assessing the fire resistance of RC beams strengthened with externally bonded FRP reinforcement (i.e., bond-critical applications) since the FRP-to-concrete interface should have lost its bond capacity almost completely around this temperature. For contact-critical applications (e.g., FRP-confined concrete columns), further experimental studies may be needed to establish how the elastic modulus and the strength of FRP sheets degrade beyond  $200^{\circ}\text{C}$  so that the residual strength of columns at much higher temperatures can be accurately predicted.

A linear-elastic stress-strain relationship is adopted to describe the tensile behaviour of unidirectional FRP laminates at elevated temperatures based on the coupon test observations of Chowdhury et al. (2011) and Wang et al. (2011). The CTE of unidirectional FRP laminates in the longitudinal direction is much lower than that in the transverse direction. This is because the longitudinal properties of unidirectional

FRPs are dominated by the reinforcing fibres while their transverse properties are governed by the matrix. For example, the longitudinal CTE of unidirectional CFRP is generally close to zero (ACI 2008) and can be either negative or positive depending on the fibres used, the fibre orientation and the fibre volumetric fraction. In the present study, unidirectional FRP laminates are assumed to exhibit orthotropic thermal behaviour, and the CTE values found from fire tests are used if they are available. However, if test values are not available, the CTEs in the longitudinal and transverse directions of CFRP laminates are assumed to be  $0.3 \times 10^{-6} / ^\circ\text{C}$  and  $33 \times 10^{-6} / ^\circ\text{C}$  based on the test data of Klamer (2006).

#### ***7.2.4 Interfaces at elevated temperatures***

For insulated FRP-strengthened RC members under fire conditions, the bond behaviour of FRP-to-concrete and reinforcing steel-to-concrete interfaces becomes important. Bond degradations at both interfaces at elevated temperatures may significantly affect the cracking behaviour of concrete and the occurrence of debonding failure in insulated FRP-strengthened RC beams. However, such bond degradations have received little attention in existing FE modelling work. In the present FE model, the shear bond-slip responses of both steel-to-concrete and FRP-to-concrete interfaces at elevated temperatures are explicitly considered; a perfectly rigid contact condition is assumed for their normal direction.

For steel-to-concrete interfaces, the CEB-FIP (1993) bond-slip model is employed to describe shear interactions at ambient temperature. Reductions in bond strength and interfacial fracture energy are then incorporated into this model to reflect bond degradations at elevated temperatures. The study presented in Chapter 6 on RC beams exposed to fire has demonstrated that an FE model with appropriate modelling of the steel-to-concrete interfacial behaviour leads to more accurate predictions of deflections. Therefore, the bond-slip model given in Chapter 6 and described by the equations below [Eq. (7.2)] is also adopted in the present FE model:

$$\tau_{s,T} = \tau_{max,T} \left( \frac{s}{s_1} \right)^{0.4} \quad s \leq s_1 \quad (7.2a)$$

$$\tau_{s,T} = \tau_{max,T} \quad s_1 < s \leq s_2 \quad (7.2b)$$

$$\tau_{s,T} = \tau_{max,T} - \frac{\tau_{max,T} - \tau_{f,T}}{s_3 - s_2} (s - s_2) \quad s_2 < s \leq s_3 \quad (7.2c)$$

$$\tau_{s,T} = \tau_{f,T} \quad s > s_3 \quad (7.2d)$$

where  $\tau_{s,T}$  is the shear bond stress at temperature  $T$ ;  $s$  is the interfacial slip between reinforcing steel and concrete;  $s_1$ ,  $s_2$  and  $s_3$  are assumed to be independent of temperature and are equal to 0.6 mm, 0.6 mm, and 1.0 mm respectively;  $\tau_{max,T}$  is the peak value of shear bond stress at temperature  $T$ , which depicts bond strength degradations at elevated temperatures and is determined by the “lower-bound” trend curve in Section 6.4; and  $\tau_{f,T}$  ( $= 0.15\tau_{max,T}$ ) is the residual bond strength at large slips ( $>1.0$  mm). Fig. 7.2a shows a typical set of temperature-dependent bond-slip curves where the bond stresses at elevated temperatures are normalized by the peak bond stress at ambient temperature (i.e.,  $\tau_{max,0}$ ) for clear presentation. The properties of concrete and tensile steel reinforcement used for producing the results in this figure are those of Blontrock’s (2003) tests.

For FRP-to-concrete interfaces, Chapter 5 collected the existing double-lap shear test data of FRP-to-concrete bonded joints at elevated temperatures and developed a temperature-dependent two-parameter bond-slip model. The proposed bond-slip model was validated through comparisons with 79 shear tests on FRP-to-concrete bonded joints. Thus, this model [Eq. (7.3a)] is employed in the present FE model; the two key parameters of the model, the interfacial fracture energy  $G_f$  and the interfacial brittleness index  $B$ , are calculated from the following formulae:

$$\tau_{f,T} = 2G_{f,T}B_T(e^{-B_T\delta} - e^{-2B_T\delta}) \quad (7.3a)$$

$$\frac{G_{f,T}}{G_{f0}} = \frac{1}{2} \times \tanh\left(-c_2 \times \left(\frac{T}{T_{g,a}} - c_3\right)\right) + \frac{1}{2} \quad (7.3b)$$

$$\frac{B_T}{B_0} = \frac{(1-d_1)}{2} \times \tanh\left(-d_2 \times \left(\frac{T}{T_{g,a}} - d_3\right)\right) + \frac{(1+d_1)}{2} \quad (7.3c)$$

where  $\tau_{f,T}$  is the shear bond stress at temperature  $T$ ;  $\delta$  is the interfacial slip between FRP and concrete;  $G_{f0}$  and  $G_{f,T}$  are the interfacial fracture energies at ambient and elevated temperatures, respectively;  $B_0$  and  $B_T$  are the interfacial brittleness indices at ambient and elevated temperatures, respectively;  $T_{g,a}$  ( $^{\circ}\text{C}$ ) is the glass transition temperature of the bonding adhesive; and  $c_2= 3.21$ ,  $c_3= 1.31$ ,  $d_1= 0.485$ ,  $d_2= 14.1$  and  $d_3= 0.877$  are constants determined from least-squares regression analysis of test data. Fig. 7.2b shows a typical set of temperature-dependent bond-slip curves for FRP-to-concrete interfaces, where the properties of concrete and FRP are those of Blontrock's (2003) tests, in which an epoxy bonding adhesive with a  $T_{g,a}$  of  $62^{\circ}\text{C}$  was used. For clear comparison, the bond stresses at elevated temperatures are also normalized by the peak bond stress at ambient temperature (i.e.,  $\tau_{f,0}$ ). As explained in Section 5.3.4, the values of  $B_0$  and  $G_{f0}$  may vary over a wide range and depend mainly on the tensile strength of concrete and the properties of adhesive (Dai et al. 2005; Lu et al. 2005; Toutanji et al. 2011). For simplicity, the interfacial fracture energy  $G_{f0}$  can be estimated from Lu et al.'s (2005) model; a simple reference value of 10.4 may be used for  $B_0$  according to Dai et al. (2005) if a conventional bonding adhesive is used.

## 7.3 FINITE ELEMENT ANALYSIS

### 7.3.1 Procedure of Analysis

The FE software package ABAQUS (2008) was used to realize the proposed FE model. The temperature-dependent bond-slip models described above were implemented into ABAQUS as user-defined nonlinear spring elements and cohesive elements for steel-to-concrete and FRP-to-concrete interfaces, respectively. The constitutive models for concrete, steel and FRP were defined within the framework of the software package. The modelling of insulated FRP-strengthened RC beams exposed to fire was undertaken using a sequentially coupled thermo-mechanical procedure. This procedure means that the mechanical analysis depends on the heat transfer analysis, but no reverse dependency exists. Therefore, this procedure generally consists of two steps: (a) a heat transfer analysis to obtain the temperature

distribution in the structure; and (b) a mechanical response analysis based on the results of the heat transfer analysis.

### ***7.3.2 Heat transfer analysis***

In the heat transfer analysis of the present study, the concrete, reinforcing steel, FRP and fire insulation were modelled using eight-node continuum (DC3D8), two-node link (DC1D2), shell (DS4) and eight-node continuum (DC3D8) thermal elements, respectively. The thermal properties of concrete and steel were determined according to EN 1992-1-2 (2004). Information on the thermal conductivity, specific heat and density of FRP laminates at ambient and elevated temperatures is very limited in the existing literature. For the heat transfer analysis in the present FE model, the values suggested by Griffis et al. (1981) were adopted. For fire insulation materials, their actual thermal properties reported in the corresponding fire tests were used in the heat transfer analysis.

### ***7.3.3 Mechanical Response Analysis***

The mechanical response analysis can be divided into two stages: (a) the beam is first loaded at ambient temperature; and (b) the temperatures from the heat transfer analysis are next imposed to simulate the action of fire while the applied load is maintained until the fire limit state of the beam is reached. During the mechanical response analysis, the FE mesh was kept the same as that used in the preceding heat transfer analysis, but the thermal elements were replaced with stress elements, which were the eight-node continuum element with reduced integration (C3D8R) for concrete, the two-node link element (T3D2) for the reinforcing steel, and a shell element with reduced integration (S4R) for the FRP. The contribution of fire insulation was ignored in the mechanical response analysis. Two different types of elements available in ABAQUS may be used to describe interfacial bond-slip responses: link elements and contact elements. In this study, the three-dimensional cohesive element COH3D8 (a contact element) and the nonlinear spring element Spring 2 (a link element) were employed to implement the bond-slip relationships of FRP-to-concrete and steel-to-concrete interfaces, respectively. The spring element is simpler but was not used to represent the FRP-to-concrete interface as the significant

effect of interfacial damage cannot be described by the spring element (Chen et al. 2012). A maximum element size of 25 mm was used for the concrete in numerical modelling on the basis of a mesh convergence study conducted on RC beams exposed to fire (Chapter 6). Matching element sizes were used to represent the FRP and the reinforcing steel as well as the interfaces. Detailed description of the mechanical response analysis can be found in Section 6.5.3.

## **7.4 VALIDATION OF THE FE MODEL**

Three series of fire tests on FRP-strengthened RC beams were selected and simulated to illustrate the capability and accuracy of the proposed FE model. The first series of tests was conducted by Blontrock et al. (2000) and consists of two control RC beams tested at ambient temperature, two control RC beams tested under fire conditions, and six CFRP-strengthened RC beams tested under fire conditions; the latter six beams were strengthened with pultruded CFRP plates and protected with different fire insulation systems. The second series includes only one beam, which was tested by Gao et al. (2010) and protected with a U-shaped cladding board. The last series consists of two CFRP-strengthened RC T-beams, which were protected with two different insulation thicknesses and tested by Williams et al. (2008). These three test series were chosen because all the necessary test data needed by the FE simulations were clearly reported. Table 7.1 summarizes the geometric dimensions and reinforcement details of all these beams as well as the material properties of concrete, steel, FRP laminates and fire insulation layers. It should be noted that recently Ahmed and Kodur (2011a) also reported the fire endurance tests of five FRP-strengthened RC beams. However, the focus of these tests was on the effects of the anchorage configuration, the restraint condition and the type of fire exposure. As these aspects are beyond the scope of the present study, these five beams were not simulated in the present study.

### ***7.4.1 Blontrock et al.'s Tests***

Blontrock et al. (2000) reported in detail fire tests conducted on ten un-strengthened and FRP-strengthened RC beams. Each test beam had a total length of 3.15 m, and the fire-exposed portion of those beams in the fire furnace was 2.85 m long. All the

beams had a section of 200 mm × 300 mm, and were reinforced with two  $\phi 16$  steel tension bars and two  $\phi 12$  steel compression bars. Beam 1 (i.e., reference RC beam) and Beam 2 (i.e., reference RC beam strengthened with a CFRP plate) were statically loaded to failure at ambient temperature to determine their load-carrying capacities. Beams 3 and 4 (two identical plain RC beams) and Beams 5 to 10 (CFRP-strengthened RC beams) were tested under the ISO 834 standard fire exposure. Beams 5 to 10 were each strengthened with a 100 mm x 1.2 mm CFRP plate and were then protected with different fire insulation systems. Beam 5 was protected by gluing to its bottom surface a 25 mm thick plate of Promatect H, which is a fire resistant material with a thermal conductivity of 0.175 W/m. $^{\circ}$ C at ambient temperature. Beam 6 was protected by a U-shaped Promatect H insulation system, with a 40 mm thick layer for the bottom and a 25 mm thick layer for the two sides. Beam 7 differed from Beam 6 only in the thicknesses of the insulation layer: the bottom insulation layer was 25 mm thick and the side insulation layer was 12 mm thick. Beam 8 had the same sectional protection system as Beam 6, but the fire insulation was applied only to the anchorage zones of the CFRP plate over a length of 800 mm from each end of the fire exposed zone. Beams 9 and 10 were protected with a mechanically-fastened flat insulation system, with a 25 mm thick layer of Promatect H for Beam 9 and a 25 mm thick layer of Promatect 100 for Beam 10. Promatect 100 is also a fire resistant material, with a thermal conductivity of 0.285 W/m. $^{\circ}$ C at ambient temperature. All the ten beams were simulated using the proposed FE model, and the predictions are compared with the test data in Figs. 7.4 to 7.6. For the RC beams (i.e., Beams 3 and 4), the fire tests were terminated when the mid-span deflections increased abruptly after about 90 min fire-exposure. The insulated FRP-strengthened RC beams were not tested until failure, but the fire-exposure time of testing was at least as long as the fire resistance of the un-protected and un-strengthened RC beams (i.e., Beams 3 and 4).

Fig. 7.3 shows comparisons between the predicted and the measured load-deflection curves for the two reference beams (i.e., Beams 1 and 2). Both the predicted and the measured curves of Beam 2 feature three points at which the slope of the curve changes abruptly. These three points correspond to concrete cracking, yielding of longitudinal steel reinforcement and debonding of CFRP plate respectively.

Compared to Beam 1, Beam 2 exhibits significantly improved performance in terms of both stiffness and strength as a result of CFRP strengthening. The predicted ultimate loads of Beams 1 and 2 are 67.02 kN and 106.51 kN respectively, which are very close to the corresponding test values of 68.3 kN and 105.5 kN respectively (Blontrock et al. 2000). The excellent agreement between the FE predictions and the test data demonstrates the accuracy of the proposed FE model for ambient temperature behaviour.

In Fig. 7.4, the measured rebar temperatures and mid-span deflections of Beams 3 and 4 under the standard ISO 834 fire exposure are seen to be in close agreement with the FE predictions throughout the fire exposure period. The slight differences that appear during the later stages of fire exposure are probably due to the effect of concrete cracks on heat penetration. This effect is not considered in the proposed FE model.

Fig. 7.5 shows comparisons between the predicted and the measured temperatures and deflections for the six insulated CFRP-strengthened RC beams. For Beam 5, the glued flat insulation system fell off from the bottom surface of the beam only after 7 minutes of fire exposure; therefore, the convective and radiative thermal boundary was imposed on the surface of the fire insulation layer only for the first 7 minutes and then on the RC beam surface for the remaining fire exposure time. The measured and the predicted rebar temperatures and mid-span deflections of Beam 5 are seen to be in close agreement (Fig. 7.5a) for the entire period of fire exposure. Since the applied load ( $2 \times 40.6$  kN, i.e., two point loads with each being 40.6 kN) on Beam 5 was much higher than that (i.e.,  $2 \times 30.6$  kN) on the un-protected RC beams (Beams 3 and 4), the deflection rate of Beam 5 at early fire exposure stages was much higher than that of un-protected RC beams (Fig. 7.4).

In Figs. 7.5b-7.5d, the predicted temperatures of the steel reinforcement and the FRP-to-concrete interface are compared with the test data of the successfully protected beams (i.e., Beams 6 to 8). The FE model provides fairly accurate predictions of the test results except for some small differences at around 80-100 °C. The test results exhibit a plateau while the FE predictions do not. This temperature

plateau was possibly due to the migration of moisture from the insulation material to the surface of the CFRP due to the better moisture-resistance of the latter, which led to moisture accumulation on the CFRP surface. As a result, the heat absorbed from the fire allowed the evaporation of moisture over there, which was an energy absorption process and caused the temperature plateau. Once the moisture was fully evaporated, the measured temperature increased quickly. Such moisture evaporation and migration mechanisms cannot be captured by the heat transfer analysis of the proposed FE model. However, it is believed that ignoring the temperature plateau has a marginal effect on the evaluation of fire resistance because the plateau occurs only at temperatures of around 100 °C.

In Figs. 7.5b to 7.5d, the measured mid-span deflections as a function of fire exposure time are compared with the test values for Beams 6 to 8. The agreement between the predicted and the measured values is excellent at all the stages of fire exposure. A change in trend can be identified in each of the deflection response curves (Figs. 7.5b-7.5c) at about 15-50 minutes after the commencement of fire exposure. These turning points are believed to have been caused by the gradual debonding of the CFRP laminate since the temperature at the CFRP-to-concrete interface at this time already exceeds the glass transition temperature of the bonding adhesive (i.e., 62 °C).

For Beams 9 and 10, the fire insulation layer gradually detached from the beam from around 45 minutes after the commencement of fire exposure. For this reason, only heat transfer analysis was carried out for these two beams. In Figs. 7.5e and 7.5f, the predicted temperatures of the steel reinforcement and the FRP-to-concrete interface are compared with their measured values. Within the first 40 minutes of fire exposure, the predicted temperatures of the FRP-to-concrete interface agree closely with the measured values. Afterwards, the FE predictions underestimate the measured temperatures as expected; this underestimation is due to the detachment of the fire insulation layer, which was not considered in the FE model. The same observation can be made about the temperatures of the steel reinforcement.

#### ***7.4.2 Gao et al.'s Tests***

Three full-scale rectangular RC beams strengthened with CFRP sheets were tested by Gao et al. (2010) under the ISO 834 standard fire condition to examine the effect of end anchorage configuration for the CFRP reinforcement. As the effect of end anchorage configuration is beyond the scope of this study, only Beam III which had no end anchorage is considered here. This beam, with a 200 mm × 500 mm cross section and a total length of 6.0 m, was reinforced with two 16 mm steel tension bars and two 12 mm steel compression bars. The beam was strengthened with two layers of 200 mm wide CFRP sheets with each layer having a normal thickness of 0.167 mm, and then protected with a 40 mm thick U-shaped calcium silicate cladding board system. During the fire exposure test, the temperatures of the CFRP-to-concrete interface at the mid-span and the quarter-span cross-sections of the beam were measured by thermocouples. Since the author heard cracking/popping sound at about 80 minutes after the fire initiation, the test was terminated to avoid the collapse of the beam specimen in the fire furnace; therefore, the observed ultimate mid-span deflection was less than  $L/20$ .

In Fig. 7.6a, the predicted and the measured temperatures at the mid-height of the RC beam are compared, showing close agreement. Fig. 7.6b shows that at the bottom of the beam, the predicted temperatures of the CFRP-to-concrete interface deviate significantly from the measured values after 60 to 80 minutes of fire exposure. The measured temperatures show a plateau at around 60 minutes of fire exposure and then a more rapid increase between 80 minutes and 100 minutes of fire exposure. This plateau is much more significant than those observed in Figs. 7.5b-7.5d, probably due to the different moisture contents of insulation materials. It should be noted that such a plateau does not exist in Fig. 7.6a since no FRP laminate was present between the insulation layer and the concrete substrate.

In Fig. 7.6c, the predicted and the measured mid-span deflections of the insulated CFRP-strengthened RC beam are compared, showing close agreement. Within the first 50 minutes of fire exposure, the beam maintains its stiffness. Afterwards, the deflection increases much more rapidly with the exposure time, resulting in a sharp change in slope of the deflection curve. A small change in slope is also seen at around 60 minutes of fire exposure when the temperature of the CFRP-to-concrete

interface exceeded the glass transition temperature of the bonding adhesive (i.e., 73°C). Another slope change is seen at around 75 minutes of fire exposure, when debonding of the CFRP laminate occurred. This is similar to the deflection response of Beam 6 in Blontock et al.'s (2000) test (Fig. 7.5b). Overall, the predicted deflections are slight larger than the measured values both before and after the loss of composite action between the CFRP laminate and the concrete. This is probably due to the temperature plateau phenomenon (i.e., overestimation of temperatures by the FE model) as discussed above.

### **7.4.3 William et al.'s Tests**

William et al. (2008) reported the fire tests of two T-beams strengthened with CFRP plates and protected with a sprayed fire insulation system. The fire insulation system included a plaster-based VG layer and a fire-resistant texture coating. The VG insulation layer, covering the entire beam length, was 25 mm thick for Beam I and 38 mm thick for Beam II. The fire-resistant coating had a thickness of 0.1 mm for both beams. Due to experimental errors, the imposed loading was partially lost at about 30 minutes of fire exposure, resulting in a substantial reduction in deflection [see Williams et al. (2008) for details]. Therefore, only heat transfer analysis was carried out for these two beams to validate the present FE model.

Fig. 7.7 presents the measured temperatures of the FRP-to-concrete interface, the corner rebar and the unexposed surface respectively in comparison with FE predictions. Figs. 7.7a, 7.7c and 7.7e are for Beam I, while Figs. 7.7b, 7.7d and 7.7f are for Beam II. In each diagram, measured results at several locations along the beam length are presented to provide more details of the test data. Once again, the FE model is seen to provide satisfactory predictions of the test results for the entire fire exposure period. Indeed, the temperatures predicted by the present FE model are more accurate than the FE predictions obtained by Williams et al. (2008) (Figs. 7.7a-7.7f). This improved accuracy may be attributed to the more reasonable choice of material thermal parameters as well as thermal boundary conditions for heat transfer analysis in the present FE model; this information was not reported by Williams et al. (2008).

## 7.5 FIRE RESISTANCE DESIGN OF INSULATED FRP-STRENGTHENED RC BEAMS

For RC beams strengthened with externally bonded FRP laminates, the glass transition temperature of the bonding adhesive is generally either similar to or lower than the glass transition temperature of the FRP; the former is the case if wet layup FRP sheets are used, while the latter is generally true if pre-fabricated FRP plates are used. Therefore, a conservative fire insulation approach for FRP-strengthened RC beams is to ensure that the temperature of the FRP-to-concrete interface stays below the glass transition temperature of the bonding adhesive. For such insulated beams, the structural performance deteriorates under fire exposure as a result of degradations of the following three components: the RC beam, the FRP laminate, and the bond. To achieve an in-depth understanding of the role of each component and develop a design method for the insulation system, a parametric study was conducted using the validated FE model as part of the present study.

In the parametric study, four performance scenarios of Beams 6 and 7 from Blontrock et al.'s (2000) study under fire exposure were explored, covering two different insulation layer thicknesses: (1) an un-strengthened RC beam, also approximating an un-protected FRP-strengthened RC beam; (2) an insulated un-strengthened RC beam, also approximating an insulated FRP-strengthened RC beam but with the contribution of the FRP laminate ignored; (3) an insulated FRP-strengthened RC beam with degradations of the FRP-to-concrete interface; and (4) an insulated FRP-strengthened RC beam with perfect bonding assumed for the FRP-to-concrete interface (i.e., the corresponding node pairs of FRP and concrete were tied in the FE model to eliminate any interfacial slips). The third scenario reflects the actual situation as examined in Section 7.4.1 while the other three cases represent simplifications to different degrees.

Figs. 7.8a and 7.8b show the time-deflection responses of these two beams for the four different scenarios. Overall, less stiffness degradation is seen for the insulated beams in Fig. 7.8a than that seen in Fig. 7.8b because the insulation layer of the beams in Fig. 7.9b is thinner. It is not surprising that the stiffness of the un-insulated beam degrades faster than that of the insulated beams in both Figs. 7.9a and 7.9b.

During the early stage of fire exposure (e.g., within the first 20 minutes), the deflection of the insulated FRP-strengthened RC beam is smaller than that of the insulated un-strengthened RC beam due to the contribution of the externally bonded FRP plate ( Figs. 7.8a and 7.8b). As the fire exposure time further increases, ignoring the degradation of the FRP-to-concrete interface leads to a significant underestimation of the deflection because bond degradation leads to losses of the FRP strengthening effect. When the composite action between FRP and concrete is totally lost, the deflection performance of the insulated RC beam becomes similar to that of the insulated FRP-strengthened RC beam. Therefore, during the later fire exposure stage, the absence of the FRP strengthening system has little effect on the performance of the insulated FRP-strengthened RC beam.

Fig. 7.9 present the predicted temperatures of the rebars as well as those of the bottom surface of the RC beam to examine the effect of ignoring the FRP strengthening system in heat transfer analysis for Beams 6 and 7 of Blontrock et al.'s (2000) study. The bottom surface of the RC beam coincides with the fire insulation-to-concrete interface if the existence of the FRP strengthening system is ignored, or the FRP-to-concrete interface if the existence of the FRP strengthening system is considered. It is clearly seen that the absence of the FRP strengthening system has a very small effect on the temperature response of an insulated FRP-strengthened RC beam during the entire period of fire exposure. The above comparisons indicate that, as far as the fire resistance is concerned, an insulated FRP-strengthened RC beam can be conservatively but closely represented by an insulated RC beam in practice (i.e., with the contribution of the FRP laminate ignored). This leads to a much simpler approach as there is then no need to model the complex degradation mechanism of the FRP strengthening system as well as its interface with the RC beam during a fire. This observation also means that, in the practical design of fire insulation for an FRP-strengthened RC beam, the role of an insulation layer is to protect the original RC beam rather than the FRP strengthening system itself. This fire resistance design approach is generally much more cost-effective than one that aims at keeping the temperature of the FRP-to-concrete interface or that of the FRP laminate stays below the glass transition temperature. The latter approach normally

leads to a very thick insulation layer, which compromises the attractiveness of the FRP strengthening technology.

## **7.6 CONCLUSIONS**

An advanced FE model for the fire performance simulation of insulated FRP-strengthened RC beams has been presented in this chapter. In this FE model, rational and reliable material constitutive laws for all components of the beam are included, and in particular, the responses of FRP-to-concrete and steel-to-concrete interfaces at elevated temperatures are carefully considered. The accuracy of the FE model was demonstrated by comparing its predictions for both thermal and structural responses with available test data. The validated FE model was subsequently used to examine how the degradation of the FRP-to-concrete interface affects the performance of the beam and how the FRP strengthening system enhances the fire resistance. The numerical results and discussions presented in the paper also allow the following conclusions to be drawn:

- (1) With the inclusion of a temperature-dependent bond-slip model for the FRP-to-concrete interface in the FE model, the time-dependent deflection response of insulated FRP-strengthened RC beams can be accurately predicted for the entire period of fire exposure.
- (2) It is important to account for interfacial slips between FRP and concrete, as the fire resistance of an insulated FRP-strengthened RC beam may otherwise be substantially overestimated;
- (3) For practical design purposes, the fire resistance of an insulated FRP-strengthened RC beam can be closely and conservatively approximated by that of an insulated RC beam. That is, the contribution of the FRP strengthening system to fire resistance can be ignored, which considerably simplifies the design procedure.
- (4) In most cases, the concept of protecting the RC beam rather than the FRP strengthening system leads to a more practical and cost-effective insulation

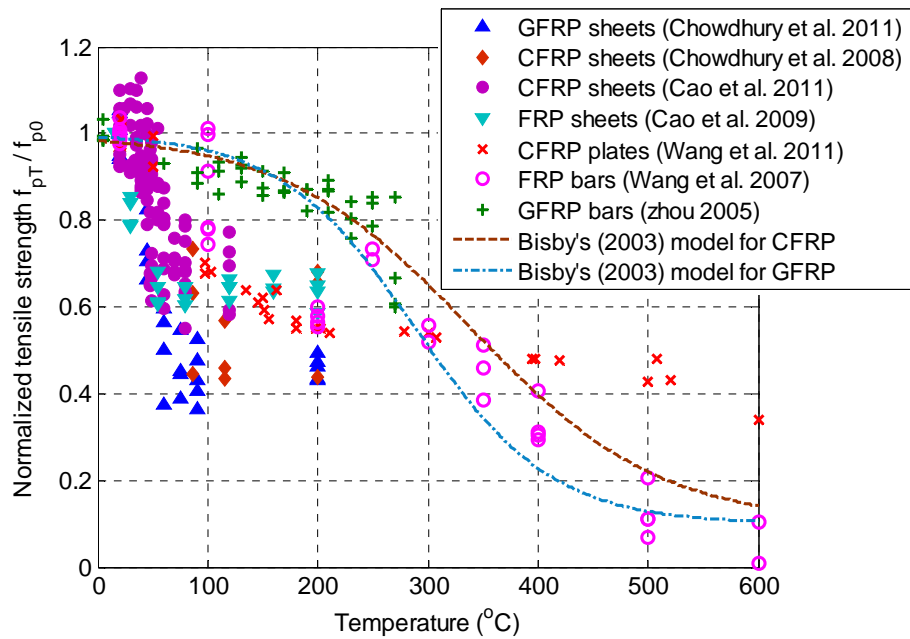
design.

## 7.7 REFERENCES

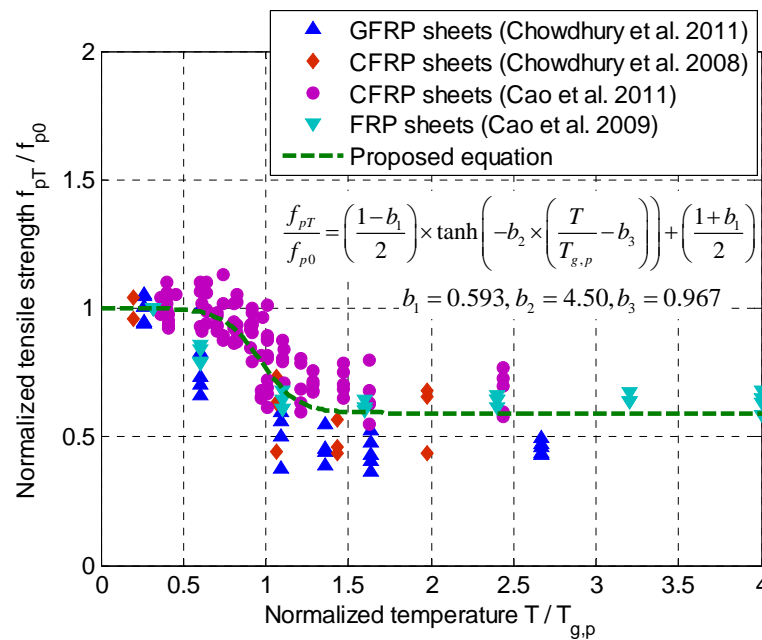
- ABAQUS. (2008). *ABAQUS Standard User's Manual*, Volumes I-III, Version 6.8. Hibbitt, Karlsson & Sorensen, Inc., Pawtucket, America.
- Adelzadeh, M., Benichou, N., and Green, M.F. (2012). "Behaviour of fibre reinforced polymer -strengthened T-beams and slabs in fire." *Proceedings of the ICE, Structures and Buildings*, Vol. 165, No. 7, pp. 361-371.
- American Concrete Institute (ACI). (2008). "Guide for the design and construction of externally bonded FRP systems for strengthening concrete structures." *ACI 440.2R-08*, Farmington Hills, Michigan, America.
- Ahmed, A. (2010). "Behavior of FRP-strengthened reinforced concrete beams under fire conditions." PhD thesis, Michigan State University, Michigan, America.
- Ahmed, A., and Kodur, V.K.R. (2011a). "The experimental behavior of FRP-strengthened RC beams subjected to design fire exposure." *Engineering Structures*, Vol. 33, No. 7, pp. 2201-2211.
- American Society of Civil Engineers (ASCE). (1992). *Structural Fire Protection*. Manuals and Reports on Engineering Practice No. 78, ASCE Committee on Fire Protection, Structural Division, American Society of Civil Engineers, New York, America.
- Bisby, L.A. (2003). "Fire behavior of fiber-reinforced polymer (FRP) reinforced or confined concrete." PhD thesis, Queen's University, Kingston, Ontario, Canada.
- Bisby, L.A., Kodur, V.K.R., and Green, M.F. (2005). "Fire endurance of Fiber-reinforced polymer- confined concrete columns." *ACI Structural Journal*, Vol. 102, No. 6, pp. 883-891.
- Blontrock, H., Taerwe, L., and Vandeveldel, P. (2000). "Fire tests on concrete beams strengthened with fiber composite laminates." *Proceeding of the Third Ph.D. Symposium in Civil Engineering*, Vienna, Austria, pp. 151-161.
- Blontrock, H. (2003). "Analysis and modeling of the fire resistance of concrete elements with externally bonded FRP reinforcement." PhD thesis, Ghent University, Ghent, Belgium.
- Cao, S.H., Wu, Z.S., and Wang, X. (2009). "Tensile properties of CFRP and hybrid FRP composites at elevated temperatures." *Journal of Composite Materials*, Vol. 43, No. 4, pp. 315-330.
- Cao, S.H., Wang, X., and Wu, Z.S. (2011). "Evaluation and prediction of temperature-dependent tensile strength of unidirectional carbon fiber-reinforced polymer composites." *Journal of Reinforced Plastics and Composites*, Vol. 30, No. 9, pp. 799-807.
- Comite Euro-International du Beton - Federation International de la Precontrainte (CEB-FIP). (1993). *CEB-FIP Model Code 90*, Thomas Telford Ltd., London.

- Chen, G.M., Teng, J.G., and Chen, J.F. (2011). "Finite-element modeling of intermediate crack debonding in FRP-plated RC beams." *Journal of Composites for Construction*, ASCE, Vol. 15, No. 3, pp. 339-353.
- Chen, G.M., Chen, J.F., and Teng, J.G. (2012). "Behaviour of FRP-to-concrete interfaces between two adjacent cracks: A numerical investigation on the effect of bondline damage", *Construction and Building Materials*, Vol. 28, No. 1, pp. 584-591.
- Chowdhury, E.U., Bisby, L.A., Green, M.F., and Kodur, V.K.R. (2007). "Investigation of insulated FRP-wrapped reinforced concrete columns in fire." *Fire Safety Journal*, Vol. 42, No. 6-7, pp. 452-460.
- Chowdhury, E.U., Eedson, R., Bisby, L.A., Green, M.F., Benichou, N., and Kodur, V.K.R. (2008). "Mechanical characterization of fibre reinforced polymers for numerical fire endurance modelling." *Proceeding of the Fifth International Conference-Structures in Fire*, Singapore, pp. 499-507.
- Chowdhury, E.U., Eedson, R., Green, M.F., Bisby, L.A., and Benichou, N. (2011). "Mechanical characterization of fiber reinforced polymers materials at high temperature." *Fire Technology*, Vol. 47, No. 4, pp. 1063-1080.
- Dai, J.G., Ueda, T., and Sato, Y. (2005). "Development of the nonlinear bond stress-slip model of fiber reinforced plastics sheet-concrete interfaces with a simple method." *Journal of Composites for Construction*, ASCE, Vol. 9, No. 1, pp. 52-62.
- EN 1992-1-2 (2004). *Eurocode 2: Design of Concrete Structures --- Part 1-2: General Rules --- Structural Fire Design*, British Standards Institution, London, UK.
- Gao, W.Y., Hu, K.X., and Lu, Z.D. (2010). "Fire resistance experiments of insulated CFRP strengthened reinforced concrete beams." *China Civil Engineering Journal*, Vol. 43, No. 3, pp. 15-23 (in Chinese).
- Griffis, C.A., Masmura, R.A., and Chang, C.I. (1981). "Thermal response of graphite epoxy composite subjected to rapid heating." *Journal of Composite Materials*, Vol. 15, No. 5, pp. 427-442.
- Han, L.H., Zheng, Y.Q., and Teng, J.G. (2006). "Fire resistance of RC and FRP-confined RC columns." *Magazine of Concrete Research*, Vol. 58, No. 8, pp. 533-546.
- Hawileh, R.A., Naser, M., Zaidan, W., and Rasheed, H.A. (2009). "Modeling of insulated CFRP-strengthened reinforced concrete T-beam exposed to fire." *Engineering Structures*, Vol. 31, No. 12, pp. 3072-3079.
- Klamer, E. (2006). "The influence of temperature on concrete structures strengthened with externally bonded CFRP." Research Report, Eindhoven University of Technology, Eindhoven, Netherlands.
- Kodur, V.K.R., Bisby, L.A., and Green, M.F. (2006). "Experimental evaluation of the fire behavior of insulated fibre-reinforced-polymer-strengthened reinforced concrete columns." *Fire Safety Journal*, Vol. 41, No. 7, pp. 547-557.

- Kodur, V.K.R., Dwaikat, M.M.S., and Dwaikat, M.B. (2008). "High-temperature properties of concrete for fire resistance modelling of structures." *ACI Material Journal*, Vol. 105, No. 5, pp. 517-527.
- Kodur, V.K.R., and Ahmed, A. (2010). "Numerical model for tracing the response of FRP-strengthened RC beams exposed to fire." *Journal of Composites for Construction*, ASCE, Vol. 14, No. 6, pp. 730-742.
- Liu, F.T., Wu, B., and Wei, D.M. (2009). "Failure modes of reinforced concrete beams strengthened with carbon fiber sheet in fire." *Fire Safety Journal*, Vol. 44, No. 7, pp. 941-950.
- Lu, X.Z., Teng, J.G., Ye, L.P., and Jiang, J.J. (2005). "Bond-slip models for FRP sheets/plates bonded to concrete." *Engineering Structures*, Vol. 27, No. 6, pp. 920-937.
- Mouritz, A. P., and Gibson, A. G. (2006). *Fire properties of polymer composite materials*, Springer, Dordrecht, Netherlands.
- Toutanji, H., Han, M. and Ghorbel, E. (2011). "Interfacial Bond Strength Characteristics of FRP and RC Substrates." *Journal of Composites for Construction*, ASCE, Vol.16, No.1, pp. 35-46.
- Wang, Y.C., Wong, P.M.H., and Kodur, V. (2007). "An experimental study of the mechanical properties of fibre reinforced polymer (FRP) and steel reinforcing bars at elevated temperatures." *Composite Structures*, Vol. 80, No. 1, pp. 131-140.
- Wang, K., Young, B., and Smith, S.T. (2011). "Mechanical properties of pultruded carbon fibre-reinforced polymer (CFRP) plates at elevated temperatures." *Engineering Structures*, Vol. 33, No. 7, pp. 2154-2161.
- Williams, B. (2004). "Fire performance of FRP-strengthened reinforced concrete flexural members." PhD thesis, Queen's University, Kingston, Ontario, Canada.
- Williams, B., Kodur, V.K.R., Green, M.F., and Bisby, L.A. (2008). "Fire endurance of fiber-reinforced polymer strengthened concrete T-beams." *ACI Structural Journal*, Vol. 105, No. 1, pp. 60-67.
- Wu, B., and Wan, Z.J. (2009). "Experimental investigation into fire resistance of reinforced concrete beams strengthened in flexure with Carbon Fiber Sheets." *Journal of South China University of Technology*, Vol.40, No.6, pp.26-41 (in Chinese).
- Zhou, C.D. (2005). "Fire performance of GFRP reinforced concrete." Research Report, Department of Civil Engineering, Tongji University, Shanghai, China (in Chinese).

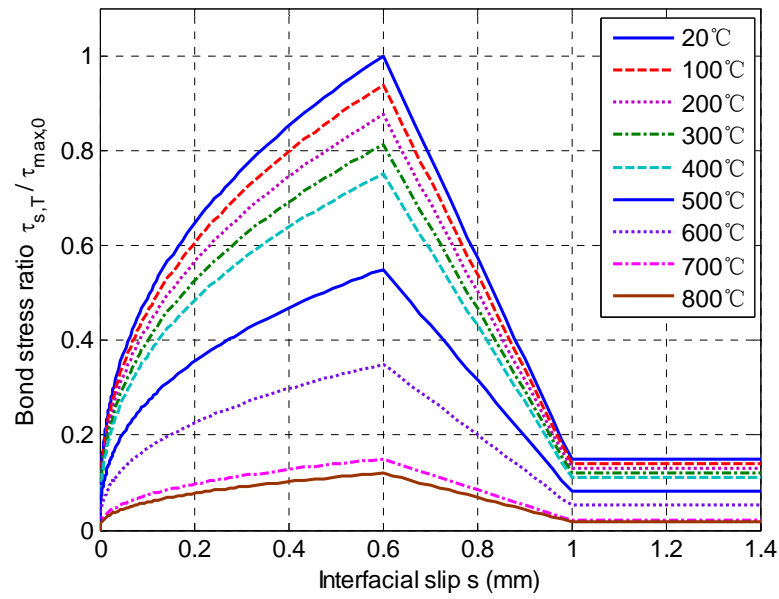


(a) Effect of temperature on normalized tensile strength

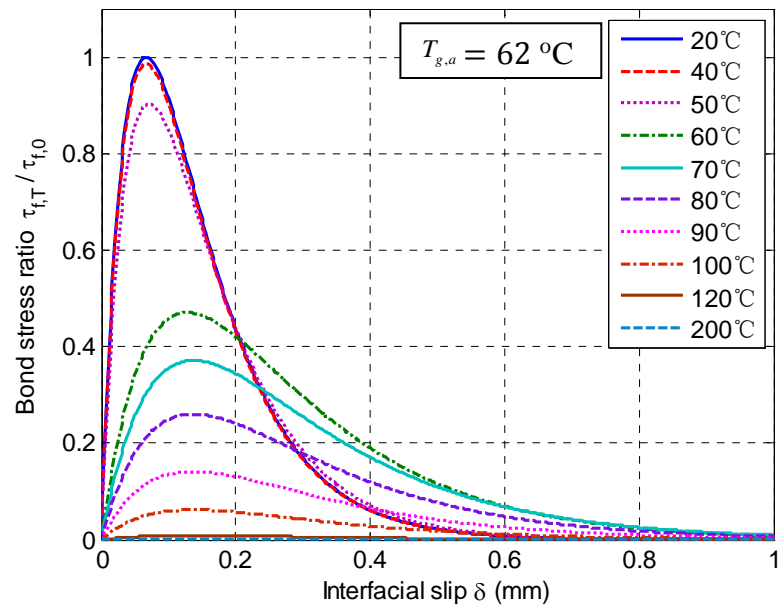


(b) Effect of normalized temperature on normalized tensile strength

**Fig. 7.1** Variation of tensile strength of FRP sheets with temperature.



(a) Steel-to-concrete interface



(b) FRP-to-concrete interface

**Fig. 7.2** Bond-slip curves of steel-to-concrete and FRP-to-concrete interfaces at elevated temperatures.

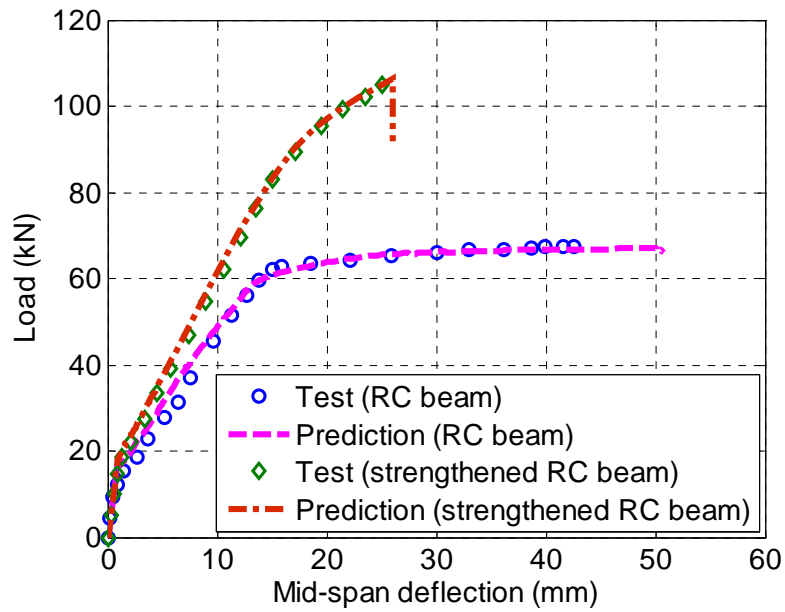


**Fig. 7.3** Load-deflection curves of Blontrock et al.'s (2000) reference beams.

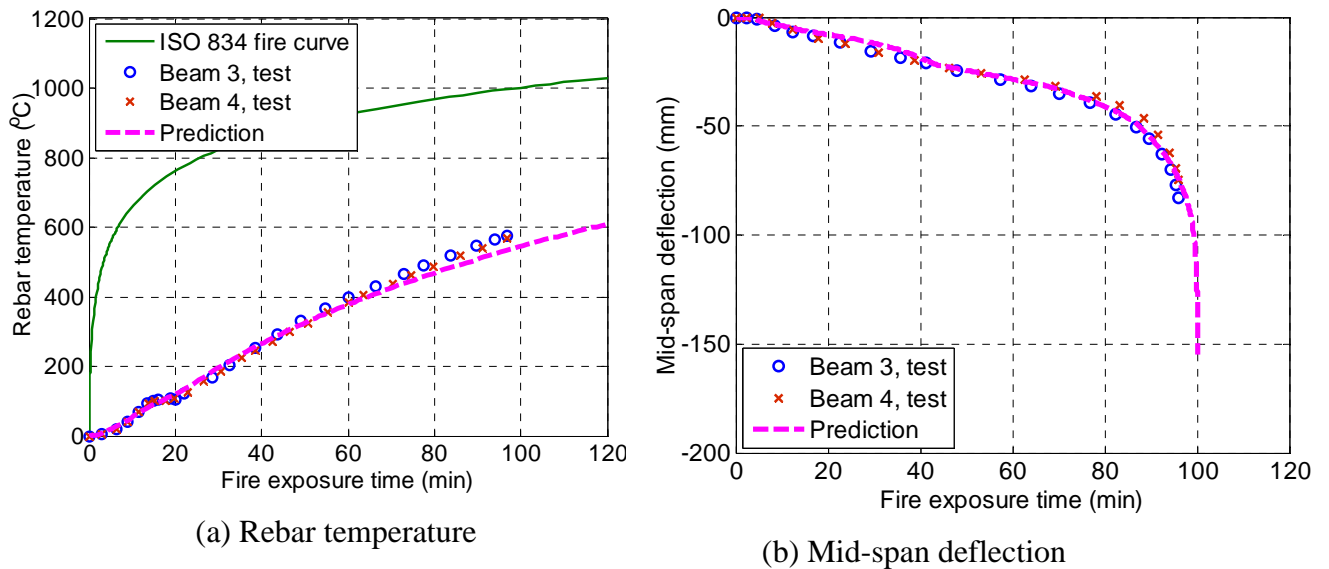
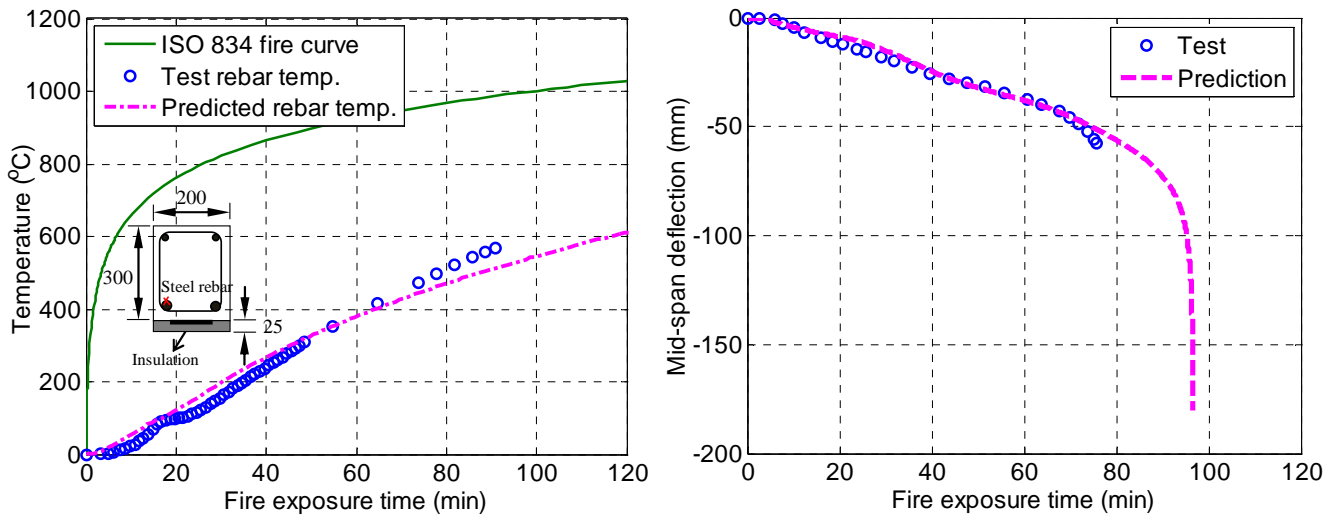
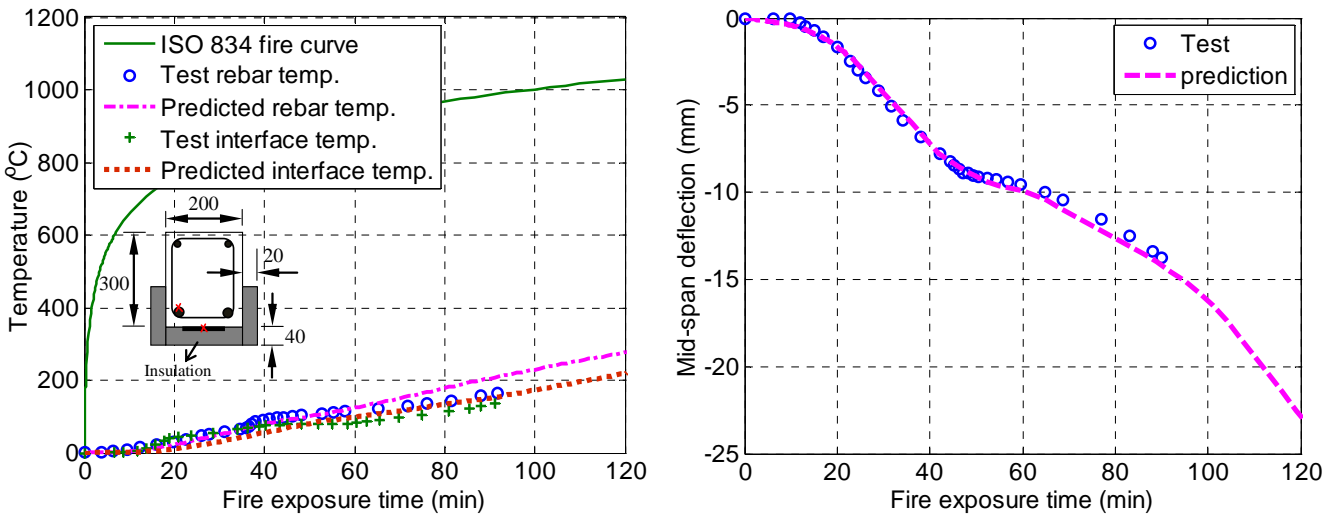


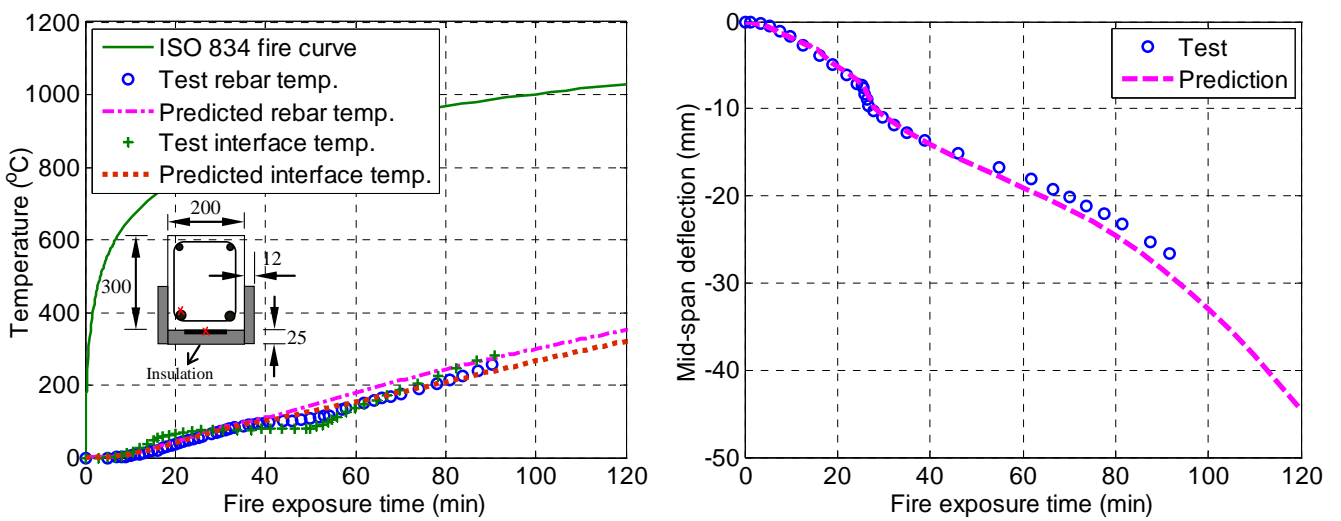
**Fig. 7.4** Fire responses of plain RC beams tested by Blontrock et al. (2000).



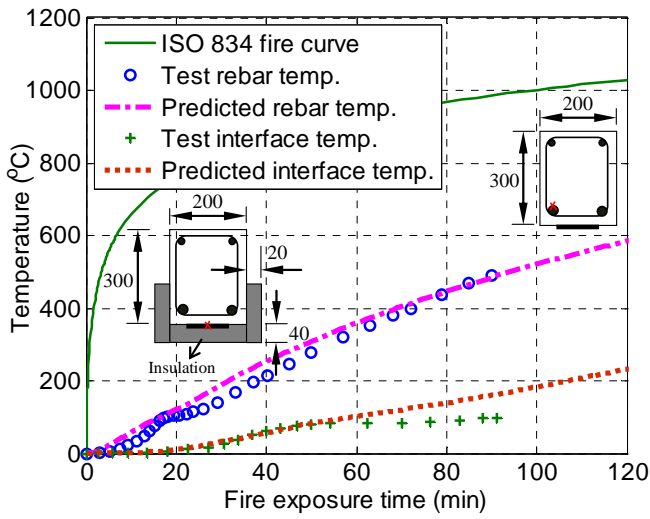
(a) Beam 5



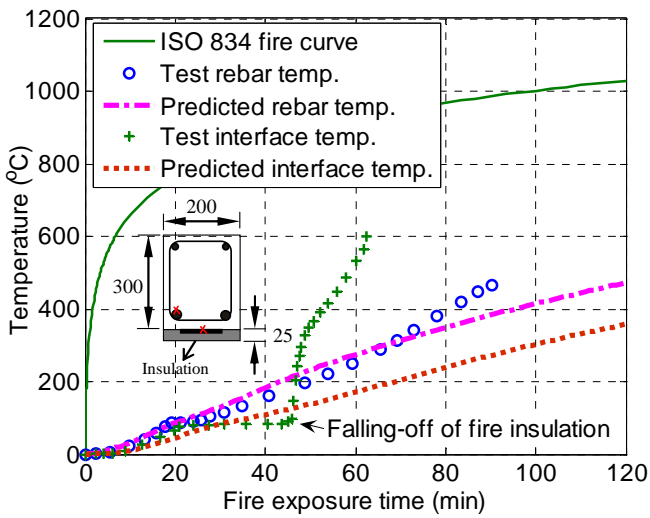
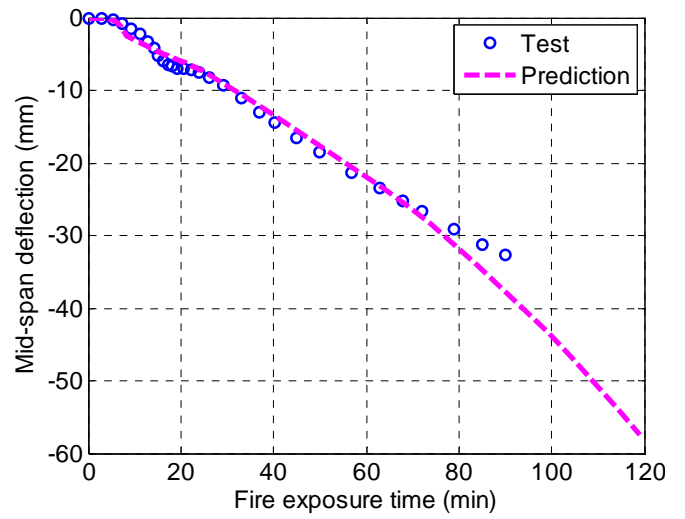
(b) Beam 6



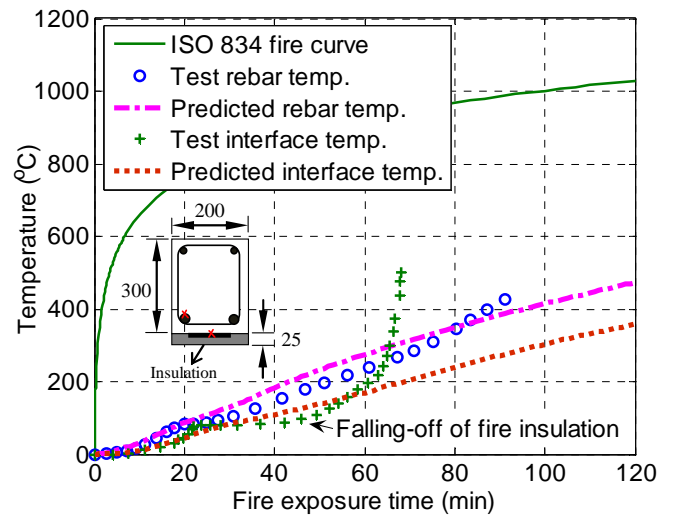
(c) Beam 7



(d) Beam 8

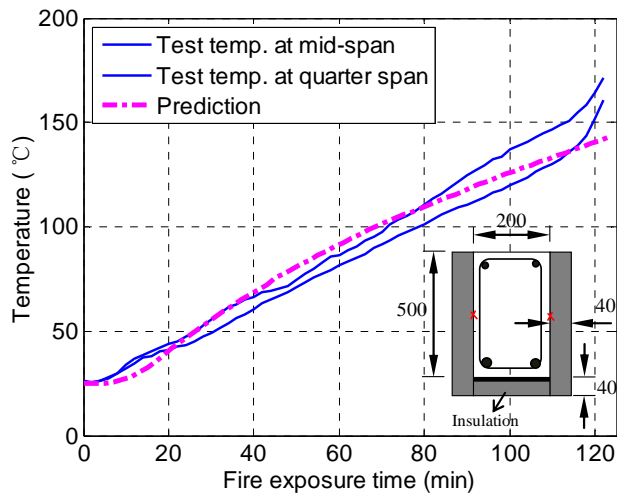


(e) Beam 9

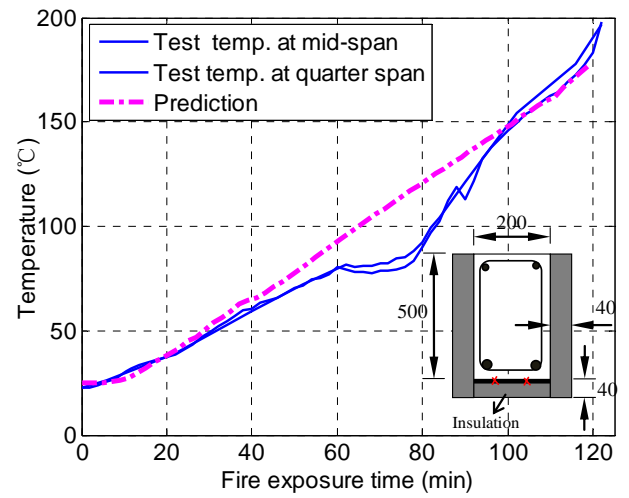


(f) Beam 10

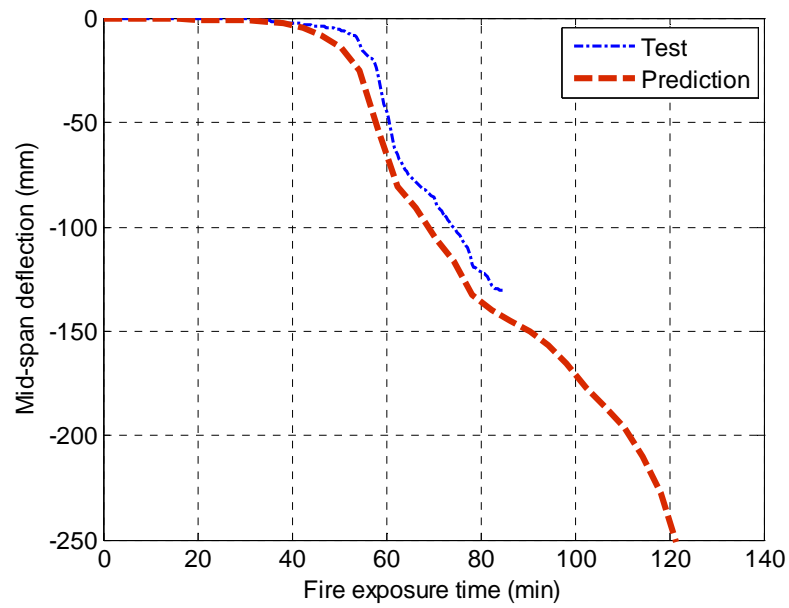
**Fig. 7.5** Fire responses of insulated CFRP-strengthened RC beams tested by Blontrock et al. (2000).



(a) Mid-height temperature

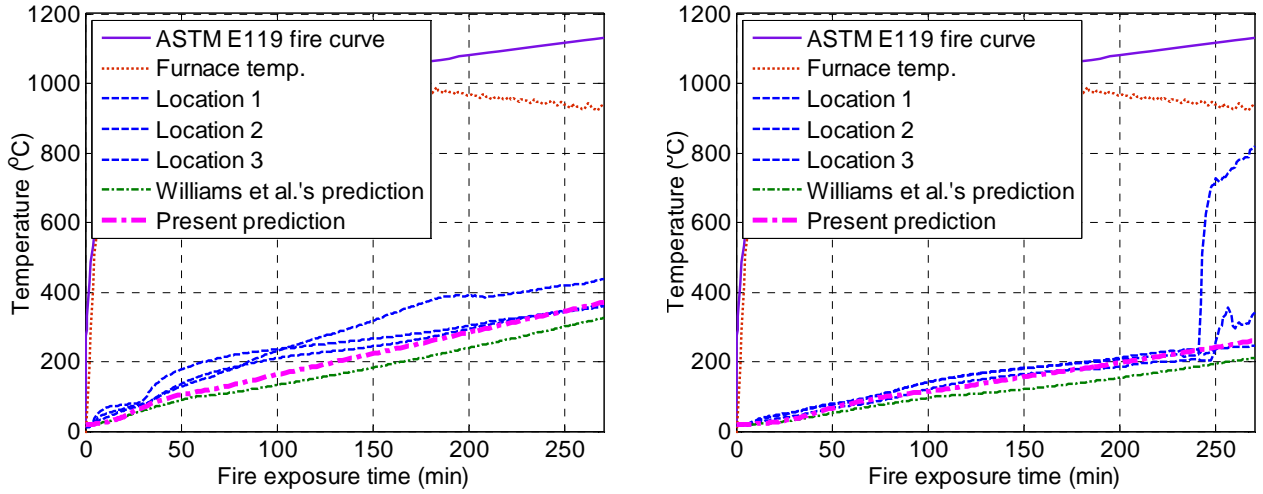


(b) Bottom surface temperature

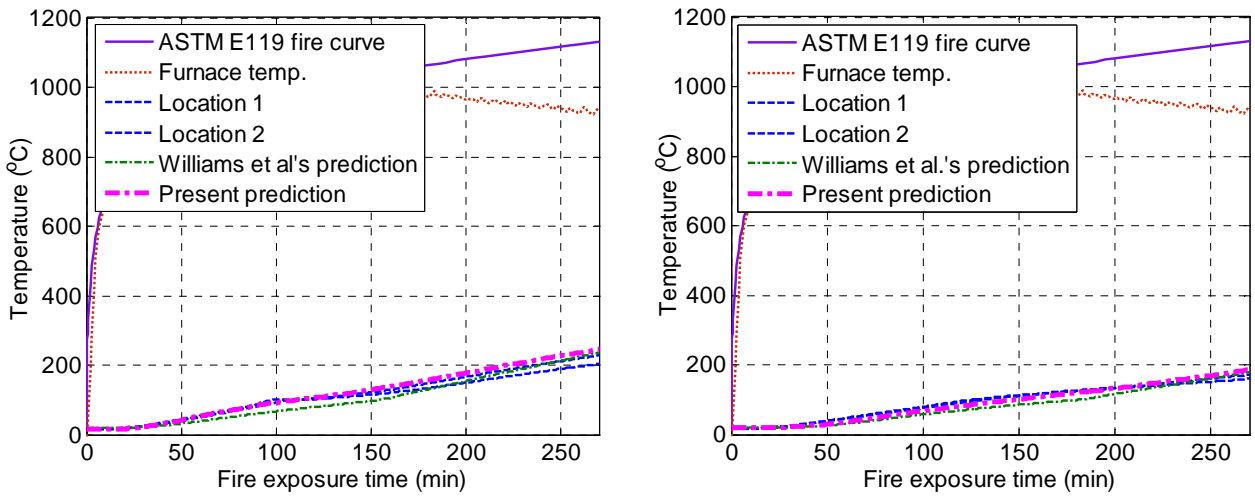


(c) Mid-span deflection

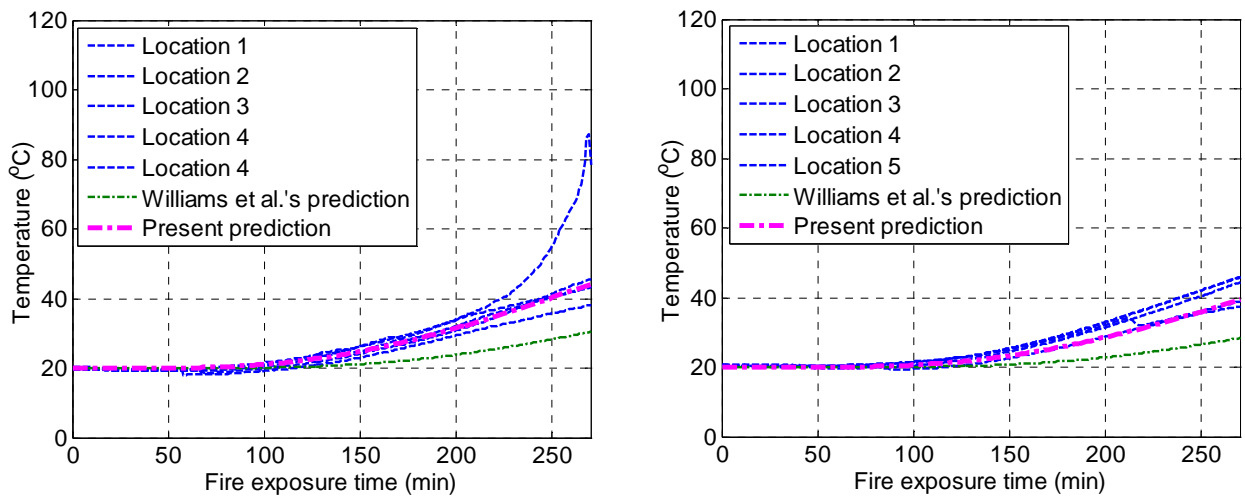
**Fig. 7.6** Fire responses of the insulated CFRP-strengthened RC beam tested by Gao et al. (2010).



(a) FRP-to-concrete interface temperature

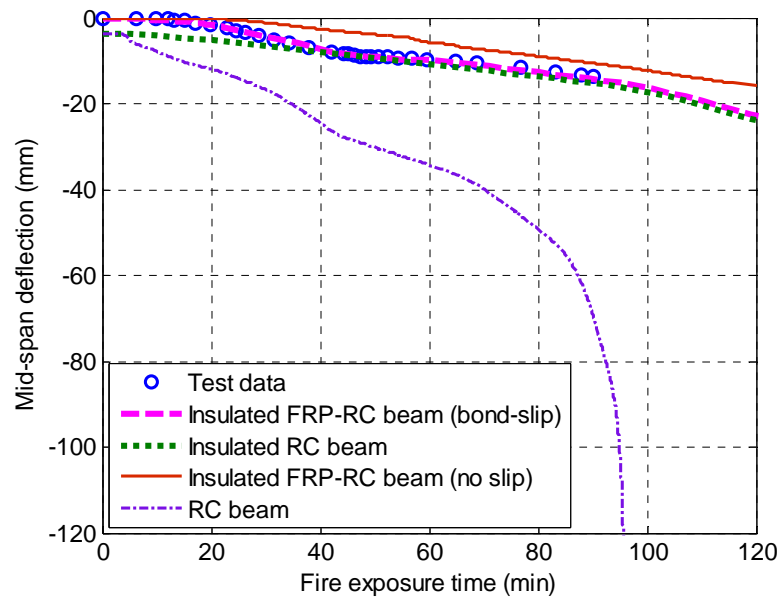


(b) Corner rebar temperature

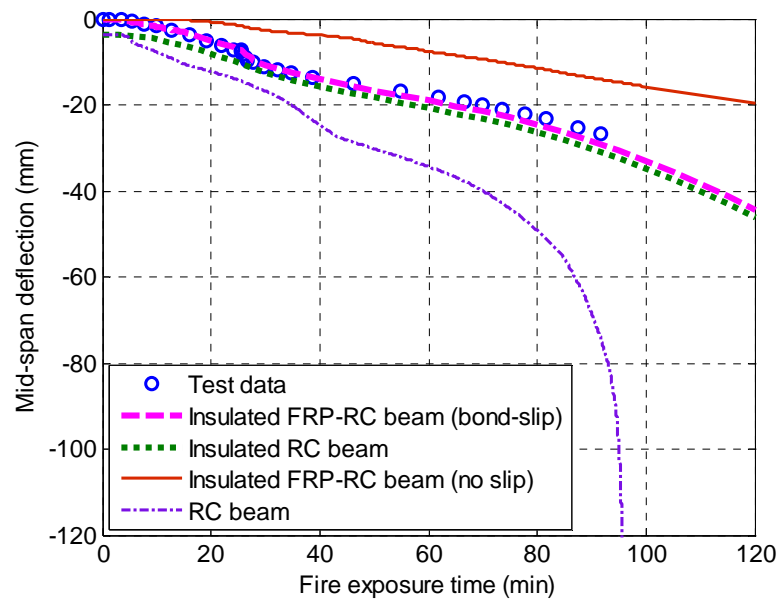


(c) Unexposed surface temperature

**Fig. 7.7** Temperatures of CFRP-strengthened RC T-beams tested by Williams et al. (2008).

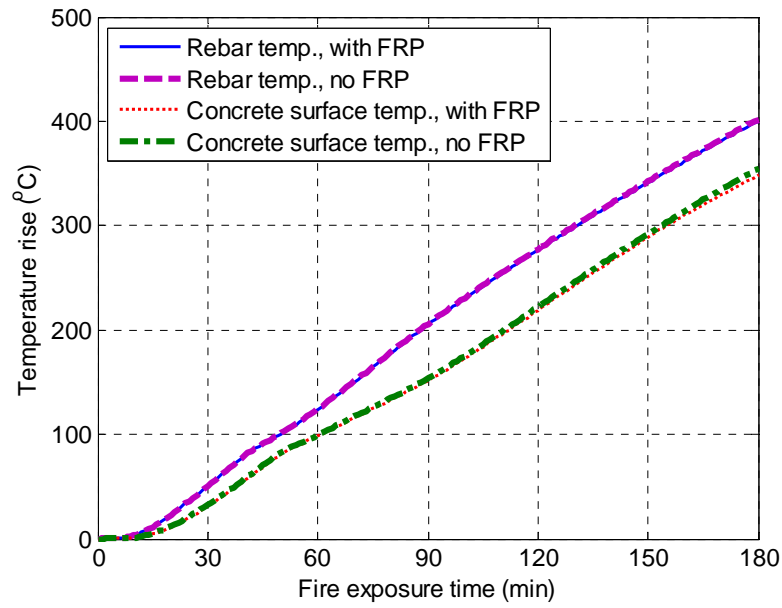


(a) Beam 6 of Blontrock et al. (2000)

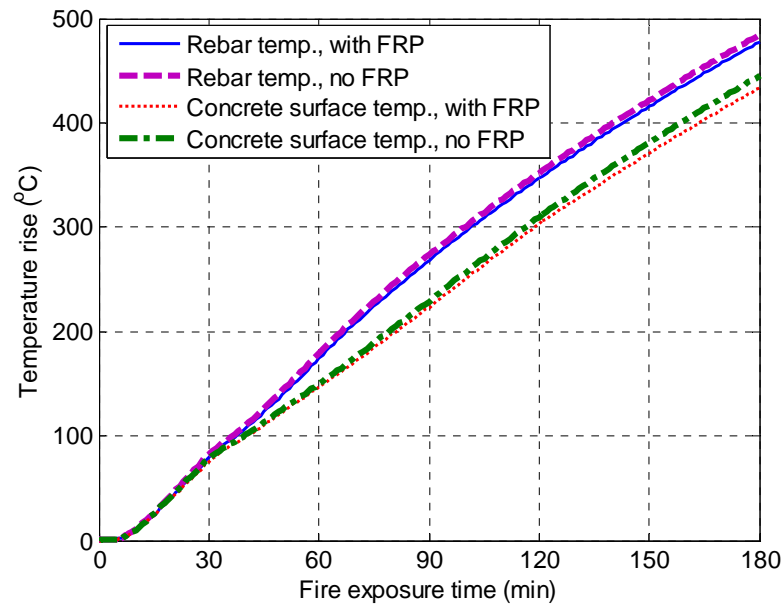


(b) Beam 7 of Blontrock et al. (2000)

**Fig. 7.8** Effect of bond degradation on mid-span deflection.



(a) Beam 6 of Blontrock et al. (2000)



(b) Beam 7 of Blontrock et al. (2000)

**Fig. 7.9** Effect of FRP strengthening system on temperatures in an insulated FRP-strengthened RC beam.

**Table 7.1** Material and geometrical properties of insulated FRP-strengthened RC beams.

| Series                                 |   | Series I                     | Series II                       | Series III                                   |
|--|---|------------------------------|---------------------------------|--|
| Source                                 |   | Blontrock et al. (2000)      | Gao et al. (2010)               | Williams et al. (2008)                       |
| Cross-section (mm)                     |   | 200 × 300                    | 200 × 500                       | T-beam: Web: 300 × 250<br>Flange: 1220 × 150 |
| Length (mm)                            |   | 3150                         | 6000                            | 3900   |
| Fire exposure span (mm)                |   | 2850                         | 4500                            | 3810   |
| Reinforcement                          | Top bars                                    | 2 Ø 10 mm                    | 2 Ø 12 mm                       | 2 Ø 10 mm                                    |
|  | Bottom bars                                 | 2 Ø 16 mm                    | 2 Ø 16 mm                       | 2 Ø 20 mm                                    |
| Concrete cylinder strength $f_c$ (MPa) |   | 57.5                         | 22.95                           | 41   |
| Load during fire                       |   | 2 × 40.6 kN                  | 4 × 30.2 kN                     | 34 kN/m                                      |
| Concrete cover thickness (mm)          |   | 25                           | 20                              | 40   |
| FRP                                    | Type  | CFRP plates                  | CFRP sheets                     | CFRP plates                                  |
|  | Thickness (mm)                              | 1.2                          | 0.334                           | 1.0  |
|  | Tensile strength (MPa)                      | 3180                         | 2600                            | 1076   |
|  | Elastic modulus (MPa)                       | 184                          | 160                             | 71.8   |
| Insulation                             | Scheme                                      | U-shaped or flat-shaped      | U-shaped                        | U-shaped                                     |
|  | Thickness (mm)                              | 12 ~ 40                      | 40                              | 25 or 38                                     |
|  | Material                                    | Promatect-H or Promatect-100 | Calcium silicate cladding board | Vermiculite-gypsum (VG) layer                |
|  | Density (kg/m <sup>3</sup> )                | 870                          | 244.7                           | 351  |
|  | Specific heat (J/kg.°C)                     | 840                          | 790                             | 1176.3                                       |
|  | Thermal conductivity <sup>a</sup> (W/m. °C) | 0.175 or 0.285               | 0.0603                          | 0.1158                                       |

<sup>a</sup> At ambient temperature.

## CHAPTER 8

# SIMPLE METHOD FOR PREDICTING TEMPERATURES IN BARE AND INSULATED RC BEAMS EXPOSED TO A STANDARD FIRE

### 8.1 INTRODUCTION

In the performance-based design approach, the fire resistance of the structure needs to be accurately evaluated, which requires the accurate prediction of temperature fields in the structure. A generic approach for temperature field analysis is to employ the FE or the finite-difference (FD) method using the available software packages. However, structural engineers often prefer a simpler approach as they may not have the expertise to deal with the complexity involved in such numerical computations within the tight timeframe of a design task. This chapter is concerned with the development of such a simple, design-oriented method given in explicit, closed-form expressions for temperature fields in un-protected RC beams (i.e., bare RC beams) and insulated RC beams for use in fire safety design.

Attempts have been made in the past to develop simple design-oriented methods for the prediction of temperature profiles in RC members subjected to one-dimensional heat transfer (Hertz 1981; Harmathy 1993) or two-dimensional heat transfer (Wickstrom 1986; Desai 1995, 1998; Abbasi 2003; Abbasi and Hogg 2005). Wickstrom (1986) presented a method for predicting temperatures in fire-exposed RC structures. For the standard ISO 834 fire curve and normal weight concrete, this method needs only two input parameters: the fire-exposure time and the concrete depth. Wickstrom's (1986) method was used by Eamon and Jensen (2012) to

determine the 500 °C isotherm and the temperature history of steel reinforcement in the fire resistance analysis of pre-stressed RC beams. Desai (1995, 1998) assumed that the isotherms of a rectangular RC beam are parallel to the exposed surfaces of the beam, and then proposed a simple equation to determine these isotherms. Desai's (1995, 1998) method is governed by three factors: the fire-exposure time, the width of beam cross-section, and the ratio between overall beam height and beam width. More recently, Abbasi and Hogg (2005) developed a formula to predict temperatures of FRP rebars in FRP-reinforced concrete beams exposed to fire. Under the standard ISO 834 fire curve, the rebar temperature was assumed to be influenced only by the fire-exposure time and the concrete cover thickness. Rafi (2010) and Nigro et al. (2012) proposed best-fit curves for the temperature responses of FRP bars based upon fire tests of FRP-reinforced concrete beams and slabs. It should be noted that the above-mentioned methods have all been assessed only using a limited test database, and the differences between model predictions and experimental results may be substantial.

For structural members protected with fire insulation materials, most of the available formulae are provided for calculating the temperatures of insulated steel members in fire. In deriving these formulae, different methods were employed including the separation of variables approach (Wickstrom 1985), the Laplace transform approach (Melinek and Thomas 1987) and the Green's function approach (Wang et al. 2005). Simplified formulae were also provided in fire design codes for calculating the temperature profiles in insulated steel members under fire conditions (ECCS 1983; Bennetts et al. 1987; EN 1993-1-2 2005). Detailed descriptions and comparisons of these different formulae can be found in Wong and Ghajel (2003) and Zhang et al. (2012). However, it should be noted that all these formulae were obtained by solving a simplified one-dimensional condensed heat transfer model based on a lumped capacitance concept. That is, the temperature field inside the steel section is assumed

to be uniform and the temperature difference between the fire gas and the insulation surface (i.e., interfacial thermal resistance) is ignored (Carslaw and Jaeger 1995; Wang et al. 2005; Zhang et al. 2012). Theoretically, these formulae are not applicable to insulated concrete members because the temperature gradient in concrete section is usually significant due to the low thermal conductivity of concrete materials. Besides, the thermal resistance at the fire-to-insulation interface cannot be ignored due to the relatively high heat capacity of concrete materials.

Since concrete is an excellent thermal barrier for the internal steel reinforcement, fire insulation is generally not needed for conventional RC beams (Khoury 2008). As a result, very limited studies were carried out to investigate the effect of insulation or coating on the fire performance of RC members (Wickstrom and Hadziselimovic 1996; Zhou and Zhang 2003; Hodhod et al. 2009). Wickstrom and Hadziselimovic (1996) assumed the additional fire-resistant coating as an equivalent concrete layer for temperature field analysis of insulated RC beams exposed to a standard fire. The thickness of the equivalent concrete layer was determined based upon the assumption that the insulated RC section and the RC section enlarged by the equivalent concrete layer yield the same fire exposure period when the temperature of the internal steel reinforcement reached 500°C. A linear relationship was developed by Wickstrom and Hadziselimovic (1996) for the concrete cover thickness and the thickness of the equivalent concrete layer. However, the proposed linear relationship is only suitable for high density insulation coatings with a large thermal conductivity (i.e., larger than 0.2 W/m·°C), since for light-weight insulation materials with a low thermal conductivity less than 0.2 W/m·°C at room temperature (widely used for fire protection of FRP-strengthened RC members), this relationship is obviously nonlinear [see Eqs. (8.24)-(8.25) for more details]. Besides, such an approximate approach proposed by Wickstrom and Hadziselimovic (1996) focused on the temperature evolution at the location of internal steel reinforcement; as a result, it is not applicable for insulated FRP-strengthened RC members, in which the

temperatures of the insulation-to-FRP/concrete interfaces may become more critical as compared to that of the internal steel reinforcement.

This chapter aims to develop an explicit design-oriented solution for predicting temperatures in bare and insulated RC beams under a standard fire exposure. Three steps of work are included in the chapter: (1) to establish a simple yet accurate method for the prediction of temperature fields in RC beams under a standard fire exposure as an alternative to the complex FE or FD analysis; (2) to treat the fire insulation layer as an equivalent concrete layer and establish an appropriate relationship between their thicknesses according to their thermal properties; (3) to predict the temperature fields in insulated FRP-strengthened RC beams (i.e., equivalent to un-protected RC beams with enlarged concrete sections) exposed to a standard fire using the explicit formulae developed in the preceding two steps. The explicit temperature analyses will serve as the basis for the development of design-oriented approaches for the fire resistance analysis of insulated FRP-strengthened RC beams in the next chapter.

## **8.2 EXISTING METHODS FOR TEMPERATURE PREDICTIONS**

The temperature fields of an RC beam exposed to a standard fire depends on several factors, such as the fire-exposure time, the beam width, the aggregate type and the moisture content of concrete. Many studies have been carried out to determine the temperature fields of RC beams, but most of them were conducted using an FE or FD software package. Only three simple methods have been found in the published literature for predicting the temperature fields of RC beams under a standard fire exposure as summarized below.

### 8.2.1 Wickstrom's Method

For an RC beam made of normal weight concrete and exposed to the ISO 834 standard fire, Wickstrom's (1986) method predicts the temperature rise  $\Delta T(x, y)$  at a given point  $(x, y)$  in the concrete at the fire-exposure time  $t$  by the following equation:

$$\Delta T(x, y) = [n_w(n_x + n_y - 2n_x n_y) + n_x n_y] \Delta \theta_f \quad (8.1)$$

where  $\Delta \theta_f$  is the temperature rise of the standard ISO 834 fire curve;  $n_w$  is the ratio between the temperature rise of the beam surface to that of the fire, which depends on the fire-exposure time and is given by:

$$n_w = 1 - 0.0616 t^{-0.88} \quad (8.2)$$

In Eq. (8.2),  $t$  (in hours) is the fire exposure time;  $n_x$  (or  $n_y$ ) is a function of fire-exposure time and the ratio between the thermal diffusivity of the RC beam (i.e.,  $\alpha$ ) and a reference value  $\alpha_c$  (i.e.,  $\alpha_c = 417 \times 10^{-9} \text{ m}^2 \text{ s}^{-1}$ ):

$$n_x = 0.18 \ln \left( \frac{\alpha}{\alpha_c} \times \frac{t}{x^2} \right) - 0.81 \quad (8.3)$$

where  $x$  (in m) is the distance between the point under consideration and the fire-exposed surface in the beam width direction. A similar equation is used to calculate  $n_y$  by replacing  $x$  with  $y$  in the beam height direction. It should be noted that Eq. (8.3) only holds if

$$x \text{ (or } y) \geq 2h - 3.6(0.0015t)^{0.5} \quad (8.4)$$

where  $h$  (in m) is the dimension of the RC beam in the direction under consideration.

### 8.2.2 Desai's Method

Desai (1995, 1998) adopted a simple equation to predict the temperature profiles of rectangular RC beams based on his own experimental results and those of some others [e.g., Lin et al. (1988) and Wade (1991)]. The temperature  $T$ , ( $^{\circ}\text{C}$ ) of a contour at a distance  $x$  (in mm) from the fire-exposed surfaces of the beam was assumed to be influenced by the following factors:

- a)  $t$ , the fire-exposure time (in min);
- b)  $b$ , the width of beam cross-section (in mm); and
- c)  $r$ , the ratio between beam height and beam width.

Desai's (1998) equation is as follows:

$$T = (D - Ax + Bx^2 - Cx^3)/r^{0.25} \quad (8.5)$$

where

$$A = 3.33 \left[ 3 + 0.0033 t + \left( \frac{100-t}{b} \right) \right] \quad (8.6)$$

$$B = 0.085 \quad (8.7)$$

$$C = 0.000221 \quad (8.8)$$

$$D = 475 r^{7/12} - (b - 105 t^{1/3}) \quad (8.9)$$

The applicability of Eq. (8.5) is limited to beams satisfying the following two conditions:  $100\text{mm} < b < 300\text{mm}$  and  $1 < r < 3$ . If  $r \leq 1.5$ , then it is assumed that  $r = 1.5$  in the calculation. The initial temperature calculated by Eq. (8.5) varies from negative values to positive ones depending on the beam geometry and the distance from the fire-exposed surfaces, which is an undesirable feature. In the comparisons presented later in the chapter, the temperature rise is taken as the temperature predicted using Eq. (8.5) minus the initial temperature of a standard fire (i.e.,  $20^\circ\text{C}$ ).

### ***8.2.3 Abbasi and Hogg's Method***

Abbasi and Hogg's (2005) method was developed only for predicting the temperatures of FRP rebars in beams subjected to the standard ISO 834 fire. In this method, the difference between the rebar temperature and the fire temperature, after 30 minutes of fire exposure, is assumed to be in the following exponential form:

$$\theta - T = A' \exp(-\beta \cdot t) \quad (8.10)$$

where  $\theta$  and  $T$  are the fire temperature and the rebar temperature, respectively;  $A'$  is an empirical constant and  $= 767$ ;  $t$  is the fire exposure time (in min);  $\beta$ , being the gradient of  $\ln [(\theta - T)/A']$  versus  $t$  curves, was derived from fire test data by regression analysis and has the following exponential form:

$$\beta = a' \exp\left(\frac{b'}{c'+d'}\right) \quad (8.11)$$

where  $c'$  (in mm) is the concrete cover thickness;  $a'$ ,  $b'$  and  $d'$ , being empirical constants determined from regression of test data, are as follows:

$$a' = 0.001, b' = 7.602, d' = -23.623 \quad (8.12)$$

By the combined use of Eqs. (8.10)~(8.12), the rebar temperature in the beam subjected to the standard ISO fire can be obtained as follows:

$$T = \theta - 767 \exp \left\{ - \left[ 0.001 \cdot \exp \left( \frac{7.602}{c' - 23.623} \right) \right] \cdot t \right\} \quad (8.13)$$

As this method was derived on the basis of fire test data after 30 minutes of fire exposure, the initial temperature calculated by Eq. (8.13) (i.e.,  $t=0$ ) is always equal to  $-747$  °C, which is unreasonable. Again for comparison purposes in the chapter, the temperature rise is taken as the predicted temperature minus the initial temperature of a standard fire (i.e.,  $20$  °C).

### **8.3 PROPOSED METHOD FOR TEMPERATURES IN BARE RC BEAMS**

#### ***8.3.1 General***

The proposed method for predicting temperature fields in RC beams consists of two steps: (1) determination of the temperature distribution along the mid-width vertical line of beam cross-section; and (2) determination of temperature profiles in corner regions of beam cross-section with due consideration of two-dimensional heat transfer from both the bottom and the side surfaces. The first step can be divided into two sub-steps: 1) when the width of the beam is wide enough, the prediction of the mid-width temperatures can in fact be approximated as a one-dimensional heat transfer problem; 2) the one-dimensional temperature distribution can then be modified for use in relatively narrow beams with due consideration of the beam width effect.

### **8.3.2 FE Analyses**

In both the above two steps of work, parametric FE analyses were undertaken with the following two purposes: (1) to investigate the influences of each parameter on the sectional temperature distributions; and (2) to provide sufficient temperature data for regression analysis to derive and validate the explicit predictive method. Details of the FE model for heat transfer analysis of RC beam under a standard fire exposure can be found in Chapter 6.

Table 8.1 provides a summary of the cross-sections used in the FE parametric study. It should be noted that, the effect of the moisture content of concrete is taken into account by adjusting the specific heat capacity to represent the latent heat of water evaporation. An early study conducted by Harmathy (1965) showed that the presence of moisture in building components is beneficial to their fire resistance if it is not so excessive as to trigger the spalling of concrete. Therefore, a slightly lower-than-normal moisture content of 1.5% by weight (i.e.,  $u = 1.5\%$ ) was assumed in the FE analysis to ensure conservative predictions (Hertz 1981; Biondini and Nero 2011). According to EN 1992-1-2 (2004), a peak value (i.e.,  $c_{c,peak}$ ) of 1.470 kJ/kg was adopted for the specific heat capacity of concrete to implicitly consider the latent heat of evaporation component. The thermal properties of steel are not considered in the FE analysis since the effects of steel reinforcement are usually negligible in heat transfer analysis (Rodrigo et al. 2010; Biondini and Nero 2011). In other words, the temperature of internal steel reinforcement is taken to be equal to that of concrete at the same location.

### **8.3.3 Factors Governing Temperature Fields**

The temperature response at a given point of an RC beam is certainly affected by its location and exposure time. Desai (1995, 1998) reported that the temperature distribution over the cross-section of an RC beam exposed to fire is influenced by the beam width  $b$  and the beam depth-to-width ratio  $r$ . To clarify the effects of these two parameters, a parametric FE study was conducted to examine the temperature distributions over the mid-width vertical line of the cross-section for five different beam widths and height-to-width ratios (Table 8.1). These results are presented in Figs. 8.1a and 8.1b, and suggest that, for a given beam width (here  $b = 200$  mm), the temperature rises at the five different depths (i.e., 5 mm, 25 mm, 50 mm, 100 mm, and 200 mm) from the beam bottom are independent of the depth-to-width ratio (varying from 1.0 to 3.0 with the beam depth increasing from 200 mm to 600 mm); the different depth-to-width ratios lead to similar temperature evolutions at a given location. By contrast, when the depth-to-width ratio is kept constant (e.g.,  $r=1.0$ ), the beam width has a significant effect on the time-dependent temperature evolutions at all locations (Fig. 8.1b), particularly when the depth of location is large (e.g., 200 mm in Fig. 2b). For example, when the beam width increases from 200 mm to 600 mm, the temperature rise changes from 542 °C to 368 °C at the 50 mm concrete depth while from 322 °C to 27 °C at the 200 mm concrete depth after a two-hour fire exposure. Based on these numerical results, the beam width, rather than the depth-to-width ratio, needs to be considered as a key parameter in developing a simple predictive model for temperatures.

#### ***8.3.4 Mid-Width Temperatures in Wide Beams***

FE analyses revealed that, when the beam width is larger than 500 mm, the temperature distribution over the mid-width vertical line of the cross-section can be obtained from a one-dimensional heat transfer analysis. That is, the effect of heat transfer from the two beam sides on this temperature distribution is negligible.

Therefore, a beam cross-section of 600 mm in width by 600 mm in depth was employed in the FE analysis to generate the time-dependent temperature data for the one-dimensional temperature distribution prediction. Fig. 8.2 shows the FE predictions for the evolving temperature rises at different concrete depths over the mid-width vertical line of the cross-section. It is obvious that the temperatures are influenced by the concrete depth  $d$  and the fire exposure time  $t$ . The temperature rises more quickly for locations with a smaller depth as expected. Therefore, the temperature rise ( $\Delta T$ , in °C) at a point located at a distance  $d$  (in mm) from the bottom surface of the beam is governed by the following two factors:

- a)  $t$ , the fire exposure time (in min); and
- b)  $d$ , the distance from the fire-exposed surface (in mm).

Thus, the temperature rise  $\Delta T$  at a point of the mid-width line can be expressed as:

$$\Delta T = \theta_{d,120} k_t k_b \quad (8.14)$$

where  $\theta_{d,120}$  is the reference temperature rise at  $t = 120$  min for a certain depth  $d$  and a beam width of 600 mm;  $k_t$  accounts for the effect of fire exposure time; and  $k_b$  accounts for the effect of beam width. For wide beams,  $k_b = 1$ .  $\theta_{d,120}$  is chosen as the reference temperature rise because a 120-minute duration represents a typical fire-resistance rating of RC beams in existing design codes [e.g., BS 8110-2 (1985), EN 1992-1-2 (2004), FIP/CEB report (2004), ACI 216.1 (2007) and AS 3600 (2009)].  $\theta_{d,120}$  can be expressed as an exponential function based on least-squares regression of the present FE numerical results:

$$\theta_{d,120} = a_0 \cdot \exp(a_1 d) + a_2 \quad (8.15)$$

where  $a_0 = 8.73 \times 10^2$ ,  $a_1 = -1.77 \times 10^{-2}$ , and  $a_2 = 4.53$  for siliceous aggregate concrete (Fig. 8.3a);  $a_0 = 8.96 \times 10^2$ ,  $a_1 = -1.88 \times 10^{-2}$ , and  $a_2 = 1.88$  for calcareous aggregate concrete (Fig. 8.3b).

The value of  $k_t$  can be found using Fig. 8.4, in which the temperature rises at different depths with the fire exposure time are normalized by the reference temperature  $\theta_{d,120}$ . For depths larger than 200 mm, their curves are not provided because temperatures at these locations were found to be low (below 100 °C) after a three-hour standard fire exposure (see Fig. 8.2 for more details). Because degradations of concrete in both strength and stiffness below 100 °C are negligible, the temperature rises at concrete depths beyond 200 mm are assumed to be the same as those at 200 mm for simplicity. This simplification is believed to have little influence on the fire resistance prediction of RC beams. Temperature rises at locations not directly represented by the curves in Fig. 8.4 can be obtained by linear interpolation. In addition, FE results (not given here to save space) showed that the curves in Fig. 8.2 are applicable to both siliceous and calcareous aggregate RC beams.

The values of  $k_t$  can also be alternatively represented using an algebraic equation which is more convenient for use with spreadsheets in design calculations. It was found by trial and error that the Morgan-Mercer-Flodin (MMF) function (Morgan et al. 1975) is suitable for describing time-dependent temperature rises at all concrete depths. The MMF function was originally developed to describe the nutritional response of higher organisms and has the following form:

$$k_t = \frac{t_1 t_2 + t_3 t^4}{t_2 + t^4} \quad (8.16)$$

where  $t_{i(i=1,2,3,4)}$  are functions of the concrete depth. A regression process indicated that  $t_{i(i=1,2,3,4)}$  can be expressed as polynomials:

$$t_{i(i=1,2,3,4)} = m_1 + m_2 \cdot d + m_3 \cdot d^2 + m_4 \cdot d^3 + m_5 \cdot d^4 \quad (8.17)$$

where the coefficients  $m_{i(i=1,2,3,4,5)}$  were determined through least-square regression analysis of the FE data presented in Fig. 8.4, and their values are provided in Table 8.2. The curves predicted using the above two formulae [i.e., Eqs. (8.16) and (8.17)] are presented in Fig. 8.5 for different concrete depths. The close agreement between the predicted curves and the FE data demonstrates the accuracy of Eqs. (8.16) and (8.17) in predicting the values of  $k_t$  value.

### **8.3.5 Effect of Beam Width**

To quantify the beam width effect, FE analyses were carried out to compare the mid-width temperature distributions for five different beam widths (the beam depth is identical, i.e., 600 mm) (Table 8.1). Fig. 8.6 illustrates the effect of beam width (i.e., from 200 mm to 600 mm) on temperatures at different concrete depths (i.e., from 5 mm to 200 mm) over the mid-width line of beam cross-section at  $t = 120$  min. The results are all normalized by  $\theta_{d,120}$  for a 600 mm wide beam. As the concrete depth increases, the effect of beam width is clearly seen to become more significant. In addition, the temperature at a given concrete depth decreases as the beam width increases. Using a curve-fitting software package available freely at <[www.curveexpert.webhop.biz](http://www.curveexpert.webhop.biz)>, the exponential function given below was found to lead to the best representation of the FE temperature data (Fig. 8.6):

$$k_b = \exp \left[ b_0 + \frac{b_1}{b/200} + b_2 \ln(b/200) \right] \quad (8.18)$$

where the parameters  $b_0$ ,  $b_1$  and  $b_2$  are functions of the concrete depth as given below:

$$b_0 = -1.31 \times 10^{-1} - 1.45 \times 10^{-2}d + 5.81 \times 10^{-5}d^2 \quad (8.19a)$$

$$b_1 = 1.71 \times 10^{-1} - 2.04 \times 10^{-2}d - 3.42 \times 10^{-5}d^2 \quad (8.19b)$$

$$b_2 = 7.39 \times 10^{-2} + 6.59 \times 10^{-3}d - 4.12 \times 10^{-5}d^2 \quad (8.19c)$$

To validate the expression proposed for  $k_b$ , the curves predicted by Eq. (8.19) are shown in Fig. 8.6 as continuous lines. In the same figure, the symbols represent the FE temperature data, with different symbols corresponding to different concrete depths. The close agreement between the predictions of Eq. (8.19) and the FE results confirms the accuracy of expression for  $k_b$ .

Combining Eqs. (8.14), (8.15) and (8.18) as well as Fig. 8.4 [or Eq. (8.16)], the temperature distribution over the mid-width vertical line of beam cross-section can be obtained. Fig. 8.7 compares the predictions of the method proposed herein (using Fig. 8.4) with those obtained from FE analyses for a 600 mm  $\times$  600 mm cross-section. The excellent agreement between the results from the two sources demonstrates that the explicit formulae have properly captured the effects of fire exposure time  $t$ , the concrete depth  $d$  and the beam width  $b$ .

### ***8.3.6 Temperatures of Corner Concrete***

The temperatures of points in corner regions depend on their distances from both the bottom surface and the two side surfaces of the beam. A logarithmic function used

by Wickstrom (1986) is modified to predict the two-dimensional temperature response with due consideration of the two distances:

$$\Delta T = \left\{ \left[ \ln \left( \frac{\theta_x}{\theta_y} + 1 \right) + 1 \right] \cdot \theta_y \cdot m(y) \cdot n \left( \frac{y}{x} \right) \right\} k_t k_b \quad (8.20)$$

where  $x$  is the distance between the point under consideration and the beam bottom surface or the nearer beam side surface, whichever is larger, while  $y$  is the smaller one;  $\theta_x$  and  $\theta_y$  are calculated according to Eq. (8.15) by replacing  $d$  with  $x$  and  $y$ , respectively. The functions  $m(y)$  and  $n \left( \frac{y}{x} \right)$  are introduced here into Wickstrom's (1986) original function to account for the interactive effect of the two distances mentioned above on heat transfer. Both functions were obtained through regression analysis of FE temperature data for 120 locations in the corner regions of the beam cross-section (i.e., 600 mm  $\times$  600 mm). The detailed regression process is not presented here as it was conducted using routine least-squares analysis. As a result, the expressions for  $m(d)$  and  $n \left( \frac{y}{x} \right)$  were obtained as follows:

$$m(y) = 7.59 \times 10^{-1} + 4.37 \times 10^{-3}y - 1.71 \times 10^{-5}y^2 \quad (8.21a)$$

$$n \left( \frac{y}{x} \right) = 1.26 - 1.32 \left( \frac{y}{x} \right) + 8.81 \times 10^{-1} \left( \frac{y}{x} \right)^2 \quad (8.21b)$$

Eq. (8.21) was derived from regression analysis of FE temperature data for RC beams made of siliceous aggregate. It is also taken to be accurate for RC beams made of calcareous aggregate as demonstrated in the following section. The influence of aggregate type on temperature fields was already considered in deriving the equation for the reference temperature [i.e., Eq. (8.15)].

## 8.4 VERIFICATION OF THE PROPOSED METHOD FOR BARE RC BEAMS

Three well-reported fire tests of RC beams from independent sources are used to verify the accuracy of the proposed method for predicting temperatures in RC beams under a standard fire exposure (Lin et al. 1981; Dotreppe and Franssen 1985; Wu et al. 1993). Figs. 8.8 to 8.10 show comparisons between predictions from the proposed method and the test results. Predictions from the three existing methods (i.e., Wickstrom 1986; Desai 1998; Abbasi and Hogg 2005) are also presented in these figures for comparison. In Wickstrom's (1986) method, the thermal diffusivity of concrete (i.e.,  $\alpha_c$ ) is an important parameter. Wickstrom (1986) suggested a value of  $417 \times 10^{-9} \text{ m}^2 \cdot \text{s}^{-1}$  for  $\alpha_c$ , and this value was adopted in making predictions using Wickstrom's (1986) method for comparison in Figs. 8.8a, 8.9a and 8.10a. According to Eamon and Jensen (2012), the actual thermal diffusivity may vary between 0.75 and 1.5 times this recommended value, depending on the aggregate type, density of concrete, temperature and some other factors.

Figs. 8.8a-8d show comparisons between the test data and the predictions at two concrete depths along the mid-width vertical line of cross-section for the RC beams tested by Wu et al. (1993). This series of fire tests included three RC beams made of calcareous aggregate concrete. All three beams were designed to have an identical section of 200 mm  $\times$  300 mm and tested under the ISO 834 standard fire exposure. The test data in Figs. 8.8a~8.8d were averaged from thermocouple readings of these three RC beams. Since the methods of Wickstrom (1986) and Abbasi and Hogg (2005) lead to negative temperature values during the early stage of fire exposure, which is obviously incorrect, only the positive values are shown in these figures (Figs. 8.8a and 8.8c). During the later stages of fire exposure, Wickstrom's (1986) method seems to capture closely the trend of temperature response (Fig. 8.8a),

whereas predictions of the other two methods (Desai 1998; Abbasi and Hogg 2005) deviate substantially from the test results (Figs. 8.8b and 8.8c). The temperatures predicted by the proposed method agree closely with the test data although there is some over-estimation during later stages for larger concrete depths (i.e., above 100 mm from the bottom of the beam). This over-estimation may be attributed to the higher moisture content of the test beams, which is about 3.5% and much larger than the value assumed in the present analysis (i.e., 1.5%). In the thin layer of concrete adjacent to the fire-exposed surfaces, the moisture can be released into the air during the heating process, but the moisture further away from the surface moves towards the inner colder region of concrete due to pore pressure-induced flow. As a result, the effect of moisture on temperature changes is more significant for the inner concrete. It should be noted that the above-mentioned over-estimation leads to a more conservative fire resistance design for RC beams.

Figs. 8.9a-8.9d compare the predictions of rebar temperatures from the proposed method with the test data of Lin et al. (1981) for a simply-supported RC beam made of calcareous aggregate under the ASTM E119 standard fire exposure. The beam had a section of 305 mm × 355 mm, with the bottom and the side concrete covers of corner tension bars being 25 mm and 38 mm respectively. The methods of Wickstrom (1986) and Abbasi and Hogg (2005) both lead to substantial over-estimations, particularly during the later stages of fire exposure (Figs. 8.9a and 8.9c). Desai's (1998) method gives close predictions of the test data, probably because Desai's (1998) method was based on Lin et al.'s (1988) test results; the concrete properties and the beam dimensions of Lin et al.'s (1988) tests are similar to those of the specimen from Lin et al. (1981) under consideration here. The proposed method is by far the most accurate method among all the methods (Fig. 8.9d), indicating its accuracy for both the ASTM E119 and the ISO-834 standard fire exposures. The two

standard fire scenarios are in fact similar, and indeed for a long fire exposure time, their difference in severity of exposure is negligible (Harmathy et al. 1987).

The last test specimen was conducted by Dotreppe and Franssen (1985) who reported only the fire test of one simply-supported RC beam made of siliceous aggregate. The beam had a width of 200 mm and a depth of 600 mm. The bottom concrete cover of steel rebars was 40 mm. Comparisons between test and predicted results for the temperature responses of the central tension rebar are given in Figs. 8.10a-8.10d. These comparisons indicate again that the proposed method provides consistent and satisfactory predictions of the test results throughout the entire fire exposure period, while the three existing methods lead to underestimations or overestimations of the test results to different extents (Figs. 8.10a-8.10c).

## **8.5 PROPOSED METHOD FOR TEMPERATURES IN INSULATED RC BEAMS**

### ***8.5.1 General***

The above sections are concerned with an explicit solution for predicting the temperatures in bare RC beams exposed to a standard fire. It is expected that such a solution can also be extended to insulated RC beams if the fire insulation layer is approximated as an equivalent concrete layer (Wickstrom and Hadziselimovic 1996). In other words, the temperature analysis of an insulated RC beam turns into that of a bare RC beam with an enlarged cross-section by the equivalent concrete layer. Figs. 8.11a and 8.11b shows a schematic of the one-dimensional heat transfer in an RC member with a fire insulation layer and an equivalent concrete layer, respectively. Thus, it is clear that the key is to determine the thickness of the equivalent concrete layer by relating it to the thickness and thermal properties of the fire insulation layer.

### 8.5.2 Transformation of a Fire Insulation Layer to an Equivalent Concrete Layer

Both the thickness ( $d_i$ ) and the thermal properties (i.e.,  $\lambda_a$ ,  $c_a$  and  $\rho_a$  for thermal conductivity, specific heat capacity and density, respectively) of the fire insulation layer influence the temperature field of an insulated RC member under fire exposure. Therefore, the thickness of an equivalent concrete layer (i.e.,  $d_{equ}$ ) is assumed to be expressed as a function of these parameters as follows:

$$d_{equ} = d_a k_\lambda k_{\rho c} \quad (8.22)$$

where  $d_a$  is the thickness of a concrete layer equivalent to a reference insulation layer, which has the thickness of  $d_i$  and specific thermal properties (i.e.,  $\lambda_a=0.10$  W/m·K;  $\rho_a c_a=750$  kJ/m<sup>3</sup>·K). The two specific values entitled to the insulation layer represent typical thermal properties of a light-weight insulation material at elevated temperatures (Wong and Ghajel 2003).  $k_\lambda$  and  $k_{\rho c}$  are two coefficients to consider the parametric effects of  $\lambda_a$  and  $\rho_a c_a$ , respectively.

To obtain the relationship between  $d_a$  and  $d_i$  for the fire insulation layer with the above-mentioned reference thermal properties, FE analyses were conducted on an insulated one-dimensional concrete member (Fig. 8.11a) to determine the time-dependent temperature evolution at the insulation-to-concrete interface under the ISO-834 standard fire exposure. In the FE analyses,  $\lambda_a$  and  $\rho_a c_a$  are assigned with the reference values while the value of  $d_i$  is changed. The analytical results are shown in Fig. 8.12a. Similarly, FE analyses were also conducted on an un-protected one-dimensional concrete member (Fig. 8.11b) to generate another group of temperature curves, which show the evolution of temperatures with time at different concrete depths (Fig. 8.12b). Through comparing Fig. 8.12a and Fig. 8.12b, it appears that any temperature curve in Fig. 8.12a can be approximated using a curve

interpolation in Fig. 8.12b if an appropriate concrete depth is chosen. In other words, it is possible to find out how thick an equivalent concrete layer should be in order to provide the same thermal barrier effect as an insulation layer does. To realize this approximation, a least-squares minimization process was performed for a given insulation thickness for the first four-hour fire exposure to find out the most appropriate concrete depth. The four-hour duration was chosen as it represents the maximum fire resistance rating adopted by the current fire design codes for RC beams [e.g., BS 8110-2 (1985), EN 1992-1-2 (2004), ACI 216.1 (2007) and AS 3600 (2009)].

Taking the 5 mm insulation thickness as an example, at first, the temperature rises for different concrete thicknesses  $\theta_{d_{ai}}$  ( $d_{ai}$  represents the concrete depths with a 5 mm interval along the thickness direction, since a 5 mm element size was used in the FE analysis) were normalized by the temperature rise  $\theta_{d_5}$  for the 5 mm insulation layer (Fig. 8.12a). The approximate value for  $d_a$  can be determined through least-squares minimization of the difference between the normalized value  $\theta_{d_{ai}}/\theta_{d_5}$  and 1.0. That is, regression analyses were conducted by increasing the equivalent concrete layer  $d_{ai}$  step by step (i.e., a 5 mm thickness interval) to find out the minimal value of the following function:

$$f(d_{ai}) = \sum_{i=1}^{240} [\theta_{d_{ai}}/\theta_{d_5} - 1]^2 \quad (8.23)$$

where  $i$  is the time interval for calculation (i.e., one minute). Fig. 8.13 shows the change of  $f(d_{ai})$  with  $d_{ai}$ . From this figure, it clearly seen that the minimum value of  $f(d_{ai})$  can be found when the thickness of concrete layer lies in between 35 mm to 40 mm when the thickness of the insulation layer is 5 mm. Therefore, the exact value for  $d_a$  can be further identified using a 0.1 mm increase of the thickness of concrete layer following a similar analytical procedure (see Fig. 8.13). The

temperatures corresponding to small step increases of the concrete thicknesses were obtained by a linear interpolation process. It can be found in Fig. 8.13 that 36.5 mm is the most appropriate thickness for the concrete layer, which is equivalent to a 5 mm thick fire insulation layer.

Fig. 8.14 shows the comparisons of the temperature profiles along the concrete member thickness direction, which were predicted based on a concrete member with a 5 mm thick fire insulation layer and concrete member with an additional 36.5 mm thick equivalent concrete layer, respectively. The original point of the  $x$  axis represents the interface between the fire insulation layer and the concrete member or the interface between the additional equivalent concrete layer and the original concrete member. The excellent agreement between the two cases indicates that, if the thickness of an equivalent concrete layer is selected in such a way that the temperature at the interface between the fire insulation layer and the original concrete beam is well predicted, the temperature profiles along the member thickness direction underneath the insulation layer can also be well predicted. Therefore, the soundness of the equivalent concrete thickness concept is further demonstrated for the temperature analysis of insulated concrete members exposed to the standard fire.

By repeating the above work, the relationship between the equivalent concrete thickness,  $d_a$ , and the fire insulation thickness,  $d_i$ , can be found as follows (Fig. 8.15):

$$d_a = c_1 \cdot d_i^{c_2} \quad (8.24)$$

where  $c_1 = 13.34$  and  $c_2 = 6.49 \times 10^{-1}$ . Both are empirical factors derived from the least-squares regression analysis.

Once the relationship between  $d_a$  and  $d_i$  for the reference thermal properties is found, further work is needed to investigate the parametric effects of thermal properties of the insulation layer (i.e.,  $k_\lambda$  and  $k_{\rho c}$ ). To achieve this objective, extensive FE parametric analyses were carried out on insulated one-dimensional concrete members. For these analyses, eight different thicknesses of fire insulation layer, nine different thermal conductivities and seven different products of specific heat capacity and density were investigated. Figs. 8.16a and 8.16b show the interfacial temperatures for these different thermal conductivities and different products of specific heat capacity and density, respectively (the thickness of fire insulation layer in these figures is 20 mm, i.e.,  $d_i = 20$  mm). It is obvious that the change of thermal conductivity leads to a dramatic change of the temperature responses, whereas the change of product of specific heat capacity and density does not. Through a least-squares optimization procedure, the two coefficients,  $k_\lambda$  and  $k_{\rho c}$ , which reflect the impact of the thermal conductivity as well as the product of specific heat capacity and density of insulation materials on the thickness of the equivalent concrete layer, respectively, can be obtained as follows ( Figs. 8.17 and 8.18):

$$k_\lambda = e_1 \cdot (\lambda_a)^{e_2} \quad (8.25)$$

and

$$k_{\rho c} = f_1 + f_2 \cdot (\rho_a c_a) \quad (8.26)$$

where  $e_1$ ,  $e_2$ ,  $f_1$  and  $f_2$  are the functions of the thickness of the insulation layer as follows:

$$e_1 = 7.93 \times 10^{-2} + 1.42 \times 10^{-2} d_i - 2.89 \times 10^{-4} d_i^2 + 1.78 \times 10^{-6} d_i^3 \quad (8.27)$$

$$e_2 = -9.36 \times 10^{-1} + 3.06 \times 10^{-2} d_i - 6.91 \times 10^{-4} d_i^2 + 4.72 \times 10^{-6} d_i^3 \quad (8.28)$$

$$f_1 = 9.81 \times 10^{-1} + 1.28 \times 10^{-3} d_i - 1.60 \times 10^{-4} d_i^2 + 1.01 \times 10^{-6} d_i^3 \quad (8.29)$$

$$f_2 = 2.42 \times 10^{-5} - 1.54 \times 10^{-6} d_i + 2.14 \times 10^{-7} d_i^2 - 1.34 \times 10^{-9} d_i^3 \quad (8.30)$$

The calculated results (i.e., equivalent concrete thicknesses) using the above equations are plotted in Figs. 8.17 and 8.18 with dotted lines, which are in close agreement with the FE parametric studies (i.e., different symbols for different insulation thicknesses). It should be mentioned that all the above equations were obtained by assuming constant thermal properties for an insulation layer during the fire exposure. In reality, the thermal properties of an insulation material may change with the elevated temperatures. In such a case, an incremental procedure needs to be adopted to determine the time-dependent temperature responses of an insulated concrete member. Following such an approach, the thermal properties of an insulation layer can be entitled using an effective mean temperature of its overall depth obtained at the adjacent preceding time step. Since the temperature gradient along the insulation thickness is nonlinear, the effective mean temperature of the insulation layer is not equal to the average value of the temperatures of the inner side ( $T_i$ ) and the outer side ( $T_o$ ). For a better calculation accuracy, the effective mean temperature of the insulation layer can be calculated using  $(\frac{1}{3}T_o + \frac{2}{3}T_i)$  according to the recommendation by Melinek and Thomas (1987). A trial temperature calculation process of several insulated concrete beams (see the next section for more details) shows that, once a small enough time step (e.g., 1~2 minutes) is adopted, the above-mentioned incremental procedure can achieve a satisfactory accuracy.

## **8.6 VERIFICATION OF THE PROPOSED METHOD FOR INSULATED RC BEAMS**

Two successfully insulated beams (i.e., Beams 6 and 7) from Blontrock et al. (2000)'s test and another two insulated FRP-strengthened RC beams reported by Williams et al. (2008) were selected to validate the proposed explicit solution for the temperature analysis of insulated concrete beams. In Blontrock et al.'s (2000) test, Beam 6 was protected by a U-shaped Promatect H insulation system with a 40 mm thickness for the bottom and a 25 mm thickness for the two sides. Beam 7 had the similar protection system as Beam 6, but the bottom was protected with a 25 mm thick Promatect H and the thickness of the side insulation was 12 mm. These two beams were chosen for comparisons because they were successfully protected throughout the entire fire exposure, while the fire insulation of the other FRP-strengthened RC beams failed during the fire exposure.

Figs. 19a and 19b compare the tested and predicted temperatures of steel rebar and at the interface between the concrete and the fire insulation layer by ignoring the existence of externally bonded FRP strengthening laminates. As the thermal properties of Promatect H vary with elevated temperatures, the equivalent concrete thickness of the insulation layer was accordingly changed with the time increase of the fire exposure, and therefore, an incremental procedure was adopted to calculate the temperature fields of the insulated beam section. It is seen in these two figures that the explicit solution provides excellent agreement with the FE numerical results. Both the proposed method and the FE analysis give fairly accurate predictions of test data except a slight difference at the temperature around 100 °C. This slight difference is induced by the moisture migration and evaporation during the fire exposure, which is explained in detail in Section 7.4.1. Such a slight difference in

temperature response is believed to have a marginal effect on the fire resistance analysis of insulated FRP-strengthened RC beams as demonstrated in Section 7.5.

Another two insulated FRP-strengthened RC beams tested by Williams et al. (2008) were protected with a two-component coating system, which consisted of a plaster-based vermiculite/gypsum (VG) layer and a fire-resistant texture coating. The VG layer insulation was applied with a thickness of 25 mm for Beam I and 38mm for Beam II along the entire beam length. The fire-resistant coating was installed with the same thickness of 0.1 mm for both beams. As reported by Williams et al. (2008), the texture coating was burnt out within 4 minutes after the initiation of the fire test. Therefore, the fire-resistant coating was ignored and only the VG insulation was considered in both the proposed explicit solution and the FE analysis. During the temperature calculation process, an incremental procedure was also adopted regarding the temperature-dependent thermal properties of VG insulations.

Fig. 8.20 provides comparisons of the temperatures measured at the FRP-to-concrete interface by three thermocouples against the values predicted by the FE analysis and the explicit solution. During the analyzing process, the flanges of T-section were ignored due to its negligible effect on the interfacial temperatures. That means, a rectangular section with the depth of 400 mm and the width of 300 mm (i.e., the web width of the T-section) was assumed for the analysis. Besides, the predicted temperatures by Williams et al. (2008) using numerical heat transfer models are also provided in the figure for comparisons. It is indicated that, at the early stages of the fire tests, Williams et al.'s model, the FE analysis and the proposed explicit solution lead to similar predictions while at the latter stages the FE analysis and the explicit solution yield better agreement with the test data. This better accuracy is attributed to a more reasonable consideration of the thermal boundary conditions for heat transfer analyses, which was not provided in Williams et al.'s (2008) model.

It should be also noted that the furnace temperature is different from the surface temperature of the exposed insulated RC beams due to the convective and radiative heat exchanges between the hot gases and the beam surfaces. Wickstrom and Hadziselimovic (1996) defined a ratio of the beam surface temperature rise to that of the fire temperature using the symbol “ $n_w$ ” (i.e., interfacial thermal resistance) and proposed an equation to predict it. However, in the existing literature, the surface temperature of insulated FRP-strengthened RC beams exposed to fire were rarely available. Only Williams et al. (2008) measured the surface temperatures in their fire tests using three thermocouples for each beam specimen.

The proposed explicit solution can be employed to predict the surface temperatures of beam specimens as well. Fig. 8.21 compares the predicted surface temperatures of Williams et al.’s (2008) tested beams and the measured values. The predicted results by Wickstrom and Hadziselimovic’s equation (1996) are also presented for comparison purpose. In the figure, the test results are the average values of readings measured by three thermocouples and represented by the ratio (i.e.,  $n_w$ ) of the beam surface temperature rise to the furnace temperature rise. It is seen that the present explicit solution tends to slightly underestimate the measured values at around 30 minutes after the beginning of the fire tests, probably due to the unstable heat release of fire during that period. Afterwards, reasonably good agreement is seen between the predictions and the test results. Overall, the explicit solution performs much better than the proposed equation by Wickstrom and Hadziselimovic (1996). Therefore, the proposed explicit solutions for temperature analyses of bare and insulated RC beams can predict reasonably well not only the temperature profiles inside the RC beams but also the interfacial temperatures between the fire insulation layer and the inner concrete.

## **8.7 CONCLUSIONS**

This chapter has presented an accurate yet simple method for predicting temperatures in bare and insulated RC beams exposed to the standard fire. In formulating the simple method for bare RC beams, the FE model was used for parametric studies to identify the influencing parameters and to generate temperature data for regression analyses. In this simple method, the temperature at any point of a beam cross-section is given as a function of its coordinates, the beam width and the fire exposure time. Predictions from the proposed simple method were compared with numerical predictions from FE analyses as well as fire test data. These comparisons showed that the proposed method provides more accurate predictions of the fire test results than the three existing methods of the same kind. For insulated RC beams, the fire insulation layer is regarded as an equivalent concrete layer and thus the temperature analysis of an insulated concrete beam becomes that of a bare concrete beam with an enlarged section. Based on extensive parametric studies on the one-dimensional heat transfer analyses of bare and insulated concrete members using the FE model, the relationship between the thickness of the fire insulation layer and that of the equivalent concrete layer is obtained; that is, the thickness of the equivalent concrete layer can be expressed as the function of the thickness and the thermal properties of the insulation materials. The explicit solution for insulated RC beams has also been validated by comparing the temperature predictions with those obtained from FE parametric analyses as well as existing standard fire tests. Due to their explicit forms, the proposed simple methods for both bare and insulated RC beams can be easily implemented into a spreadsheet for direct use in practical fire safety design.

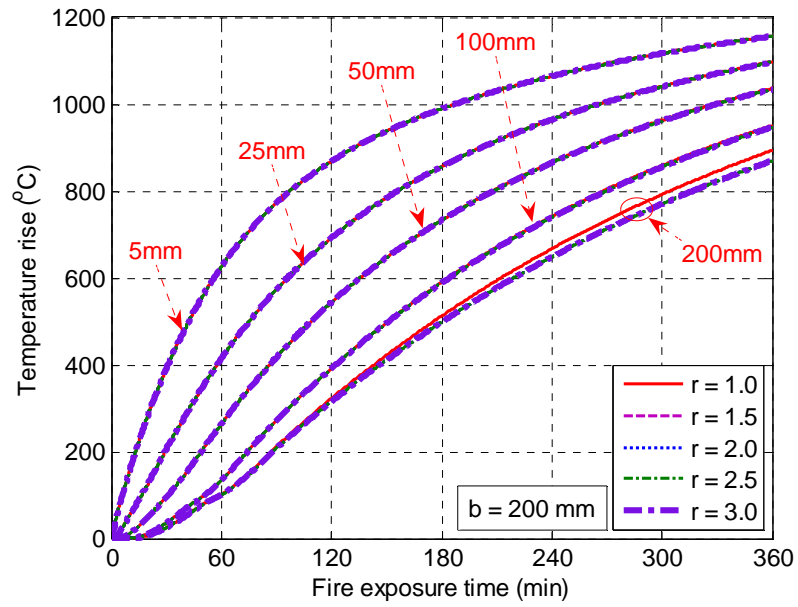
## **8.8 REFERENCES**

- Abbasi, A. (2003). "Behavior of GFRP rebars reinforced concrete elements under elevated temperature and fire." Ph.D. thesis, Queen Mary University of London, London, UK.
- Abbasi, A., and Hogg, P.J. (2005). "A model for predicting the properties of the constitutive of a glass fiber rebar reinforced concrete beam at elevated temperatures simulating a fire test." *Composites Part B: Engineering*, Vol. 36, No. 5, pp. 384-393.
- ACI 216.1. (2007). *Code Requirements for Determining Fire Resistance of Concrete and Masonry Construction Assemblies*, American Concrete Institute, Michigan, America.
- AS 3600. (2009). *Concrete Structures*, Standards Association of Australia, Sydney, Australia.
- Bennetts, I.D., Proe, D.J., and Thomas, I.R. (1987). *Guidelines for Assessment of Fire Resistance of Structural Steel Members*, Australian Steel Institute, Australia.
- Biondini, F.M., and Nero, A. (2011). "Cellular finite beam element for nonlinear analysis of concrete structures under fire." *Journal of Structural Engineering*, ASCE, Vol. 137, No. 5, pp. 543-558.
- Blontrock, H., Taerwe, L., and Vandeveld, P. (2000). "Fire tests on concrete beams strengthened with fiber composite laminates." *Proceeding of the Third Ph.D. Symposium in Civil Engineering*, Vienna, Austria, pp. 151-161.
- BS 8110-2. (1985). *Structural Use of Concrete --- Part 2: Code of Practice for Special Circumstances*, British Standards Institute, Milton Keynes, UK.
- Carslaw, H.S., and Jaeger, J.C. (1995). *Conduction of Heat in Solids*, Second Edition, Clarendon Press, Oxford, England.
- Desai, S.B. (1995). "Shear resistance at normal and high temperatures of reinforced concrete members with links and central bars." Ph.D. thesis, City University London, London, UK.
- Desai, S.B. (1998). "Design of reinforced concrete beams under fire exposure conditions." *Magazine of Concrete Research*, Vol. 50, No. 1, pp. 75-83.
- Dotreppe, J.C., and Franssen, J.M. (1985). "The use of numerical models for the fire analysis of reinforced concrete and composite structures." *Engineering Analysis*, Vol. 2, No. 2, pp. 67-74.
- Eamon, C.D., and Jensen, E. (2012). "Reliability analysis of prestressed concrete beams exposed to fire." *Engineering Structures*, Vol. 43, pp. 69-77.

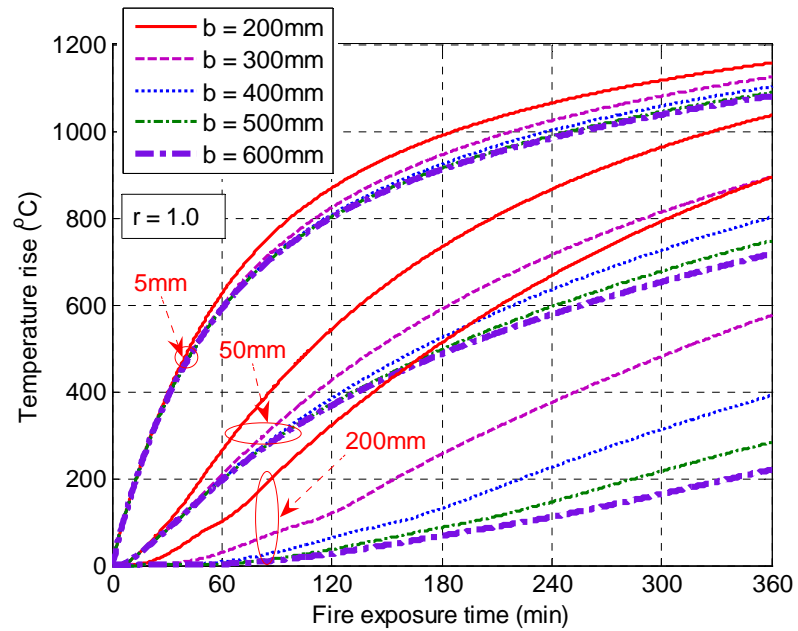
- European Convention for Constructional Steelwork (ECCS). (1983). *European Recommendations for the Fire Safety of Steel Structures*, Elsevier Scientific Publishing Company, Amsterdam.
- EN 1992-1-2 (2004). *Eurocode 2: Design of Concrete Structures --- Part 1-2: General Rules --- Structural Fire Design*, British Standards Institution, London, UK.
- EN 1993-1-2 (2005). *Eurocode 3: Design of Steel Structures --- Part 1-2: General Rules --- Structural Fire Design*, British Standards Institution, London, UK.
- Federation International de la Precontrainte-Comite Euro-International du Beton (FIP/CEB) (2004). *FIP/CEB Report on Methods of Assessment of the Fire Resistance of Concrete Structural Members*, Cement and Concrete Association, Slough. UK.
- Harmathy, T.Z. (1965). "Effect of moisture on the fire endurance of building elements." *Moisture in Materials in Relation to Fire Tests*, ASTM STP 385, American Society for Testing and Materials, pp.74-95.
- Harmathy, T.Z., Sultan, M.A., and MacLaurin, J.W. (1987). "Comparison of severity of exposure in ASTM E119 and ISO 834 fire resistance tests." *Journal of Testing and Evaluation*, Vol. 15, No. 6, pp. 371-375.
- Harmathy, T.Z. (1993). *Concrete Design and Construction Series: Fire Safety Design and Concrete*, Longman Scientific and Technical, London, UK.
- Hertz, K. (1981). "Simple temperature calculations of fire exposed concrete constructions." *Report No. 159*, Institute of Building Design, Technical University of Denmark, Lyngby, Denmark.
- Hodhod, O.A., Rashad, A.M., Abdel-Razek, M.M., and Ragab, A.M. (2009). "Coating protection of loaded RC columns to resist elevated temperature." *Fire Safety Journal*, Vol. 44, No. 2, pp. 241-249.
- Khoury, G.A. (2008). "Passive fire protection of concrete structures." *Proceedings of the Institution of Civil Engineers -Structures and Buildings*, Vol. 161, No. 3, pp. 135-145.
- Lin, T.D., Gustafarro, A.H., and Abrams, M.S. (1981). "Fire Endurance of Continuous Reinforced Concrete Beams." *RD 072.01B*, Research and Development Bulletin, Portland Cement Association, Skokie, Illinois, America.
- Lin, T.D., Ellingwood, B., and Piet, O. (1988). "Flexural and shear behavior of reinforced concrete beams during fire tests." *NBS-GCR-87-536*, U.S. Department of Commerce, National Institute for Science and Technology, Center for Fire Research, Gaithersburg, MD, America.

- Melinek, S.J., and Thomas, P.H. (1987). "Heat flow to insulated steel." *Fire Safety Journal*, Vol. 12, No. 1, pp. 1-8.
- Morgan, P.H., Mercer, L.P., and Flodin, N.W. (1975). "General model for nutritional responses of higher order mechanisms." *Proceedings of the National Academy of Sciences of the United States of America*, Vol. 72, No. 11, pp. 4327-4331.
- Nigro, E., Cefarelli, G., Bilotta, A., Manfredi, G., and Cosenza, E. (2012). "Behavior of FRP reinforced concrete slabs in case of fire: theoretical models and experimental tests." *Advances in Structural Engineering*, Vol. 15, No. 4, pp. 637-652.
- Rafi, M.M. (2010). *Fire Performance of FRP Reinforced Concrete Beams: Experimental and Theoretical Studies*, LAP Lambert Academic Publishing, Germany.
- Rodrigo, B.C., Jaoao, B.M., and Ricardo, H.F. (2010). "Interaction diagram for reinforced concrete sections subjected to fire." *Engineering Structures*, Vol. 32, No. 9, pp. 2832-2838.
- Wade, C. (1991). "Method for fire engineering design of structural concrete beams and floor systems." *BRANZ Technical Recommendation No. 8*, Building Research Association of New Zealand, Wellington, New Zealand.
- Wang, Z.H., Au, S.K., and Tan, K.H. (2005). "Heat transfer analysis using a Green's function approach for uniformly insulated steel members subjected to fire." *Engineering Structures*, Vol. 27, No. 10, pp. 1551-1562.
- Wickstrom, U. (1985). "Temperature analysis of heavily-insulated steel structures exposed to fire." *Fire Safety Journal*, Vol. 9, No. 3, pp. 281-285.
- Wickstrom, U. (1986). "A very simple method for estimating temperatures in fire exposed concrete structures." *New Technology to Reduce Fire Losses and Costs*, S.J. Grayson and D.A. Smith, eds., Elsevier Applied Science, London, pp.186-194.
- Wickstrom, U., and Hadziselimovic, E. (1996). "Equivalent concrete layer thickness of a fire protection insulation layer." *Fire Safety Journal*, Vol. 26, No. 4, pp. 295-302.
- Williams, B., Kodur, V.K.R., Green, M.F., and Bisby, L. (2008). "Fire endurance of fiber-reinforced polymer strengthened concrete T-beams." *ACI Structural Journal*, Vol. 105, No. 1, pp. 60-67.
- Wong, M.B., and Ghojel, J.I. (2003). "Sensitivity analysis of heat transfer formulations for insulated structural steel components." *Fire Safety Journal*, Vol. 38, No. 2, pp. 187-201.

- Wu, H.J., Lie, T.T., and Hu, J.Y. (1993). "Fire resistance of beam-slab specimens --- experimental studies." Internal Report No. 641, Institute for Research in Construction, National Research Council Canada, Canada.
- Zhang, C., Li, G.Q., and Wang, Y.C. (2012). "Sensitivity study on using different formulae for calculating the temperature of insulated steel members in natural fires." *Fire Technology*, Vol. 48, No. 2, pp. 343-366.
- Zhou, X., and Zhang, J. (2003). "A theoretical study of the effect of coatings on concrete members under fire." *Magazine of Concrete Research*, Vol. 55, No. 2, pp. 143-149.



(a) Effect of the depth-to-width ratio



(b) Effect of the beam width

**Fig. 8.1** Effects of beam dimensions on mid-width temperature rises

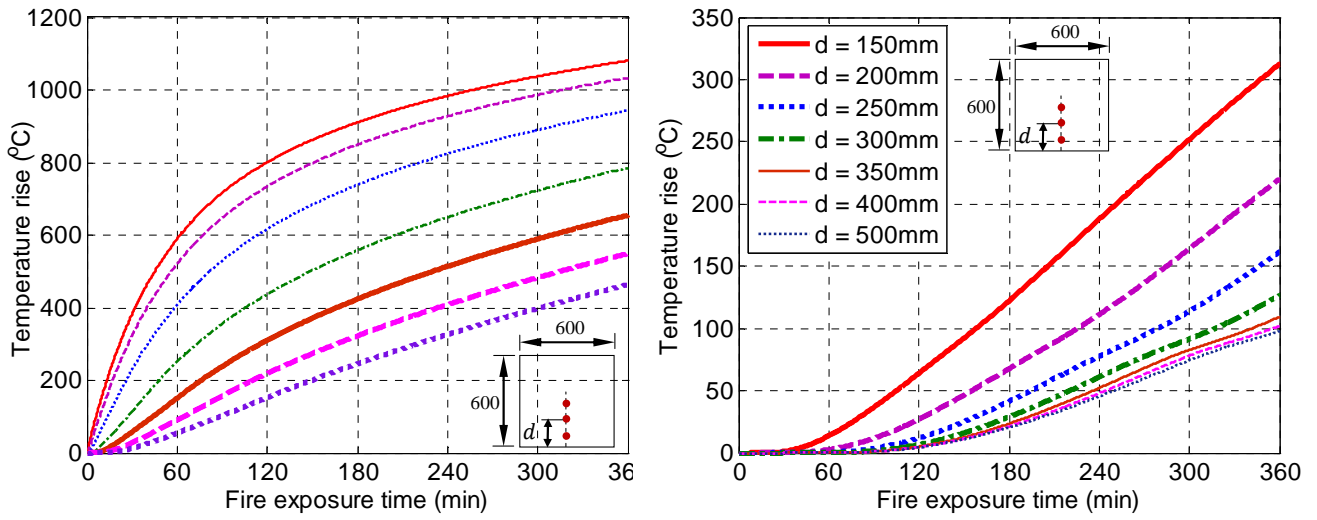
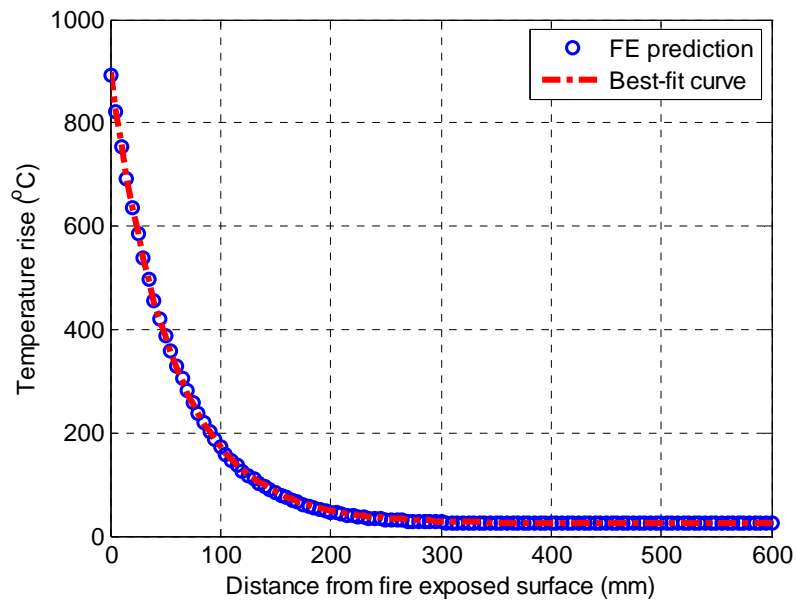
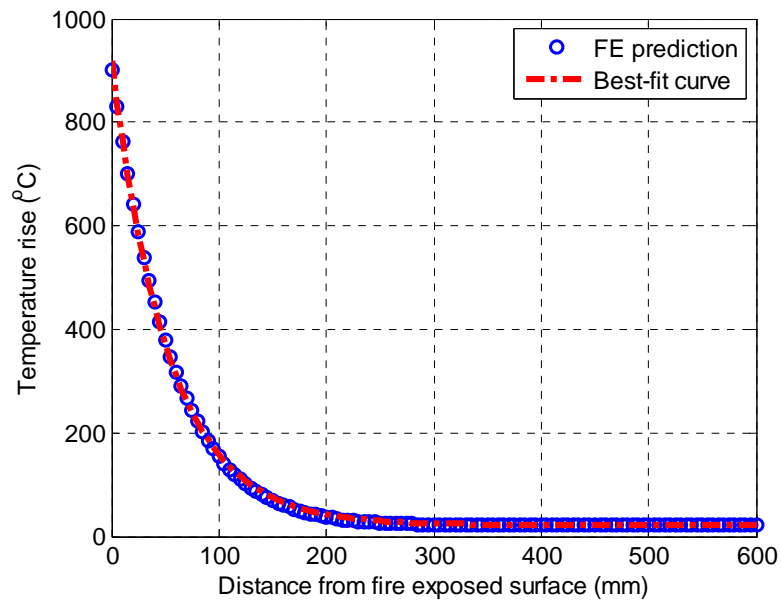


**Fig. 8.2** Mid-width temperature rises in a wide beam.



(a) Siliceous aggregate concrete

**Fig. 8.3**  $\theta_{d,120}$  defined as a function of distance from fire exposed surface.



(b) Calcareous aggregate concrete

**Fig. 8.3**  $\theta_{d,120}$  defined as a function of distance from fire exposed surface (Cont'd).

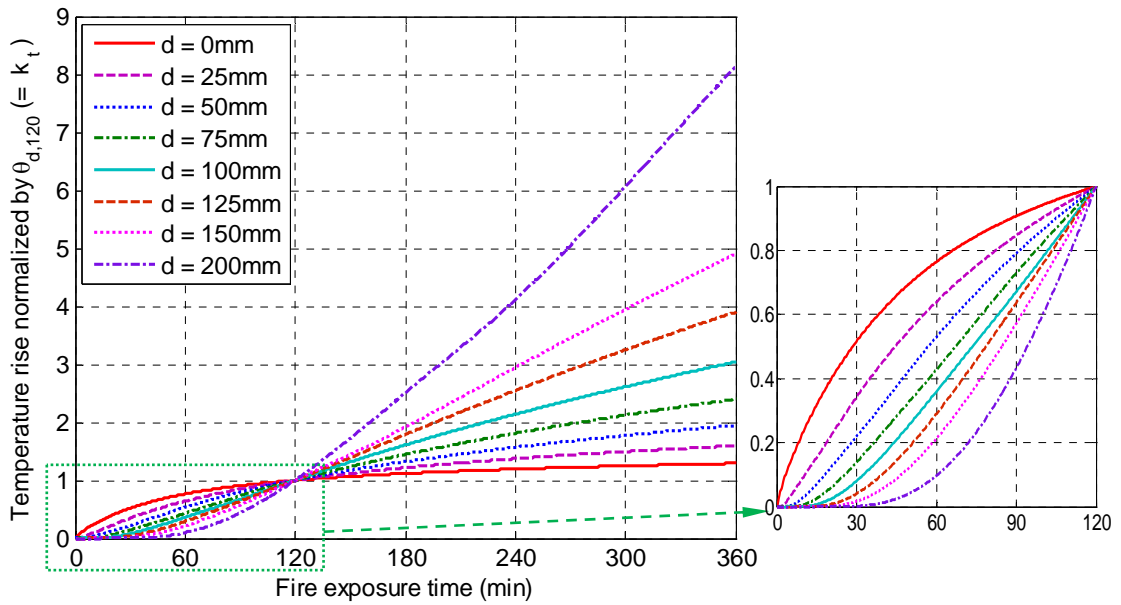


**Fig. 8.4** Temperature rises at different concrete depths with the fire exposure time.

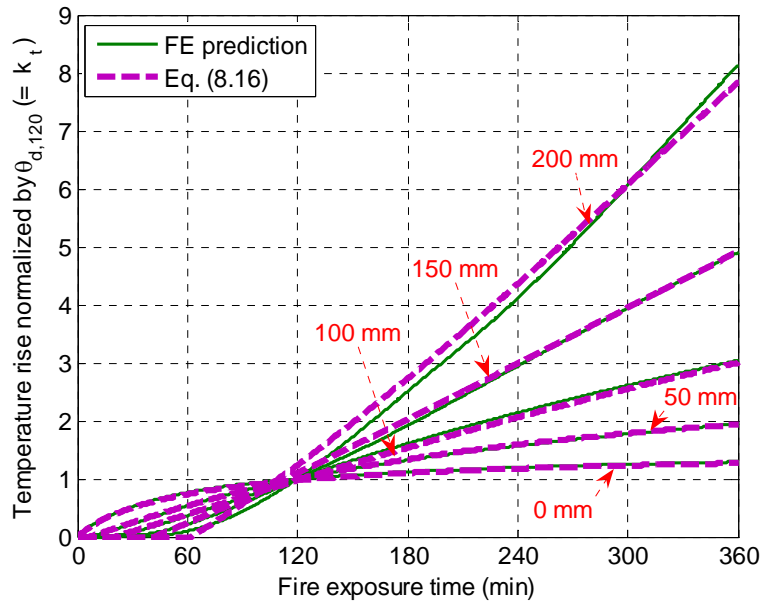


**Fig. 8.5** Comparisons of temperature rises at different concrete depths with the fire exposure time: predictions by proposed empirical equations vs. FE results.

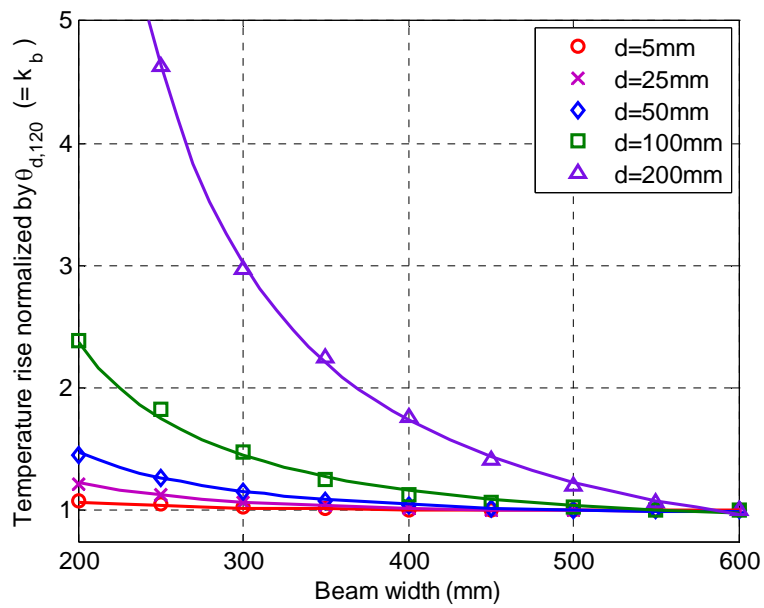
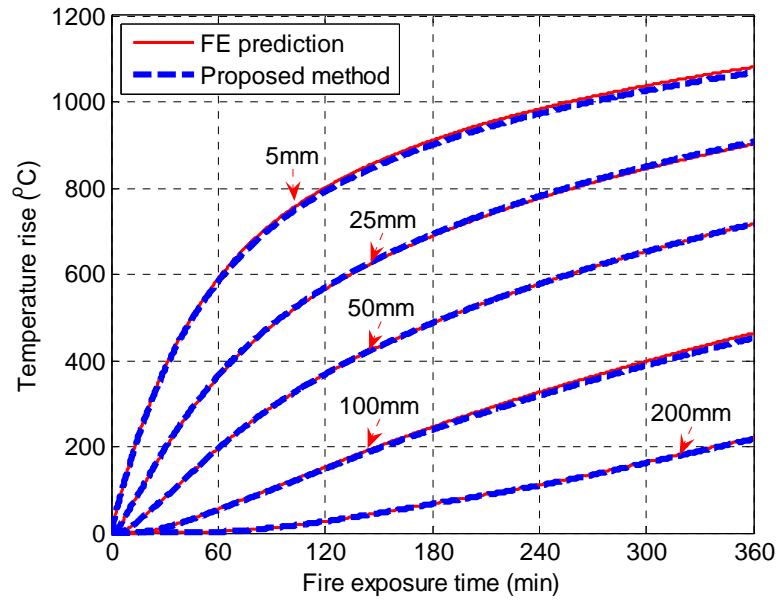
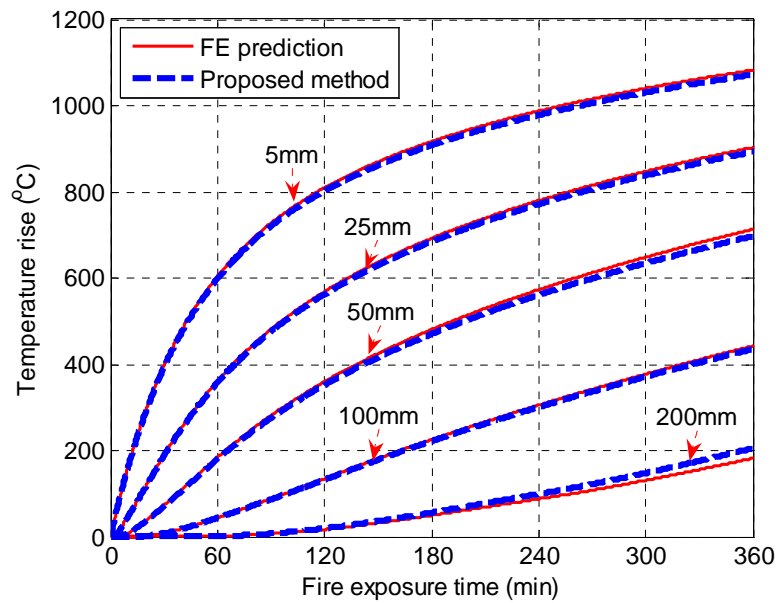


**Fig. 8.6** Effect of beam width on temperature rises at different concrete depths.

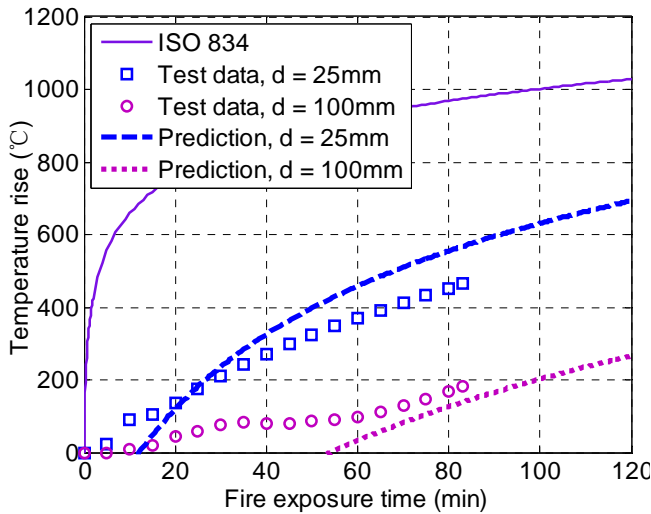


(a) Siliceous aggregate concrete beam

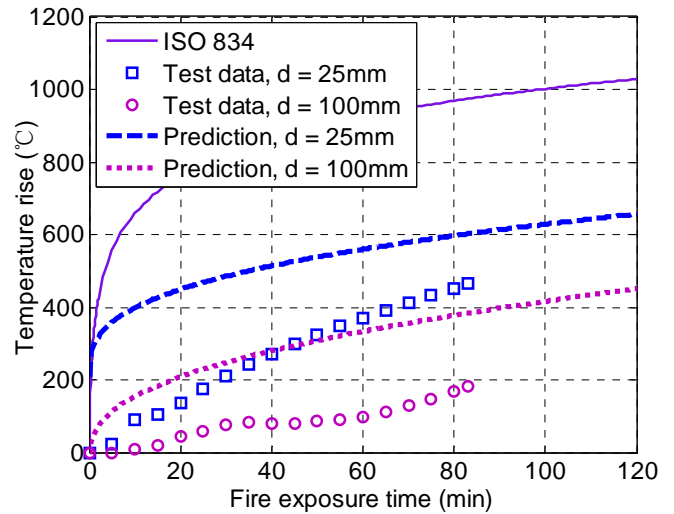


(b) Calcareous aggregate concrete beam

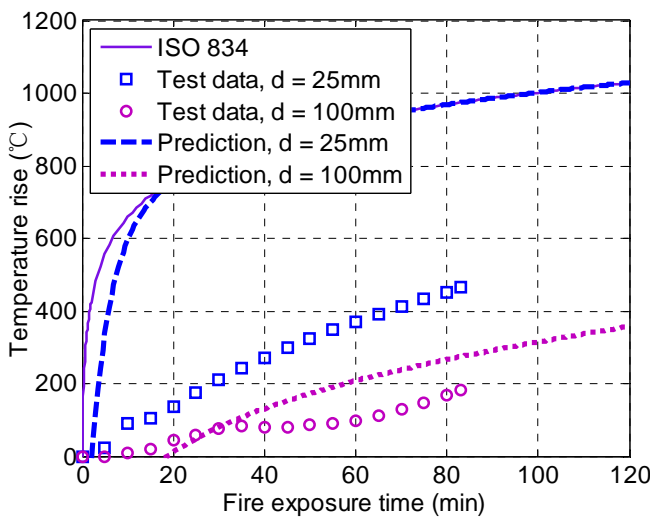
**Fig. 8.7** Mid-width temperature rises with exposure time: proposed explicit solution vs. FE prediction.



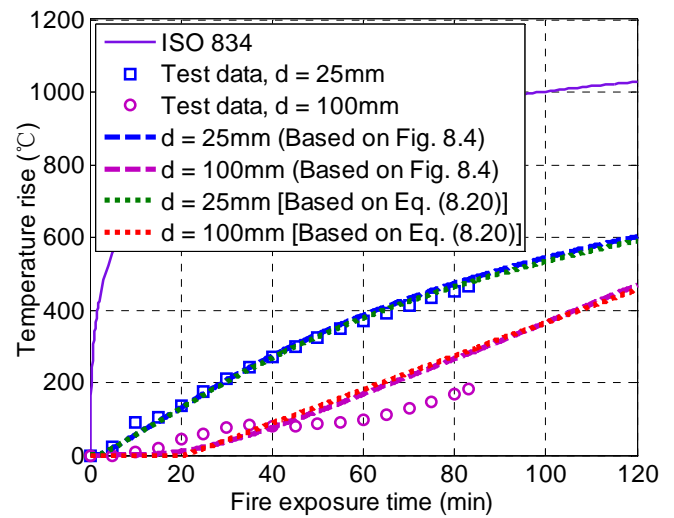
(a) Wickstrom (1986)



(b) Desai (1998)

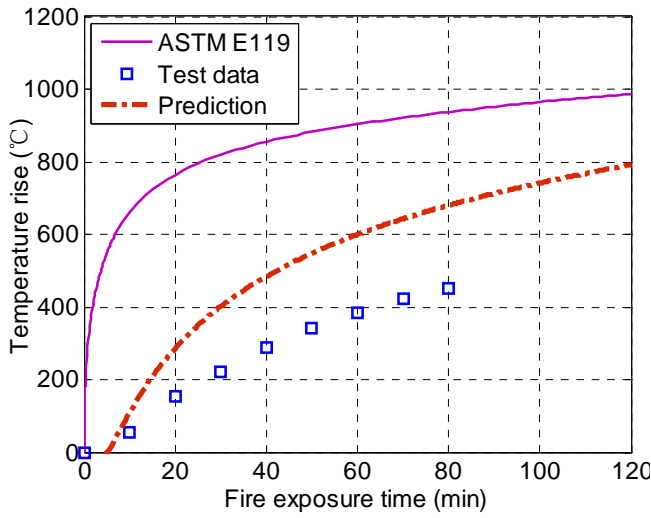


(c) Abbasi and Hogg (2005)

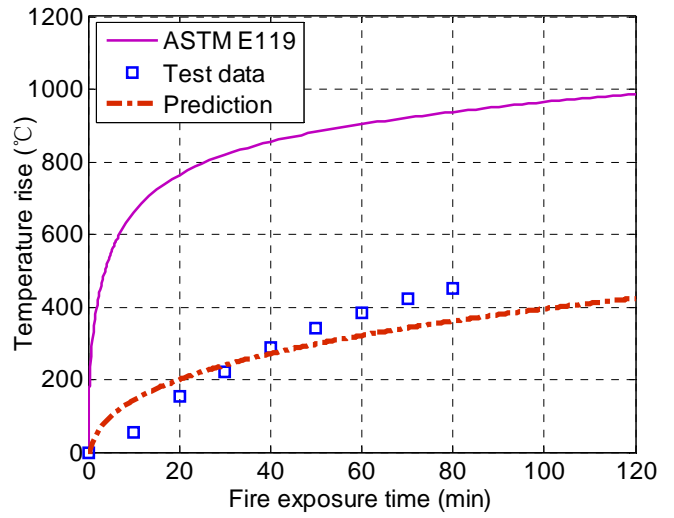


(d) Proposed method

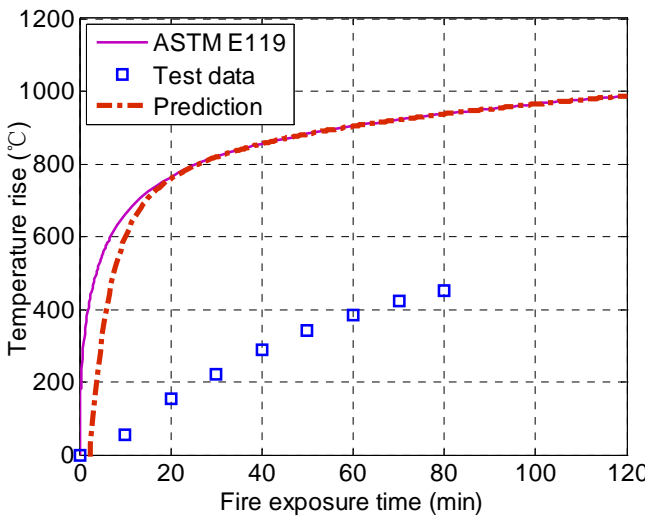
**Fig. 8.8** Comparisons between predictions from simple methods and test data for Wu et al.'s (1993) beams.



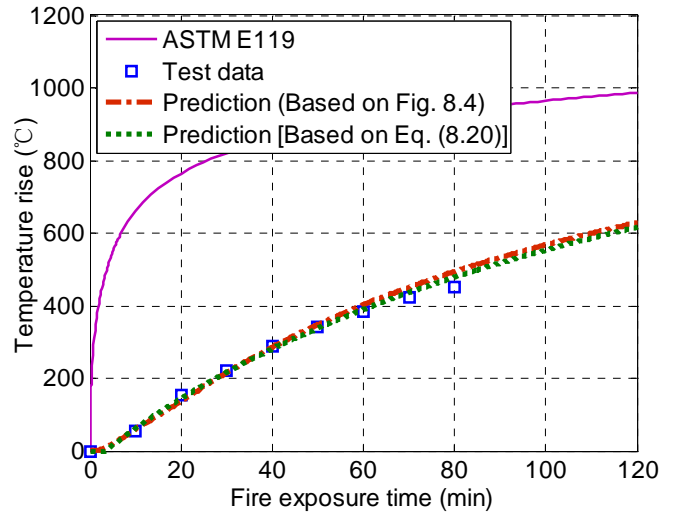
(a) Wickstrom (1986)



(b) Desai (1998)

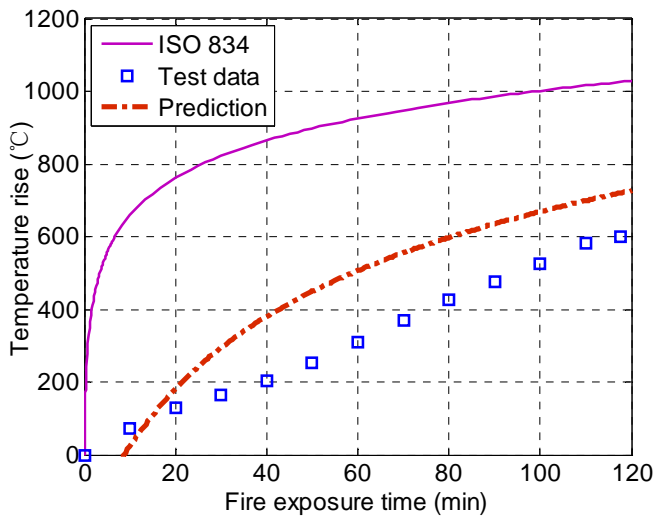


(c) Abbasi and Hogg (2005)

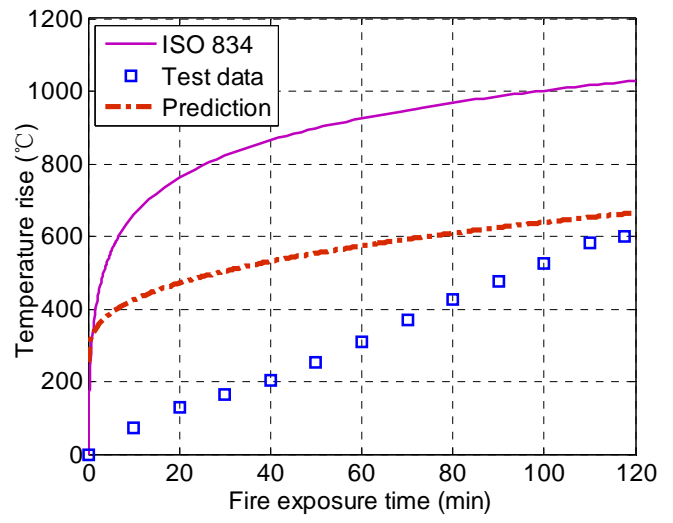


(d) Proposed method

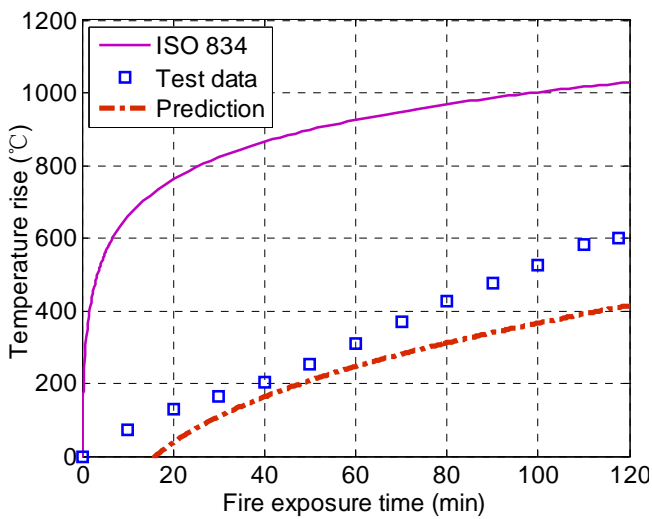
**Fig. 8.9** Comparisons between predictions from simple methods and test data for Lin et al.'s (1981) beam.



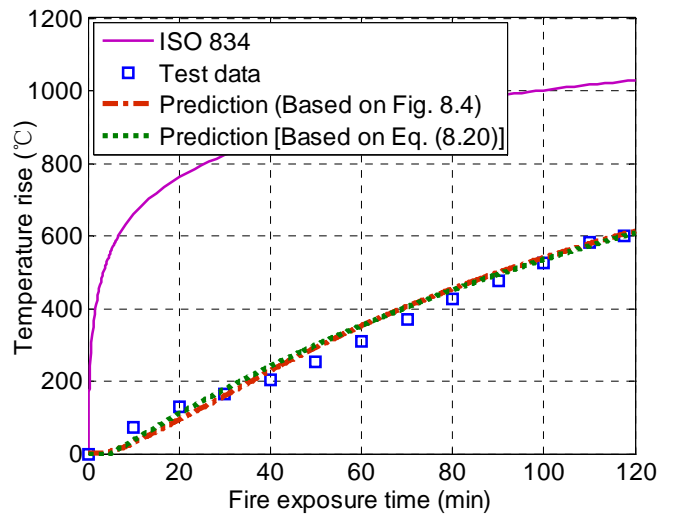
(a) Wickstrom (1986)



(b) Desai (1998)



(c) Abbasi and Hogg (2005)



(d) Proposed method

**Fig. 8.10** Comparisons between predictions from simple methods and test data for Dotrepe and Franssen's (1985) beam.

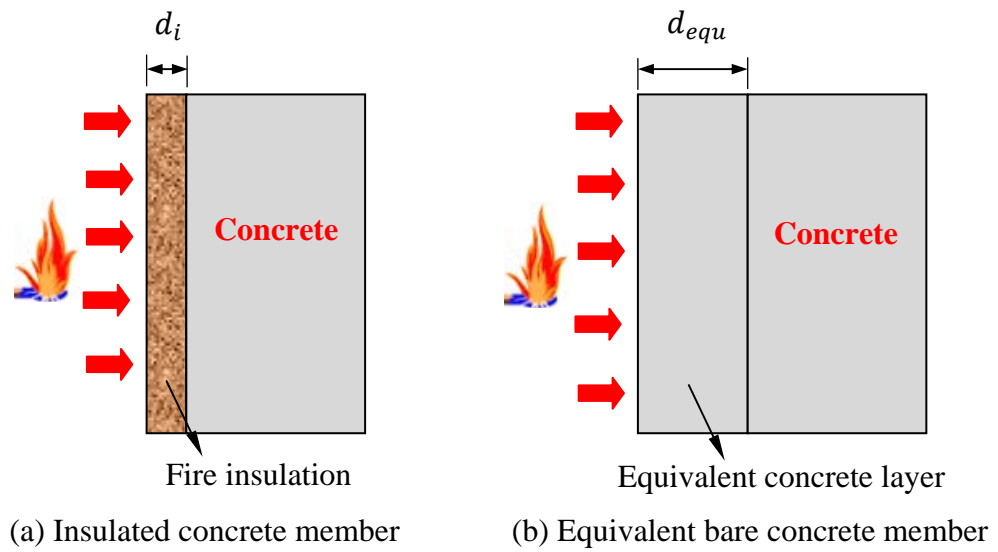
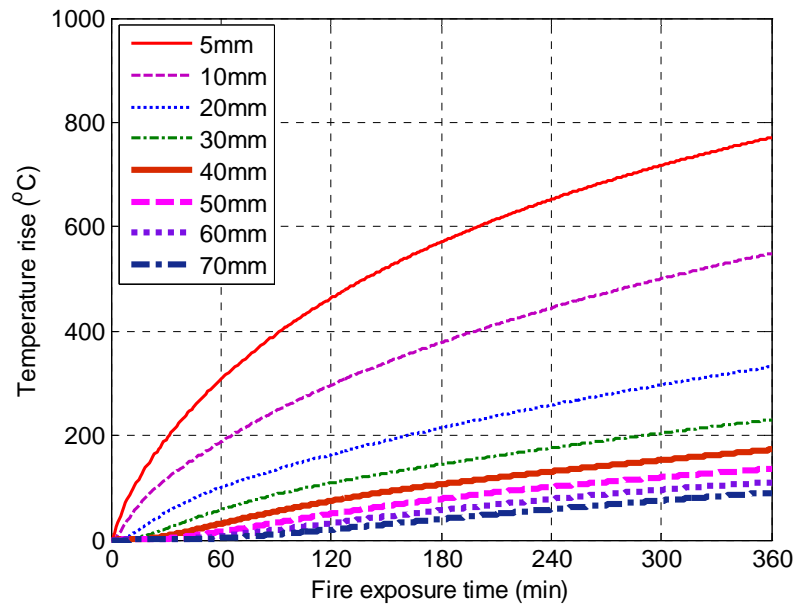
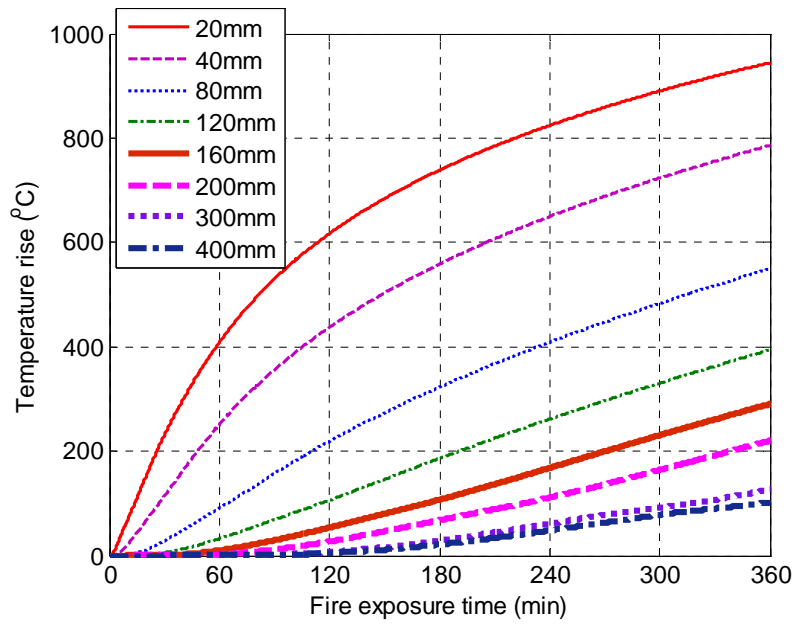


**Fig. 8.11** One-dimensional heat transfer problem.



(a) Temperature rises at the insulation layer-to-concrete interface with different insulation thicknesses

**Fig. 8.12** Comparisons of temperature profiles between bare and insulated concrete members.



(b) Temperatures at different concrete depths in a bare concrete member

**Fig. 8.12** Comparisons of temperature profiles between bare and insulated concrete members (Cont'd).

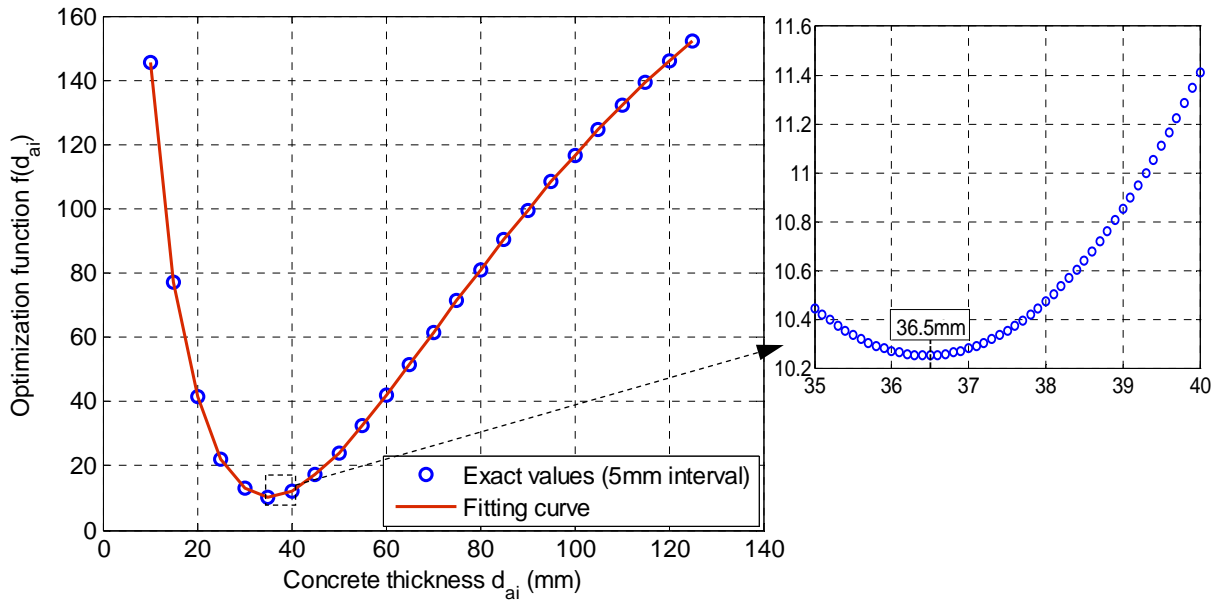


**Fig. 8.13** Optimization function vs. equivalent concrete thickness.

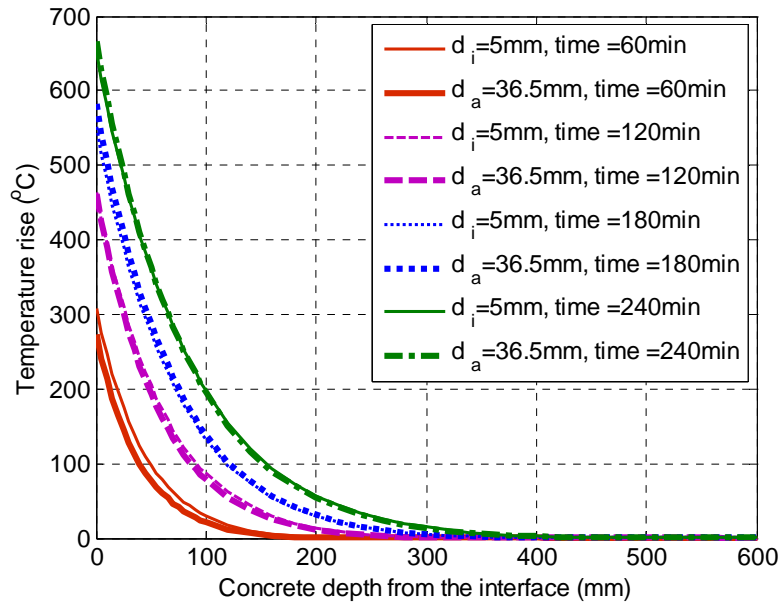


**Fig. 8.14** Temperature profiles along the thickness direction in the insulated concrete member and the equivalent bare concrete member.

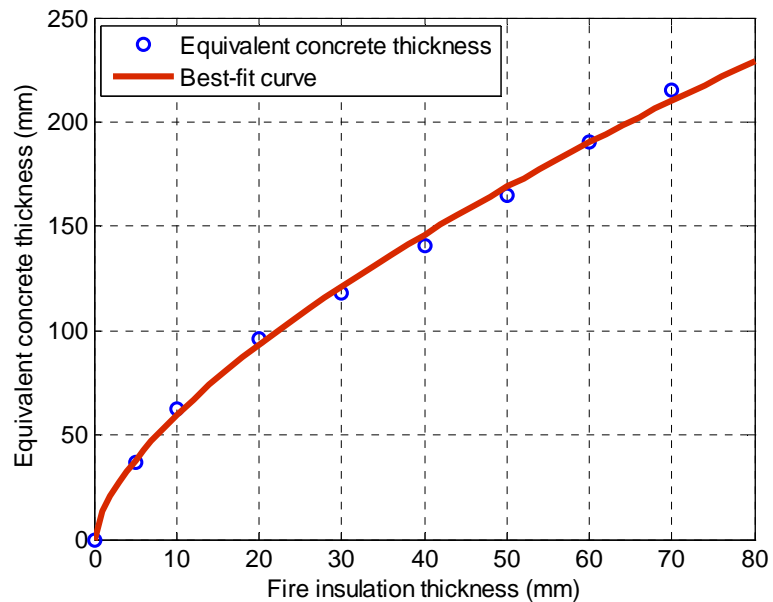
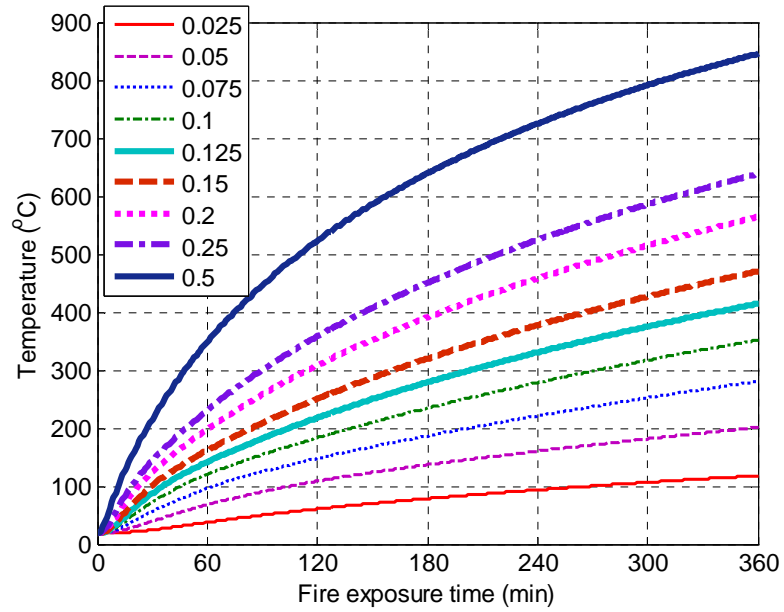
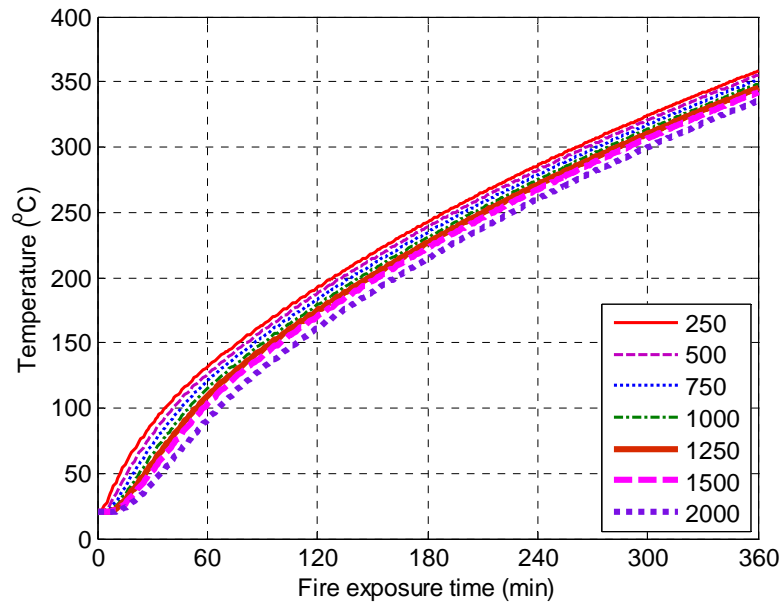


**Fig. 8.15** Determination of  $d_a$  as a function of fire insulation thickness.



(a) Effect of the thermal conductivity ( $\lambda_a$ , unit: W/m.K)



(b) Effect of the product of specific heat capacity and density ( $\rho_a c_a$ , unit: kJ/m<sup>3</sup>.K)

**Fig. 8.16** Temperature history at the fire insulation layer-to-concrete interface as a function of fire exposure time.

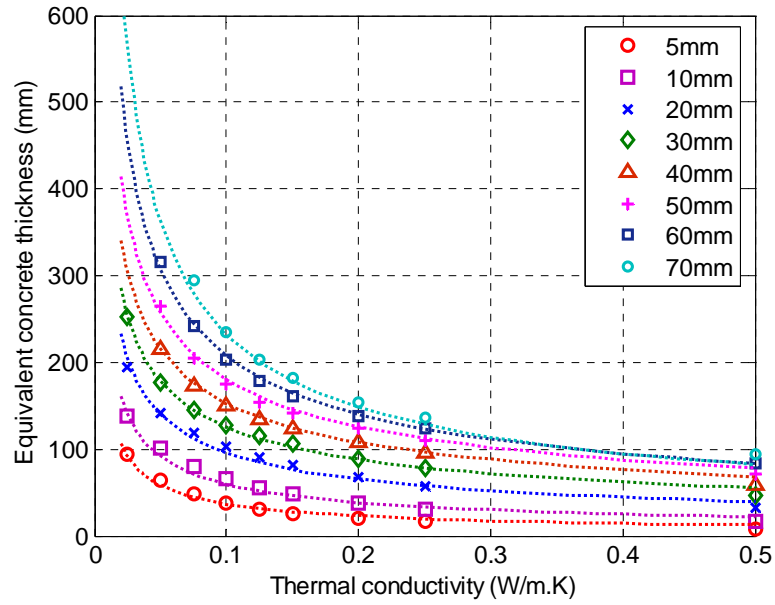


**Fig. 8.17** Effect of the thermal conductivity ( $\lambda_a$ ) on the equivalent concrete thickness.

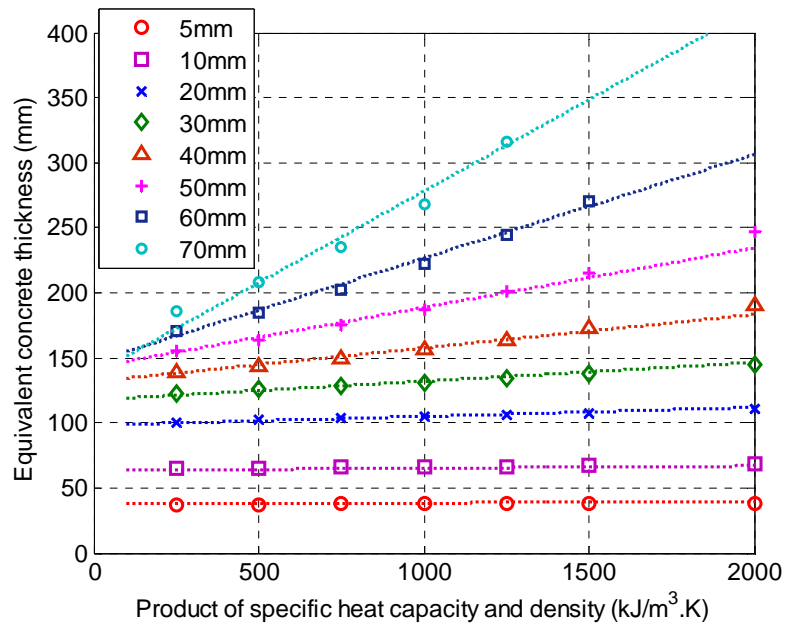


**Fig. 8.18** Effect of the product of specific heat capacity and density ( $\rho_a c_a$ ) on the equivalent concrete thickness.

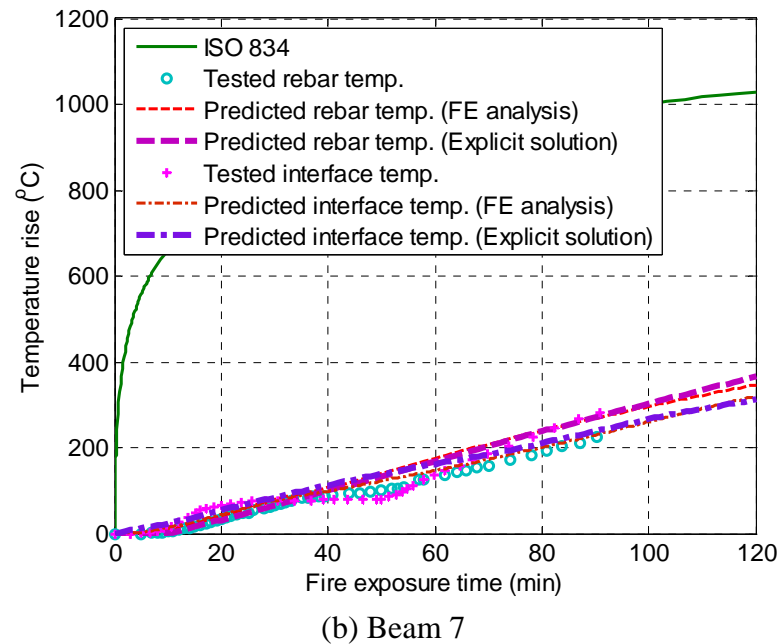
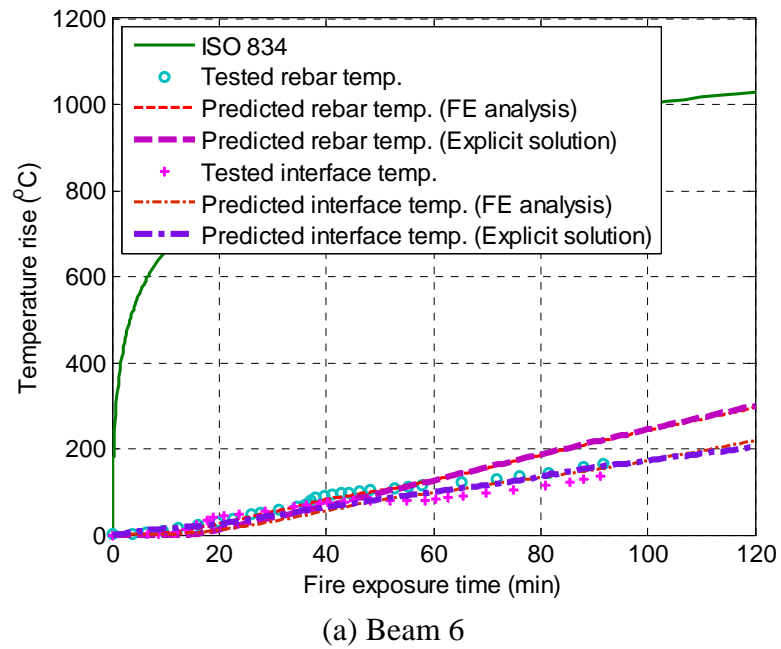
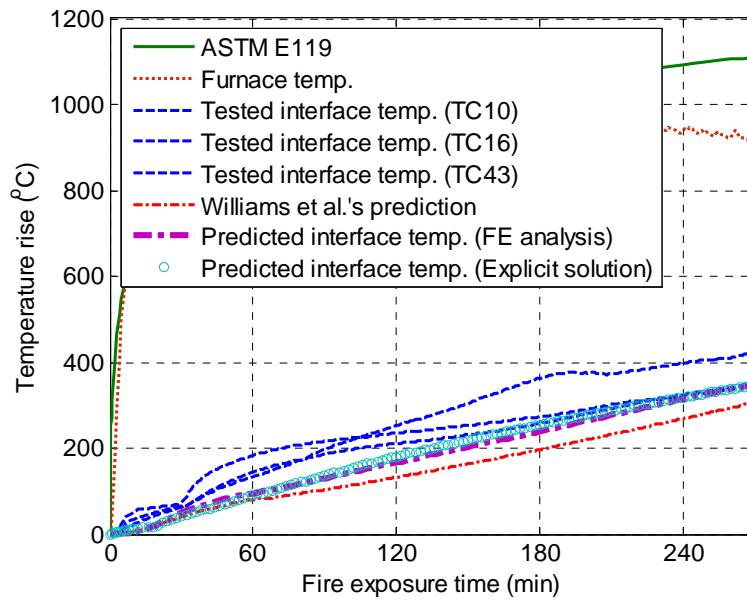
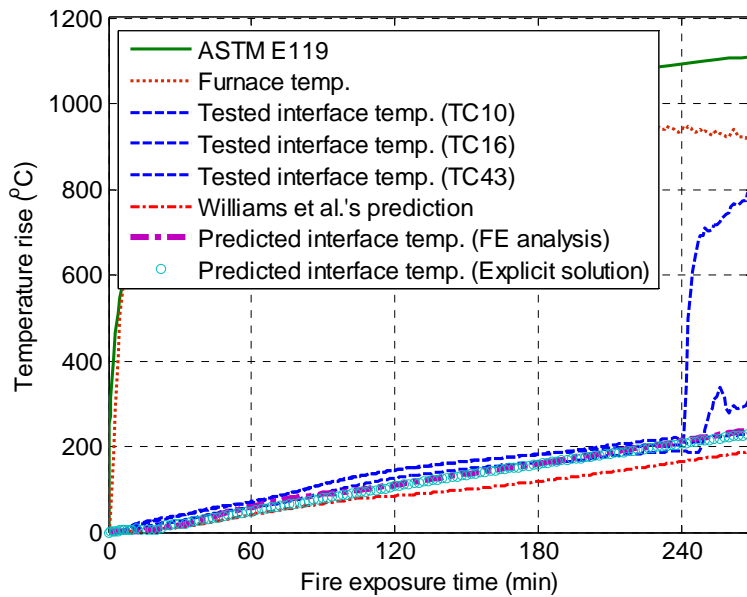


**Fig. 8.19** Predicted and measured temperature results for the insulated concrete beams tested by Blontrock et al. (2000).

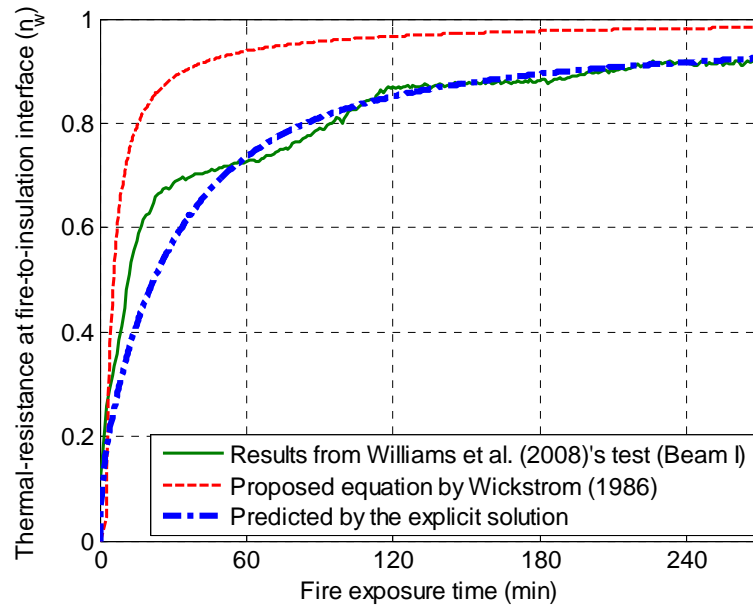


(a) Beam I

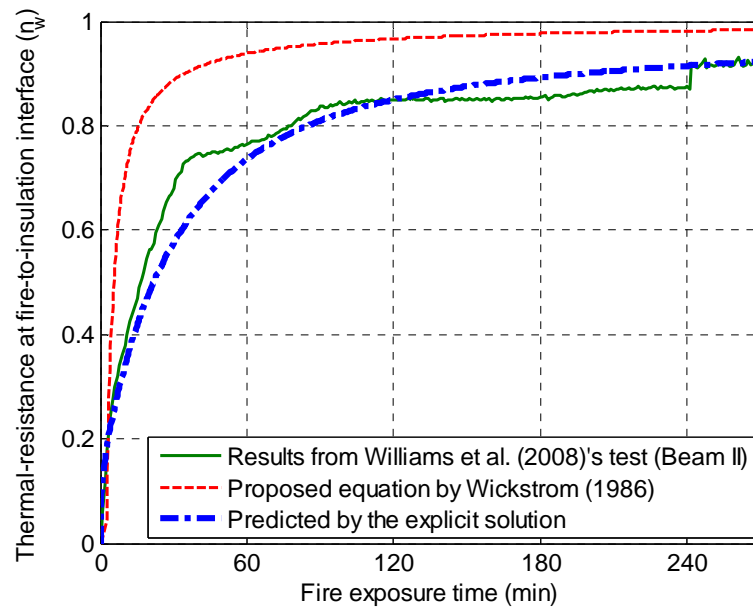


(b) Beam II

**Fig. 8.20** Predicted and measured temperature results for the insulated concrete beams tested by William et al. (2008).



(a) Beam I



(b) Beam II

**Fig. 8.21** Comparisons of thermal resistance at the fire-to-insulation interface for beams tested by Williams et al. (2008).

**Table 8.1** Cross-sections examined in the FE parametric study

| Purpose                                  |                                      | Parameter | Cross-section (mm × mm)                      |
|--|--------------------------------------|-----------|--|
| Identification of significant parameters | Depth-to-width ratio                 |           | 200×200; 200×300; 200×400; 200×500; 200×600. |
|  | Beam width                           |           | 200×200; 300×300; 400×400; 500×500; 600×600. |
| Formulation of the simple method         | Mid-width temperatures in wide beams |           | 600×600                                      |
|  | Beam width                           |           | 200×600; 300×600; 400×600; 500×600; 600×600. |
|  | Temperatures of corner concrete      |           | 600×600                                      |

**Table 8.2** Coefficients  $m_i$  determined through least-square regression analysis

|       | $0 \text{ mm} \leq d \leq 75 \text{ mm}$   | $75 \text{ mm} < d \leq 200 \text{ mm}$  |
|-------|--|--|
| $t_1$ | $m_1=-4.34 \times 10^{-3}, m_2=-4.34 \times 10^{-3}, m_3=1.27 \times 10^{-4},$<br>$m_4=-1.73 \times 10^{-6}, m_5=8.85 \times 10^{-9}.$ | $m_1=-8.40 \times 10^{-1}, m_2=3.69 \times 10^{-2}, m_3=-5.53 \times 10^{-4},$<br>$m_4=3.15 \times 10^{-6}, m_5=-6.54 \times 10^{-9}.$ |
| $t_2$ | $m_1=4.85 \times 10^1, m_2=-4.49 \times 10^{-1}, m_3=2.41 \times 10^{-1},$<br>$m_4=-5.37 \times 10^{-3}, m_5=7.15 \times 10^{-5}.$     | $m_1=-6.02 \times 10^4, m_2=2.23 \times 10^3, m_3=-2.97 \times 10^1,$<br>$m_4=1.63 \times 10^{-1}, m_5=-3.05 \times 10^{-4}.$          |
| $t_3$ | $m_1=1.531, m_2=2.54 \times 10^{-2}, m_3=1.28 \times 10^{-4},$<br>$m_4=-4.31 \times 10^{-7}, m_5=9.64 \times 10^{-9}.$                 | $m_1=1.73 \times 10^2, m_2=-6.17, m_3=7.70 \times 10^{-2},$<br>$m_4=-3.84 \times 10^{-4}, m_5=7.09 \times 10^{-7}.$                    |
| $t_4$ | $m_1=9.29 \times 10^{-1}, m_2=-1.19 \times 10^{-3}, m_3=1.72 \times 10^{-4},$<br>$m_4=-2.03 \times 10^{-6}, m_5=1.02 \times 10^{-8}.$  | $m_1=2.18, m_2=-3.99 \times 10^{-2}, m_3=4.31 \times 10^{-2},$<br>$m_4=-1.75 \times 10^{-6}, m_5=2.48 \times 10^{-9}.$                 |

# PERFORMANCE-BASED APPROACH FOR PREDICTING THE FIRE RESISTANCE OF FRP- STRENGTHENED RC BEAMS

### 9.1 INTRODUCTION

Design guidelines for FRP-strengthened RC structures at ambient temperature are widely available. However, these guidelines do not provide performance-based fire-resistance design approaches although some prescriptive provisions have existed by ignoring the contribution of the FRP strengthening system in a fire event (ACI 2008; fib 2001).

To correct the above deficiency, this chapter presents a performance-based approach for the fire-resistance design of FRP-strengthened RC beams. The approach provides a three-level (i.e., I, II and III) design concept based on a tradeoff between the strength contribution of the FRP strengthening system and the required fire resistance rating. Fig. 9.1 provides a description of this three-level design concept, in which the horizontal axis represents the strength contribution provided by the FRP strengthening system and the vertical axis is the required fire-resistance period. It is clearly seen that, when a low level of fire resistance (i.e., Level I) is required, fire insulation is not needed as the pre-strengthening RC beam can satisfy the required fire resistance rating even under the new service load, regardless of the extent of FRP strengthening. However, as FRP composites are flammable and the ignition process generates densely toxic fumes and promotes flame spread (Bisby 2003), a thin coating or cement mortar layer is thus needed to protect the FRP composites.

This thin coating/mortar layer contributes little to the fire performance of the strengthened beams, and therefore, it can be ignored during the fire performance evaluation of FRP-strengthened RC beams. As a consequence, the fire resistance evaluation of FRP-strengthened RC beams turns out to be that of un-protected RC beams (i.e., bare RC beams). The tabulated methods specified in existing design codes (BS 8110-2 1985; FIP/CEB report 2004; EN 1992-1-2 2004; ACI 216.1 2007; AS 3600 2009) and a simple design equation provided in the previous research (Kodur and Dwaikat 2011) can be adopted for the fire resistance evaluation of RC beams. However, the tabulated method is prescriptive and just specifies some deemed-to-satisfy requirements on the minimum member dimensions and the minimum concrete cover depths for the steel reinforcement. These requirements are empirical and rely heavily on the limited fire test results of RC beams. Therefore, the applicability of using a tabulated method for the fire resistance evaluation of RC beams is controversial (Dwaikat and Kodur 2011). Furthermore, it has been demonstrated that the tabulated method does not always lead to a conservative fire resistance prediction of RC beams (Kodur and Dwaikat 2011). More recently, Kodur and Dwaikat (2011) conducted a parametric study to investigate the fire performance of RC beams using a fiber-section model (i.e., macroscopic finite element model as stated in their study) and proposed an explicit design equation for the fire resistance assessment. This equation was established based on the modification of the tabulated method specified in the AS 3600 code (2009) with due consideration of the impact of various factors, such as the fire load ratio, the section geometries, the aggregate type of concrete and the restraint conditions of RC beams. However, this equation was proposed for RC beams under a normal service load in which the fire load ratio is around 50 percent of the load-carrying capacity at room temperature. Therefore, the proposed equation may not be suitable for the fire resistance evaluation of un-protected FRP-strengthened RC beams, since under this situation the un-protected RC beams are subjected to a higher fire load ratio due to the loss of FRP

strengthening. As an alternative to the fiber-section model, the advanced FE model proposed in Chapter 6 is a generic analytical approach, which can be directly adopted for parametric studies and to propose a design method for the fire resistance evaluation of un-protected RC beams, especially under high fire load ratios.

The highest level (i.e., Level III in Fig. 9.1) for the fire-resistance design of FRP-strengthened RC beams assumes that the FRP strengthening system needs to remain effective during fire events. In this case, a thick fire insulation layer is required to protect the FRP strengthening system below a threshold temperature. However, this threshold is not an exact temperature, since various types of bonding adhesives and polymer matrixes of FRPs are commercially available. Furthermore, the threshold temperature should not be a constant value when the same bonded system is applied to strengthen RC beams with different dimensions. Therefore, Burke et al. (2013) recommended conducting full-scale loaded fire endurance tests to determine the threshold temperature for a specific bonding adhesive and/or polymer matrix. Nevertheless, this threshold temperature is typically defined using the glass transition temperature,  $T_g$ , of the epoxy primer, bonding adhesive, or the polymer matrix of the FRP composites, leading to an almost full contribution of the FRP strengthening system during the fire and eventually a conservative fire resistance design (Kodur et al. 2007).

For the intermediate level (i.e., Level II in Fig. 9.1), the fire insulation allows the protected RC beam to maintain a sufficient portion of its pre-fire strength, even if the FRP strengthening system is rendered useless. In other words, the FRP-strengthened RC beam is partially protected and the main purpose of using fire insulation is to retard the temperature increases of the internal concrete and the steel reinforcement, while the temperature control for the FRP strengthening system is no longer a paramount concern.

For the highest level of fire design (i.e., to protect the FRP strengthening system as well as the RC beam), the fire resistance design of the fully insulated FRP-strengthened RC beam converts directly to a temperature analysis problem. The explicit method developed in Chapter 8 for predicting the temperature distributions of insulated beam sections can be directly used to determine the thickness of the fire insulation layer, which is needed to ensure the temperature of FRP laminate below its  $T_g$  during the required fire duration. Therefore, this chapter focuses on developing detailed solutions for the fire resistance design of FRP-strengthened RC beams under the other two lower levels (i.e., Levels I and II).

This chapter consists of two main parts. The first part presents detailed FE parametric studies in which factors influencing the fire resistance of un-protected FRP-strengthened RC beams (i.e., equivalent to RC beams) are carefully considered. The fire resistance results generated from the FE parametric studies are then used to develop an explicit design equation with due consideration of the impact of various factors adopted in the preceding FE parametric studies. The accuracy of the proposed equation is validated by comparing its predictions with fire-resistance data from both FE parametric studies and existing standard fire tests on RC beams in the literature. The second part presents a simple design-oriented method to assess the moment capacity of insulated FRP-strengthened RC beams under fire by ignoring the contribution of FRP strengthening system (i.e., the FRP strengthening system is assumed to be totally lost). In this simple design-oriented method, the “500 °C isotherm method” is used to predict the moment capacity of insulated RC beams in combination with the temperature field predictions of insulated beam sections (described in Chapter 8). The proposed design-oriented method is validated through comparisons with the fire resistance data generated from parametric studies using the advanced FE model (developed in Chapter 7). The use of advanced FE model to

generate the fire resistance data is because in existing literature this data on insulated FRP-strengthened RC beams are very scarce.

## **9.2 AN EXPLICIT SOLUTION FOR PREDICTING THE FIRE RESISTANCE OF UN-PROTECTED FRP-STRENGTHENED RC BEAMS**

### ***9.2.1 FE parametric study***

Detailed FE parametric studies were carried out to investigate the effects of various influencing parameters on the fire resistance of un-protected RC beams exposed to the standard fire. Before the parametric studies, the load-carrying capacities of reference RC beams at room temperature were determined at first. Details of the factors adopted in the parametric analyses and the obtained numerical results are presented below.

#### ***9.2.1.1 Determination of the influencing parameters***

Previous numerical studies (Kodur et al. 2007; Kodur and Dwaikat 2011) revealed that the span-to-depth ratio ( $l/d$ ), fire load ratio (i.e., the ratio of the fire load to the load-carrying capacity of an RC beam at room temperature,  $\gamma$ ), concrete cover depth ( $c$ ), reinforcement ratio of tension steel rebars (ratio of the area of total tension steel rebars to that of the gross section,  $\rho_s$ ), aggregate type of concrete ( $\mu_{ag}$ ), rebar placement of tension steel reinforcement (ratio of the total area of corner tension rebars to the total area of tension rebars,  $\frac{A_{sc}}{A_{st}}$ ), and beam width ( $b$ ) have influences on the fire resistance of RC beams. Some other factors, such as concrete spalling and the axial and rotational restraint conditions of beams, were also found to affect the fire resistance of RC beams (Dwaikat and Kodur 2009, 2010; Kodur and Dwaikat 2010; Choi and Shin 2011; Wu and Liu 2009). However, they are not considered in the present study, since most of the RC beams needed to be strengthened are made of

normal strength concrete and concrete spalling is a minor concern. Both the rotational and axial restraints affect the fire resistance of RC beams (Wu and Liu 2009; Kodur and Dwaikat 2010, 2011). However, in a real RC building under fire events, the restraint conditions of an RC beam are extremely complicated and may change during the fire due to the deformation process of the adjacent columns, which further influences the force and moment interaction at the beam-to-column joint as well as its failure mechanism. Therefore simply supported RC beams were analyzed in the present FE parametric studies based on a simple and conservative concern (Kodur and Dwaikat 2011).

The parameters adopted in the extensive FE studies include three different concrete cross-sections (250mm×250mm, 250mm×450mm and 250mm×600mm), four different concrete cover depths (20mm, 30mm, 40mm and 50mm), five different ratios of tension steel reinforcement (0.3%, 0.9%, 1.2%, 1.5% and 2.4%), five different fire-load ratios (0.1, 0.3, 0.5, 0.7 and 0.9), two aggregate types (calcareous and siliceous aggregate), six different placements of tension rebars ( $A_{sc}/A_{st} = 1, 3/4, 2/3, 1/2, 1/3$  and  $1/4$ , as shown in Fig. 9.2), and seven different beam widths (200mm, 250mm, 300mm, 350mm, 400mm, 450mm, 600mm). As the simulated specimens have the same span (i.e., 4 m), three different cross-sections in fact correspond to three different span-to-depth ratios. Besides, the concrete cover depth specified in the parametric studies represents the clear distance from the side and bottom surface to the exterior surface of tension steel reinforcement. In all simulated RC beams, the compressive strength of concrete and the yield strength of steel rebars were assumed respectively as 30 MPa and 375 MPa (i.e., the measured yield strength of the HRB 335 steel reinforcement typically used in China based on previous experiences). The ISO 834 standard fire curve was adopted as the fire scenario. Table 9.1 presents a summary of the properties of all the beams and the influencing parameters adopted in the FE studies. For the purpose of saving computational efforts, when

investigating the effects of aggregate type and placement of tension rebars, FE parametric studies were conducted under a fixed cross-section (i.e., 250 mm × 250 mm). Different beam widths correspond to different thermal diffusions in the sections. In the FE parametric studies, fourteen RC beams with seven different beam widths and a fixed beam depth of 450 mm as well as under two different fire load ratios were analyzed to investigate the beam width effect. In total, the FE parametric studies included 512 simply supported RC specimens.

The four-point loading scheme (Fig. 9.3a) is generally recommended to investigate the fire resistance of RC beams in existing fire test codes (BS 476-20 1987; ISO 834-1 1999; ASTM E119 2008). However, it is difficult to determine the moment capacity of the beam section using this loading scheme in displacement-controlled FE analyses. Therefore, in order to ascertain the fire load ratio of the simulated beam specimens, conventional two-point loading scheme (Fig. 9.3a) is used to determine the ultimate loads of RC beams at room temperature. However, it is more common that RC beams are subjected to uniformly distributed loads along the span direction in an actual RC building. To investigate the loading scheme effect, Fig. 9.3b presents the results of a trial FE simulation on a typical RC beam under four different loading schemes (i.e., one-point load, two-point loads, four-point loads and uniformly distributed loads). The predicted time-dependent mid-span deflections are compared in Fig. 9.4b. It is seen that the uniformly distributed loading scheme and the four-point loading scheme lead to the similar deformation response. Therefore, the four-point loading scheme was adopted in the present FE parametric studies for fire performance evaluation.

### *9.2.1.2 FE analytical results on the load-deflection responses of RC beams at room temperature*

The FE model developed in Chapter 6 was used to determine the load-deflection responses of reference RC beams at room temperature. These reference RC beams have different geometrical dimensions and different reinforcement ratios of tensile steel rebars. Table 9.2 summarizes the beam section properties and the values of other parameters as well as the predicted load-carrying capacities of RC beams. As expected, the strength and stiffness of the reference RC beams are remarkably increased with the tension steel reinforcement ratio (Fig. 9.4). Besides, the beams reinforced with a normal steel reinforcement ratio (i.e.,  $\rho_s = 0.9\%$ ,  $1.2\%$  or  $1.5\%$ ) achieves good deformation ductility while this ductility is significantly reduced when the RC beams are over-reinforced (e.g.,  $\rho_s = 2.4\%$ ) or under-reinforced (e.g.,  $\rho_s = 0.3\%$ ). In addition, the load-carrying capacity of the RC beams is largely dependent on the tension steel reinforcement ratio.

### *9.2.1.3 Definition of the fire resistance period*

Various performance criteria are used to define the fire resistance of RC members in existing fire test codes, including stability-related criteria in terms of the maximum deflection and the rate of deflection, integrity-based criteria that prevent fire and gas penetration through the member, and insulation-based criteria that limit the temperature reached at the unexposed side of the member (ASTM E119 2008; ISO 834-1 1999; BS 476-20 1987). Integrity and insulation-based criteria are usually associated with compartment/separating walls and floors. For RC beams in the present study, the fire resistance period is defined to be reached:

- (1) when the maximum mid-span deflection of the beam exceeds  $l/20$  at any fire exposure time; or
- (2) when the rate of mid-span deflection exceeds  $l^2/9000d$ .

where  $l$  is the clear span of the test specimen and  $d$  is the beam depth, both in millimeters.

In some previous studies, the strength (i.e., the moment capacity of beams under fire) or the critical temperature of tension rebars (e.g., 593 °C) is also suggested as an index to define the fire resistance period of RC beams (Kodur and Dwaikat 2007, 2011; Dwaikat and Kodur 2011). However, Kodur and Dwaikat (2007, 2011) showed that the fire resistance defined based upon the deflection or the rate of deflection is most conservative, regardless of the applied fire load ratios. Therefore, only these two indices are used to define the fire resistance period of RC beams in the present analyses. Fig. 9.5 gives an example of two sets of RC beams reinforced with two steel reinforcement ratios of tension rebars and five different fire load ratios, demonstrating that the FE analysis can produce sufficiently large deflection and deflection rate to define the fire resistance period.

### ***9.2.2 FE Parametric Results vs. Predictions by Existing Design Methods***

The FE predictions of the fire resistance periods of 512 beam specimens are compared with the calculated results based upon the tabulated methods (Figs. 9.6 to 9.10) and the simple design equation proposed by Kodur and Dwaikat (2011) (Fig. 9.10). Appendix A provides the relevant design tables provided in existing design codes (i.e., tabulated design methods), such as BS 8110-2 (1985), FIP/CEB report (2004), ACI 216.1 (2007), EN 1992-1-2 (2004) and AS 3600 (2009). It should be noted that, the concrete cover depth defined in BS 8110-2 (1985) and ACI 216.1 (2007) is the clear distance from the concrete surface to the exterior surface of the tension rebar, whereas it is the axis distance between the concrete surface and the centroid of tension reinforcement in FIP/CEB report (2004), EN 1992-1-2 (2004) and AS 3600 (2009). Figs. 9.6 to 9.9 clearly indicate that the fire resistance

predictions by the tabulated methods deviate obviously from FE parametric results. The tabulated methods underestimate the fire resistance of RC beams at lower fire load ratios, while provide unsafe designs at higher fire load ratios. The poor performance of the tabulated methods is mainly due to the omit of some key parameters. On the other hand, the fire resistance periods predicted by Kodur and Dwaikat's (2011) equation agree reasonably well with the FE prediction when the fire load ratio is around 0.5, but not so well when the fire load ratio is lower (Fig. 9.10). The major drawback of Kodur and Dwaikat's (2011) equation lies that it may overestimate the fire resistance periods and provide an unsafe design for some RC beams under high fire load ratios (e.g.,  $\gamma \geq 0.7$ ). As explained earlier, for FRP-strengthened RC beams without fire insulation, the fire resistance design converts to the problem of an un-protected RC beam under a higher fire load ratio because the service load sustained by the FRP strengthening system transfers onto the existing RC beam during fire. Therefore, for the fire resistance design of un-protected FRP-strengthened RC beams, refined formulae are deemed necessary especially under high fire load ratios.

### ***9.2.3 Simple Design Formulae***

#### *9.2.3.1 Configuration of the formulae*

FE prediction results of 512 beam specimens included in four series (i.e., Series I, II, III and IV) were used to deduce the formulae for predicting the fire resistance period. Series I consists of 300 beam specimens to account for the four key influencing parameters (i.e., reinforcement ratio, concrete cover depth, span-to-depth ratio, and fire load ratio) that affect the structural behavior of RC beams exposed to fire. Series II and III both consist of 100 RC beams that consider the effects of the concrete aggregate type (i.e.,  $\mu_{ag}$ ) and the placement of tension steel rebars [i.e.,  $\xi \left( \frac{A_{sc}}{A_{st}} \right)$ ].

Twelve beams are added in Series IV to investigate the beam width effect [i.e.,  $\phi(b)$ ]. A generic equation as shown in Eq. (9.1) is thus proposed to take into account the influences of all the factors on the fire resistance periods of RC beams:

$$R\left(\gamma, c, \rho, \frac{l}{d}, \frac{A_{sc}}{A_{st}}, \mu_{ag}, b\right) = \varphi(\gamma) \times \omega(c, \rho_s) \times \psi\left(\frac{l}{d}, \rho_s\right) \times \xi\left(\frac{A_{sc}}{A_{st}}\right) \times \mu_{ag} \times \phi(b) \quad (9.1)$$

where  $R$  is the fire resistance period (in min);  $\varphi(\gamma)$  accounts for the effect of the fire load ratio;  $\omega(c, \rho_s)$  accounts for the combined effect of the concrete cover depth and the tension reinforcement ratio;  $\psi\left(\frac{l}{d}, \rho_s\right)$  accounts for the effect of the span-to-depth ratio under different tension reinforcement ratios;  $\xi\left(\frac{A_{sc}}{A_{st}}\right)$ ,  $\phi(b)$ ,  $\mu_{ag}$  account for the effects of the placement of tension rebars, the beam width and the type of concrete aggregate, respectively.

#### 9.2.3.2 Function $\varphi(\gamma)$ for fire load ratio

Fig. 9.11 shows the relationship between the fire resistance period and the fire load ratio. RC beam specimens in the figure have a 250 mm  $\times$  250 mm dimension, a 30 mm concrete cover depth, and a 1.2% reinforcement ratio. It is obvious that the fire resistance decreases with the fire load ratio and a polynomial curve can be used to accurately fit the FE results as follows:

$$\varphi(\gamma) = a_1 + a_2 \cdot \gamma + a_3 \cdot \gamma^2 + a_4 \cdot \gamma^3 \quad (9.2)$$

where  $a_1$ ,  $a_2$ ,  $a_3$ , and  $a_4$  are constants, and the least-squares regression suggests that:  $a_1 = 2.92 \times 10^2$ ;  $a_2 = -8.15 \times 10^2$ ;  $a_3 = 1.17 \times 10^3$ ;  $a_4 = -6.13 \times 10^2$ .

### 9.2.3.3 Function $\omega(c, \rho_s)$ for the combined effect of concrete cover depth and tension steel reinforcement ratio

Fig. 9.12 shows the relationship between the fire resistance period and the concrete cover depth in cases of different reinforcement ratios. In the figure, all the analyzed RC beams have the section of 250 mm  $\times$  250 mm (series I in Table 9.1) and their fire resistance periods are normalized by the value obtained for the case of 30 mm concrete cover depth and 1.2% reinforcement ratio (i.e., Section 9.2.3.2). With the increase of concrete cover depth, the normalized fire resistance periods are shown to increase approximately linearly, and the slopes are different for RC beams with different tensile reinforcement ratios. Therefore, a linear function is proposed as follows to describe the combined effect of concrete cover depth and tension steel reinforcement ratio:

$$\omega(c, \rho_s) = \omega_0 + \omega_1 \cdot c \quad (9.3)$$

where  $\omega_0$  and  $\omega_1$  are the functions of the tension steel reinforcement ratio and given by:

$$\omega_0 = b_0 + b_1 \cdot \rho_s + b_2 \cdot \rho_s^2 \quad (9.4a)$$

$$\omega_1 = c_0 + c_1 \cdot \rho_s + c_2 \cdot \rho_s^2 \quad (9.4b)$$

where  $b_0 = 4.06 \times 10^{-1}$ ;  $b_1 = -4.37 \times 10^{-2}$ ;  $b_2 = 1.84 \times 10^{-2}$ ;  $c_0 = 2.11$ ;  $c_1 = -2.83 \times 10^{-3}$ ;  $c_2 = -4.69 \times 10^{-2}$ .

#### 9.2.3.4 Function $\psi\left(\frac{l}{d}, \rho_s\right)$ for beam span-to-depth ratio

Three different beam depths were adopted to investigate the influence of the beam span-to-depth ratio on the fire resistance period. The FE results generated for the other two beam depths (i.e., 450 mm and 600 mm in Table 9.1) are normalized using the RC beams with the 250 mm depth as the reference. Fig. 9.13 illustrates the relationship between the normalized fire resistance period and the tension reinforcement ratio in cases of three different beam span-to-depth ratios (i.e., represented by three different symbols). Since the RC beams with the 250 mm depth are the reference beams, the normalized fire resistance periods are all equal to 1.0. The effect of concrete cover depth on these normalized values is negligible as the tendency obtained from four different concrete cover depths was found to be very similar. Through the least-squares regression analysis, the following equations can be used to describe the relationships between the normalized fire resistance and the steel reinforcement ratio at different beam span-to-depth ratios:

$$\psi\left(\frac{l}{d}, \rho\right) = \psi_0 + \psi_1 \cdot \rho + \psi_2 \cdot \rho^2 \quad (9.5)$$

where

$$\psi_0 = 1.78 - 1.03 \times 10^{-1} \cdot \left(\frac{l}{d}\right) + 3.39 \times 10^{-3} \cdot \left(\frac{l}{d}\right)^2 \quad (9.6a)$$

$$\psi_1 = 6.80 - 1.64 \times 10^{-1} \cdot \left(\frac{l}{d}\right) + 7.61 \times 10^{-3} \cdot \left(\frac{l}{d}\right)^2 \quad (9.6b)$$

$$\psi_2 = -1.15 \times 10^{-1} + 4.36 \times 10^{-2} \cdot \left(\frac{l}{d}\right) - 2.27 \times 10^{-3} \cdot \left(\frac{l}{d}\right)^2 \quad (9.6c)$$

### 9.2.3.5 Coefficient $\mu_{ag}$ for aggregate type of concrete

In another series of parametric studies (series II in Table 9.2), a total of 100 RC beams made with calcareous aggregate concrete were simulated. Fig. 9.14 shows the detailed FE analytical results of these 100 beams in comparison with those of their counterparts made of siliceous aggregate concrete. It seems that the fire resistance of RC beams made of calcareous aggregates is slightly higher than that of their siliceous counterparts. An average value  $\mu_{ag} = 1.04$  can be used to describe the above difference.

### 9.2.3.6 Function $\xi \left( \frac{A_{sc}}{A_{st}} \right)$ for placement of tension steel rebars

Even if the reinforcement ratio is the same, the placement of tension steel rebars also influences the fire resistance of RC beams. Steel reinforcement located at the corner of the beam section degrades faster due to the two-dimensional heat penetration effect (Fig. 9.2). Fig. 9.15 presents the relationship between the fire resistance period and the placement of tension steel rebars (i.e.,  $\frac{A_{sc}}{A_{st}}$ ) in cases of different concrete cover depths. In total, 100 specimens (Series III in Table 9.2) were simulated by the FE model. In Fig. 9.15, the fire resistance is also normalized by that of the reference RC beams for which  $\frac{A_{sc}}{A_{st}} = \frac{2}{3}$ . It is seen that the normalized fire resistance is linearly proportional to the ratio of  $\frac{A_{sc}}{A_{st}}$ , regardless of the concrete cover depth. The following functions can be used to describe the above linear relationships:

$$\xi \left( \frac{A_{sc}}{A_{st}} \right) = \xi_1 + \xi_2 \cdot \left( \frac{A_{sc}}{A_{st}} \right) \quad (9.7)$$

where

$$\xi_1 = 1.54 - 6.81 \times 10^{-3} \cdot c \quad (9.8a)$$

$$\xi_2 = -7.91 \times 10^{-1} + 9.73 \times 10^{-3} \cdot c \quad (9.8b)$$

### 9.2.3.7 Function $\phi(b)$ for beam width

The last factor considered is the beam width, which influences the heated perimeters as well as the thermal diffusions in beam sections. Even with the same tension reinforcement ratio, the degradation of tension rebars at elevated temperatures may decrease with the increase of beam width from the thermal response point of view. Therefore, 14 RC beams with an identical beam depth of 450 mm but seven different beam widths (series IV in Table 9.2) were analyzed under two different fire load ratios ( $\gamma = 0.5$  and  $0.7$ ) to investigate the beam width effect. Fig. 9.16 shows the relationship between the normalized fire resistance periods of RC beams (i.e., normalized by the fire resistance of the 250 mm width beam) and the normalized beam widths (i.e., normalized by 250 mm). It is clearly seen that there is an approximately linear relationship between two of them. This relationship seems to be independent of the fire load ratio and a unique modification factor for beam width  $\phi(b)$  can be expressed as follows:

$$\phi(b) = d_0 + d_1 \left( \frac{b}{250} \right) \quad (9.9)$$

where the constants  $d_0$  and  $d_1$  are  $3.80 \times 10^{-1}$  and  $6.20 \times 10^{-1}$  respectively.

With the assistance of the proposed functions in sections 9.2.3.2~9.2.3.7, the fire resistance of RC beams with different parameters exposed to the standard fire can be explicitly obtained using Eq. (9.1). Figs. 9.11-9.16 evaluate the performance of Eq. (9.1) by comparing the predicted results (dotted lines in these figures) with the FE results (discrete symbols in these figures) for RC beams with different combinations of influencing parameters. The excellent agreement proves that the proposed

functions can capture the complex variations well for the fire resistance design of RC beams with different design parameters.

#### ***9.2.4 Validation of the Proposed Design Formulae***

Figures 9.17a to 9.17d show the comparisons between the calculated fire resistance periods (i.e., continuous lines) based upon Eq. (9.1) and the data generated from the preceding FE analyses for RC beams with different parameters. In general, the predictions by the proposed explicit equation exhibit excellent agreement with the FE results, demonstrating that it has properly captured the effects of all relevant influencing parameters. If the fire resistance details of all the 512 beam specimens are collected together, Fig. 9.18 shows that the average ratio of the equation predictions to the FE results is 1.0, and the coefficient of variation (COV) is 4.355%. This excellent agreement is expected as the proposed simple design equation is regressed from the FE parametric studies. Regarding this fact, the fire resistance periods of 60 more RC beams, in which some of the influencing parameters are different from those adopted in the preceding FE parametric analyses, were assessed using both the proposed explicit equation and the advanced FE model. The influencing parameters of these 60 RC beams are illustrated in Table 9.3. Fig. 9.19 shows the comparison between the calculated fire resistance and the FE results of these 60 beam specimens. It is well demonstrated that the proposed explicit design equation is able to predict the fire resistance of RC beams.

The proposed equation was also used to predict the fire resistance of twelve RC beams obtained from the standard fire tests in the existing literature for further verification. Among the 12 RC beams, three were tested by Wu et al. (1993), one was tested by Lin et al. (1981), one was tested by Dotreppe and Franssen (1985), one was tested by Hertz (1985), and the other six beams were carried out by Blontrock et

al. (2000), Dwaikat and Kodur (2009) and Choi and Shin (2011) as the reference beams to investigate the fire performance of FRP-strengthened RC beams and high strength concrete beams. Fire test results on RC beams at early times (i.e., before 1970s) are excluded from the comparison, since most of these fire tests were conducted on small specimens and some of them were related to the post-fire residual strength evaluation. Table 9.4 summarizes the section geometries and material properties of all the preceding twelve beams together with their measured and predicted fire resistance periods. It should be mentioned that, the measured fire resistance of the RC beams tested by Lin et al. (1981) and Dotreppe and Franssen (1985) were determined by the FE modeling as reported in Chapter 6, since the original fire tests were terminated before the mid-span deflection reached the defined fire limit state. Fig. 9.20 shows the comparison between the fire resistance predictions (i.e., based on the simple design equation) and the measured fire resistance data. Very close agreement is seen in this figure with a scatter less than 10%. Only the beam N5 tested by Choi and Shin (2011) exhibits a conservative prediction. That is because this beam has an extremely thick concrete cover (i.e., 60 mm from the exterior surface of tension reinforcement to the surface of the beam), which exceeds the maximum cover depth (i.e., 50mm) assumed in the present FE parametric analyses. Owing to this thick concrete cover, the two corner rebars may be well protected under fire exposure. The effect of the tension rebar placement [i.e.,  $\xi\left(\frac{A_{sc}}{A_{st}}\right)$ ] considered in the present simple design equation may amplify the strength degradation of these two corner rebars and thus underestimate the actual fire resistance performance.

Overall, the proposed simple equation proves to be an efficient and reliable tool for the fire resistance evaluation of RC beams exposed to the standard fire. Nevertheless, the applicability of Eq. (9.1) is limited to the following ranges of parameters:  $0.1 \leq \gamma \leq 0.9$ ,  $20 \text{ mm} \leq c \leq 50 \text{ mm}$ ,  $0.3\% \leq \rho_s \leq 2.4\%$ ,  $6.67 \leq \frac{L}{d} \leq 16$ ,  $\frac{1}{4} \leq \frac{A_{sc}}{A_{st}} \leq 1$ ,

and  $200 \text{ mm} \leq b \leq 600 \text{ mm}$ , which were adopted in the FE parametric analyses and almost cover the parameter variations of RC beams commonly used in practice

### **9.3 SIMPLE METHOD FOR PREDICTING THE FIRE RESISTANCE OF INSULATED FRP-STRENGTHENED RC BEAMS**

The FE model developed in Chapter 7 has proven to be an efficient method to evaluate both the thermal and the mechanical responses of insulated FRP-strengthened RC beams, upon which their fire resistance can be well defined. However, as the commercially available insulation materials have different temperature-dependent thermal properties, it is impossible to develop an explicit formula to predict the fire resistance of insulated FRP-strengthened RC members with due consideration of various insulation products. Therefore, the well known “500 °C isotherm method” (Anderberg 1978, EN 1992-1-2 2004), in combination with the simple method for predicting the temperature distributions of insulated beam sections (Chapter 8), is adopted to form a simple design-oriented method for the fire resistance design of insulated FRP-strengthened RC beams.

#### ***9.3.1 The 500 °C Isotherm Method***

As a simple handy calculation method recommended by EN 1992-1-2 (2004), the “500 °C isotherm method” (Anderberg 1978) has been widely applied to evaluate the load-carrying capacity of RC beams subjected to fire exposure. In this method, the compressive zone of concrete in the beam section is reduced by eliminating its strength at the locations where the temperatures are greater than 500 °C, while the concrete is assumed to retain its full strength at locations where the temperatures are less than 500 °C.

If the fire exposure duration is  $t$  (in min), the 500 °C isotherm in the fire-exposed beam section can be properly determined using the simple and explicit method proposed in Chapter 8. As illustrated in Fig. 9.21a, if the distance between the 500 °C isotherm and the nearest beam side is  $x_{500}(t)$ , the reduced width of the concrete compression zone can be expressed as:

$$b'(t) = b - 2x_{500}(t) \quad (9.10)$$

Assuming this fire-exposed section is loaded to failure, the stress profiles in concrete and steel reinforcement are illustrated in Fig. 9.21.b. If taking the moment to the compression steel reinforcement, the force and moment equilibrium equations can be written as:

$$\begin{cases} b'(t) \cdot \beta y_c(t) \cdot \alpha f_c + \sum_{j=1}^n A_{c,j} \cdot f_{yc,j}(\theta_{c,j}) - \sum_{i=1}^m A_{t,i} \cdot f_{yt,i}(\theta_{t,i}) = 0 \\ M_R(t) = b'(t) \cdot \beta y_c(t) \cdot \alpha f_c \cdot [\beta y_c(t) - d'] + \sum_{i=1}^m A_{t,i} \cdot f_{yt,i}(\theta_{t,i}) \cdot (d - d') \end{cases} \quad (9.11)$$

where  $y_c(t)$  is the height of neutral axis;  $\beta y_c(t)$  is the height of equivalent compressive stress block in which  $\beta = 0.8$  (EN 1992-1-1);  $A_{t,i}$  and  $f_{yt,i}(\theta_{t,i})$  are the area of the  $i^{th}$  tension steel rebar and its tensile stress at temperature  $\theta_{t,i}$ ;  $A_{c,j}$  and  $f_{yc,j}(\theta_{c,j})$  are the area of the  $j^{th}$  compression steel rebar and its compressive stress at temperature  $\theta_{c,j}$ ;  $d$  and  $d'$  are the depths of the centroids of the tension and compression steel reinforcement;  $m$  and  $n$  are the total numbers of tension and compression steel rebars, respectively; and  $M_R(t)$  is the moment capacity of the fire-exposed RC section at the time  $t$ . The factor  $\alpha$ , a coefficient defined the effective strength, is recommend with the value of 1.0 according to EN 1992-1-1 (2004). The stress degradations of tension and compression steel rebars at elevated temperatures [i.e.,  $f_{yc,j}(\theta_{c,j})$  and  $f_{yt,i}(\theta_{t,i})$ ] are determined based on EN 1992-1-2 (2004).

### 9.3.2 Validation of The Proposed Simple Design-Oriented Method

Since the fire tests on insulated FRP-strengthened RC beams are scarce, and in the existing literature most of the fire tests were terminated before the fire limit states were reached. Therefore, the advanced FE model developed in Chapter 7 was used to produce the fire resistance data for validation of the proposed design-oriented method. The parameters adopted in the FE analyses are summarized in Table 9.5; in total, 60 insulated CFRP-strengthened RC beams were designed and simulated. All the beams were assumed to be protected by a U-shaped insulation system and exposed to the ISO 834 standard fire. The mechanical properties of CFRP laminates and the thermal properties of the insulation material were determined according to Blontrock et al.'s (2000) tests, while the cylinder compressive strength of concrete and the yield strength of steel reinforcement were assumed as 30 MPa and 375 MPa, respectively.

Table 9.6 presents the predicted load-carrying capacities of CFRP-strengthened RC beams (i.e.,  $P_{u,FRP}$ ) and un-strengthened reference RC beams (i.e.,  $P_{u,RC}$ ) at room temperature. Two different thicknesses of CFRP laminates (i.e., 0.3mm and 1.2 mm) and two different tensile reinforcement ratios (i.e., 0.8% and 1.2%) were adopted in the FE parametric studies. Table 9.7 summarizes the fire load ratios (i.e.,  $\gamma$ ), the corresponding fire loads (i.e.,  $P = \gamma P_{u,FRP}$ ) on the CFRP-strengthened RC beams, and the ratio of the fire loads to the load-carrying capacities of their un-strengthened counterparts (i.e.,  $P/P_{u,RC}$ ). It is seen that, when a high fire load ratio is applied on a CFRP-strengthened RC beam (i.e.,  $\gamma = 0.7$ ), the fire load may be higher than the load-carrying capacity of the RC beam prior to its strengthening. Under this situation, the proposed design-oriented method is not applicable, since full fire insulation is deemed necessary to activate the FRP strengthening effect during the fire exposure. In other words, the highest level (i.e., Level III) for fire resistance design is required.

Except for these fully protected beams, the fire resistance periods of the other insulated FRP-strengthened RC beams can be predicted by the proposed design-oriented method.

Fig. 9.22 shows the moment capacity versus the fire exposure time relationships for insulated FRP-strengthened RC beams with two different steel reinforcement ratios and five different fire insulation thicknesses. It can be seen that, with the thickness increase of the fire insulation layer, a more gentle reduction of the moment capacity during the fire exposure is vividly illustrated. In order to determine the fire resistance of the simulated RC beams, the predicted moment capacity versus the fire exposure time curves are compared with the bending moment induced by the applied fire loads. Fig. 9.23 provides two examples of how to find the fire resistance periods of insulated FRP-strengthened RC beams with different fire load ratios. The predicted fire resistance periods of these beams are also compared with the FE predictions as shown in Fig. 9.24. It is seen that both approaches lead to similar predictions despite that the former is based on the strength failure criterion while the latter is based on the deflection failure criterion. Therefore, the simple design-oriented method can be used for practical fire-resistance design of insulated FRP-strengthened RC beams as an alternative to the precise FE model.

#### **9.4 DESIGN APPLICABILITY FOR FRP-STRENGTHENED RC BEAMS**

Although the proposed performance-based design approach is applicable to a large range of design parameters, the following limitations have also been noted when the explicit design equation and the design-oriented method are applied for the fire resistance evaluation of un-protected and insulated FRP-strengthened RC beams.

(1) The proposed simple design equation offers a practical approach for evaluating the fire resistance of RC beams exposed to the standard fire, which is normally much more severe than a real (natural) fire. The main difference between the standard fire curve and the real fire curve is that the former is characterized by a continuous temperature increase while the latter has both a heating phase and a subsequent decay phase. For any real compartment fire, the proposed equation leads to a conservative fire resistance evaluation. Where necessary, it can also be modified with due consideration of different fire-exposure intensities experienced in the standard fire and the real fire (Kodur et al. 2010).

(2) The temperature field analysis established for insulated FRP-strengthened RC beams has been validated for regularly shaped RC sections (i.e., rectangular sections). For T-shaped RC beams, this approach may provide a conservative fire resistance assessment. This is because the compression zone of a T-beam section is protected by the adjacent slab parts from the direct heat penetration. In addition, the T-shaped geometrical configuration also reduces the thermal radiation due to the shadow effect (Wickstrom 2001). Therefore, using the explicit method proposed in Chapter 8, the predicted temperatures of the concrete compression zones of T-beams are higher than the actual values.

(3) The design-oriented method established for insulated FRP-strengthened RC beams is based on an assumption that the beam failure is due to the tension steel yielding. It is not applicable to those beams failing in brittle shear. This brittle shear was indeed observed in some existing fire tests in which a flat insulation layer was used to protect the FRP-strengthened RC beam (i.e., only the bottom surface of the beam was protected) (Liu et al. 2009). Therefore, for insulated FRP-strengthened RC beams with the flat insulation system, advanced FE modeling is strongly recommended for use to evaluate their fire performance.

## 9.5 CONCLUSIONS

This chapter provides a performance-based approach for the fire resistance design of FRP-strengthened RC beams. A three-level design concept has been proposed based on the tradeoff between the strength contribution of FRP strengthening system and the required fire resistance rating. For FRP-strengthened RC beams without fire insulation (i.e., the lowest level), extensive FE parametric studies were carried out to investigate the influences of various governing parameters. The results generated from the FE parametric results were used for regression to derive a simple design equation to predict the fire resistance of RC beams. The validity of the proposed equation has been demonstrated.

For insulated FRP-strengthened RC beams (i.e., equivalent to insulated RC beams) exposed to the standard fire, a design-oriented method has been established based on the well-known “500 °C isotherm method” to enable the prediction of their time-dependent moment capacity. The fire resistance results obtained from the design-oriented method are in good agreement with the FE predictions. However, the former is more attractive for use in practical design due to its simplicity yet good accuracy.

## 9.6 REFERENCES

- American Concrete Institute (ACI). (2008). “Guide for the design and construction of externally bonded FRP systems for strengthening concrete structures.” *ACI 440.2R-08*, Farmington Hills, Michigan, America.
- ACI 216.1. (2007). *Code Requirements for Determining Fire Resistance of Concrete and Masonry Construction Assemblies*, American Concrete Institute, Michigan, America.
- Anderberg, Y. (1978). “Analytical fire engineering design of reinforced concrete structures based on real fire characteristics.” *Proceedings of the Eighth Congress*

- of the *Federation Internationale de la Precontrainte*, Concrete Society, London, pp. 112-123.
- AS 3600. (2009). *Concrete Structures*. Standards Association of Australia, Sydney, Australia.
- ASTM E119. (2008). *Standard Test Methods for Fire Test of Building Construction and Materials*. American Society for Testing and Materials, Pennsylvania, America.
- Bisby, L.A. (2003). "Fire behavior of fiber-reinforced polymer (FRP) reinforced or confined concrete." Ph.D. thesis, Queen's University, Kingston, Ontario, Canada.
- Blontrock, H., Taerwe, L., and Vandeveld, P. (2000). "Fire tests on concrete beams strengthened with fiber composite laminates." *Proceeding of the Third Ph.D. Symposium in Civil Engineering*, Vienna, Austria, pp. 151-161.
- BS 8110-2. (1985). *Structural Use of Concrete--- Part 2: Code of Practice for Special Circumstance*. British Standards Institute, Milton Keynes, UK.
- BS 476-20. (1987). *Fire Tests on Building Materials and Structures --- Part 20: Methods for Determination of the Fire Resistance of Elements of Construction (General Principles)*. British Standards Institute, Milton Keynes, UK.
- Burke, P.J., Bisby, L.A., and Green, M.F. (2013). "Effects of elevated temperature on near surface mounted and externally bonded FRP strengthening systems for concrete." *Cement and Concrete Composites*, Vol. 35, No. 1, pp. 190-199.
- Choi, E.G. and Shin, Y.S. (2011). "The structural behavior and simplified thermal analysis of normal-strength and high-strength concrete beams under fire." *Engineering Structures*, Vol. 33, No. 4, pp. 1123-1132.
- Dotreppe, J.C. and Franssen, J.M. (1985). "The use of numerical models for the fire analysis of reinforced concrete and composite structures." *Engineering Analysis*, Vol. 2, No. 2, pp. 67-74.
- Dwaikat, M.B., and Kodur, V.K.R. (2009). "Response of restrained concrete beams under design fire exposure." *Journal of Structural Engineering*, ASCE, Vol. 135, No. 11, pp. 1408-1417.
- Dwaikat, M.B., and Kodur, V.K.R. (2010). "Fire induced spalling in high strength concrete beams." *Fire Technology*, Vol. 46, No. 1, pp. 251-274.
- Dwaikat, M.B., and Kodur, V.K.R. (2011). "Comparison of fire resistance of RC beams from different codes of practice." *ACI Special Publication SP255*, Vol. 255, pp. 125-146.
- Eamon, C.D., and Jensen, E. (2013). "Reliability analysis of RC beams exposed to fire." *Journal of Structural Engineering*, Vol. 139, No. 2, pp. 212-220.

- EN 1992-1-2 (2004). *Eurocode 2: Design of Concrete Structures --- Part 1-2: General Rules --- Structural Fire Design*, British Standards Institution, London, UK.
- Fédération International du Béton (fib). (2001). “Externally bonded FRP reinforcement for RC structures.” *fib Bulletin 14*, fib Task Group 9.3, fib, Lausanne, Switzerland.
- FIP/CEB (2004). *FIP/CEB Report on Methods of Assessment of the Fire Resistance of Concrete Structural Members*, Cement and Concrete Association, Slough. UK.
- Hertz, K. (1981). “Simple temperature calculations of fire exposed concrete constructions.” *Report No. 159*, Institute of Building Design, Technical University of Denmark, Lyngby, Denmark.
- Hertz, K. (1985). *Analysis of prestressing concrete structures exposed to fire*, Technical University of Denmark, Lyngby, Denmark.
- ISO 834-1 (1999). *Fire Resistance Tests --- Elements of Building Construction --- Part 1: General Requirement*. International Organization for Standardization, Geneva, Switzerland.
- Kodur, V.K.R. and Dwaikat, M.B. (2007). “Performance-based fire safety design of reinforced concrete beams.” *Journal of Fire Protection Engineering*, Vol. 17, No. 4, pp. 293-320.
- Kodur, V.K.R. and Dwaikat, M.B. (2010). “Effect of fire induced restraint on fire resistance of reinforced concrete beams.” *Journal of Structural Fire Engineering*, Vol. 1, No. 2, pp. 73-88.
- Kodur, V.K.R. Pakala, P., and Dwaikat, M.B. (2010). “Energy based time equivalent approach for evaluating fire resistance of reinforced concrete beams.” *Fire Safety Journal*, Vol. 45, No. 4, pp. 211-220.
- Kodur, V.K.R. and Dwaikat, M.B. (2011). “Design equation for predicting fire resistance of reinforced concrete beams.” *Engineering Structures*, Vol. 33, No. 2, pp. 602-614.
- Lin, T.D., Gustaferro, A.H. and Abrams, M.S. (1981). *Fire Endurance of Continuous Reinforced Concrete Beams.* RD 072.01B, Research and Development Bulletin, Portland Cement Association, America.
- Liu, F.T., Wu, B., and Wei, D.M. (2009). “Failure modes of reinforced concrete beams strengthened with carbon fiber sheet in fire.” *Fire Safety Journal*, Vol. 44, No. 7, pp. 941-950.
- Nigro, E., Cefarelli, G., Bilotta, A., Manfredi, G., and Cosenza, E. (2012). “Behavior of FRP reinforced concrete slabs in case of fire: theoretical models and

- experimental tests.” *Advances in Structural Engineering*, Vol. 15, No. 4, pp. 637-652.
- Rafi, M.M. and Nadjai, A. (2010). “Behavior of hybrid (steel-CFRP) and CFRP bar-reinforced concrete beams in fire.” *Journal of Composite Materials*, Vol. 45, No. 15, pp. 1573-1584.
- Rigberth, J. (2000). “Simplified design of fire exposed concrete beams and columns.” *Report No.5063*, Department of Fire Safety Engineering, Lund University, Sweden.
- Wickstrom, U. (2001). “Calculation of heat transfer to structures exposed to fire - shadow effects.” *Interflam 2001*, Edinburgh, UK.
- Wu, B. and Lu, J.Z. (2009). “A numerical study of the behaviour of restrained RC beams at elevated temperatures.” *Fire Safety Journal*, Vol. 44, No. 4, pp. 522-531.
- Wu, H.J., Lie, T.T. and Hu, J.Y. (1993). “Fire resistance of beam-slab specimens --- experimental studies.” Internal Report No. 641, Institute for Research in Construction, National Research Council Canada, Canada.

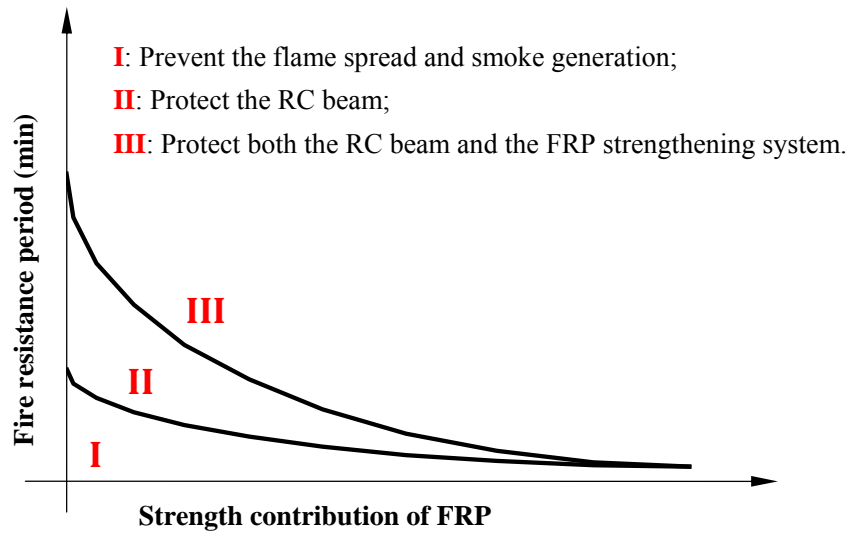


**Fig. 9.1** Schematic of three-level performance-based fire resistance design

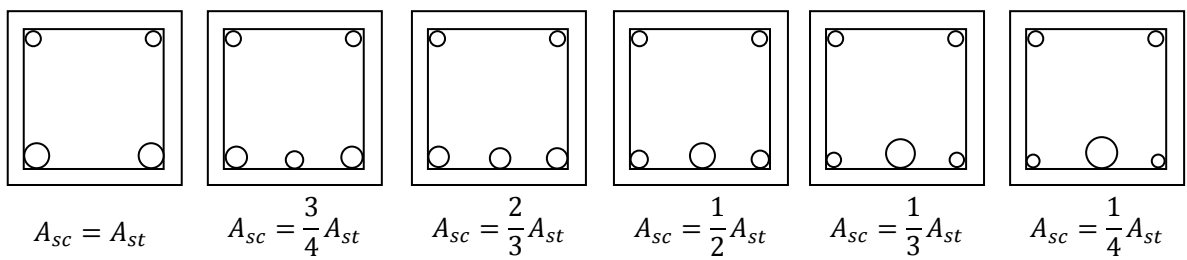
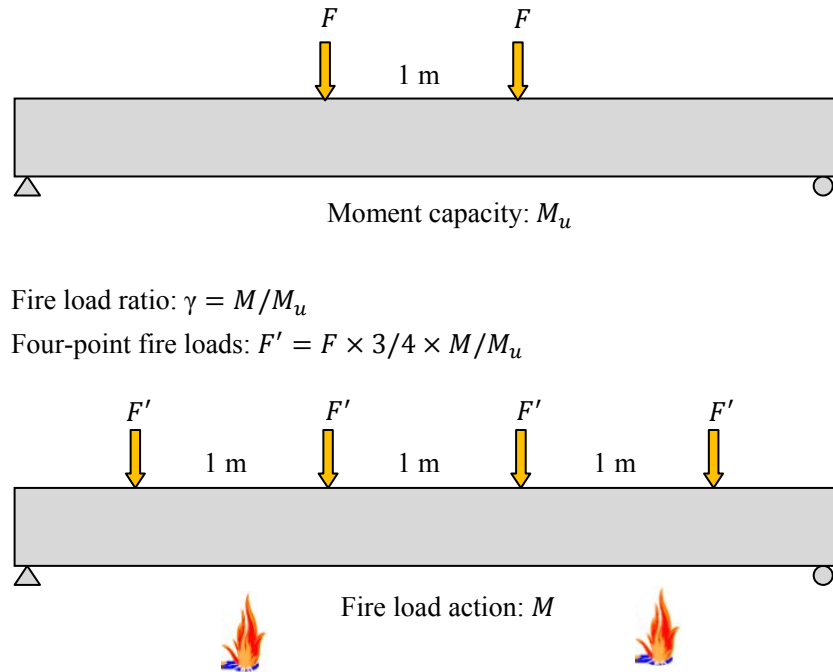
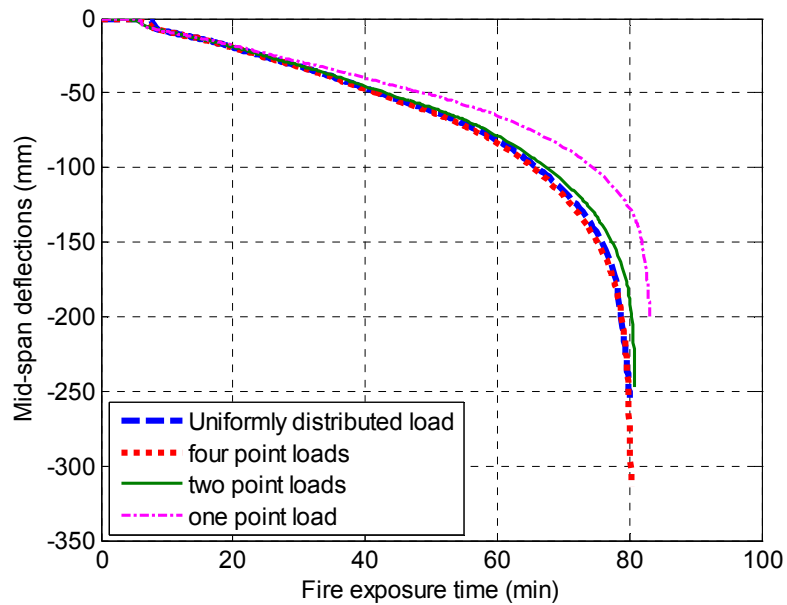


**Fig. 9.2** Effect of placement of tension steel rebars.



(a) Loading schemes on RC beams at ambient and elevated temperatures



(b) Time-dependent deflection responses of an RC beam subjected to different loading schemes

**Fig. 9.3** Effects of loading scheme

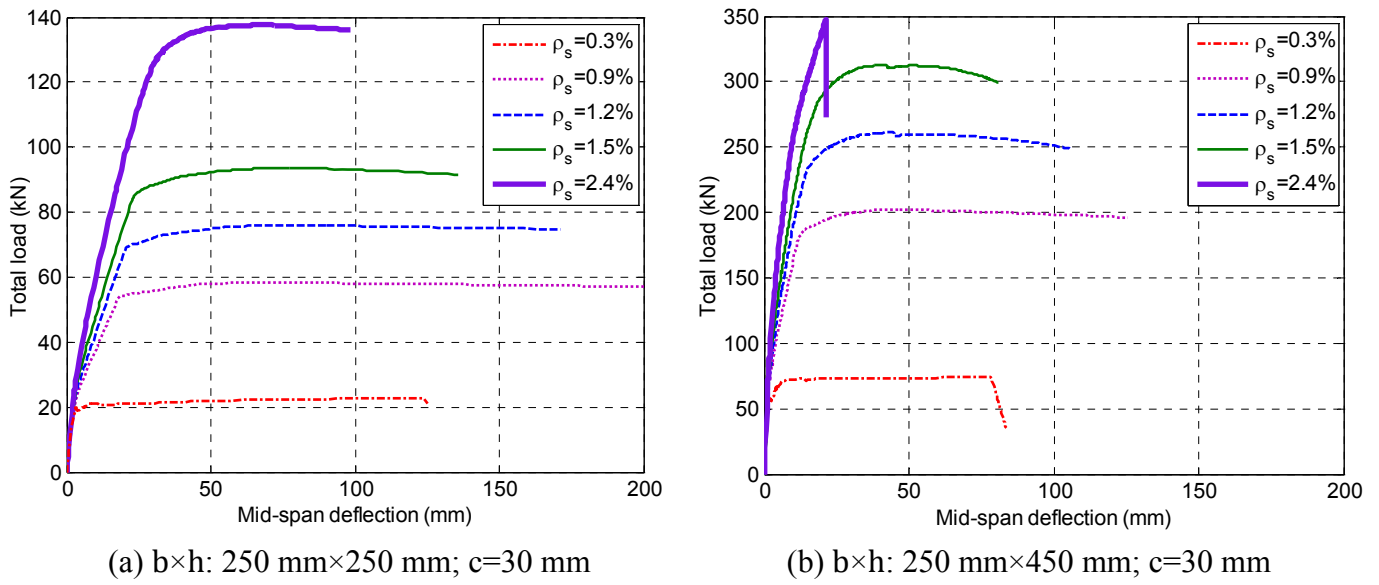


**Fig. 9.4** Load-deflection responses of RC beams with different design parameters at ambient temperature.

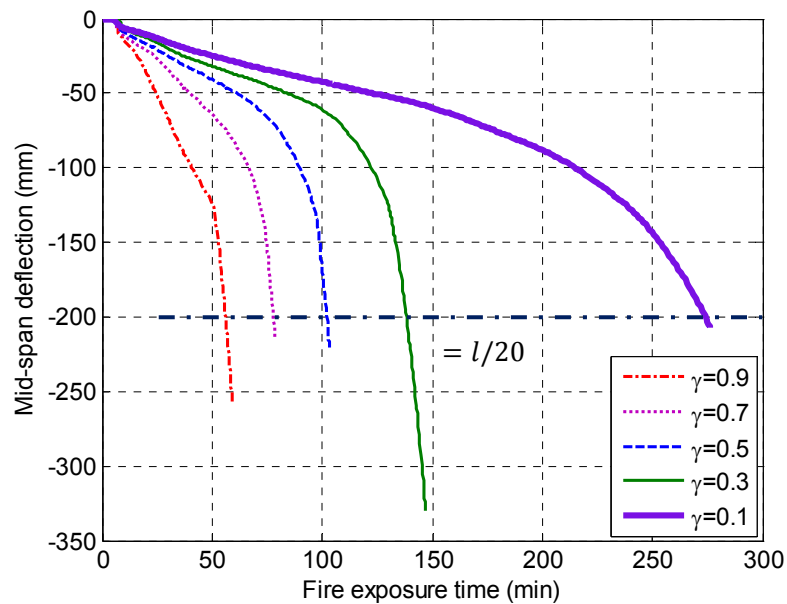
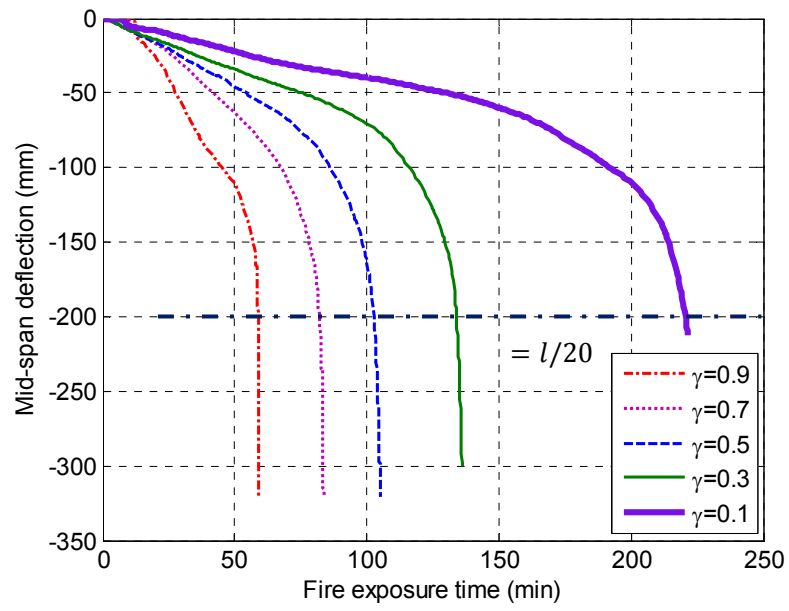


**Fig. 9.5** Determination of fire-resistance periods of RC beams.



(b)  $b \times h \times c$ : 250 mm  $\times$  250 mm  $\times$  30 mm;  $\rho_s = 1.2\%$

**Fig. 9.5** Determination of fire-resistance periods of RC beams (Cont'd).

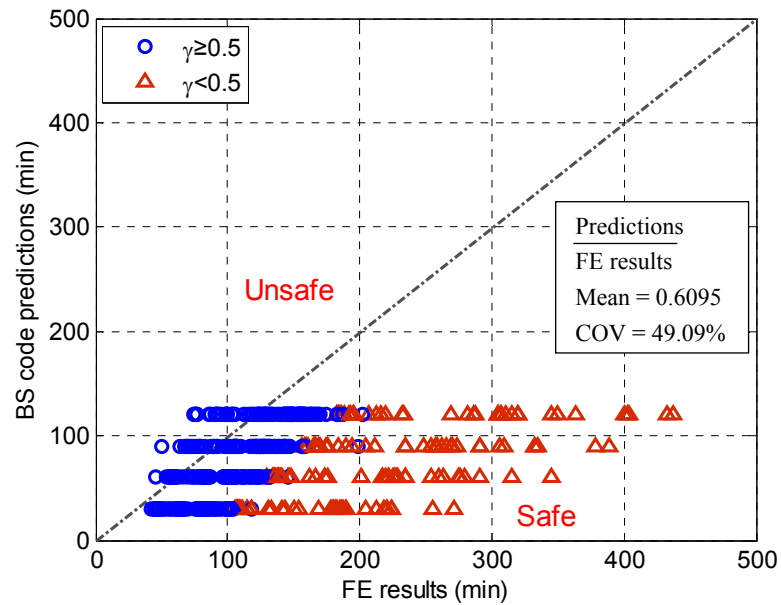


**Fig. 9.6** Comparison between BS 8110 code predictions and FE results

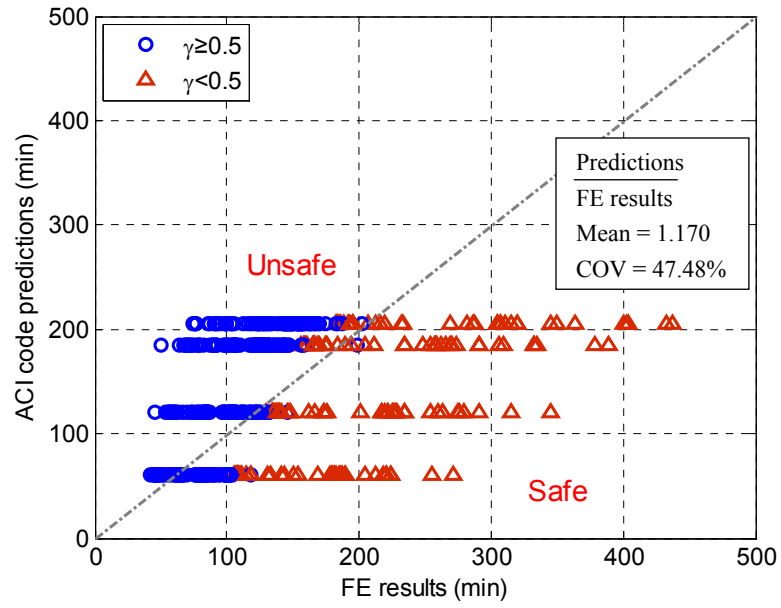


**Fig. 9.7** Comparison between ACI code predictions and FE results

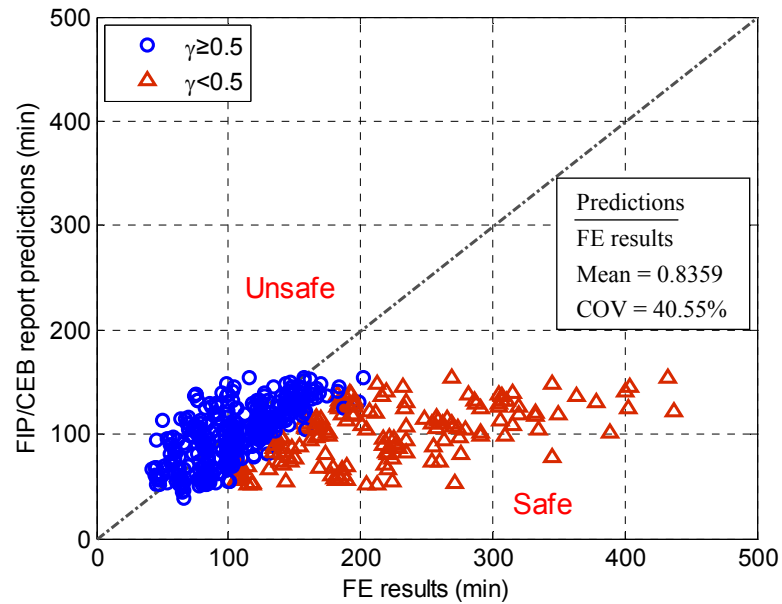


**Fig. 9.8** Comparison between FIP/CEB report predictions and FE results

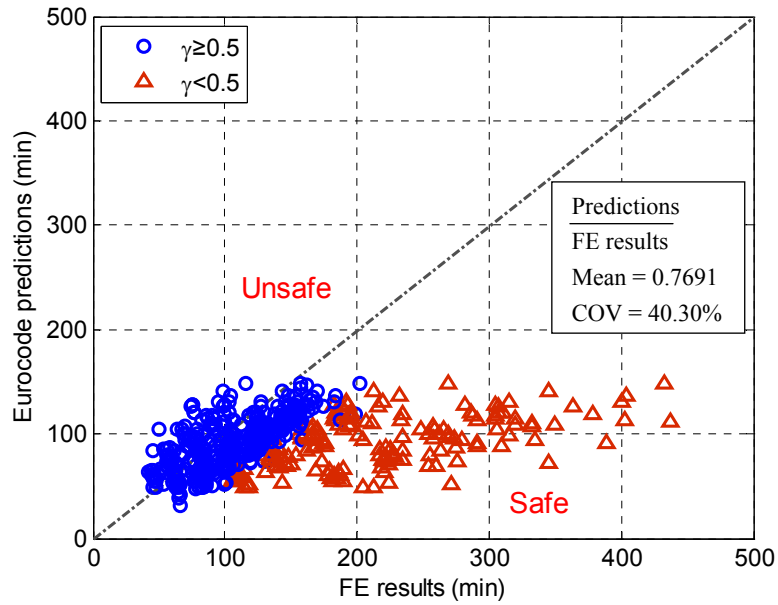


**Fig. 9.9** Comparison between Eurocode predictions and FE results.

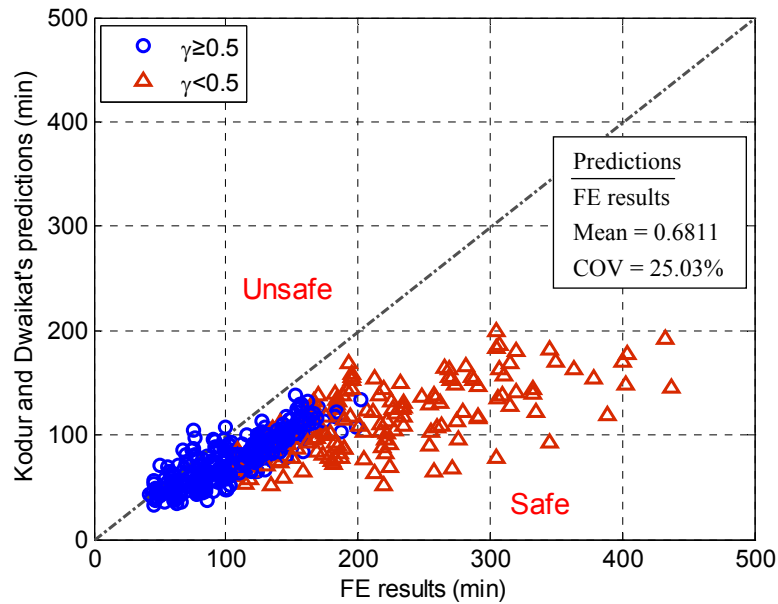


**Fig. 9.10** Comparison between Kodur and Dwaikat's (2011) predictions and FE results.

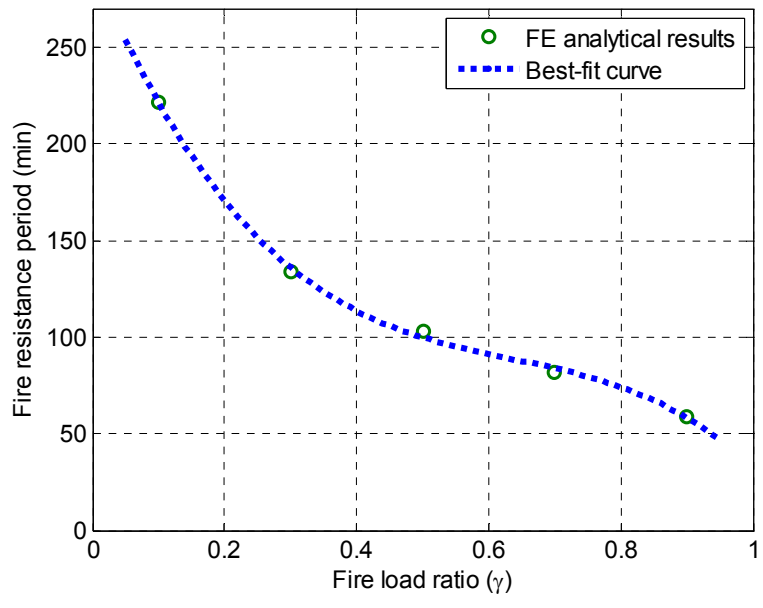


**Fig. 9.11** Effect of fire load ratio

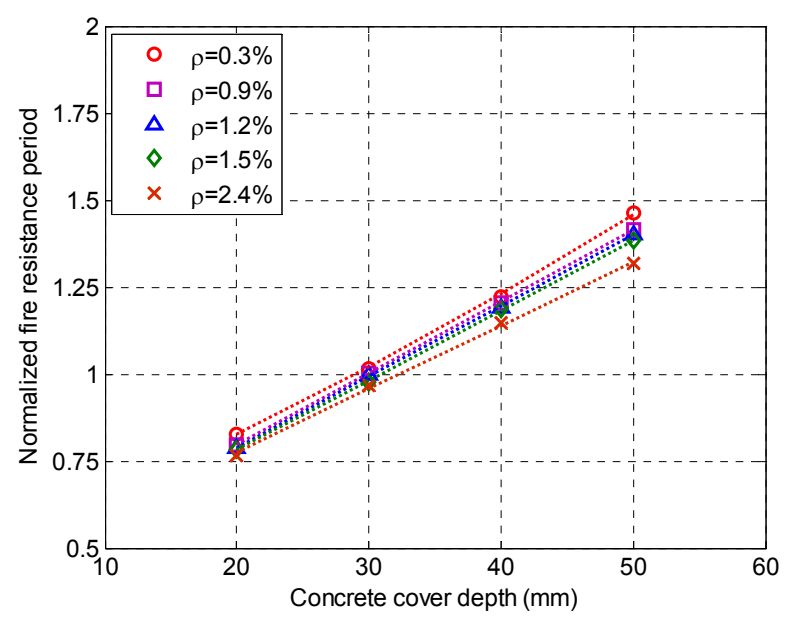


**Fig. 9.12** Combined effects of concrete cover and ratio of tension steel reinforcement.

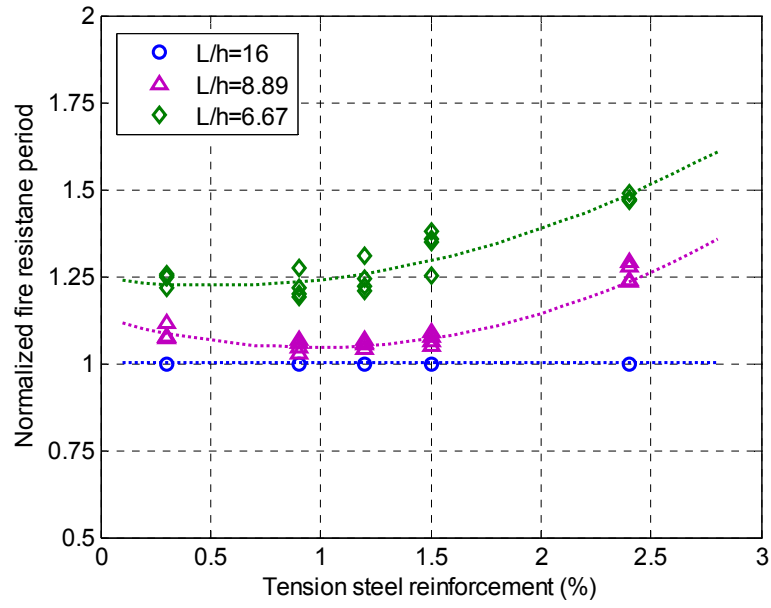


**Fig. 9.13** Effect of span-to-depth ratio

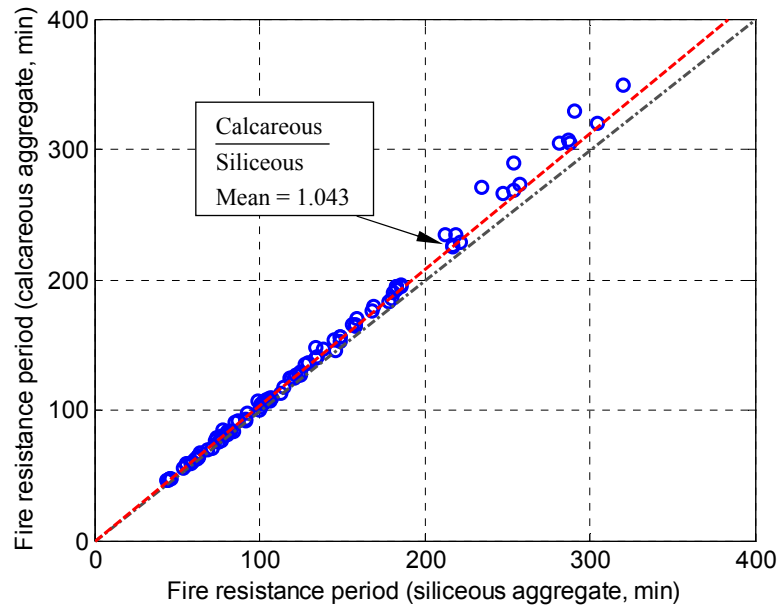


**Fig. 9.14** Effect of aggregate type

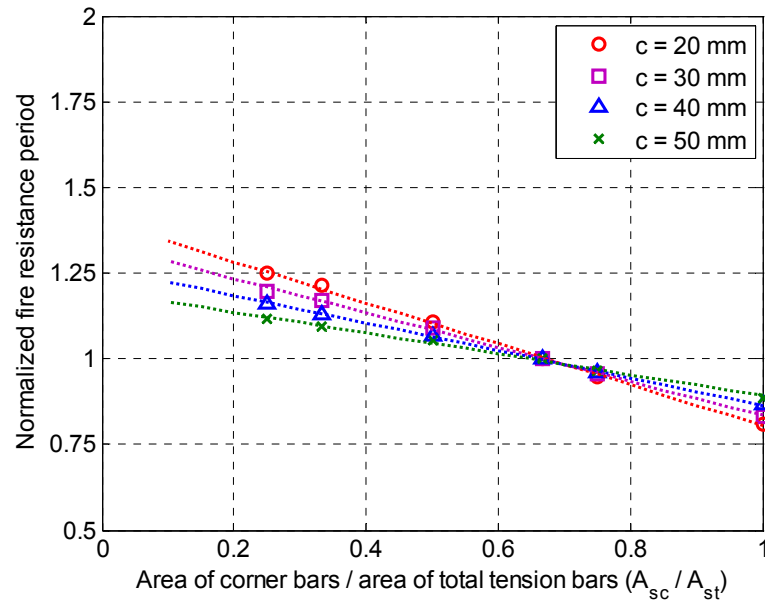


**Fig. 9.15** Effect of rebar placement of tension steel reinforcement

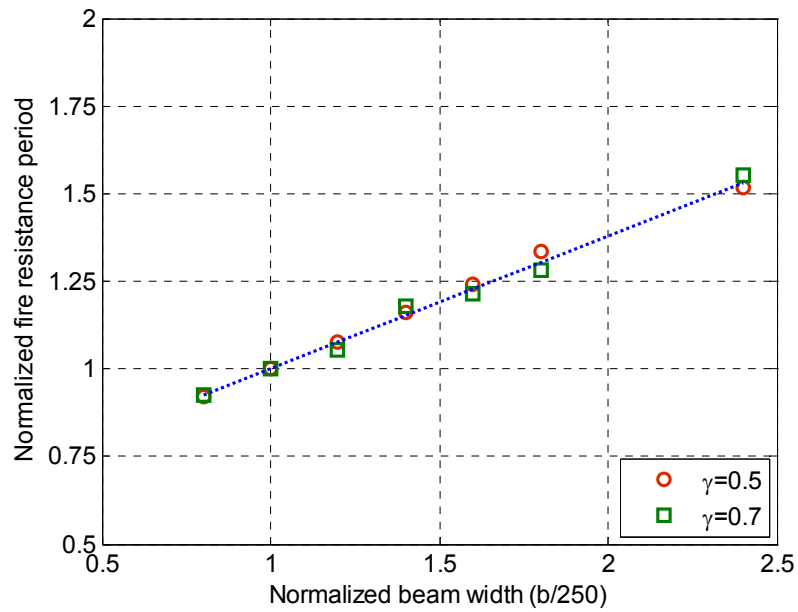
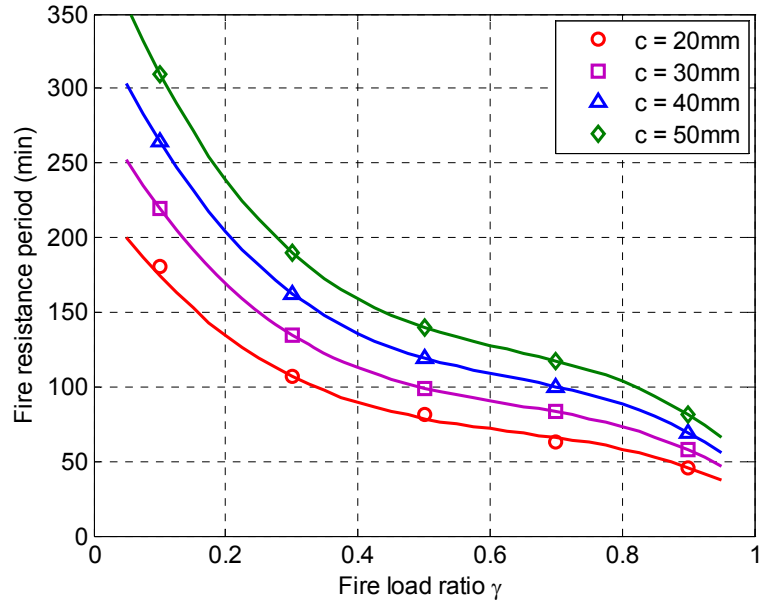
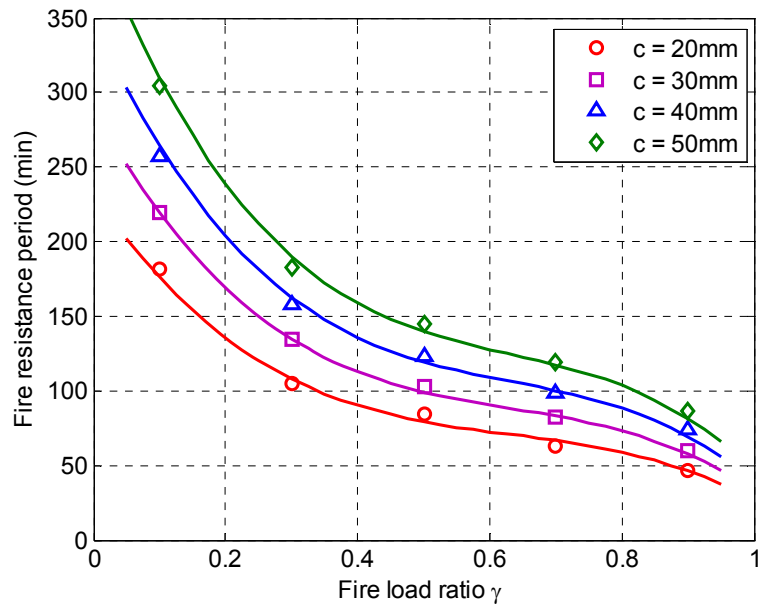


**Fig. 9.16** Effect of beam width

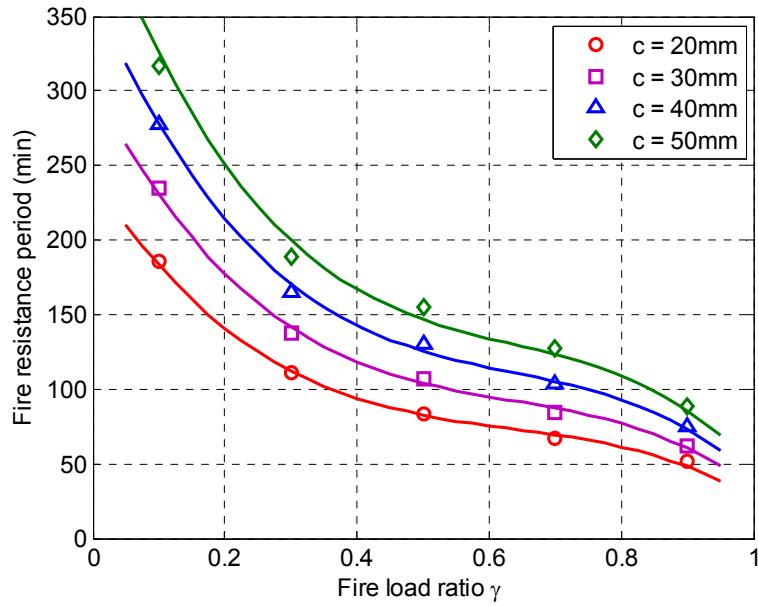


(a)  $b \times h$ : 250 mm $\times$ 250 mm;  $\rho_s = 1.2\%$

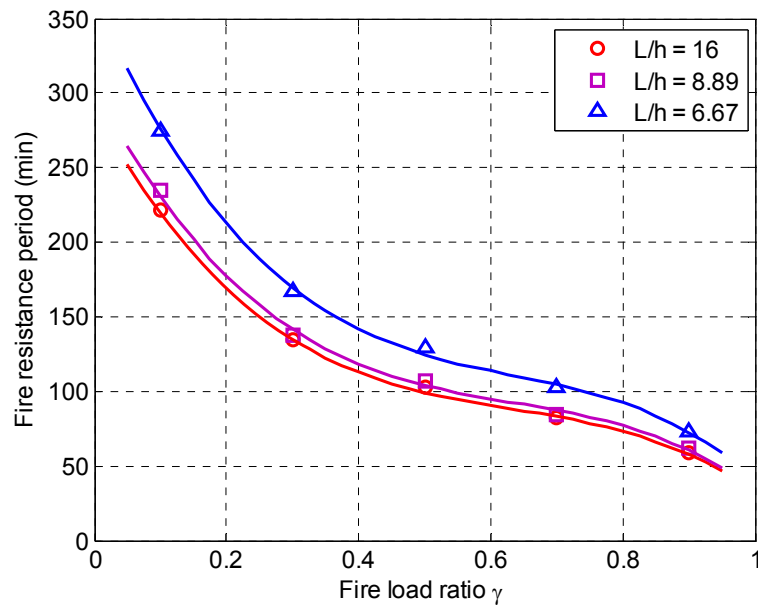


(b)  $b \times h$ : 250 mm $\times$ 250 mm;  $\rho_s = 0.9\%$

**Fig. 9.17** Comparisons between calculated fire resistance periods and data from FE parametric studies.



(c)  $b \times h$ : 250 mm $\times$ 450 mm;  $\rho_s = 1.2\%$



(d)  $b = 250\text{ mm}$ ,  $\rho_s = 1.2\%$ ;  $c = 30\text{ mm}$

**Fig. 9.17** Comparisons between calculated fire resistance periods and data from FE parametric studies (Cont'd).

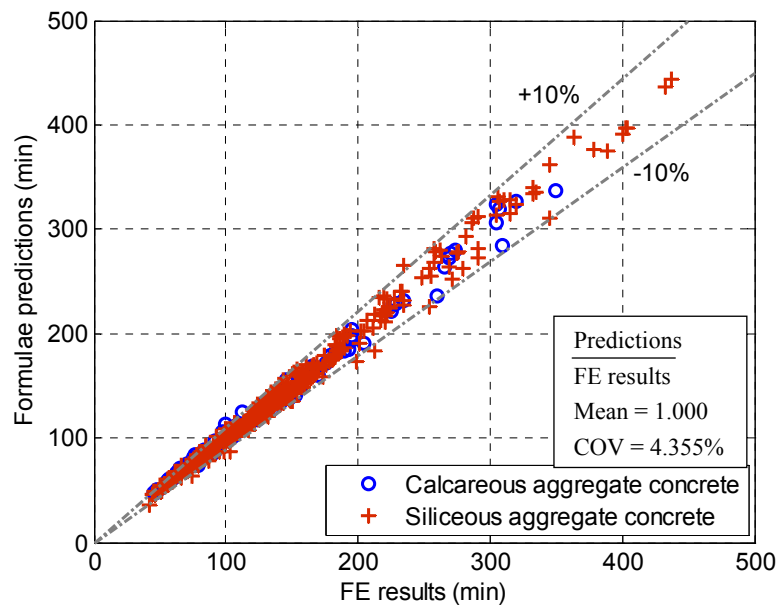


**Fig. 9.18** Comparison between the formulae predictions and the FE results (512 beams in total).

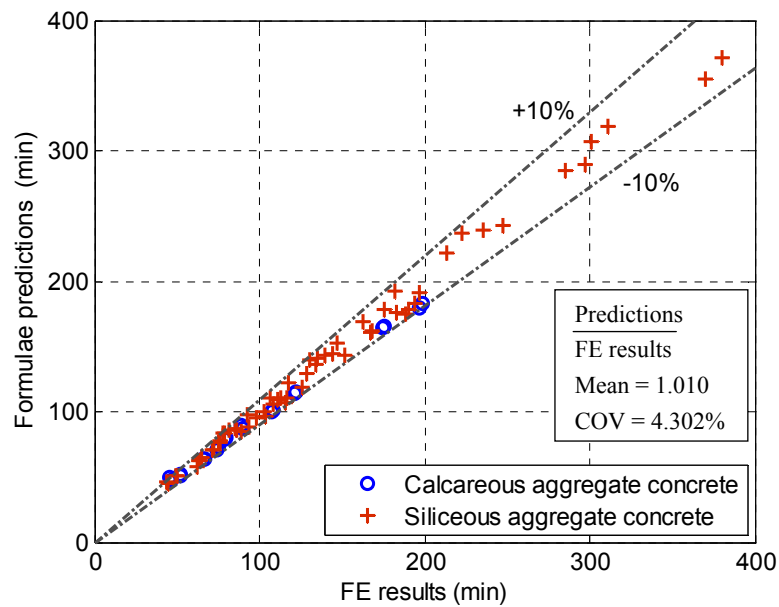


**Fig. 9.19** Comparison between the formulae predictions with the data from further FE parametric analyses (60 beams in total).

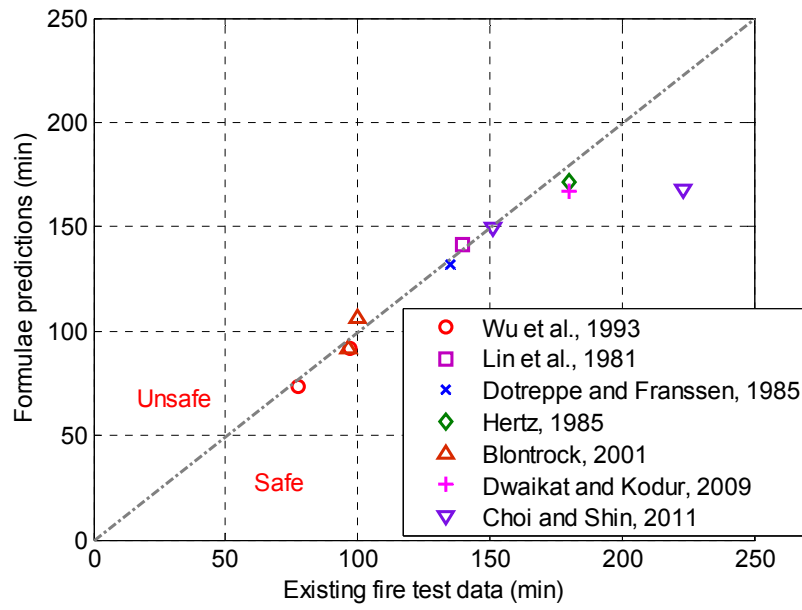


**Fig. 9.20** Comparison between formulae predictions and existing test data.

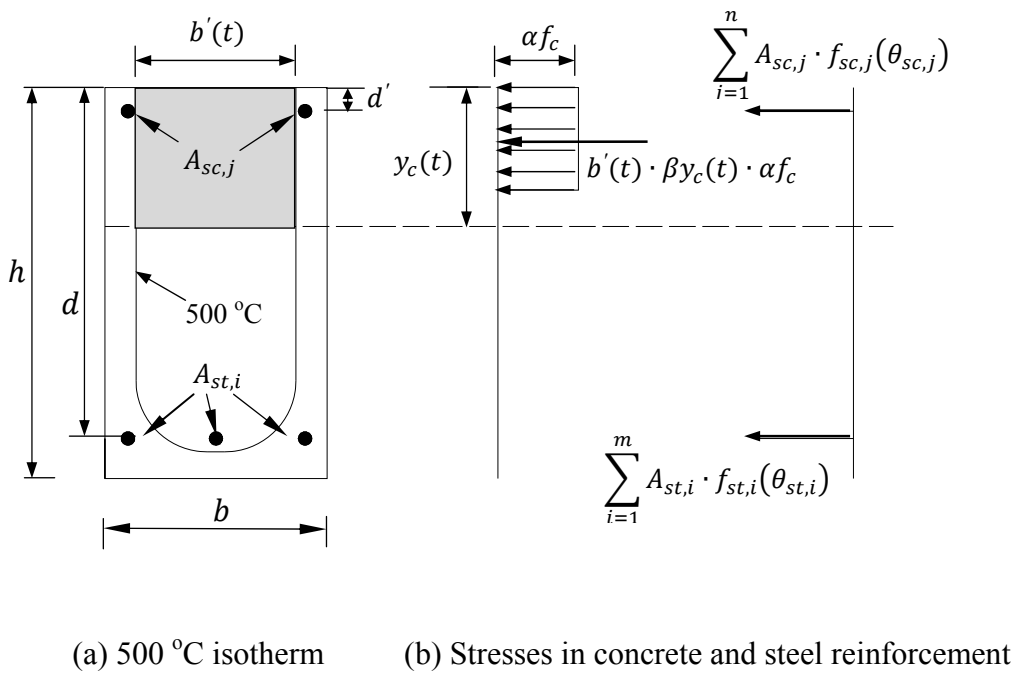


**Fig. 9.21** Schematic of the 500 °C isotherm method.

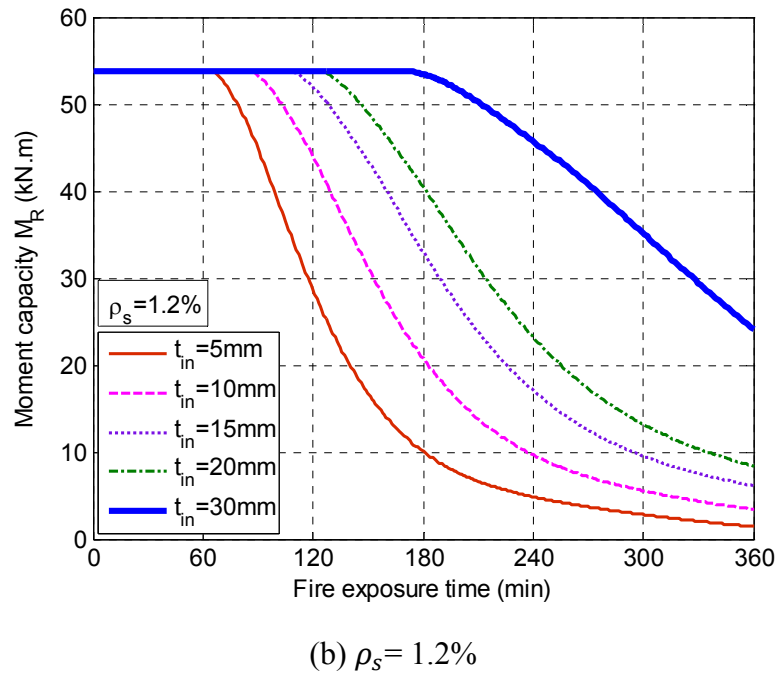
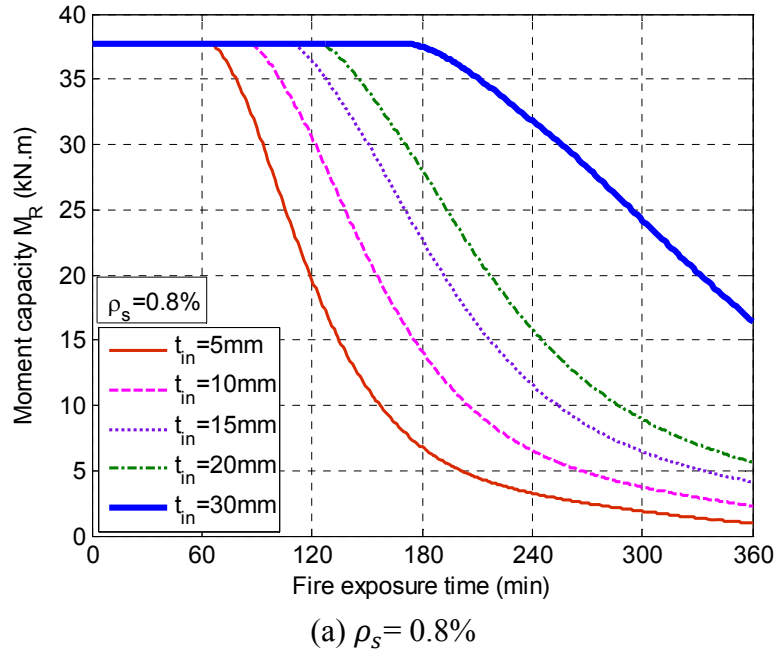
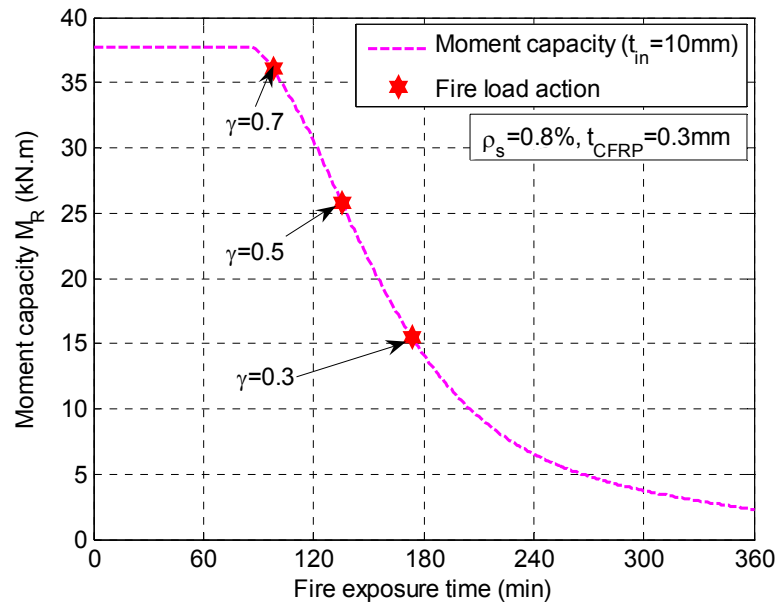
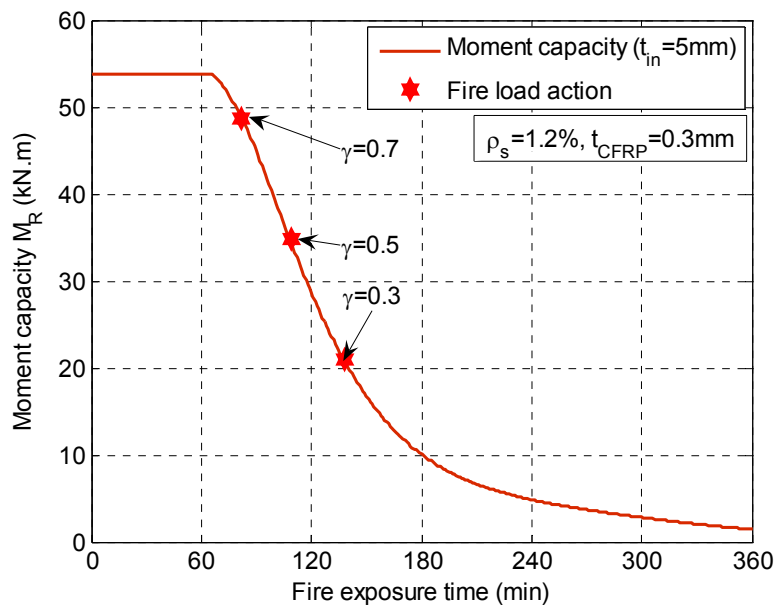


**Fig. 9.22** Effect of insulation thickness on the time-dependent moment capacity



(a)  $\rho_s = 0.8\%$ ;  $t_{CFRP} = 0.3\text{mm}$ ;  $t_{in} = 10\text{mm}$ .



(b)  $\rho_s = 1.2\%$ ;  $t_{CFRP} = 0.3\text{mm}$ ;  $t_{in} = 5\text{mm}$ .

**Fig. 9.23** Determination of fire resistance period of insulated CFRP-strengthened RC beams.

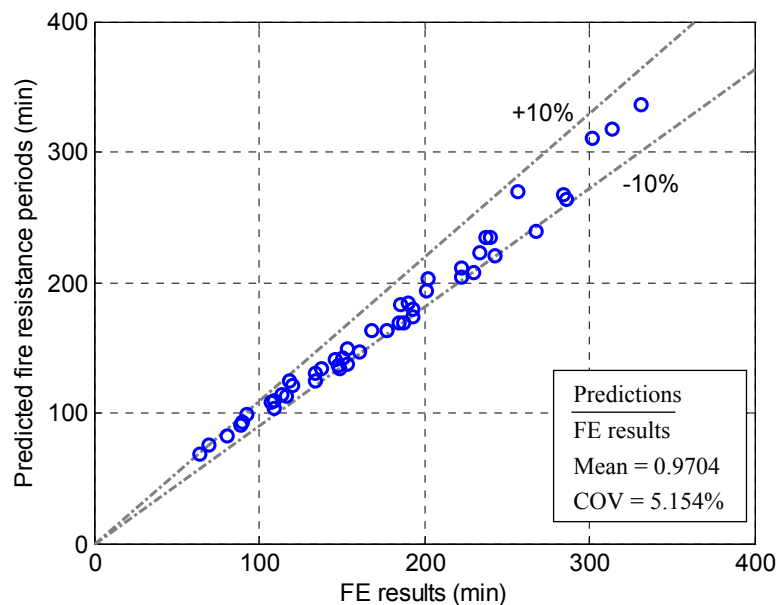


**Fig. 9.24** Comparison between predicted fire resistance periods and FE results for insulated CFRP-strengthened RC beams.

**Table 9.1** Design parameters of RC beams used in FE parametric analyses.

| Series     | Aggregate type       | Dimension (mm)           |       |          | Design parameters |          |                 |
|------------|----------------------|--------------------------|-------|----------|-------------------|----------|-----------------|
|            |                      | Section ( $b \times h$ ) | $l/d$ | $c$ (mm) | $\rho_s$ (%)      | $\gamma$ | $A_{sc}/A_{st}$ |
| <b>I</b>   | Siliceous aggregate  | $250 \times 250$         | 16    | 20       | 0.3               | 0.1      | $2/3$           |
|            |                      |                          |       | 30       | 0.9               | 0.3      |                 |
|            |                      |                          |       | 40       | 1.2               | 0.5      |                 |
|            |                      |                          |       | 50       | 1.5               | 0.7      |                 |
|            |                      |                          |       |          | 2.4               | 0.9      |                 |
| <b>II</b>  | Calcareous aggregate | $250 \times 250$         | 16    | 20       | 0.3               | 0.1      | $2/3$           |
|            |                      |                          |       | 30       | 0.9               | 0.3      |                 |
|            |                      |                          |       | 40       | 1.2               | 0.5      |                 |
|            |                      |                          |       | 50       | 1.5               | 0.7      |                 |
|            |                      |                          |       |          | 2.4               | 0.9      |                 |
| <b>III</b> | Siliceous aggregate  | $250 \times 250$         | 16    | 20       | 0.3               |          | 1               |
|            |                      |                          |       | 30       | 0.9               |          | $3/4$           |
|            |                      |                          |       | 40       | 1.2               | 0.5      | $2/3$           |
|            |                      |                          |       | 50       | 1.5               |          | $1/2$           |
|            |                      |                          |       |          | 2.4               |          | $1/3$           |
| <b>IV</b>  | Siliceous aggregate  | $200 \times 450$         | 8.89  | 30       | 1.2               | 0.5      | $2/3$           |
|            |                      | $250 \times 450$         |       |          |                   |          |                 |
|            |                      | $300 \times 450$         |       |          |                   |          |                 |
|            |                      | $350 \times 450$         |       |          |                   |          |                 |
|            |                      | $400 \times 450$         |       |          |                   |          |                 |
|            |                      | $450 \times 450$         |       |          |                   |          |                 |
|            |                      | $600 \times 450$         |       |          |                   |          |                 |

**Table 9.2** Load-carrying capacity of beams at room temperature for parametric study.

| Beam           |                     | Load-carrying capacity $P_u$ (kN) |                |                |                |                |
|----------------|---------------------|-----------------------------------|----------------|----------------|----------------|----------------|
| Dimension (mm) | Concrete cover (mm) | $\rho_s=0.3\%$                    | $\rho_s=0.9\%$ | $\rho_s=1.2\%$ | $\rho_s=1.5\%$ | $\rho_s=2.4\%$ |
| 250 × 250      | 20                  | 23.13                             | 62.18          | 81.27          | 99.55          | 146.43         |
|                | 30                  | 22.94                             | 58.28          | 75.99          | 93.59          | 137.58         |
|                | 40                  | 23.42                             | 55.38          | 71.06          | 86.35          | 127.24         |
|                | 50                  | 24.59                             | 52.65          | 67.02          | 80.50          | 116.96         |
| 250 × 450      | 20                  | 75.78                             | 211.22         | 267.21         | 303.04         | 329.92         |
|                | 30                  | 73.83                             | 202.38         | 261.18         | 312.74         | 347.86         |
|                | 40                  | 72.62                             | 199.34         | 254.49         | 307.08         | 349.32         |
|                | 50                  | 72.02                             | 191.17         | 246.73         | 296.15         | 350.43         |
| 250 × 600      | 20                  | 135.26                            | 374.65         | 414.00         | 420.39         | 434.37         |
|                | 30                  | 135.25                            | 365.28         | 443.98         | 459.75         | 464.11         |
|                | 40                  | 130.52                            | 356.38         | 441.88         | 454.62         | 461.90         |
|                | 50                  | 127.85                            | 346.35         | 431.61         | 448.64         | 461.67         |

**Table 9.3** Design parameters of RC beams used in further FE parametric analyses.

| Series    | Aggregate type                      | Dimension (mm) |       |          | Parameters   |          |                 |
|-----------|-------------------------------------|----------------|-------|----------|--------------|----------|-----------------|
|           |                                     | Cross-section  | $l/d$ | $c$ (mm) | $\rho_s$ (%) | $\gamma$ | $A_{sc}/A_{st}$ |
| <b>I</b>  | Siliceous and calcareous aggregates | 200 × 400      | 10    | 20       | 0.8          | 0.1      | 2/3             |
|           |                                     |                |       |          |              | 0.3      |                 |
|           |                                     |                |       |          |              | 0.5      |                 |
|           |                                     |                |       |          |              | 0.7      |                 |
|           |                                     |                |       |          |              | 0.9      |                 |
| <b>II</b> | Siliceous aggregate                 | 300 × 400      | 10    | 30       | 0.8          | 0.1      | 2/3             |
|           |                                     |                |       |          |              | 0.3      |                 |
|           |                                     | 300 × 600      | 6.67  | 40       | 1.2          | 0.5      |                 |
|           |                                     |                |       |          |              | 0.7      |                 |
|           |                                     |                |       |          |              | 0.9      |                 |

**Table 9.4** Comparisons between existing fire test data with formulae predictions

| Specimen <sup>a</sup>   | BI-BII                      | BIII  | B-124             | RC beam                      | B1                  | B3-B4                   | B5     | B1                       | N4                   | N5    |       |
|-------------------------|-----------------------------|-------|-------------------|------------------------------|---------------------|-------------------------|--------|--------------------------|----------------------|-------|-------|
| Source                  | Wu et al. (1993)            |       | Lin et al. (1981) | Dotreppe and Franssen (1985) | Hertz (1985)        | Blontrock et al. (2000) |        | Dwaikat and Kodur (2009) | Choi and Shin (2011) |       |       |
| Cross-section (mm)      | 200×400                     |       | 305×355           | 200×600                      | 285×580             | 200×300                 |        | 254×406                  | 250×400              |       |       |
| Span (m)                | 5.1                         |       | 6.1               | 6.5                          | 8.0                 | 2.85                    |        | 3.66                     | 4.5                  |       |       |
| Tension rebars          | 1φ14 and 2φ12               |       | 4φ19              | 3φ20                         | 3φ22 and 1φ25       | 2φ16                    |        | 3φ19                     | 3φ22                 |       |       |
| $f_c$ (MPa)             | 24.2                        |       | 29.46             | 15                           | 25                  | 58.2                    |        | 58.2                     | 21                   |       |       |
| $f_{sy}/f_{su}^b$ (MPa) | 240/380                     |       | 435.8/--          | 300/--                       | 420/--              | 591/699                 |        | 420/705                  | 439/--               |       |       |
| Cover (mm)              | 25                          |       | 25                | 40                           | 29.375 <sup>c</sup> | 25                      |        | 38                       | 50                   | 60    |       |
| Aggregate type          | Calcareous                  |       | Siliceous         | Siliceous                    | Siliceous           | Siliceous               |        | Calcareous               | Siliceous            |       |       |
| Fire load               | Distributed (kN/m)          |       | 4 points (kN)     | 2 points (kN)                | Distributed (kN/m)  | 2 points (kN)           |        | 2 points (kN)            | 2 points (kN)        |       |       |
|                         | 7.55                        | 11.39 | 20                | 32.5                         | 11                  | 30.6                    | 40.6   | 50                       | 43.55                |       |       |
| R<br>(min)              | $R_{test}$                  | 97.1  | 77.4              | 139.5                        | 135                 | 180                     | 100    | 96.5                     | 180                  | 151   | 167   |
|                         | $R_{pred}$                  | 91.99 | 73.3              | 141.7                        | 132.1               | 171.4                   | 106.4  | 92.1                     | 167.1                | 149.3 | 211.3 |
|                         | $\frac{R_{pred}}{R_{test}}$ | 0.948 | 0.947             | 1.015                        | 0.977               | 0.952                   | 1.0627 | 0.955                    | 0.928                | 0.989 | 0.753 |

<sup>a</sup> Some of the specimen names are assigned by the author as they are not available in the original papers.

<sup>b</sup>  $f_{su}$  is the measured ultimate strength of steel rebars.

<sup>c</sup> Concrete cover is determined as the average value of these four steel rebars.

**Table 9.5** Design parameters of insulated FRP-strengthened RC beams for FE parametric analyses

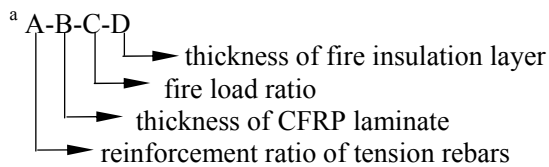
| Aggregate type      | Dimension (mm)     |       |          | Parameters   |                 |                                   |          |  |
|---------------------|--------------------|-------|----------|--------------|-----------------|-----------------------------------|----------|--|
|                     | Cross-section (mm) | $l/d$ | $c$ (mm) | $\rho_s$ (%) | $A_{sc}/A_{st}$ | CFRP thickness ( $t_{CFRP}$ : mm) | $\gamma$ | Fire insulation thickness ( $t_{in}$ : mm) |
| Siliceous aggregate | $250 \times 250$   | 16    | 25       | 0.8          | 2/3             | 0.3                               | 0.3      | 5  |
|                     |                    |       |          |              |                 |                                   |          | 10   |
|                     |                    |       |          |              |                 |                                   |          | 15   |
|                     |                    |       |          |              |                 |                                   |          | 20   |
|                     |                    |       |          |              |                 |                                   |          | 30   |

**Table 9.6** Load-carrying capacities of reference and FRP-strengthened RC beams.

| Dimension (mm)   | Concrete cover (mm) | $\rho_s$ (%) | CFRP thickness ( $t_{CFRP}$ : mm) | Load-carrying capacity $P_u$ (kN) |
|------------------|---------------------|--------------|-----------------------------------|-----------------------------------|
| $250 \times 250$ | 25                  | 0.8          | --                                | 51.00                             |
|                  | 25                  | 0.8          | 0.3                               | 68.65                             |
|                  | 25                  | 0.8          | 1.2                               | 100.06                            |
|                  | 25                  | 1.2          | --                                | 77.86                             |
|                  | 25                  | 1.2          | 0.3                               | 92.87                             |
|                  | 25                  | 1.2          | 1.2                               | 117.65                            |

**Table 9.7** Fire resistance predictions of insulated CFRP-strengthened RC beams.

| Name <sup>a</sup>   | Fire load |             |       |            |              | Fire resistance period (min) |                           |                     |
|---------------------|-----------|-------------|-------|------------|--------------|------------------------------|---------------------------|---------------------|
|                     | $\gamma$  | $P_{u,FRP}$ | $P$   | $P_{u,RC}$ | $P/P_{u,RC}$ | $R_{FE}$ <sup>b</sup>        | $R_{Simple}$ <sup>c</sup> | $R_{Simple}/R_{FE}$ |
| 0.8%-0.3mm-0.3-5mm  | 0.3       | 68.65       | 20.60 | 51.00      | 0.4039       | 148.50                       | 134                       | 0.9024              |
| 0.8%-0.3mm-0.3-10mm | 0.3       | 68.65       | 20.60 | 51.00      | 0.4039       | 193.34                       | 174                       | 0.9000              |
| 0.8%-0.3mm-0.3-15mm | 0.3       | 68.65       | 20.60 | 51.00      | 0.4039       | 240.45                       | 234                       | 0.9732              |
| 0.8%-0.3mm-0.3-20mm | 0.3       | 68.65       | 20.60 | 51.00      | 0.4039       | 286.00                       | 264                       | 0.9231              |
| 0.8%-0.3mm-0.3-30mm | 0.3       | 68.65       | 20.60 | 51.00      | 0.4039       | > 360                        | > 360                     | N.A.E               |
| 0.8%-1.2mm-0.3-5mm  | 0.3       | 100.06      | 30.02 | 51.00      | 0.5886       | 116.59                       | 113                       | 0.9692              |
| 0.8%-1.2mm-0.3-10mm | 0.3       | 100.06      | 30.02 | 51.00      | 0.5886       | 160.55                       | 147                       | 0.9156              |
| 0.8%-1.2mm-0.3-15mm | 0.3       | 100.06      | 30.02 | 51.00      | 0.5886       | 201.16                       | 194                       | 0.9644              |
| 0.8%-1.2mm-0.3-20mm | 0.3       | 100.06      | 30.02 | 51.00      | 0.5886       | 242.74                       | 220                       | 0.9063              |
| 0.8%-1.2mm-0.3-30mm | 0.3       | 100.06      | 30.02 | 51.00      | 0.5886       | 330.95                       | 336                       | 1.0153              |
| 0.8%-0.3mm-0.5-5mm  | 0.5       | 68.65       | 34.33 | 51.00      | 0.6731       | 109.00                       | 104                       | 0.9541              |
| 0.8%-0.3mm-0.5-10mm | 0.5       | 68.65       | 34.33 | 51.00      | 0.6731       | 147.50                       | 136                       | 0.9220              |
| 0.8%-0.3mm-0.5-15mm | 0.5       | 68.65       | 34.33 | 51.00      | 0.6731       | 185.21                       | 169                       | 0.9125              |
| 0.8%-0.3mm-0.5-20mm | 0.5       | 68.65       | 34.33 | 51.00      | 0.6731       | 222.65                       | 204                       | 0.9162              |
| 0.8%-0.3mm-0.5-30mm | 0.5       | 68.65       | 34.33 | 51.00      | 0.6731       | 301.95                       | 311                       | 1.0300              |
| 0.8%-1.2mm-0.5-5mm  | 0.5       | 100.06      | 50.03 | 51.00      | 0.9809       | 64.42                        | 69                        | 1.0711              |
| 0.8%-1.2mm-0.5-10mm | 0.5       | 100.06      | 50.03 | 51.00      | 0.9809       | 89.29                        | 91                        | 1.0192              |
| 0.8%-1.2mm-0.5-15mm | 0.5       | 100.06      | 50.03 | 51.00      | 0.9809       | 113.64                       | 114                       | 1.0032              |
| 0.8%-1.2mm-0.5-20mm | 0.5       | 100.06      | 50.03 | 51.00      | 0.9809       | 133.67                       | 130                       | 0.9725              |
| 0.8%-1.2mm-0.5-30mm | 0.5       | 100.06      | 50.03 | 51.00      | 0.9809       | 185.82                       | 183                       | 0.9848              |
| 0.8%-0.3mm-0.7-5mm  | 0.7       | 68.65       | 48.06 | 51.00      | 0.9423       | 69.76                        | 76                        | 1.0894              |
| 0.8%-0.3mm-0.7-10mm | 0.7       | 68.65       | 48.06 | 51.00      | 0.9423       | 93.07                        | 99                        | 1.0637              |
| 0.8%-0.3mm-0.7-15mm | 0.7       | 68.65       | 48.06 | 51.00      | 0.9423       | 118.59                       | 124                       | 1.0456              |
| 0.8%-0.3mm-0.7-20mm | 0.7       | 68.65       | 48.06 | 51.00      | 0.9423       | 145.63                       | 141                       | 0.9682              |
| 0.8%-0.3mm-0.7-30mm | 0.7       | 68.65       | 48.06 | 51.00      | 0.9423       | 202.24                       | 203                       | 1.0038              |
| 0.8%-1.2mm-0.7-5mm  | 0.7       | 100.06      | 70.04 | 51.00      | 1.3733       | N.A.                         | N.A.                      | N.A.                |
| 0.8%-1.2mm-0.7-10mm | 0.7       | 100.06      | 70.04 | 51.00      | 1.3733       | N.A.                         | N.A.                      | N.A.                |
| 0.8%-1.2mm-0.7-15mm | 0.7       | 100.06      | 70.04 | 51.00      | 1.3733       | N.A.                         | N.A.                      | N.A.                |
| 0.8%-1.2mm-0.7-20mm | 0.7       | 100.06      | 70.04 | 51.00      | 1.3733       | N.A.                         | N.A.                      | N.A.                |
| 0.8%-1.2mm-0.7-30mm | 0.7       | 100.06      | 70.04 | 51.00      | 1.3733       | N.A.                         | N.A.                      | N.A.                |



<sup>b</sup>  $R_{FE}$ : Fire resistance period predicted by the FE modeling.

<sup>c</sup>  $R_{Simple}$ : Fire resistance period predicted by the proposed simple approach.

**Table 9.7** Fire resistance predictions of insulated CFRP-strengthened RC beams (cont'd).

| Name                | Fire load |             |       |            |              | Fire resistance period (min) |              |                     |
|---------------------|-----------|-------------|-------|------------|--------------|------------------------------|--------------|---------------------|
|                     | $\gamma$  | $P_{u,FRP}$ | $P$   | $P_{u,RC}$ | $P/P_{u,RC}$ | $R_{FE}$                     | $R_{Simple}$ | $R_{Simple}/R_{FE}$ |
| 1.2%-0.3mm-0.3-5mm  | 0.3       | 92.87       | 27.86 | 77.89      | 0.3577       | 153.10                       | 138          | 0.9014              |
| 1.2%-0.3mm-0.3-10mm | 0.3       | 92.87       | 27.86 | 77.89      | 0.3577       | 192.66                       | 180          | 0.9343              |
| 1.2%-0.3mm-0.3-15mm | 0.3       | 92.87       | 27.86 | 77.89      | 0.3577       | 237.66                       | 235          | 0.9888              |
| 1.2%-0.3mm-0.3-20mm | 0.3       | 92.87       | 27.86 | 77.89      | 0.3577       | 284.53                       | 267          | 0.9384              |
| 1.2%-0.3mm-0.3-30mm | 0.3       | 92.87       | 27.86 | 77.89      | 0.3577       | > 360                        | > 360        | N.A.E <sup>e</sup>  |
| 1.2%-1.2mm-0.3-5mm  | 0.3       | 117.65      | 35.29 | 77.89      | 0.4532       | 134.25                       | 125          | 0.9311              |
| 1.2%-1.2mm-0.3-10mm | 0.3       | 117.65      | 35.29 | 77.89      | 0.4532       | 177.23                       | 163          | 0.9197              |
| 1.2%-1.2mm-0.3-15mm | 0.3       | 117.65      | 35.29 | 77.89      | 0.4532       | 222.19                       | 211          | 0.9496              |
| 1.2%-1.2mm-0.3-20mm | 0.3       | 117.65      | 35.29 | 77.89      | 0.4532       | 267.76                       | 239          | 0.8926              |
| 1.2%-1.2mm-0.3-30mm | 0.3       | 117.65      | 35.29 | 77.89      | 0.4532       | > 360                        | > 360        | N.A.E               |
| 1.2%-0.3mm-0.5-5mm  | 0.5       | 92.87       | 46.44 | 77.89      | 0.5962       | 109.38                       | 109          | 0.9965              |
| 1.2%-0.3mm-0.5-10mm | 0.5       | 92.87       | 46.44 | 77.89      | 0.5962       | 150.40                       | 142          | 0.9441              |
| 1.2%-0.3mm-0.5-15mm | 0.5       | 92.87       | 46.44 | 77.89      | 0.5962       | 190.44                       | 184          | 0.9662              |
| 1.2%-0.3mm-0.5-20mm | 0.5       | 92.87       | 46.44 | 77.89      | 0.5962       | 230.28                       | 208          | 0.9032              |
| 1.2%-0.3mm-0.5-30mm | 0.5       | 92.87       | 46.44 | 77.89      | 0.5962       | 313.44                       | 318          | 1.0145              |
| 1.2%-1.2mm-0.5-5mm  | 0.5       | 117.65      | 58.82 | 77.89      | 0.7553       | 89.70                        | 93           | 1.0368              |
| 1.2%-1.2mm-0.5-10mm | 0.5       | 117.65      | 58.82 | 77.89      | 0.7553       | 120.26                       | 121          | 1.0062              |
| 1.2%-1.2mm-0.5-15mm | 0.5       | 117.65      | 58.82 | 77.89      | 0.7553       | 153.43                       | 149          | 0.9711              |
| 1.2%-1.2mm-0.5-20mm | 0.5       | 117.65      | 58.82 | 77.89      | 0.7553       | 187.31                       | 169          | 0.9022              |
| 1.2%-1.2mm-0.5-30mm | 0.5       | 117.65      | 58.82 | 77.89      | 0.7553       | 256.94                       | 270          | 1.0508              |
| 1.2%-0.3mm-0.7-5mm  | 0.7       | 92.87       | 65.01 | 77.89      | 0.8347       | 80.31                        | 83           | 1.0335              |
| 1.2%-0.3mm-0.7-10mm | 0.7       | 92.87       | 65.01 | 77.89      | 0.8347       | 107.75                       | 108          | 1.0023              |
| 1.2%-0.3mm-0.7-15mm | 0.7       | 92.87       | 65.01 | 77.89      | 0.8347       | 137.59                       | 134          | 0.9739              |
| 1.2%-0.3mm-0.7-20mm | 0.7       | 92.87       | 65.01 | 77.89      | 0.8347       | 167.96                       | 163          | 0.9705              |
| 1.2%-0.3mm-0.7-30mm | 0.7       | 92.87       | 65.01 | 77.89      | 0.8347       | 233.55                       | 223          | 0.9548              |
| 1.2%-1.2mm-0.7-5mm  | 0.7       | 117.65      | 82.35 | 77.89      | 1.0574       | N.A. <sup>d</sup>            | N.A.         | N.A.                |
| 1.2%-1.2mm-0.7-10mm | 0.7       | 117.65      | 82.35 | 77.89      | 1.0574       | N.A.                         | N.A.         | N.A.                |
| 1.2%-1.2mm-0.7-15mm | 0.7       | 117.65      | 82.35 | 77.89      | 1.0574       | N.A.                         | N.A.         | N.A.                |
| 1.2%-1.2mm-0.7-20mm | 0.7       | 117.65      | 82.35 | 77.89      | 1.0574       | N.A.                         | N.A.         | N.A.                |
| 1.2%-1.2mm-0.7-30mm | 0.7       | 117.65      | 82.35 | 77.89      | 1.0574       | N.A.                         | N.A.         | N.A.                |

<sup>d</sup>N.A. = Not applicable as the applied fire load on FRP-strengthened RC beams are larger than the load-carrying capacity of the reference RC beams.

<sup>e</sup>N.A.E. = Not able to estimate as the fire resistance period is longer than 360 min.

## Appendix A

**Table 9. A1** Minimum dimensions for RC beams provided by BS 8110-2 (1985)

| Material properties<br>and support conditions |       | Minimum dimensions for a fire resistance rating (mm) |     |      |     |     |     |
|---|-------|--|-----|------|-----|-----|-----|
|   |       | 0.5h   | 1h  | 1.5h | 2h  | 3h  | 4h  |
| Simply supported beam<br>dense concrete       | width | 80   | 120 | 150  | 200 | 240 | 280 |
|   | cover | 20   | 30  | 40   | 50  | 70  | 80  |
| Simply supported beam<br>lightweight concrete | width | 80   | 100 | 130  | 160 | 200 | 250 |
|   | cover | 15   | 20  | 35   | 45  | 55  | 65  |
| Continuous beam<br>dense concrete             | width | 80   | 80  | 120  | 150 | 200 | 240 |
|   | cover | 20   | 20  | 35   | 50  | 60  | 70  |
| Continuous beam<br>lightweight concrete       | width | 60   | 80  | 90   | 110 | 150 | 200 |
|   | cover | 15   | 20  | 25   | 35  | 45  | 65  |

**Table 9. A2** Minimum dimensions and axial distances for simply supported RC beams provided by FIP/CEB code (1978).

| Fire resistance<br>ratings | Minimum dimensions (mm)                     |     |     |     |
|----------------------------|---|-----|-----|-----|
|                            | Possible combinations of $a$ and $b_{\min}$ |     |     |     |
| R 30                       | $b_{\min} = 80$                             | 120 | 160 | 200 |
|                            | $a = 25$                                    | 15  | 10  | 10  |
| R 60                       | $b_{\min} = 120$                            | 160 | 200 | 300 |
|                            | $a = 40$                                    | 35  | 30  | 25  |
| R 90                       | $b_{\min} = 150$                            | 200 | 250 | 400 |
|                            | $a = 55$                                    | 45  | 40  | 35  |
| R 120                      | $b_{\min} = 200$                            | 240 | 300 | 500 |
|                            | $a = 65$                                    | 55  | 50  | 45  |
| R 180                      | $b_{\min} = 240$                            | 300 | 400 | 600 |
|                            | $a = 80$                                    | 70  | 65  | 60  |
| R 240                      | $b_{\min} = 280$                            | 350 | 500 | 700 |
|                            | $a = 90$                                    | 80  | 75  | 70  |

**Table 9. A3** Minimum cover thickness and beam width requirements for fire resistance design in RC beams provided by ACI 216.1 (2007)

| Support condition | Beam width, mm | Cover for corresponding fire-resistance rating, mm |             |         |         |         |
|-------------------|----------------|--|-------------|---------|---------|---------|
|                   |                | 1 hour   | 1-1/2 hours | 2 hours | 3 hours | 4 hours |
| Restrained beam   | 125            | 20   | 20          | 20      | 25      | 30      |
|                   | 175            | 20   | 20          | 20      | 20      | 20      |
|                   | $\geq 250$     | 20   | 20          | 20      | 20      | 20      |
| Unrestrained beam | 125            | 20   | 25          | 30      | NP*     | NP      |
|                   | 175            | 20   | 20          | 20      | 45      | 75      |
|                   | $\geq 250$     | 20   | 20          | 20      | 25      | 45      |

\*Not Permitted

**Table 9. A4** Minimum dimensions and axial distances for simply supported RC beams provided by EN 1992-1-2 (2004) and AS 3600 (2009).

| Fire resistance ratings | Minimum dimensions (mm)                     |     |     |     |
|-------------------------|---|-----|-----|-----|
|                         | Possible combinations of $a$ and $b_{\min}$ |     |     |     |
| R 30                    | $b_{\min} = 80$                             | 120 | 160 | 200 |
|                         | $a = 25$                                    | 20  | 15  | 15  |
| R 60                    | $b_{\min} = 120$                            | 160 | 200 | 300 |
|                         | $a = 40$                                    | 35  | 30  | 25  |
| R 90                    | $b_{\min} = 150$                            | 200 | 300 | 400 |
|                         | $a = 55$                                    | 45  | 40  | 35  |
| R 120                   | $b_{\min} = 200$                            | 240 | 300 | 500 |
|                         | $a = 65$                                    | 60  | 55  | 50  |
| R 180                   | $b_{\min} = 240$                            | 300 | 400 | 600 |
|                         | $a = 80$                                    | 70  | 65  | 60  |
| R 240                   | $b_{\min} = 280$                            | 350 | 500 | 700 |
|                         | $a = 90$                                    | 80  | 75  | 70  |

# CONCLUSIONS AND RECOMMENDATIONS

## 10.1 CONCLUSIONS

### *10.1.1 Conclusions on Bond-Slip Behavior of FRP-to-Concrete Interfaces at Elevated Temperatures*

A set of closed-form analytical solutions for the Mode II debonding behavior of FRP-to-concrete bonded joints subjected to combined thermal and mechanical loadings have been proposed in Chapters 3 and 4. In these theoretical analyses, five different bond-slip models are adopted to represent different bond-slip characteristics of FRP-to-concrete interfaces. Explicit closed-form expressions for the full-range interfacial shear stress, the interfacial slip, the axial stress in the FRP laminates as well as the load-displacement relationship of FRP-to-concrete bonded joints have been derived for each of the five bond-slip models. Based on the results and discussion presented in Chapters 3 and 4 in this dissertation, the following conclusions can be drawn.

- (1) The bond-slip characteristics of the FRP-to-concrete interface have been found to affect the bond stress transfer mechanism and the propagation of debonding when the interface is subjected to combined thermal and mechanical loadings.
- (2) Provided that the material properties are not affected by the temperature variations, a temperature rise leads to an linear increase in the debonding

load of the bonded joint due to the existence of initial thermal stresses at the interface. The exact value of the debonding load increase depends on the stiffness of the FRP plate and the range of temperature variation. For example, when a 2.4 mm thick FRP plate is used, a temperature increase of 50 °C (e.g., from an installation temperature of 20 °C to a high service temperature of 70 °C) leads to approximately a 26% increase in the debonding load.

- (3) If a sufficiently long bond length is provided (i.e., a bond length larger than the effective bond length), the debonding load of an FRP-to-concrete bonded joint depends only on the interfacial fracture energy and the temperature variation but is independent of the shape of bond-slip models.
- (4) The effective bond length increases with a positive temperature variation and the increase rate depends on the bond-slip characteristics. The increase rates of elastic-brittle and elastic-plastic-brittle bond-slip models are much higher than those of the other three bond-slip models (i.e., rigid-softening, bi-linear and exponential models).

Using the proposed analytical solutions, a general approach has been presented to interpret and describe the bond-slip behavior of FRP-to-concrete interfaces at elevated temperatures. Existing shear test data on FRP-to-concrete bonded joints at room and elevated temperatures were collected from the literature and a nonlinear temperature-dependent local bond-slip model for FRP-to-concrete interfaces has been formulated based on a careful analysis of the test data. The two key parameters employed in the bond-slip model, the interfacial fracture energy  $G_f$  and the interfacial brittleness index  $B$ , were determined from regression analysis of existing test data at elevated temperatures. During the interpretation of the test data and the

derivation of  $G_f$  and  $B$ , the influences of both temperature-induced thermal stress and temperature-induced bond degradation were carefully considered. The interfacial fracture energy  $G_f$  has been found to be initially almost constant but start to decrease when the temperature close to the glass transition temperature; the interfacial brittleness index  $B$  also exhibits a similar decreasing trend, but the decrease was almost completed before reaching the glass transition temperature. The proposed temperature-dependent bond-slip model provides a reasonably close representation of the test data upon which it is based, despite the large scatter of the test data.

### ***10.1.2 Conclusions on Advanced FE Modeling of FRP-Strengthened RC Beams***

Advanced FE models have been developed in Chapters 6 and 7 for accurate predictions of the fire performance of conventional RC beams, which are equivalent to un-protected FRP-strengthened RC beams, and insulated FRP-strengthened RC beams, respectively. In these models, rational and reliable constitutive laws are considered for concrete, reinforcing steel, FRP laminate as well as the interfaces of steel-to-concrete and FRP-to-concrete at elevated temperatures. The FE predictions of both the thermal and the mechanical responses of the un-protected and insulated FRP strengthened RC beams are found to be in close agreement with the existing standard fire test results. The following conclusions can be drawn based on the numerical results in these two chapters:

- (1) The bond-slip model of the interface between reinforcing steel and concrete at elevated temperatures that has been considered in the FE model enables more accurate predictions of deflections for RC beams exposed to fire.
- (2) The proposed FE model incorporated into the bond-slip model of FRP-to-concrete interface at elevated temperatures can captured the deflection response of insulated FRP-strengthened RC beams for the entire period of

fire exposure. A perfect bond assumption between FRP and concrete adopted in previous numerical studies has been demonstrated to produce an overestimated fire resistance prediction of an insulated FRP-strengthened RC beam.

- (3) For practical design purposes, the fire resistance of an insulated FRP-strengthened RC beam can be closely and conservatively approximated by that of an insulated RC beam, i.e., the contribution of the FRP strengthening system to the fire resistance can be ignored.
- (4) Numerical results also reveal that, in most cases, the concept of protecting the RC beam rather than the FRP strengthening system leads to a more practical and cost-effective insulation design.

### ***10.1.3 Conclusions on Performance-Based Approach for Predicting the Fire Resistance of FRP-Strengthened RC Beams***

An accurate yet simple method for predicting temperatures in bare and insulated RC beams exposed to a standard fire have been developed in Chapter 8. In this simple method for bare RC beams, the temperature at any point of a beam cross-section is given as a function of its coordinates, the beam width and the fire exposure time. For insulated RC beams, the fire insulation is regarded as an equivalent concrete layer and thus the temperature analysis of an insulated concrete beam becomes that of a bare concrete beam with an enlarged section exposed to fire. The thickness of the equivalent concrete layer is expressed as the function of thickness and thermal properties of the insulation materials. The proposed simple method for bare and insulated RC beams has been validated as the temperature predictions agreed well

with those obtained from FE parametric analyses as well as existing standard fire tests.

Subsequently, Chapter 9 presents a performance-based approach for the fire resistance design of FRP-strengthened RC beams, and it provides a three-level design conception based on a tradeoff between the strength contribution of FRP strengthening system and the required fire resistance rating. For un-protected FRP-strengthened RC beams, extensive FE parametric studies were carried out to investigate the influence of various influencing parameters on the fire resistance of the beams. Based on the FE analytical results, a simple design equation has been developed for the fire resistance assessment. For insulated FRP-strengthened RC beams, the well-known “500 °C isotherm method” has been adopted in combination with the simple method for temperature predictions of insulated beam sections to assess the moment capacity of insulated RC beams under the standard fire exposure. The reliability of the proposed simple method for predicting fire resistance of insulated RC beams has been demonstrated through comparing the fire resistance predictions with the results obtained from the accurate FE parametric studies. It should be noted that the design approaches for both RC beams and insulated FRP-strengthened RC beams are obtained based on the simply supported beams exposed to the standard fire. In real RC structures, the continuous beams exposed to fire are more complicated due to the negative moments at the supporting regions and the moment redistributions between the different spans and the beam-column joints. However, as stated by Kodur and Dwaikat (2011), the simply supported beams were analyzed in this dissertation to achieve a simple and conservative concern.

## **10.2 RECOMMENDATIONS FOR FURTHER RESEARCH**

This dissertation focuses on the performance-based fire resistance design for externally bonded FRP-strengthened RC beams. Further research is required to fully characterize the complicated behavior of FRP composites and FRP strengthened RC members at elevated temperatures as follows:

- (1) Additional tensile tests on FRP sheets and plates at elevated temperatures are required for various FRP composites available in the market to understand their mechanical behavior under fire, since the test data is extremely limited in the existing literature. The additional tests would help to refine the temperature-dependent mechanical models proposed for FRP laminates [e.g., Eqs. (5.16) and (7.1)] for different types of FRP laminates.
- (2) Existing test results on the bond performance of FRP-to-concrete interfaces at elevated temperatures were mainly related to the externally bonded FRP reinforcement. More tests and analyses are needed to investigate the bond performance of near-surface mounted (NSM) reinforcement at elevated temperatures.
- (3) Only Palmieri et al. (2012) and Burke et al. (2013) conducted fire endurance tests on insulated concrete beams strengthened with NSM FRP reinforcement. Besides, only Ahmed and Kodur (2011) carried out fire tests on externally bonded FRP-strengthened RC beams to investigate the effects of fire scenarios (i.e., standard fire and parametric fire), anchorage schemes, and restraint conditions. Further full-scale fire tests on FRP-strengthened RC beams are recommended to investigate the effects of different strengthening systems, different anchorage schemes, different types of fire exposure and restraint conditions, etc.
- (4) The phenomena of moisture migration and evaporation in concrete and insulation materials, which were widely witnessed by the measured

temperature data in existing fire tests, should be incorporated into the heat transfer analysis to improve the accuracy of temperature predictions, particularly at the early stages of fire exposure.

- (5) While much emphasis of existing fire tests in the literature were placed on the behavior of FRP-strengthened RC beams during fire, an important issue to be further studied is the post-fire residual strength of FRP-strengthened RC members. A good understanding on the post-fire residual strength of FRP-strengthened RC members is useful for the damage assessment and the subsequent proposal of remedy actions on FRP-strengthened RC members after fire exposure.

### 10.3 REFERENCES

- Ahmed, A., and Kodur, V. (2011). "The experimental behavior of FRP-strengthened RC beams subjected to design fire exposure." *Engineering Structures*, Vol. 33, No. 7, pp. 2201-2211.
- Burke, P.J., Bisby, L.A., and Green, M.F. (2013). "Effects of elevated temperature on near surface mounted and externally bonded FRP strengthening systems for concrete." *Cement and Concrete Composites*, Vol. 35, No. 1, pp. 190-199.
- Kodur, V.K.R. and Dwaikat, M.B. (2011). "Design equation for predicting fire resistance of reinforced concrete beams." *Engineering Structures*, Vol. 33, No. 2, pp. 602-614.
- Palmieri, A., Matthys, S., and Taerwe, L. (2012). "Experimental investigation on fire endurance of insulated concrete beams strengthened with near surface mounted FRP bar reinforcement." *Composites Part B: Engineering*, Vol. 43, No. 3, pp. 885-895.